THE PHYSICS AND CHEMISTRY OF SOLIDS

AN INTERNATIONAL JOURNAL

VOLUME 20 1961

EDITORS

Editor-in-Chief HARVEY BROOKS *Cambridge, Mass.*

Associate Editors H. B. G. CASIMIR *Eindhoven*; G. J. DIENES *Brookhaven*; JACQUES FRIEDEL *Paris*

E. M. LIFSHITZ *Moscow*

Supported by an International Advisory Editorial Board

Vol. 20
1961

Copyright © 1962
Pergamon

PERGAMON PRESS

NEW YORK · LONDON · PARIS · LOS ANGELES

THE JOURNAL OF THE PHYSICS AND CHEMISTRY OF SOLIDS

Editors

PROF. HARVEY BROOKS (*Editor-in-Chief*), 217 *Pierce Hall, Harvard University, Cambridge* 38, *Mass. U.S.A.*

PROF. Dr. H. B. G. CASIMIR, *N.V. Philips' Gloeilampenfabrieken, Eindhoven, The Netherlands*

DR. G. J. DIENES, *Brookhaven National Laboratory, Upton, Long Island, New York, U.S.A.*

PROF. JACQUES FRIEDEL, *Service de Physique des Solides, Faculte des Sciences (Group II), B.P. No.* 11, *Orsay (S. & O.) France*

PROF. E. M. LIFSHITZ, *Institute for Physical Problems, Vorobievskoye Chaussee,* 2, *Moscow, V-*334, *U.S.S.R.*

Editorial Advisory Board

U.S.A.

E. N. ADAMS, Pittsburgh
D. ALPERT, Illinois
L. APKER, Schenectady
J. BARDEEN, Illinois
D. S. BILLINGTON, Oak Ridge
R. G. BRECKENRIDGE, Cleveland
LEO BREWER, Berkeley, Calif.
E. BURSTEIN, Penn.
J. A. BURTON, New Jersey
N. CABRERA, Virginia
G. C. DANIELSON, Iowa
J. C. FISHER, Schenectady
F. HERMAN, Princeton
CONYERS HERRING, New Jersey
A. R. VON HIPPEL, Cambridge, Mass.
J. H. HOLLOMON, Schenectady
W. V. HOUSTON, Houston
H. B. HUNTINGTON, Troy
H. M. JAMES, Purdue
C. KITTEL, Berkeley, Calif.
W. KOHN, La Jolla, Calif.
J. A. KRUMHANSL, Ithaca
A. W. LAWSON, Riverside, Calif.
H. W. LEVERENZ, Princeton
O. T. MARZKE, Pittsburgh
B. T. MATTHIAS, New Jersey
L. R. MAXWELL, Silver Spring
JOSEPH E. MAYER, La Jolla, Calif.
J. W. MITCHELL, Charlottesville
E. W. MONTROLL, Maryland
DAVID PINES, Princeton
GEORGE T. RADO, Washington, D.C.
H. REISS, Canoga Park, Calif.
J. R. REITZ, Cleveland
A. ROSE, Princeton
R. SMOLUCHOWSKI, Princeton
F. H. SPEDDING, Iowa
D. TURNBULL, Schenectady
J. H. VAN VLECK, Cambridge, Mass.
B. E. WARREN, Cambridge, Mass.
EUGENE P. WIGNER, Princeton
B. H. ZIMM, La Jolla, Calif.

Canada

R. E. BURGESS, Vancouver
D. K. C. MACDONALD, Ottawa
W. B. PEARSON, Ottawa

United Kingdom

A. CHARLESBY, Shrivenham, Berks.
W. J. DUNNING, Bristol
I. ESTERMANN, London
F. C. FRANK, Bristol
H. K. HENISCH, Reading
H. JONES, London
A. B. PIPPARD, Cambridge
M. H. L. PRYCE, Bristol
O. C. SIMPSON, Baldock
R. A. SMITH, Sheffield
K. W. H. STEVENS, Nottingham
F. C. TOMKINS, London

France

E. F. BERTAUT, Grenoble
A. GUINIER, Orsay
LOUIS NÉEL, Grenoble
LOUIS WEIL, Grenoble

Germany

M. BORN, Bad Pyrmont
ULRICH DEHLINGER, Stuttgart
R. HILSCH, Göttingen
G. LEIBFRIED, Aachen
E. MOLLWO, Erlangen
H. PICK, Stuttgart
H. WELKER, Erlangen

Italy

F. G. FUMI, Pavia

Czechoslovakia

J. TAUC, Praha

Japan

TOSHINOSUKE MUTO, Tokyo

The Netherlands

A. MICHELS, Amsterdam
G. W. RATHENAU, Amsterdam

Sweden

J. O. LINDE, Stockholm
PER-OLOV LÖWDIN, Uppsala

Switzerland

G. BUSCH, Zurich
P. SCHERRER, Zurich

U.S.S.R.

G. S. ZHDANOV, Moscow

Publishing Offices

American Continent: Pergamon Press, Inc., 122 *East* 55*th Street, New York* 22, *N.Y.*

Rest of the World: Pergamon Press Ltd., Headington Hill Hall, Oxford.

Issued in parts. Annual Subscription: (A) for Libraries, £35 (*U.S.A.* $100.00); (*B*) *for subscribers who write directly to the publisher certifying that the subscription is for their own personal use,* £5 5*s.* (*U.S.A.* $15.00) *including postage.*

Surcharge for airmail subscriptions:

U.S.A. and South America	$28.00 (£10) per annum
Far East	$40.00 (£14) per annum
European countries	£5 ($14.00) per annum

Copyright © 1962 Pergamon Press Ltd.

PERGAMON PRESS, INC.

121 EAST 55TH STREET, NEW YORK 22, N.Y. 4 & 5 FITZROY SQUARE, LONDON W.1

CONTENTS LISTS FOR VOLUME 20, NOS. 1–4

Volume 20 Numbers 1/2

page

N. G. Bäcklund: An experimental investigation of the electrical and thermal conductivity of iron and some dilute iron alloys at temperatures above 100°K . . . 1
R. Kikuchi: Statistical dynamics of crystalline diffusion—II. Vacancy mechanism . . . 17
R. Kikuchi: Statistical dynamics of crystalline diffusion—III. Self-diffusion in an order–disorder system . 35
J. S. Smart: Magnetic short-range order and specific heat in ferromagnets and antiferromagnets . . 41
G. Leman: Sur la structure électronique des impuretés métalliques dans l'approximation des liaisons fortes . 50
F. Bassani and V. Celli: Energy-band structure of solids from a perturbation on the "empty lattice" . 64
H. B. Huntington and A. R. Grone: Current-induced marker motion in gold wires . . . 76
A. R. Grone: Current-induced marker motion in copper . . . 88
J. W. Cahn and R. Kikuchi: Theory of domain walls in ordered structures—I. Properties at absolute zero 94
V. Garino-Canina: Quelques propriétés physiques dépendant de défauts de structure dans l'oxyde de germanium pur et vitreux . . . 110
P. Koenig, D. W. Lynch and G. C. Danielson: Infrared absorption in magnesium silicide and magnesium germanide . . . 122
M. B. Webb: Knight shifts and quadrupole effects in Al alloys . . . 127
W. E. Spicer: The problem of exciton induced photoemission from CdS . . . 134
M. Balarin und F. Hilbert: Die Einwirkung energiereicher Ionen auf Metalloberflächen . . . 138
J. C. Thompson and B. A. Younglove: Thermal conductivity of silicon at low temperatures . . . 146
D. T. Keating and S. Krasner: Mechanical and radiation induced faulting in sodium azide . . . 150

Letters to the Editor:

A. Corciovei: The effect of magnetic anisotropy in cobalt ferromagnetic thin films . . . 162
R. P. Chasmar: Electron mobility in indium arsenide . . . 164
L. Červinka, S. Krupička and V. Syneček: To the existence of tetragonally distorted $Mn^{3+}O_6^{2-}$ octahedra in cubic $MnFe_2O_4$ . . . 167
G. E. Smith: The effective mass of holes in bismuth . . . 168
C. H. Neuman, D. Lazarus and D. B. Fitchen: Enhanced nonequilibrium diffusion in plastically deformed AgZn . . . 170

Volume 20 Numbers 3/4

F. Lappe: The energy of electron–hole pair formation by X-rays in PbO . . . 173
R. R. Hake, D. H. Leslie and T. G. Berlincourt: Electrical resistivity, Hall effect and superconductivity of some b.c.c. titanium–molybdenum alloys . . . 177
R. Blinc, S. Detoni, I. Levstek, M. Pintar, S. Poberaj and M. Schara: Electron spin resonance of irradiated ferroelectric tri-glycine sulfate . . . 187
J. Tauc and A. Abrahám: Optical investigation of the band structure of Ge–Si alloys . . . 190
K. V. Rao: On the dielectric loss and thermal bleaching of calcite irradiated by X-rays . . . 193
C. Haas and M. M. G. Corbey: Measurement and analysis of the infrared reflection spectrum of semiconducting SnS . . . 197
A. Lawley and R. W. Cahn: A high temperature X-ray study of ordering in iron–aluminium alloys . . . 204
A. J. W. Moore and J. F. Nicholas: Atomic configurations in ideally flat surfaces—I. Construction of models of surfaces in face-centred and body-centred cubic crystals . . . 222
J. F. Nicholas: Atomic configurations in ideally flat surfaces—II. Description of surface for an arbitrary crystal structure . . . 230
H. Meyer: The susceptibility of NO in β-quinol clathrates . . . 238
J. H. van Vleck: Theory of the magnetic susceptibility of the nitric oxide clathrate . . . 241
D. B. Medved: Photoconductivity and chemisorption kinetics in sintered zinc oxide semiconductor . . . 255
P. Manca: A relation between the binding energy and the band-gap energy in semiconductors of diamond and zinc-blende structure . . . 268
M. Green and K. H. Maxwell: The adsorption of chlorine on clean germanium surfaces . . . 274
B. W. Levinger and D. R. Frankl: Cyclotron resonance measurements of the energy band parameters of germanium . . . 281
A. Houghton: Specific heat and spin susceptibility of dilute alloys . . . 289

page

F. E. KARASZ and J. A. POPLE: A theory of fusion of molecular crystals—II. Phase diagrams and relations with solid state transitions 294
M. NACHMAN, I. MAXIM and T. BRAUN: Radiation induced chemisorption of oxygen on chromia 307

Letters to the Editor:

S. H. CHARAP: Concerning the theory of anisotropic magnetization 315
D. G. WICKHAM, N. MENYUK and K. DWIGHT: Evidence for canted magnetic moments in manganous stannate (Mn_2SnO_4) 316
J. W. CORBETT and G. D. WATKINS: Stress-induced alignment of anisotropic defects in crystals . . . 319

Book Reviews:

H. C. GATOS (with J. W. FAUST, Jr. and W. J. LAFLEUR): "The Surface Chemistry of Metals and Semiconductors" (reviewed by Gert Ehrlich) 321
J. R. O'CONNOR and J. SMILTENS (Editors): "Silicon Carbide—A High Temperature Semiconductor" (reviewed by D. Warschauer) 322

Errata:

L. GILDART, J. M. KLINE and D. M. MATTOX: Some semiconducting properties of bismuth trisulphide . 324
E. DANIEL: Sur la résistivité et le displacement de Knight d'alliages liquides de sodium 324

Tôme 20 Nos 1/2

N. G. BÄCKLUND: Etude expérimentale de la conductibilité électrique et thermique du fer et de quelques alliages dilués de fer à des températures supérieures à 100°K. 1
R. KIKUCHI: Dynamique statistique de la diffusion dans les cristaux—II. Mécanisme pour les lacunes . . 17
R. KIKUCHI: Dynamique statistique de la diffusion cristalline—III Auto-diffusion dans un système ordre-désordre 35
J. S. SMART: Ordre magnétique à courte distance et chaleur spécifique dans les ferromagnétiques et les antiferromagnétiques 41
G. LEMAN: Sur la structure électronique des imputetés métalliques dans l'approximation des liaisons fortes . 50
F. BASSANI et V. CELLI: Structure de bandes dans les solides par perturbation du "reseau vide." . . . 64
H. B. HUNTINGTON et A. R. GRONE: Déplacement dû au courant de repères dans des fils d'or . . . 76
A. R. GRONE: Déplacement induit par le courant de repères dans le cuivre 88
J. W. CAHN et R. KIKUCHI: Théorie des parois de domaines dans les structures ordonnées I—Propriétés au zéro absolu 94
V. GARINO-CANINA: Quelques propriétés physiques dépendant de défauts de structure dans l'oxyde de germanium pur et vitreux 110
P. KOENIG, D. W. LYNCH et G. C. DANIELSON: Absorption infra-rouge dans le siliciure et le germaniure de magnésium 122
M. B. WEBB: Déplacement de Knight et effets quadrupolaires dans les alliages d'aluminium 127
W. E. SPICER: Le problème de la photoémission induite dans CdS par les excitons 134
M. BALARIN und F. HILBERT: Les effets d'ions riches en énergie sur des surfaces métalliques 138
J. C. THOMPSON et B. A. YOUNGLOVE: Conductibilité thermique du Silicium à basse température . . 146
D. T. KEATING et S. KRASNER: Fautes d'empilement induites mécaniquement et par irradiation dans le nitrure de sodium 150

Lettres au Rédacteur:

A. CORCIOVEI: L'effet de l'anisotropie magnétique dans les films minces de cobalt ferromagnétique . . 162
R. P. CHASMAR: Mobilité électrique dans l'arseniure d'indium 164
L. ČERVINKA, S. KRUPIČKA et V. SYNEČEK: L'existence d'une distorsion tétragonale des octaèdres $Mn^{3+}O_6^{2-}$ dans $MnFe_2O_4$ cubique 167
G. E. SMITH: La masse effective des trous dans le Bismuth 168
C. H. NEUMAN, D. LAZARUS et D. B. FITCHEN: Augmentation de la diffusion hors de l'équilibre dans Ag Zn plastiquement déformé. 170

Tôme 20 Nos 3/4

F. LAPPE: L'énergie de formation par rayonnement X de paires électron-trou dans PbO 173
R. R. HAKE, D. H. LESLIE et T. G. BERLINCOURT: Résistivité électrique, effet Hall et supraconductivité de quelques alliages Titane-Molybdène cubiques centrés 177
R. BLINC, S. DETONI, I. LEVSTEK, M. PINTAR, S. POBERAJ et M. SCHARA: Résonance de spin électronique dans le sulfate de triglycine ferroélectrique irradié 187

Vol. 2
196

page

J. Tauc et A. Abrahám: Recherches optiques sur la structure de bande des alliages Ge–Si. 190
K. V. Rao: Perte diélectrique et blanchiment thermique de la calcite irradiée aux rayons X 193
C. Haas et M. M. G. Corbey: Mesure et analyse du spectre de réflexion infra-rouge de SnS semi-conducteur 197
A. Lawley et R. W. Cahn: Etude aux rayons X à haute température de l'ordre dans les alliages Fer-Aluminium 204
A. J. W. Moore et J. F. Nicholas: Configurations atomiques dans les surfaces idéalement planes—I. Construction de modèles de surfaces dans les cristaux cubiques centrés et cubiques faces centrées . . 222
J. F. Nicholas: Configurations atomiques dans les surfaces idéalement planes—II. Description de la surface pour une structure cristalline arbitraire 230
H. Meyer: Susceptibilité de NO dans les clathrates β quinol 238
J. H. van Vleck: Théorie de la susceptibilité magnétique du clathrate de l'oxyde nitrique 241
D. B. Medved: Cinétique de la photoconductivité et de l'adsorption chimique dans l'oxyde de zinc fritté semi-conducteur 255
P. Manca: Une relation entre l'énergie de liaison et la largeur de bande interdite pour les semi-conducteurs de la structure du diamant et de la blende 268
M. Green et K. H. Maxwell: L'adsorption du chlore par des surfaces propres de germanium . . . 274
B. W. Levinger et D. R. Frankl: Mesures par résonance cyclotron des paramètres des bandes d'énergie du germanium 281
A. Houghton: Chaleur spécifique et susceptibilité de spin dans les alliages dilués 289
F. E. Karasz et J. A. Pople: Une théorie de la fusion des cristaux moléculaires—II. Diagrammes de phases et transitions à l'état solide 294
M. Nachman, I. Maxim et T. Braun: Adsorption chimique induite par radiation de l'oxygène dans Cr_2–O_3 . 307

Lettres au Rédacteur:

S. H. Charap: Sur la théorie de l'aimantation anisotrope 315
D. G. Wickham, N. Menyuk et K. Dwight: Preuve de l'existence de moments magnétiques formant un angle dans le manganate stanneux 316
J. W. Corbett et G. D. Watkins: Alignement par contrainte de défauts anisotropes dans les cristaux . . 319

Revue des Livres:

H. C. Gatos (avec J. W. Faust, Jr. et W. J. LaFleur): "The Surface Chemistry of Metals and Semiconductors" (revu par Gert Ehrlich) 321
J. R. O'Connor et J. Smittens (Éditeurs) "Silicon Carbide—A High Temperature Semiconductor" (revu par D. Warschauer) 322

Errata:

L. Gildart, J. M. Kline et D. M. Mattox: Quelques propriétés du trisulfure de bismuth semi-conducteur 324
E. Daniel: Sur la résistivité et le déplacement de Knight d'alliages liquides de sodium 324

Band 20 Nr. 1/2

N. G. Bäcklund: Eine experimentelle Untersuchung der elektrischen und thermischen Leitfähigkeit des Eisens und einiger verdünnter Eisenlegierungen oberhalb von 100°K 1
R. Kikuchi: Statistische Dynamik der Diffusion in Kristallen—II. Der Leerstellenmechanismus . . 17
R. Kikuchi: Statistische Dynamik der Diffusion in Kristallen—III. Selbstdiffusion in einem teilweise geordneten System 35
J. S. Smart: Magnetische Nahordnung und spezifische Wärme in ferromagnetischen und antiferromagnetichen Stoffen 41
G. Leman: Über die Elektronenstruktur metallischer Veruneinigungen in der Näherung starker Bindungen . 50
F. Bassani und V. Cetti: Bestimmung der Energiebandtruktur von Festkörpern durch eine Störung des "leeren Gitters" 64
H. B. Huntington und A. R. Grone: Sichtbare durch Ströme hervorgerufene Bewegung in Golddrähten . 76
A. B. Grone: Sichtbare durch Ströme hervorgerufene Bewegung in Kupfer 88
J. W. Cahn und R. Kikuchi: Die Theorie der Domänenwände in geordneten Strukturen—I. Eigenschaften am absoluten Nullpunkt 94
V. Garino-Canina: Einige von Strukturfehlern abhängige physikalische Eigenschaften des reinen, glasartigen Germaniumoxyds 110
P. Koenig, D. W. Lynch und G. C. Danielson: Infrarote Absorption in Magnesiumsilizid und Magnesiumgermanid 122
M. B. Webb: Knightverschiebungen und Quadrupoleffekte in Al-Legierungen 127
W. E. Spicer: Das Problem der durch Exzitonen induzierten Photoemission von CdS 134

Vol. 20
1961

page

M. Balarin und F. Hilbert: Die Einwirkung energiereicher Ionen auf Metalloberflächen 138
J. C. Thompson und B. A. Younglove: Die Wärmeleitfähigkeit von Silizium bei tiefen Temperaturen . . 146
D. T. Keating und S. Krasner: Durch Verformung und Bestrahlung hervorgerufene Stapelfehler in Natriumazit 150

Briefe an der Herausgebar:

A. Corciovei: Der Einfluss der magnetischen Anisotropie in dünnen ferromagnetischen Kobaltfilmen . 162
R. P. Chasmar: Die Elektronenbeweglichkeit in Indiumarsenid 164
L. Červinka, S. Krupička und V. Syneček: Die Existenz tetragonal verzerrter $Mu^{3+}O_6^{2-}$-Oktaeder in kubischem $MnFe_2O_4$ 167
G. E. Smith: Die effektive Masse von Löchern in Wismut 168
C. H. Neuman, D. Lazarus und D. B. Fitchen: Die Beschleunigung der Diffusion im Nichtgleichgewicht bei plastisch verformtem AgZn 170

Band 20 Nr. 3/4

F. Lappe: Die Bildungsenergie von durch Röntgenstrahlen erzeugten Elektron–Loch Paaren in PbO . . 173
R. R. Hake, D. H. Leslie und T. G. Berlincourt: Elektrischer Widerstand, Halleffekt und Supraleitung in einigen kubisch-raumzentrierten Titan–Molybdan–Legierungen 177
R. Blinc, S. Detoni, I. Levstek, M. Pintar, S. Poberaj und M. Schara: Elektronspinresonanz von bestrahltem, ferroelektrischem Triglyzinsulfat 187
J. Tauc und A. Abrahám: Optische Untersuchung der Bandstruktur von Ge–Si–Legierungen 190
K. V. Rao: Über dielektrische Verluste und das thermische Entfärben von mit Röntgenstrahlen bestrahltem Kalzit 193
C. Haas und M. M. G. Corbey: Messung und Analyse des infraroten Reflexionsspektrums von halbleitendem SnS. 197
A. Lawley und R. W. Cahn: Eine Untersuchung der Ordnungseinstellung in Eisen–Aluminium–Legierungen bei hohen Temperaturen mit Röntgenstrahlen 204
A. J. W. Moore und J. F. Nicholas: Atomkonfigurationen in ideal ebenen Oberflächen—I. Zur Konstruktion von Modelloberflächen in flächen-raumzentrierten kubischen Kristallen 222
J. F. Nicholas: Atomkonfigurationen in ideal ebenen Oberflächen—II. Beschreibung von Oberflächen bei einer beliebigen Kristallstruktur 230
H. Meyer: Die Suszeptibilität von NO in β-Quinol-Chlathraten 238
J. H. van Vleck: Theorie der magnetischen Suszeptibilität der Stichoxyd-Chlathrate 241
D. B. Medved: Photoleitfähigkeit und Kinetik der Chemisorption in gesintertem und halbleitendem Zinkoxyd 255
P. Manca: Eine Beziehung zwischen der Bindungsenergie und der Bandenergielücke in Halbleitern der Diamant und Zinkblendestruktur 268
M. Green und K. H. Maxwell: Die Adsorption von Chlor an reinen Germaniumoberflächen 274
B. W. Levinger und D. R. Frankl: Messungen der Energiebandparameter des Germaniums mit der Zyklotronresonanz 281
A. Houghton: Spezifische Wärme und Spinsuszeptibilität verdünnter Legierungen 289
F. E. Karasz und J. A. Pople: Eine Theorie zur Bildung von Molekülkristallen —II. Phasendiagramme und Beziehungen zu den Umwandlungen im festen Zustand 294
M. Nachman, I. Maxim und T. Braun: Durch Bestrahlung induzierte Chemisorption des Sauerstoffs auf Chromoxyd 307

Briefe an der Herausgeber:

S. H. Charap: Zur Theorie der anisotropen Magnetisierung 315
D. G. Wickham, N. Menyuk und K. Dwight: Hinweise auf antiparallele magnetische Momente in Manganstannat (Mn_2SnO_4) 316
J. W. Corbett und G. D. Watkins: Ordnungseinstellung bei anisotropen Fehlstellen in Kristallen unter dem Einfluss einer Spannung 319

Buchbesprechungen:

H. C. Gatos (mit J. W. Faust und W. J. LaFleur): "The Surface Chemistry of Metals and Semiconductors" (besprochen von G. Ehrlich) 321
J. R. O'Connor und J. Smiltens (Herausgebern): "Silicon Carbide—A. High Temperature Semiconductor" (besprochen von D. Warschauer) 322

Errata:

L. Gildart, J. M. Kline und D. M. Mattox: Einige Halbleitereigenschaften von Wismuttrisulfid . . 324
E. Daniel: Über den spezifischen Widerstand und über die Verschiebung der flussigen Natriumlegierungen nach der Methode Knight 324

Vol. 2
196

Том 20 На. 1/2

page

Н. Г. Беклунд: Экспериментальное исследование электрической и тепловой проводимости железе и некоторых разбавленных сплавов железа при температурах выше 100°K 1
Р. Кикучи: Статистическая динамика диффузии в кристаллах. II. Механизм вакансий 17
Р. Кикучи: Статистическая динамика диффузии в кристаллах. III. Самодиффузия в упорядоченной системе 35
Дж. С. Смарт: Магнитный ближний порядок и теплоемкость ферромагнетиков и антиферромагнетиков 41
Г. Леман: обэлектронной структуре металлических примесей в приближении силрной связи . . . 50
Ф. Бассани, В. Челли: Структура энергетических полос в твердых тедах согласно теории "пустой решетки" 64
Г. Б. Хантингтон, А. Р. Грон: Движение маркеров в золотых проволоках, индуцированное током. . 76
А. Р. Грон: Движение маркеров в меди, индуцированное током 88
Дж. В. Кан, Р. Кикучи: Теория доменных стенок в уиорядоченных структурах–I. Свойства при абсолютном нуле 94
В. Г. Ганина: Некоторые физические свойства окиси германия, Зависщие от дефектов структуры . . 110
П. Кениг, Д. В. Линч, Г. Даниельсон: Инфракрасное поглощение в силициде магния и в германиде магния 122
М. Б. Вебб: Найтовское смещение и квадрупольные эффекты в сплавах алюминия 127
В. Е. Спайсер: Проблема экситонной индуцированной фотоэмиссии CdS 134
М. Баларин, Ф. Гильберт: Влияние энергичных ионов на металлическую поверхность 138
Дж. Томпсон, В. А. Юнглав: Теплопроводность кремния при низких температурах 146
Д. Т. Китинг, С. Краснер: Дефекты в азиде натрия, индуцированные механиуескими и радиационными воздействиями 150

Письмо в Редакцию:

А. Корчовей: Эффект магнитной анизотропии в ферромагнитных тонких пленках кобальта . . 162
Р. П. Часмар: Электронная подвижность в арсенидеиндия 164
Л. Червинка, С. Крупичка, В. Синичек: О существовании тетрагонально деформированных октаэдров $Mn^{3+}O_6^{2-}$ в кубическом $MnFe_2O_4$ 167
Г. Е. Смит: Эффективная масса дырок в висмуте 168
К. Нейман, Д. Лазарус, Д. Б. Флитчен: Усиление неравновесной диффузии в пластически деформированном AgZn 170

Vol. 20
1961

Том 20 На. 3/4

Ф. Лаппе: Энергия образования электронно-дырочных пар X-лучами в PbO 173
Р. Р. Хейк, Д. Лесли, Т. Берлинкур: Электрическое сопотивление, эффект Холла и сверхпроводимость некоторых об емноцентрированных сплавов титана и молибдена 177
Р. Блинк, С. Детони, И. Левстек, М. Пинтар, С. Побераж, М. Шара: Электронный спиновый резонанс в облученном ферроэлектрическом триглицин-сульфате 187
Дж. Таук, А. Абрагам: Оптическое исследование зонной структуры сплавов Ge–Si 190
К. В. Рао: Диэлектрические потери и тепловое обесцвечивание кальцита, облученного X-лучами. . 193
К. Хааз, М. Корбей: Измерение и анализ спектра инфракрасного поглощения полупроводящего SnS . 197
А. Лоулей, Р. Кан: Рентгеновское исследование упорядочения в сплавах железа и алюминия при высоких температурах 204
А. Мур, Дж. Ф. Николас: Атомная конфигурация идеально плоских поверхностей. I. Конструкция моделей поверхности в гранеи обчемно-центрированных кубических кристаллах 222
Д. Ф. Николас: Атомная конфигурация идеально плоских поверхностей. п. Описание поверхности при произвольной кристаллической структуре 230
Г. Мейер: Восприимчивость NO в β-хинол-клатратах 238
Дж. Г. ван Флек: Теория магнитной восприимчивости NO -клатрата 241
Д. Б. Медвед: Фотопроводимость и кинетика хемисорбции спеченного полупроворолящего ZnO . . 255
П. Манка: Соотношение между энергией связи и энергетической щелью в полупроводниках со структурой типа алмаза и цинковой обманки 268
М. Грин, К. Максвелл: Адсорбция хлора на чистой поверхности германия 274
Б. В. Левинджер, Д. Р. Франкль: Измерение параметров энергетических зон в германии методом циклотронного резонанса 281
А. Хоутон: Теплоемкость и спиновая восприимчвость разведенных сплавов 289
Ф. Е. Караз, Дж. А. Попл: Теория плавления молекулярных кристаллов. II. Фазовая диаграмма и взаимоотношения с переходами в твердом состоянии 294
М. Нахман, И. Максим, Т. Браун: Хемисорбция кислорода на хроме, индуцированная облучением . 307

Письмо в Ре дакцию: page

С. Чарап: К теории анизотропного намагничивания 315
Д. Викхам, Н. Мениук, К. Двайт: Свидетельство о наклонных магнитых моментах в (Mn_2SnO_4) . 316
Дж. В. Корбетт, Г. Д. Уоткинс: Ориентация под влияием напряжений анизотропных дефектов в кристаллах 319

Рецензия на книги:

С. Гатос, В. Фауст, В. ЛаФлэр: "The Surface Chemistry of Metals and Semiconductors" (рецензнт Герт Эрлих) 321
Р. О Коннер, Дж. Смилтзнс (редактори): "Silicon Carbide—A High Temperature Semiconductor" (рецснзент Д. Варщаузр) 322

Опеуатка:

Л. Гилдарт, Дж. Клин, Д. М. Маттокс: Некоторвые полупроводниковые свйства трисульфида висмута 324
Е. Данисль: О сопротивлении и смещении найта в жидких сплавах натрия. 324

AUTHOR INDEX TO VOLUME 20

(B) denotes book review (E) denotes erratum

Abrahám, A. 190

Bäcklund, N. G. 1
Balarin, M. 138
Bassani, F. 64
Berlincourt, T. G. 177
Blinc, R. 187
Braun, T. 307

Cahn, J. W. 94
Cahn, R. W. 204
Celli, V. 64
Červinka, L. 167
Charap, S. H. 315
Chasmar, R. P. 164
Corbett, J. W. 319
Corbey, M. M. G. 197
Corciovei, A. 162

Daniel, E. 324 (E)
Danielson, G. C. 122
Detoni, S. 187
Dwight, K. 316

Ehrlich, G. 321 (B)

Fitchen, D. B. 170
Frankl, D. R. 281

Garino-Canina, V. 110
Gildart, L. 324 (E)
Green, M. 274
Grone, A. R. 76, 88

Haas, C. 197
Hake, R. R. 177
Hilbert, F. 138
Houghton, A. 289
Huntington, H. B. 76

Karasz, F. E. 294
Keating, D. T. 150
Kikuchi, R. 17, 35, 94
Kline, J. M. 324 (E)
Koenig, P. 122
Krasner, S. 150
Krupička, S. 167

Lappe, F. 173
Lawley, A. 204
Lazarus, D. 170
Leman, G. 50
Leslie, D. H. 177
Levinger, B. W. 281
Levstek, I. 187
Lynch, D. W. 122

Manca, P. 268
Mattox, D. M. 324 (E)
Maxim, I. 307
Maxwell, K. H. 274
Medved, D. B. 255
Menyuk, N. 316
Meyer, H. 238
Moore, A. J. W. 222

Nachman, M. 307
Neuman, C. H. 170
Nicholas, J. F. 220, 230

Pintar, M. 187
Poberaj, S. 187
Pople, J. A. 294

Rao, K. V. 193

Schara, M. 187
Smart, J. S. 41
Smith, G. E. 168
Spicer, W. E. 134
Syneček, V. 167

Tauc, J. 190
Thompson, J. C. 146

Warschauer, D. 322 (B)
Watkins, G. D. 319
Webb, M. B. 127
Wickham, D. G. 316

Younglove, B. A. 146

Van Vleck, J. H. 241

BACK NUMBERS OF PREVIOUS VOLUMES AVAILABLE

Vol. 2
196

J. Phys. Chem. Solids Pergamon Press 1961. Vol. 20, Nos. 1/2, pp. 1–16. Printed in Great Britain.

AN EXPERIMENTAL INVESTIGATION OF THE ELECTRICAL AND THERMAL CONDUCTIVITY OF IRON AND SOME DILUTE IRON ALLOYS AT TEMPERATURES ABOVE 100°K

N. G. BÄCKLUND

Physics Dept., Royal Institute of Technology, Stockholm 70, Sweden.

(*Received* 15 *September* 1960)

Abstract—Conductivity measurements have been performed at 90–300°K on iron of high purity and dilute alloys of this metal with Mn, Ni or Si. For the elimination of the parasitic thermal losses in the heat-conductivity measurements a special method has been worked out. The validity of the Wiedemann–Franz–Lorenz law (W–F–L law) for the investigated substances is examined. This analysis is extended to about 1300°K by use of conductivity values for iron and steels given in the literature. It is found that the part of the heat-resistivity of the electrons caused by lattice vibrations is fairly independent of temperature, in accordance with a previous statement by LINDE for non-transition metals. A modified form of the W–F–L law, written $K_e(\rho+\tilde{\rho}_0) = LT$, is put forward, and it is shown that this is generally valid for transition as well as non-transition metals at temperatures above the T^5-region of ρ. The constant $\tilde{\rho}_0$ of the suggested formula can be obtained from electrical measurements. If expressed as $K_g = K-K_e$, the lattice conductivity of iron shows an anomalous change at the Curie point, being much larger in the state of spontaneous magnetization than in the paramagnetic state. The spin-disorder part of the electrical resistivity is found to be proportional to T^3 in the temperature range < 1000°K. Some abnormal behaviour of the residual resistivity of iron when measured on wires of varying diameters is discussed. The general results of the investigation concerning ρ, K_e and K_g are given in the form of graphs of conductivity and resistivity-quantities as functions of temperature.

1. INTRODUCTION

WHILE the transport properties of commercial steels have been extensively investigated, there is remarkable lack of systematic research on the theoretically more interesting dilute iron alloys. YENSEN's[1] electrical resistivity measurements on binary iron alloys concerned only values at room temperature. Even the measurements on pure iron are scanty, especially those of the thermal conductivity.

A fairly complete collection of existing thermal conductivity data for iron and commercial steels at normal and low temperatures is included in a review by POWELL and BLANPIED[2]. To these some later measurements have to be added.[3,4,5] The properties of commercial steels at elevated temperatures have been investigated and surveyed by—among others—POWELL[6,7,8]. PALLISTER[9] has brought together his own and other investigators' values of the electrical resistivity of iron above the ice point. Finally, CLEAVES' and THOMPSON's[10] survey of iron data should be mentioned. Their exhaustive tables of electrical resistivity measurements illustrate the relativity of the concept "pure annealed iron".

An interesting result of these earlier measurements is that the thermal conductivities for steels seem to converge towards a fairly low value at about 900°C. In the low temperature region the thermal conductivity of iron shows the usual maximum, which, however, is remarkably small compared with that of most other pure metals. The electrical resistivity curve shows, as do those of other ferromagnetic metals, a knee at the Curie point.

Regarding the question of the validity of the

Wiedemann–Franz–Lorenz law for iron and iron alloys, the results given in the literature are rather confusing. The following investigation is an attempt to obtain more reliable information on this problem, but it also offers the possibility of studying the behaviour of the lattice conductivity at temperatures above 100°K. Unfortunately, the theories of the lattice conductivity, exhaustively surveyed by KLEMENS[11,12], do not pay any attention to the ferromagnetic state.

The Wiedemann–Franz–Lorenz law in the case of normal metals

This law (in the following denoted W–F–L law) connects the electrical resistivity ρ and the electronic part K_e of the heat conductivity of metals by the relation

$$\frac{K_e\rho}{T} = L \tag{1}$$

where T is absolute temperature and L the Lorenz constant.

Using the Matthiessen relation

$$\rho = \rho_t + \Delta\rho \tag{2}$$

which splits up the electrical resistivity into a temperature-dependent part ρ_t equal to the resistivity of the pure metal and an approximately temperature-independent part $\Delta\rho$ due to impurities and other crystal disturbances, equation (1) can be written

$$\frac{1}{K_e} = \frac{\rho_t}{LT} + \frac{\Delta\rho}{LT} \tag{3}$$

in terms of thermal resistivity quantities.

Experimentally it is established that the thermal resistivity caused by impurity atoms or structural defects is fairly accurately described by the term $\Delta\rho/LT$ of equation (3), (GRÜNEISEN and GOENS[13]). Regarding the effect of the atomic vibrations on the thermal resistivity, which should be accounted for by the term ρ_t/LT in the equation, the question is more complicated. Thus in the low temperature region (range of non-linear behaviour of the $\rho(T)$ curve) the W–F–L law fails totally. It has no theoretical basis in that temperature range either. But also in the range of straight line behaviour of the $\rho(T)$ curve some doubts exist regarding the validity of the law as regards the lattice-vibration term of the equation.

In a paper of 1952, LINDE[14] has discussed this problem on the basis of conductivity data for Cu, Ag, Au and Al and some Cu alloys given in the literature (temperature range 90–700°K). LINDE's investigation, which was entirely empirical, resulted in the conclusion that the heat-conductivity of normal (non-transition) metals is to be considered as independent of temperature with a fairly high degree of accuracy as long as the $\rho(T)$ curve can be approximated by a straight line. This was later confirmed by a low-temperature investigation by KEMP *et al.*[15]. The deviation from the W–F–L law was (even when correction was properly made to the lattice conductivity) found to be fairly large and increased with decreasing temperature in the temperature region studied.

On basis of these results LINDE writes the W–F–L law

$$\frac{1}{K_e} = \frac{1}{K_0} + \frac{\Delta\rho}{LT} \tag{4}$$

where $1/K_0$ denotes the constant electronic heat-resistivity of the pure metal, which he relates to the temperature-coefficient α of the electric resistivity by

$$\frac{1}{K_0} = \frac{\alpha}{L}\rho_{0°C} \tag{5}$$

(By a misprint the quantity L is lost in LINDE's expression.) Apparently equation (3) is (as pointed out by LINDE) closely analogous to Matthiessens' rule, equation (2), for the electrical resistivity of alloys and seems to have about the same degree of validity.

LINDE's investigation was restricted to the behaviour of normal metals (non-transition metals) and alloys with such a metal as the basic metal. It may, however, be of great interest to test his suggestion of a constant electronic heat-resistivity term for the case of a transition metal, especially a ferromagnetic one. This will be done in the following, (Section 6) after due extension of equation (4).

2. THE SAMPLES

For the measurements a series of binary iron alloys, including also pure iron, was available. It had been delivered, in the 1920's by Heraeus, Inc., Hanau, Germany, in the form of wires with

Vol. 2
196

1·0 and 2·0 mm diameter. In addition, there was very pure iron from Philip's Research Labs., Eindhoven, Holland (supplied by Mr. J. D. FAST), in the form of wires of 2·5 mm diameter. This iron and the alloys were kindly given for this investigation by G. BORELIUS. Finally there was a rod 5·0 mm in diameter, of spectroscopically standardized pure iron from Johnson and Matthey, Inc., London. In Table 1 some data for the alloys and the pure metals investigated are put together. The solute concentrations of the alloys given in the table were obtained by chemical analysis with an accuracy of one or two units in the second decimal.

In order to obtain specimens of suitable form for the heat-conductivity measurements of the alloys, the original wires were re-melted and rolled into bars with a cross section of about 15 mm^2 and a length of 100 mm. The melting was performed with a high-frequency furnace in sealed silica tubes, filled with argon to a pressure of about 120 mm Hg at room temperature. The tubes were placed in graphite crucibles during the melting. The heating of the charge, thus occurred by two mechanisms—first, indirectly via the graphite and second, directly by currents in the charge. The apparently difficult task of melting these high-melting alloys in quartz tubes was in this manner solved successfully.

The melts were, after a short rolling, annealed at 1100°C for two hours in evacuated silica tubes in order to remove segregation inhomogenities. Then they were rolled to the final form for the measurements and annealed at about 500°C for 10 hr to remove the cold-work effects.

The pure-iron specimens were not re-melted but were given the same final annealing as the alloy samples. In the case of iron no. 1, several pieces of the original wire were coupled in parallel to increase the cross section of the sample for the thermal-conductivity measurements.

3. THE HEAT-CONDUCTIVITY MEASUREMENTS

The heat-conductivity measurements were performed with the apparatus shown in Fig. 1 by measuring an established temperature-gradient along the sample with two iron–constantan thermocouples. The apparatus was alternately submerged in liquid oxygen, solid carbon-dioxide or an ice–water mixture. It consists of a brass can (a) which encloses the sample (b) and which is exhausted through a german-silver tube (c). The thermocouples (d) from the sample are joined to leads of the same material, which are pressed by plates (e) against the lid of the brass-can to obtain thermal contact. The filaments are also pressed against the wall of the german-silver tube by an inner tube (f) acting as a spring. The filaments leave the apparatus through small holes in an

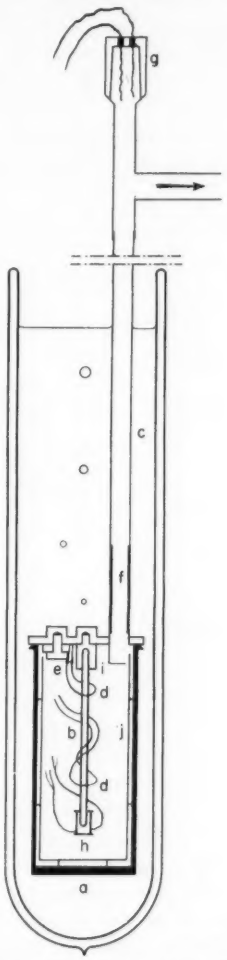

FIG. 1. The apparatus for the thermal conductivity measurements. (a) is the brass can, (b) the sample, (c) a german-silver tube, (d) thermocouples, (e) and (f) thermal-contact arrangements for the leads, (g) acrylic-plaster cap, (h) heating body, (i) specimen holder, (j) aluminum-foil reflector.

acrylic-plaster cap (g) which is sealed with picein. The specimens were soldered inside a wire-wound heating-body (h) and inside a bolt (i) which was screwed to the lid of the can. In order to diminish the heat radiation and obtain better reproducibility the heating-body was wrapped in aluminum foil and a reflector of cashed aluminum foil (j) was inserted. The brass can was sealed by soldering.

The two carefully calibrated thermocouples had a diameter of 0·25 mm and were soldered to the specimen. Their positions were fixed by two thin grooves, cut across the specimen 50 mm apart, and were checked with an optical comparator. The other junctions were held at a carefully controlled reference temperature close to room temperature and very exactly the same for both couples. The temperature gradient of the sample was regulated to lie between 1–2 °C/cm. The thermoelectric forces as well as the power supply to the heating-body were measured with a precision potentiometer. A stationary state could be reached about 1 hr after setting the current.

In the apparatus used the separately heated shield is omitted, which normally is applied in heat conductivity measurements to prevent heat transport by radiation. The thermal loss through radiation and through conduction in the leads was instead determined by remeasuring the conductivity after changing the sample dimensions. Assuming that the emissivity was approximately the same for all the samples, additional measurements on a shortened rod of one of the alloys and on a single piece of one of the iron wires (no. 1) also used in parallel as described above were sufficient. (In the case of samples with more widely varying emissivities gold plating of the bars would be a better solution of the problem.) The corrections applicable to the primary conductivity values were (with small variations for different samples) about 0·05 W/cm-degree when measured in ice, 0·02 W/cm-degree in solid carbon dioxide and 0·007 W/cm-degree in liquid oxygen.

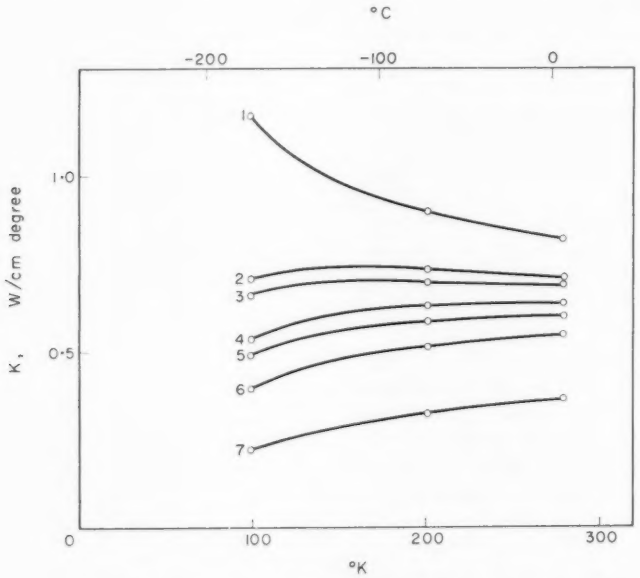

FIG. 2. The thermal conductivity results. For the curve numbers, see Table 1.

Results

The thermal conductivity values, corrected as outlined above are given in Fig. 2 as functions of the mean-temperature of the samples. In the

neighbourhood of 100°K the slopes of the curves could be determined by repeated measurements with varied energy supply to the heating coil, thus influencing the mean temperature of the sample. These slopes have been used to trace the interpolated parts of the curves.

The values obtained for the iron from Johnson and Matthey are not represented in Fig. 2 but are about 0·007 units lower than that of iron no. 1 at 280°K and 0·013 units lower at 100°K, in very good agreement with values obtained by ROSENBERG[2] for material from the same source.

4. THE ELECTRICAL-RESISTIVITY MEASUREMENTS

The electrical resistivity values to be analysed in the following (Sections 5, 6) were measured on the bar-shaped samples used for the heat-conductivity measurements. The apparatus used was provided with two steel edges 50 mm apart as potential probes, and could in its entirety be put into an oil bath at room temperature, or into some thermostatic medium, such as liquid oxygen or solid carbon dioxide. The cross sections of the samples were obtained indirectly by measuring their length, weight and density. The distance between the edges, serving as potential probes, was determined with an optical comparator. The electrical measurements were performed with a high-precision (thermoelectric-free) potentiometer of Diesselhorst type.

Results

The electrical resistivity results are shown in Table 1 and Fig. 3. The extrapolation to zero temperature, which is of minor interest for the present investigation, is made with the assumption that the additional resistivity caused by alloying is linearly dependent on temperature. The residual resistivity values of the Fe–Mn and Fe–Ni alloys (nos. 2–5), thus obtained, agree almost exactly with earlier results for thin filament samples of the same alloys obtained by measurements in the liquid helium region.[16] (For the Fe–Si alloys there is a considerable disagreement.)

Regarding the absolute resistivity-values of the pure-iron specimens there exists some confusion. In fact our measurements on thinner samples, rolled to different cross section, before annealing at 500–700°C, have given increasing resistivity with decreasing cross section. The reason for this peculair behaviour may be that it is very difficult to remove the effect of cold-working completely from iron specimens by annealing, or it can be a phenomenon of a more complicated nature, where such properties as the grain size and the size of the

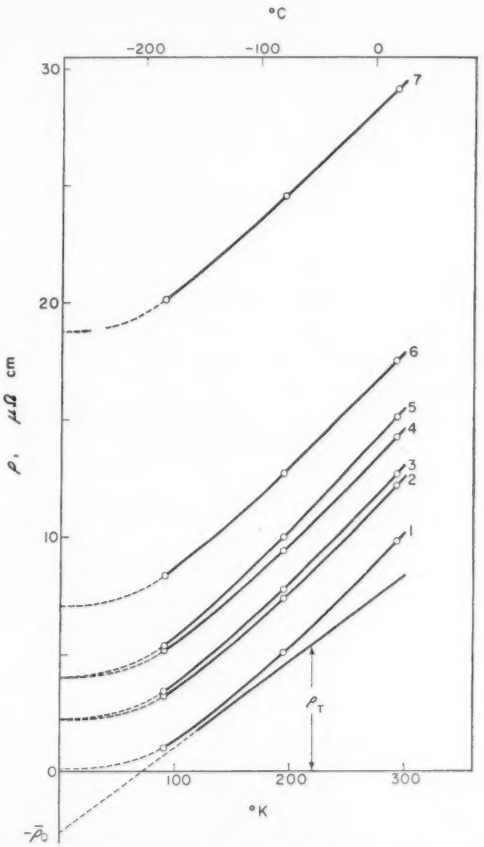

FIG. 3. The electrical resistivity results. For the curve numbers, see Table 1. The ρ_T line accords with equation (11).

Weiss domains are involved. The resistivity values given in Table 1 are representative for the materials in the state as obtained from the producer (without subsequent rolling or annealing). The points in Fig. 3 thus do not exactly correspond to the values in Table 1. A small difference between the resistivity values of the Fe–Mn alloys in the two types of samples can—as special experiments have

Table 1. *Composition and electrical resistivity at* 20°C *of the original materials. The values in parenthesis are the lowest values observed after annealing* (*The solute* Mn *may be attended with some impurity*).

Curve no.	Solute	at. per cent	ρ at 20°C μ ohm-cm	Supplier
2	Mn	0·26	12·3	Heraeus A.G.
4	Mn	0·53	14·6	
3	Ni	0·90	12·6	
5	Ni	1·81	15·1	
6	Si	1·17	17·5	
7	Si	2·89	29·0	
	—		9·74 (9·68)	
1	—		9·92 (9·80)	Philips Res. Lab.
	—		(9·87)	Johnson and Matthey, inc.

shown—be ascribed to a change in the concentration in the melting process, caused by a chemical reaction between Mn and SiO_2.

From the data of Table 1, the following mean values of the atomic resistivity increases of Mn, Ni and Si in iron at 20°C are obtained:

Mn	Ni	Si	
(9·3)	3·0	6·7	μ ohm-cm/at. per cent

The value for Mn in Fe is remarkably high, considering that the two metals are neighbours in the periodic table. It is also higher than the corresponding quantity derived by YENSEN[1] (6·9 μ ohm-cm/at. per cent). The values for Ni and Si agree fairly well with YENSEN's values. Since the values of the manganese concentrations given by the manufacturer (cited in Ref. (16)) are considerably higher than those obtained by chemical analyses (Table 1) one should until further evidence not trust the purity of the present Fe–Mn alloys. The total atomic impurity concentration should however be proportional to the Mn concentrations of Table 1.

5. THE SCATTERING TERMS IN THE ELECTRICAL RESISTIVITY

Besides the two scattering sources for electrons in normal metals, namely thermal vibrations and crystal imperfections (impurity atoms, dislocations etc.) there is, in the case of transition metals, the narrow and incomplete *d*-band which can trap the more movable *s*-electrons. This scattering process has also in recent years been treated with increased success as a spin-disorder scattering. For a survey of this topic, see MOTT and STEVENS[17] and COLES[18]. As the term "s-d scattering" may as well be used as a short-name for spin-disorder scattering it will here stand for this additional "transition-metal scattering" irrespective of any models.

The electrical resistivity of a transition metal can evidently be written as

$$\rho = \rho_T + \rho_S + \rho_I \tag{6}$$

where ρ_T is caused by thermal scattering, ρ_S by s-d scattering and ρ_I by crystal imperfections. The present investigations are limited to the temperature region where $\rho_T(T)$ is approximately linear and thus the Grüneisen–Borelius relation,[19]

$$\frac{\rho T}{\rho\theta} = -0{\cdot}17 + 1{\cdot}17\frac{T}{\theta} \tag{7}$$

should apply (θ = Debye temperature). Deviations from the linearity occurring at higher temperatures have been discussed by MOTT[20].

The impurity resistivity ρ_I is approximately independent of temperature, as stated by Matthiessen's rule. The s-d resistivity-term ρ_S should, according to the theory of spin-disorder scattering,[21,22] be independent of temperature for magnetic metals well above the Curie point.

In order to separate the resistivity of pure iron

in terms of thermal and s-d scattering, valid in an intermediate temperature region, the present resistivity values have been analysed together with those of PALLISTER[9] at elevated temperatures and it was found that the $\rho(T)$ dependence with a surprisingly high degree of accuracy can be written as

$$\rho = a+bT+cT^3 \qquad (8)$$

373°K, has the equation (μ ohm-cm)

$$\rho = -2{\cdot}4+3{\cdot}65\times10^{-2}T+0{\cdot}64\times10^{-6}T^3 \qquad (9)$$

The deviation at higher temperatures is consistent with the behaviour of the non-ferromagnetic 8th-group metals Pt and Pd. They show in contrast to normal metals a decreasing temperature derivative $d\rho/dT$ when the temperature is raised.[20]

In equation (9) the cubic term undoubtedly

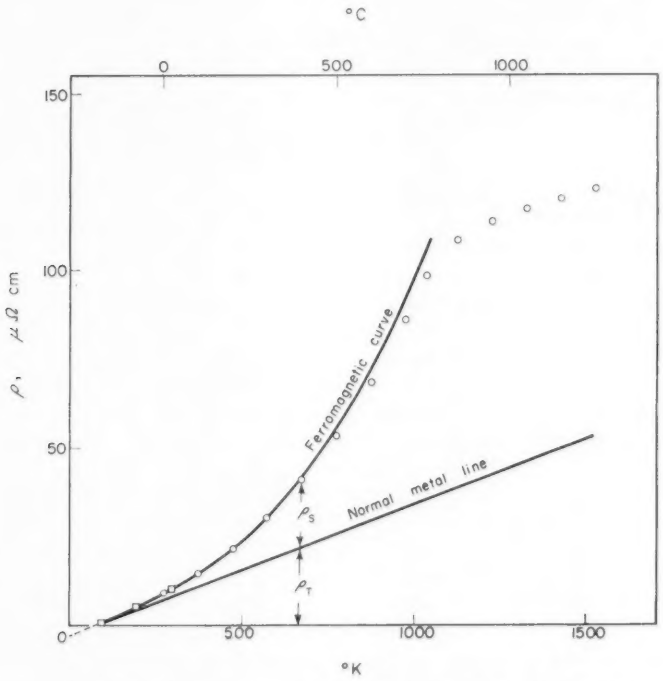

FIG. 4. The temperature variation of the electrical resistivity of iron and the curve of equation (9).

□ present measurements, ○ PALLISTER's measurements. The ρ_T line accords with equation (11).

where a, b and c are constants. (The same form of equation can of course be applied to iron alloys, since deviations from the Matthiessen rule enter the bT term.) With T^2 or T^4 instead of T^3 a much poorer fit to the experimental data is obtained. A comparison between a curve according to equation (8) up to the Curie point and experimental points is shown in Fig. 4. The curve which has been adjusted to fit the experimental values (corrected to correspond at 20°C) at 195°K, 273°K and

represents the s-d scattering in the ferromagnetic state

$$\rho_S = 0{\cdot}64\times10^{-6}T^3 \,(T < T_{\text{Curie}}) \qquad (10)$$

Further evidence in support of the cubic temperature proportionality of ρ_S is that it leads to a temperature function for the spontaneous magnetization which fits the experimental results very well. This will be discussed in a following paper where equation (8) also will be applied to resistance data of nickel.

Vol. 20
1961

The linear part of equation (9) should correspond mainly to thermal scattering. With $\rho = 9{\cdot}7\ \mu$ ohm-cm for ideal iron at 20°C we obtain

$$\rho_T = -2{\cdot}6 + 3{\cdot}65 \times 10^{-2} T \qquad (11)$$

corresponding to a Debye temperature $\theta = 490$°K when identified with equation (7). In Fig. 4 and Fig. 3 a straight line corresponding to equation (11) is drawn. This line gives the resistivity that iron would have at temperatures above the "T^5-region" if it were a normal metal (i.e. disregarding the s-d scattering). In a better approximation the line should have a weak positive curvature corresponding to a decreasing θ in equation (7) caused by the thermal expansion.

6. THE HEAT CONDUCTION BY THE ELECTRONS (W–F–L LAW)

The invalidity of the classical W–F–L law (equation 1) for iron at intermediate temperatures is easily established since the law with the experimental ρ-values inserted gives values of K_e bigger than the total experimental K even at 100–200°K. This is avoided if LINDE's suggestion of a temperature-independent contribution to the electronic heat-resistivity from the lattice vibrations is applied. His suggestion will here be used as a postulate which, as seen by the reasonableness of the resulting lattice conductivities, seems to be realistic.

The electronic thermal-resistivity $W_e = 1/K_e$ can be separated into terms due to thermal scattering (W_{eT}), s-d scattering (W_{eS}) and impurity scattering (W_{eI}) and corresponding to the electrical resistivity terms of equation (6).

$$W_e = W_{eT} + W_{eS} + W_{eI} \qquad (12)$$

Here W_{eI} indubitably can be derived from ρ_I by the W–F–L law. Since the centers of the spin-disorder scattering are considered as localized in the lattice[18] like those of the impurity scattering, permitting a relaxation time to be defined, W_{eS} should also be obtainable from ρ_T by the W–F–L law. As regards the constant term W_{eT} it cannot be obtained from equation (5), which is not generally applicable to transition metals, but from

$$W_{eT} = \frac{1}{L} \times \frac{d\rho_T}{dT} \qquad (13)$$

which should be valid in the region where $\rho_T(T)$ is linear. It is advantageous to transform this equation to get T in the denominator. Writing

$$\rho_T = -\bar{\rho}_0 + bT \qquad (14)$$

where the constant $\bar{\rho}_0 \approx 2{\cdot}6\ \mu$ ohm-cm for iron according to equation (11), the electronic heat conductivity will appear as

$$W_{eT} = \frac{\rho_T + \bar{\rho}_0}{LT} \qquad (15)$$

and the W–F–L law should be written

$$W_e = \frac{\rho_T + \bar{\rho}_0}{LT} + \frac{\rho_S}{LT} + \frac{\rho_I}{LT} \qquad (16)$$

where the different scattering-sources are separated. Using equation (6) for the total electrical resistivity the law will be expressed by

$$W_e = \frac{1}{K_e} = \frac{\rho + \bar{\rho}_0}{LT} \qquad (17)$$

This modified W–F–L law should apply to both normal metals and transition metals at all temperatures above the low temperature region, where the linearity of $\rho_T(T)$ ceases. This means for iron, strictly speaking, above about 120°K; consequently a small systematic error can be expected to influence the values calculated for 100°K in the following.

If a physical meaning could be given to the quantity $\bar{\rho}_0$ it should probably be connected to the zero-point energy as pointed out by BORELIUS[23]. As was shown above ρ_0 can be determined by a study of $\rho(T)$ in the intermediate temperature region.

Figure 5 shows as functions of $1/T$ the electronic thermal resistivities of the samples 1–7 as derived from equation (17) with $\bar{\rho}_0 = 2{\cdot}66\ \mu$ ohm-cm and $L = 2{\cdot}45 \times 10^{-8}$ V^2/deg^2. To see the high-temperature behaviour, curves are also drawn, based on the electric resistivity values of PALLISTER[9] for pure iron, and POWELL[8] for two commercial steels. The figure illustrates very clearly how the different scattering processes [the three terms of equation (12) or (16)] influence the electronic heat-resistivity. The thermal scattering causes, as postulated, a constant resistivity W_{eT}

marked in the figure. (If the temperature variation of the Debye temperature were considered the line would curve upwards to the left.) The impurity scattering adds a resistivity term proportional to $1/T$ and the s-d scattering causes a resistivity term passing a maximum at the Curie point, being proportional to T^2 below and to $1/T$ above this temperature. The convergence of the curves towards W_{eT}, when T increases, is evident. The maximum at the Curie point explains a weak minimum in K earlier observed at 800–900°C and by POWELL[8] connected to the α–γ transformation. The weakness of this minimum as compared with the sharpness of the W_e maximum, can be ascribed partly to the inverse representation in Fig. 5, and partly to a simultaneous decrease in the lattice conductivity as will be shown in the following.

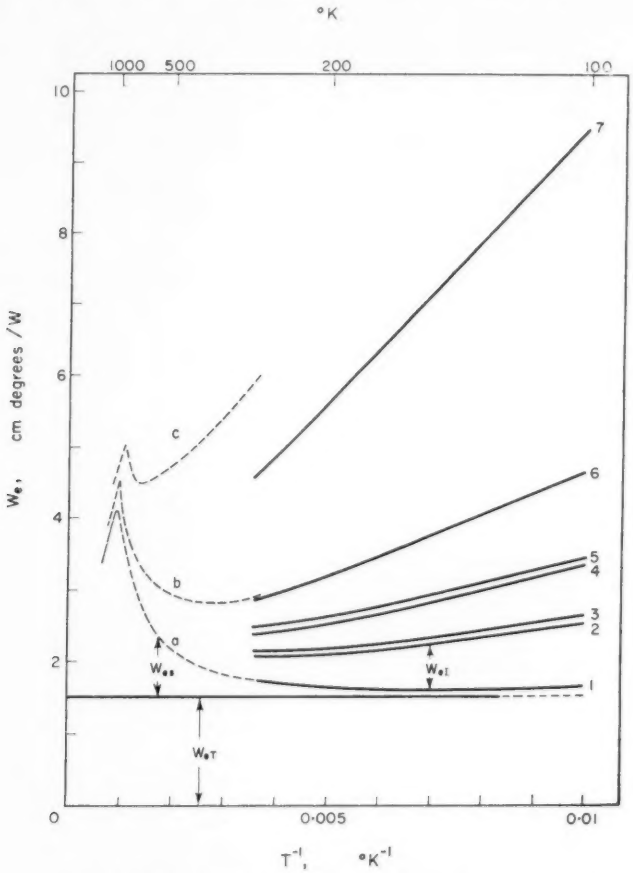

FIG. 5. The electronic thermal resistivity according to equation (17) plotted vs. the inverted temperature. The curves 1–7 are based on the present measurements (numbers according to Table 1), curve (a) on PALLISTER'S[9] measurements on iron ($\rho_{0°C} = 8{\cdot}86$ μ ohm-cm) and the curves (b) and (c) on POWELL'S[8] measurements on commercial steels ($\rho_{0°C} = 16{\cdot}97$ μ ohm-cm and $37{\cdot}4$ μ ohm-cm respectively).

Figure 6 shows the electronic heat-conductivity as a function of temperature. It should be remarked that the maxima here are caused by the s-d scattering. For comparison a horizontal line

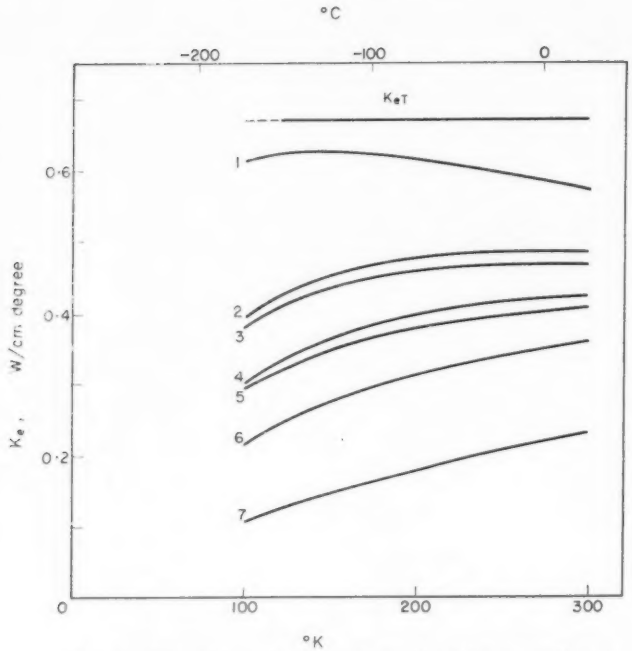

FIG. 6. The electronic thermal conductivity according to equation (17), plotted vs. the temperature. For the numbers, see Table 1. The curve marked K_eT represents "normal-metal iron", the s-d scattering being dismissed.

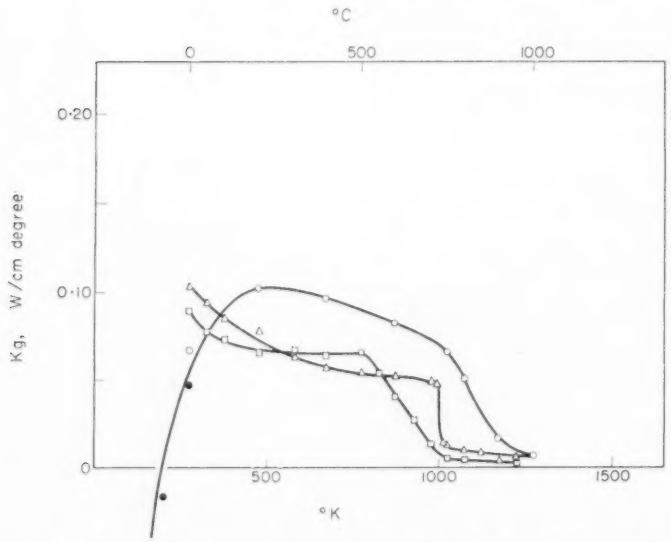

FIG. 7. The lattice thermal conductivity of iron and alloy steels derived by the classical W–F–L law equations (1) and (18). ● deduced from the present measurements on iron no. 1 (the value obtained for 100°K is −0·66 W/cm-degree); ○, △ and □ from POWELL's measurements on iron[7] and two commercial steels,[8] respectively.

($K_{eT} = 1/W_{eT}$) corresponding to "normal metal iron" is drawn.

7. THE HEAT CONDUCTION BY THE LATTICE

When the electronic thermal conductivity K_e can be determined separately, the lattice thermal conductivity K_g is obtained as

$$K_g = K - K_e \qquad (18)$$

equation (18), using POWELL's values of ρ and K for iron and two commercial steels at elevated temperatures and the present values for iron no. 1 at decreased temperatures. Below about 500°K the apparent lattice conductivity for iron decreases with decreasing temperature, which is inconsistent with the theories in this field. At lower temperatures the lattice conductivity even becomes negative.

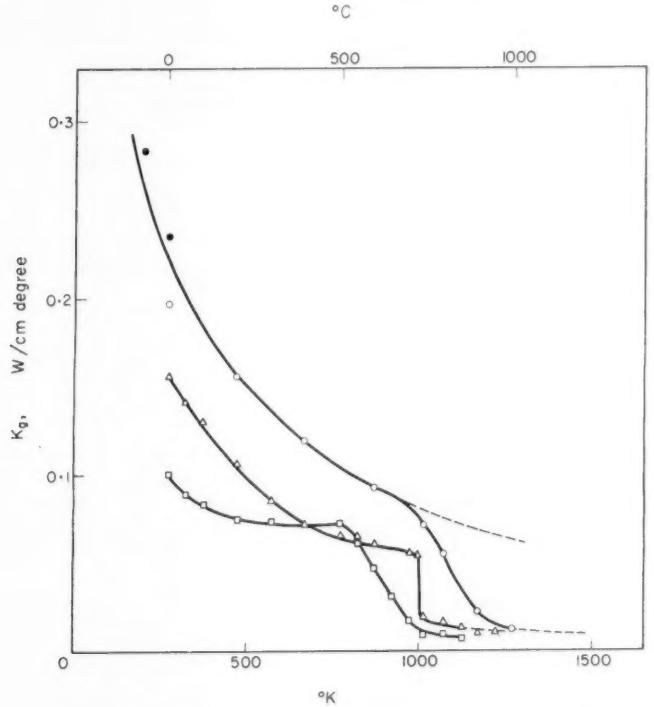

FIG. 8. The data of Fig. 7 derived by the modified law equations (17) and (18). (The value for iron no. 1 at 100°K is 0·56 W/cm-degree.)

where K is the total experimental heat conductivity. (A possible energy-transport by spin interactions is until further notice considered as unimportant or included in K_g.) As a consequence of the invalidity of the classical W–F–L law it has been considered impossible to determine the lattice conductivity at temperatures above 90°K and for pure metals or alloys with an additional resistance less than about 1 μ ohm-cm.[11,12] This is illustrated by Fig. 7 showing the lattice conductivity of iron as calculated by equation (1) and

If the calculations instead are based on the modified W–F–L law, equation (17), the resulting lattice conductivity will appear more plausible as Fig. 8 shows. An interesting observation is the rapid fall of the curve at the Curie point, indicating that the lattice conductivity (as defined by equation (18)) is bigger in the magnetically ordered state than in the disordered state. As can be concluded from POWELL's discussions of his results, the different character of the curves of Fig. 8 in the neighbourhood of the Curie temperature can be

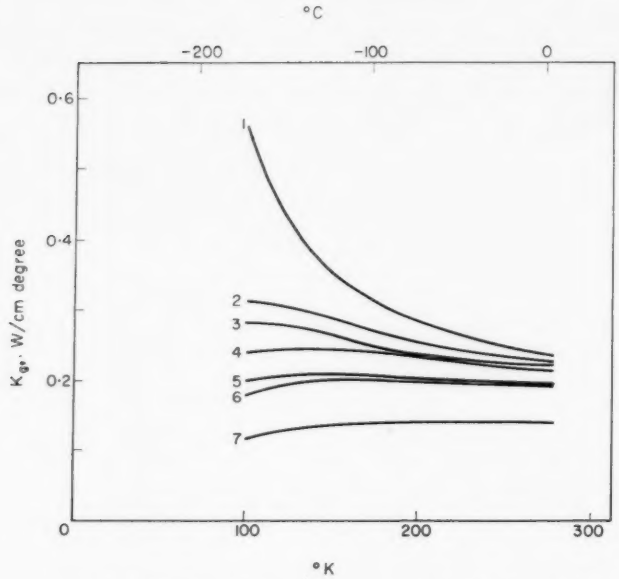

FIG. 9. The lattice thermal conductivity of the samples 1–7 according to equations (17) and (18). For the curve numbers, see Table 1.

explained by variations in the heat treatment and the method of measurement.

The lattice conductivity of the samples, computed with use of the modified W–F–L law equation (17) and equation (18) is shown in Fig. 9. The effect of alloying is evident.

To illustrate the influence of the different phonon scattering processes Fig. 10 shows the

Table 2. Temperature variation of the lattice thermal resistivity for various interaction mechanisms. From KLEMENS[12]

	Scattering mechanism	$W_g(T)$
Low temperatures $T < \theta$	External boundaries	T^{-3}
	Grain boundaries	T^{-3}
	Thin sheets embedded in crystal of continuous orientation	T^{-1}
	Stacking faults	T^{-1}
	Conduction electrons in metals	T^{-2}
	Dislocations (strain field)	T^{-2}
	Dislocations (core)	T^{0}
	Long cylinders	T^{0}
	Point defects	T^{1}
	Umklapp processes	$T^{-3}\exp(-\theta/AT)$
High temperatures $T > \theta$	Umklapp processes	T^{1}
	All imperfections	T^{0}
	Conduction electrons in metals	T^{0}

resistivity quantity $W_g = 1/K_g$. It has to be compared to Table 2, cited from KLEMENS[12] and giving the theoretical temperature dependence of W_g as caused by different scattering sources at high and at very low temperatures, where the specific heat can respectively be assumed constant and proportional to T^3. The lattice thermal conductivity is, as is known, roughly a product of the heat-capacity S of the lattice per unit volume, the sound velocity v and the mean free path l of the phonons:

$$K_g = \frac{1}{W_g} = \frac{1}{3} Svl \qquad (19)$$

The contribution to the lattice thermal-resistivity from the different scattering sources, thermal vibrations (W_{gT}), electrons (W_{gE}) and crystal defects (W_{gI}) are approximately additive:

$$W_g = W_{gT} + W_{gE} + W_{gI} \qquad (20)$$

The curves of Fig. 10 (as those of Figs. 5, 6 and 9) are traced closely in accordance with the interpolated curves of K and ρ (Figs. 2 and 3). The quantitative conclusions which can be drawn from Fig. 10 are limited for several reasons. The right ends of the curves are sensitive to possible errors in the measurements and the left ends extend into a region where the validity of equation (17) is probably restricted ($\rho(T)$ not linear), resulting in somewhat too low values for W_g. A deviation of some 0·1 unit seems reasonable. Also, the choice of a value for $\bar{\rho}_0$ affects the curves.

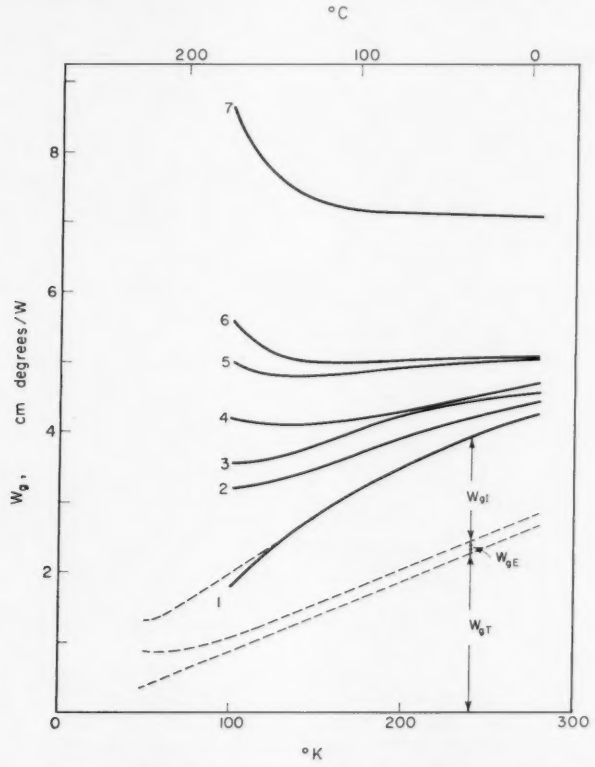

FIG. 10. The data of Fig. 9 given in terms of resistivity quantities. For the dashed curves, see the text.

A comparison of the data of Fig. 10 and Table 2 shows that the curves are mainly of the high-temperature type, though some low-temperature

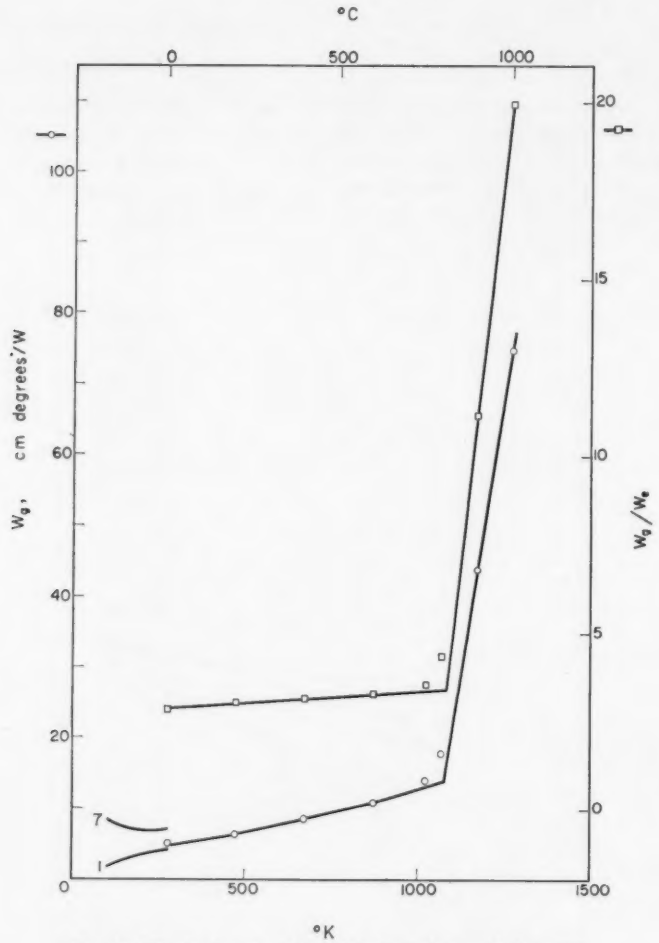

FIG. 11. The lattice thermal resistivity and the ratio between the lattice and electronic thermal-resistivities for iron at elevated temperatures. The curves are based on equations (17) and (18) and POWELL'S[7] measurements on iron. The outermost curves (1 and 7) of Fig. 10 are inserted for comparison.

behaviour can be traced in their rising left ends. It can be concluded that the solutes Mn, Si and Ni form the same sequence with regard to their ability to scatter phonons as that found for the electron scattering (Section 4), and that the increase in W_{gI} caused by alloying is proportional to the alloy concentration, at least for the alloys nos. 2–5. It should be remarked that the iron of curve no. 1 is not identical with the iron used for the alloys.

The average slope of curve no. 1 in the higher temperature region should be ascribed to the thermal scattering. To picture the general behaviour of $W_{gT}(T)$ in the temperature region of the measurements the following approximations of equation (19) are applied:

$$\frac{1}{W_{gT}} \propto Sl \propto C_p \frac{1}{N_p} \propto C_p[\exp(\theta/2T)-1] \quad (21)$$

Here C_p is the molar heat-capacity (at constant

pressure) and N_p the density of phonons with an energy exceeding the value $k\theta/2$ (k = Boltzmann constant, θ = Debye temperature) which according to PEIERLS[24] should be necessary for an Umklapp process. In this equation AUSTIN's selected values[10] for C_p are inserted, after correction for the electronic heat-capacity with the function used by HOFMAN *et al.*[25], whose value for θ also is used (432°K). Choosing the proportionality constant for equation (21) to give the proper slope (according to Fig. 11) we obtain W_{gT} as represented by a broken line in Fig. 10.

The evaluation of the terms W_{gE} and W_{gI} of equation (20) is a more complicated problem. Anyhow W_{gE} should be constant in the temperature region where W_{eT} is constant, i.e. above about 120°K (Fig. 3 and equation (15)). Provided that the electrons interact equally with phonons of all polarizations the high-temperature value of W_{gE} can be rated according to MAKINSON[26] from the relation

$$W_{gE} = W_{eT} \times \frac{8}{27}\pi^2 N_e^2 \qquad (22)$$

where N_e denotes the number of free electrons per atom. Taking the value of W_{eT} from Fig. 5 and assuming for example $N_e = 0{\cdot}2$ for iron we obtain $W_{gE} = 0{\cdot}2$ W/cm-degree, leaving a considerable fraction of the total resistivity to W_{gI}. This case is illustrated in Fig. 10. If, on the other hand, the electrons interact more weakly with transverse lattice-waves than with longitudinal waves, W_{gE} can be the dominating term of W_g. A bigger value for N_e would have the same effect, W_{gI} disappears for $N_e \approx 0{\cdot}6$. Only in the first case, or in a compromise case favouring the term W_{gI}, is it, however, possible to interpret the subtleties of the experimental curvatures in Fig. 10. Thus only a strong scattering by point defects can explain the slope of curve no. 1 below about 200°K. Here the possibility of an additional scattering associated with the disordered spins must be considered (not discussed in the literature as yet). The alloy curves are characterized by a considerable scattering of "T^{-1} or T^{-2} type" (Table 2), causing their positive curvature and their convergence to the right. The influence on W_g of the dislocations introduced by alloying (or an extensive strain-field around the solute atoms) obviously quite overshadows that of the solute atoms themselves, at least at lower temperatures.

In Fig. 11, the circles show the lattice heat-resistivity of iron as derived from POWELL's measurements with the aid of equations (17) and (18). In this figure the outermost curves of Fig. 10 are also inserted. The effect of the spontaneous magnetization appears very distinctly. The knee of the slightly idealized interpolation line indicates the paramagnetic Curie point (about 1100°K) rather than the ferromagnetic one (1043°K)—as also could be expected theoretically. The effect studied is still more evident for the ratio between the lattice resistivity and the electronic heat resistivity (W_g/W_e) also given in the figure.

Considering the strength of the magnetization effect on W_g at the Curie point it seems unlikely that it can to any essential extent be correlated with scattering of phonons by electrons or dislocations, but perhaps largely with an additional scattering associated with disordered spins as mentioned above. The stepformed anomaly of the $K_g(T)$ curve (Fig. 8) seems, however, to point to a considerable influence of some subtractional effect in K_g. The anomaly in the sound velocity that can theoretically be expected to accompany the magnetostriction phenomenon is insufficient to cause this effect, but the ferromagnetic heat-capacity anomaly is of the order of magnitude required. In fact, it would be remarkable if the latter anomaly had no equivalence in the heat conductivity. In the numerical study of equation (21) the magnetic specific heat (although small) was included in C_p. This means that the lattice waves were assumed to carry also the spin excitation energy. Approaching the Curie temperature the curves of the W_g components would all show a negative curvature making an analysis rather complicated. It would perhaps be more satisfying to separate the quantity W_g of equation (18) into one term (K_p) for "non-magnetic" phonon conductivity applying to the theories underlaying Table 1, and one term (K_s) for the thermal conductivity to be associated with the spin interactions (by spin waves and/or another mechanism).

$$K_g = K_p + K_s \qquad (23)$$

but this problem may be treated in a following investigation.

The interpretation of the W_g curves of Fig. 10

on the basis of the present matter obviously has some degree of freedom. It is however constrained, since the components of K_g and W_g must be less than the entirety and since the general temperature variation of W_{gE} and W_{gT} (or properly W_{pE} and W_{pT}) is known. Thus if the W_{gE} curve of Fig. 10 is essentially displaced upwards it will cross the experimental curve. In other words, if N_e is considerably bigger than 0·2 electrons per atom (0·6–0·8 may be reasonable) the steeping slope of curve 1 below about 200°K has to be explained by a (spin wave?) term entering K_s. (This is the temperature range where the spin-wave model of the spontaneous magnetization has been successful.) If on the other hand the W_{gT} curve is raised (perhaps to diminish the W_{gI} term), an avoidance of a passage over the experimental curve at higher temperatures (Fig. 11) would necessitate an assumption that the effect of K_s, discussed above for the Curie point region, is of importance even at room temperature.

Acknowledgements—I am much indebted to Professor J. O. LINDE for his proposal of these measurements and for many valuable discussions. The investigation has been supported by a grant from the Swedish Natural Science Research Council.

REFERENCES

1. YENSEN T. D., *Trans. Amer. Soc. Metals* **27,** 801 (1939).
2. POWELL R. L. and BLANPIED W. A., *NBS Circular* 556 (1954).
3. CHARI M. S. R. and DE NOBEL J., *Physica* **25,** 73 (1959).
4. KEMP W. R. G., KLEMENS P. G. and WHITE G. K., *Aust. J. Phys.* **9,** 180 (1956).
5. KEMP W. R. G., KLEMENS P. G. and TAINSH R. J., *Ann. Phys., Lpz.* (7) **5,** 35 (1959).
6. POWELL R. W., *Iron and Steel Inst.* (*Alloy Steels Res. Committee*), *Spec. Rep.* **24,** 215, 253 (1939).
7. POWELL R. W., *Proc. Phys. Soc. Lond.* **51,** 407 (1939).
8. POWELL R. W., *Iron and Steel Inst.* (*Alloy Steels Res. Committee*) Paper No. 23 (1946).
9. PALLISTER P. R., *J. Iron St. Inst.* **161,** 87 (1949).
10. CLEAVES H. E. and THOMPSON J. G., *The Metal Iron.* McGraw-Hill, New York (1935).
11. KLEMENS P. G., *Handbuch der Physik* Vol. XIV p. 198. Springer, Berlin (1956).
12. KLEMENS P. G., *Solid State Physics* Vol. VII p. 1. Academic Press, New York (1958).
13. GRÜNEISEN E. and GOENS E., *Z. Phys.* **44,** 615 (1927).
14. LINDE J. O., *Arkiv för Fysik* **4,** 541 (1952).
15. KEMP W. R. G., KLEMENS P. G., SREEDHAR A. K. and WHITE G. K., *Proc. Roy. Soc.* **233,** 480 (1956).
16. LINDE J. O., BÄCKLUND N. G. and HUMBLE S. G., *Bull. IIF*, Annexe 1959–1 (in press).
17. MOTT N. F. and STEVENS K. W. H., *Phil. Mag.* **2,** 1364 (1957).
18. COLES B. R., *Advanc. Phys.* **7,** 40 (1958).
19. BORELIUS G., *Ann. Phys., Lpz.* (5) **8,** 261 (1931).
20. MOTT N. F. and JONES H., *The Theory of the Properties of Metals and Alloys.* Oxford University Press (1936).
21. FRIEDEL J. and DE GENNES P., *J. Phys. Chem. Solids* **4,** 71 (1958).
22. WEISS R. J. and MAROTTA A. S., *J. Phys. Chem. Solids* **9,** 302 (1959).
23. BORELIUS G., *Canad. J. Phys.* **34,** 1336 (1956).
24. PEIERLS R., *Ann. Phys., Lpz.* **3,** 1055 (1929).
25. HOFMANN J. A., PASKIN A., TAUER K. J. and WEISS R. J., *J. Phys. Chem. Solids* **1,** 45 (1956).
26. MAKINSON R. E. B., *Proc. Camb. Phil. Soc.* **34,** 474 (1938).

J. Phys. Chem. Solids Pergamon Press 1961. Vol. 20, Nos. 1/2, pp. 17–34. Printed in Great Britain.

STATISTICAL DYNAMICS OF CRYSTALLINE DIFFUSION II. VACANCY MECHANISM

RYOICHI KIKUCHI

Hughes Research Laboratories, A Division of Hughes Aircraft Company, Malibu, California

(*Received* 31 *August* 1960)

Abstract—The method of treating diffusion of atoms in crystals developed in the first paper of this series is applied to the vacancy mechanism of atomic migration in substitutional alloys. The method is used on a body centered cubic binary system (including vacancies) with the chemical potential gradient along a [100] direction. The system is isothermal and a flow of atoms is maintained by two particle reservoirs of different chemical potentials placed at the two ends of the system. First, the path probability $\mathscr{G}$ for change of state during a short time interval is written in terms of the *path parameters* by using the pair approximation of the cluster-variation method and following the recipe previously proposed by the author. The most probable change of state is then derived by maximizing $\mathscr{G}$ with respect to the path parameters. The relations between the atomic fluxes and the chemical potential gradients are derived for the stationary state. Onsager's reciprocal relation holds. The limiting case for no chemical potential gradient becomes identical with the state derived from the equilibrium theory.

When the pressure gradient in the system is neglected, the diffusion coefficient for B atoms in the matrix of A atoms is given as

$$D_{\mathrm{B}}^{*} = 28x_3 \frac{\theta_{\mathrm{A}}\theta_{\mathrm{B}} \exp(\epsilon_{\mathrm{M}} - \epsilon_{\mathrm{A}})/kT}{7\theta_{\mathrm{A}} + 2\theta_{\mathrm{B}} \exp(\epsilon_{\mathrm{M}} - \epsilon_{\mathrm{A}})/2kT},$$

where x_3 is the mole fraction of vacancies in the lattice, θ_{A} (or θ_{B}) is the probability for a unit jump of an A atom (or a B atom) into an adjacent vacancy per unit time, and ϵ_{M} and ϵ_{A} are potential energies for an A–B pair and an A–A pair, respectively. By setting $\theta_{\mathrm{A}} = \theta_{\mathrm{B}}$ and $\epsilon_{\mathrm{M}} = \epsilon_{\mathrm{A}}$, the self-diffusion coefficient for A atoms is derived as

$$D^{*} = (28/9)x_3\theta_{\mathrm{A}}.$$

1. INTRODUCTION

IN THE first paper of this series,[1] diffusion of atoms in crystals is discussed with the assumption that the direct exchange mechanism is operating. Although SDD I served the purpose of explaining the method, it is generally accepted[2] that the direct exchange mechanism is not likely to be the main process of atomic migration in solids. One of the more realistic elementary processes of migration is the vacancy mechanism. The Kirkendall effect[3–5] found in face centered cubic structures supported the theory that the vacancy mechanism is the leading one operating in them.[6] Although previously doubted,[7] the recent observation of the Kirkendall effect in a body centered cubic structure[8] suggests that the vacancy mechanism is the main mechanism in this structure also.

In applying the cluster-variation method,[9] the b.c.c. structure is mathematically much easier to use than the f.c.c. structure because the pair approximation gives good results for the former wheras the tetrahedron approximation (which is much bulkier than the pair approximation) is necessary for the latter in order to obtain reasonable accuracy. In view of these considerations, the b.c.c. structure has been selected for this paper.

The discussion will be limited to the binary system, where B atoms diffuse through the matrix of A atoms. The general program pursued in this paper is similar to that dealt with in SDD I.

2. PROBLEM

We have an alloy consisting of A and B atoms and vacancies in a b.c.c. structure; Fig. 1 shows a

side view of the lattice. The system has a uniform temperature T, but a concentration gradient exists along a [100] direction.

A co-ordinate axis is introduced along the [100] direction, with the origin at one of the (100) planes. In Fig. 1, $\nu-1$, ν, $\nu+1$, ... indicate the co-ordinates of corresponding planes measured in units of interplanar distance. Notice that the Greek letter ν is an integer. The interstitial planes have co-ordinates of half integers, which will be

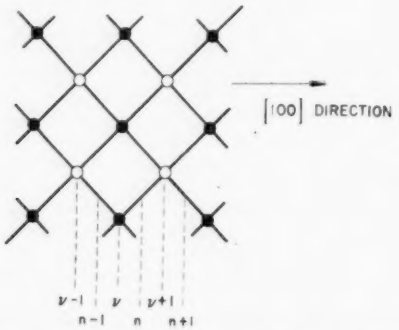

FIG. 1. Side view of the body centered cubic lattice. ν's number the lattice planes perpendicular to the gradient, which exists along the [100] direction. n's number the bonds between planes. The open circles are at the body-center position of cubes made of the solid circles and vice versa. Lines connecting lattice points indicate bonds on which the adjacent atoms can interchange.

denoted by $n-1$, n, $n+1$, ... When n and ν appear in an equation simultaneously, they are connected by

$$n = \nu+\tfrac{1}{2}. \tag{2.1}$$

A lattice point on the ν^{th} lattice plane will be called a "ν^{th} lattice point". Similarly, the expression "an n^{th} bond" will be used to indicate a bond between the ν^{th} and the $(\nu+1)^{\text{th}}$ planes.

We assume that an atom can migrate only when a vacancy happens to occur next to it and they interchange places. This interchange takes place by means of thermal agitation, and the parameter θ_A (or θ_B) indicates the probability of a unit jump of an A atom (or a B atom) into an adjacent vacancy per unit time. These probability parameters are to be evaluated using quantum mechanics or the rate process theory if the detailed mechanisms of the atomic jump are specified; however, in this paper, they will be treated as given parameters in the same sense as the energy levels are given for equilibrium statistical mechanics.

In general, θ_A depends on the configuration of atoms surrounding the A atom, but such dependence will be neglected here, although future modification of the treatment may be able to take the effect of surrounding atomic configurations into account.

We further assume the nearest neighbor interaction for atomic pairs, as is usual for the order–disorder problem. The definitions of the interaction potentials, ϵ_A, etc., are listed in Table 2; it is assumed that an atom–vacancy pair has no potential. Since the system is classical, each atom contributes $3kT$ to the energy of vibration (k is the Boltzmann constant and T the absolute temperature). This paper considers the problem of expressing the relation between the concentration gradients and the flow of atoms in terms of the probabilities of atomic interchange θ's, the interaction energies ϵ's, and the temperature of the heat bath T.

In order to maintain the steady flow of atoms across the system, it is brought into contact with two particle reservoirs, I and II. Each reservoir is infinitely large: the first occupies the range $-\infty < \nu \leqslant 0$, the second occupies $L \leqslant \nu < \infty$, and the range of the system is $0 \leqslant \nu \leqslant L$. A reservoir is characterized mathematically by the requirement that the probability for a unit jump, $\theta^{(\mathrm{I})}$ or $\theta^{(\mathrm{II})}$, in a reservoir is very large compared with a unit jump, θ, for the system. When this condition is satisfied, even though particles are either flowing out from or flowing into the reservoir, the latter is always practically in equilibrium in comparison with the system in question.

In order to treat θ_A for the system and for the reservoirs in a unified manner, we regard it as a function of the position of a bond and introduce a notation $\theta_A{}^{(n)}$ defined as

$$\theta_A{}^{(n)}=\begin{cases}\theta_A{}^{(\mathrm{I})} & \text{for the reservoir I, } -\infty<n\leqslant -1/2\\ \theta_A & \text{for the system } \quad 1/2\leqslant n\leqslant L-1/2\\ \theta_A{}^{(\mathrm{II})} & \text{for the reservoir II, } L+1/2\leqslant n<\infty.\end{cases} \tag{2.2}$$

$\theta_B{}^{(n)}$ is similarly defined.

In order to maintain the temperature of the system constant, it is placed in contact with a large heat bath of temperature T. How to take the effect

of the heat bath into account was discussed thoroughly in ICP[10]; and we shall use only the result here. Experimentally, the vibrating lattice, or the system of phonons, can be regarded as the heat bath for the system of interest.

In this paper the possibility of creating and destroying vacancies will be ignored, i.e. the volume of the system is kept constant, primarily in order to simplify the mathematics. Although this assumption does not seem to impair the generality of the treatment to any extent, a calculation based on constancy of pressure[5] will be left for future investigation.

3. VARIABLES

The system is assumed homogeneous in a plane perpendicular to the direction of the gradient. This assumption allows us to define parameters $x_i^{(\nu)}(t)$'s, which indicate the probability for finding certain configurations at a ν^{th} lattice point at time t. They are listed in Table 1 and obey the normalization

$$\sum_{i=1}^{3} x_i^{(\nu)}(t) = 1. \tag{3.1}$$

Table 1. Probability for finding configurations at a lattice point for the vacancy mechanism; v indicates a vacancy

ν^{th}	Probability
A	$x_1^{(\nu)}(t)$
B	$x_2^{(\nu)}(t)$
v	$x_3^{(\nu)}(t)$

Along with x_i's, we introduce the probability parameters $y_i^{(n)}(t)$'s for a bond (see Table 2). Since the concentration of vacancies is always small,[2] we neglect the occurrence of vacancy pairs. The geometrical consideration leads to the following relations among x's and y's:

$$\begin{aligned} x_1^{(\nu)} &= y_1^{(n)}+y_2^{(n)}+y_5^{(n)} = y_1^{(n-1)}+y_3^{(n-1)}+y_6^{(n-1)} \\ x_2^{(\nu)} &= y_3^{(n)}+y_4^{(n)}+y_7^{(n)} = y_2^{(n-1)}+y_4^{(n-1)}+y_8^{(n-1)} \\ x_3^{(\nu)} &= y_6^{(n)}+y_8^{(n)} = y_5^{(n-1)}+y_7^{(n-1)} \end{aligned} \tag{3.2}$$

All the quantities in these relations are for the same time instant t; n and ν are connected by (2.1).

Table 2. Probability for finding atomic pair configurations on a bond in the case of the vacancy mechanism

ν^{th} $(\nu+1)^{\text{th}}$	Probability	Energy
A — A	$y_1^{(n)}(t)$	ϵ_A
A — B	$y_2^{(n)}(t)$	ϵ_M
B — A	$y_3^{(n)}(t)$	ϵ_M
B — B	$y_4^{(n)}(t)$	ϵ_B
A — v	$y_5^{(n)}(t)$	
v — A	$y_6^{(n)}(t)$	
B — v	$y_7^{(n)}(t)$	
v — B	$y_8^{(n)}(t)$	

As a result of thermal agitation, an atom and a vacancy may interchange places during a small time interval τ. The X's and Y's in Tables 3 and 4 denote probabilities for finding configurations of change. They will be called the *path probability parameters* as distinct from x's and y's, which are the *state probability parameters*. In defining the path probabilities, configurations in which two atomic jumps occur next to each other in the lattice are omitted on the basis that these configurations appear with a probability proportional to τ^2, which is an order of magnitude smaller than those defined in Table 4.

Geometrical considerations lead to the following relations among the probability parameters. First, for a lattice point, $x_i(t)$ and $x_i(t+\tau)$ of Table 1 are expressed by $X_i(t;\tau)$ of Table 3 as

$$\begin{aligned} x_1(t) &= X_1+4(X_4+X_8) \\ x_2(t) &= X_2+4(X_5+X_9) \\ x_3(t) &= X_3+4(X_6+X_7+X_{10}+X_{11}). \end{aligned} \tag{3.3a}$$

$$\begin{aligned} x_1(t+\tau) &= X_1+4(X_6+X_{10}) \\ x_2(t+\tau) &= X_2+4(X_7+X_{11}) \\ x_3(t+\tau) &= X_3+4(X_4+X_5+X_8+X_9). \end{aligned} \tag{3.3b}$$

Table 3. Definition of path parameters $X_i^{(\nu)}$ for a lattice point on the ν^{th} lattice plane for the vacancy mechanism. The vertical arrows are used when there is no change at the point during the time τ. The diagonal arrows indicate interchange of atoms and vacancies. α_i is the number of configurations having the same probability X_i

$(\nu-1)^{\text{th}}$	ν^{th}	$(\nu+1)^{\text{th}}$	Probability	α_i
	A ↓ A		$X_1^{(\nu)}(t;\tau)$	1
	B ↓ B		$X_2^{(\nu)}(t;\tau)$	1
	v ↓ v		$X_3^{(\nu)}(t;\tau)$	1
	A ↘ v ↙		$X_4^{(\nu)}(t;\tau)$	4
	B ↘ v ↙		$X_5^{(\nu)}(t;\tau)$	4
	v ↘ A ↙		$X_6^{(\nu)}(t;\tau)$	4
	v ↘ B ↙		$X_7^{(\nu)}(t;\tau)$	4
	A ↘ ↙ v		$X_8^{(\nu)}(t;\tau)$	4
	B ↘ ↙ v		$X_9^{(\nu)}(t;\tau)$	4
	v ↘ ↙ A		$X_{10}^{(\nu)}(t;\tau)$	4
	v ↘ ↙ B		$X_{11}^{(\nu)}(t;\tau)$	4

In (3.3a), (3.3b), and in the following discussion, unless it is otherwise indicated $x_i(t)$, $y_i(t)$, X_i, and Y_{ij} are for $x_i^{(\nu)}(t)$, $y_i^{(n)}(t)$, $X_i^{(\nu)}(t;\tau)$, and $Y_{ij}^{(n)}(t;\tau)$, respectively. For a bond, the definitions given in Tables 2 and 4 lead to the following relations.

$$
\begin{aligned}
y_1(t) &= Y_{11}+4(Y_{12}+Y_{14})+3(Y_{13}+Y_{15})\\
y_2(t) &= Y_{21}+4(Y_{22}+Y_{24})+3(Y_{23}+Y_{25})\\
y_3(t) &= Y_{31}+4(Y_{32}+Y_{34})+3(Y_{33}+Y_{35})\\
y_4(t) &= Y_{41}+4(Y_{42}+Y_{44})+3(Y_{43}+Y_{45})\\
y_5(t) &= Y_{51}+Y_{56}+4(Y_{52}+Y_{54})+3(Y_{53}+Y_{55})\\
y_6(t) &= Y_{61}+Y_{66}+4(Y_{62}+Y_{64})+3(Y_{63}+Y_{65})\\
y_7(t) &= Y_{71}+Y_{76}+4(Y_{72}+Y_{74})+3(Y_{73}+Y_{75})\\
y_8(t) &= Y_{81}+Y_{86}+4(Y_{82}+Y_{84})+3(Y_{83}+Y_{85})
\end{aligned}
\tag{3.4a}
$$

$$
\begin{aligned}
y_1(t+\tau) &= Y_{11}+4(Y_{52}+Y_{62})+3(Y_{53}+Y_{63})\\
y_2(t+\tau) &= Y_{21}+4(Y_{54}+Y_{82})+3(Y_{55}+Y_{83})\\
y_3(t+\tau) &= Y_{31}+4(Y_{64}+Y_{72})+3(Y_{65}+Y_{73})\\
y_4(t+\tau) &= Y_{41}+4(Y_{74}+Y_{84})+3(Y_{75}+Y_{85})\\
y_5(t+\tau) &= Y_{51}+Y_{66}+4(Y_{12}+Y_{22})+3(Y_{13}+Y_{23})\\
y_6(t+\tau) &= Y_{61}+Y_{56}+4(Y_{14}+Y_{34})+3(Y_{15}+Y_{35})\\
y_7(t+\tau) &= Y_{71}+Y_{86}+4(Y_{32}+Y_{42})+3(Y_{33}+Y_{43})\\
y_8(t+\tau) &= Y_{81}+Y_{76}+4(Y_{24}+Y_{44})+3(Y_{25}+Y_{45})
\end{aligned}
\tag{3.4b}
$$

The relations among X's and Y's are derived from Tables 3 and 4 as

$$
\begin{aligned}
X_1^{(\nu)} &= Y_{11}^{(n)}+Y_{21}+Y_{51}\\
&\quad +4(Y_{12}+Y_{22}+Y_{52}+Y_{54})\\
&\quad +3(Y_{13}+Y_{23}+Y_{53}+Y_{55})\\
X_2^{(\nu)} &= Y_{31}^{(n)}+Y_{41}+Y_{71}\\
&\quad +4(Y_{32}+Y_{42}+Y_{72}+Y_{74})\\
&\quad +3(Y_{33}+Y_{43}+Y_{73}+Y_{75})\\
X_3^{(\nu)} &= Y_{61}^{(n)}+Y_{81}\\
X_4^{(\nu)} &= Y_{56}^{(n)} = Y_{15}^{(n)}+Y_{25}\\
X_5^{(\nu)} &= Y_{76}^{(n)} = Y_{35}^{(n)}+Y_{45}\\
X_6^{(\nu)} &= Y_{66}^{(n)} = Y_{63}^{(n)}+Y_{83}
\end{aligned}
$$

Vol. 2
196

$$
\begin{aligned}
X_7^{(\nu)} &= Y_{86}^{(n)} = Y_{65}^{(n)} + Y_{85} \\
X_8^{(\nu)} &= Y_{14}^{(n)} + Y_{24} \\
X_9^{(\nu)} &= Y_{34}^{(n)} + Y_{44} \\
X_{10}^{(\nu)} &= Y_{62}^{(n)} + Y_{82} \\
X_{11}^{(\nu)} &= Y_{64}^{(n)} + Y_{84}
\end{aligned}
\qquad (3.5a)
$$

$$
\begin{aligned}
X_1^{(\nu+1)} &= Y_{11}^{(n)} + Y_{31} + Y_{61} \\
&\quad + 4(Y_{14} + Y_{34} + Y_{62} + Y_{64}) \\
&\quad + 3(Y_{15} + Y_{35} + Y_{63} + Y_{65}) \\
X_2^{(\nu+1)} &= Y_{21}^{(n)} + Y_{41} + Y_{81} \\
&\quad + 4(Y_{24} + Y_{44} + Y_{82} + Y_{84}) \\
&\quad + 3(Y_{25} + Y_{45} + Y_{83} + Y_{85}) \\
X_3^{(\nu+1)} &= Y_{51}^{(n)} + Y_{71} \\
X_4^{(\nu+1)} &= Y_{12}^{(n)} + Y_{32} \\
X_5^{(\nu+1)} &= Y_{22}^{(n)} + Y_{42} \\
X_6^{(\nu+1)} &= Y_{52}^{(n)} + Y_{72} \\
X_7^{(\nu+1)} &= Y_{54}^{(n)} + Y_{74} \\
X_8^{(\nu+1)} &= Y_{66}^{(n)} = Y_{13}^{(n)} + Y_{33} \\
X_9^{(\nu+1)} &= Y_{86}^{(n)} = Y_{23}^{(n)} + Y_{43} \\
X_{10}^{(\nu+1)} &= Y_{56}^{(n)} = Y_{53}^{(n)} + Y_{73} \\
X_{11}^{(\nu+1)} &= Y_{76}^{(n)} = Y_{55}^{(n)} + Y_{75}
\end{aligned}
\qquad (3.5b)
$$

Among the path parameters previously defined, all the $Y_{ij}^{(n)}$'s, except $Y_{i1}^{(n)}$'s for $i = 1, 2, \ldots, 8$

Table 4. Definition of path parameters $Y_{ij}^{(n)}$ for a bond between the ν^{th} and the $(\nu+1)^{\text{th}}$ planes for the vacancy mechanism. β_{ij} is the number of configurations having the same probability Y_{ij}. Diagonal dotted crossed arrows indicate atomic interchange occurring on an adjacent bond between ν and $\nu+1$ planes. Diagonal solid crossed arrows are for atomic interchange between either $\nu+1$ and $\nu+2$ or $\nu-1$ and ν planes.

(a) ν $\nu+1$	Probability	β_{ij}	(b) ν $\nu+1$	Probability	β_{ij}
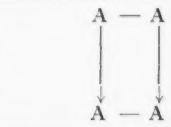	$Y_{11}^{(n)}$	1		$Y_{21}^{(n)}$	1
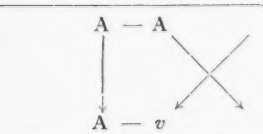	$Y_{12}^{(n)}$	4	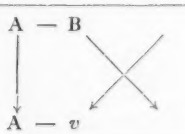	$Y_{22}^{(n)}$	4
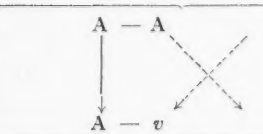	$Y_{13}^{(n)}$	3	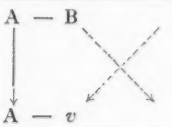	$Y_{23}^{(n)}$	3
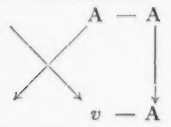	$Y_{14}^{(n)}$	4	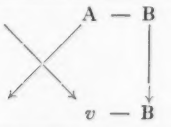	$Y_{24}^{(n)}$	4
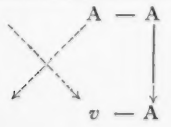	$Y_{15}^{(n)}$	3	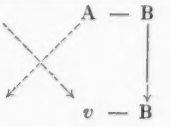	$Y_{25}^{(n)}$	3

Table 4. (Contd.)

(c) ν $\nu+1$	Probability	β_{ij}	(d) ν $\nu+1$	Probability	β_{ij}
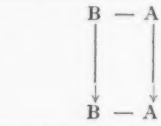	$Y_{31}^{(n)}$	1	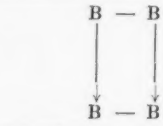	$Y_{41}^{(n)}$	1
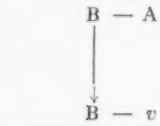	$Y_{32}^{(n)}$	4	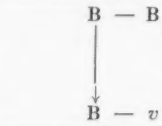	$Y_{42}^{(n)}$	4
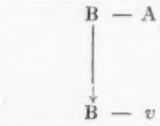	$Y_{33}^{(n)}$	3	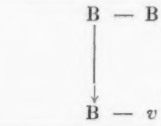	$Y_{43}^{(n)}$	3
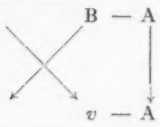	$Y_{34}^{(n)}$	4	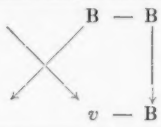	$Y_{44}^{(n)}$	4
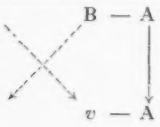	$Y_{35}^{(n)}$	3	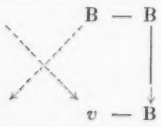	$Y_{45}^{(n)}$	3

$(-\infty < n < \infty)$, will be regarded as independent. The relations existing among the independent parameters as seen in (3.6) necessitate the use of 16 Lagrange multipliers for each value of n when the path probability is maximized with respect to the independent variables in a later section.

The $Y_{i1}^{(n)}$ for $i = 1, \ldots, 8$ are considered as dependent variables and are defined in (3.4a), where $y_i^{(n)}(t)$ are regarded as given. The $X_i^{(\nu)}$ for $i = 1$, 2, and 3 are given from (3.3a), (3.5a), and (3.5b) as

$$X_1^{(\nu)} = x_1^{(\nu)} - 4(Y_{56}^{(n)} + Y_{66}^{(n-1)})$$

$$X_2^{(\nu)} = x_2^{(\nu)} - 4(Y_{76}^{(n)} + Y_{86}^{(n-1)})$$

$$X_3^{(\nu)} = x_3^{(\nu)} - 4(Y_{66}^{(n)} + Y_{86}^{(n)} + Y_{56}^{(n-1)} + Y_{76}^{(n-1)}). \tag{3.6}$$

In order to discuss change of state variables in time t, we introduce the parameters J's:

$$J_A^{(n)} = Y_{56}^{(n)} - Y_{66}^{(n)}$$

$$J_B^{(n)} = Y_{76}^{(n)} - Y_{86}^{(n)}. \tag{3.7}$$

Here $J_A^{(n)}$ denotes the net flux of A atoms through an n^{th} bond toward the positive direction of n. We define the change of state variables as

$$\Delta x_i^{(\nu)}(t;\tau) = x_i^{(\nu)}(t+\tau) - x_i^{(\nu)}(t). \tag{3.8}$$

$\Delta y_i^{(n)}(t;\tau)$ are analogously defined. Use of (3.7), (3.3), and (3.5) leads to

$$\Delta x_1^{(\nu)} = 4(J_A^{(n-1)} - J_A^{(n)})$$

$$\Delta x_2^{(\nu)} = 4(J_B^{(n-1)} - J_B^{(n)}). \tag{3.9}$$

Vol. 2
196

Table 4 (Contd.)

(e) ν $\nu+1$	Probability	β_{ij}	(f) ν $\nu+1$	Probability	β_{ij}
	$Y_{51}^{(n)}$	1	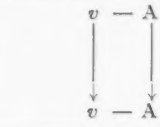	$Y_{61}^{(n)}$	1
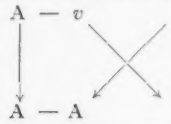	$Y_{52}^{(n)}$	4	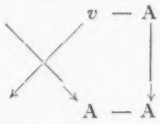	$Y_{62}^{(n)}$	4
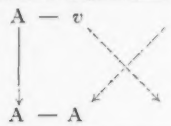	$Y_{53}^{(n)}$	3	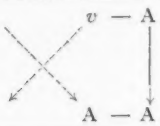	$Y_{63}^{(n)}$	3
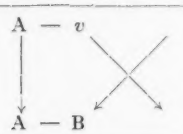	$Y_{54}^{(n)}$	4	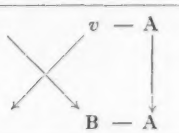	$Y_{64}^{(n)}$	4
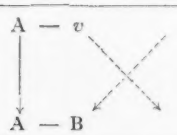	$Y_{55}^{(n)}$	3	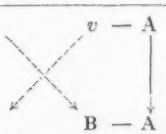	$Y_{65}^{(n)}$	3
	$Y_{56}^{(n)}$	1		$Y_{66}^{(n)}$	1

From (3.4) and (3.5), the change of y_i's are

$$\begin{aligned}
\Delta y_1 &= 4(Y_{52}+Y_{62}-Y_{12}-Y_{14}) \\
&\quad +3(Y_{53}+Y_{63}-Y_{13}-Y_{15}) \\
\Delta y_2 &= 4(Y_{54}+Y_{82}-Y_{22}-Y_{24}) \\
&\quad +3(Y_{55}+Y_{83}-Y_{23}-Y_{25}) \\
\Delta y_3 &= 4(Y_{64}+Y_{72}-Y_{32}-Y_{34}) \\
&\quad +3(Y_{65}+Y_{73}-Y_{33}-Y_{35}) \\
\Delta y_4 &= 4(Y_{74}+Y_{84}-Y_{42}-Y_{44}) \\
&\quad +3(Y_{75}+Y_{85}-Y_{43}-Y_{45}). \qquad (3.10)
\end{aligned}$$

In (3.9) and (3.10), all the quantities are for $(t;\tau)$, and the Y_{ij}'s are for (n). Using (3.2), we can express Δy_i's for $i = 5, \ldots, 8$ as a linear combination of Δx_i's and Δy_i's in (3.10). Further from (3.2) we see that not four but only three of expressions (3.10) are independent. In later sections the notations $(3.9)_0$ and $(3.10)_0$ will be used to indicate equations which are derived from (3.9) and (3.10) by setting $\Delta x_i^{(\nu)}$ and $\Delta y_i^{(n)}$ to zero.

4. PATH PROBABILITY

The recipe for writing the path probability

Table 4 (Contd.)

(g) ν $\nu+1$	Probability	β_{ij}	(h) ν $\nu+1$	Probability	β_{ij}
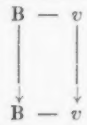	$Y_{71}^{(n)}$	1		$Y_{81}^{(n)}$	1
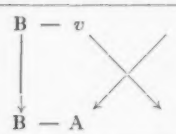	$Y_{72}^{(n)}$	4	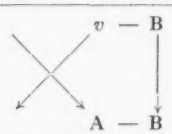	$Y_{82}^{(n)}$	4
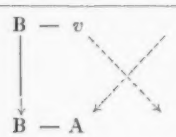	$Y_{73}^{(n)}$	3	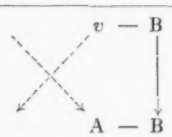	$Y_{83}^{(n)}$	3
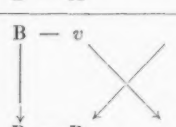	$Y_{74}^{(n)}$	4	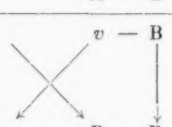	$Y_{84}^{(n)}$	4
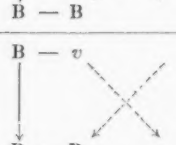	$Y_{75}^{(n)}$	3	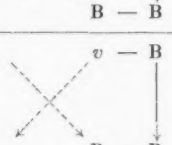	$Y_{85}^{(n)}$	3
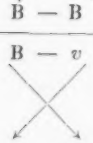	$Y_{76}^{(n)}$	1	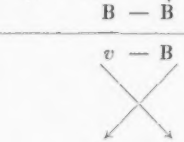	$Y_{86}^{(n)}$	1

$\mathscr{G}(t;\tau)$ was derived in ICP.[10] It says that $\ln \mathscr{G}(t;\tau)$ is made of three terms. The first, $\ln \mathscr{G}_1(t;\tau)$, is the quantum mechanical probability for occurrence of a special path and is written as

$$\ln \mathscr{G}_1(t;\tau) = 4N \sum_{n=-\infty}^{\infty} [(Y_{56}^{(n)} + Y_{66}^{(n)}) \ln(\tau\theta_A^{(n)}) + (Y_{76}^{(n)} + Y_{86}^{(n)}) \ln(\tau\theta_B^{(n)})], \quad (4.1)$$

where N is the number of lattice points in one lattice plane perpendicular to the direction of the concentration gradient. The second term, $\ln \mathscr{G}_2(t;\tau)$, comes from the energy exchange with the heat reservoir and takes the form

$$\ln \mathscr{G}_2(t;\tau) = -[E(t+\tau)-E(t)]/2kT + \text{const.}, \quad (4.2)$$

where $E(t)$ is the energy of the system plus the particle reservoirs at time t, and T is the temperature of the heat bath. Using Table 2, we can write

$$E(t+\tau)-E(t) = 4N \sum_{n=-\infty}^{\infty} [\epsilon_A \Delta y_1^{(n)} + \epsilon_B \Delta y_4^{(n)} + \epsilon_M(\Delta y_2^{(n)} + \Delta y_3^{(n)})] + N \sum_{\nu=-\infty}^{\infty} 3kT[\Delta x_1^{(\nu)} + \Delta x_2^{(\nu)}]. \quad (4.3)$$

It may be noticed here that, because of (3.9), the last term for the kinetic energy does not contribute to the path probability. The third term, $\ln \mathcal{G}_3(t;\tau)$, represents the number of different paths having the same probability and is written using the cluster-variation method:[9,10]

$$\ln \mathcal{G}_3(t;\tau) = N \sum_{n=-\infty}^{\infty} [7 \sum_{i=1}^{11} \alpha_i X_i^{(\nu)} \ln X_i^{(\nu)} - 4 \sum_{i=1}^{8} \sum_j \beta_{ij} Y_{ij}^{(n)} \ln Y_{ij}^{(n)}]. \quad (4.4)$$

The complete path probability $\mathcal{G}$ is readily constructed from the three terms:

$$\ln \mathcal{G}(t;\tau) = \sum_{i=1}^{3} \ln \mathcal{G}_i(t;\tau). \quad (4.5)$$

5. MOST PROBABLE PATH

When the values $x_i(t)$ and $y_i(t)$ at t are given, the most probable values of $x_i(t+\tau)$ and $y_i(t+\tau)$ are derived by maximizing the path probability $\mathcal{G}(t;\tau)$ with respect to the path parameters. As was mentioned in Section III, the number of independent variables Y_{ij} is 36 for each n. Differentiation leads to 36 simultaneous equations, which are to be combined with 16 subsidiary conditions for determining the Lagrange multipliers, for each value of n. Although the number of variables is unusually large, the equations can be handled without difficulty, since when the time interval τ is small it can be safely assumed that the transition probabilities are linear in τ. The results for the most probable path are summarized as follows.

First, we define $\Lambda_i^{(n)}$ and $\Gamma_i^{(n)}$ as

$$\begin{aligned}
\Lambda_1^{(n)} &= K_A y_1^{(n)} + K_M y_3^{(n)} \\
\Lambda_2^{(n)} &= K_A y_1^{(n)} + K_M y_2^{(n)} \\
\Lambda_3^{(n)} &= K_M y_2^{(n)} + K_B y_4^{(n)} \\
\Lambda_4^{(n)} &= K_M y_3^{(n)} + K_B y_4^{(n)}
\end{aligned} \quad (5.1a)$$

$$\begin{aligned}
\Gamma_1^{(n)} &= K_A^{-1} y_5^{(n)} + K_M^{-1} y_7^{(n)} \\
\Gamma_2^{(n)} &= K_A^{-1} y_6^{(n)} + K_M^{-1} y_8^{(n)} \\
\Gamma_3^{(n)} &= K_M^{-1} y_5^{(n)} + K_B^{-1} y_7^{(n)} \\
\Gamma_4^{(n)} &= K_M^{-1} y_6^{(n)} + K_B^{-1} y_8^{(n)},
\end{aligned} \quad (5.1b)$$

where

$$K_A = \exp(\epsilon_A/2kT); \quad (5.2)$$

K_B and K_M are derived from (5.2) when ϵ_A is changed to ϵ_B and ϵ_M, respectively.

Using these quantities, we can write the solutions as

$$\begin{aligned}
&Y_{12}^{(n)} : Y_{32}^{(n)} : Y_{56}^{(n+1)} = Y_{13}^{(n)} : Y_{33}^{(n)} : Y_{66}^{(n)} = K_A y_1^{(n)} : K_M y_3^{(n)} : \Lambda_1^{(n)} \\
&Y_{14}^{(n)} : Y_{24}^{(n)} : Y_{66}^{(n-1)} = Y_{15}^{(n)} : Y_{25}^{(n)} : Y_{56}^{(n)} = K_A y_1^{(n)} : K_M y_2^{(n)} : \Lambda_2^{(n)} \\
&Y_{22}^{(n)} : Y_{42}^{(n)} : Y_{76}^{(n+1)} = Y_{23}^{(n)} : Y_{43}^{(n)} : Y_{86}^{(n)} = K_M y_2^{(n)} : K_B y_4^{(n)} : \Lambda_3^{(n)} \\
&Y_{34}^{(n)} : Y_{44}^{(n)} : Y_{86}^{(n-1)} = Y_{35}^{(n)} : Y_{45}^{(n)} : Y_{76}^{(n)} = K_M y_3^{(n)} : K_B y_4^{(n)} : \Lambda_4^{(n)} \\
&Y_{52}^{(n)} : Y_{72}^{(n)} : Y_{66}^{(n+1)} = Y_{53}^{(n)} : Y_{73}^{(n)} : Y_{56}^{(n)} = K_A^{-1} y_5^{(n)} : K_M^{-1} y_7^{(n)} : \Gamma_1^{(n)} \\
&Y_{62}^{(n)} : Y_{82}^{(n)} : Y_{56}^{(n-1)} = Y_{63}^{(n)} : Y_{83}^{(n)} : Y_{66}^{(n)} = K_A^{-1} y_6^{(n)} : K_M^{-1} y_8^{(n)} : \Gamma_2^{(n)} \\
&Y_{54}^{(n)} : Y_{74}^{(n)} : Y_{86}^{(n+1)} = Y_{55}^{(n)} : Y_{75}^{(n)} : Y_{76}^{(n)} = K_M^{-1} y_5^{(n)} : K_B^{-1} y_7^{(n)} : \Gamma_3^{(n)} \\
&Y_{64}^{(n)} : Y_{84}^{(n)} : Y_{76}^{(n-1)} = Y_{65}^{(n)} : Y_{85}^{(n)} : Y_{86}^{(n)} = K_M^{-1} y_6^{(n)} : K_B^{-1} y_8^{(n)} : \Gamma_4^{(n)}
\end{aligned} \quad (5.3a)$$

$$\begin{aligned}
Y_{56}^{(n)} &= \tau\theta_A^{(n)} y_5^{(n)} (x_1^{(\nu)} x_3^{(\nu+1)})^{-7} (\Lambda_1^{(n-1)} \Gamma_2^{(n+1)})^4 (\Lambda_2^{(n)} \Gamma_1^{(n)})^3 \\
Y_{66}^{(n)} &= \tau\theta_A^{(n)} y_6^{(n)} (x_1^{(\nu+1)} x_3^{(\nu)})^{-7} (\Lambda_2^{(n+1)} \Gamma_1^{(n-1)})^4 (\Lambda_1^{(n)} \Gamma_2^{(n)})^3 \\
Y_{76}^{(n)} &= \tau\theta_B^{(n)} y_7^{(n)} (x_2^{(\nu)} x_3^{(\nu+1)})^{-7} (\Lambda_3^{(n-1)} \Gamma_2^{(n+1)})^4 (\Lambda_4^{(n)} \Gamma_3^{(n)})^3 \\
Y_{86}^{(n)} &= \tau\theta_B^{(n)} y_8^{(n)} (x_2^{(\nu+1)} x_3^{(\nu)})^{-7} (\Lambda_4^{(n+1)} \Gamma_3^{(n-1)})^4 (\Lambda_3^{(n)} \Gamma_4^{(n)})^3.
\end{aligned} \quad (5.3b)$$

In these equations, all the Y's are for $(t;\tau)$ and all the y's and x's are for (t).

Equation (5.3) provides the desired solution of the problem. By combining it with (3.9) and (3.10),

we can trace the change of state of a system starting from any arbitrarily given initial state.

6. DIFFUSION COEFFICIENT

Although in a sense the problem was solved when (5.3) was obtained, our final goal is to derive the expression of the diffusion coefficient. For this purpose, we discuss the stationary state and expand the state variables in terms of the small deviation from equilibrium. This deviation occurs when chemical potential gradients exist across the system.

The stationary state is defined as one in which the state variables $x_i^{(\nu)}$ and $y_i^{(n)}$ are independent of time. For this case, Equation (3.9) leads to the requirement that

$$J_A^{(n)} = J_A \text{ independent of } n,$$
$$J_B^{(n)} = J_B \text{ independent of } n. \tag{6.1}$$

In the stationary state, the $\Delta y_i^{(n)} (i = 1, ..., 4)$ in (3.10) vanish. Let us indicate the equations in which the $\Delta y_i^{(n)}$ of (3.10) are equated to zero by $(3.10)_0$.

Equation (3.10) is transformed in two steps. First (5.3a) and (5.3b) are used to write Y_{ij}'s in terms of y_i's, Λ_i's and Γ_i's. Next, taking into account (3.7) and (6.1), we introduce Y_{i60}'s so as to write

$$\begin{aligned} Y_{56}^{(n)} &= Y_{560}^{(n)} + J_A/2 \\ Y_{66}^{(n)} &= Y_{560}^{(n)} - J_A/2 \\ Y_{76}^{(n)} &= Y_{760}^{(n)} + J_B/2 \\ Y_{86}^{(n)} &= Y_{760}^{(n)} - J_B/2. \end{aligned} \tag{6.2}$$

As was mentioned at the end of Section III, only three out of the four equations of $(3.10)_0$ are independent. We may chose Δy_2, Δy_3, and $\Delta y_1 - \Delta y_4$ and arrive at the following equations:

$$\begin{aligned} &[4Y_{760}^{(n+1)} + 3Y_{760}^{(n)}]\left[\frac{K_M^{-1} y_5^{(n)}}{\Gamma_3^{(n)}} - \frac{K_M y_2^{(n)}}{\Lambda_3^{(n)}}\right] \\ &+ [4Y_{560}^{(n-1)} + 3Y_{560}^{(n)}]\left[\frac{K_M^{-1} y_8^{(n)}}{\Gamma_2^{(n)}} - \frac{K_M y_2^{(n)}}{\Lambda_2^{(n)}}\right] \\ &- \frac{J_B}{2}\left[\frac{K_M^{-1} y_5^{(n)}}{\Gamma_3^{(n)}} + \frac{K_M y_2^{(n)}}{\Lambda_3^{(n)}}\right] + \frac{J_A}{2}\left[\frac{K_M^{-1} y_8^{(n)}}{\Gamma_2^{(n)}} + \frac{K_M y_2^{(n)}}{\Lambda_2^{(n)}}\right] = 0 \end{aligned} \tag{6.3a}$$

$$\begin{aligned} &[4Y_{760}^{(n-1)} + 3Y_{760}^{(n)}]\left[\frac{K_M^{-1} y_6^{(n)}}{\Gamma_4^{(n)}} - \frac{K_M y_3^{(n)}}{\Lambda_4^{(n)}}\right] \\ &+ [4Y_{560}^{(n+1)} + 3Y_{560}^{(n)}]\left[\frac{K_M^{-1} y_7^{(n)}}{\Gamma_1^{(n)}} - \frac{K_M y_3^{(n)}}{\Lambda_1^{(n)}}\right] \\ &+ \frac{J_B}{2}\left[\frac{K_M^{-1} y_6^{(n)}}{\Gamma_4^{(n)}} + \frac{K_M y_3^{(n)}}{\Lambda_3^{(n)}}\right] - \frac{J_A}{2}\left[\frac{K_M^{-1} y_7^{(n)}}{\Gamma_1^{(n)}} + \frac{K_M y_3^{(n)}}{\Lambda_1^{(n)}}\right] = 0 \end{aligned} \tag{6.3b}$$

$$\begin{aligned} &[4Y_{560}^{(n+1)} + 3Y_{560}^{(n)}]\left[\frac{K_A^{-1} y_5^{(n)}}{\Gamma_1^{(n)}} - \frac{K_A y_1^{(n)}}{\Lambda_1^{(n)}}\right] + [4Y_{560}^{(n-1)} + 3Y_{560}^{(n)}]\left[\frac{K_A^{-1} y_6^{(n)}}{\Gamma_2^{(n)}} - \frac{K_A y_1^{(n)}}{\Lambda_2^{(n)}}\right] \\ &- [4Y_{760}^{(n+1)} + 3Y_{760}^{(n)}]\left[\frac{K_B^{-1} y_7^{(n)}}{\Gamma_3^{(n)}} - \frac{K_B y_4^{(n)}}{\Lambda_3^{(n)}}\right] - [4Y_{760}^{(n-1)} + 3Y_{760}^{(n)}]\left[\frac{K_B^{-1} y_8^{(n)}}{\Gamma_4^{(n)}} - \frac{K_B y_4^{(n)}}{\Lambda_4^{(n)}}\right] \end{aligned}$$

$$+\frac{J_A}{2}\left[-\frac{K_A{}^{-1}y_5{}^{(n)}}{\Gamma_1{}^{(n)}}-\frac{K_A y_1{}^{(n)}}{\Lambda_1{}^{(n)}}+\frac{K_A{}^{-1}y_6{}^{(n)}}{\Gamma_2{}^{(n)}}+\frac{K_A y_1{}^{(n)}}{\Lambda_2{}^{(n)}}\right]$$

$$+\frac{J_B}{2}\left[\frac{K_B{}^{-1}y_7{}^{(n)}}{\Gamma_3{}^{(n)}}+\frac{K_B y_4{}^{(n)}}{\Lambda_3{}^{(n)}}-\frac{K_B{}^{-1}y_8{}^{(n)}}{\Gamma_4{}^{(n)}}-\frac{K_B y_4{}^{(n)}}{\Lambda_4{}^{(n)}}\right]=0. \tag{6.3c}$$

Equations (6.1) and (6.3) hold in a stationary state, however steep the gradient may be. They may be regarded as the recurrence equations or difference equations which determine the properties at $n+1$ when those at n and $n-1$ are known. We can solve the whole profile of *state* parameters x's and y's across the system by *integrating* these difference equations using the appropriate procedure when the boundary conditions for the two particle reservoirs are specified. When, however, we are mainly interested in only the diffusion coefficients, it will not be necessary to use such a general process. The short-cut method of deriving these coefficients is to expand (6.1) and (6.3) in terms of local gradients of state variables.

Thus far, we have confined the discussion to the discrete lattice structure of the system. Now we shall relax the restriction and introduce the *continuum approximation*, which assumes that the variation of local properties is gradual enough from plane to plane so that the local state variables can be regarded as continuous functions of position. The local values of chemical potentials for the two atomic species will be denoted by $\alpha_A{}^{(n)}$ and $\alpha_B{}^{(n)}$ and their gradients denoted by $\dot{\alpha}_A{}^{(n)}$ and $\dot{\alpha}_B{}^{(n)}$ where the dot indicates a derivative with respect to n. (As will be seen in the Appendix, $\alpha_A{}^{(n)}$ and $\alpha_B{}^{(n)}$ are defined as the ordinary chemical potential divided by kT, but for convenience we shall call $\alpha_A{}^{(n)}$ the "chemical potential".) The local values $\alpha_A{}^{(n)}$ and $\alpha_B{}^{(n)}$ are defined as the value of chemical potentials in an equilibrium system specified by the same atomic composition as that at the location of present interest. Now the local state variables $x_i{}^{(\nu)}$ and $y_i{}^{(n)}$ in (6.1) and (6.3) are regarded as functions of local values of chemical potentials and their derivatives, $\alpha_A{}^{(n)}$, $\dot{\alpha}_A{}^{(n)}$, etc., and they will be written as

$$y_i{}^{(n)}=y_{ie}{}^{(n)}+\delta y_i{}^{(n)}. \tag{6.4}$$

Here $y_{ie}{}^{(n)}$ is the value of $y_i{}^{(n)}$ with no chemical potential gradients, and $\delta y_i{}^{(n)}$ is expected to be a linear combination of $\dot{\alpha}^{(n)}$'s when the latter quantities are small. This technique of expansion in terms of deviation from local equilibrium was first introduced by KIKUCHI and CAHN in their work on the structure of phase boundaries.[11] When $x_i{}^{(\nu)}$ and $y_i{}^{(n)}$ occur in the same equation, the former is expanded around the point n by using the relation (2.1) for ν and n:

$$x_i{}^{(\nu)}=x_i{}^{(n)}-\tfrac{1}{2}\dot{x}_i{}^{(n)}+\ldots. \tag{6.5}$$

In accordance with the expansions (6.4) and (6.5), Equations (6.1) and (6.3) are regarded as being made of the zeroth order and first order terms with respect to the deviations δ's. In (6.3), $Y_{i60}{}^{(n)}$ and $Y_{i60}{}^{(n+1)}$ differ only by the amount of the order of the deviations. Therefore, the zeroth order equations derivable from (6.3a) and (6.4b) are

$$Y_{760}{}^{(n)}\left[\frac{K_M{}^{-1}y_{5e}{}^{(n)}}{\Gamma_{3e}{}^{(n)}}-\frac{K_M y_{2e}{}^{(n)}}{\Lambda_{3e}{}^{(n)}}\right]+Y_{560}{}^{(n)}\left[\frac{K_M{}^{-1}y_{8e}{}^{(n)}}{\Gamma_{2e}{}^{(n)}}-\frac{K_M y_{2e}{}^{(n)}}{\Lambda_{2e}{}^{(n)}}\right]=0$$

$$Y_{760}{}^{(n)}\left[\frac{K_M{}^{-1}y_{6e}{}^{(n)}}{\Gamma_{4e}{}^{(n)}}-\frac{K_M y_{3e}{}^{(n)}}{\Lambda_{4e}{}^{(n)}}\right]+Y_{560}{}^{(n)}\left[\frac{K_M{}^{-1}y_{7e}{}^{(n)}}{\Gamma_{1e}{}^{(n)}}-\frac{K_M y_{3e}{}^{(n)}}{\Lambda_{1e}{}^{(n)}}\right]=0, \tag{6.6}$$

where the subscript e indicates the zeroth order quantity. The equilibrium properties of the system are derivable from (6.6); This is shown as follows.

In (6.6), quantities in square brackets are *state*

variables, while $Y_{i60}^{(n)}$'s depend on θ's and are *path* quantities; thus, all of the square brackets vanish individually to yield

$$\frac{\Lambda_{1\varepsilon}^{(n)}}{\Gamma_{1\varepsilon}^{(n)}} = \frac{K_M y_{3\varepsilon}^{(n)}}{K_M^{-1} y_{7\varepsilon}^{(n)}} = \frac{K_A y_{1\varepsilon}^{(n)}}{K_A^{-1} y_{5\varepsilon}^{(n)}}$$

$$\frac{\Lambda_{2\varepsilon}^{(n)}}{\Gamma_{2\varepsilon}^{(n)}} = \frac{K_M y_{2\varepsilon}^{(n)}}{K_M^{-1} y_{8\varepsilon}^{(n)}} = \frac{K_A y_{1\varepsilon}^{(n)}}{K_A^{-1} y_{6\varepsilon}^{(n)}}$$

$$\frac{\Lambda_{3\varepsilon}^{(n)}}{\Gamma_{3\varepsilon}^{(n)}} = \frac{K_M y_{2\varepsilon}^{(n)}}{K_M^{-1} y_{5\varepsilon}^{(n)}} = \frac{K_B y_{4\varepsilon}^{(n)}}{K_B^{-1} y_{7\varepsilon}^{(n)}}$$

$$\frac{\Lambda_{4\varepsilon}^{(n)}}{\Gamma_{4\varepsilon}^{(n)}} = \frac{K_M y_{3\varepsilon}^{(n)}}{K_M^{-1} y_{6\varepsilon}^{(n)}} = \frac{K_B y_{4\varepsilon}^{(n)}}{K_B^{-1} y_{8\varepsilon}^{(n)}}, \qquad (6.7)$$

where the expressions at the far right follow from (5.1). Equation (6.7) automatically satisfies the zeroth order equation derived from (6.3c). The zeroth order terms of (3.7) combined with (6.1) give

$$Y_{56\varepsilon}^{(n)} = Y_{66\varepsilon}^{(n)}$$
$$Y_{76\varepsilon}^{(n)} = Y_{86\varepsilon}^{(n)}. \qquad (6.8)$$

The $Y_{56\varepsilon}^{(n)}$ in this equation may not be the same as $Y_{560}^{(n)}$ introduced in (6.2), but the difference is of the first order.

It is easy to show that (6.7) and (6.8) are equivalent to those equations derived in the Appendix directly from minimization of *state* free energy. The immediate consequence of this equivalence is that

$$y_{2\varepsilon}^{(n)} = y_{3\varepsilon}^{(n)},\ y_{5\varepsilon}^{(n)} = y_{6\varepsilon}^{(n)},\ y_{7\varepsilon}^{(n)} = y_{8\varepsilon}^{(n)}. \qquad (6.9)$$

As for Λ's and Γ's, it is convenient to introduce the following parameter Ω's:

$$\Omega_A^{(n)} = q_A^{(n)} K_A^{-1} + q_B^{(n)} K_M^{-1}$$
$$\Omega_B^{(n)} = q_A^{(n)} K_M^{-1} + q_B^{(n)} K_B^{-1}, \qquad (6.10)$$

where q_A and q_B are the equilibrium quantities introduced in (A.3). Using (6.10), we can write

$$\Lambda_{1\varepsilon}^{(n)} = \Lambda_{2\varepsilon}^{(n)} = q_{A\varepsilon}^{(n)} \Omega_{A\varepsilon}^{(n)}$$
$$\Lambda_{3\varepsilon}^{(n)} = \Lambda_{4\varepsilon}^{(n)} = q_{B\varepsilon}^{(n)} \Omega_{B\varepsilon}^{(n)}$$
$$\Gamma_{1\varepsilon}^{(n)} = \Gamma_{2\varepsilon}^{(n)} = \lambda_\varepsilon^{(n)} \Omega_{A\varepsilon}^{(n)}$$
$$\Gamma_{3\varepsilon}^{(n)} = \Gamma_{4\varepsilon}^{(n)} = \lambda_\varepsilon^{(n)} \Omega_{B\varepsilon}^{(n)}. \qquad (6.11)$$

Here λ is also the equilibrium quantity introduced in the Appendix. Using these relations for (5.3b), we can write for (6.8)

$$Y_{56\varepsilon}^{(n)} = \tau\theta_A^{(n)} y_{5\varepsilon}^{(n)} [y_{5\varepsilon}^{(n)} (\Omega_{A\varepsilon}^{(n)})^2 / (x_{1\varepsilon}^{(n)} x_{3\varepsilon}^{(n)})]^7$$
$$Y_{76\varepsilon}^{(n)} = \tau\theta_B^{(n)} y_{7\varepsilon}^{(n)} [y_{7\varepsilon}^{(n)} (\Omega_{B\varepsilon}^{(n)})^2 / (x_{2\varepsilon}^{(n)} x_{3\varepsilon}^{(n)})]^7. \qquad (6.12)$$

From the first order terms of (6.3a), (6.3b), (6.3c) and (3.2), we derive

$$\delta y_1^{(n)} = \delta(y_2^{(n)} + y_3^{(n)}) = \delta y_4^{(n)}$$
$$= \delta(y_5^{(n)} + y_6^{(n)}) = \delta(y_7^{(n)} + y_8^{(n)}) = 0, \qquad (6.13)$$

where we used the fact that

$$x_1^{(\nu)} + x_1^{(\nu+1)} = 2x_1^{(n)} + O(\ddot{x}_1^{(n)}), \qquad (6.14)$$

which follows from (6.5). The relations in (6.13) were anticipated because $y_1^{(n)}$, $y_2^{(n)} + y_3^{(n)}$, $y_4^{(n)}$, $y_5^{(n)} + y_6^{(n)}$, and $y_7^{(n)} + y_8^{(n)}$ are symmetric with respect to the reversal of the direction of gradients. Thus, the nontrivial first order equation derived from (6.3) is as follows:

$$\frac{7Y_{760}^{(n)}}{\Lambda_{3\varepsilon}^{(n)}} \delta \ln \frac{y_5^{(n)} \Lambda_3^{(n)}}{y_2^{(n)} \Gamma_3^{(n)}} + \frac{7Y_{560}^{(n)}}{\Lambda_{2\varepsilon}^{(n)}} \delta \ln \frac{y_8^{(n)} \Lambda_2^{(n)}}{y_2^{(n)} \Gamma_2^{(n)}} - \frac{J_B}{\Lambda_{3\varepsilon}^{(n)}} + \frac{J_A}{\Lambda_{2\varepsilon}^{(n)}} = 0, \qquad (6.15)$$

where the δ notation denotes the deviation from equilibrium values similar to that used in (6.4). The J's in (6.15) can be expressed in δ's from the first order terms of (3.7) combined with (6.1):

$$J_A = Y_{56\varepsilon}^{(n)} \delta \ln(Y_{56}^{(n)} / Y_{66}^{(n)})$$
$$J_B = Y_{76\varepsilon}^{(n)} \delta \ln(Y_{76}^{(n)} / Y_{86}^{(n)}). \qquad (6.16)$$

Equation (6.15), with J's replaced by (6.16), is regarded as determining $\delta y_2^{(n)}$ in terms of chemical potential gradients $\dot{\alpha}$'s. We then use the δy_2 thus obtained in (6.16) to arrive at the linear relations between J's and $\dot{\alpha}$'s.

The δ operation in (6.16) works as the ordinary differentiation. From (6.16) and (5.3b), using relations derived in the Appendix, we have

$$J_A / Y_{56\varepsilon}^{(n)} = -\dot{\alpha}_A^{(n)} + 2\delta \ln(y_5^{(n)} \Lambda_1^{(n)} / \Gamma_1^{(n)})$$
$$J_B / Y_{76\varepsilon}^{(n)} = -\dot{\alpha}_B^{(n)} + 2\delta \ln(y_7^{(n)} \Lambda_3^{(n)} / \Gamma_3^{(n)}) \qquad (6.17)$$

In deriving (6.17), we used relations like

$$\delta \ln \Lambda_1^{(n+1)} = \delta \ln \Lambda_1^{(n)} + \frac{d}{dn} \ln \Lambda_{1e}^{(n)} \quad (6.18)$$

When we substitute (6.17) in (6.15) and rearrange terms, we use the relations

$$\begin{aligned} \delta \ln y_8^{(n)} &= -\delta \ln y_7^{(n)} \\ \delta \ln \Gamma_2^{(n)} &= -\delta \ln \Gamma_1^{(n)} \\ \delta \ln \Lambda_2^{(n)} &= -\delta \ln \Lambda_1^{(n)}, \end{aligned} \quad (6.19)$$

which follow from (6.13), (5.1), and (6.11). We also introduce the notation

$$\Phi^{(n)} = \delta \ln(y_5^{(n)} / y_2^{(n)} y_7^{(n)}) \quad (6.20)$$

and write (6.15) as

$$\frac{Y_{56e}^{(n)}}{\Lambda_{1e}^{(n)}} [7\Phi^{(n)} - 5\delta \ln(y_5^{(n)} \Lambda_1^{(n)} / \Gamma_1^{(n)}) - \dot{\alpha}_A^{(n)}] + \frac{Y_{76e}^{(n)}}{\Lambda_{3e}^{(n)}} [7\Phi^{(n)} + 5\delta \ln(y_7^{(n)} \Lambda_3^{(n)} / \Gamma_3^{(n)}) + \dot{\alpha}_B^{(n)}] = 0. \quad (6.21)$$

Now, use of (5.1), (6.10), (6.11), (6.13) and the Appendix leads to

$$\begin{aligned} \delta \ln(y_5^{(n)} \Lambda_1^{(n)} / \Gamma_1^{(n)}) &= \Phi^{(n)} q_{Be}^{(n)} K_M^{-1} / \Omega_{Ae}^{(n)} \\ \delta \ln(y_7^{(n)} \Lambda_3^{(n)} / \Gamma_3^{(n)}) &= -\Phi^{(n)} q_{Ae}^{(n)} K_M^{-1} / \Omega_{Be}^{(n)}, \end{aligned} \quad (6.22)$$

which allows (6.17) to be written as

$$\begin{aligned} J_A &= Y_{56e}^{(n)} [-\dot{\alpha}_A^{(n)} + 2\Phi^{(n)} q_{Be}^{(n)} K_M^{-1} / \Omega_{Ae}^{(n)}] \\ J_B &= Y_{76e}^{(n)} [-\dot{\alpha}_B^{(n)} - 2\Phi^{(n)} q_{Ae}^{(n)} K_M^{-1} / \Omega_{Be}^{(n)}]. \end{aligned} \quad (6.23a)$$

For $\Phi^{(n)}$ in (6.23a), we use the expression solved from (6.21) and (6.22):

$$\Phi^{(n)} = \frac{1}{\Delta_1^{(n)}} \left[\frac{Y_{56e}^{(n)}}{\Lambda_{2e}^{(n)}} \dot{\alpha}_A^{(n)} - \frac{Y_{76e}^{(n)}}{\Lambda_{3e}^{(n)}} \dot{\alpha}_B^{(n)} \right] \quad (6.23b)$$

with

$$\Delta_1^{(n)} = Y_{56}^{(n)} (7K_A y_{1e}^{(n)} + 2K_M y_{2e}^{(n)}) / (\Lambda_{1e}^{(n)})^2 + Y_{76}^{(n)} (7K_B y_{4e}^{(n)} + 2K_M y_{2e}^{(n)}) / (\Lambda_{3e}^{(n)})^2. \quad (6.23c)$$

Equations (6.23) give the general expression for the linear relation between the fluxes and the chemical potential gradients. It is easy to see with the aid of (6.11) that (6.23a) satisfies ONSAGER's reciprocal relation[12] as is expected: the coefficient of $\dot{\alpha}_B^{(n)}$ in J_A is equal to that of $\dot{\alpha}_A^{(n)}$ in J_B. It would be worthwhile to repeat here the meaning of some of the quantities used in these expressions: J_A is the net flux of A atoms through a bond, and since the state is stationary, J_A is the same for all bonds. $Y_{56e}^{(n)}$ is derived from (5.3b) and is written in (6.12), where $\theta_A^{(n)}$ is the quantum mechanical probability for interchange of an A atom with a vacancy as discussed in (2.2). $y_{1e}^{(n)}$, $x_{1e}^{(n)}$, $q_{Ae}^{(n)}$, etc., are local equilibrium values of the corresponding quantities and they satisfy relations in the Appendix. Ω's are defined in (6.10), and K's in (5.2). α_A is the reduced chemical potential, i.e. the chemical potential divided by kT for an A atom. The dot above α_A indicates a derivative with respect to n, which is the distance (measured in units of the interplanar distance) along the gradient of the chemical potential.

For further discussion, it seems convenient to use the auxiliary variables $s^{(n)}$ introduced in the Appendix. Because of the relations

$$\begin{aligned} K_M^{-1} q_B^{(n)} / \Omega_A^{(n)} &= \exp(-s^{(n)} + w_B) \operatorname{sech}(s^{(n)} - w_B) \\ K_M^{-1} q_{Ae}^{(n)} / \Omega_B^{(n)} &= \exp(s^{(n)} + w_A) \operatorname{sech}(s^{(n)} + w_A) \end{aligned} \quad (6.24)$$

which come from the Appendix, with w's defined in (A.9), we can express (6.23) as follows:

$$\begin{aligned} J_A &= -Y_{56e}^{(n)} [\dot{\alpha}_A^{(n)} - 2\Phi^{(n)} \exp(-s^{(n)} + w_B) \operatorname{sech}(s^{(n)} - w_B)] \\ J_B &= -Y_{76e}^{(n)} [\dot{\alpha}_B^{(n)} + 2\Phi^{(n)} \exp(s^{(n)} + w_A) \operatorname{sech}(s^{(n)} + w_A)], \end{aligned} \quad (6.25a)$$

where

$$\Phi^{(n)} = [Y_{56e}^{(n)} \dot{\alpha}_A^{(n)} \exp(-s^{(n)} + w_B) \operatorname{sech}(s^{(n)} - w_B) - Y_{76e}^{(n)} \dot{\alpha}_B^{(n)} \exp(s^{(n)} + w_A) \operatorname{sech}(s^{(n)} + w_A)] / \Delta_2^{(n)} \quad (6.25b)$$

and

$$\Delta_2^{(n)} = Y_{56e}^{(n)}[7+2\exp(-2s^{(n)}+2w_B)]\,\mathrm{sech}^2(s^{(n)}-w_B)+Y_{76e}^{(n)}[7+2\exp(2s^{(n)}+2w_A)]\,\mathrm{sech}^2(s^{(n)}+w_A). \tag{6.25c}$$

From (6.12)

$$Y_{56e}^{(n)} = \tau\theta_A^{(n)}\frac{x_3^{(n)}}{2}\frac{\exp(s^{(n)}+w_A-w_B)}{\cosh(s^{(n)}+w_A-w_B)}\times\left[\frac{1-2x_3^{(n)}}{x_1^{(n)}}\frac{\exp(s^{(n)}+w_A+w_B)\cosh^2(s^{(n)}-w_B)}{[e^{2(w_A+w_B)}+\cosh(2s^{(n)})]\cosh(s^{(n)}+w_A-w_B)}\right]^7$$

$$Y_{76e}^{(n)} = \tau\theta_B^{(n)}\frac{x_3^{(n)}}{2}\frac{\exp(-s^{(n)}-w_A+w_B)}{\cosh(s^{(n)}+w_A-w_B)}\times\left[\frac{1-2x_3^{(n)}}{x_2^{(n)}}\frac{\exp(-s^{(n)}+w_A+w_B)\cosh^2(s^{(n)}+w_A)}{[e^{2(w_A+w_B)}+\cosh(2s^{(n)})]\cosh(s^{(n)}+w_A-w_B)}\right]^7. \tag{6.26}$$

Equations (6.23) or (6.25) give the general law of diffusion in binary systems for any value of the concentration. However, in applying the equations it should be kept in mind that the jumping probabilities θ_A and θ_B can and probably do, sometimes strongly, depend on the concentration, and also that the possible dependence of θ_A on the configuration of atoms surrounding the atom making a jump is neglected in this paper.

7. SELF-DIFFUSION

The simplest application of (6.23) is the self diffusion, which occurs when A and B atoms are isotopes. Since the chemical properties of A and B atoms are the same, we have

$$\epsilon_A = \epsilon_M = \epsilon_B$$

and

$$K_A = K_M = K_B. \tag{7.1}$$

Also, for the unit jump

$$\theta_A^{(n)} = \theta_B^{(n)} \equiv \theta^{(n)}. \tag{7.2}$$

When these relations are used on the equations in the previous section it is easy to derive the following results. Equation (6.23) combined with (6.26) may be written as

$$\begin{aligned} 4J_A &= -\tau(D_A^{(n)}x_1^{(n)}\dot{\alpha}_A^{(n)}+D_M^{(n)}x_2^{(n)}\dot{\alpha}_B^{(n)}) \\ 4J_B &= -\tau(D_M^{(n)}x_2^{(n)}\dot{\alpha}_A^{(n)}+D_B^{(n)}x_2^{(n)}\dot{\alpha}_B^{(n)}), \end{aligned} \tag{7.3}$$

where the coefficients are now

$$D_A^{(n)} = \tfrac{4}{9}x_3^{(n)}\Theta^{(n)}\left[7+\frac{2x_1^{(n)}}{x_1^{(n)}+x_2^{(n)}}\right]$$

$$D_M^{(n)} = \tfrac{4}{9}x_3^{(n)}\Theta^{(n)}\frac{2x_1^{(n)}}{x_1^{(n)}+x_2^{(n)}}$$

$$D_B^{(n)} = \tfrac{4}{9}x_3^{(n)}\Theta^{(n)}\left[7+\frac{2x_2^{(n)}}{x_1^{(n)}+x_2^{(n)}}\right] \tag{7.4}$$

with

$$\Theta^{(n)} = \frac{\theta^{(n)}}{1-x_3^{(n)}}\left[1-\frac{x_3^{(n)}}{1-x_3^{(n)}}\right]^7 \tag{7.5}$$

The sum of the two fluxes in (7.3) is

$$J_A+J_B = -\tau x_3^{(n)}\Theta^{(n)}[x_1^{(n)}\dot{\alpha}_A^{(n)}+x_2\dot{\alpha}_B^{(n)}] \tag{7.6}$$

The Gibbs–Duhem relation states that the last factor is related to the change of local pressure when the temperature is constant:

$$x_1^{(n)}\dot{\alpha}_A^{(n)}+x_2^{(n)}\dot{\alpha}_B^{(n)} = -v\dot{p}^{(n)}/kT, \tag{7.7}$$

where v is the volume of a unit cell and $p^{(n)}$ is the local pressure in the n^{th} bond.

If the two particle reservoirs are so chosen that in the stationary state

$$J_A+J_B = 0, \tag{7.8}$$

the last three equations require that the internal pressure is everywhere the same. This is the condition of ordinary self-diffusion experiments. When (7.7) vanishes, equation (A.7) gives

$$\dot{x}_3^{(n)} = 0, \tag{7.9}$$

which when inserted into (A.7) again gives

$$\dot{\alpha}_A^{(n)} = -\dot{x}_2^{(n)}/x_1^{(n)} \text{ and } \dot{\alpha}_B^{(n)} = \dot{x}_2^{(n)}/x_2^{(n)}. \tag{7.10}$$

Vol. 2
196

Use of (7.10) in (7.3) leads to

$$4J_B = -4J_A = -\tau[D_A^{(n)} - D_M^{(n)}]\dot{x}_2^{(n)}. \tag{7.11}$$

The diffusion constant D_B^* for B atoms is defined as

$$4J_B = -\tau D_B^* \dot{x}_2^{(n)}, \tag{7.12}$$

where 4 in front of J_B comes from the four bonds connecting a lattice point with its four neighbors on an adjacent plane. From (7.12), (7.11), and (7.4), we obtain

$$D_B^* = D_A^{(n)} - D_M^{(n)} = \frac{28}{9}\frac{\theta^{(n)} x_3^{(n)}}{1-x_3^{(n)}}\left[1 - \frac{x_3^{(n)}}{1-x_3^{(n)}}\right]^7. \tag{7.13}$$

Under ordinary circumstances, the concentration of vacancies $x_3^{(n)}$ is less than 10^{-3} so that we can safely write

$$D_B^* = \tfrac{28}{9}\theta^{(n)} x_3^{(n)}. \tag{7.14}$$

BARDEEN and HERRING[5] estimated the error when $D_A^{(n)}$ is used for D_B^*. In our case, equations (7.4) and (7.13) lead to

$$\frac{D_B^*}{D_A} = 7\left[7 + \frac{2x_1^{(n)}}{1-x_3^{(n)}}\right]^{-1}. \tag{7.15}$$

This quantity is called the correlation factor f by LECLAIRE and LIDIARD[13] and has been studied extensively by COMPAAN and HAVEN[14]. Their value, which was confirmed recently by SCHOEN and LOWEN[15], is

$$f = 0{\cdot}727 \tag{7.16}$$

for the b.c.c. lattice. The present expression (7.15) leads to

$$f = 7/9 \tag{7.17}$$

when the reasonable substitutions, $x_3^{(n)} \ll 1$ and $x_1^{(n)} \approx 1$, are made. The value in (7.16) is more accurate than our 7/9, which is based on the cluster variation approximation.

It should be pointed out that (7.17) agrees with the known value[16] of the correlation factor derived by counting the nearest neighbor correlations but neglecting the farther correlations. It may also be worth noting that the diffusion coefficient D_B^* is sometimes[17] written as

$$D_B^* = r^2\Gamma f/6, \tag{7.18}$$

where r is the distance moved by the atom in each jump (nearest neighbor distance), Γ the average number of jumps made by each isotopic atom in unit time, and f the correlation factor. In our notation

$$r = \sqrt{3}$$
$$\Gamma = 8x_3^{(n)}\theta^{(n)}. \tag{7.19}$$

The present result (7.14) agrees with (7.18) when (7.19) and (7.17) are substituted in it.

8. DILUTE DIFFUSION

Another case of practical interest occurs when the concentration of diffusion particles is very small. The case in which the concentration of B atoms is small is expressed mathematically by the condition that $s^{(n)}$ is very large:

$$\exp(s^{(n)}) \gg 1,$$
$$s^{(n)} \gg w_A + w_B, \qquad w_A - w_B. \tag{8.1}$$

This requirement combined with (A.12) leads to

$$\frac{x_2^{(n)}}{x_1^{(n)}} = \exp[-2(s^{(n)} - w_A - w_B)]. \tag{8.2}$$

When w_A and w_B are arbitrary, in contrast with the case of self-diffusion, we cannot choose the stationary values of fluxes J_A and J_B such that the Gibbs–Duhem relation holds everywhere in the system. This means that even when the two particle reservoirs are under the same pressure, the local internal pressure in the steady state varies along the direction of particle flow. Thus, rigorously speaking, the local pressure and its gradient can be determined only by solving the complete two-boundary-value problem including the system and the two reservoirs.

For practical purposes, however, if the two particle reservoirs are under the same pressure, we may expect that the local pressure of the system would not be too far from the reservoir pressure or that the local pressure gradient would not be large. If this is the case, we may use the Gibbs–Duhem relation as a tolerable approximation.

When we accept this approximation, the diffusion constant $D_B^{*(n)}$ for the B atoms is defined by (7.12). When (8.1) is the case, equation (A.13) gives

$$\dot{\alpha}_B^{(n)} = \frac{\dot{x}_2^{(n)}}{x_2^{(n)}} + \ldots \tag{8.3}$$

so that the Gibbs–Duhem relation, (7.10) and (7.3) give the expression

$$D_B{}^{*(n)} = D_{BB}{}^{(n)} - D_{AB}{}^{(n)} \frac{x_2{}^{(n)}}{x_1{}^{(n)}}. \qquad (8.4)$$

For $D_{BB}{}^{(n)}$ and $D_{AB}{}^{(n)}$ we must use the corresponding coefficients in (6.25) rather than the simplified expressions in (7.3). After expansion in terms of $\exp(-s^{(n)})$, and assuming $x_3{}^{(n)} \ll 1$, we arrive at the result;

$$D_B{}^{*(n)} = 28 x_3{}^{(n)} \frac{\theta_A \theta_B \exp(-4w_A)}{7\theta_A + 2\theta_B \exp(-2w_A)}. \qquad (8.5)$$

It should be noted here that the diffusion coefficient $D_B{}^{*(n)}$ for the B atoms critically depend on θ_A, i.e. the quantum mechanical jumping probability for A atoms. It is interpreted on a physical basis as follows.

If $\theta_A \gg \theta_B$, then when a vacancy happens to occur next to a B atom it is highly probable that the vacancy will migrate away from the B atom before the latter jumps into the vacancy, thus causing a small diffusion coefficient for B proportional to θ_B. If $\theta_A \ll \theta_B$, then a B atom will interchange position very rapidly with a vacancy which happens to lie next to it, but this B-atom–vacancy pair will not migrate rapidly because interchanges of positions between the vacancy and surrounding A atoms are necessary for any mass motion of the B-atom–vacancy pair. Thus the rate determining factor in this case is θ_A.

The factor $\exp(-4w_A) = \exp(\epsilon_M - \epsilon_A)/kT$ in (8.5) can be interpreted as follows. This factor is larger when $\epsilon_M \gg \epsilon_A$. If this is the case, it would be difficult to break a B-atom–vacancy pair once it is formed because, in effect, an A–A bond has to be changed to an A–B bond in breaking the pair. This leads to a similar situation when $\theta_A \ll \theta_B$ and the migration of B atoms is controlled by θ_A. If on the other hand $\epsilon_M \ll \epsilon_A$, even when a vacancy happens to lie next to a B atom the former will quickly drift away, since the conversion of an A–A bond into an A–B bond is an easy process. Hence this case is similar to $\theta_A \gg \theta_B$.

Equation (8.5) has an apparent resemblance to those derived previously[13,16] and the above interpretation of the equation is based on the same physical observation as proposed before.[13] It may be emphasized here, however, that one of the essentially new features of the present paper, and consequently of equation (8.5), is that the interaction with the heat bath is taken into account correctly for the first time.

It is probably worth pointing out here that θ_A in (8.5) is the same as θ_A appearing in the self-diffusion expression (7.14), whereas θ_B in (8.5) is not necessarily the same as θ_B used in the expression for the self-diffusion of B-atoms. The reason for this second point is that the probability for a unit jump depends on the surrounding atoms and θ_B in (8.5) is for the case in which a B atom exists along in the matrix of A atoms, whereas θ_B used in the self-diffusion expression of B atoms is for the case in which all the atoms are B atoms.

9. SUMMARY

The method of treating diffusion of atoms in crystals developed in the first paper of this series[1] is applied to the case of the vacancy mechanism of atomic migration in substitutional alloys. The method is used on a binary system including vacancies of a b.c.c. structure in which the gradients of chemical potentials are along a [100] direction. The system is isothermal and a flow of atoms is maintained by two particle reservoirs of different chemical potentials placed at the two ends of the system. First, the path probability $\mathscr{G}$ is written in terms of the path parameters by using the pair approximation of the cluster-variation method and following the recipe previously proposed by the author.[10] The most probable change of state is derived by maximizing $\mathscr{G}$ with respect to the path parameters.

The relations between the atomic fluxes and the gradients of chemical potentials are derived for the stationary state. ONSAGER's reciprocal relation holds. The limiting case of no chemical potential gradient is identical with the state derived from the equilibrium theory.

When the pressure gradient in the system is neglected, the diffusion coefficient for B atoms in the matrix of A atoms is given as

$$D_B{}^* = 28 x_3 \frac{\theta_A \theta_B \exp(\epsilon_M - \epsilon_A)/kT}{7\theta_A + 2\theta_B \exp(\epsilon_M - \epsilon_A)/2kT}, \qquad (9.1)$$

where x_3 is the mole fraction of vacancies in the lattice, θ_A is the probability per unit time for a unit jump of an A atom into an adjacent vacancy,

Vol. 2
196

and ϵ_M and ϵ_A are potential energies for an A–B and A–A pair respectively. By setting $\theta_A = \theta_B$ and $\epsilon_M = \epsilon_A$, the self-diffusion coefficient for A atoms is derived as

$$D^* = (28/9)x_3\theta_A. \tag{9.2}$$

REFERENCES

1. KIKUCHI R., *Ann. Phys., Paris* **11,** 306 (1960). This paper will be cited as SDD I.
2. SEITZ F., *Phase Transformations in Solids*, Chapter 4. John Wiley, New York (1951).
3. KIRKENDALL E. O., *Trans. Amer. Inst. Min. (Metall.) Engrs.* **147,** 104 (1942). See also SMIGELSKAS A. D. and KIRKENDALL E. O., *Trans. Amer. Inst. Min. (Metall.) Engrs.* **171,** 130 (1947).
4. SEITZ F., *Acta Cryst., Camb.* **3,** 355 (1950); *Phys. Rev.* **74,** 1513 (1948).
5. BARDEEN J. and HERRING C., *Imperfections in Nearly Perfect Crystals*, Chapter 10. John Wiley, New York (1952).
6. HUNTINGTON H. B. and SEITZ F., *Phys. Rev.* **61,** 315, 325 (1942).
7. LECLAIRE A. D., *Progress in Metal Physics*, Vol. IV, Chapter 6. Interscience, New York (1953).
8. SHEWMON P. C. and BECHTOLD J. H., *Acta Met.* **3,** 452 (1955).
9. KIKUCHI R., *Phys. Rev.* **81,** 988 (1951).
10. KIKUCHI R., *Ann. Phys., Paris* **10,** 127 (1960). This paper will be referred to as ICP hereafter.
11. CAHN J. W. and KIKUCHI R., *Bull. Amer. Phys. Soc.* (ser. 2) **4,** 182 (1959).
12. ONSAGER L., *Phys. Rev.* **37,** 405 (1931); **38,** 2265 (1931).
13. LECLAIRE A. D. and LIDIARD A. B., *Phil. Mag.* **1,** 518 (1956).
14. COMPAAN K. and HAVEN Y., *Trans. Faraday Soc.* **52,** 786 (1956).
15. SCHOEN A. H. and LOWEN R. W., *Bull. Amer. Phys. Soc.* (ser. 2) **5,** 280 (1960).
16. See for instance LIDIARD A. B., *Phil. Mag.* (7) **46,** 1218 (1955).
17. See for instance LIDIARD A. B., *Nuovo Cim. Suppl.* (10) **7,** 620 (1958).

APPENDIX

EQUILIBRIUM STATE

The equilibrium state of a binary system with vacancies in a b.c.c. lattice can be calculated using the pair approximation as follows. The system of interest is composed of A and B atoms and vacancies. We assume no long-range order so that all the lattice points are equivalent. Tables 1 and 2 are used in defining probabilities for finding configurations at a lattice point and on a bond, with the modification that we do not need superscripts (ν) nor (n) for specifying the location and the argument (t) is not necessary since the system does not change in time. We can also use the simplification resulting from the symmetry of the system that

$$y_2 = y_3,\ y_5 = y_6,\ y_7 = y_8. \tag{A.1}$$

The normalization for x_i's is (3.1). Equation (3.2) holds for the geometrical relation between x's and y's.

The standard procedure for the cluster-variation method[10] applied to the pair approximation leads to the following form of the Helmholtz free energy F for a system composed of M lattice points:

$$\frac{F}{MkT} = \frac{4}{kT}(\epsilon_A y_1 + 2\epsilon_M y_2 + \epsilon_B y_4) - 7(x_1 \ln x_1 + x_2 \ln x_2 + x_3 \ln x_3)$$
$$+ 4(y_1 \ln y_1 + 2y_2 \ln y_2 + y_4 \ln y_4 + 2y_5 \ln y_5 + 2y_7 \ln y_7). \tag{A.2}$$

The equilibrium state is derived by minimizing F for given values of x_1 and x_2. We may use y_1, y_2, and y_4 as the independent variable and employ a Lagrange multiplier $4(2 \ln \lambda + 1)$ for the subsidiary condition, i.e. the last equation of (3.2). The relations derived by the minimization procedure can be expressed by using auxiliary parameters q_A and q_B in the following form:

$$\begin{aligned} y_1 &= q_A{}^2 K_A{}^{-2} \\ y_2 &= q_A q_B K_M{}^{-2} \\ y_4 &= q_B{}^2 K_B{}^{-2} \\ y_5 &= \lambda q_A \\ y_7 &= \lambda q_B, \end{aligned} \tag{A.3}$$

where λ in the Lagrange multiplier has the value

$$\lambda = x_3(q_A + q_B)^{-1}. \tag{A.4}$$

Here K_A, etc., are defined in (5.2). The q_A and q_B are to be determined from the first three equations of (3.2):

$$\begin{aligned} x_1 &= q_A(q_A K_A{}^{-2} + q_B K_M{}^{-2} + \lambda) \\ x_2 &= q_B(q_A K_M{}^{-2} + q_B K_B{}^{-2} + \lambda). \end{aligned} \tag{A.5}$$

Without going into the general solution of these equations for q's, let us examine the expression for the chemical potentials. The chemical potential μ_A for A atoms is defined as the partial derivative of the Helmholtz

free energy with respect to the total number of A atoms in the system with the following parameters of the system fixed: the temperature, the volume, and the number of B atoms. Since the volume of the system is proportional to M and the number of A atoms in a system is Mx_1, the definition gives

$$\alpha_A \equiv \frac{\mu_A}{kT} = \frac{1}{MkT}\left(\frac{\partial F}{\partial x_1}\right)_{T,\,M,\,x_2,\,y_1,\,y_2,\,y_4}$$
$$= 7\ln x_1 + 7\ln x_3 + 8\ln y_5 - 16\ln\lambda \quad \text{(A.6)}$$

Here we used the fact that F of (A.2) is a minimum with respect to y_1, y_2, and y_4 in equilibrium. For convenience here, we shall call the quantity α_A "the chemical potential". The chemical potential for a B atom, α_B, is derived in a similar manner.

When the given parameters x_1 and x_2 are considered functions of a certain variable n, the derivative of α_A of (A.6) with respect to n is written as

$$\dot{\alpha}_A = 7\left(-\frac{\dot{x}_1}{x_1} + \frac{\dot{x}_3}{x_3} + 8\frac{\dot{y}_5}{y_5} - 16\frac{\dot{\lambda}}{\lambda}\right), \quad \text{(A.7)}$$

where a dot indicates the derivative with respect to n. This relation and the corresponding one for $\dot{\alpha}_B$ were used for (6.17).

In some cases it seems more convenient to introduce an auxiliary parameter s rather than using q_A and q_B. Let us define s by

$$\exp(4s) = y_1/y_4 = (q_A/q_B)^2 \exp[4(w_B - w_A)], \quad \text{(A.8)}$$

where in order to simplify the notation we write

$$w_A = (\epsilon_A - \epsilon_M)/4kT$$
$$w_B = (\epsilon_B - \epsilon_M)/4kT. \quad \text{(A.9)}$$

Now we use s and x_3 as the independent variable in place of q_A and q_B. It is easy to show that

$$y_1 = (\tfrac{1}{2} - x_3)e^{2s}\{\exp[2(w_A + w_B)] + \cosh(2s)\}^{-1}$$
$$y_4 = (\tfrac{1}{2} - x_3)e^{-2s}\{\exp[2(w_A + w_B)] + \cosh(2s)\}^{-1} \quad \text{(A.10)}$$

$$y_2 = (\tfrac{1}{2} - x_3)\exp[2(w_A + w_B)]\{\exp[2(w_A + w_B)] + \cosh(2s)\}^{-1}$$
$$y_5 = \frac{x_3}{2}\exp(s + w_A - w_B)\operatorname{sech}(s + w_A - w_B)$$
$$y_7 = \frac{x_3}{2}\exp(-s - w_A + w_B)\operatorname{sech}(s + w_A - w_B). \quad \text{(A.11)}$$

When x_1 and x_2 are given, the parameters x_3 and s are to be solved from

$$x_3 = 1 - x_1 - x_2$$
$$x_1 - x_2 = (1 - 2x_3)\sinh(2s)\{\exp[2(w_A + w_B)] + \cosh(2s)\}^{-1} + x_3\tanh(s + w_A - w_B). \quad \text{(A.12)}$$

Using s, we write the chemical potential gradients in (A.6) as

$$\dot{\alpha}_A = \frac{-8\dot{x}_3}{x_3(1-2x_3)} + \frac{8P(P\dot{x}_1 - Q\dot{x}_2)}{R} - 7\left(\frac{\dot{x}_1}{x_1} - \frac{\dot{x}_3}{x_3}\right)$$
$$\dot{\alpha}_B = \frac{-8\dot{x}_3}{x_3(1-2x_3)} - \frac{8Q(P\dot{x}_1 - Q\dot{x}_2)}{R} - 7\left(\frac{\dot{x}_2}{x_2} - \frac{\dot{x}_3}{x_3}\right), \quad \text{(A.13)}$$

where P, Q, and R are defined as

$$P = e^{s + w_A - w_B}[e^{2(w_A + w_B)} + \cosh(2s)] - 2\sinh(2s)\cosh(s + w_A - w_B)$$
$$Q = e^{-s - w_A + w_B}[e^{2(w_A + w_B)} + \cosh(2s)] + 2\sinh(2s)\cosh(s + w_A - w_B)$$
$$R = 2(1 - 2x_4)[e^{2(w_A + w_B)}\cosh(2s) + 1]\cosh^2(s + w_A - w_B) + x_4[e^{2(w_A + w_B)} + \cosh(2s)]^2. \quad \text{(A.14)}$$

Vol. 2
196

J. Phys. Chem. Solids Pergamon Press 1961. Vol. 20, Nos. 1/2, pp. 35–40. Printed in Great Britain.

STATISTICAL DYNAMICS OF CRYSTALLINE DIFFUSION III. SELF-DIFFUSION IN AN ORDER–DISORDER SYSTEM

RYOICHI KIKUCHI

Hughes Research Laboratories, Malibu, California

(*Received* 24 *October* 1960)

Abstract—Self-diffusion coefficient in a β-brass type order–disorder alloy is derived theoretically using the path probability method of irreversible cooperative phenomena and the cluster-variation technique, assuming the vacancy mechanism of atomic migration. The diffusion coefficient is expressed in terms of the probability for a unit jump of an atom into its adjacent vacancy, and near-neighbor interaction potentials between atoms. It is shown that at the Curie point the diffusion coefficient decreases more rapidly on the ordered side than the disordered side; this result agrees with experiment qualitatively.

I. INTRODUCTION

ATOMIC diffusion in order–disorder alloys is a challenging problem, particularly from the theoretical point of view, since the simple random-walk approach does not work.

KUPER *et al.*[1] experimentally investigated the influence of order on diffusion in Cu–Zn, but there does not seem to have been any theoretical analysis published on this subject.* The path-probability method for irreversible cooperative phenomena proposed by the author[2] is well suited for studying this problem and the present paper reports an analysis of a simple case in this general field.

Applications of this method to atomic diffusion were reported in two previous publications,[3,4] of which the second one, referred to as (II) hereafter, is for the vacancy mechanism of atomic diffusion in a binary solid solution of an arbitrary atomic concentration. The result of (II) will be used here with minor modifications in discussing the self-diffusion in a 50–50 AB type alloy of b.c.c. structure using the vacancy mechanism.

In order to simplify the analysis we assume that the density of A is a constant 50 per cent throughout the system and that the atomic species B is a mixture of B and its isotope B*. Furthermore, it is assumed that the concentration of B* is uniform in a (100) plane and the gradient of B* exists along a [100] direction.

The important aspect which makes the treatment of self-diffusion simpler compared with diffusion of impurities in an order–disorder system is that in a (100) plane B and B* are mixed completely randomly among themselves. The general approach developed in this paper is applicable to the impurity diffusion, but with tedious mathematical machinery.

II. AB SYSTEM IN EQUILIBRIUM

In the following analysis the results of the paper (II) will be quoted without explanation. Equation (II 5.3) means equation (5.3) in (II). First we apply the results of (II) to the ordered equilibrium state of an AB system with vacancies.

In Fig. of (II) the alternating (100) planes (i.e. the solid-circle planes and the open-circle planes) belong to the two sublattices, which we will call the 0^{th} and the 1^{st} sublattices. We modify Tables 1 and 2 of (II) and define probability parameters as shown in Tables 1 and 2 below. In Table 2 of (II) y's were defined with the ν^{th} point always on the left. In Table 2 of this paper, y_i is for a configuration

* After the paper had been submitted, four publications by SLIFKIN, TOMIZUKA, LIDIARD, ELCOCK and MCCOMBIE (Refs. 6 to 9) on the same subject were brought to the author's attention. He acknowledges the indebtedness to Dr. TOMIZUKA and the referee. The approach of the present paper is enough different from these previous works to justify its publication.

in which the 0^{th} point is on the left, and y_{1i} is when the 1^{st} point is on the left. In contrast to (II), in the present case there is no concentration gradient so that, for instance, y_2 and y_{13} are equal as shown in Table 2.

The results in Sections V and VI of (II) hold when we use y_i for $y_i^{(n)}$ and y_{1i} for $y_i^{(n+1)}$. (The reversed choice, y_{1i} for $y_i^{(n)}$ and y_i for $y_i^{(n+1)}$, is equivalent to the following analysis.) We will define Λ_i and Γ_i as in (II 5.1a) and (II 5.1b) dropping the superscript (n).

The path parameters Y_{ij} are defined following Table 4 of (II), with ν and $\nu+1$ identified with the 0^{th} and 1^{st} sublattices and with the superscript (n) dropped.

In equilibrium, the currents vanish so that

Table 1. *Definition of probability parameters for configurations at a point*

0^{th} sublattice	Prob.	1^{st} sublattice	Prob.
A	x_{01}	A	x_{11}
B	x_{02}	B	x_{12}
v	x_{03}	v	x_{13}
(a)		(b)	

Table 2. *Definition of probability parameters for configurations of a bond*

Sublattices 0^{th} 1^{st}	Probability	
A—A	y_1	y_{11}
A—B	y_2	y_{13}
B—A	y_3	y_{12}
B—B	y_4	y_{14}
A—v	y_5	y_{16}
v—A	y_6	y_{15}
B—v	y_7	y_{18}
v—B	y_8	y_{17}

(II 6.7) holds when we drop the subscript (e) and the superscript (n). Of the four equations in (II 6.7) the following three are independent:

$$y_1y_4K_A^2K_B^2 = y_2y_3K_M^4 \tag{2.1}$$

$$y_2y_6y_7 = y_3y_5y_8 \tag{2.2}$$

$$K_A^2y_1y_7y_8 = K_B^2y_4y_5y_6. \tag{2.3}$$

When the currents vanish, (II 3.7) combined with (II 5.3b) yields

$$(y_2/y_3)^8 = (x_{01}x_{12}/x_{11}x_{02})^7 \tag{2.4}$$

$$(y_5/y_6)^8 = (x_{01}x_{13}/x_{11}x_{03})^7. \tag{2.5}$$

It can be shown that the cluster-variation technique[5] of equilibrium cooperative phenomena leads to exactly the same equations (2.1) through (2.5). Here K's are defined as

$$K_A = \exp(\epsilon_A/2kT), \text{ etc.,} \tag{2.6}$$

ϵ_A, ϵ_B and ϵ_M being the interaction potentials between A–A, B–B and A–B pairs, respectively.

Since the need arises later we copy Y_{76} from (II 5.3b):

$$Y_{76} = \tau\theta_B y_7(x_{02}x_{13})^{-7}(\Lambda_4\Gamma_3)^7. \tag{2.7}$$

Here θ_B is the probability that a B atom jumps into an adjacent vacancy per unit time, and τ is a short time interval.

Let us now solve (2.1) through (2.5) for the probability parameters. In deriving these equations the concentration of vacancies, which we will write as σ, is assumed given so that

$$x_{03}+x_{13} = 2\sigma. \tag{2.8}$$

Because of the fact that the total number of A atoms is equal to that of B atoms, we can write

$$x_{01}+x_{11} = x_{02}+x_{12} = 1-\sigma. \tag{2.9}$$

It is convenient to express the solutions of (2.1) through (2.5) by means of new variables g's as

$$\begin{aligned}
y_1 &= g_1(x_{01}x_{11})^{7/8}K_A^{-2} \\
y_2 &= g_2(x_{01}x_{12})^{7/8}K_M^{-2} \\
y_3 &= g_3(x_{02}x_{11})^{7/8}K_M^{-2} \\
y_4 &= g_4(x_{02}x_{12})^{7/8}K_B^{-2} \\
y_5 &= g_5(x_{01}x_{13})^{7/8} \\
y_6 &= g_6(x_{03}x_{11})^{7/8} \\
y_7 &= g_7(x_{02}x_{13})^{7/8} \\
y_8 &= g_8(x_{03}x_{12})^{7/8}.
\end{aligned} \tag{2.10}$$

Vol. 2
196

When (2.10) is substituted in (2.1) through (2.5) we derive

$$g_2 = g_3 \tag{2.11}$$

$$g_5 = g_6 \tag{2.12}$$

$$g_7 = g_8 \tag{2.13}$$

$$g_1 g_4 = g_2^2 \tag{2.14}$$

$$g_1/g_4 = (g_5/g_7)^2. \tag{2.15}$$

A new variable ϕ may be introduced so that from the last two equations we write

$$g_1 = \phi^2 g_4, \quad g_2 = \phi g_4, \quad g_5 = \phi g_7. \tag{2.16}$$

When (2.10) through (2.16) are used in (II 5.1), Λ_4 and Γ_3 are expressed as

$$\begin{aligned} \Lambda_4 &= g_4 (x_{02})^{7/8} \Omega_4 \\ \Gamma_3 &= g_7 (x_{13})^{7/8} \Omega_3 \end{aligned} \tag{2.17}$$

with

$$\begin{aligned} \Omega_3 &= \phi (x_{01})^{7/8} K_{\mathrm{M}}^{-1} + (x_{02})^{7/8} K_{\mathrm{B}}^{-1} \\ \Omega_4 &= \phi (x_{11})^{7/8} K_{\mathrm{M}}^{-1} + (x_{12})^{7/8} K_{\mathrm{B}}^{-1}. \end{aligned} \tag{2.18}$$

The rest of Λ's and Γ's can be written in terms of g's, x's and appropriately defined Ω's, but they are not used in this paper.

We now note here that (2.10) and (2.17) reduce (2.7) to

$$Y_{76} = \tau \theta_{\mathrm{B}} g_7^8 (g_4 \Omega_3 \Omega_4)^7. \tag{2.19}$$

In order to evaluate (2.19), let us introduce variables r, s and q as

$$\begin{aligned} 2x_{01} &= (1-\sigma) e^{8r} \operatorname{sech} 8r; \\ 2x_{02} &= (1-\sigma) e^{-8s} \operatorname{sech} 8s; \\ 2x_{11} &= (1-\sigma) e^{-8r} \operatorname{sech} 8r; \\ 2x_{12} &= (1-\sigma) e^{8s} \operatorname{sech} 8s; \\ x_{03} &= \sigma e^{-8q} \operatorname{sech} 8q; \\ x_{13} &= \sigma e^{8q} \operatorname{sech} 8q. \end{aligned} \tag{2.20}$$

Use of (2.20) in (2.18) leads to

$$\begin{aligned} \Omega_3 \Omega_4 = [(1-\sigma)/2]^{7/4} [&\phi^2 (\operatorname{sech} 8r)^{7/4} K_{\mathrm{M}}^{-2} \\ &+ (\operatorname{sech} 8s)^{7/4} K_{\mathrm{B}}^{-2} \\ &+ 2\phi \cosh(7r+7s) (\operatorname{sech} 8r \operatorname{sech} 8s)^{7/8} K_{\mathrm{M}}^{-1} K_{\mathrm{B}}^{-1}]. \end{aligned} \tag{2.21}$$

Use of (2.20) and (2.10) in

$$1-2\sigma = y_1 + y_2 + y_3 + y_4, \tag{2.22}$$

which follows from (II 3.2), yields

$$\begin{aligned} 1-2\sigma = g_4 [(1-\sigma)/2]^{7/4} [&\phi^2 (\operatorname{sech} 8r)^{7/4} K_{\mathrm{A}}^{-2} \\ &+ (\operatorname{sech} 8s)^{7/4} K_{\mathrm{B}}^{-2} \\ &+ 2\phi \cosh(7r+7s) (\operatorname{sech} 8r \operatorname{sech} 8s)^{7/8} K_{\mathrm{M}}^{-2}]. \end{aligned} \tag{2.23}$$

Combining the relations

$$\begin{aligned} x_{03} &= y_6 + y_8 \\ x_{13} &= y_5 + y_7 \end{aligned} \tag{2.24}$$

and using (2.10) and (2.20), we derive

$$\begin{aligned} \sigma \frac{\cosh^8 q}{\cosh 8q} = g_7^8 \left(\frac{1-\sigma}{2} \right)^7 \\ \times \left[\frac{\phi \cosh 7r}{(\cosh 8r)^{7/8}} + \frac{\cosh 7s}{(\cosh 8s)^{7/8}} \right]^8. \end{aligned} \tag{2.25}$$

It should be noted that r, s and q vanish in the disordered state.

When we put $\sigma = 0$ in the relations of this section, we recover the well-known results of the order–disorder phenomenon of β-brass.

III. CURRENT IN A–B–B* SYSTEM

We consider a system in which part of the B atoms in a 50–50 AB alloy are replaced by B*, an isotope of B. The definitions of the probability parameters in Table 1 are modified as in Table 3.

Here in anticipation of the concentration gradient

Table 3. Definition of probability parameters for a point in A–B–B system with vacancies*

ν^{th} lattice point	Prob.
A	$\bar{x}_1^{(\nu)}$
B	$\bar{x}_2^{(\nu)}$
B*	$\bar{x}_2^{(\nu)*}$
v	$\bar{x}_3^{(\nu)}$

of B* along the [100] direction, the superscript (ν) is used indicating the lattice plane on which the point lies. The ν^{th} plane is defined in Fig. 1 of (II).

Since an A atom cannot tell the difference between B and B*, the latter two species are completely mixed randomly among themselves. Even when there is a gradient in the concentration of B*, the system is identical with that of the previous section if $\bar{x}_2^{(\nu)}+\bar{x}_2^{(\nu)*}$ is identified with $x_2^{(\nu)}$. Now we identify the even ν point as the 0^{th} sublattice point and the odd ν as the 1^{st} sublattice. Then we have the relations:

$$\begin{aligned} x_{01} &= \bar{x}_1^{(2\mu)} & x_{11} &= \bar{x}_1^{(2\mu+1)} \\ x_{02} &= \bar{x}_2^{(2\mu)}+\bar{x}_2^{(2\mu)*} & x_{12} &= \bar{x}_2^{(2\mu+1)}+\bar{x}_2^{(2\mu+1)*} \\ x_{03} &= \bar{x}_3^{(2\mu)} & x_{13} &= \bar{x}_3^{(2\mu+1)} \end{aligned} \tag{3.1}$$

where μ is an integer. We further introduce a parameter $\rho_\nu(t)$ and $\rho_\nu^*(t)$ by

$$\begin{aligned} \rho_\nu(t) &= \bar{x}_2^{(\nu)}/x_{\nu 2} \\ \rho_\nu^*(t) &= x_2^{(\nu)*}/x_{\nu 2} \end{aligned} \tag{3.2}$$

where $x_{\nu 2}$ stands for x_{02} or x_{12} depending on whether ν is even or odd.

Table 4. Path probabilities for atomic migration of B atoms*

Sublattices $(2\mu)^{\text{th}}$ $(2\mu+1)^{\text{th}}$	Probability
B*—v ↘ ↙ v—B*	$Y_{76}\rho_{2\mu}^*(t)$
v—B* ↘ ↙ B*—v	$Y_{86}\rho_{2\mu+1}^*(t)$

Because of the complete randomness among B and B*, we can write for instance $y_7\,\rho_{2\mu}^*(t)$ for the probability of finding a pair B*—v when B* is on a 0^{th} point. Using the similar argument for the path probabilities, we have the relations shown in Table 4 for the configurations of our direct interest.

The number of B* atoms moving toward the right in time τ through an n^{th} bond is denoted by $\bar{J}_{\text{B}}^{(n)*}$. Similar to (II 3.7), we can write

$$\bar{J}_{\text{B}}^{(n)*}(t) = Y_{76}\rho_\nu^*(t) - Y_{86}\rho_{\nu+1}^*(t). \tag{3.3}$$

Remember that a ν^{th} bond is between an n^{th} and an $(n+1)^{\text{th}}$ point as seen in Fig. 1 of (II).

Although the gradient of B* exists, the concentration of B+B* is in equilibrium with A atoms so that

$$Y_{76} = Y_{86}. \tag{3.4}$$

When the system is in a steady state, the current of B*, equation (3.3), is independent of n so that we may drop it to write

$$\bar{J}_{\text{B}}^* = Y_{76}(\rho_{2\mu}^*-\rho_{2\mu+1}^*) = Y_{76}(\rho_{2\mu+1}^*-\rho_{2\mu+2}^*). \tag{3.5}$$

Taking the average of these two, we obtain

$$\bar{J}_{\text{B}}^* = Y_{76}(\rho_{2\mu}^*-\rho_{2\mu+2}^*)/2, \tag{3.6a}$$

and similarly

$$\bar{J}_{\text{B}}^* = Y_{76}(\rho_{2\mu+1}^*-\rho_{2\mu+3}^*)/2. \tag{3.6b}$$

Now we introduce an averaged density $\bar{x}_2^{(2m)*}$ of B* over adjacent even and odd lattice planes, and define

$$\begin{aligned} \bar{x}_2^{(2m)*} &= (\bar{x}_2^{(2\mu)*}+\bar{x}_2^{(2\mu+1)*})/2 \\ \bar{x}_2^{(2m+1)*} &= (\bar{x}_2^{(2\mu+1)*}+\bar{x}_2^{(2\mu+2)*})/2. \end{aligned} \tag{3.7}$$

The Greek superscripts are for lattice planes and the Roman superscripts are for interstitial points. From (3.7) we may write

$$\bar{x}_2^{(2m)*}-\bar{x}_2^{(2m+1)*} = (\bar{x}_2^{(2\mu)*}-\bar{x}_2^{(2\mu+2)*})/2 \tag{3.8}$$

which may be transformed using (3.2), as

$$\bar{x}_2^{(2m)*}-\bar{x}_2^{(2m+1)*} = x_{02}(\rho_{2\mu}^*-\rho_{2\mu+2}^*)/2. \tag{3.9a}$$

Similarly,

$$\bar{x}_2^{(2m+1)*}-\bar{x}_2^{(2m+2)*} = x_{12}(\rho_{2\mu+1}^*-\rho_{2\mu+3}^*)/2. \tag{3.9b}$$

Combining (3.6) and (3.9), we derive

$$(1-\sigma)\bar{J}_{\text{B}}^* = (x_{02}+x_{12})\bar{J}_{\text{B}}^* = Y_{76}(\bar{x}_2^{(2m)*}-\bar{x}_2^{(2m+2)*})/2 \tag{3.10}$$

The diffusion coefficient D for B* atoms may be

Vol. 2
1961

defined as

$$4\bar{J}_B^* = -\tau D(\bar{x}_2^{(2m+2)*} - \bar{x}_2^{(2m)*})/2. \quad (3.11)$$

The 4 in front of $\bar{J}_B^*$ comes from the four bonds coming out from one lattice point toward right.

Comparison of (3.10) and (3.11) yields

$$D = 8Y_{76}/(1-\sigma)\tau. \quad (3.12)$$

Using (2.19) in this we may write

$$D = 8\theta_B g_7^8 (g_4\Omega_3\Omega_4)^7/(1-\sigma) \quad (3.13)$$

where (2.21), (2.23) and (2.25) are to be used.

IV. DIFFUSION COEFFICIENT

The self-diffusion coefficient D is expressed in terms of r, s, q and ϕ in (3.13) combined with the results in Section II. In order to evaluate it, we assume that the concentration of vacancies, σ, is very small compared with unity. This assumption allows us to use for r and s defined in (2.20) the values for the AB type order–disorder alloy without vacancies. In other words we use the following results:

$$r = s \quad (4.1a)$$

$$\phi = K_B^{-1}/K_A^{-1}, \quad (4.1b)$$

and further

$$r = s = 0 \text{ in the disordered state} \quad (4.2a)$$

$$\sinh 8r/\sinh 6r = K_A K_B K_M^{-2} \text{ in the ordered state.} \quad (4.2b)$$

These relations can be derived from Section II by putting $\sigma = 0$.

Using (4.1) in (2.21), (2.23) and (2.25), we simplify them as

$$\Omega_3\Omega_4 = \frac{K_B^{-2}}{(2\cosh 8r)^{7/4}}\left[\frac{K_M^{-2}}{K_A^{-2}} + 2\frac{K_M^{-1}}{K_A^{-1}}\cosh 14r + 1\right] \quad (4.3)$$

$$1 = \frac{2g_4K_B^{-2}}{(2\cosh 8r)^{7/4}}\left[1 + \frac{K_A K_B}{K_M^2}\cosh 14r\right], \quad (4.4)$$

$$\sigma\frac{\cosh^8 q}{\cosh 8q} = \frac{g_7^8}{2^7}\left(\frac{K_B^{-1}}{K_A^{-1}} + 1\right)^8 \frac{\cosh^8 7r}{\cosh^7 8r}. \quad (4.5)$$

When (4.3) through (4.5) together with (4.2a) are substituted in (3.13), we have the diffusion coefficient in the disordered state as

$$D_d = 8\sigma\theta_B(1+e^{\beta(\epsilon+u)})^{14}(1+e^{2\beta\epsilon})^{-7}(1+e^{2\beta u})^{-8} \quad (4.6)$$

where we introduced

$$\epsilon = (\epsilon_A + \epsilon_B - 2\epsilon_M)/4$$

$$u = (\epsilon_A - \epsilon_B)/4. \quad (4.7)$$

For the ordered state (4.2b) is to be used instead of (4.2a), and the result is

$$D_o = 8\sigma\theta_B\frac{\cosh^8 q}{\cosh 8q}\frac{\cosh^7 8r}{\cosh^8 7r} \times \frac{[e^{2\beta(\epsilon+u)} + 2e^{\beta(\epsilon+u)}\cosh 14r + 1]^7}{(1+e^{2\beta u})^8(1+e^{2\beta\epsilon}\cosh 14r)^7}. \quad (4.8)$$

We can estimate the approximate behavior of q as follows. When the number of vacancies is small, the ratio of x_{03} and x_{13} is the ratio of Boltzmann factors for creating a vacancy on a 0^{th} and on a 1^{st} sublattice points. Thus the ratio derived from (2.20), can be approximated as

$$e^{-16q} = \frac{\exp[-\beta 8(\epsilon_A x_{11} + \epsilon_B x_{12})]}{\exp[-\beta 8(\epsilon_A x_{01} + \epsilon_B x_{02})]} \quad (4.9)$$

which yields

$$q = 2\beta u(x_{11} - x_{01}) = -2\beta u\tanh 8r. \quad (4.10)$$

Equations (4.6) and (4.8) combined with the solutions of (4.2b) for given values of the interaction potentials, ϵ_A, ϵ_B and ϵ_M, and with the jumping probability θ_B provide the self-diffusion coefficient as a function of temperature. Detailed numerical calculation of this temperature dependence is not the purpose of the present paper, but we will examine the behavior of the diffusion coefficient at the Curie point, in other words we examine the value

$$Q = \left[\left(\frac{d\ln D_o}{d\beta} - \frac{d\ln D_d}{d\beta}\right)\Big/ 56\frac{r\,dr}{d\beta}\right]_{T=T_c}. \quad (4.11)$$

In evaluating this quantity we use (4.6), (4.8) and (4.10) together with

$$e^{2\beta\epsilon} = 4 \text{ at } T = T_c. \quad (4.12)$$

At T_c, r and q vanish, but $r\,dr/d\beta$ is finite and positive. Thus simple arithmetic leads to

$$Q = -(16\beta u)^2 - \frac{97}{[\sqrt{(3)}+2e^{\beta u})^2} \times \left[\left(\sqrt{(3)} - \frac{149}{97}e^{\beta u}\right)^2 + \left\{1-\left(\frac{149}{194}\right)^2\right\}4e^{2\beta u}\right]. \tag{4.13}$$

This shows that, independent of the sign of $u = (\epsilon_A - \epsilon_B)/4$, Q is always negative:

$$Q < 0. \tag{4.14}$$

This agrees with the experimental observation[1] shown below schematically, except for the difference of about 50°C between the order–disorder transition point and the break point in the ln D vs. β curve.

Equation (4.13) shows that two origins contribute to negative value of Q. The first term of (4.13) comes from the difference $x_{03} - x_{13}$ or from the fact that the number of vacancies becomes not equal for the 0th and the 1st sublattices. The second term of (4.13) represents the effect of ordering of A and B atoms.

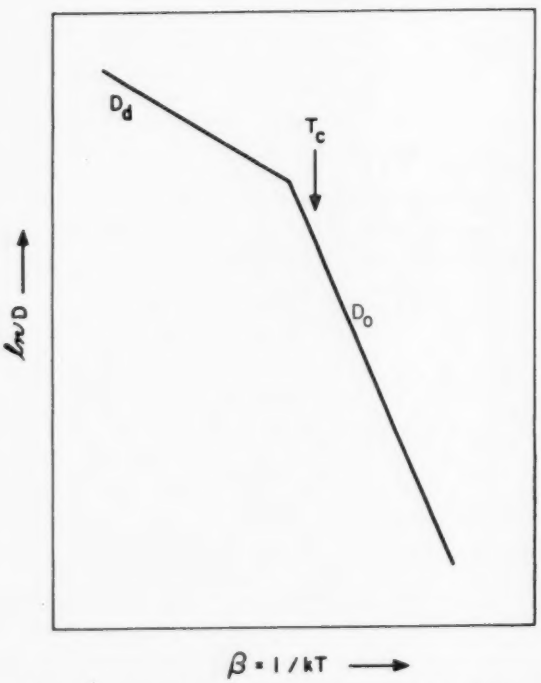

FIG. 1. Schematic behavior of the self-diffusion coefficient D as a function of temperature. D_d and D_o are for disordered and the ordered states, respectively. The Curie point is indicated by an arrow.

5. SUMMARY

Self-diffusion coefficient in a β-brass type order–disorder alloy is derived theoretically using the path probability method[2] of irreversible cooperative phenomena and cluster-variation technique,[5] assuming the vacancy mechanism of atomic migration. The diffusion coefficient is expressed in terms of the probability for a unit jump of an atom into its adjacent vacancy, and near-neighbor interaction potentials between atoms. It is shown that at the Curie point the diffusion coefficient decreases more rapidly on the ordered side than the disordered side; this result agrees with experiment[1] qualitatively.

REFERENCES

1. KUPER A. B., LAZARUS D., MANNING J. R. and TOMIZUKA C. T., *Phys. Rev.* **104,** 1536 (1956).
2. KIKUCHI R., *Ann. Phys., Paris* **10,** 127 (1960).
3. KIKUCHI R., *Ann. Phys., Paris* **11,** 306 (1960).
4. KIKUCHI R., *J. Phys. Chem. Solids*, preceding paper.
5. KIKUCHI R., *Phys. Rev.* **81,** 988 (1951).
6. SLIFKIN L. and TOMIZUKA C. T., *Phys. Rev.* **104,** 1803 (1956).
7. LIDIARD A. B., *Phys. Rev.* **106,** 823 (1957).
8. ELCOCK E. W. and MCCOMBIE C. W., *Phys. Rev.* **109,** 605 (1958).
9. ELCOCK E. W., *Proc. Phys. Soc. Lond.* **73,** 250 (1959).

Vol. 2
1961

J. Phys. Chem. Solids Pergamon Press 1961. Vol. 20, Nos. 1/2, pp. 41–49. Printed in Great Britain.

MAGNETIC SHORT RANGE ORDER AND SPECIFIC HEAT IN FERROMAGNETS AND ANTIFERROMAGNETS

J. S. SMART

Office of Naval Research, Department of the Navy, Washington 25, D.C. and IBM Research Center, Yorktown Heights, New York

(*Received* 9 *December* 1960)

Abstract—The OGUCHI method is extended to allow for both first and second nearest interactions. The results are used to calculate the magnetic short range order parameters and the magnetic specific heat above the transition temperature for both ferromagnets and antiferromagnets.

INTRODUCTION

IN THE past few years, considerable interest has been shown in the problem of determining exchange interactions in magnetic materials by comparison of the appropriate experimental data with theoretical predictions.[1–4] A principal difficulty has been one of obtaining sufficiently precise theoretical expressions for the various physical properties of ferromagnets and antiferromagnets. Such relatively sophisticated methods as the Bethe–Peierls–Weiss and constant coupling approximations[5,6] are considered to give reasonably good quantitative results but they have the severe limitation that they are restricted, because of computational complexities, to systems in which the exchange interactions are between nearest neighbors only. The experimental evidence, on the other hand, indicates that in many, if not most, ferromagnets and antiferromagnets interactions between more than one set of neighbors are required to explain their magnetic properties. So far, the only theoretical treatment developed for taking more than one set of interactions into account is the molecular field method.[7,8] This method has proved invaluable in studying magnetic problems but it is well known that the results must be considered to be only semi-quantitative at the best and to be wrong in many details. It is highly desirable that more quantitative theoretical methods be developed for studying systems which have two, and perhaps more, sets of exchange interactions.

Several years ago, OGUCHI[9] described a simple theoretical model of magnetic systems which was based on treating the interaction of an arbitrary pair of atoms exactly and treating their interaction with the remainder of the crystal by an effective field approximation. The OGUCHI theory is probably the simplest method which predicts such details as (a) short range order above the transition temperature, (b) different values of $kTc/|J|$ for ferromagnets and antiferromagnets, and (c) lack of saturation of antiferromagnetic sublattices at 0°K. The method is closely related to the constant coupling approximation and actually gives the same results as the constant coupling approximation for the short range order, energy, and specific heat above the transition temperature.

The purpose of this note is to point out that the OGUCHI method can be applied to systems having both first and second nearest neighbor interactions without getting involved in a great deal of laborious calculation. We give below an illustrative calculation for the special case of a body-centered cubic lattice with spin $\frac{1}{2}$ per atom. Any of the usual thermomagnetic properties of ferromagnets or antiferromagnets can be obtained by this procedure; in our sample calculation, we derive expressions for the short range order parameters and the magnetic specific heat above the transition temperature.

As is usual in considering second nearest neighbor interactions on a body-centered cubic lattice, we subdivide the lattice into four interpenetrating face-centered cubic lattices, A, B, C, and D. To treat second nearest neighbors on a proper basis, the OGUCHI pair of atoms must be enlarged to a cluster of four atoms, one from each sublattice. Such a cluster, which includes four nearest neighbor interactions and two second nearest neighbor interactions, is shown in Fig. 1

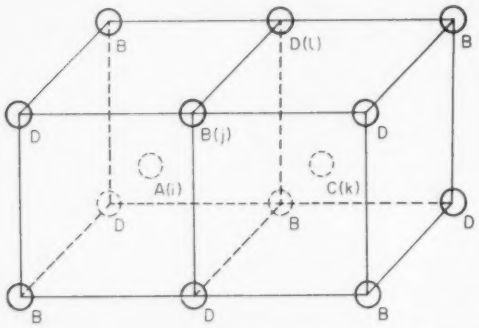

FIG. 1. Body-centered cubic lattice showing the four face-centered cubic sublattices A, B, C, D. The atoms i, j, k, l form a cluster of four of the kind referred to in equation (1).

by the four atoms designated i, j, k, and l. The Oguchi Hamiltonian for the cluster is then

$$\mathscr{H}_{\mathrm{cl}} = -2J_1(\boldsymbol{S}_i+\boldsymbol{S}_k)\cdot(\boldsymbol{S}_j+\boldsymbol{S}_l)-2J_2(\boldsymbol{S}_i\cdot\boldsymbol{S}_k+\boldsymbol{S}_j\boldsymbol{S}_l) -\mathscr{A}S_{iz}-\mathscr{B}S_{jz}-\mathscr{C}S_{kz}-\mathscr{D}S_{lz} \quad (1)$$

Here J_i is the exchange interaction between i^{th} nearest neighbors. The coefficients $\mathscr{A}$, $\mathscr{B}$, $\mathscr{C}$, and $\mathscr{D}$ are defined by:

$$\begin{aligned}
\mathscr{A} &= 2J_1(\tfrac{1}{2}z_1-1)(S_{\mathrm{B}}+S_{\mathrm{D}})+2J_2(z_2-1)S_{\mathrm{C}}+g\beta H_0\\
\mathscr{B} &= 2J_1(\tfrac{1}{2}z_1-1)(S_{\mathrm{A}}+S_{\mathrm{C}})+2J_2(z_2-1)S_{\mathrm{D}}+g\beta H_0\\
\mathscr{C} &= 2J_1(\tfrac{1}{2}z_1-1)(S_{\mathrm{B}}+S_{\mathrm{D}})+2J_2(z_2-1)S_{\mathrm{A}}+g\beta H_0\\
\mathscr{D} &= 2J_1(\tfrac{1}{2}z_1-1)(S_{\mathrm{A}}+S_{\mathrm{C}})+2J_2(z_2-1)S_{\mathrm{B}}+g\beta H_0
\end{aligned} \quad (2)$$

where $z_1 = 8$ and $z_2 = 6$ are the first and second nearest neighbor numbers and S_A, S_B, S_C, and S_D are the expectation values of S_z for the respective sublattices.

The diagonalization of $\mathscr{H}_{\mathrm{cl}}$ is discussed in some detail in the Appendix. In the succeeding sections we merely give the results of immediate interest to our sample calculations.

SHORT RANGE ORDER

In this section, expressions are given for the short range order parameters

$$\tau_1 = 4\langle \boldsymbol{S}_i\cdot\boldsymbol{S}_j\rangle \quad (3a)$$

$$\tau_2 = 4\langle \boldsymbol{S}_i\cdot\boldsymbol{S}_k\rangle \quad (3b)$$

above the transition temperature. $\boldsymbol{S}_i$ and $\boldsymbol{S}_j$ are the spin operators for a pair of nearest neighbors and $\boldsymbol{S}_i$ and $\boldsymbol{S}_k$ the spin operators for a pair of second nearest neighbors. The possible values of τ_1 and τ_2 range between $+1$ and -3.

The partition function above the transition temperature and in zero applied field is (see the Appendix)

$$Z_{\mathrm{cl}}(j_1,j_2) = 5\exp(2j_1+j_2)+6\exp(-j_2) +3\exp(-2j_1+j_2)+\exp(-3j_2)+\exp(-4j_1+j_2) \quad (4)$$

where $j_i = J_i/kT$. For the short range order parameters, we find

$$\tau_1 = Z_{\mathrm{cl}}^{-1}[5\exp(2j_1+j_2)-3\exp(-2j_1+j_2) -2\exp(-4j_1+j_2)] \quad (5a)$$

$$\tau_2 = Z_{\mathrm{cl}}^{-1}[5\exp(2j_1+j_2)-6\exp(-j_2) +3\exp(-2j_1+j_2)-3\exp(-3j_2)+\exp(-4j_1+j_2)] \quad (5b)$$

These equations are valid for any combination of signs of j_1 and j_2 and thus hold for both ferromagnets and antiferromagnets. Considering the temperature range in which equations (4) and (5) should hold, one might expect them to be valid only above the transition temperature predicted by the OGUCHI method, which is believed to be considerably higher than the exact transition temperature. However, in view of the close relation between the OGUCHI and constant coupling approximations in the paramagnetic region, it seems likely that equations (4) and (5) can be used with reasonable confidence for any temperature above the exact transition temperature.

Before discussing the general properties of these equations, it is of interest to look at some special cases. If $J_1 = 0$, the system breaks up into two

Vol. 2
196

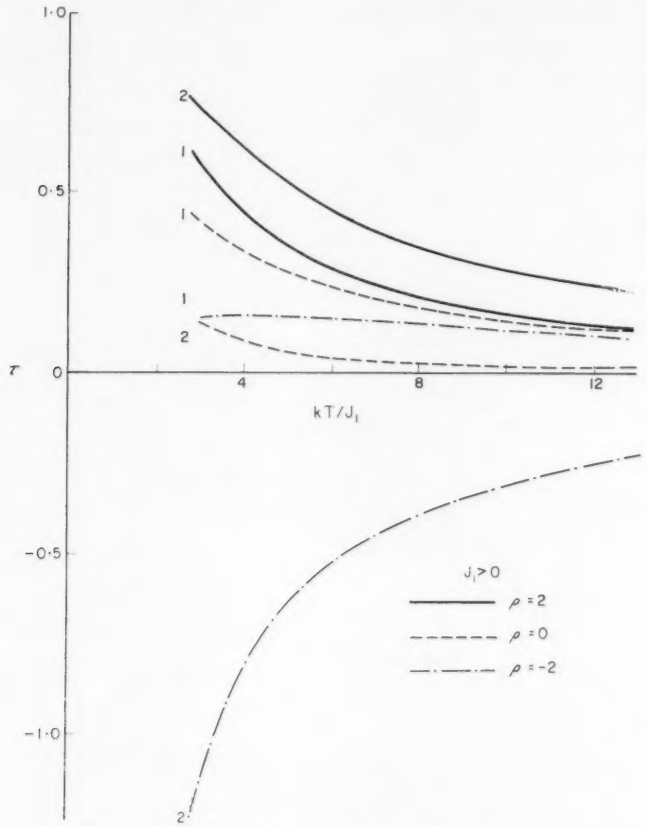

FIG. 2. τ_1 and τ_2 as a function of kT/J_1 for $J_1 > 0$.
——, $\rho = 2$; – – – –, $\rho = 0$; — — — —, $\rho = -2$.

independent simple cubic lattices. As the cluster of four atoms includes two from each simple cubic lattice, our results should reduce to the OGUCHI pair approximation for the simple cubic lattice. We find, as expected,

$$Z_{c1}(0, j_2) = 9\exp(j_2) + 6\exp(-j_2) + \exp(-3j_2) = (Z_{\text{pair}})^2 \tag{6}$$

and

$$\tau_1 = 0, \tag{7a}$$

reflecting the fact that the two simple cubic lattices are not coupled in any way.

$$\tau_2 = 3[1-\exp(-2j_2)]/[3+\exp(-2j_2)] = \tau_{\text{pair}} \tag{7b}$$

If $J_2 = 0$, we have a body-centered cubic lattice with nearest neighbor interactions only; inasmuch as the central cluster contains four atoms, our results provide some improvement over the OGUCHI pair approximation for the same lattice. We find, for example,

$$\tau_1 = [5\exp(2j_1) - 3\exp(-2j_1) - 2 \times \exp(-4j_1)]/[5\exp(2j_1) + 3 \times \exp(-2j_1) + \exp(-4j_1) + 7] \tag{8}$$

This result should be compared with the formula derived from the pair approximation*

$$\tau_1 = 3[1-\exp(-2j_1)]/[3+\exp(-2j_1)] \tag{9}$$

* Note that equations (7b) and (9) are identical in form; this occurs because τ_1 is independent of z in the pair approximation.

The two expressions appear to be considerably different, but turn out to give very similar numerical results. For example, equation (9) gives $\tau_1(j_N) = -3/7$, and equation (8) gives $\tau_1(j_N) = -17/40$, where j_N is the reduced reciprocal Néel point for the pair theory.

and J_2 antiferromagnetism of the second kind. The type of long range order which actually prevails depends of course on ρ, the critical value being $\rho = -2/3$.[10] Thus, for $\rho = -2$, the ordering is the second kind, with second nearest neighbors arranged antiferromagnetically, and

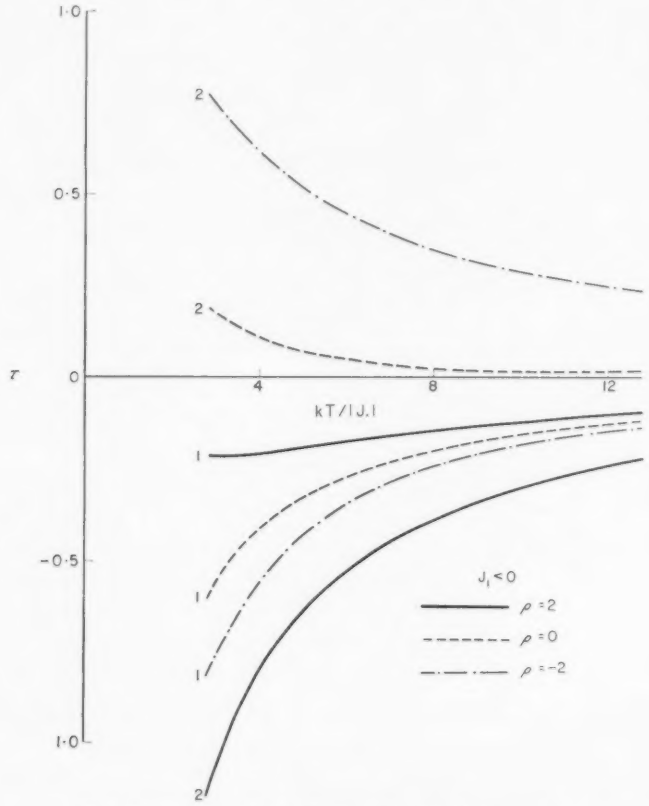

FIG. 3. τ_1 and τ_2 as a function of $kT/|J_1|$ for $J_1 < 0$. ——, $\rho = 2$; – – – –, $\rho = 0$; — — — —, $\rho = -2$.

Figures 2 and 3 show τ_1 and τ_2 as functions of the reduced temperature $kT/|J_1|$ for $J_1 > 0$ and $J_1 < 0$, respectively, and for $\rho = J_2/J_1 = 2$, 0, and -2. As might be expected, the behavior of the short range order parameters τ_1 and τ_2 reflect the kind of long range order which occurs below the transition temperature in each particular case. For example, if J_1 is positive and J_2 is negative, there is obviously a competition between the interactions, with J_1 tending to produce ferromagnetism first nearest neighbors showing no order, despite their positive interaction. In an analogous fashion, we see from Fig. 2 that for this case τ_2 is large and negative while τ_1 is small and positive and actually has a maximum near $kT/|J_1| = 4$. The behavior of τ_1 and τ_2 in the other cases can be related in the same way to competition or cooperation between the two sets of interactions.

The results of our calculations suggest that it may be possible to determine J_1 and J_2 for actual

crystals from experimental data on the temperature variation of τ_1 and τ_2. Our results are of course limited to spin $\frac{1}{2}$ and to a particularly simple lattice and thus are not applicable to most known ferromagnets and antiferromagnets. However, it should be possible to extend the calculations to more realistic cases without seriously increasing the computational labor, although machine assistance on the numerical work would probably be desirable. The experimental determination of τ_1 and τ_2 is of course not a trivial problem but, as can be seen from the figures, because of the very sensitive way in which these two quantities depend on J_1 and J_2, even very rough measurements would provide useful information about the exchange interactions.

MAGNETIC SPECIFIC HEAT

The magnetic contribution to the specific heat can in principle be obtained from the partition function by the usual statistical mechanical formulas. However, a certain amount of caution is required in proceeding from the properties of an individual cluster to the macroscopic properties of the crystal. Inspection of Fig. 1 shows that a b.c.c. crystal of N atoms could be constructed with $N/4$ clusters of the type considered; however, the Hamiltonian operator for the crystal is not the sum of the Hamiltonian operators for the clusters (nor any fixed multiple of it) because the simple summation neglects one-third of the second nearest neighbor interactions. In order to avoid this difficulty, we approach the problem in another way. The total internal energy, U, should be the sum of the energies of all nearest neighbor interactions plus the sum of the energies of all second nearest neighbor interactions. There are $Nz_1/2$ nearest neighbor pairs and $Nz_2/2$ second nearest neighbor pairs. Then

$$U = \frac{Nz_1}{2}(-2J_1\langle \boldsymbol{S}_i \cdot \boldsymbol{S}_j\rangle) + \frac{Nz_2}{2}(-2J_2\langle \boldsymbol{S}_i \cdot \boldsymbol{S}_k\rangle) = -\frac{NJ_1}{4}[z_1\tau_1 + z_2\tau_2], \tag{10}$$

and combining with equations (5a) and (5b)

$$U = -\frac{NJ_1}{Z_{c1}}\{5(2+\tfrac{3}{2}\rho)\exp[(\rho+2)j_1] - 9\rho\exp(-\rho j_1) + 3(\tfrac{3}{2}\rho-2)\exp[(\rho-2)j_1] - \tfrac{9}{2}\rho\exp(-3\rho j_1) + (\tfrac{3}{2}\rho-4)\exp[(\rho-4)j_1]\} \tag{11}$$

The specific heat may be obtained from

$$C = -\frac{J_1}{kT^2}\frac{\partial U}{\partial j_1}. \tag{12}$$

The result is

$$\frac{C}{Nk} = \left(\frac{j_1}{Z_{c1}}\right)^2\{60(\rho+1)(3\rho+2)\exp(2j_1) + 240\exp(2\rho j_1) + 20(2\rho+1)(3\rho+1)\exp[(2-2\rho)j_1] + 180\exp[(2\rho-2)j_1] + 36(\rho-1)(3\rho-2)\exp(-2j_1) + 36\rho^2\exp(-4\rho j_1) + 12(\rho-2)(3\rho-4)\exp(-4j_1) + 12(2\rho-1)(3\rho-1)\exp[-(2\rho+2)j_1] + 12\exp[(2\rho-6)j_1] + 8(\rho-1)(3\rho-2)\exp[-(2\rho+4)j_1]\} \tag{13}$$

Figures 4 and 5 show C as a function of j_1^2 for $J_1 > 0$ and $J_1 < 0$, respectively and for various values of ρ. The principal experimental problem in measuring the magnetic specific heat is that of separating it from the lattice specific heat. However, as in the case of the short range order parameters, the theoretical results are sufficiently sensitive to variations in J_1 and J_2 to make even semi-quantitative experimental data useful.

Vol. 20
1961

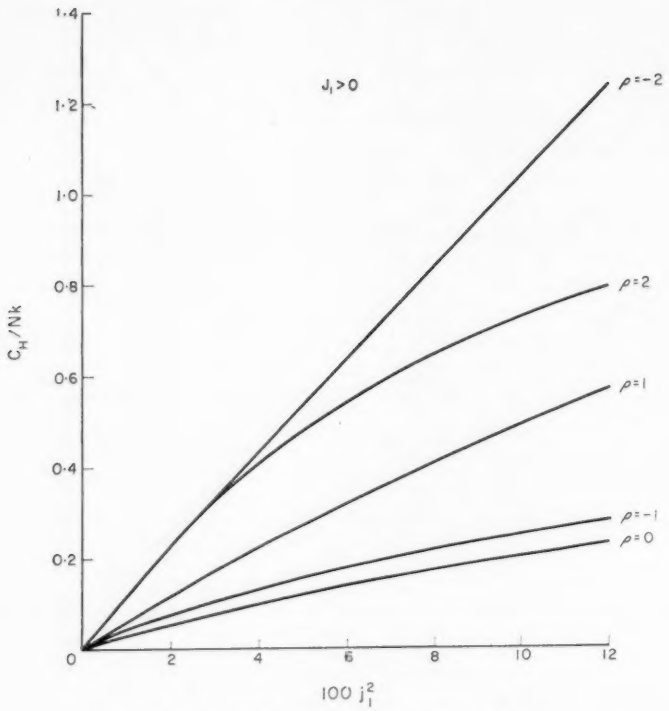

FIG. 4. C_H/Nk as a function of j_1^2 for $J_1 > 0$.

REFERENCES

1. HOFMANN J. A., PASKIN A., TAUER K. J. and WEISS R. J., *J. Phys. Chem. Solids* **1,** 45 (1956).
2. WOTJOWICZ P. J., *Phys. Rev.* **107,** 429 (1957).
3. GILLEO M. A., *Phys. Rev.* **109,** 777 (1958).
4. SMART J. S., *J. Phys. Chem. Solids* **11,** 97 (1959).
5. WEISS P. R., *Phys. Rev.* **74,** 1493 (1948).
6. KASTELEYN P. W. and VAN KRANENDONK J., *Physica* **22,** 317, 367 (1956).
7. NÉEL L., *Ann. Phys., Paris* **3,** 137 (1948).
8. ANDERSON P. W., *Phys. Rev.* **79,** 705 (1950).
9. OGUCHI T., *Prog. Theor. Phys. Osaka.* **13,** 148 (1955).
10. SMART J. S., *Phys. Rev.* **86,** 968 (1952).
11. KIKUCHI R., *Ann. Phys., Paris* **4,** 1 (1958).

APPENDIX

The diagonalization of the Hamiltonian is discussed in somewhat more detail and generality than is necessary for the purpose of this paper because some of the results may be useful in other applications of the OGUCHI method. It is convenient to divide the Hamiltonian into two parts,

$$\mathscr{H}_{\mathrm{cl}} = \mathscr{H}_{\mathrm{ex}} + \mathscr{H}' \tag{14}$$

where $\mathscr{H}_{\mathrm{ex}}$ is the exchange part (the first two terms of equation (2)) and $\mathscr{H}'$ is the effective field part. To set up the Hamiltonian matrix, we use a representation in which $\mathscr{H}_{\mathrm{ex}}$ is diagonal, and noting that $\mathscr{H}_{\mathrm{ex}}$ has the form as the Hamiltonian for four atoms at the corners of a square, we use the eigenfunctions previously obtained by KIKUCHI[11] for this problem. There will be a quintuplet, three triplets, and two singlets. The wave functions are:

$$\psi_2^{-2} = \alpha\alpha\alpha\alpha$$

$$\psi_2^{-1} = \tfrac{1}{2}[\beta\alpha\alpha\alpha + \alpha\beta\alpha\alpha + \alpha\alpha\beta\alpha + \alpha\alpha\alpha\beta]$$

$$\psi_2^{0} = \frac{1}{\sqrt{(6)}}[\alpha\alpha\beta\beta + \beta\beta\alpha\alpha + \alpha\beta\beta\alpha + \beta\alpha\alpha\beta + \alpha\beta\alpha\beta + \beta\alpha\beta\alpha]$$

$$\psi_2^{-1} = \tfrac{1}{2}[\alpha\beta\beta\beta + \beta\alpha\beta\beta + \beta\beta\alpha\beta + \beta\beta\beta\alpha]$$

$$\psi_2^{-2} = \beta\beta\beta\beta$$

$$\psi_{1a}^{1} = \tfrac{1}{2}[-\beta\alpha\alpha\alpha - \alpha\beta\alpha\alpha + \alpha\alpha\beta\alpha + \alpha\alpha\alpha\beta]$$

$$\psi_{1a}^{0} = \frac{1}{\sqrt{(2)}}[\alpha\alpha\beta\beta - \beta\beta\alpha\alpha]$$

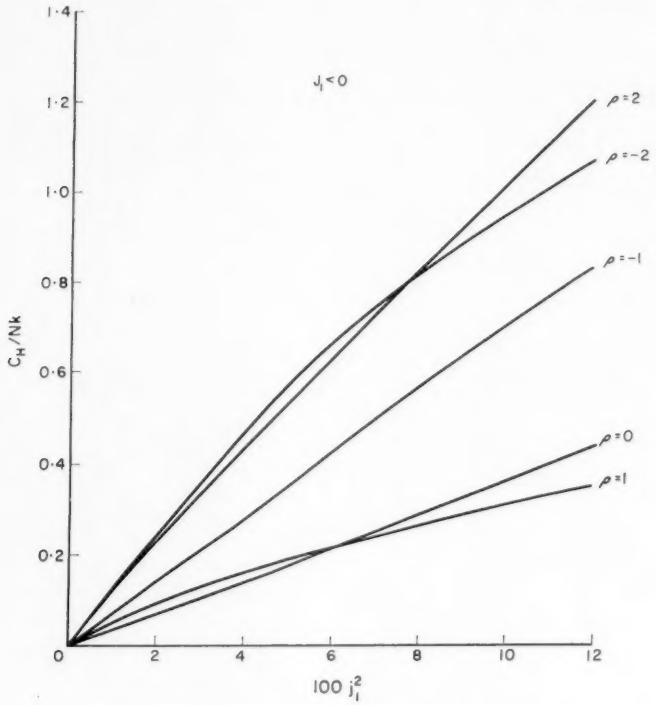

FIG. 5. C_H/Nk as a function of j_1^2 for $J_1<0$.

$$\psi_{1a}^{-1} = \tfrac{1}{2}[\alpha\beta\beta\beta+\beta\alpha\beta\beta-\beta\beta\alpha\beta-\beta\beta\beta\alpha]$$

$$\psi_{1b}^{-1} = \tfrac{1}{2}[-\beta\alpha\alpha\alpha+\alpha\beta\alpha\alpha+\alpha\alpha\beta\alpha-\alpha\alpha\alpha\beta]$$

$$\psi_{1b}^{0} = \frac{1}{\sqrt{(2)}}[\alpha\beta\beta\alpha-\beta\alpha\alpha\beta]$$

$$\psi_{1b}^{-1} = \tfrac{1}{2}[\alpha\beta\beta\beta-\beta\alpha\beta\beta-\beta\beta\alpha\beta+\beta\beta\beta\alpha]$$

$$\psi_{1c}^{1} = \tfrac{1}{2}[-\beta\alpha\alpha\alpha+\alpha\beta\alpha\alpha-\beta\beta\alpha\beta+\alpha\alpha\alpha\beta]$$

$$\psi_{1c}^{0} = \frac{1}{\sqrt{(2)}}[\alpha\beta\alpha\beta-\beta\alpha\beta\alpha]$$

$$\psi_{1c}^{-1} = \tfrac{1}{2}[\alpha\beta\beta\beta-\beta\alpha\beta\beta+\beta\beta\alpha\beta-\beta\beta\beta\alpha]$$

$$\psi_{0a} = \tfrac{1}{2}[\alpha\alpha\beta\beta+\beta\beta\alpha\alpha-\alpha\beta\beta\alpha-\beta\alpha\alpha\beta]$$

$$\psi_{0b} = \frac{1}{(\sqrt{21})}[\alpha\alpha\beta\beta+\beta\beta\alpha\alpha+\alpha\beta\beta\alpha+\beta\alpha\alpha\beta-2\alpha\beta\alpha\beta-2\beta\alpha\beta\alpha] \quad (15)$$

The eigenvalues of $\mathscr{H}_{ex}$ depend only on the total spin and are given by:

$$E_2 = -2J_1-J_2$$

$$E_{1a} = E_{1b} = J_2$$

$$E_{1c} = 2J_1-J_2$$

$$E_{0a} = 3J_2$$

$$E_{0b} = 4J_1-J_2 \quad (16)$$

The effective field term $\mathscr{H}'$ will have non-vanishing matrix elements connecting states of the same $M_s = S_{1z}+S_{1z}+S_{kz}+S_z$. By grouping the states according to M_s, the 16×16 matrix can be split into two 1×1 matrices ($M_s = \pm 2$), two 4×4 matrices ($M_s = \pm 1$), and one 6×6 matrix ($M_s = 0$). Moreover, each matrix element of $\mathscr{H}'$ is a multiple of one of the following four factors.

$$\mathscr{P} = \mathscr{A}+\mathscr{B}-\mathscr{C}-\mathscr{D} = -2(z_2-1)J_2(S_A+S_B-S_C-S_D)$$

$$\mathscr{Q} = \mathscr{A}-\mathscr{B}-\mathscr{C}+\mathscr{D} = -2(z_2-1)J_2(S_A-S_B-S_C+S_D)$$

$$\mathscr{R} = \mathscr{A}-\mathscr{B}+\mathscr{C}-\mathscr{D} = -2[(z_1-2)J_1-(z_2-1)J_2](S_A-S_B+S_C-S_D)$$

$$\mathscr{F}+4g\beta H_0 = \mathscr{A}+\mathscr{B}+\mathscr{C}+\mathscr{D} = 2[(z_1-2)J_1+(z_2-1)J_2](S_A+S_B+S_C+S_D)+4g\beta H_0$$

The matrix elements of $\mathscr{H}_{cl}$ are:

$-2J_1-J_2 \pm \frac{1}{2}(\mathscr{F}+4g\beta H_0)$ $\quad M_s = \pm 2$

$\psi_2^{\pm 1}$	$\psi_{1a}^{\pm 1}$	$\psi_{1b}^{\pm 1}$	$\psi_{1c}^{\pm 1}$	
$-2J_1-J_2$ $\pm \frac{1}{4}(\mathscr{F}+4g\beta H_0)$	$-\frac{1}{4}\mathscr{P}$	$-\frac{1}{4}\mathscr{Q}$	$-\frac{1}{4}\sim$	
$-\frac{1}{4}\mathscr{P}$	J_2 $\mp \frac{1}{4}(\mathscr{F}+4g\beta H_0)$	$\pm \frac{1}{4}\mathscr{R}$	$\pm \frac{1}{4}\mathscr{Q}$	$M_s = \pm 1$
$-\frac{1}{4}\mathscr{Q}$	$\pm \frac{1}{4}\mathscr{R}$	J_2 $\mp \frac{1}{4}(\mathscr{F}+4g\beta H_0)$	$\pm \frac{1}{4}\mathscr{P}$	
$-\frac{1}{4}\mathscr{R}$	$\pm \frac{1}{4}\mathscr{Q}$	$\pm \frac{1}{4}\mathscr{P}$	$2J_1-J_2$ $\mp \frac{1}{4}(\mathscr{F}+4g\beta H_0)$	

ψ_2^0	ψ_{1a}^0	ψ_{1b}^0	ψ_{1c}^0	ψ_{0a}	ψ_{0b}	
J_2	0	0	$-\frac{1}{2\sqrt{(3)}}\mathscr{P}$	$-\frac{1}{2\sqrt{(2)}}\mathscr{P}$	$-\frac{1}{2\sqrt{(6)}}\mathscr{P}$	
0	J_2	0	$-\frac{1}{2\sqrt{(3)}}\mathscr{Q}$	$\frac{1}{2\sqrt{(2)}}\mathscr{Q}$	$-\frac{1}{2\sqrt{(6)}}\mathscr{Q}$	
0	0	$2J_1-J_2$	$-\frac{1}{2\sqrt{(3)}}\mathscr{R}$	0	$\frac{1}{\sqrt{(6)}}\mathscr{R}$	$M_s = 0$
$-\frac{1}{2\sqrt{(3)}}\mathscr{P}$	$-\frac{1}{2\sqrt{(3)}}\mathscr{Q}$	$-\frac{1}{2\sqrt{(3)}}\mathscr{R}$	$-2J_1-J_2$	0	0	
$-\frac{1}{2\sqrt{(2)}}\mathscr{P}$	$\frac{1}{2\sqrt{(2)}}\mathscr{Q}$	0	0	$3J_2$	0	
$-\frac{1}{2\sqrt{(6)}}\mathscr{P}$	$-\frac{1}{2\sqrt{(6)}}\mathscr{Q}$	$\frac{1}{\sqrt{(6)}}\mathscr{R}$	0	0	$4J_1-J_2$	

These sub-matrices can then be diagonalized by the usual procedures but the resulting expressions for the eigenvalues and eigenfunctions are very cumbersome. Fortunately, because of the nature of the terms $\mathscr{P}$, $\mathscr{Q}$, $\mathscr{R}$, and $\mathscr{F}$, the calculations can be greatly simplified for many important special cases. As an example, we

Vol. 2
196

have been considering the properties of ferromagnets and antiferromagnets above their transition temperatures; such cases are characterized, for any magnitude of applied field, by

$$S_A = S_B = S_C = S_D$$

or

$$\mathscr{P} = \mathscr{Q} = \mathscr{R} = 0$$

Thus all off-diagonal elements vanish in this case and the functions (15) are the eigenfunctions for the paramagnetic state. The partition function is

$$\begin{aligned} Z_{c1}(j_1, j_2, y) &= [2\cosh 2y + 2\cosh y + 1]\exp(2j_1 + j_2) \\ &+ [2\cosh y + 1][2\exp(-j_2) + \exp(-2j_1 + j_2)] \\ &+ \exp(-3) + \exp(-4j_1 + j_2) \end{aligned} \tag{17}$$

where $y = \frac{1}{4}(\mathscr{F} + 4g\beta H_0)/kT$. In this paper, we are only interested in the properties in zero external field, so that we set $H_0 = 0$ and $\mathscr{F} = 0$, obtaining equation (4).

The eigenfunctions and eigenvalues for the paramagnetic state obviously apply to the ferromagnetic state as well. On the other hand, for antiferromagnetism of the first kind, the results are not particularly simple unless $H_0 = 0$, in which case

$$S_A = -S_B = S_C = -S_D = 0,$$

and

$$\mathscr{F} = \mathscr{P} = \mathscr{Q} = 0.$$

For antiferromagnetic ordering of the second kind in zero external field, the usual two-fold degeneracy exists if we assume, as the OGUCHI method does, the existence of only one antiferromagnetic axis. We may have either

$$S_A = S_B = -S_C = -S_D = 0,$$

and

$$\mathscr{F} = \mathscr{Q} = \mathscr{R} = 0.$$

or

$$S_A = -S_B = -S_C = S_D = 0,$$

and

$$\mathscr{F} = \mathscr{P} = \mathscr{R} = 0.$$

These relations may be employed to simplify greatly the calculation of the thermomagnetic properties of a system having a given type of magnetic ordering. The fact that such a calculation can be made, of course, does not guarantee that the particular kind of ordering will be stable. Questions of stability must be answered by other methods, such as calculating the relevant free energies.

J. Phys. Chem. Solids Pergamon Press 1961. Vol. 20, Nos. 1/2, pp. 50–63. Printed in Great Britain.

SUR LA STRUCTURE ELECTRONIQUE DES IMPURETES METALLIQUES DANS L'APPROXIMATION DES LIAISONS FORTES

G. LEMAN

Physique des Solides, Faculté des Sciences, Orsay (S. et O.) France

(*Received* 17 *December* 1960)

Résumé—La structure électronique des impuretés métalliques est étudiée dans l'approximation des liaisons fortes. On montre, sur l'exemple simple d'une chaine linéaire, que seules certaines des fonctions d'onde stationnaires (dans ce cas, les fonctions symétriques) sont appréciablement perturbées. On établit directement divers résultats généraux sur la densité de charge déplacée par un atome d'impureté et ses relations avec le déphasage des fonctions d'onde au niveau de Fermi. La généralisation possible de ces résultats à trois dimensions est discutée qualitativement.

Abstract—The electronic structure of metallic impurities is studied in the tight binding approximation. It is shown, on the simple example of a linear chain, that only some stationary wave functions (in this case, the symmetric ones) are appreciably perturbed. Various general results are obtained directly, concerning the density of charge displaced by an impurity atom and its relations to the phase shift of the wave functions at the Fermi level. The possible extension to three dimensions of these results is discussed qualitatively.

INTRODUCTION

L'ETUDE de la modification de la densité électronique produite dans un cristal parfait, par un potentiel perturbateur quelconque est importante dans l'étude de phénomènes physiques divers comme les propriétés électriques et magnétiques des métaux et alliages.[1,2] Nous avions déjà traité ce problème d'une façon purement formelle dans le modèle de KRONIG et PENNEY[3]. L'avantage de ce modèle était d'établir rigoureusement certains résultats importants : décroissance exponentielle de la perturbation pour les électrons d'une bande pleine, oscillations de charge dont la longueur d'onde est inversement proportionnelle à la distance du niveau de Fermi au bas ou au sommet de la bande dans le cas d'une bande peu remplie ou presque pleine. Mais la généralisation à trois dimensions de ce modèle n'offrait aucun intérêt pratique, les conditions réelles de potentiel étant beaucoup trop différentes du modèle choisi.

Dans cet article, nous considérons le même problème de la chaine linéaire perturbée localement, mais en le traitant dans l'approximation des liaisons fortes. Cette approximation semble rendre compte de façon assez satisfaisante de la structure électronique de bandes étroites, comme la bande *d* des métaux de transition.[4,5] Il y a donc un intérêt physique évident à étudier la structure électronique des impuretés métalliques dans cette approximation.

Ce problème a déjà été étudié par KOSTER et SLATER[6]; et nous utilisons en fait une méthode identique à la leur. Notre seule originalité est de mettre l'accent sur l'emploi, pour le continuum de la bande, des ondes *stationnaires*, ce qui nous permet d'obtenir très simplement des résultats généraux sur les densités de charge déplacée par un atome d'impureté. L'essentiel de cet article porte sur l'étude détaillée d'une impureté de substitution dans une chaine linéaire. Nous montrons brièvement comment la même méthode permet en principe d'étudier les problèmes à trois dimensions.

Nous devons souligner que le même type de *méthode* peut être utilisé chaque fois que, dans une structure cristalline, on ne considère que des

interactions entre premiers voisins : spectres de phonons[7] ou d'ondes de spin d'une impureté; ordre local dans les alliages.[8] Les *résultats* obtenus concernant la densité de charge déplacée sont d'autre part des cas particuliers des résultats généraux démontrés par BLANDIN[9]. Après avoir exposé le principe de la méthode et donné les équations déterminant la fonction d'onde perturbée (Section 1), nous les appliquerons à la chaîne linéaire et introduirons le déphasage (Section 2), ce qui nous permettra d'aboutir rapidement à l'évaluation de la modification de densité électronique à grande distance (Section 3) et de la charge déplacée (Section 4). Enfin, nous montrons qualitativement comment ces résultats pourraient être généralisés à trois dimensions (Section 5).

1. METHODE GENERALE

Nous considérons un cristal composé d'atomes semblables dans lequel on introduit une impureté de substitution. Les équations que nous allons établir pour déterminer la fonction d'onde perturbée sont en principe valables pour un cristal à une ou trois dimensions de structure quelconque. Nous désignerons les potentiels atomiques par V_j et le potentiel perturbateur par V_0'; si l'impureté est plus attractive que les atomes du réseau, on aura

$$V_0' < V_j < 0$$

L'origine étant au centre de la maille perturbée, nous prenons comme fonction d'onde de l'électron itinérant :

$$\Psi = A_0'\psi_0'(\boldsymbol{r}) + \sum_j{}' A_j'\psi_j(\boldsymbol{r}-\boldsymbol{R}_j) \qquad (1)$$

où les ψ_j sont des fonctions d'onde atomiques pour les atomes du réseau, la somme, indiquée par $\sum'$, étant faite sur tous les sites $j \neq 0$. ψ_0' est la fonction d'onde atomique de même type angulaire, dans la maille origine. Ces fonctions satisfont aux équations :

$$\Delta\psi_0'(\boldsymbol{r}) + 2(E_0' - V_0')\psi_0'(\boldsymbol{r}) = 0 \qquad (2)$$

$$\Delta\psi_j(\boldsymbol{r}-\boldsymbol{R}_j) + 2(E-V_j)\psi_j(\boldsymbol{r}-\boldsymbol{R}_j) = 0;\ j \neq 0 \qquad (3)$$

On a choisi le système d'unités atomiques $\hbar = m = e = 1$.

En l'absence de perturbation, la fonction d'onde totale serait :

$$\Psi_0(\boldsymbol{r}) = A_0\psi_0(\boldsymbol{r}) + \sum_j{}' A_j\psi_j(\boldsymbol{r}-\boldsymbol{R}_j) \qquad (4)$$

où $\psi_0(\boldsymbol{r})$ satisfait à l'équation (3) pour $j = 0$.

L'énergie de l'électron dans le réseau perturbé étant $\mathscr{E}$, l'équation d'évolution de sa fonction d'onde sera :

$$\Delta\Psi + 2(\mathscr{E} - V_0' - \sum_j{}' V_j')\Psi = 0 \qquad (5)$$

c'est-à-dire en tenant compte de (1),

$$A_0'(\mathscr{E} - E_0' - \sum_k{}' V_k)\psi_0' + (\mathscr{E} - E - V_0')\sum_j{}' A_j'\psi_j - \sum_{k\neq j}{}' \sum_j{}' A_j'V_kV_j = 0 \qquad (6)$$

Pour déterminer les coefficients A_0', A_j', on multiplie (6) par $\psi_0'^*$ ou ψ_j^* et on intègre sur tout le volume du cristal, en faisant les hypothèses suivantes :

(*a*) Chaque potentiel atomique, y compris celui de l'impureté, n'a de valeurs notables que dans la maille correspondante. On aura donc :

$$\int \psi_j^* V_l\psi_k \simeq 0 \quad \text{si } l \neq j \neq k$$

$$\int \psi_j^* V_k\psi_k \simeq 0 \quad \text{si } j \text{ et } k \text{ ne sont pas premiers voisins.} \qquad (7)$$

(*b*) De plus, contrairement à ce que l'on fait habituellement dans l'approximation des liaisons fortes, nous supposerons que les fonctions d'onde atomiques de même type centrées sur des sites différents, sont quasi orthogonales.

$$\int \psi_j^* \psi_k\, d\tau \simeq \delta_{jk} \qquad (8)$$

A_0' et les A_j' relatifs aux premiers voisins de l'origine sont alors donnés par :

$$A_0'[\mathscr{E} - E_0' - \sum_{\substack{j \text{ voisin} \\ \text{de } 0}} \int |\psi_0'|^2 V_j\, d\tau] = \sum_{\substack{j \text{ voisin} \\ \text{de } 0}} A_j' \int \psi_0'^* V_0'\psi_j\, d\tau \qquad (9)$$

$$-A'_0 \int \psi_j^* V_j \psi'_0 \, d\tau + A'_j [\mathscr{E} - E - \int \psi_j^* V'_0 \psi_j \, d\tau]$$

$$- \sum_{\substack{i \text{ voisin} \\ \text{de } j}}{}' A'_i \int \psi_j^* V_j \psi_i \, d\tau$$

$$- A'_j \sum_{\substack{i \text{ voisin} \\ \text{de } j}}{}' \int |\psi_j|^2 V_i \, d\tau = 0 \qquad (10)$$

Pour les atomes non premiers voisins de l'origine, l'équation (10) s'écrira :

$$A'_j [\mathscr{E} - E - \sum_{\substack{i \text{ voisin} \\ \text{de } j}} \int |\psi_j|^2 V_i \, d\tau]$$

$$= \sum_{\substack{i \text{ voisin} \\ \text{de } j}} A'_i \int \psi_j^* V_j \psi_i \, d\tau \qquad (11)$$

Ces équations (9), (10) et (11) déterminent complètement la fonction Ψ à un facteur de normalisation près, pour une structure cristalline donnée.

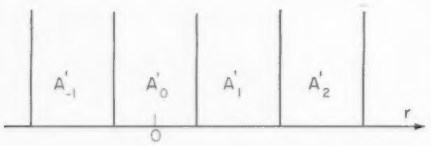

FIG. 1. Chaîne linéaire d'atomes identiques avec une impureté de substitution dans la maille origine. Les A'_j sont les coefficients du développement de la fonction d'onde stationnaire en fonctions d'onde atomiques.

Si la structure possède une symétrie suffisante, la détermination de Ψ et, par conséquent, celle de la charge électrique déplacée, ne semble pas présenter de difficultés insurmontables. Cependant, nous nous restreindrons, pour le moment, au cas plus simple de la chaîne linéaire, en indiquant seulement le principe d'une généralisation possible.

2. CHAINE LINEAIRE. DETERMINATION DE LA FONCTION D'ONDE

On suppose que l'origine, placée, au centre de la maille perturbée (Fig. 1), est un centre de symétrie pour toute la chaîne des N atomes, N pouvant devenir infiniment grand.

Compte tenu des approximations (7), il y a cinq intégrales de recouvrement à considérer, soit en prenant des fonctions atomiques réelles :

$$\dagger\alpha = \int \psi'_0 V'_0 \psi_{\pm 1} \, dr = \int \psi'_0 V_{\pm 1} \psi_{\pm 1} \, dr \qquad (12)$$

$$\beta = \int \psi_j V_j \psi_{j\pm 1} \, dr$$

$$\gamma = \int \psi_j^2 V_{j\pm 1} \, dr$$

$$\gamma_0 = \int \psi_0'^2 V_{\pm 1} \, dr$$

$$\gamma'_0 = \int \psi_{\pm 1}^2 V'_0 \, dr$$

En l'absence de perturbation, il n'y a plus évidemment que deux intégrales différentes puisque :

$$\alpha = \beta$$

$$\gamma = \gamma_0 = \gamma'_0 \qquad (13)$$

En fait, dans le cristal parfait, l'intégrale γ est beaucoup moins importante que l'intégrale de recouvrement β. La perturbation introduite par l'impureté ne modifie pas beaucoup cet état de choses. Nous montrons dans l'appendice A que les différences $\gamma - \gamma_0$ et $\gamma - \gamma'_0$ sont petites par rapport à γ. On peut donc considérer, avec une bonne approximation, que

$$\gamma \sim \gamma_0 \sim \gamma'_0 \ll \beta \qquad (14)$$

C'est ce que nous ferons désormais, laissant en appendice le traitement plus complet basé sur des valeurs différentes de γ, γ_0 et γ'_0.

---

† *Note:* Ces deux intégrales sont égales à l'ordre d'approximation considéré ici, parce que

$$\int \psi'_0 V'_0 \psi_1 \, dr - \int \psi'_0 V_1 \psi_1 \, dr$$

$$= (E'_0 - E) \int \psi_1 \psi_0 \, dr$$

$$+ \frac{1}{2} \int \left[\psi_1 \frac{d^2 \psi'_0}{dr^2} - \frac{\psi'_0 d^2 \psi_1}{dr^2} \right] dr$$

le premier terme du second membre est nul, dans l'approximation (8), le second terme est rigoureusement nul, quand on intègre de $-\infty$ à $+\infty$.

2.1 *Fonction d'onde non perturbée*

En l'absence de perturbation, les équations (9) (10) et (11) s'écrivent :

$$A_0(\mathscr{E}-E-2\gamma)=\beta(A_{+1}+A_{-1}) \qquad (15)$$

$$A_{\pm1}(\mathscr{E}-E-2\gamma)=\beta(A_0+A_{\pm2}) \qquad (16)$$

$$A_j(\mathscr{E}-E-2\gamma)=\beta(A_{j+1}+A_{j-1}) \qquad (17)$$

D'après le théorème de Bloch, une solution pour les A_j dans le réseau parfait est de la forme e^{ijka}, où a est la période du réseau. Par conséquent :

$$\frac{\mathscr{E}-E-2\gamma}{\beta}=\frac{A_{j+1}+A_{j-1}}{A_j}=2\cos ka \qquad (18)$$

Les valeurs permises de l'énergie $\mathscr{E}$ sont réparties dans une bande de largeur -4β, si $\beta<0$, c'est à dire si la fonction d'onde atomique est

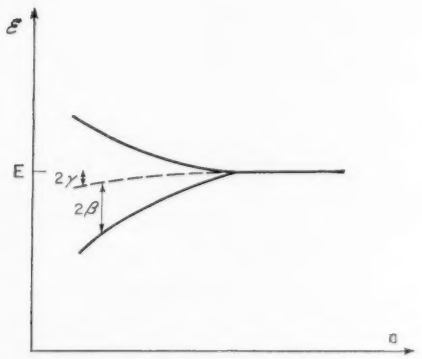

FIG. 2. Variations de l'énergie des électrons d'un réseau linéaire en fonction de la distance interatomique (explications dans le texte).

symétrique. Au bas de la bande, on a : $k=0$, au sommet de la bande $k=\pi/a$. L'énergie correspondant au milieu de la bande (c'est à dire pour $k=\pi/2a$) est décalée de 2γ par rapport au niveau d'énergie de l'atome libre (Fig. 2).

La fonction d'onde stationnaire Ψ_0 est nécessairement symétrique ou antisymétrique. Elle sera symétrique si

$$A_0\neq 0$$
$$A_j=A_{-j}$$

ce qui donne, compte tenu des équations (15) à (18),

$$\Psi_{0S}=A_0[\psi_0(r)+\sum_j{}'\,\psi_j(r-ja)\cos jka] \qquad (19)$$

où $A_0=\sqrt{(2/N)}$ si la fonction d'onde est normalisée sur une chaîne de N atomes.

On aura un état stationnaire antisymétrique, si

$$A_0=0$$
$$A_j=-A_{-j}$$

Par conséquent,

$$\Psi_{0A}=A\sum_j{}'\,\psi_j(r-ja)\sin jka \qquad (20)$$

où k est le nombre d'onde, des ondes de Bloch, relié à l'énergie $\mathscr{E}$ par la relation (18) et $A=\sqrt{(2/N)}$ est le facteur de normalisation.

2.2 *Fonction d'onde perturbée*

On introduit maintenant une impureté de substitution dans la maille origine avec les conditions aux limites suivantes :

(a) L'origine est un centre de symétrie de la chaîne. Par conséquent, la fonction d'onde perturbée Ψ est encore symétrique ou antisymétrique.

(b) La densité électronique n'est pas modifiée, en moyenne, à grande distance; ou encore : les ondes électroniques perturbées sont simplement déphasées par rapport aux ondes stationnaires non perturbées.

Les coefficients de la fonction Ψ sont donnés par les équations (9) (10) et (11) qui s'écrivent maintenant :

$$A'_0(\mathscr{E}-E'_0-2\gamma)=\alpha(A'_1+A'_{-1}) \qquad (21)$$

$$-A'_0\alpha+A'_{\pm1}(\mathscr{E}-E-2\gamma)=\beta A'_{\pm2} \qquad (22)$$

$$A'_j(\mathscr{E}-E-2\gamma)=\beta(A'_{j+1}+A'_{j-1});\ |j|\geqslant 2 \qquad (23)$$

A cause de la condition (b), on aura encore:

$$\frac{\mathscr{E}-E-2\gamma}{\beta}=2\cos ka$$

c'est-à-dire

$$2A'_j\cos ka=A'_{j+1}+A'_{j-1}\ \text{pour}\ |j|\geqslant 2$$

Les coefficients A_j' peuvent donc toujours s'écrire sous l'une des deux formes

$$A_j' = B\cos(jka+\eta) \tag{24}$$

$$A_j' = C\sin(jka+\eta') \tag{25}$$

suivant que la fonction d'onde est symétrique ou antisymétrique. Autrement dit :

$$\Psi_S = B\left[\frac{A_0'}{B}\psi_0'(r) + \sum_j{}' \psi_j'(r-ja)\cos(jka+\eta)\right] \tag{26}$$

$$\Psi_A = C\sum_j{}' \psi_j(r-ja)\sin(jka+\eta') \tag{27}$$

la quantité A_0'/B et les déphasages η et η' étant complètement déterminés par les équations (21) et (22). Nous montrons dans l'appendice A que η' est nul dans l'approximation (14).

Les états antisymétriques ne sont donc pratiquement pas modifiés par la perturbation. Seuls les états symétriques, dont nous allons maintenant calculer le déphasage, interviendront dans la charge électrique déplacée.

2.3 *Déphasage des états symétriques*

2.3.1. *Calcul du déphasage.* En remplaçant A_1' et A_2' respectivement par $B\cos(ka+\eta)$ et $B\cos(2ka+\eta)$ dans les équations (21) et (22), on obtient :

$$\frac{A_0'}{B} = \frac{2\alpha\cos(ka+\eta)}{2\beta\cos ka+\Delta E} = \frac{\beta\cos\eta}{\alpha} \tag{28}$$

où l'on a posé $\Delta E = E - E_0'$

Introduisons les quantités sans dimension :

$$p = \frac{\beta^2-\alpha^2}{\alpha^2} \tag{29}$$

$$b = \frac{\beta\Delta E}{2(\alpha^2-\beta^2)} \tag{30}$$

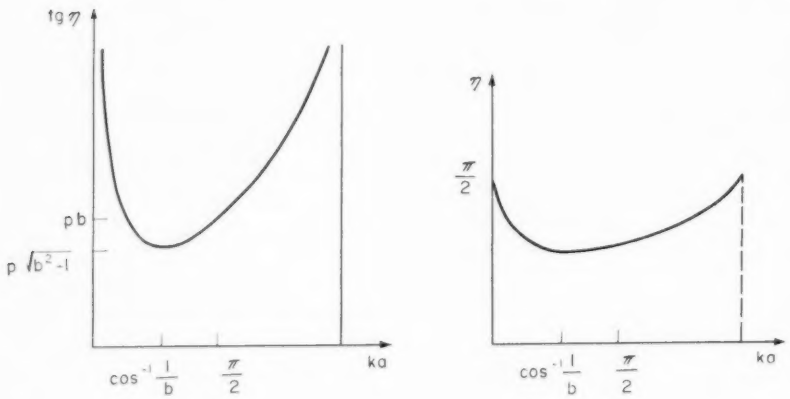

(a) (b)

FIG. 3. Comportement du déphasage des états symétriques dans une bande.

le déphasage η des états symétriques sera donné par :

$$\operatorname{tg}\eta = \frac{p(b-\cos ka)}{\sin ka} \tag{31}$$

2.3.2. *Variations du déphasage dans la bande.* Nous allons étudier le comportement du déphasage quand on fait varier k de 0 à π/a. Nous le ferons dans le cas d'une impureté plus attractive que les atomes du réseau et pour des fonctions d'onde atomiques symétriques, c'est-à-dire avec

$$\begin{gathered} V_0' < V_j < 0 \\ \Delta E > 0 \\ \beta < \alpha < 0 \end{gathered} \tag{32}$$

Vol. 2
196

Cette dernière condition traduit le fait que la fonction d'onde ψ_0' s'étend moins loin que ψ_j.

Nous montrons dans l'appendice B qu'il est raisonnable de penser que la quantité b est supérieure à l'unité.

Puisque p est positif, $\operatorname{tg}\eta$ sera positive dans l'intervalle considéré, variant de $+\infty$ à $+\infty$ en passant par la valeur $(\operatorname{tg}\eta)_{\min} = p\sqrt{(b^2-1)}$ pour $ka = \cos^{-1} 1/b$ (Fig. 3a). Le déphasage η (Fig. 3b) varie donc de $\pi/2$ à $\pi/2$ en restant toujours compris entre 0 et $\pi/2$.

Les résultats sont absolument analogues dans le cas d'une impureté moins attractive que les

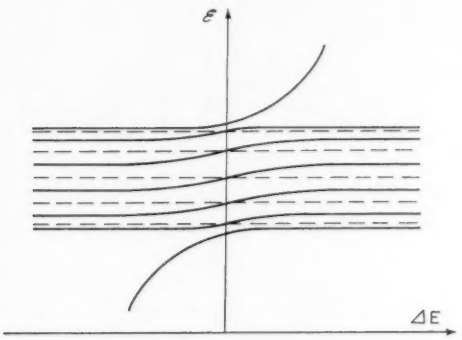

FIG. 4. Niveaux d'énergie perturbés en fonction de l'énergie de perturbation : en trait plein, les états symétriques; en pointillé, les états antisymétriques (d'après KOSTER et SLATER).

atomes du réseau. Le déphasage change simplement de signe, ce qui confirme ce qu'avaient déjà montré KOSTER et SLATER[6], à savoir qu'un état lié symétrique disparaît au sommet de la bande et qu'un autre apparaît dans le bas de la bande quand la perturbation change de signe (Fig. 4).

L'expression (31) permet de calculer les déphasages en fonction de k à partir des niveaux d'énergie atomiques E et E_0' et des intégrales de recouvrement α et β. Il est évident que faire de tels calculs dans le cas d'une chaine linéaire ne présenterait guère d'intérêt physique; mais il est important de montrer, d'une manière générale, comment la connaissance des déphasages permet d'évaluer simplement la charge déplacée et la perturbation de densité électronique : nous allons d'abord calculer celle-ci à grande distance de l'impureté.

3. FORME ASYMPTOTIQUE DE LA PERTURBATION DE DENSITE ELECTRONIQUE

Il s'agit d'évaluer, pour les grandes valeurs de r,

$$\Delta\rho(r) = \int_0^{k_M} [\Psi_S^2(r)n(k) - \Psi_{0S}^2(r)n_0(k)]\,dk. \quad (33)$$

L'intégration est faite sur tous les électrons d'une bande jusqu'au niveau de Fermi. On a introduit les densités d'états avec et sans perturbation. Nous n'avons pas tenu compte des états antisymétriques qui ne sont pas modifiés par la perturbation.

Puisque les ondes perturbées sont simplement déphasées par rapport aux ondes stationnaires non perturbées, on peut donc prendre la même densité d'états $n(k) = n_0(k) = N^a/\pi$ dans l'intégrale (33) à condition que Ψ_S et Ψ_{0S} soient normalisées de la même façon. D'après le théorème de VON LAUE[3,10], en effet, l'impureté ne modifie pas, à grande distance, la répartition des densités électroniques. On écrira donc :

$$\Psi_S = \sqrt{(2/N)} \sum_j \cos(jka+\eta)\psi_j(r-ja) \quad (34)$$

Négligeant alors les produits de fonctions d'ondes atomiques centrées sur des sites différents, on obtient pour les grandes valeurs de r

$$\Delta\rho(r) = 2a/\pi \sum_j \psi_j^2(r-ja) \times \int_0^{k_M} [\cos^2(jka+\eta) - \cos^2 jka]\,dk \quad (35)$$

c'est-à-dire :

$$\Delta\rho(r) = a/\pi \sum_j \psi_j^2(r-ja) \times \int_0^{k_M} [\cos 2jka(\cos 2\eta - 1) - \sin 2jka \sin 2\eta]\,dk \quad (36)$$

où $\eta(k)$ est une fonction lentement variable déterminée par l'équation (31). En intégrant par parties et remarquant que $\sin 2\eta(0) = 0$, on obtient finalement pour la modification de densité électronique à grande distance de l'impureté au

premier ordre en $1/j$

$$\Delta\rho(r) = 2/\pi \sum_j \psi_j^2(r-ja)$$

$$\times \frac{\sin\eta(k_M)\cos[2j\,k_M a+\eta(k_M)]}{j} \qquad (37)$$

Cette expression ne dépend que de la valeur du déphasage au niveau de Fermi. On voit donc que la présence d'un potentiel perturbateur dans la chaîne linéaire produit des oscillations de charge dont l'amplitude, décroissant avec la distance comme $1/r$, est uniquement fonction du déphasage au niveau de Fermi et dont la longueur d'onde est directement liée à la position du niveau de Fermi dans la bande.

Précisons ces résultats:

(a) *Bande peu remplie*

Le niveau de Fermi étant proche du bas de la bande, c'est-à-dire k_M étant petit, on voit immédiatement que la modification de densité électronique oscille lentement : elle se comporte comme

$$\frac{\cos(2k_M r+\eta)}{r}$$

dont la longueur d'onde est inversement proportionnelle à $2\,k_M$.

(b) *Bande à moitié pleine*

Si le niveau de Fermi est au milieu de la bande, soit $k_M = \pi/2a$, la longueur d'onde des oscillations de charge sera $2a$. En d'autres termes, la modification de densité électronique change de signe quand on passe d'une maille à la maille voisine. Ce résultat avait déjà été établi par COULSON[11].

(c) *Bande pleine*

Si le niveau de Fermi se trouve dans une bande interdite, l'intégration sur k dans l'équation (35) doit être effectuée entre les limites 0 et π/a. La modification de densité électronique s'écrit alors

$$\Delta\rho(r) = a/\pi \sum_j \psi_j^2(r-ja)$$

$$\times \int_0^{\pi/a} \cos(2jka+\eta)\,dk \qquad (38)$$

Remplaçant $\eta(k)$ par sa valeur (31), on peut alors calculer l'intégrale dans le plan complexe (Appendice C).

On constate que, pour une bande pleine, la modification de densité électronique est une fonction exponentiellement décroissante de la distance. Nous[3] avions déjà établi ce résultat pour un modèle de KRONIG et PENNEY à une dimension.

(d) *Bande presque pleine*

Supposons enfin que le niveau de Fermi soit proche du sommet de la bande et posons

$$\Delta k = \frac{\pi}{2} - k_M. \qquad (39)$$

On peut alors considérer que la modification de densité électronique est celle que produiraient les électrons d'une bande pleine et les trous d'une bande peu remplie. Puisqu'à grande distance, la contribution d'une bande pleine est négligeable, les oscillations de charge seront en

$$\frac{\cos(2\Delta k r+\eta)}{r}$$

dont la longueur d'onde est inversement proportionnelle à Δk.

Il est clair que la perturbation introduit également des états liés dont l'amplitude décroît exponentiellement avec la distance : ces états ne contribuent pratiquement pas à la charge électrique à grande distance de l'impureté, sauf pour des perturbations très faibles où la décroissance exponentielle est très lente.

4. CHARGE DEPLACEE

4.1. *Charge totale déplacée*

Nous avons étudié, jusqu'ici, la modification de densité électronique en un point r en faisant l'intégration (33) sur tous les états occupés. Nous voudrions maintenant obtenir la charge totale déplacée en intégrant sur toute la chaîne linéaire. Considérons d'abord les électrons de nombre d'onde k. La charge totale de ces électrons, déplacée par le potentiel perturbateur, sera :

$$\left(\frac{\partial\rho}{\partial k}\right)_{\text{tot}} = 2\int_0^{Na/2} (\Psi_S^2 - \Psi_{0S}^2)\,dr \qquad (40)$$

Vol. 2
1961

où nous ferons tendre N vers l'infini. Pour pouvoir garder la densité d'états $n_0(k)$ en l'absence de perturbation, il faudra ici encore prendre $B = A_0 = \sqrt{(2/N)}$ dans les états symétriques qui vont, seuls, contribuer à la charge déplacée. Les fonctions d'onde atomiques sont normalisées sur toute la chaîne. En tenant compte de (26) et (28) et en négligeant les produits de fonctions atomiques centrées sur des sites différents, on obtient :

$$\left(\frac{\partial\rho}{\partial k}\right)_{\text{tot}} = \frac{4}{N}\left(\frac{\beta^2}{\alpha^2}\cos^2\eta - 1\right)\int_0^{Na/2}\psi_0'^2\,dr$$

$$+\frac{4}{N}\sum_j{}'\left[\cos^2(jka+\eta) - \cos^2 jka\right]\times\int_0^{Na/2}\psi_j^2\,dr. \tag{41}$$

c'est-à-dire :

$$\left(\frac{\partial\rho}{\partial k}\right)_{\text{tot}} = \frac{2}{N}\left[\frac{\beta^2}{\alpha^2}\cos^2\eta - 1 - 2\sin\eta\sum_j{}'\sin(2jka+\eta)\right] \tag{42}$$

Puisque nous faisons tendre N vers l'infini, on ne considèrera que la valeur moyenne de la somme sur j, soit :

$$\overline{Im\sum_j{}'\exp i[(2jka+\eta)]}$$

si bien que :

$$\left(\frac{\partial\rho}{\partial k}\right)_{\text{tot}} = \frac{2}{N}\cos^2\eta\left[\frac{\beta^2}{\alpha^2} - 1 - \text{tg}\eta\,\text{cotg}\,ka\right] \tag{43}$$

Le déphasage $\eta(k)$ est donné par la relation (31). Si l'on fait intervenir sa dérivée par rapport à k, la charge totale déplacée pour les électrons de nombre d'onde k s'exprimera très simplement, par la relation :

$$\boxed{\left(\frac{\partial\rho}{\partial k}\right)_{\text{tot}} = \frac{2}{Na}\frac{\partial\eta}{\partial k}} \tag{44}$$

Pour tous les électrons de nombre d'onde compris entre k_1 et k_2, la charge totale déplacée est donc, en faisant intervenir la densité d'états $N\alpha/\pi$

$$\rho_{\text{tot}} = \frac{2}{\pi}[\eta(k_2) - \eta(k_1)] \tag{45}$$

En particulier, pour tous les électrons de nombre d'onde compris entre $k = 0$ et k_M, la charge totale déplacée, en ce qui concerne les électrons de la bande, serait :

$$\rho_{\text{tot}} = \frac{2}{\pi}\left(\eta_M - \frac{\pi}{2}\right) \tag{46}$$

Il faut noter cependant qu'en prenant $k = 0$, comme limite inférieure d'intégration, on ne compte que la moitié de l'état symétrique non perturbé correspondant à $k = 0$, si bien que la charge totale déplacée dans la bande vaut :

$$\rho_{\text{tot}} = \frac{2}{\pi}(\eta_M - \pi) \tag{47}$$

Tenant compte enfin de l'état lié introduit par la perturbation, on obtient la charge totale déplacée en écrivant simplement :

$$\rho_{\text{tot}} = \frac{2}{\pi}\eta_M \tag{48}$$

4.2 *Charge délocalisée*

Comment se répartit cette charge totale déplacée? Elle peut être essentiellement localisée dans la maille origine pour y former la charge d'écran de l'impureté ou, au contraire, elle pourra être répartie plus ou moins uniformément sur tous les sites du réseau. Essayons donc de déterminer la charge délocalisée et pour cela d'évaluer d'abord la charge déplacée localement dans la maille origine, c'est-à-dire d'effectuer l'intégration (40) entre les limites $-a/2$ et $+a/2$, ce qui donne pour des électrons de nombre d'onde k

$$\left(\frac{\partial\rho}{\partial k}\right)_{\text{loc}} = \frac{2}{N}\cos^2\eta\left(\frac{\beta^2}{\alpha^2} - 1 - \text{tg}^2\eta\right) \tag{49}$$

ce que l'on peut écrire, en tenant compte des relations (29), (43) et 44)

$$\left(\frac{\partial\rho}{\partial k}\right)_{\text{loc}} = \frac{2}{Na}\frac{p - \text{tg}^2\eta}{p - \text{tg}\,\eta\,\text{cotg}\,ka}\frac{\partial\eta}{dk} \tag{50}$$

La charge électrique déplacée localement dans

la maille origine sera donc :

$$\rho_{\text{loc}} = +\frac{2}{\pi}\int_{\pi/2}^{\eta_M}\left(\frac{p-\text{tg}^2\eta}{p-\text{tg}\,\eta\,\text{cotg}\,ka}\right)\partial\eta \quad (51)$$

η_M étant le déphasage au niveau de Fermi.

Un calcul immédiat donne, avec (31),

$$\text{cotg}\,ka = \frac{\text{tg}\,\eta+\epsilon b\sqrt{[\text{tg}^2\eta-p^2(b^2-1)}}{p(b^2-1)} \quad (52)$$

La détermination $\epsilon = +1$ doit être prise quand ka se trouve dans l'intervalle 0, $\cos^{-1}1/b$ (Fig. 3b), l'autre détermination $\epsilon = -1$ correspondant à $\cos^{-1}1/b \leqslant ka \leqslant \pi$. Rappelons que pour $ka = \cos^{-1}1/b$, η passe par un minimum de valeur $\text{tg}^{-1}p\sqrt{(b^2-1)}$.

On trouve alors, en posant $q = p\sqrt{(b^2-1)}$, que la charge localisée dans la bande vaut :

$$\rho_{\text{loc}} = \frac{2}{\pi}\frac{p}{p-1}\Big|\eta+2\,\text{arc tg}\left\{\frac{-\text{tg}\,\eta+\sqrt{(\text{tg}^2\eta-q^2)}}{p(1+\epsilon b)}\right\}+\frac{\epsilon b}{\sqrt{(1+q^2)}}\,\text{arc tg}\sqrt{\left(\frac{1+q^2}{\text{tg}^2\eta-q^2}\right)}\Big|_{\pi/2}^{\eta_M} \quad (53)$$

L'expression (53) est exacte mais ne permet pas de donner facilement une interprétation physique du résultat, tant que l'on n'a pas de données précises sur les valeurs de p, b, q, c'est-à-dire sur ΔE et les intégrales de recouvrement α et β. Nous nous contenterons d'évaleur l'ordre de grandeur de ρ_{loc} quand la perturbation est forte, c'est-à-dire pour les grandes valeurs de p et b. Nous le ferons pour une bande peu remplie et pour une bande à moitié pleine.

(a) *Bande peu remplie.* Si $\eta_M = \pi/2-\delta$, $\delta \ll 1$, on obtient pour la charge localisée dans la bande

$$\rho_{\text{loc}} = -\frac{2}{\pi}pb\delta$$

Si la perturbation est assez forte, l'état lié est presque entièrement localisé dans la maille origine, si bien que la charge localisée totale sera

$$\rho_{\text{loc}} = +\frac{2}{\pi}(\pi-pb\delta) \quad (54)$$

Puisque la charge totale déplacée est alors,

$$\rho_{\text{tot}} = \frac{2}{\pi}\left(\frac{\pi}{2}-\delta\right) \quad (55)$$

on voit que la charge délocalisée sera de l'ordre de

$$\rho_{\text{délocc}} = \frac{2}{\pi}\left(-\frac{\pi}{2}+pb\delta\right) \quad (56)$$

En d'autres termes, la charge délocalisée est de l'ordre de la charge totale changée de signe. Par conséquent, l'introduction d'une impureté de substitution dans une chaîne linéaire, où la dernière bande d'énergie était peu remplie, produit un état lié localisé dans la maille origine et une répulsion des électrons de la bande : il y a une faible charge d'écran localisée dans la bande [$-2/\pi pb\delta$ dans (54)], la majeure partie de la charge déplacée par répulsion étant répartie sur les différents sites atomiques. Ce résultat était prévisible, puisque pour une bande peu remplie, la modification de densité électronique oscille très lentement.

(b) *Bande à moitié pleine.* Si l'on suppose que le niveau de Fermi est tel que $k_M a = \cos^{-1}1/b$, correspondant au minimum du déphasage :

$\eta_M = \text{tg}^{-1}q$, l'expression (53) donne exactement, en prenant $\epsilon = +1$,

$$\rho_{\text{loc}} = \frac{2}{\pi}\frac{p}{p-1}\left(\eta_M-\frac{\pi}{2}-k_M a + \frac{b}{\sqrt{(1+q^2)}}\times\frac{\pi}{2}\right)$$

Pour une perturbation forte, les quantités p et b sont grandes par rapport à l'unité. Dans ce cas, k_M a est voisin de $\pi/2$; la charge localisée dans la bande sera

$$\rho_{\text{loc}} \simeq \frac{2}{\pi}\left(-\frac{\pi}{2}+\frac{1}{b}\right)$$

et la charge localisée totale, en supposant l'état lié complètement localisé, est :

$$\rho_{\text{loc}} \simeq \frac{2}{\pi}\left(\frac{1}{b}+\frac{\pi}{2}\right)$$

Vol. 20
1961

Puisque la charge totale vaut, dans ce cas,

$$\rho_{\text{tot}} \simeq \frac{2}{\pi}\left(\frac{\pi}{2} - \frac{1}{pb}\right)$$

on obtient pour la charge délocalisée, quand la bande est à moitié pleine :

$$\rho_{\text{déloc}} \simeq -\frac{2}{\pi}\left(+\frac{1}{pb} + \frac{1}{b}\right)$$

La charge délocalisée est faible : c'est dire que, quand la bande est à moitié pleine, la charge déplacée est essentiellement localisée dans la maille origine; il y a une importante charge d'écran et les électrons de la bande sont faiblement repoussés en dehors de la maille origine : ce résultat s'accorde à la faible longueur d'onde des oscillations de charge, qui est, dans ce cas, de l'ordre de deux distances interatomiques.

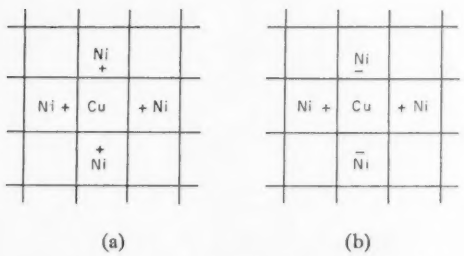

FIG. 5. Impureté de substitution dans un cristal de Ni

(a) Les fonctions d'onde stationnaires ayant la symétrie cubique sont les seules qui ne soient pas nulles sur l'atome de Cu et correspondent aux états symétriques de la chaîne linéaire.

(b) Les fonctions d'onde stationnaires n'ayant pas la symétrie cubique sont nulles dans la maille origine où se trouve l'impureté.

5. GENERALISATION à 3 DIMENSIONS

Les équations (9) (10) et (11) qui permettent de déterminer les coefficients A_j' de la fonction d'onde perturbée sont valables pour un cristal à trois dimensions de structure quelconque et n'importe quelle impureté, pourvu que les approximations de liaisons fortes restent valables. Il est clair qu'une grande symétrie dans la structure cristalline faciliterait la détermination des A_j'. Or c'est le cas des métaux de transition de symétrie cubique, dont les électrons $3d$ se traitent assez bien dans l'approximation des liaisons fortes.

Prenons, par exemple, un cristal de Ni, cubique centré, où nous remplaçons un atome de Ni par un atome de Cu. Pour généraliser le traitement que nous avons fait da la chaîne linéaire, il faut résoudre deux problèmes : déterminer les coefficients A_j de la fonction d'onde non perturbée et ensuite exprimer les A_j' en fonction des A_j par l'intermédiaire de déphasages. En d'autres termes, il faut trouver, à trois-dimensions, l'analogue des états stationnaires symétriques et anti-symétriques de la chaîne linéaire. Seuls les états ayant toutes les symétries du cube peuvent avoir des valeurs non nulles sur le site central (Fig. 5a et b). Ce serait donc l'analogue des états symétriques de la chaîne linéaire. Ils seront en particulier les seuls à être fortement perturbés par l'atome d'impureté.

CONCLUSION

Nous avons traité les électrons d'un métal pur, dans l'approximation de liaisons fortes, par des ondes stationnaires qui sont de deux sortes, pour une chaîne linéaire : états symétriques et antisymétriques. Si nous introduisons dans ce métal une impureté de substitution conservant la symétrie du système, les ondes stationnaires perturbées sont simplement déphasées par rapport aux ondes stationnaires non perturbées. Nous avons montré, dans le cas de la chaîne linéaire, que les états antisymétriques n'étaient pratiquement pas déphasés. Ayant calculé le déphasage des états symétriques, nous avons pu établir un certain nombre de résultats généraux que nous allons brièvement résumer :

(1) La présence de l'impureté modifie la densité électronique à grande distance en introduisant des oscillations de charge, dont l'amplitude décroît avec la distance comme $1/r$ et dépend seulement de la valeur du déphasage au niveau de Fermi.

(2) Pour les électrons d'une bande pleine, l'amplitude des oscillations de charge décroît exponentiellement avec la distance à partir de l'impureté : les électrons des couches internes complètement remplies ne subissent donc pratiquement pas l'influence de l'impureté.

(3) Si la bande de valence est très peu remplie ou presque pleine, les oscillations de charge ont une grande longueur d'onde égale à $1/2\Delta k$, en appelant Δk la distance du niveau de Fermi au bas ou au sommet de la bande.

(4) La charge totale déplacée par l'impureté, y compris l'état lié qui apparaît en dehors de la bande, s'exprime simplement en fonction du déphasage au niveau de Fermi, dans le cas d'une chaîne linéaire

$$\rho_{\text{tot}} = \frac{2}{\pi}\eta_M$$

(5) La connaissance du déphasage au niveau de Fermi permet enfin d'exprimer exactement, en fonction des niveaux d'énergie atomiques de l'impureté et des atomes du réseau, la portion de la charge déplacée localement dans le voisinage de l'impureté, c'est-à-dire de la charge d'écran. Un calcul numérique dans le cas d'un réseau linéaire ne présente guère d'intérêt physique et nous nous sommes contentés de considérer le cas des fortes perturbations : on montre alors que, si la bande est très peu remplie, les électrons liés sont localisés au voisinage de l'impureté, tandis que les électrons de la bande peu remplie sont repoussés sur des sites atomiques voisins. Si la bande est à moitié pleine, au contraire, la majeure partie de la charge d'écran se produit dans la maille de l'impureté.

Ces résultats semblent en accord avec les longueurs d'ondes des oscillations de charge dans l'un et l'autre cas.

Remerciement—Ce travail nous a été suggéré par Monsieur le Professeur J. FRIEDEL qui nous a constamment aidé de ses conseils. Nous lui exprimons très vivement notre reconnaissance.

BIBLIOGRAPHIE

1. DANIEL E., *J. Phys. Radium* **20,** 769 (1959).
2. FRIEDEL J., LEMAN G. and OLSZEWSKI S., *J. Appl. Phys.*, sous presse.
3. LEMAN G., *J. Phys. Chem. Solids* **13,** 221 (1960).
4. ASDENTE M., à paraître.
5. BELDING E. F., *Phil. Mag.* **4,** 1145 (1959).
6. KOSTER G. F. and SLATER J. C., *Phys. Rev.* **95,** 1167 (1954).
7. MONTROLL E. W. and POTTS R. B., *Phys. Rev.* **100,** 525 (1955).
8. BÉAL M. T., *J. Phys. Chem. Solids* **15,** 72 (1960).
9. BLANDIN A., *Ann. Phys., Paris*, à paraître.
10. VON LAUE M., *Ann. Phys., Lpz.* **44,** 1197 (1914).
11. COULSON C. A., communication privée.

APPENDICE A : CALCUL DES DEPHASAGES

Nous avons supposé pour établir la valeur (31) du déphasage que les intégrales de recouvrement γ, γ_0 et γ_0' étaient égales, leur valeur étant beaucoup moins grande que celle de α et β.

(1) *Valeur de cette approximation*

Montrons d'abord que cette approximation est justifiée, au moins pour les petites perturbations. Supposons que le potentiel de l'impureté satisfasse à la condition

$$V_0' < V_0(1+\epsilon)$$

où ϵ est un nombre indépendant de r, et petit devant l'unité. La fonction d'onde atomique de l'électron dans le potentiel V_0' pourra s'écrire

$$\psi_0' = \psi_0 + \sum_n a_n\psi_n$$

où les a_n sont petits par rapport à l'unité et les ψ_n sont des fonctions atomiques d'énergie différente de E_0.

On aura donc, d'une part :

$$\gamma_0 = \int \psi_0'^{*} V_1\, dr = \int \psi_0^2 V_1\, dr + \sum_{n,m} \int a_n a_m \psi_n \psi_m V_1\, dr$$

c'est-à-dire

$$\gamma_0 = \gamma + \sum_{n,m} a_n a_m \int \psi_n\psi_m V_1\, dr$$

et par conséquent

$$|\gamma_0 - \gamma| \ll |\gamma| \qquad \text{(A.1)}$$

puisque les a_n sont petits par rapport à l'unité.

D'autre part,

$$|\gamma_0'| = |\int \psi_1^2 V_0'\, dr| < |\int \psi_1^2 V_0(1+\epsilon)\, dr|$$

$$|\gamma_0'| < |\gamma|(1+\epsilon) \qquad \text{(A.2)}$$

Ici encore, la différence $|\gamma_0' - \gamma|$ est petite par rapoprt à $|\gamma|$, ce qui justifie l'approximation que nous avons faite. Nous allons maintenant évaluer exactement les déphasages, sans tenir compte de l'approximation $\gamma \sim \gamma_0 \sim \gamma_0'$.

(2) *Déphasage des états symétriques*

Les coefficients de la fonction d'onde perturbée sont donnés par les équations (9) (10) et (11), qui s'écrivent maintenant :

$$A_0'(\mathscr{E} - E_0' - 2\gamma_0) = \alpha(A_{+1}' + A_{-1}') \qquad \text{(A.3)}$$

$$-A_0'\alpha + A_{\pm 1}'(\mathscr{E} - E - \gamma - \gamma_0') = \beta A_{\pm 2}' \qquad \text{(A.4)}$$

$$A'_j(\mathscr{E}-E-2\gamma) = \beta(A'_{j+1}+A'_{j-1}) \quad |j| \geqslant 2. \tag{A.5}$$

En remplaçant A'_1 et A'_2 respectivement par $B\cos(ka+\eta)$ et $B\cos(2ka+\eta)$ on obtient :

$$\frac{A'_0}{B} = \frac{2\alpha\cos(ka+\eta)}{2\beta\cos ka+\Delta E+2(\gamma-\gamma_0)} = \frac{\beta\cos\eta}{\alpha} + \frac{\gamma-\gamma'_0}{\alpha}\cos(ka+\eta)$$

et le déphasage η est donné par la relation :

$$\operatorname{tg}\eta = \frac{\cos ka\left[\alpha^2-\beta^2-(\gamma-\gamma'_0)\left(\frac{\Delta E}{2}+\gamma-\gamma_0+\beta\cos ka\right)\right]-\beta\left(\frac{\Delta E}{2}+\gamma-\gamma_0\right)}{\sin ka\left[\alpha^2-(\gamma-\gamma_0)\left(\frac{\Delta E}{2}+\gamma-\gamma_0+\beta\cos ka\right)\right]} \tag{A.6}$$

En tenant compte de (A.1) et (A.2), on retrouve bien l'expression (31) pour le déphasage η des états symétriques.

(3) *Déphasage des états antisymétriques*

Pour les états antisymétriques, on doit avoir :

$$A'_0 = 0$$
$$A'_j = A_{-j}$$

et les coefficients A'_j ont la forme générale

$$A'_j = C\sin(jka+\eta') \qquad j \geqslant 1$$

L'équation (A.4) donne immédiatement le déphasage η' :

$$\operatorname{tg}\eta' = \frac{(\gamma'_0-\gamma/\beta)\sin ka}{1+(\gamma-\gamma'_0/\beta)\cos ka}$$

c'est-à-dire, puisque

$$\left|\frac{\gamma-\gamma'_0}{\beta}\right| \ll 1,$$

$$\operatorname{tg}\eta' \simeq \left(\frac{\gamma'_0-\gamma}{\beta}\right)\sin ka \tag{A.7}$$

Les états antisymétriques sont donc très peu modifiés par la perturbation. Quand k varie de 0 à π/a, η' varie de 0 à 0 en restant faiblement positif ou négatif suivant que l'impureté est moins ou plus attractive que les atomes du réseau.

APPENDICE B : ETUDE DU PARAMETRE b

Nous voulons comparer les deux quantités

$$\Delta E = E_0-E'_0 \text{ et } \frac{2(\alpha^2-\beta^2)}{\beta}$$

dans le cas d'une impureté attractive. (ΔE positif) avec des fonctions d'onde atomiques telles que

$$\beta < \alpha < 0 \tag{B.1}$$

Nous posons

$$b = \frac{\beta\Delta E}{2(\alpha^2-B^2)}$$

et nous allons montrer que b est supérieur à l'unité à la fois pour les fortes et petites perturbations.

(1) Si la perturbation est assez forte pour que ΔE soit supérieur à la demi-largeur de bande, c'est-à-dire si :

$$\Delta E > -2\beta \tag{B.2}$$

$$b > \frac{-2\beta^2}{2\alpha^2-2\beta^2}$$

donc $b > 1$

Physiquement, cette condition sera assez souvent réalisée. Elle peut l'être de 2 manières : β petit ou ΔE grand. La premiere manière implique que la matrice a un paramètre cristallin suffisamment grand pour que la bande d'énergie considérée soit raisonnablement étroite. La seconde correspond à une impureté de substitution telle que V'_0 soit assez différent de V_0.

(2) A l'opposé, intéressons-nous maintenant au cas des petites perturbations. Nous posons

$$V'_0 = V_0-\epsilon(r) \tag{B.3}$$

avec

$$|\epsilon(r)| \ll |V_0| \tag{B.4}$$

Notons que $\epsilon(r)$ est négatif quand l'impureté est plus attractive que les atomes du réseau.

La nouvelle fonction d'onde atomique dans la maille origine, correspondant à l'énergie E'_0, peut s'écrire :

$$\psi'_0 = \sum_n a_n\psi^0_n \tag{B.5}$$

L'indice supérieur 0 rappelle que les fonctions d'onde atomiques considérées sont centrées sur l'origine. Dans le développement (B.5)

$$a_0 \sim 1$$

et

$$a_n = \frac{\int \psi_0^0 \epsilon(r) \psi_n^0 \, dr}{E_0 - E_n} \tag{B.6}$$

Il nous faut évaluer les parties principales des deux quantités ΔE et $2(\alpha^2-\beta^2)/\beta$.

La premiere représente la modification du niveau d'énergie E_0 au premier ordre. Par conséquent :

$$E_0' - E_0 = -\Delta E = \int \psi_0^0 \epsilon(r) \psi_0^0 \, dr \tag{B.7}$$

D'autre part,

$$\beta = \int \psi_0^0 V_1 \psi_0^1 \, dr \tag{B.8}$$

et

$$\alpha = \int \psi_0' V_1 \psi_1 \, dr = \beta + \sum_{n \neq 0} a_n \int \psi_n^0 V_1 \psi_0^1 \, dr \tag{B.9}$$

Au premier ordre des coefficients a_n, on aura :

$$\frac{2(\alpha^2-\beta^2)}{\beta} \sim 4 \sum_{n \neq 0} a_n \int \psi_n^0 V_1 \psi_0^1 \, dr \tag{B.10}$$

Dans cette expression,

$$\int \psi_n^0 V_1 \psi_0^1 \, dr$$

est de l'ordre de β et les a_n sont donnés par (B.6). Dire que b est supérieur à l'unité revient donc à prouver que :

$$-\int \psi_0^0 \epsilon(r) \psi_0^0 \, dr > \sum_{n \neq 0} \frac{4\beta}{E_0 - E_n} \int \psi_0^0 \epsilon(r) \psi_n^0 \, dr \tag{B.11}$$

Les deux intégrales sont du même ordre de grandeur. Le terme $E_0 - E_n$ représente la distance en énergie des niveaux atomiques, c'est-à-dire approximativement la distance du milieu de la bande considérée aux milieux des autres bandes. Il suffit alors que la largeur de la bande ($|4\beta|$) soit inférieure à celle des bandes interdites voisines pour que l'inéquation (B.11) soit vérifiée.

On peut donc raisonnablement conclure que b est supérieur à l'unité, pour les petites comme pour les fortes perturbations.

APPENDICE C : ELECTRONS D'UNE BANDE PLEINE

Nous voulons calculer la modification de la densité électronique pour des électrons d'une bande pleine, c'est-à-dire effectuer l'intégrale

$$\Delta\rho(r) = \frac{Na}{\pi} \sum_j A_0^2 \psi_j^2(r - ja) \int_0^{\pi/a} \cos 2(jka + \eta) \, dk \tag{C.1}$$

Le déphasage étant donné par :

$$\operatorname{tg} \eta = p \frac{(b - \cos ka)}{\sin ka} \tag{C.2}$$

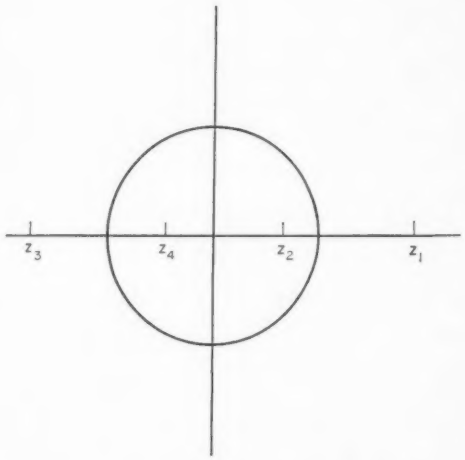

FIG. 6. Position des pôles de J par rapport au cercle unité (explications dans le texte).

où p est positif et $b > 1$ (nous nous bornons au cas d'une impureté plus attractive que les atomes de la matrice), on peut décomposer l'intégrale (C.1) en une somme d'intégrales du type

$$J = \int_{-\pi/a}^{\pi/a} \frac{\exp(imka) \, dk}{\sin^2 ka + p^2(b - \cos ka)^2} \tag{C.3}$$

où m vaut

$$2j, \; 2j \pm 1, \; 2j \pm 2.$$

Nous pouvons donc dire que le comportement

asymptotique de la modification de densité électronique est celui de $J(m)$ avec m grand.

Posons $\exp(ika) = z$ et intégrons sur le cercle unité (Fig. 6)

$$J = \frac{4}{ia} \int_C \frac{z^{m+1}\, dz}{[(p+1)z^2 - 2pbz + p - 1][(p-1)z^2 - 2pbz + p + 1]} \qquad \text{(C.4)}$$

les quatre pôles de la fonction à intègrer valent :

$$z_1 = \frac{pb + \sqrt{(q^2+1)}}{p+1}$$

$$z_2 = \frac{pb - \sqrt{(q^2+1)}}{p+1}$$

$$z_3 = \frac{pb + \sqrt{(q^2+1)}}{p-1}$$

$$z_4 = \frac{pb - \sqrt{(q^2+1)}}{p-1}$$

On a utilisé $q^2 = p^2(b^2-1)$ qui est nécessairement positif. Les quatre pôles sont donc tous réels et deux d'entre eux z_2 et z_4 se trouvent nécessairement à l'intérieur du cercle unité.

Finalement,

$$J = \frac{8\pi}{a(p^2-1)}(\rho_2 + \rho_4)$$

ρ_2 et ρ_4 sont les résidus relatifs aux pôles z_2 et z_4 et sont donc proportionnels à z_2^{m+1} ou z_4^{m+1}, c'est-à-dire de la forme $\exp(-s_1 m)$ ou $\exp(-s_2 m)$ avec s_1 et s_2 positifs.

L'intégrale $J(m)$ se comporte donc pour les grandes valeurs de m comme $\exp(-s_1 m)$, si $s_1 > s_2$, et la modification de densité électronique pour les électrons d'une bande pleine décroît exponentiellement quand on s'éloigne de l'impureté.

ol. 20
1961

J. Phys. Chem. Solids Pergamon Press 1961. Vol. 20, Nos. 1/2, pp. 64–75. Printed in Great Britain.

ENERGY-BAND STRUCTURE OF SOLIDS FROM A PERTURBATION ON THE "EMPTY LATTICE"*†

F. BASSANI

Argonne National Laboratory, Argonne, Illinois

and

V. CELLI

University of Illinois, Urbana, Illinois

(*Received* 19 *September* 1960; *revised* 14 *December* 1960)

Abstract—A simple perturbation approach is developed to obtain the energy-band structure of solids. The unperturbed Hamiltonian consists of the kinetic part and of a uniform potential; the perturbing operator is the crystal potential plus a term which originates from the requirement that valence and conduction states be orthogonal to the inner states. This amounts to an approximation to the O.P.W. method.

Reasons are given for the validity of such a simple scheme and applications are made to the case of the diamond lattice and of the zincblende lattice.

It is shown how features of the energy-band structure depend on the symmetry of the lattice, on the lattice parameter and on the "core states" of the atomic components. Numerical results obtained for diamond, silicon and BN are in fair agreement with recent calculations.

An energy-band structure consistent with experimental information is obtained for Ge and GaAs by fixing the values of a few parameters.

1. INTRODUCTION

IN THE past few years a number of calculations of the energy-band structure of solids have been published[1] and in the case of many monatomic solids the energies of a number of valence and conductions states have been computed with a remarkable amount of labor.

An examination of the results obtained on different elements having the same lattice symmetry and a comparison with results of calculations on fictitious crystals[2,3,4] seem to indicate that the relative positions of the energy levels at symmetry points of the Brillouin zone and the general energy-band structure are quite independent of the lattice potential. The important regularities characteristic of the monovalent metals in the body centered cubic structure have been discussed by COHEN and HEINE[5] on the basis of a simplified model derived from the Wigner–Seitz method.

It is recognized that similar regularities exist for every crystal symmetry. We want to point out that they can be most easily explained in the framework of the Orthogonalized Plane Wave (O.P.W.) method. The reason why this can be done is the same one which is responsible for the good convergence of the O.P.W. method itself, namely the approximate cancellation of the Fourier coefficients of the crystal potential against the terms arising from the procedure of orthogonalization of the trial wave functions to the core states. As recognized by PHILLIPS and KLEINMAN[6], the effect of orthogonalization is formally equivalent to the addition of a repulsive term in an effective Hamiltonian acting on the non-orthogonalized trial wave functions. Though this extra term does not have in general the simple form of a

* Based on work performed under the auspices of the U.S. Atomic Energy Commission.

† Supported in part by the Air Force Research and Development Command, Air Force Contract AF 49–638–420.

potential function of coordinates $V_r(\boldsymbol{r})$, PHILLIPS and KLEINMAN found that an approximate "effective potential" $V_r(\boldsymbol{r})$ can be simply constructed from the O.P.W. method. ANTONCIK[7] makes use of the same idea, but approximates the repulsive potential by a formula derived from the statistical theory of the atom. The calculations performed using these simplifications give good results in the case of diamond,[8] where only s core states are present, but are not so accurate in the case of silicon.[9] The idea of a repulsive potential has been mainly successful in the formulation of an interpolation scheme,[10] in which the high Fourier coefficients of $V_r(\boldsymbol{r})$ are assumed to cancel exactly the high Fourier components of the crystal potential and the low Fourier components are chosen to fit a few calculated or experimental values.

The justification of these procedures first suggested by COHEN[11] will be used here to show that the combined effect of the crystal potential and the repulsive term can be treated as a perturbation on the eigenstates of a uniform potential. In this scheme the first and second order corrections to the energy of a level can be visualized as arising from the core states of the atoms composing the crystal and from the first few Fourier coefficients of the crystal potential and thus a criterion is given for predicting the positions of energy levels belonging to different irreducible representations of the group of the wave vector $\boldsymbol{k}$.

This simple approach will be shown to give qualitative information on the energy-band structure of crystals with diamond and zincblende type structure. A quantitative application of the method to the case of diamond, silicon and boron nitride gives results in good agreement with previous calculations. A simplified interpolation scheme has been set up in this framework, which is shown to reproduce the band structure obtained by PHILLIPS for Ge[10] and is further applied to the case of gallium arsenide.

2. PERTURBATION APPROACH TO THE O.P.W. METHOD

Let $H = H_0 + V(\boldsymbol{r})$ be the one-electron Hamiltonian of the crystal and let ψ_c be the wave functions of the core states, which satisfy the equations $H\psi_c = E_c\psi_c$, where E_c is the atomic eigenvalue for the core state c. The unperturbed Hamiltonian H_0 is the sum of the kinetic energy and the Fourier coefficient $V(0)$ of the potential, so that the space average of $V(\boldsymbol{r})$ can be taken to be zero.

The eigenfunction $\psi^\alpha(\boldsymbol{k},\boldsymbol{r})$ of a valence or conduction state associated with the irreducible representation α of the group of $\boldsymbol{k}$ is determined in the O.P.W. method by putting

$$\psi^\alpha(\boldsymbol{k},\boldsymbol{r}) = \phi^\alpha(\boldsymbol{k},\boldsymbol{r}) - \sum_c (\psi_c,\phi^\alpha)\psi_c(\boldsymbol{k},\boldsymbol{r})$$

and expanding ϕ in the appropriate set of symmetrized linear combinations of plane waves. The Schrödinger equation can be transformed into:

$$(H+R)\phi = E\phi \tag{1}$$

where the operator R is defined by:

$$R\phi = \sum_c (E-E_c)\,(\psi_c,\phi)\psi_c. \tag{1'}$$

It is clear that the function ϕ is not uniquely defined. In fact, adding to ϕ any arbitrary combination of core wave-functions we obtain a wave function ϕ' which satisfies equations (1) and (1') and gives the same results for $\psi^\alpha(\boldsymbol{k},\boldsymbol{r})$ and E. It is possible in principle to remove this indeterminacy from ϕ by substituting R in equation (1) with an operator R' defined by:

$$R'\phi = \sum_c (\psi_c, A\phi)\psi_c \tag{1''}$$

where A is any chosen operator. Then the solutions of the equation:

$$(H+R')\phi = E\phi \tag{2}$$

also satisfy equation (1) because by multiplying equation (2) on the left by ψ_c and integrating we obtain, for every value of the index c:

$$(\psi_c,A\phi) = (E-E_c)\,(\psi_c,\phi). \tag{3}$$

However, now the function ϕ belonging to a given eigenvalue E is uniquely defined because of equation (3).

Several choices of A are possible: (a) for $A = 0$, ϕ reduces to the eigenfunction ψ; (b) for $A = E-H$ equation (3) becomes an identity and gives back the equations (1) and (1'); (c) for $A = -V$, equation (1) becomes:

$$H_0\phi + V\phi - \sum_c (\psi_c,V\phi)\psi_c = E\phi \tag{4}$$

and this shows that the orthogonalization has the effect of subtracting from $V\phi$ that part which can be expanded over the core states, that is a large fraction of the potential V near the nuclei is cancelled. The most convenient choice depends on the method used to solve equation (2).

In the present paper $V+R'$ will be treated as a perturbation and R' will be defined by choosing the operator A in such a way that $\phi^\alpha(\boldsymbol{k},\boldsymbol{r})$ be as close as possible to a combination of a few plane waves of the appropriate symmetry. Rules have been given in detail by HERMAN[12] and others to construct such combinations. In short the "empty lattice" analysis is first performed, grouping into a set all the plane waves of the form $\exp[i(\boldsymbol{k}+\boldsymbol{h}_i)\boldsymbol{r}]$ belonging to the same eigenvalue of H_0,

$$W_i^0 = V(0)+\frac{\hbar^2}{2m}|\boldsymbol{k}+\boldsymbol{h}_i|^2.$$

As usual, $\boldsymbol{k}$ indicates the reduced wave vector and $\boldsymbol{h}_i$ a reciprocal lattice vector. Out of every set one then forms linear combinations $S_i^\alpha(\boldsymbol{k},\boldsymbol{r})$ which transform according to a given irreducible representation α of the group of the $\boldsymbol{k}$ vector. Matrix elements of $V+R'$ between S_i^α and S_j^β will vanish for $\alpha\neq\beta$, so that the correct zero order linear combinations are directly obtained by symmetry arguments, unless the same irreducible representation appears more than once in a given set or it appears in two sets which lie close in energy in the empty lattice.

To obtain general formulae let us consider the case of two quasi-degenerate or degenerate states $S_1^\alpha(\boldsymbol{k},\boldsymbol{r})$ and $S_2^\alpha(\boldsymbol{k},\boldsymbol{r})$ having energies W_1^0 and W_2^0 with $W_1^0\leqslant W_2^0$. The perturbed wave functions of these states are expanded as follows:

$$\phi = c_1S_1+c_2S_2+{\sum_j}' a_jS_j$$

where S_1 and S_2 appear only in the zero-order combination $S_1^0=c_1S_1+c_2S_2$ which is normalized to unity. For the lower energy level we set $E_1=W_1^0+W_1'+W_1''$. Substituting into (2) and considering zero and first-order terms together we obtain:

$$\begin{aligned} c_1(S_1,(H+R')S_1)+c_2(S_1,(V+R')S_2) &= (W_1^0+W_1')c_1 \\ c_1(S_2,(V+R')S_1)+c_2(S_2,(H+R')S_2) &= (W_1^0+W_1')c_2 \end{aligned} \tag{5}$$

Solving equation (5) one obtains the first-order correction to the energy and the zero-order correct wave function S_1^0. For the coefficients a_j we obtain:

$$a_j=\frac{(S_j,(V+R')S_1^0)}{W_1^0-W_j^0}$$

The energy to second order is then formally given by the same expression as for a non-degenerate level; but now S_1^0 needs not to be an eigenfunction of the unperturbed Hamiltonian.

$$E_1=(S_1^0,(H+R')S_1^0)+{\sum_j}'\frac{(S_1^0,(V+R')S_j)\,(S_j,(V+R')S_1^0)}{W_1^0-W_j^0} \tag{6}$$

The question arises at this point as to which is the most convenient form of the operator R' to be inserted into equations (5) and (6). In the Appendix we show that the requirement that ϕ be as close as possible to S_1^0 is consistent with considering $R'\phi$ as the sum of a first order term.

$$R_1'\phi=\sum_c(W_1^0-E_c)\,(\psi_c,\phi)\psi_c$$

and a second order correction

$$R_2'\phi=\sum_c W_1'(\psi_c,\phi)\psi_c$$

The first order term is the one used in obtaining W_1' and S_1^0 from equation (5). When both terms are substituted into equation (6) the second order correction to the energy becomes:

$$W_1''=W_1'\sum_c|(\psi_c,S_1^0)|^2+{\sum_j}'\frac{|(S_1^0,VS_j)+\sum_c(W_1^0-E_c)\,(S_1^0,\psi_c)(\psi_c,S_j)|^2}{W_1^0-W_j^0} \tag{7}$$

The perturbation formulae so obtained reduce to the ones previously derived in the appendix of Ref. (2) in the case of well separated unperturbed eigenvalues.

The problem of checking the convergence of the method cannot be treated without considering higher order terms in the perturbation expansion,

Vol. 20
1961

which is extremely unpractical. The confidence that the present method gives a reliable picture and can be used in practice lies mainly in the cancellation between the attractive potential and the repulsive term, which makes the matrix elements of the perturbation very small. As in the case of the O.P.W. method[6,7] a great simplification is introduced if the repulsive operator R' is substituted by a repulsive potential appropriate to the core state and independent of ϕ since then the present approach does not differ from the usual free electron perturbation theory except for the fact that the perturbation is now the total potential $V+R'$ instead of the crystal potential V. The perturbation method in this simplified form has been presented in 1954 by ANTONCIK[7], who applied it to some metals of the b.c.c. structure. The accuracy of the results obtained in this way depends on the choice of the repulsive potential and is poorer in general than in our more consistent approach; in the case of Si for instance, the error introduced into the first order perturbation term by choosing the repulsive effective potential suggested by KLEINMAN and PHILLIPS[9] or the one used by ANTONCIK[7] would not be negligible. This simplification however can be probably accepted when the method is used as an interpolation scheme, where the values of the Fourier coefficients of the total potential are chosen *a posteriori*; it becomes then very similar to the interpolation scheme used by PHILLIPS[10] on Si and Ge and by HARRISON[13] on some polyvalent metals.

The present formulation allows one to draw up some qualitative rules for the sequence of the energy levels at a given symmetry point of the Brillouin zone. From formulae (5) and (6) one sees that the lowest energy levels in the empty lattice will be the lowest levels in the perturbed crystal too. The first order correction is generally positive, its magnitude depends on the structure of the matrix element determined from the irreducible representation considered and on the core eigenstates which belong to the same irreducible representation. *s*-Like states will have a larger term than *p*-like states and *d*-like states because the orthogonality coefficients are larger. In the second order correction the interaction with higher unperturbed states decreases the energy and the interaction with lower unperturbed states increases the energy, the correction decreasing as the states are farther apart. The preceding arguments are mostly valid at symmetry points, where the group theoretical classification of the plane waves is of great advantage.

In proximity of a symmetry point the number of levels to be treated as quasi-degenerate becomes larger. It is then convenient to resort to the perturbation approach discussed by KANE[14]. In the following applications to the study of the energy-band structure of solids in the diamond and zincblende structure we shall be concerned only with energy levels at special points. In a more detailed study of experimental data the effect of spin–orbit interaction should also be considered.

3. THE DIAMOND LATTICE STRUCTURE: NUMERICAL RESULTS FOR Si AND DIAMOND

The perturbation approach described in Section (2) will now be tested for crystals with the diamond structure.

We will consider unperturbed energy values up to the energy

$$8\frac{\hbar^2}{2m}\left(\frac{2\pi}{a}\right)^2$$

where a is the lattice constant. The value of $V(0)$ can be estimated in the same way as by HERMAN and WOODRUFF[15] or can be directly inferred from experimental data.[9] The effect of the perturbation on the various energy levels is obtained from formulae (5), (6) and (7). The symmetry analysis given in Table 1, Ref. (2), in Table 2 of HERMAN's paper[12] and in Table 5 of CASELLA's paper[4] enables one to obtain explicit expressions for the energy levels at the symmetry points Γ ($\boldsymbol{k}=0$),

$$X\left(\boldsymbol{k}=\frac{2\pi}{a}(1,0,0)\right) \text{ and } L\left(\boldsymbol{k}=\frac{2\pi}{a}(\tfrac{1}{2},\tfrac{1}{2},\tfrac{1}{2})\right)$$

as functions of the Fourier coefficients of the crystal potential $V(\boldsymbol{h}_i)$, of the orthogonality coefficients

$$(\psi_c, S_i^{\alpha}(\boldsymbol{k}))$$

and of the core energies E_c.

Qualitative considerations can be immediately drawn in the way indicated in Section (2). At the point $\boldsymbol{k}=0$ the lowest lying valence level is expected to be Γ_1. There will be a splitting of the levels $\Gamma_{2'}$, $\Gamma_1(2)$, $\Gamma_{25'}$, and Γ_{15} which come next in

the empty lattice. The first order perturbation increases the energy of $\Gamma_1(2)$ and $\Gamma_{2'}$ more than that of Γ_{15} and $\Gamma_{25'}$ for light elements because the repulsion from s-states is larger than that from p-states and $\Gamma_1(2)$ is further raised at second order by the positive interaction with $\Gamma_1(1)$. The second order correction lowers $\Gamma_{25'}$ with respect to Γ_{15} because of the interaction with the set $\langle 200 \rangle$ in the former case. The sequence of the energy levels at the Γ point in the diamond structure is then:

$$\Gamma_1 < \Gamma_{25'} < \Gamma_{15} \sim \Gamma_{2'} < \Gamma_1(2)$$

This is verified in calculations on C, Si and pseudocrystals. However, HERMAN's calculations for Ge[16] give $\Gamma_{2'}$ lower than Γ_{15}; we think that this can be attributed to the presence of d-core states which raise Γ_{15} with respect to $\Gamma_{2'}$ which is an s-like state.

In lattice constant and consequently an increase in the energy gap as experimentally observed.[17]

Quantitative results can also be obtained from formulae (5), (6), and (7) with a small amount of labor. We have carried out the calculations for silicon using the same core states and crystal potential as KLEINMAN and PHILLIPS[9]* rather than the expressions given by WOODRUFF[15], which one of us used in a previous O.P.W. calculation.[18] In Table 1 we give our numerical results and for comparison the results obtained by KLEINMAN and PHILLIPS, who used their "effective potential method" but introduced corrections to make it equivalent to a complete O.P.W. method. The difference in the results due to our use of the perturbation approach is seen to be not significantly large with a maximum difference of about 0·1 Ry for the level $L_{3'}$. The agreement can still

Table 1. *Energy levels at points* Γ, X, L *in* Si (*in* Ry)

Irr. rep.	Γ_1	$L_{2'}$	X_1	L_1	X_4	$L_{3'}$	$\Gamma_{25'}$	$X_1(2)$	Γ_{15}	L_3	$L_1(2)$
Present calculations	−2·35	−2·15	−2·08	−2·00	−1·73	−1·60	−1·57	−1·32	−1·32	−1·22	−1·19
KLEINMAN and PHILLIPS[9]	−2·32	−2·11	−2·01	−1·96	−1·77	−1·70	−1·56	−1·38	−1·35	−1·28	−1·18

At the other symmetry points of the Brillouin zone also, the sequence of the energy levels at each point can be inferred in the same way and is in agreement with the calculations performed and with the experimental evidence available. However, very little can be said in this qualitative way about the relative position of energy levels at different symmetry points.

It is to be expected from the present approach that an increase in the lattice constant will contract the energy scale of the empty lattice eigenvalues and consequently will make the separation between final energy levels smaller. This is in agreement with the experimental observation that the energy gap and the valence band width decrease going from diamond to silicon to germanium. On this basis one can also explain qualitatively the effect of pressure on the energy gap; an increase in pressure will cause a decrease

be improved by including more plane waves in the perturbation expansion since this will lower our energies for the states $L_{3'}$ and L_3 by a few hundredths of a Rydberg and have a much smaller effect on the other states. However, the main interest of this calculation is that of showing that perturbation corrections of order higher than second are small enough to have a negligible effect on the general energy-band structure. The quantitative application of this procedure to the case of diamond has also been made but in this case we felt justified to use for the operator R' in equations (5) and (6) the effective repulsive potential evaluated by KLEINMAN and PHILLIPS[8]. The results for s-like states are quite good but, as expected,

* We are very grateful to Dr. KLEINMAN for giving us the new values of the "orthogonality coefficients" which were not reproduced in the paper of Ref. (9).

Vol. 2
1961

the p-like states Γ_{15}, $\Gamma_{25'}$, X_4, L_3 and $L_{3'}$ do not show the same good convergence because of the absence of the repulsive terms in this case. However, the relative position of these states is obtained correctly and, by adding a constant value ($-0{\cdot}3$ Ry) to compensate for the neglect of plane waves of higher energy, we can still reproduce the correct energy-band structure. In Table 2 our results are given together with the results reported by KLEINMAN and PHILLIPS[8], which are extrapolations of HERMAN's previous results.[15] The general energy band structure is the same but the states $L_{3'}$, L_3, $L_1(2)$ are about 0·1 Ry higher in our calculations. We feel that this is not an essential disagreement and can be sensibly reduced just by including a larger number of plane waves in the perturbation approach.

Table 2. Energy levels at points Γ, X, L in diamond (in Ry)

	Γ_1	$L_{2'}$	X_1	L_1	X_4	$L_{3'}$	$\Gamma_{25'}$	Γ_{15}	$X_1(2)$	L_3	$L_1(2)$
Present results	−2·44	−1·98	−1·66	−1·48	−1·30	−1·02	−0·79	−0·36	−0·23	−0·04	−0·03
HERMAN's results	−2·41	−1·97	−1·64	−1·55	−1·29	−1·14	−0·80	−0·35	−0·28	−0·14	−0·14

We have not performed numerical calculations of this kind on Ge but we might expect that the effect of orthogonalizing to the d-core states will be to raise the energies of the states Γ_{15} and L_3 with respect to that of the predominantly s-like states $\Gamma_{2'}$ and $L_1(2)$.

4. THE ZINCBLENDE STRUCTURE: NUMERICAL RESULTS FOR BN

This structure consists of two f.c.c. lattices made of different atoms, one of the lattices being obtained from the other by a translation $a(\frac{1}{4}, \frac{1}{4}, \frac{1}{4})$, a being the lattice constant. The symmetry analysis of the Brillouin zone has been given by PARMENTER[19] and we will use his notations. HERMAN[20] and CALLAWAY[21] have made qualitative considerations on the energy bands by considering the crystal potential as a perturbation on the diamond lattice potential; along the same line KLEINMAN and PHILLIPS[22] have given results for BN; other calculations and experimental data are reviewed by CALLAWAY[1] and by WELKER and WEISS[23]. An O.P.W. calculation has been done by KOBAYASI on SiC.[24]

The application to this structure of the perturbation procedure described in Section (2) has been carried out in detail. The Crystal Symmetry Combinations of Plane Waves (C.S.C.P.W.) are chosen to be the same as in the diamond structure at the points Γ and L. At these points the number of irreducible representations for the zincblende structure is half as much as for diamond, because the group of the $\boldsymbol{k}$ vector for the diamond structure is the direct product of that of the zincblende structure times the group composed by identity and inversion. The situation is different at the point X, where the two-dimensional irreducible representation X_1 in diamond splits into X_1 and X_3 (one dimensional) in zincblende, and similarly X_2 splits into X_2 and X_4. The other irreducible representations of diamond X_3 and X_4 coalesce into X_5. In order to get real matrix elements we found it convenient to use for X_1 and X_3 new C.S.C.P.W.'s obtained by taking the origin at a lattice point. The irreducible representations which appear in the lowest empty-lattice levels are given in Table 3. The C.S.C.P.W.'s can be taken from previous papers on the diamond structure[12] except those belonging to the irreducible representations X_1 and X_3 which are given in Table 4. A connection between the matrix elements of the zincblende and the diamond lattice can be established by dividing the crystal potential and the repulsive terms in two parts, which are symmetric and antisymmetric about the middle point of the two nearest atoms. The method of Section (2) enables one to derive explicit expressions for the energy values of all irreducible representations listed in Table 3. We do not think it necessary to give tables for them, but rather we will discuss

Table 3. Symmetry analysis of the "Empty Lattice" in the zincblende structure

Number of plane waves		Empty lattice eigenvalues in units $\frac{\hbar^2}{2m}\times\frac{4\pi^2}{a^2}$	Irreducible representations
Point Γ $k=0$	1	$(0,0,0)^2$	$\Gamma_1(s)$
	8	$(1,1,1)^2$	$2\Gamma_1, 2\Gamma_{15}(p,d)$
	6	$(2,0,0)^2$	$\Gamma_{15}, \Gamma_1, \Gamma_{12}(d)$
	12	$(2,2,0)^2$	$\Gamma_1, 2\Gamma_{15}, \Gamma_{25}, \Gamma_{12}$
Point X $k=\frac{2\pi}{a}(1,0,0)$	2	$(1,0,0)^2$	$X_1(s,p,d), X_3(s,p,d)$
	4	$(0,1,1)^2$	$X_1, X_3, X_5(p,d)$
	8	$(1,2,0)^2$	$X_1, X_3, 2X_5, X_2(p,d), X_4(p,d)$
	8	$(2,1,1)^2$	$2X_1, 2X_3, 2X_5$
Point L $k=\frac{2\pi}{a}(1/2,1/2,1/2)$	2	$(1/2,1/2,1/2)^2$	$2L_1(s,p,d)$
	6	$(3/2,1/2,1/2)^2$	$2L_1, 2L_3(p,d)$
	6	$(1/2,3/2,3/2)^2$	$2L_1, 2L_3$
	6	$(5/2,1/2,1/2)^2$	$2L_1, 2L_3$
	2	$(3/2,3/2,3/2)^2$	$2L_1$

N.B.—The core states which belong to a given irreducible representation are indicated in parentheses every time the irreducible representation appears first.

the qualitative features as done for the diamond structure.

At the point Γ the lowest eigenvalue will be Γ_1. The first order correction to the energy of this state contains only the symmetric part of the potential and is very close to that for the diamond structure. The second order correction is expected to be larger than in the diamond structure because of terms from the antisymmetric part of the potential. The second eigenvalue of Γ_1 is degenerate in zero order and as a result of the splitting in first order due to the antisymmetric perturbation this level will be lowered with respect to the corresponding $\Gamma_{2'}$ of the diamond structure. The next irreducible representation Γ_{15} is also degenerate in zero order and the effect of the antisymmetric potential to first order will be to lower $\Gamma_{15}(1)$ with respect to $\Gamma_{25'}$ of the diamond structure and to raise $\Gamma_{15}(2)$ with respect to Γ_{15} of the diamond structure. The expected order of the energy levels will then be:

$$\Gamma_1 \ll \Gamma_{15}(1) < \Gamma_1(2) \sim \Gamma_{15}(2).$$

The relative positions of $\Gamma_1(2)$ and $\Gamma_{15}(2)$ depend on the core states which are present; if there are

Table 4. Crystal symmetry combinations of plane waves in the zincblende structure with the origin at a lattice point for the wave vector $\mathbf{k} = 2\pi/a\,(100)$ (point X)

Set of plane waves	C.S.C.P.W. for X_1 and X_3
$\langle 100\rangle$	$1/\sqrt{2}[(100)\pm(\bar{1}00)]$
$\langle 011\rangle$	$1/2\ [(011)+(0\bar{1}\bar{1})\pm(0\bar{1}1)\pm(01\bar{1})]$
$\langle 120\rangle$	$1/\sqrt{8}\ [(120)+(1\bar{2}0)+(102)+(10\bar{2})\pm(\bar{1}20)\pm(\bar{1}\bar{2}0)\pm(\bar{1}02)\pm(\bar{1}0\bar{2})]$
$\langle 211\rangle$	$1/\sqrt{8}\ [211)+(2\bar{1}\bar{1})+(\bar{2}11)+(\bar{2}\bar{1}\bar{1})\pm(\bar{2}1\bar{1})\pm(\bar{2}\bar{1}1)\pm(2\bar{1}1)\pm(21\bar{1})]$
	$1/\sqrt{8}\ [(211)+(2\bar{1}\bar{1})-(\bar{2}11)-(\bar{2}\bar{1}\bar{1})\pm(\bar{2}1\bar{1})\pm(\bar{2}\bar{1}1)\mp(2\bar{1}1)\mp(21\bar{1})]$

N.B.—In any of the combinations of plane waves the first choice of signs gives a combination belonging to X_1, and the second choice the combination belonging to X_3.

other core states besides ($1s$) we may expect $\Gamma_1(2)$ to lie lower than $\Gamma_{15}(2)$.

A similar analysis at the point L, also with the help of the Table 3, gives the sequence:

$$L_1(1) < L_1(2) \ll L_3(1) \ll L_1(3) \approx L_3(2).$$

If p or d core states are present, we expect $L_1(3)$ to be lower than $L_3(2)$.

At the point X the levels X_1 and X_3 correspond to the twice degenerate level X_1 of diamond. They differ by a consistent change in sign of the antisymmetric terms in all matrix elements. The levels X_5 correspond to the levels X_4 of the diamond structure. The sequence of levels that we expect will be:

$$X_1(1) < X_3(1) < X_5(1) < X_1(2) < X_3(2) < X_5(2).$$

An energy gap exists and the material is an insulator when $\Gamma_{15}(1)$, $L_3(1)$ and $X_5(1)$ are all lower than the levels appearing next in the sequences. This appears always to be the case for the compounds which are known to crystallize in this structure.

We have made numerical computations for BN using the parameters reported by KLEINMAN and PHILLIPS[22] and their repulsive potential approximation to the operator R', as we have done for diamond, because only the core state $1s$ is present. As in the case of diamond the convergence of p-like states is rather poor and the same correction $-0{\cdot}3$ Ry has been added to the states Γ_{15}, X_5, and L_3. The results so obtained from our usual perturbation on the "empty lattice" are shown in Table 5 together with the results of KLEINMAN and PHILLIPS[22] obtained from a perturbation on the diamond lattice. While the general energy-band structure in both approximations displays the same physical features, increase in the energy gap with respect to diamond and splitting of the valence band into two separated bands, the quantitative results do not show the same good agreement as in the cases of Si and diamond. A complete O.P.W. calculation on BN is in progress.

It is a rather difficult task to predict the relative positions of levels of the same band at different points of the Brillouin zone because the difference is very small and is rather sensitive to the particular elements which form the structure. In the case of BN the minimum of the lowest conduction band was found at the point X (see Table 5), but for the elements with p and d core states as GaAs, InSb, CdS ... we may expect the minimum to be at the center of the zone and to be the state $\Gamma_1(2)$ since the effect of p and d core states is to increase the energies of X_1, X_3, L_1 and Γ_{15} with respect to that of $\Gamma_1(2)$ as can be seen from Table 3 and more clearly from the matrix elements of the perturbation. These considerations are in agreement with the results obtained by SHAKIN and BIRMAN[25] in ZnS with the Wigner–Seitz method.

5. ENERGY BAND STRUCTURE OF Ge AND GaAs

It seems of interest to use the present method as an interpolation scheme for the case of Ge and GaAs, where the large number of electrons would make the calculation of the parameters quite laborious. These two crystals are very similar having the same kind of core states and lattice constants nearly equal, $a = 5{\cdot}647$ Å in Ge and $a = 5{\cdot}635$ Å in GaAs. For both of them we approximate the repulsive operator R' of Section (2) with an effective potential depending on the core states. The quantity $V+R'$ which appears as a perturbation on the "empty lattice" is called the total potential and we consider its Fourier coefficients as disposable parameters as PHILLIPS has done with the O.P.W. method.[10] We assume

Table 5. *Energy values at the symmetry points* Γ, X *and* L *in* BN (*in* Ry)

	Γ_1	L_1	X_1	$L_1(2)$	X_5	X_3	L_3	Γ_{15}	$X_1(2)$	$\Gamma_{15}(2)$	$X_3(2)$	$\Gamma_1(2)$	$L_1(3)$
Present calculations	−2·52	−2·24	−2·17	−1·45	−1·34	−1·33	−1·06	−0·95	−0·45	−0·32	−0·17	−0·14	−0·13
KLEINMAN and PHILLIPS	−2·48	−2·16	−2·07	−1·42	−1·21	−1·37	−1·26	−1·16	−0·39	−0·11	−0·29	−0·31	−0·20

that the effect of the perturbation on the "empty lattice" can be represented by giving appropriate values to a few Fourier coefficients of the total potential and that the other Fourier coefficients are zero because of the cancellation between the crystal potential and the repulsive term near the nucleus. The constant part of the crystal potential does not have any effect on the relative positions of the energy bands in our approximation, but the first order correction contains a term arising from the core states, which has the effect of raising the energy of s-like states more than that of other states. Unlike PHILLIPS[10] we take this effect into account by allowing for two Fourier coefficients with wave vector 0, one $V_s(0)$ for s-like states and the other $V_p(0)$ for non s-like states. Their difference is taken as one of the parameters and can be fitted to give the experimental energy gap of Ge. The other values of the parameters are chosen according to estimates of their order of magnitude and to the requirement of reproducing the experimental energy levels. The experience with Si, diamond and BN suggests that the Fourier coefficients of the total potential can be represented as functions of $|K|^2$ in the way indicated in Fig. 1 for the symmetric part to be considered in the case of Ge (see Fig. 2 of Ref. (3) for comparison with the case of Si). For the Fourier coefficients of the antisymmetric part of the potential we assume a behavior as indicated in Fig. 2. In this way the energy-band structure of Ge is made to depend on the values of the parameters $V_s(0)-V_p(0)$, $V_S(3)$ and $V_S(11)$, the other Fourier coefficients of the potential being considered negligible; the energy-band structure of GaAs is made to depend on the same quantities plus the additional parameter $V_A(3) = V_A(4)$. Using this scheme the calculation of the energy levels becomes very simple. For the lowest valence state Γ_1 for instance the formula is:

$$E_{\Gamma_1} = V_s(0) - \frac{4|V_S(3)|^2}{3\left(\frac{2\pi}{a}\right)^2} - \frac{4|V_A|^2}{3\left(\frac{2\pi}{a}\right)^2} - \frac{6|V_A|^2}{4\left(\frac{2\pi}{a}\right)^2}.$$

In other cases the method of Section (2) has been used to split the degeneracies and the quasi-degeneracies. The sets of plane waves $\langle 300\rangle$ and $\langle 221\rangle$ at the point X and $\langle \frac{5}{2}, \frac{3}{2}, \frac{1}{2}\rangle$ at the point L have also been considered in addition to those reported in Table 3; their effect is that of lowering the higher states at the points L and X by about 0·02 Ry. We have performed calculations with slightly different sets of values for the parameters and in all cases we have obtained basically the same energy-band structure with differences of the order of 0·01 Ry; since this is the order of magnitude of the energy separation of the various

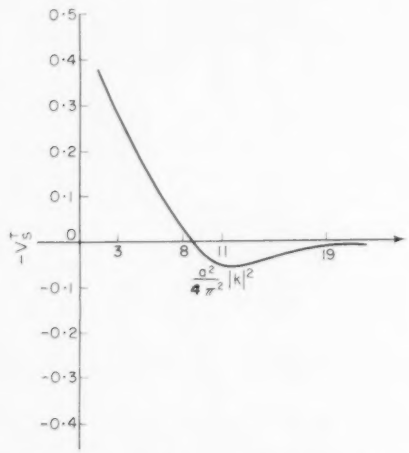

FIG. 1. Fourier coefficients of the total effective potential assumed for Ge (in Ry).

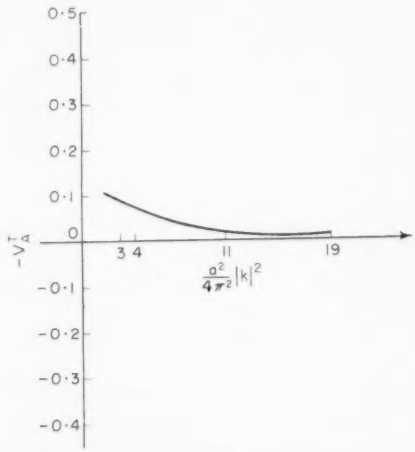

FIG. 2. Antisymmetric Fourier coefficients of the total effective potential assumed for GaAs (in Ry).

In other cases the method of Section (2) has been used to split the degeneracies and the quasi-degeneracies. The sets of plane waves $\langle 300\rangle$ and $\langle 221\rangle$ at the point X and $\langle \frac{5}{2}, \frac{3}{2}, \frac{1}{2}\rangle$ at the point L have also been considered in addition to those reported in Table 3; their effect is that of lowering the higher states at the points L and X by about 0·02 Ry. We have performed calculations with slightly different sets of values for the parameters and in all cases we have obtained basically the same energy-band structure with differences of the order of 0·01 Ry; since this is the order of magnitude of the energy separation of the various

Vol. 2
1961

Table 6. Energy values at the points Γ, X, L *in* Ge *and in* GaAs (*in* Ry)

Irr. rep.	Energy in Ge	Irr. rep.	Energy in GaAs
Γ_1	−0·80	Γ_1	−0·84
$L_{2'}$	−0·69	L_1	−0·81
X_1	−0·51	X_1	−0·78
		X_3	−0·34
L_1	−0·36	L_1	−0·34
X_4	−0·12	X_5	−0·14
$L_{3'}$	−0·01	L_3	−0·03
$\Gamma_{25'}$	+0·09 (0·09)	Γ_{15}	+0·04 (0·03)
$\Gamma_{2'}$	+0·15 (0·15)	Γ_1	+0·14 (0·14)
L_1	+0·14 (0·14)	L_1	+0·15 ($\geqslant$0·16)
X_1	+0·20 ($\sim$0·17)	X_1	+0·19 ($\geqslant$0·18)
		X_3	+0·29
Γ_{15}	+0·34	Γ_{15}	+0·32
L_3	+0·39	L_3	+0·40

N.B.—The values in brackets are the experimental values. The scale is adjusted to $\Gamma_{25'}$ in Ge and $\Gamma_1(2)$ in GaAs. The experimental values for $L_1(3)$ and $X_1(2)$ in GaAs are the lowest limit since they are appropriate to minima in the direction [111] and [100].[26]

minima of the conduction band the choice of the parameters is rather critical if the correct order has to be obtained for energy levels at different points of the reduced zone. With $V_S(3) = -0{\cdot}230$ Ry and $V_S(11) = +0{\cdot}055$ Ry the minimum of the conduction band in Ge turns out to be the state $L_1(2)$ as experimentally observed. The values of $V_s(0)$ and $V_p(0)$ which adjust the scale for s-like and p-like states respectively are $V_s(0) = -0{\cdot}60$ Ry and $V_p(0) = -0{\cdot}64$ Ry. The results obtained for Ge are reported in Table 6 together with the experimental values as given by PHILLIPS[10]. Our results as well as the values of the parameters are very close to those of PHILLIPS[10] because of the similar interpolation schemes, however our choice of the parameters allows a better agreement with the experimental results. In Table 6 are also given the results for GaAs obtained with $V_A = -0{\cdot}075$ Ry together with the values of a few energy levels which can be inferred from the band structure assumed by EHRENREICH[25] to interpret transport properties in GaAs. The main effect of the heteropolar term V_A is seen to be that of lowering the energy of $\Gamma_{15}(1)$ in GaAs with respect to that of $\Gamma_{25'}$ in Ge with the result of increasing the energy gap by an amount in reasonable agreement with experiment; the energy of $\Gamma_1(2)$ is also slightly lowered with respect to that of $\Gamma_{2'}$ in Ge so that the minimum of the conduction band is now at the centre of the zone. While the first effect is probably a general result

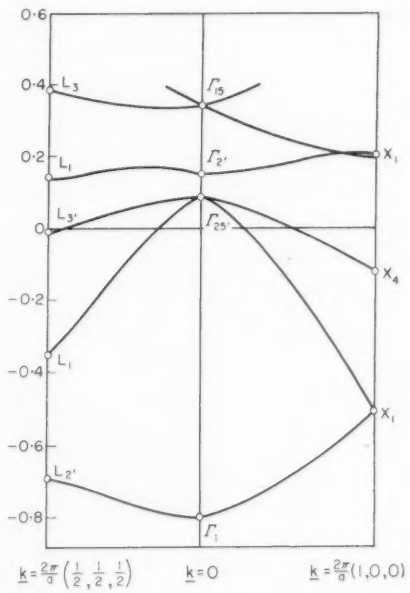

FIG. 3. Energy-band structure of Ge (energies in Ry).

of the method, the change in position of the minimum of the conduction band is strongly dependent on the choice of the parameters and on the number of plane waves considered so that little significance can be attached to it. The energy band structures of Ge and GaAs obtained by joining the points of Table 6 are sketched in Fig. 3 and Fig. 4 respectively. We have not interpolated explicity along the two symmetry lines Λ and Δ but we feel confident that the results of such

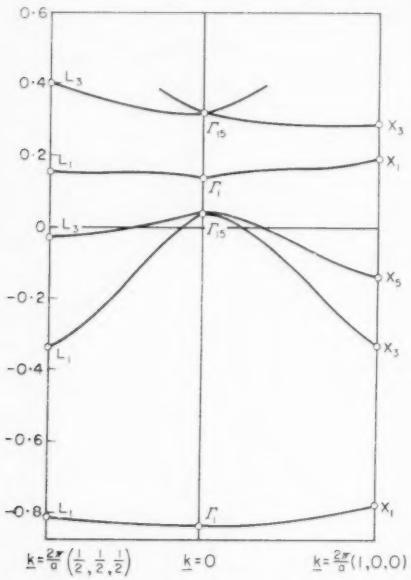

FIG. 4. Energy-band structure of GaAs (energies in Ry).

a detailed interpolation would be essentially the same as those found by PHILLIPS[10]. The predictions on some energy levels proposed by CALLAWAY for GaAs[21] are confirmed, except for the level $L_3(1)$ which is not sensibly changed from Ge. The valence band is separated into two subbands, the lowest of which appears to be very narrow; this result could be experimentally detected by soft X-ray emission as already pointed out by KLEINMAN and PHILLIPS[22].

6. CONCLUSIONS

The simplified approach we have given to derive qualitative features and quantitative results for the energy-band structure does not rule out the necessity for more precise calculations, but it is justified in view of the present uncertainty related to such calculations. Its main advantage is that of exhibiting explicitly the role of the lattice symmetry, core states and lattice parameter on the energy-band structure of different compounds. The critical role played by the few lowest Fourier coefficients of the potential with the corresponding terms from the core states explains the good results obtained in spite of the poor knowledge of the crystal potential. This also points to the conclusion that the energy-band structure is not strongly dependent on the potential and on the degree of ionicity of the crystal. We feel that our method, or the more complete O.P.W. method, could be also applied to obtain the conduction bands of ionic crystals though it may not be appropriate for the energy levels of the valence states.

Acknowledgements—We wish to thank Professor R. KNOX for his interest and for a critical reading of the manuscript and Professor M. H. COHEN for stimulating conversations.

REFERENCES

1. CALLAWAY J., *Solid State Physics* Vol. VII, p. 100. Academic Press, New York (1958); HERMAN F., *Rev. Mod. Phys.* **30,** 102 (1958).
2. BASSANI F. and CELLI V., *Nuovo Cim.* **11,** 805 (1959).
3. BASSANI F., *J. Phys. Chem. Solids* **8,** 375 (1959).
4. CASELLA R., *Phys. Rev.* **109,** 54 (1958).
5. COHEN M. H. and HEINE V., *Advanc. Phys.* **7,** 395 (1958).
6. PHILLIPS J. C. and KLEINMAN L., *Phys. Rev.* **116,** 287 (1959).
7. ANTONCIK E., *J. Chem. Phys. Solids* **10,** 314 (1959); *Czech. J. Phys.* **10,** 22 (1960); **4,** 439 (1954).
8. KLEINMAN L. and PHILLIPS J. C., *Phys. Rev.* **116,** 880 (1959).
9. KLEINMAN L. and PHILLIPS J. C., *Phys. Rev.* **118,** 1153 (1960).
10. PHILLIPS J. C., *Phys. Rev.* **112,** 685 (1958).
11. COHEN M. H., private communication.
12. HERMAN F., *Phys. Rev.* **93,** 1214 (1954).
13. HARRISON W. A., *Phys. Rev.* **118,** 1182, 1190 (1960).
14. KANE E. O., *J. Phys. Chem. Solids* **1,** 83 (1956).
15. HERMAN F., *Phys. Rev.* **88,** 1210 (1952); WOODRUFF T. O., *Phys. Rev.* **103,** 1159 (1956).
16. HERMAN F., *Physica* **20,** 801 (1954).
17. FAN H. Y., *Solid State Physics* Vol. I, p. 283. Academic Press, New York (1955); MICHELS A., VAN ECK J., MACHLUP S. and TEN SELDAM C. A., *J. Phys. Chem. Solids* **10,** 12 (1959).

18. BASSANI F., *Phys. Rev.* **108,** 263 (1957); *Nuovo Cim.* **13,** 244 (1959).
19. PARMENTER R. H., *Phys. Rev.* **100,** 573 (1955).
20. HERMAN F., *J. Electronics* **1,** 103 (1955).
21. CALLAWAY J., *J. Electronics* **2,** 230 (1957).
22. KLEINMAN L. and PHILLIPS J. C., *Phys. Rev.* **117,** 460 (1960).
23. WELKER H. and WEISS H., *Solid State Physics* Vol. III, p.1. Academic Press, New York (1956).
24. KOBAYASI S., *J. Phys. Soc. Japan* **13,** 261 (1958).
25. SHAKIN C. and BIRMAN J. L., *Phys. Rev.* **109,** 818 (1958);
BIRMAN J. L., *J. Phys. Chem. Solids* **8,** 35 (1959).
26. EHRENREICH H., *Phys. Rev.* (to appear).

APPENDIX

As an additional condition on the operator A and the function ϕ, we require that the contribution to ϕ from combinations of plane waves other than S_1 and S_2 be as small as possible. This can be simply achieved by minimizing the quantity:

$$\sum_j{}'|a_j(W_1{}^0-W_j{}^0)|^2 = \sum_j{}'|(S_j,VS_1{}^0)+\sum_c(S_j,\psi_c)(\psi_c,AS_1{}^0)|^2 \qquad \text{(A1)}$$

with respect to the parameters $(\psi_c AS_1{}^0)$. We obtain the condition:

$$\sum_j{}'(\psi_c,S_j)\{(S_j,VS_1{}^0)+\sum_{c'}(S_j,\psi_{c'})(\psi_{c'},AS_1{}^0)\}=0. \qquad \text{(A2)}$$

Using the completeness of the set $\langle S_j\rangle$ equation (A2) can be written:

$$(\psi_c,VS_1{}^0)-(\psi_c,S_1{}^0)(S_1{}^0,VS_1{}^0) +(\psi_c,AS_1{}^0)-\sum_{c'}(\psi_c,S_1{}^0)(S_1{}^0,\psi_{c'})(\psi_{c'},AS_1{}^0)=0.$$

From the definition of ψ_c and E_c and the orthogonality between $S_1{}^0$ and S_j, we finally obtain:

$$(\psi_c,S_1{}^0)\{E_c-W_1{}^0+(S_1{}^0,VS_1{}^0)\} +(\psi_c,AS_1{}^0)-\sum_{c'}(\psi_{c'},AS_1{}^0)(\psi_c,S_1{}^0)(S_1{}^0,\psi_{c'})=0. \qquad \text{(A3)}$$

The first order solution of (A3) is:

$$(\psi_c,AS_1)=(W_1{}^0-E_c)(\psi_c,S_1{}^0). \qquad \text{(A4)}$$

In this way the repulsive term which appears in equations (5) is defined and this allows us to obtain $W_1{}'$, $S_1{}^0$ and the coefficients a_j. By iteration the solution of (A3) to second order is found to be:

$$(\psi_c,AS_1)=(W_1{}^0+W_1{}'-E_c)(\psi_c,S_1{}^0). \qquad \text{(A5)}$$

This is the same result we would obtain from equation (3) by using for ϕ the zero order wave function. Since we have established it independently, we can use equation (A5), together with equation (3) to obtain to first order the following set of linear equations between the coefficients a_j:

$$\sum_j{}'a_j(\psi_c,AS_j)=(W_1{}^0-E_c)\sum_j{}'a_j(\psi_c,S_j). \qquad \text{(A6)}$$

Expressions (A5) and (A6) give equation (7) for the second order correction to the energy when substituted into equation (6).

J. Phys. Chem. Solids Pergamon Press 1961. Vol. 20, Nos. 1/2, pp. 76–87. Printed in Great Britain.

CURRENT-INDUCED MARKER MOTION IN GOLD WIRES*

H. B. HUNTINGTON and A. R. GRONE†

Rensselaer Polytechnic Institute, Troy, New York

(*Received* 9 *December* 1960)

Abstract—The motion of light transverse scratches, used as markers, has been observed on the surface of gold wires carrying current densities of about 10^4 A/cm^2 for periods of several days. Clear evidence for a mass transport caused by momentum exchange with the electron current is shown by the magnitude and direction of the marker motion—several microns a day in some cases and always toward the cathode. This motion is exhibited by scratches on the central portion whose temperature varied from 850°C to 1000°C. Water cooling maintained the ends of the wires near room temperature. In agreement with a simplified theory the marker motion appears to be proportional to the current density and the self-diffusion constant. Possible applications of this technique include (1) the indirect determination of the activation energy for diffusion and (2) the investigation of the strength of interaction between the electrons and those lattice defects which constitute the activated complexes for atom jumping. In this case a value of 2μ ohm-cm/per cent was indicated for the "specific resistivity" of the diffusing atom in gold.

I. INTRODUCTION

DURING the past thirty years numerous experiments have been carried out, particularly by German investigators, to determine the possible electrolytic effects of high current densities in alloy systems.[1] The motion of solute atoms in interstitial alloys was initially interpreted in terms of the forced motion of charged ions in the electrostatic field. This point of view ran into occasional difficulty as for example in the Au–Pb system[2] where it was found that the ions of gold migrated to the anode. It had been early pointed out by SKAUPY[3] that the electron flow might exert a "frictional" force on the metal ions which would generally tend to drive the ions against the electrostatic field. The competition between these two forces was further considered by WAGNER[4] who wished to establish a correlation between the differential increase in resistivity per added per cent solute and the net force on the solute atom. More recently measurements of marker motion in the Al–Cu system have been carried out by WEVER and SEITH[5] which showed that mass transport of both constituents took place toward the anode in the β-phase (which is an electron conductor) but that the direction of transport was reversed in the γ-phase where the current is carried by holes. This experiment has been taken as strong evidence for momentum transfer from the charge carriers to the mobile atoms, those on the point of making a diffusion jump. However, it has been pointed out by KLEMM[6] and others[7] that the inertial property of the electrons, considered as a separate system in the solid does not depend on the sign of m^*. The experiments of BARNETT[8] have shown that the electrons in a metal under acceleration with respect to the lattice show the free electron mass. On this account WEVER and SEITH have been criticized for suggesting that the sign of the momentum transfer should depend on the sign of the current carriers. We shall return to this point in the theory section.

It was natural that the next experiment should be to examine the direction of mass transport in a pure metal. In 1956 WEVER[9] observed marker motions

* Supported by The United States Atomic Energy Commission.

† Now at the Watervliet Arsenal, Watervliet, N.Y.

Vol. 2
1961

in the high temperature portions of copper specimens carrying a current density of 2×10^4 A/cm^2 for a period of one or two days. At temperatures below 950°C the markers moved toward the cathode which corresponded to mass transport toward the anode, the direction of momentum transfer from the electron current. (The transport of mobile atoms across the hottest region of the sample causes a build-up of lattice planes in the cooler regions where they come to rest and a destruction of lattice planes in the cooler region from which they come. As a result the markers fixed to the lattice appear to travel in the direction opposite to electron flow.) For temperatures above 950°C the direction of the markers was reversed.

Our first effort at observing marker motion in pure metals was applied to copper specimens but we were bothered by a lack of reproducibility which we now believe was caused by inadequate protection of the copper from atmospheric contamination. Immediately after we transferred our efforts to gold we were able to make meaningful, quantitative measurements of marker velocity as a function of current density and temperature. The dependence on temperature alone is rather close to that of the self-diffusion constant of gold. This result is in accord with the predictions of a rather simplified theory of the charge carrier–momentum transfer process, as presented in Section IV.

The final section of this paper will discuss the assumptions on which the theory rests and what is needed to develop a more thorough-going theoretical treatment. Possible future applications of the observation of moving markers in pure metal wires will also be indicated.

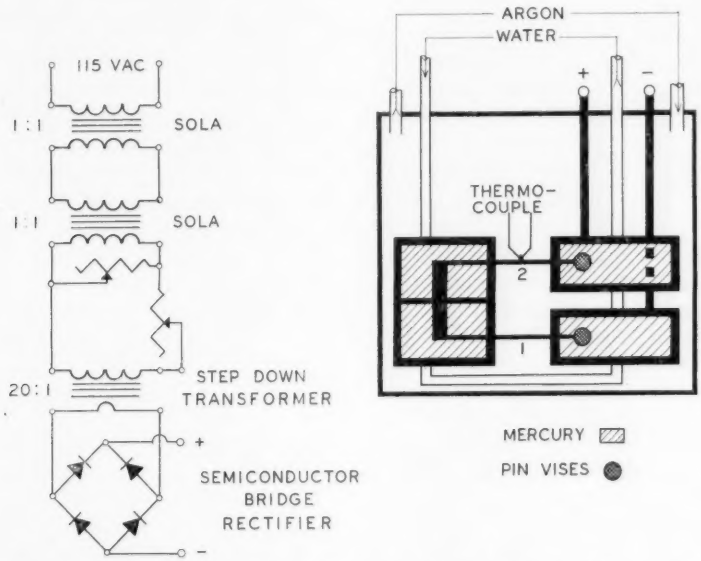

FIG. 1. Schematic of apparatus for marker motion experiment. Wire marked 1 is the sample and is observed visually through a circular port. Wire 2 acts as a monitor and is attached to a thermocouple.

II. EXPERIMENTAL PROCEDURE

The gold used in this experiment was obtained from Handy and Harman and had a purity of better than 99·97 per cent. The wires were gently rolled between glass plates to straighten them and marked with several transverse scratches applied by a razor blade. We never observed that the motion was influenced in any way by the shape or depth of the scratch.

One end of the test wire was held in a fixed clamp and the other in a pin vise floating on mercury to prevent any longitudinal stress. To give mechanical support at the higher temperatures the wire was

loosely supported a third of the way from the free end by one section of 1/8 in. long ceramic lead-through insulator.

Figure 1 shows a schematic of the experimental chamber and an associated equipment. The experiments were performed inside a brass box under an argon atmosphere, at a positive pressure. A 3 in. diameter window in the lid of the box allowed continuous measurements to be made of the marker motion during the course of a run. Both the fixed clamp and the tub holding the mercury were cooled. Provision was made for gettering the atmosphere with a Pyrex tube furnace containing calcium chips heated to 500°C. (This precaution was introduced to eliminate all traces of water vapor and oxygen during the copper experiments and its operation was probably superfluous in the case of gold.)

The d.c. current was provided by a bridge rectifier of four silicon diodes (Sarkes–Tarzian Type 5V). The a.c. voltage for the bridge was stabilized by two Sola transformers in cascade and reduced through a 20:1 step down transformer. The semiconductor bridge was protected by immersion in a water-cooled oil bath. Under this limited stabilization temperature excursions during a particular run remained within ± 15°C limits. While further reduction of temperature fluctuations, perhaps by a feedback control system, would be desirable, the technique for absolute temperature determination should be improved before additional efforts at control would be advisable.

The temperature was directly measured by an optical pyrometer (Leeds and Northrup #8615) and this instrument was in turn calibrated for the surface of the gold wire by observation of a similar specimen to which a thermocouple had been attached by a pressure contact. Welding was not used to avoid damage to the surface. (It was not practical to attach a thermocouple directly to the test wire because of the associated disturbance.) By carrying the calibrations up to the melting point of gold, a check against a fixed point was introduced and errors from both the thermocouple calibration and the uncertain thermal contact were eliminated. The precision and reproducibility of the optical pyrometer was ± 10°C in this temperature range.

In order to have a continuous temperature record of a somewhat more sensitive nature, a thermocouple was attached to a second gold wire in series with the test wire, and its response was continuously registered on a Brown Recorder. As the thermocouple on the second wire was usually at a different temperature than the test wire it was necessary to calibrate the monitor thermocouple against the test wire temperature as determined by the pyrometer. The monitor recorder so calibrated kept a running record of temperature fluctuations due to current changes only. For a given current, the test wire resistance was assumed to remain constant as long as the total length did not change.

It was possible to fix the relative temperature of different markers on the same run with greater accuracy than for markers on other wires with different surface conditions. This resulted partly from the greater relative accuracy with the pyrometer, and partly from the fact that markers on the same wire shared the same thermal fluctuations. Also the mathematical form of the temperature distribution along a wire was well known. It was a sinusoidal solution of the equation

$$\mathrm{K}J\frac{d^2T}{dx^2} = -j^2\rho(T), \tag{1}$$

which satisfied the boundary condition of low temperature at the ends of the wire and gave a symmetric maximum at the center. The current density is given by j, the Joule–Kelvin coefficient by J, the thermal conductivity by K, and the resistivity ρ was taken to be proportional to the absolute temperature T. The radial variation of temperature in the wire, as caused by radiation and convection losses from the lateral surface, was also estimated and found to be only a fraction of a degree.

The routine of a typical run went as follows: the straightened, marked wire was carefully inserted in the clamps, the box was sealed off and evacuated with a fore pump, flushed once and filled with argon. The wire was raised to temperature over a period of about five minutes and allowed to anneal for a few hours. The positions of the marks were then measured and this measurement was repeated once a day for the duration of a run which was usually a week to ten days. At the initial and final read-outs the pyrometer was used

Vol. 2
196

but it was not deemed necessary to make intermediate temperature readings if the thermocouple trace appeared normal. During each readout the positions of the scratches were read consecutively four times. For this work two instruments were used, a Hilger linear comparator microscope with a 1 μ least count and a Pye cathetometer, adaptable for horizontal measurements, with a 5 μ least count. The latter was used for some of the earlier runs only. With the Hilger the root-mean square deviation from the mean was less than 2 μ in an average group of four measurements. The day-to-day scatter in the position appeared to be somewhat larger than would have been expected from purely statistical considerations. Because of their lower reflectivity the scratch regions glowed considerably brighter than the smooth surface. Under the pure argon atmosphere thermal etching was negligible and the scratches held their shapes well. At first a light hairline was used and placed symmetrically over the center of the scratch. Later it was found easier and more reproducible to use a heavier crosshair, and to observe the point at which the crosshair, after traversing the scratch, touched the far rim.

As the distance between the end markers stayed constant generally to within experimental accuracy, they were used to establish the frame of reference for each measurement. For most of the cases where the distance between the end markers did not remain constant the explanation lay in temperature variations as could be easily verified by consulting the thermocouple trace. The appropriate corrections were simply incorporated. Occasionally part of the wire would appear to contract slightly because of bending. The direction and magnitude of the bend could be estimated by observing the change in position or focus of the wire while moving the linear comparator along the specimen.

III. RESULTS

The results of the day-to-day record for a particular run are shown in Fig. 2. While the end marks show negligible deviation the marks near the wire center move at a nearly uniform rate toward the cathode and those at the higher temperature move more rapidly. In this particular run the temperature was raised approximately 160°C after the ninth day which accounts for the sudden break in the curves. Reversing the direction of current during the course of another particular run served merely to reverse the direction of motion for all the markers.

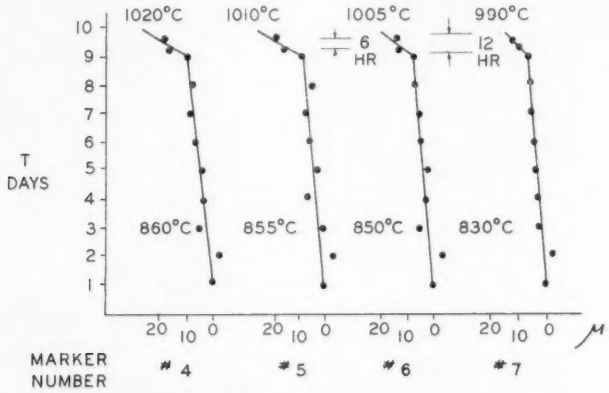

FIG. 2. Display of marker motion during a typical run. Break in curve follows change in wire temperature.

The first group of measurements (4 runs) were made with wires carrying about 30 A. Fig. 3 shows the compiled results. For each scratch the ratio of the velocity to current density is logarithmically plotted against the reciprocal of the absolute temperature. To check the influence of

current density the distance between the water-cooled supports was decreased for the next set of runs and the current increased to between 60 and 70 A. The results from these measurements are shown by the points on Fig. 4. The superimposed straight line is the best least square fit based on the 30 A data. The agreement appears to be sufficiently good to warrant the conclusion that the marker was calculated by bisecting the angle of regression. (The slope of the line in Fig. 4 was calculated by the same procedure, using the data from the 30 A runs alone.)

The slope of the best straight line through the combined data gives a pseudo-activation energy of 35 kcal/mol, or about 20 per cent lower than the most recent value for the activation energy for

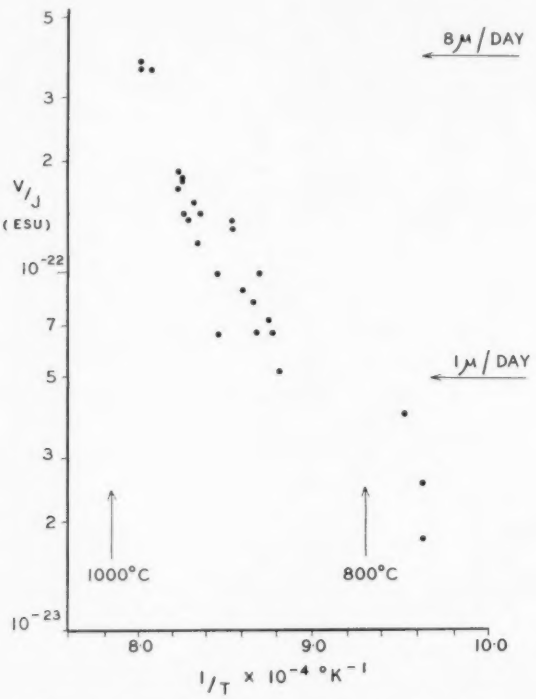

FIG. 3. Scatter plot of (v/j) vs. T^{-1} for 30 A data.

velocity is proportional to current density, at least over the range of our experiment.

While our theory does not predict that (v/j) should follow an Arhenius-type curve exactly, the expected deviation should be small, so that it was reasonable to fit these data as plotted by straight lines. Least squares analysis was applied twice to the results of the combined 30 and 60 A data. Once the (v/j) values were taken as independent and the other time the temperature was considered the independent variable. The coefficient of regression for these two analyses was 0·95. The average slope self-diffusion in gold,[10] 41·7 kcal/mol. The analysis in the next section will develop the significance of the temperature dependence further.

IV. ANALYSIS

We begin by calculating under certain simplifying assumptions, the momentum transferred per unit time to a point defect in a current-conducting metal. We treat the electrons as though they are scattered by the defect alone and consider the defect to be decoupled from the lattice. Under these rather arbitrary restrictions the scattering

takes place without the creation or annihilation of phonons. The momentum transfer to the electrons is given by m_0 times the group velocity of the Bloch wave. The x-component of the momentum transferred per unit time per unit volume to the defects is given by

$$\frac{dM_x}{dt} = -\left(\frac{1}{4\pi^3}\right)^2 \int\int\int (m_0/\hbar)\left(\frac{\partial E}{\partial k_x'} - \frac{\partial E}{\partial k_x}\right) \times f(\boldsymbol{k})\{1-f(\boldsymbol{k}')\}W_d(\boldsymbol{k}, \boldsymbol{k}')\, d\boldsymbol{k}'d\boldsymbol{k} \qquad (2)$$

$$\frac{dM_x}{dt} = \left(\frac{1}{4\pi^3}\right)^2 \int\int\int \left(\frac{m_0}{\hbar}\right) \frac{\partial E}{\partial k_x}\{f(\boldsymbol{k})[1-f(\boldsymbol{k}')] \times W_d(\boldsymbol{k}, \boldsymbol{k}') - f(\boldsymbol{k}')[1-f(\boldsymbol{k})]W_d(\boldsymbol{k}', \boldsymbol{k})\}\, d\boldsymbol{k}'d\boldsymbol{k} \qquad (3)$$

which can be simplified by the introduction of a relaxation time τ_d, defined by

$$\frac{f(\boldsymbol{k})-f_0(\boldsymbol{k})}{\tau_d} = \int \{f(\boldsymbol{k})[1-f(\boldsymbol{k}')]W_d(\boldsymbol{k}, \boldsymbol{k}') - f(k')[1-f(k)]W_d(\boldsymbol{k}'\boldsymbol{k})\}\, dk'/4\pi^3 \qquad (4)$$

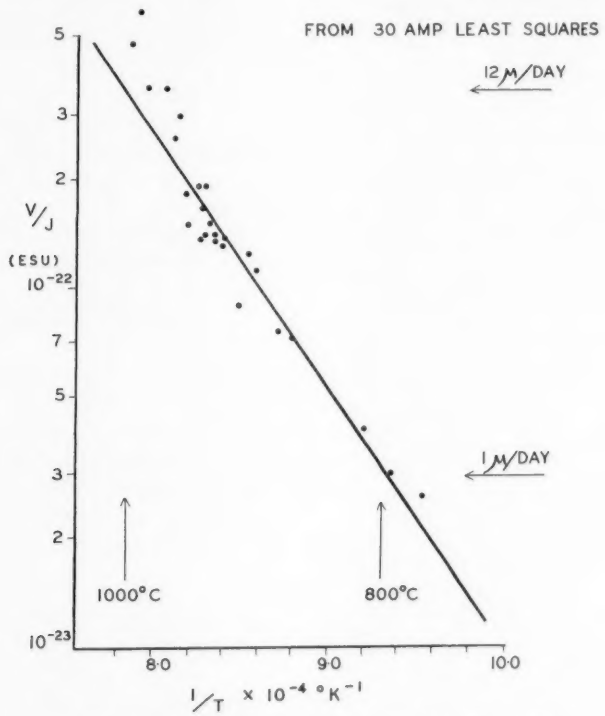

FIG. 4. Combined 30 and 60 A data for (v/j) vs. T^{-1}. Best straight line from the 30 A data superimposed on the the 60 A scatter plot.

The function $W_d(\boldsymbol{k}, \boldsymbol{k}')$ gives the transition probability per unit time that the electron in state $\boldsymbol{k}$ will jump to state $\boldsymbol{k}'$ by virtue of its interaction with the class of point defects under consideration. The distribution function for the electrons in k-space is denoted by $f(\boldsymbol{k})$. By interchanging the primed and unprimed variables of integration equation (2) can be written in the form

Here $f_0(\boldsymbol{k})$ denotes the electron distribution at equilibrium. The substitution of (4) into (3) gives

$$\frac{dM_x}{dt} = \frac{m_0}{\tau_d \hbar}\int \frac{\partial E}{\partial k_x} f(\boldsymbol{k})\, d\boldsymbol{k}/4\pi^3, \qquad (5)$$

where it has been assumed that there is a unique τ_d independent of $\boldsymbol{k}$ a common assumption for metals.

Vol. 20
1961

The current density in the x-direction j_x can be expressed

$$j_x = \frac{-e}{4\pi^3}\int f(\boldsymbol{k})\frac{\partial E(\boldsymbol{k})}{\hbar\partial k_x}d\boldsymbol{k} \tag{6}$$

it follows that

$$\frac{dM_x}{dt} = -\frac{j_x m_0}{e\tau_d}. \tag{7}$$

It appears reasonable to consider that the effect of this rate of momentum transfer is that of a continuous force against each defect. Roughly the density of electrons is 10^{23} cm^{-3} and their average speed 10^8 cm/sec in the metal. For a point defect with a quasi-classical cross section of 10^{-15} cm^2 the number of collisions would be 10^{16} sec^{-1} of which perhaps only 1 per cent would give rise to scattering, because the Exclusion Principle limits scattering to those electrons near the Fermi surface. Since the time required for an atom moving a lattice distance with thermal velocity is of the order of 10^{-13} sec (which is also approximately the time for an atomic vibration), one can conclude about 10 electrons could undergo scattering during the time of an atomic jump. While this rough estimate does not give a large number for the electron collisions during the jump time it appears to be enough to justify the assumption that the effect on the average can be approximated by a continuous force,

$$F_x = -(j_x m_0)/(e\tau_d N_d). \tag{8}$$

The density of defects is N_d. Let the contribution of the defects to the resistivity be $\rho_d = |m^*|/ne^2\tau_d$, where n is the density of the conduction electrons and m^* is their effective mass.

$$F_x = -nej_x\rho_d m_0/(N_d|m^*|) = -e\mathscr{E}_x z\frac{N\rho_d}{\rho N_d}\frac{m_0}{|m^*|} \tag{9}$$

The density of conduction electrons n has been replaced by z times the density of metallic ions N. In this form it appears that the force felt by the defects from momentum transfer of the electrons is equivalent to the force exerted by the electric field on a charge equal to the electronic charge multiplied by the following factors: z or the electron–atom ratio, the ratio of the specific resistivity per defect to the specific resistivity per normal atom, and the ratio of free to effective electron mass.

At this point, we apply the preceding analysis to the particular defect responsible for atom movements in the gold which we shall assume to be the moving vacancy (although most of the treatment will apply with small modification to the case of the moving interstitial or the interstitialcy). For an ion at the saddle point halfway from an equilibrium lattice site on its way to fill a vacancy the interaction with the flowing electrons is strong, whereas at the lattice points the same interaction is a minimum. It follows that F_x and ρ_d are functions of microscopic position. While the form of this function is not known in detail it clearly possesses the periodicity of the lattice and may be taken to be sinusoidal for simplicity. The ensuing analysis develops on a kinetic basis the modification of the Nernst–Einstein equation appropriate for the particle whose charge varies with position.

Let the variation of $\boldsymbol{F}$ along a particular jump direction y be

$$\boldsymbol{F}(y) = \boldsymbol{F}_m \sin^2(\pi y/a), \tag{10}$$

for $\boldsymbol{a}$ the jump distance. By virtue of the electron pressure the ions on the cathode side of a vacancy will find the potential barrier for jumping into the vacancy lowered and those on the anode side will find the barrier raised by a corresponding amount,

$$\Delta V_j = \int_0^{1/2a_j} \boldsymbol{F}(y)\,.\,dy = \tfrac{1}{4}a_j F_m\cos\theta_j. \tag{11}$$

The angle between $\boldsymbol{F}$ and the jump $\boldsymbol{a}_j$ is θ_j.

The net flow of atoms caused by the electron friction is given by

$$S_f = \sum_j cv_0\exp(-V/kT)a_j\cos\theta_j\sinh(\Delta V_j/kT) \tag{12}$$

where c is the concentration of ions in the metal, ν_0 is the frequency of the atomic vibrations, $\sum_j$ is a summation over all possible jumps, and V is the saddle point free energy which includes both the energy for vacancy formation and vacancy motion.

The expression (12) for the mass flow can be simplified in terms of the uncorrelated diffusion coefficient,

$$D = \tfrac{1}{2}\nu_0 \exp(-V/kT) \sum_j a_j^2 \cos\theta_j \qquad (13)$$

to give the following

$$S_f = cDF_m/2kT. \qquad (14)$$

The result (equation 14) differs from the Nernst–Einstein relation only in the factor of 2 in the denominator which enters as the average value of $\sin^2 \pi y/a$ over the path. A different choice for the form of equation (10) would lead to a somewhat different numerical factor.

The total force F_t on the moving ion consists partly of the frictional force exerted by the electrons and partly of the direct force of the electric field $\mathscr{E}$. We express F_t as $ze'\mathscr{E}$ where $e'z$ the effective charge on the ion is given by

$$e' = ze[\tfrac{1}{2}(\rho_d N/\rho N_d)m_0/|m^*| - 1]. \qquad (15)$$

The marker motion v for gold runs counter to F_t and is proportional to S_f,

$$v = \alpha S_f/c \qquad (16)$$

where $\alpha \leqslant 1$. The limiting value $\alpha = 1$ will occur only (1) if no voids are formed and (2) if the creation and annihilation of vacancies causes no changes in the lateral dimensions. It appears that void formation plays a negligible role in this experiment. In the first place no significant change in the over-all lengths of the specimens such as one would expect to find in the case of pore formation was observed during any of the runs. In addition, the interiors of two of the wires were examined metallographically[10] and no evidence for voids was found. The question of the change in lateral dimension is much more difficult to decide. It was not practical to follow the direct approach of attempting to look for a thickening of the wire on the anode side and a corresponding thinning on the cathode side since a measurement of this effect would require about a hundred times greater sensitivity to detect a comparable relative change in lateral dimension. The evidence from previous experiments involving large vacancy flux is conflicting and far from quantitative. Observations of the surface texture of tungsten wires carrying high d.c. currents[11] were systematically carried out by JOHNSON who also reported at one point changes in wire shape. Likewise studies[1] of light filaments burned by excessive d.c. currents over the period of a few hours revealed that most of the breaks occurred near one electrode. The first to look for lateral changes in a Kirkendall experiment were DA SILVA and MEHL[12] who found no appreciable effect. Some earlier electrolytic experiments[13] which reported changes in lateral dimensions were subsequently interpreted in terms of a Kirkendall effect but only inconclusively as the possibilities of other explanations, such as transport in the vapor phase, could not be ruled out. In his study of pore formation during chemical diffusion in the Cu–Ni system BARNES[14] observed over-all specimen expansion which he found to appear first in the direction of diffusion but to become quite clearly evident in the lateral directions later.

In view of the inconclusive state of the evidence as to what fraction of the vacancy creation and annihilation contributes to the change of lateral dimensions rather than the dimension parallel to diffusion, we decided to assume that such dimensional changes would be isotropic in the absence of any marked uniaxial stress. For diffusion couples where the diffusion region is small compared with the couple cross section one might expect that the shape of the specimen would constrain lateral movement as in the findings of DA SILVA and MEHL[12]. In our experiment the region where the atom movements are occurring is spread throughout the specimen and its extent is many times greater than the wire diameter. Therefore it seems reasonable to us to assume an isotropic effect and to put $\alpha = 1/3$.

If e' were strictly temperature independent then equation (15) would predict that the slope of $\ln v/j$ would give quite accurately the activation energy for diffusion. To explore the temperature dependence of e' we take for D the experimentally observed values for the coefficient of self-diffusion which is equivalent to neglecting the influence of correlation. Using the diffusion data of MAKIN *et al.*[15] and the straight line plot for (v/j) from Fig. 4, we find a variation for e' ranging from $8e$ at 800°C to $5e$ at 1000°C as shown in Fig. 5. Accordingly we have solved equation (15) for $\rho_d N/N_d$ (taking m_0/m^* to be unity for gold) and its

variation also with temperature is displayed on Fig. 5. It is gratifying to note that this quantity appears to be as one might intuitively expect relatively temperature independent within the accuracy of the measurements. Its approximate value is about 2 μ ohm cm/per cent defect. This result lies in the general range of the theoretical estimates for the values of the specific resistivities for point defects. At present this range is unfortunately quite wide. Also to date, the results of the experimental measurements of the specific resistivity of lattice defects arising from radiation damage and quenching experiments have been subject to large uncertainties because of the difficulty in knowing unequivocally the number of each kind of defect formed in any given experiment. Hopefully the sort of measurements reported here may be of use by giving a measure of the specific resistivity for a certain type of lattice defect.

To recapitulate, the important experimental support for our theoretical approach lies in the temperature independence of $(\rho_d N/N_d)$. On this basis the slope of ln v/j vs. T^{-1} is now expected to be somewhat less than that given by the activation energy for self-diffusion principally because of the temperature dependence of ρ in equation (15).

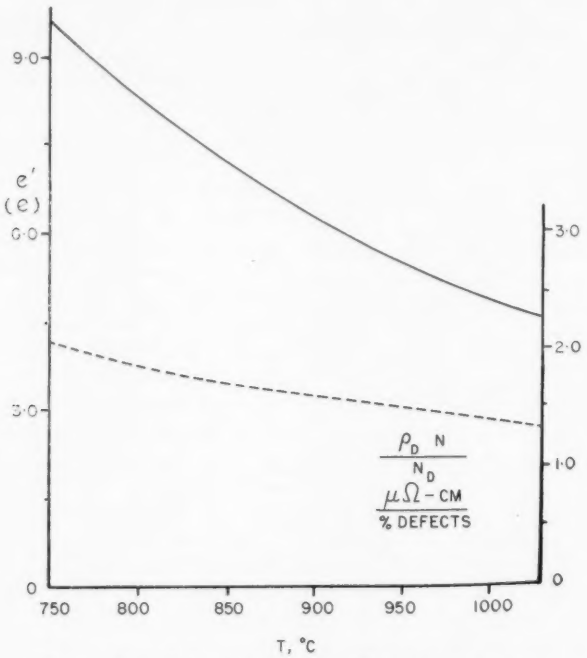

FIG. 5. Plot of e' and $(\rho_d N/N_d)$ vs. T. e' is in units of e and $(\rho_d N/N_d)$ in units of micro-ohms cm per per cent defect.

—— e'
– – – – – $\rho_d N/\rho N_d$

V. DISCUSSION

It has been shown that it is possible to make quantitative measurements on the velocity of moving markers on pure gold wires and that the variation with current density (over a limited range) and with temperature follows the predictions of a simple theory surprisingly well. The limiting factor in the precision of the measurements

is the determination of the temperature, since the requirements of the experiment preclude making direct mechanical contact with a specimen wire. Systematic errors in reading marker temperatures for any given run may amount to 10°C which is uncomfortably high for an experimental study of atom movements. In this respect WEVER's[9] technique is superior since he was able to insert a thermocouple inside hollow cylindrical specimens of considerably greater cross section. On the other hand our technique allows continuous observation of marker position at the high temperature whereas WEVER, in his earlier work at least, measured marker positions only at room temperature before and after the run.

The quantity which we have plotted v/j is directly related to the transport number TN usually reported by the German workers in this field who have taken $\alpha = 1$.

$$\alpha TN = ce(v/j) \tag{17}$$

Here e is the electronic charge in the same set of units in which j is measured. The behavior of TN, apparently independent of j and roughly proportional to D, is by no means typical. The TN for β-Cu–Al[5] was found markedly dependent on current density in a quite unexpected way. Also the general trend for the temperature dependence of e' has been a more rapid decrease with rising temperature than we have observed here. WEVER actually found a change of sign for e' in his measurements on copper at high temperature, a result which we have corroborated.[16]

A third unexpected feature which has characterized the findings so far has been the strong correlation between the direction of mass transport and the sign of the charge carriers so determined by the Hall effect. This result is difficult to understand in view of the BARNETT[8] experiment and of the fictitious inertial character of the holes. Our analysis also tends to show that direction of the electron drag is probably always toward the anode. Equation (7) shows that the transfer number is independent of m^*. The crucial consideration here is the use of $m_0 v_g$ in equation (2) to measure the change of momentum of the corresponding Bloch wave function when scattering takes place. If we had used instead the pseudo-momentum $\hbar k$ which measures the momentum of electron plus lattice built up by the field acting on the electron, then the analysis would have shown the momentum transfer to be dependent on m^*. However this result from our analysis is not really firm since we have arbitrarily ruled out momentum transfer to the lattice phonons which could conceivably cause an overbalancing effect.

It seems that there are two avenues by which valuable information could be obtained from future study of moving markers in specimens carrying high electric currents. The first of these is the determination of approximate values for the activation energy of self-diffusion of elements that possess no suitable radiotracer. Because of the difficulties with temperature measurement mentioned earlier this method could never compete in accuracy with tracer methods. In this regard a more serious difficulty is posed in the unexpectedly strong temperature variation of (e'/e) which, as has been mentioned above, has been rather frequently observed. Admittedly the process by which the charge carriers convey momentum to the ions is very imperfectly understood but also the nature of the electrostatic force on the ions is subject to uncertainty in the size of z. To take for z the nominal ionic valence assumes z free electrons completely uncoupled from the moving ion. The moving ion, in other words, reforms its screening charge from the electron distribution around its new location. Since the free-electron model is only an approximation to any actual metal, the effective ion charge may differ from z by an uncertain amount.

The second line of attack which might prove fruitful for moving marker studies is the investigation of the specific resistivity of a particular lattice defect, namely the activated complex for diffusion. Here there are several points which need future development. On the experimental side one needs to know how accurately the marker motion measures the mass transport. Much of the uncertainty arising from the dimensional changes normal to the diffusion direction and from void formation could presumably be removed by isothermal marker measurements between inert electrodes. Under these conditions one would also expect little influence from the intensity of the electric current, that is if the effects that have been observed have their origin in the deviation of the number of vacancies from the thermal equilibrium

value because of the high density vacancy flux in these experiments.

On the theoretical side the problems raised by the interpretation of the experiment are more disturbing. The investigations which measure the changes in resistivity caused by quenching, radiation damage and work hardening are always limited by the difficulty of determining the number of defects involved. Because the diffusion constant, which is accurately known, incorporates within it the density of the particular defect under study, this difficulty is avoided here and the marker motion measurements may be considered in one sense the first direct measurement of the specific resistivity of a lattice defect. The difficulty that arises here is "What defect?" It is not the activated complex for vacancy diffusion, because, for many of the electrons scattered from this complex, the momentum transfer is not to the diffusing atom itself but to its neighbors, i.e. the lattice to which they belong. It is an extremely difficult theoretical problem to determine in a rigorous way how the momentum transfer really may be divided between lattice and moving atom.

In the analysis leading to equation (9) two far-reaching assumptions were made, each open to question, first that the defect under consideration received all the momentum transferred by the scattered electrons and second that the defect was decoupled from the lattice. In this way the complication from phonon generation was artificially avoided. The only part of the activated complex which remotely fulfills the second condition is the moving atom itself. As a first approximate step one might associate the $(N\rho_d/N_d)$ obtained from fitting equations (14) and (15) with experiment with the specific resistivity of an extra ion inserted in the metal lattice without otherwise disturbing the atomic arrangement. Actually, of course, the moving atom adjoins two lattice vacancies and displaces outward from their equilibrium positions those next neighbors by which it passes. In this approximation the electron scattering from these lattice irregularities is considered independent of the scattering from the moving atom. It is difficult to estimate the size of the error involved in overlooking the interaction between the two scattering fields but it is probably considerable. (Even for atoms at their normal lattice positions there can be considerable momentum transfer from electron scattering in the neighborhood of a lattice defect, as for example in the presence of a vacancy which of itself can not take up momentum when an electron is scattered.) Perhaps the effect of the adjoining vacancies is to partially shield the moving atom from those electrons most likely to influence its motion in the jump direction, thereby making the measured specific resistivity too small. As for the second assumption that the defect is decoupled from the lattice, this is only strictly true at the exact saddle point, although the correction for this approximation is probably less important than the first point discussed. The additional assumption of a unique electronic relaxation time has been widely used and its limitation is well understood.

In brief it appears that moving marker studies may yield some quantitative information on the interaction of electrons and lattice defects, but a good deal of theoretical progress will need to be made on a rather complex scattering problem if the results can be related with confidence to the specific resistivities of lattice defects as they are ordinarily considered.

Acknowledgements—The senior author wishes to acknowledge his indebtedness to the late Professor W. SEITH for having stimulated his interest in the problem of electron momentum transfer to moving atoms.

We are much indebted to Mr. GEORGE F. ROBINSON and Mr. ROY LOVE who made important contributions to this research in its initial phases. We wish to thank Dr. EDMOND BROWN and Dr. ROBERT L. SPROULL for suggestions and valuable discussions.

REFERENCES

1. For a general review of this topic see SCHWARTZ K. E., *Elektrolytische Wanderung in flussigen und festen Metallen*. Leipzig (1940); SEITH W., *Diffusion in Metallen*. Springer-Verlag, Berlin (1955).
2. SEITH W. and ETZOLD H., *Z. Elektrochem.* **40,** 829 (1934); SCHARTZ K. and STOCKERT R., *Z. Elektrochem.* **45,** 464 (1939).
3. SKAUPY F., *Verh. Dtsch. Phys. Ges.* **16,** 156 (1914); *Z. Phys. Chem.* **58,** 560 (1907); *Phys. Z.* **21,** 597 (1920).
4. The authors are indebted to Dr. CARL WAGNER, for being permitted to see his unpublished manuscript on this topic.
5. WEVER H. and SEITH W., *Z. Elektrochem.* **59,** 942 (1955).
6. KLEMM A., *Z. Naturf.* **9a,** 1031 (1954).
7. We wish to thank Dr. LAURENCE SLIFKIN for helpful discussions of this point.

8. Barnett A. J., *Phys. Rev.* **87,** 601 (1952).
9. Wever H., *Z. Elektrochem.* **60,** 1170 (1956).
10. We are indebted to Dr. L. Girifalco and his associates at the Lewis Propulsion Laboratory, Cleveland for their careful investigation of this question.
11. Johnson R. P., *Phys. Rev.* **53,** 766 (1938); *Phys. Rev.* **54,** 459 (1939).
12. Correa L. C., Da Silva L. C. and Mehl R. F., *Trans. A.I.M.E.* **191,** 155 (1951).
13. Johnson W. A., *Trans. A.I.M.E.* **147,** 331 (1942).
14. Barnes R. S., *Proc. Phys. Soc. Lond.* **B65,** 512 (1952).
15. Makin S. M., Rowe A. H. and Le Claire A. D., *Proc. Phys. Soc. Lond.* **70,** 545 (1957).
16. See subsequent article by Grone A. R.

ol. 20
1961

J. Phys. Chem. Solids Pergamon Press 1961. Vol. 20, Nos. 1/2, pp. 88–93. Printed in Great Britain.

CURRENT-INDUCED MARKER MOTION IN COPPER*

A. R. GRONE†

Rensselaer Polytechnic Institute

(*Received* 9 *December* 1960)

Abstract—Measurements of marker motion in copper have been made from 785°C to 1040°C. The technique resembled that used for previous experiments with gold.[1] Temperature measurements were complicated by changing surface emissivity. Below 900°C markers moved towards the cathode with velocities/current densities approximately proportional to the self-diffusion coefficient, as might be expected for mass motion caused by momentum exchange with the current. Actual marker velocities were lower by approximately a factor of four than those observed in experiments with gold wires, owing to a fourfold decrease in the self-diffusion coefficient. In the temperature region below 900°C the "effective resistivity" of the activated complex appeared to be about 10^{-6} ohm m. At the higher temperatures the marker velocity goes through a maximum and finally changes sign near 1000°C. This reversal was first qualitatively noted by WEVER[2].

1. INTRODUCTION

FOR SEVERAL years mass-transport effects in pure metals and alloys have been actively investigated at the University of Münster, and more recently at the Technical University of Berlin. SEITH[3] HEUMANN[4] and WEVER[5] have reported numerous measurements of relative transport numbers, and the respective transport directions of the two constituents in binary alloys. WEVER has carried out a series of marker motion studies in pure metals, notably Cu, Ni, and Fe.

Our studies of marker motions under the influence of high electric current have been concentrated on pure metals. Though the effects in alloys are much more pronounced generally, it is felt that the simpler basic situation for the pure metal should be more conducive to a theoretical understanding of the atomistic processes involved.

This present investigation is concerned with the measurements of marker motion caused by direct currents in copper. An attempt is made to correlate the measured motions with a simplified kinetic theory model by HUNTINGTON[6].

* Supported by the United States Atomic Energy Commission.

† Presently at the Watervliet Arsenal, Watervliet, N.Y.

2. THEORETICAL BACKGROUND AND HISTORY

It has been suggested by HUNTINGTON[1,6] that a thermal defect consisting of an unscreened ion in a pure metal, moving by any mechanism of bulk diffusion, may have momentum transferred to it from the electron stream as it passes through the saddle point of the energy jump configuration. In the environment of a direct current the ion will have two forces exerted upon it. The first will be the interaction force with the electrons and the second will be the electrostatic force arising from the ionic charge. For a positive ion the sense of these two forces will be opposite, with the former acting toward the anode and the latter acting toward the cathode. As the ion is assumed to be decoupled from the lattice at the saddle point, the net ionic motion willl be determined by the difference between these forces. Within the context of the modified Nernst–Einstein equation which follows the ionic mobility will be given by the self-diffusion coefficient divided by kT. (We assume that the vacancy mechanism will predominate here, although mass transport under the above difference of forces would result for ions moving by the interstitial and interstitialcy mechanisms as well.) The ionic mobility, or average ionic velocity/net force in this case, may

Vol. 2
196

be equated to D/kT, and, assuming both the interaction and electrostatic forces to be proportional to the electric field, one obtains

$$v = DEz(e_d - e)/kT \qquad (1)$$

where

v is the average ionic velocity,
D is the self-diffusion coefficient with unity correlation,
k is the Boltzmann constant,
T is the absolute temperature,
E is the electric field,
ze_d is the effective charge due to electron-ion interactions (in the notation of the preceding paper $e_d = (e' + e)$, and ze is the charge associated with the unscreened ion.

By use of Ohm's Law and the correlation coefficient, equation (1) may be immediately rewritten,

$$v/j = D^* j\rho(e_d - e)/fkT, \qquad (2)$$

where

j is the current density,
ρ is the resistivity,
D^* is the radiotracer diffusion coefficient, and
f is the Bardeen–Herring correlation coefficient for the appropriate lattice.

For copper the valence z is taken as unity. The radiotracer diffusion data for copper[7] is used for subsequent calculations. It is necessary to correct for correlation because the measured values of D^* depend on the correlated motions of the radiotracer ions. $f = D^*/D$, and the numerical value of f for the f.c.c. lattice is $0{\cdot}78+$ [8].

The effective charge of the collision complex can be estimated[6] roughly on the basis that all the momentum of the scattered electrons goes to the moving ions, and none to the lattice phonons. Accordingly,

$$e_d = \frac{zm_0\rho_d Ne}{2|m^*|\rho N_d}, \qquad (3)$$

where $m_0/|m^*|$ is the ratio of the free electron mass to the effective mass, and is taken as unity, ρ_d/N_d is the contribution to the total resistivity of a single moving ion by virtue of direct electron–ion interaction, and ρ/N is the bulk resistivity per lattice ion. (The factor 1/2 arises from the assumed sinusoidal form for the energy barrier.) The final form for the contribution to the specific resistivity for transported ions is given by,

$$\rho_d N/N_d = 2e_d\rho/e. \qquad (3a)$$

One would not expect this quantity to be strongly temperature dependent, because the thermal vibrations of neighboring ions should not strongly affect the interaction between electrons and a particular moving ion. From equation (2), neglecting the slight temperature dependence of ρ/T, and also the temperature dependence of e_d, one would expect v/j to vary directly with the self-diffusion coefficient. One might therefore hope to estimate the activation energy for self-diffusion, Q, from the Arrhenius-type behavior of v/j.

$$v/j \sim \exp(-Q/kT). \qquad (4)$$

From experiment the average velocity of ionic transport is inferred from the velocity of the inert surface markers. In a cylindrical specimen, heated with d.c. while the ends are kept cool, ions are thought to be transported toward one electrode and vacancies are assumed to come to rest along dislocations in the direction of the opposite electrode. Planes of material will be created in the cool region towards which the mass motion is directed, and planes will be destroyed in the cooler region where the vacancies come to rest. The assumption is made that the inert markers in the hot region will be swept in the same direction as the vacancies with a motion proportional to the average velocity of the transported metal ions. (Strict equality would follow only if there were no void formation and no change in specimen shape.) Marker motion toward the cathode (mass transport toward the anode) is interpreted to mean that $e_d > e$, or, alternatively, that the electron–ion interaction force is greater that the electrostatic force on the positively charged ion.

In the pure metals investigated to date, ions are observed to move towards the anode in Ni and Au. Fe demonstrates the reverse of the expected behavior.

3. DESCRIPTION OF THE EXPERIMENTAL SYSTEM

The experimental chamber consists of a vacuum tight brass box equipped with two water-cooled steel tubs

holding mercury as seen in Fig. 1. The tubs are located near one end of the interior. Each tub is directly connected to one of the d.c. electrodes, and is otherwise insulated from the chamber. A specimen is clamped to the edge of one tub, and is constrained by a pinvise floating on the mercury surface of the opposite tub. Such an arrangement permits thermal expansion and contraction without specimen deformation. The clamped end of the wire specimen (about 3 in. long by 1/32 in. diameter) is also dipped into the mercury to preserve the thermal distribution. Specimens may be observed directly through a glass port in the chamber lid. When current passes directly through a specimen the central region is heated while the ends remain cool.

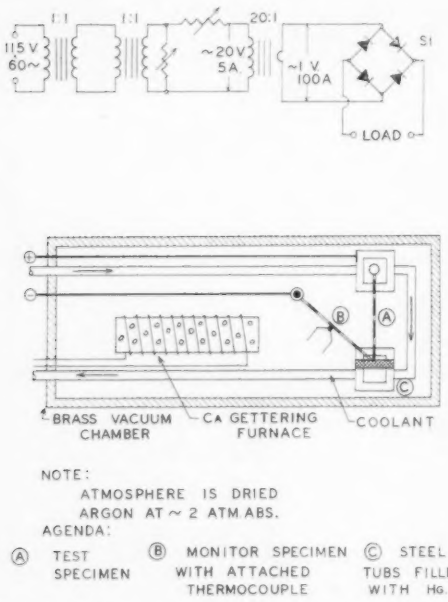

FIG. 1. Schematic of electrical circuit and pictorial sketch of the Cu marker apparatus.

The chamber is filled for each run with a dried argon atmosphere at a pressure of about 1·5 atm. Drying is accomplished by passing the argon through a Pyrex gettering tube, filled with calcium chips, and normally operated near 500°C.

The electrical circuit consists of a pair of cascade connected Sola transformers (the first of which is harmonically compensated) which feed a 20:1 stepdown transformer. The transformer output is rectified by a full-wave bridge of Sarkes–Tarzian type 5V silicon diodes. Voltage dropping and current limiting resistors provide control of the input voltage and primary loop current for the stepdown transformer. The specimen is connected directly across the bridge output. The rectifier is held at constant temperature by immersion in an oil bath cooled by running water. Typical operating conditions in the rectifier load circuit would be a d.c. voltage of one volt, and a direct current of 75 A. With a 3 in. × 1/32 in. diameter specimen, j is approximately 10^4 A/cm^2. Without regulation (except for the Solas), the average temperature excursion is of the order of $\pm$ 5°C, with occasional fast transients approaching 15°C.

A Hilger linear comparator microscope is used to measure the relative position of surface markers. The microscope is mounted directly over the chamber port, permitting the dynamic determination of marker positions. Unidirectional traverses are employed to eliminate backlash, and four traverses are normally made. If agreement from one traverse to the next is not within $\pm$ 1 μ limits (consistent with repeatability expected from a 1 μ least count instrument), the readings are continued until agreement occurs. The average of the four numbers for each marker determine the daily position, and the differences between the positions of the hot markers and the pair of cool end markers from day to day yield the marker velocities. The velocities are computed by a linear least-squares analysis of the position vs. time data.

A Leeds and Northrup optical pyrometer with a $\pm$ 7°C instrumental limit of error is used to measure temperature directly for the entire investigation. This device was calibrated against the smooth, clean surface of a test specimen in direct contact with a fine platinum/platinum–10 per cent rhodium thermocouple. Each calibration run was carried to the melting point in an inert environment. Melting normally occurred at the point where the thermocouple was fastened. This was insured by passing the thermocouple leads through the two holes in a fine ceramic insulator with the specimen positioned between the end of the insulator and the thermocouple bead. A light spring tension on the two lead wires caused the thermocouple to pull tightly against the specimen. With the precise checkpoint thus provided at melting, it was found that correction required for the thermocouple calibration because of contact losses varied between 10° and 30°C.

The filament of the pyrometer is fine enough to permit the measurement of temperature at the individual markers, for, with the particular pyrometer magnification available, the filament in the device is of the order of the marker size. The spread in the series of calibrations after the melting point corrections were applied was found to be $\pm$ 10°C.

It is not practical to leave the calibration thermocouples attached to specimens used for the collection of data. The disturbance associated with mounting a thermocouple, and the mechanical disturbance (i.e. sagging at high temperature under the weight of the couple) during the respective runs necessitate a special temperature calibration procedure. A second specimen is first placed in series with the test specimen. A thermocouple is clamped (with a fine "Stacon") to this monitor specimen. Normally this wire is somewhat shorter than the test wire. A lower center temperature results and permits one to approach the melting point with the test specimen while the monitor remains somewhat cooler.

The current is increased by steps at the start of each run, and the output of the monitor thermocouple (as displayed on a Brown recorder) is calibrated against the test specimen surface temperature as it appears to the pyrometer. Provided preferential erosion does not change the resistance ratio of the two wires at a particular temperature. such a calibration will be valid for the duration of a particular run. Customarily one of the central markers is chosen as the reference point for calibration of the monitor. An averaging of the recorder chart data throughout a run yields the temperature of the reference marker, and all other marker temperatures are obtained by simply subtracting the initial difference in temperature between each mark and the reference marker (as seen by the pyrometer) from the average value obtained from the chart. The markers are normally light razor scratches, but microhardness indentations serve equally well. There was no significant dependence of the effect on marker shape.

The sacrifice in temperature accuracy associated with the pyrometer technique employed points to the necessity of using more massive specimens so that thermocouples may be used as temperature standards. This entails a redesign of the power equipment so that sufficient current is available for heating large, hollow cylindrical specimens. Such a redesign is in progress.

4. RESULTS

Figure 2 shows the temperature dependence of v/j for all data collected. These data represent thirteen of fifteen runs made with 99·999 per cent Cu. The shortest run was four days in duration, while the longest required three weeks.

The completely unexpected saturation of the effect, with falloff and eventual reversal above 1000°C, is as yet unexplained in terms of any model.

In the region below 900°C, where the approximation of an exponential dependence of v/j on T is made roughly feasible (Fig. 3a), the data have been fitted by means of a least-squares regression analysis, with a straight line in ln v/j vs. $1/T$ (see Fig. 3). The resulting slope is 49·5 ± kcal/mole, and the regression coefficient has a value of 0·91. This result agrees with the accepted value of 47 kcal/mole[7] for the activation energy of self-diffusion rather more closely than one would expect within the stated gross limits. No attempt has been made to deduce the explicit form for the unexpected temperature dependence of e_d because of the great scatter, and both this correction and the ρ/T dependence of equation (2) are ignored in calculating an approximate activation energy at the lower temperatures.

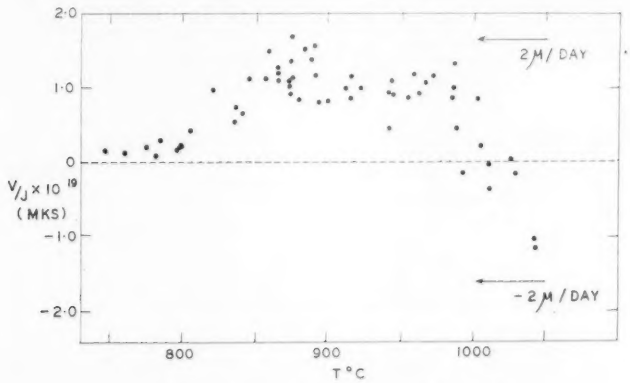

FIG. 2. Scatter plot of v/j vs. T for all data.

If is felt that the large scatter may be due to inadequate annealing, which leads to a non-standardization of grain size and number. To reduce thermal erosion during the vacuum anneal, annealing times were limited to short times (hours) at temperatures usually below 950°C, and occasionally approaching 800°C. It was thought that grain size effects should be small, and that the wires need only be softened to facilitate straightening prior to marking and mounting. However, WEVER has noticed a dependence in the mass transport in his specimens unless annealing in the

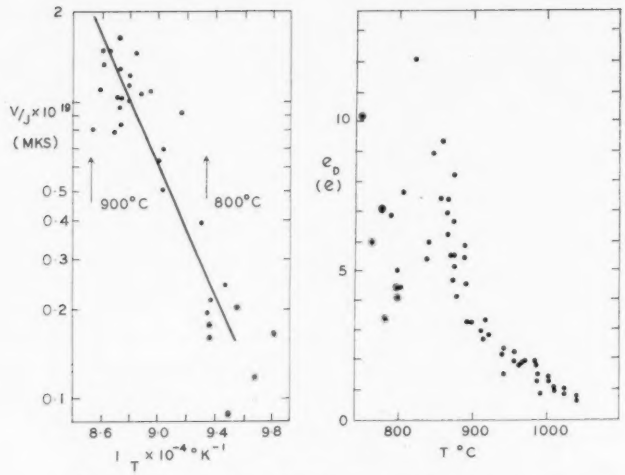

FIG. 3. Scatter plot of ln v/j vs. $1/T$ for temperature range below 900°C and scatter plot e_d vs. T.

1000°C range for about twenty-four hours is effected. Consequently a single run was attempted at low temperatures after a vacuum anneal for eight hours at 1000°C. The six circled data points on Figs. 2, 3, and 4 are from this run. The values lie near the center of the distribution of all the points in this region, but insufficient data has been collected with controlled preparation samples to have any firm statistical evidence that the precautions taken have reduced the scatter.

Figures 3 and 4 show e_d and $\rho_d N/N_d$ respectively as functions of T. Equation 18, of Ref. (6) shows that the transport is given by $\alpha TN = ce(v/j)$. These functions have been computed taking $\alpha = 1$.[6] In the preceding paper $\alpha = 1$ occurs in equation 17 for the limiting case of no void formation, and no change in the lateral dimensions, while for the case of an isotropic effect $\alpha = 1/3$. It is interesting to note that neither function changes sign with $\alpha = 1$, but such would not be the case with $\alpha = 1/3$. The apparent reduction in scatter for e_d at high temperatures occurs because of the small value of e_d itself in this region. Since e_d values are obtained by dividing the results for v/j, which have a nearly constant relative scatter, by D^* which is a well-behaved exponentially

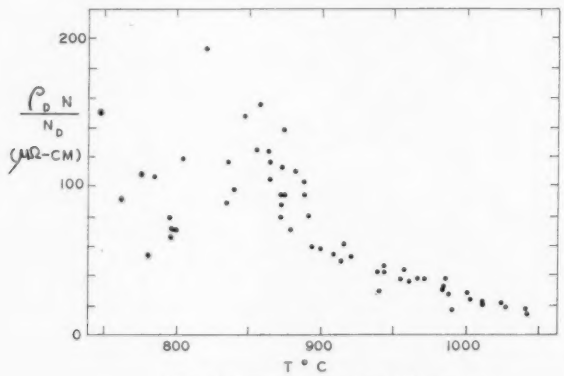

FIG. 4. Scatter plot of $\rho_d N/N_d$ vs. T.

Vol. 20
1961

increasing function of T, the effect of adding the values of $(v/j)/D^*$ to the constant electrostatic term (see equation 2) is a decrease in the absolute scatter with increasing T.

5. CONCLUSIONS AND SUMMARY

In the temperature region below 900°C the mechanism for electron–ion interaction probably follows HUNTINGTON's model. This view is supported by the fact that the actual magnitude of v/j has decreased by a factor of four with respect to gold, in agreement with the fourfold decrease in D^*. $\rho_d N/N_d$ is therefore nearly the same for the two metals. The direct transfer of momentum from electrons to diffusing ions is strongly suggested for this low temperature range.

It would be interesting to investigate the predicted linear dependence of the marker motion on current density. Such a linear effect has already been confirmed for a factor of two change in j for gold.[1,6] However, because of the relatively small motion observed with the maximum current densities available in copper (consistent with power supply and specimen geometrical requirements), no attempt was made to make similar measurements at lower values of j in copper.

Photomicrographic analysis[9] has shown some scattered pores in both the run specimens and controls. The controls in this case were simply lightly annealed stock copper wires not used in any of the experiments. Such pore formation might create "local" sinks for vacancies and noticeably reduce the effect, since the marker motion depends on vacancies ultimately coming to rest on dislocations in the cool region near the cathode. However, the sparsity of pores, and the complete absence of either a position or temperature dependence for the pore distribution, leads one to assume that the effect of small numbers of pores is negligible. In addition, copious pore formation would lead to over-all changes in specimen length, and this is not observed .

No specimen elongation except that associated with initial stress relief occurred in any of the d.c. runs, or in the single a.c. test conducted. No marker motion was obtained during the a.c. test.

The suggestion that a Sôret effect might be manifested as a motion of scratches symmetric about the central marker relative to this marker (i.e. either towards or away from it) did not appear to within the experimental sensitivity. The temperature distribution is not, of course, the most favorable for Sôret effect measurements.

Despite the fact that no statistical evidence of a grain size effect can be drawn from the single six-point run attempted, the possibility of such an effect existing should not be overlooked.

No really satisfying theoretical explanation of the anomalous behavior of copper above 900°C has yet been proposed.

Future plans in this laboratory call for the construction of a well regulated d.c. power source in the 1500 A range, the machining of high purity hollow cylindrical specimens to permit the micropositioning of thermocouples for temperature sensing, and the improvement of both chamber design and atmosphere control.

It is not anticipated that accuracies exceeding $\pm$ 0·5 μ can be exceeded with comparator microscopes or cathetometers.

Acknowledgements—The author wishes to express his indebtedness to Professor H. B. HUNTINGTON for sponsoring this research, and for his invaluable assistance in the preparation of the manuscript.

REFERENCES

1. HUNTINGTON H. B. and GRONE A. R., *Bull. Amer. Phys. Soc.* (ser. 2) **4,** 172 (1959).
2. WEVER H., *Z. Elektrochem.* **60,** 1170 (1956).
3. SEITH W. and WEVER H., *Z. Elektrochem.* **57,** 891 (1953); **59,** 942 (1955).
4. HEUMANN T., *La diffusion dans les metaux*. Bibliotheque Technique Philips, Eindhoven (1957).
5. WEVER H., Deutsche Gesellschaft für Metallkunde, Sept. (1957).
6. HUNTINGTON H. B. and GRONE A. R., *J. Phys. Chem. Solids*, preceding article.
7. KUPER A., LETAW H., Jr., SLIFKIN L., SONDER E. and TOMIZUKA C. T., *Phys. Rev.* **96,** 1224 (1954).
8. COMPAAN K. and HAVEN Y., *Trans. Faraday Soc.* **52,** 786 (1956).
9. Photomicrographic studies were conducted by L. A. GIRIFALCO and staff, NASA Lewis Research Center.

J. Phys. Chem. Solids Pergamon Press 1961. Vol. 20, Nos. 1/2, pp. 94–109. Printed in Great Britain.

THEORY OF DOMAIN WALLS IN ORDERED STRUCTURES—I. PROPERTIES AT ABSOLUTE ZERO

J. W. CAHN

General Electric Research Laboratory, Schenectady New York

and

R. KIKUCHI

Hughes Research Laboratories, A Division of Hughes Aircraft Company, Malibu, California

(*Received* 4 *August* 1960)

Abstract—The energy and entropy of domain walls in ordered structures at 0°K are computed as a function of orientation and composition. Structures, in which each atom is at a center of symmetry, are treated generally. For these the surface energy, as a function of orientation, has grooved minima for orientations containing bond direction. The surface entropy has cusped minima of zero entropy for the same orientations. Sharp peaks in surface energy as a function of composition occur at the stoichiometric point, and domain walls in nonstoichiometric crystals will have negative surface entropies. Some examples of structures in which some atoms are not at centers of symmetry are given, illustrating the major complications.

Vol. 2
196

I. INTRODUCTION

LONG-RANGE ordering is a cooperative phenomenon. It is achieved at low temperatures because the system can lower its free energy by ordering and it is maintained because it is energetically unfavorable for an individual atom to be out of step with the order imposed by its neighbors. At higher temperatures the order decreases because entropy is gained by increasing disorder, and, in addition, because it becomes energetically easier for an atom to disorder if some of its neighbors are already disordered. These two factors combined result in a very rapid decrease in order in the vicinity of a critical temperature at which the long-range order ceases.

When two (or more) ordered regions of a crystal are out of step with each other we have an antiphase domain structure. The region of contact between domains is a surface or domain wall. A certain amount of additional disorder may exist there, since atoms in the vicinity of the domain wall will have some neighbors out of step with their other neighbors. These atoms will find it easier to disorder and the domain wall becomes a region of increasing disorder which can be expected to spread into the adjacent domains as the temperature increases. A number of calculations of the nature of such a domain wall and its surface energy have been made.[1–4]

In this paper we will examine the domain wall at 0°K for a number of two- and three-dimensional structures. In subsequent papers we will examine in detail several aspects of domain walls at non-zero temperatures and compare the rigorous results obtained here with the results of more approximate methods which permit the calculation to be extended to non-zero temperatures. No general method was found to obtain rigorous results at non-zero temperatures. The only rigorous calculation by ONSAGER[1] for a two-dimensional square structure with antiferromagnetic coupling in the Ising model has not been generalized.

In the next section of this paper we will examine the orientation and composition dependence of the surface energy for a variety of structures. In the third section we will examine the surface entropies for the same structures. We will confine ourselves to the Ising model and to its ordered alloy structure analogue, in that we shall assume that the total energy of the crystal is given by the sum of

interaction energies of pairs of atoms or spins located on fixed points. For the most part, we will consider only near neighbor interactions although the techniques can usually be generalized to interactions among atoms separated by greater distances.

II. DOMAIN WALL ENERGY

The derivation of the orientation dependence of the domain wall energy in the Ising model is similar to HERRING's calculation of surface energies.[5] We will initially consider a single-domain crystal, introduce a mathematical surface

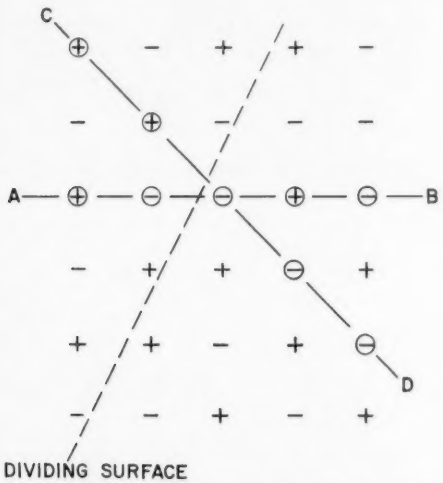

FIG. 1. Examples of chains of bonds crossing the dividing surface.

which divides the crystal into two parts, change one part into an antiphase domain, and determine the domain wall energy by the change of bond energies of pairs of atoms or spins, one of which is in each domain. The domain wall at absolute zero will be described by that dividing surface which gives the lowest energy, subject to whatever constraint we wish to place upon the surface. In ordered alloy structures (and in the antiferromagnetics in non-zero field) there may be an additional surface energy term which arises because the boundaries of the antiphase domain may not enclose an equal number of lattice points of each sublattice. Hence the formation of the new domain by exchanging the kinds of atoms on each sublattice will require an excess of one kind of atom and a deficiency of the other. This situation is most easily treated by having material reservoirs in equilibrium with the structure and including the energy change of the reservoirs in the energy of formation of the domain wall. We shall see that there will be cases in which this change is an important term. For the ferromagnetic and antiferromagnetic cases with scalar spins in zero field there is no need for such material reservoirs.

It will prove useful to treat separately those structures in which each atomic site is at a center of symmetry and then consider the structures in which this is not the case.* In addition, the ordered structures in which there are more than two sublattices and which consequently have no ferromagnetic analogue will also be treated separately.

While most of the widely studied ordered structures belong to the same crystal system as the corresponding disordered structure, there are a number that do not, e.g. AuCu, CuPt. In these there exist the possibilities of two types of domain walls, one type in which the tetragonal or hexagonal axes of the two domains are parallel to each other and another type in which they are not parallel. Since we will form new domain walls by exchanging atoms on some of the sublattices, the former type is easily achieved; the latter can usually be achieved by taking a larger unit cell and more sublattices.

A. *Domain walls in structures in which each atom is at a center of symmetry*

1. *Ferromagnetic and antiferromagnetic cases (Ising model).* Under the conditions of symmetry a

* HERRING states that his derivation applies to structures in "which all atoms are alike" and that the treatment "can be generalized to include some types of non-monatomic crystals." We find that his derivation applies to all structures in which each atom is at a center of symmetry regardless of how many different kinds of atoms or atomic sites the crystal has, and does not apply to some monatomic structures in which all atoms are alike but in which there is no center of symmetry at atomic sites, as for example, diamond cubic, graphite, and close-packed hexagonal. This may be most easily verified by considering a {111} planar dividing surface in a diamond cubic structure. The surface energy varies with position as the surface is translated normal to itself. HERRING's formula gives the mean, whereas the minimum value is called for.

given bond from one atom to another atom anywhere else in the structure is part of a continuous, straight-line chain of bonds. As long as we are within a single perfectly ordered domain these are identical except for alternating polarity if they join different kinds of atoms or spins. If we cross a dividing surface into another perfectly ordered domain of the same lattice, this row of bonds continues with bonds of the same energy except that the bond straddling the dividing surface will

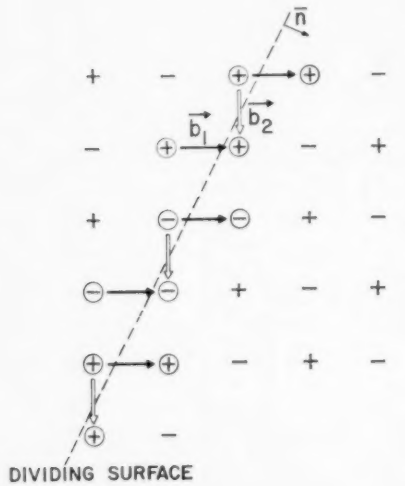

FIG. 2. Near-neighbor bonds straddling dividing surface.

be of a different kind. Thus for example in a direction along which (in a single domain) plus and minus signs alternate (line AB in Fig. 1), a plus will follow a plus or a minus will follow a minus when the chain crosses the dividing surface, and in a direction along which (in a single domain) a plus follows a plus or a minus follows a minus (line CD in Fig. 1), a plus will be followed by a minus or vice versa across the dividing surface. We may thus conceive the dividing surface as changing one bond in each straight-line chain where it crosses the chain, but because the chain is continuous it does not matter where the surface crosses the chain. If the bond energies of the ordered structure are such that the energy of each bond cut by the dividing surface is increased, then the surface cutting the minimum number of bonds of each kind will have the correct surface energy. This requirement is trivial if we consider near-neighbor bonds only. For longer range pairwise bond energies it may be severely restrictive. Without this restriction, however, the analysis that follows in this section is not valid.

With this restriction we will obtain the minimum surface energy by cutting the minimum number of bonds. This minimum number is given by the number of chains of bonds cut by a unit area of plane surface of the desired orientation (Fig. 2). If N_v is the number of atoms per unit volume, and $\boldsymbol{b}_i$ is the vector representing the i^{th} bond length and its direction, and $\Delta\epsilon(\boldsymbol{b}_i)$ is the change in energy in a bond of type $\boldsymbol{b}_i$ when it straddles a domain wall, then the surface energy E_s per unit area of a plane domain wall with unit normal $\boldsymbol{n}$ is given by

$$E_s = N_v \sum_i |\boldsymbol{b}_i \cdot \boldsymbol{n}| \Delta\epsilon(\boldsymbol{b}_i). \tag{1}$$

As HERRING showed, a polar plot of E_s as a function of $\boldsymbol{n}$ is a collection of spherical segments (called a "raspberry figure" by FRANK). Each spherical segment is of the form

$$E_s = \boldsymbol{E}_0 \cdot \boldsymbol{n} \tag{2}$$

where

$$\boldsymbol{E}_0 = N_v \sum_i \frac{|\boldsymbol{b}_i \cdot \boldsymbol{n}|}{\boldsymbol{b}_i \cdot \boldsymbol{n}} \boldsymbol{b}_i \Delta\epsilon(\boldsymbol{b}_i).$$

$\boldsymbol{E}_0$ is the diameter of a spherical segment of the raspberry figure, and is the diameter which starts at the origin of the polar plot. The boundaries between spherical segments are the planes normal to each $\boldsymbol{b}$. On crossing such a plane one of the $\boldsymbol{b} \cdot \boldsymbol{n}$ changes sign, and the surface tension plot has a discontinuity in slope there (a groove). Thus the surface tension for any domain wall in such a system at absolute zero is easily determined by specifying the $\boldsymbol{E}_0$'s and the solid angle bounding the orientations for which a sphere determined by an $\boldsymbol{E}_0$ represents a polar plot of the surface energy. The solid angles are formed by planes normal to all bond directions $\boldsymbol{b}_i$ for which $\Delta\epsilon$ differs from zero. Within any solid angle, $\boldsymbol{E}_0$ is found by performing the indicated summation.

Thus for a simple cubic structure, considering near neighbors only, the domain wall orientations over which a single sphere represents the surface

energy are bounded by orientations which are zones of the ⟨100⟩ bond directions, and the $\boldsymbol{E}_0$ vectors lie in the ⟨111⟩ directions. For a body-centered cubic structure, they are bounded by ⟨111⟩ zones giving rise to fourteen solid angles (Fig. 3): six square solid angles, with $\boldsymbol{E}_0$'s in ⟨100⟩ directions, and eight triangular solid angles, with $\boldsymbol{E}_0$'s in ⟨111⟩ directions. We shall term the domain wall whose normals lie in the solid angle around ⟨100⟩ Type I and the other domain walls Type II.

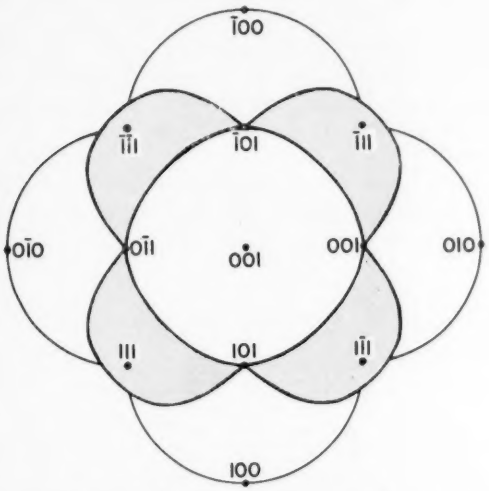

FIG. 3. Polar plot of domain wall energy for a body-centered cubic structure. The white area is Type I and the shaded area is Type II.

At this point it may be worthwhile to note that the dividing surface need not be a plane. As long as every element of its surface lies within a single solid angle in the polar plot, no chains of bonds will be crossed more than once by the dividing surface. The energy is completely determined by specifying the perimeter line of the dividing surface, since that will specify the number of chains of bonds which must be cut. The energy of the domain wall is independent of the actual shape of the dividing surface provided that every element of that surface lies entirely within one of the solid angles formed by planes normal to the bond directions $\boldsymbol{b}_i$'s.

2. *Ordered structures with two sublattices* (AB *alloy*). In an ordered alloy of the AB type consisting of two sublattices, two types of domain walls are to be distinguished. One of these is such that the wall is parallel to a crystal plane in which the two sublattices exist in equal number as shown in Fig. 4(a). The other is such that the wall is parallel to a plane in which only one kind of the two sublattices exists as shown in Fig. 4(b). The former

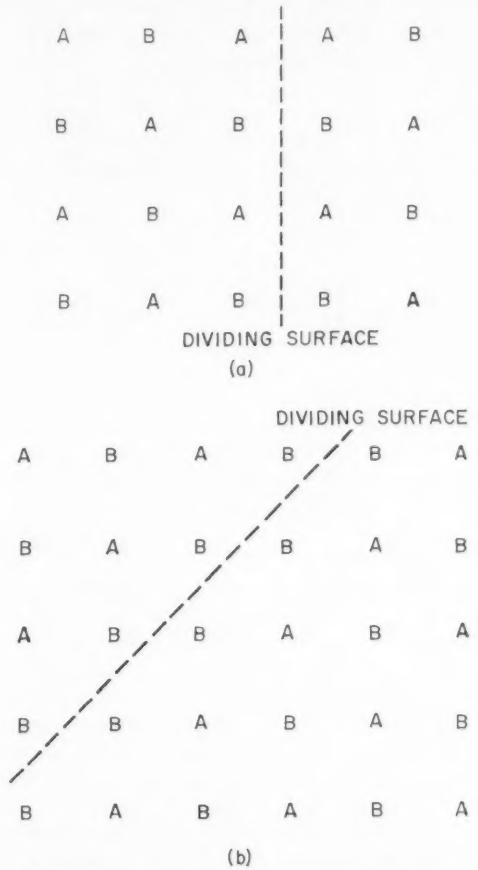

FIG. 4. Examples of dividing surfaces which do and do not alter the local concentration of atoms.

boundary can be treated in exactly the same way as for the Ising model of the previous section. The analysis of the latter type is not quite as simple as the previous case because of considerations of the changes in the amount of each species.

At any temperature but absolute zero, these changes in the amount of each species can be

Vol. 20
1961

achieved by corresponding changes in the composition of the bulk phase. At absolute zero, however, the bulk phase has a discontinuity in chemical potential at the stoichiometric composition and is therefore a very poor constant chemical-potential reservoir. For this reason it is simpler to calculate the domain wall energy for a system in contact with material reservoirs in equilibrium with the bulk ordered phase, in other words, by performing a grand canonical calculation. We will therefore look for the dividing surfaces for which $E-(\mu_A N_A+\mu_B N_B)$ is a minimum. The restriction that the chemical-potential reservoirs be in equilibrium with the bulk phase places a restriction on the chemical potentials:

$$N_A\mu_A+N_B\mu_B = E_{\text{bulk}}.$$

At the stoichiometric point, however, $\mu_A-\mu_B$ is not determined and can have a range of values, and as we shall see E_s will be a function of $\mu_A-\mu_B$.

Let us compute the energy change $E_s = \Delta E-(\mu_A-\mu_B)\Delta N_A$ when we form an antiphase domain entirely enclosed within the original domain and sufficiently large that we may ignore edge and corner effects. The purpose of enclosing one domain within the other is to avoid changes in the exterior surface of the crystal. Let us consider the interior domain formed by a parallelepiped, large in two dimensions, whose surfaces have an orientation in which each plane consists of only one kind of atom. The parallelepipeds of this orientation will, if they enclose an odd number of planes, require the operation of the material reservoirs for the creation of the antiphase domain. By simple translation of the parallelepiped, the exchange can be either A atoms for B atoms or vice versa, and the domain walls will contain two adjacent layers of either A or B atoms. To compute the energy of the domain wall, we may take the energy of AA and BB bonds as equal to zero, and the energy of an AB bond as ϵ, neglecting all but nearest neighbors. Since an AA or BB chain of bonds will gain an AB bond when it crosses the dividing surface, and an AB chain will lose an AB bond, at the dividing surface, we may write for the domain wall energy per unit area

$$E_s = N_v \sum_i S_i|\boldsymbol{b}_i \cdot \boldsymbol{n}|\epsilon_i-(N_s/2)|\mu_A-\mu_B| \quad (3)$$

where

$$S_i = \begin{cases} +1 \text{ if } \boldsymbol{b}_i \text{ refers to an AB chain} \\ -1 \text{ if } \boldsymbol{b}_i \text{ refers to either an AA or BB chain} \end{cases}$$

and the μ's are chemical potentials referred to a reference state of pure A or B of the structure upon which the ordered structure under consideration is based. These reference potentials are zero because we have taken AA and BB bond energies as zero. N_s is the number of atoms per unit area of a plane of this orientation, and the exchange of N_s atoms with the material reservoirs suffices for two surfaces. The sign of the second term is such as to take advantage of any difference between μ_A and μ_B because a surface will have either an excess of A or B if any difference in potentials exists.

The free energy of formation of an ordered structure from the elements in the near-neighbor approximation at absolute zero is

$$F = \begin{cases} -NZ\epsilon c & \text{for } c \leqslant 1/2 \\ -NZ\epsilon(1-c) & \text{for } c \geqslant 1/2. \end{cases} \quad (4)$$

Z is the coordination number and c the atom fraction of the species B. The chemical potential of each species relative to the pure component is given by

$$\mu_A = 0 \text{ and } \mu_B = -Z\epsilon \text{ for } c < 1/2$$
$$\mu_A = -Z\epsilon \text{ and } \mu_B = 0 \text{ for } c > 1/2. \quad (5)$$

For $c = 1/2$ the chemical potentials are indeterminate, subject to the restrictions:

$$\mu_A+\mu_B = -Z\epsilon$$

and

$$-Z\epsilon \leqslant \mu_A \leqslant 0. \quad (6)$$

The second term of (3) is of course absent for any crystallographic orientation in which each plane consists of equal amounts of both atoms. But because the second term is always negative, these orientations may become unstable to faceting into orientations that can take advantage of the second term. An inspection of (3) will show that for any non-zero values of $\mu_A-\mu_B$ all such orientations, except those containing bond directions, are unstable to faceting and that for sufficiently large $\mu_A-\mu_B$ even these become unstable. The upper

Vol. 2
196

limit of $\mu_A - \mu_B$ is given by (6) and is

$$\mu_A - \mu_B = Z\epsilon.$$

For this value, (3) reduces to zero energy for the closest packed orientation containing only one kind of atom, that is {11} in the two-dimensional square net, {111} in the sodium chloride structure and {100} in the cesium chloride or β-brass structure. For these directions, $N_v|\boldsymbol{b}_i \cdot \boldsymbol{n}| = N_s$. For these potentials all orientations are unstable with respect to faceting to zero energy orientations. Since these are the potentials also encountered in any crystals that deviate from the stoichiometric composition, it follows that it is always possible to create antiphase domains with no change in energy in nonstoichiometric crystals counting near neighbors only. This is illustrated in Fig. 5 for a two-dimensional square net.

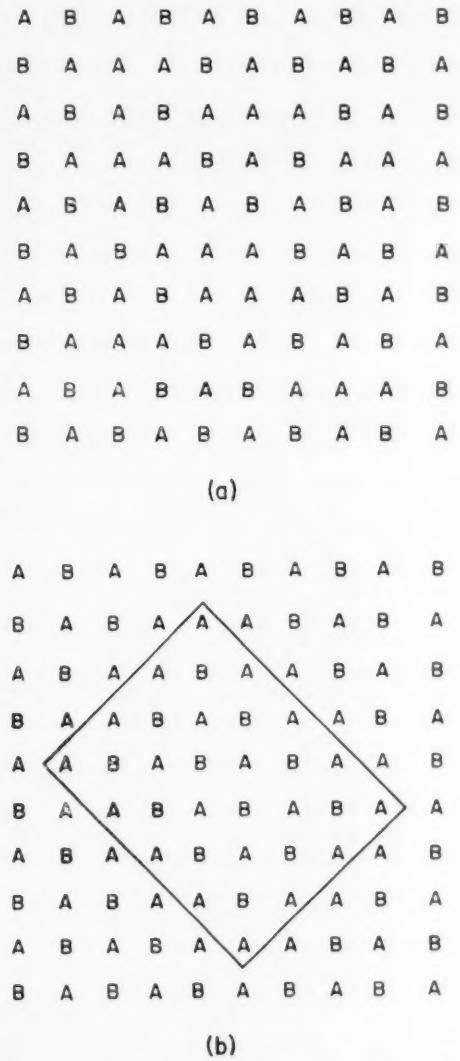

FIG. 5. Example of an antiphase domain in a nonstoichiometric crystal that can be formed with no change in energy. (a) 58 per cent A crystal with the excess A distributed at random on the B sublattice; (b) 58 per cent A crystal of the same energy with an enclosed domain.

3. *Ordered structures with more than two sublattices.* In this section we consider a domain wall between two domains, one of which may be created from the other by changing the kinds of atoms on more than two sublattices. This section covers compounds of other than equiatomic composition in which the minor component occupies one (or more) sublattices and the other component the remainder. It also covers structures in which the ordered and disordered structures belong to different crystal systems (AuCu, CuPt) in which domain walls can be formed between domains of different orientations that would be part of a single crystal if disordered. A chain of bonds of a given type, on crossing a dividing surface, may convert to any other type of bonds or continue unchanged. Thus not only the bonds straddling the dividing surface but also the interior bonds must be considered. The latter must of course cancel out except for surface terms. Let us now consider the domain wall energy of a stoichiometric AB_3 compound based on the face-centered cubic lattice (Fig. 6). There are four simple cubic sublattices. We shall consider a domain wall between two domains. In one of these the A atoms are on sublattice No. 1, in the other on No. 2. Again let us consider one domain to be in an enclosed parallelepiped that is large in two directions.

We have six types of bond chains each in two $\langle 110 \rangle$ directions. These are listed in Table 1. The $\boldsymbol{b}_{12}$ type bond is the only one which is similar to those previously encountered. There is an increase of ϵ for each chain intercepted. The $\boldsymbol{b}_{34}$ bond chains are unaffected. The remaining bond types change not only on the dividing surface but also in the interior. Let us group the $\boldsymbol{b}_{13}$ with the $\boldsymbol{b}_{24}$ and the $\boldsymbol{b}_{14}$ with the $\boldsymbol{b}_{23}$, since these have the

Vol. 20
1961

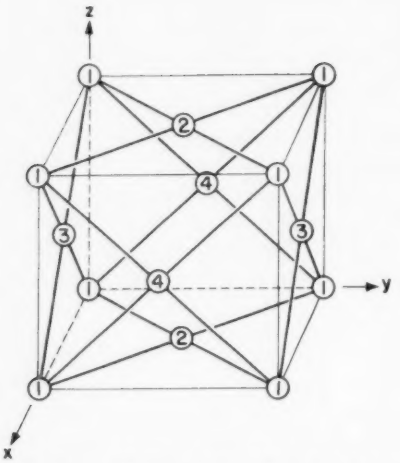

FIG. 6. The four sublattices of the AB_3 ordered structure based on the face-centered lattice.

Table 1

Bond	Directions	In exterior domain	In interior domain
$\boldsymbol{b}_{12}$	[110] [1$\bar{1}$0]	AB	BA
$\boldsymbol{b}_{13}$	[101] [10$\bar{1}$]	AB	BB
$\boldsymbol{b}_{24}$	[101] [10$\bar{1}$]	BB	AB
$\boldsymbol{b}_{14}$	[011] [01$\bar{1}$]	AB	BB
$\boldsymbol{b}_{23}$	[011] [01$\bar{1}$]	BB	AB
$\boldsymbol{b}_{34}$	[110] [1$\bar{1}$0]	BB	BB
$\boldsymbol{b}_{11}$	[100] [010] [001]	AA	BB
$\boldsymbol{b}_{22}$	[100] [010] [001]	BB	AA
$\boldsymbol{b}_{33}$, $\boldsymbol{b}_{34}$	[100] [010] [001]	BB	BB

same directions. The number of AB bonds for such paired chains having the same direction is equal to twice the number of A atoms. Therefore the change in bond energy for such pairs on forming a domain wall is proportional only to the change in the number of A atoms. Thus we may write for the surface energy of a 1–2 domain wall

$$E_s = (N_v/2)\sum |\boldsymbol{b}_{12}\cdot\boldsymbol{n}|\epsilon + (N_s/2)(\mu_A - \mu_B - 4\epsilon) \tag{7}$$

where $N_s/2$ is the increase in the number of A atoms per unit area of domain wall. The sum is only over the two $\boldsymbol{b}_{12}$ directions, so that the first terms give rise to only four $\boldsymbol{E}_0$'s in the Herring plot, two having [100] and two having [010] directions. When $\mu_A - \mu_B = 4\epsilon$, the polar plot of the domain wall energy reduces to just four spheres whose diameters lie in the (001) plane. The surface energy vanishes for the (001) surface and is non-zero for all other orientations. Since $N_s = 0$ for the (001) plane, E_s vanishes for that direction even if $\mu_A - \mu_B$ does not equal 4ϵ.

So far we have considered the 1–2 domain wall. The 3–4 has the identical orientation dependence. The 1–3 and 2–4 domain walls have $\boldsymbol{E}_0$'s in the [100] and [001] directions with zero domain wall energy for the (010) orientations, while the 1–4 and 2–3 domain walls have $\boldsymbol{E}_0$'s in the [010] and [001] directions with zero domain wall energy for the (100) orientations. It is possible to construct a three-dimensional domain structure with rectangular domains of zero domain wall energy. The only energy requirement is that of forming the junction of four domains. These require excess of A or B atoms.

It is easy to generalize the above argument to higher neighbors. Table 1 also lists next nearest neighbors. These add only a term of the following form to E_s of (7):

$$(N_v/4)\sum \{|\boldsymbol{b}_{11}\cdot\boldsymbol{n}| + |\boldsymbol{b}_{22}\cdot\boldsymbol{n}|\}\epsilon_2$$

where ϵ_2 is the energy of a next nearest neighbor AB pair, the AA and BB pair energies being set to zero. The summation is over all $\boldsymbol{b}_{11}$ and $\boldsymbol{b}_{22}$ types.

B. *Other structures*

If some atoms are not at centers of symmetry, the chain-of-bonds concept cannot be used. There appears to be no general method for obtaining results. We will consider only one two-dimensional structure, the honeycomb net (a layer of the graphite structure). In this two-dimensional structure, the dividing surface is most easily specified by a line in the dual net, each segment of which corresponds to a bond cut by the dividing surface (Fig. 7). In the ferro- and antiferromagnetic honeycomb structure the energy increase per segment in the dual net is constant; minimum energy increase is minimum length in the dual net. This means that the minimum energy domain wall will cut, at most, two of the three bond

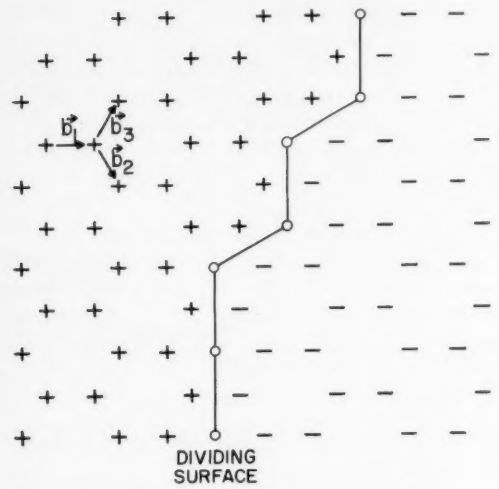

FIG. 7. The hexagonal net—and a domain wall specified by a line in the dual net. Note that no bonds of the type $\boldsymbol{b}_3$ are to be cut, even though $\boldsymbol{b}_3 \cdot \boldsymbol{n} \neq 0$.

directions and will zigzag to avoid cutting the other kind of bond. The orientation dependence of the surface energy is thus given by

$$E_s = (2\Delta\epsilon/3b)\cos\theta \qquad -\pi/6 < \theta < \pi/6 \quad (8)$$

where b is the bond length, $\Delta\epsilon$ the change in bond energy and θ the angle that the normal to the surface direction makes with the nearest bond direction. The surface energy plot (Fig. 8) is again a set of circles going through the origin, but now the minima occur when the surface is perpendicular to a bond direction instead of when it contains a bond direction.

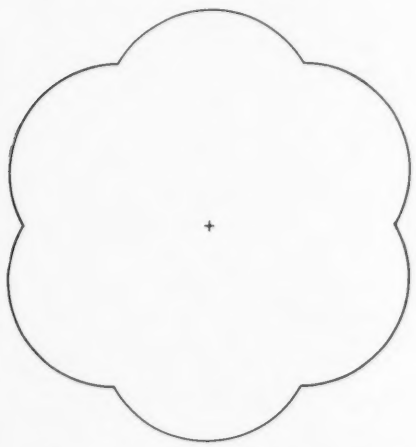

FIG. 8. The dependence of surface energy of the hexagonal net of Fig. 7 on the orientations of the normal to its average direction.

III. DOMAIN WALL ENTROPY

The domain wall entropy per unit area S_s gives the temperature coefficient of the domain wall surface tension σ

$$S_s = (E_s - \sigma)/T = -d\sigma/dT. \quad (9)$$

At absolute zero the entropy is computed by counting the number of ways a domain wall of a given average orientation and of the minimum energy can be formed. It was noted in the previous section that the energy of domain walls in the Ising model depended only on the number and kinds of bonds intersected by a dividing surface. If there is an increase in the energy of each bond that is intersected, then the minimum energy is given by dividing surfaces which intersect the minimum number of bonds, namely one per bond chain. Nonplanar dividing surfaces will give identical energies as long as each element of such surfaces are so oriented that no chain of bonds is intersected more than once. In this section we will count the number of different dividing surfaces which cut the minimum number of bonds.

A. *Two-dimensional structures*

1. *Two-dimensional square net.* Consider a finite square net with nearest-neighbor ferromagnetic interactions only. We specify the orientation of the domain wall by giving the termini of the domain wall on the edges of the net. Let these be (x_1, y_1) and (x_2, y_2)

$$x_2 - x_1 = nh_1a$$

$$y_2 - y_1 = nh_2a.$$

Here n, h_1 and h_2 are integers which we may take as positive and a is the lattice spacing. The numbers of vertical and horizontal bonds which must be cut are nh_1 and nh_2 respectively. But the sequence in which this number of horizontal and vertical bonds are cut does not affect the energy. We may specify a dividing surface by giving the sequence of cutting horizontal and vertical bonds

one at a time. The number of such zigzag curves connecting the point (x_1, y_1) with (x_2, y_2) and cutting only nh_1 and nh_2 bonds is

$$W = \frac{[n(h_1+h_2)]!}{(nh_1)!(nh_2)!}.$$

The total domain wall entropy is thus

$$S/k = \ln W = n\{(h_1+h_2)\ln(h_1+h_2) - h_1 \ln h_1 - h_2 \ln h_2\}$$

or per unit length

$$S_s/k = \{(h_1+h_2)\ln(h_1+h_2) - h_1 \ln h_1 - h_2 \ln h_2\}a^{-1}(h_1^2+h_2^2)^{-1/2} \qquad (10)$$

S_s is independent of crystal size if nh_1 and nh_2 are

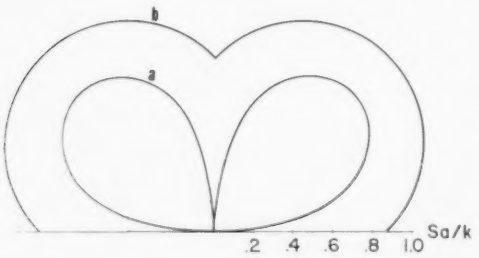

FIG. 9. Surface entropy of domain walls in the two-dimensional square net as a function of orientation: (a) entropy at absolute zero; (b) average entropy of the temperature range from absolute zero to the critical temperature.

of sufficient magnitude that Stirling's approximation for a factorial is accurate. It must be noted that this expression of S_s is rigorous.

This amount of entropy is not trivial. The average domain wall entropy for a given orientation over the temperature range of 0°K to the Curie temperature, T_c, may be defined as

$$\bar{S}_s = \frac{1}{T_c}\int_0^{T_c} S_s(T)\,dT = E_s(0)/T_c \qquad (11)$$

since the surface tension vanishes at T_c when the transition is of the second order. Fig. 9 compares the surface entropy of 0°K with the average surface entropy for that orientation. For most orientations the surface entropy at 0°K is a major fraction of the average surface entropy.

The surface entropy has a cusp for the orientations for which the polar plot of energy has a minimum. The high value of the entropy for other orientations will result in a rapid decrease in surface tension anisotropy with increasing temperature.

2. *Honeycomb net.* The domain wall can be visualized as consisting of mixtures of cuts of only two kinds of bonds corresponding to two directions in the dual net. Since the energy is determined only by the number of cuts, it is immaterial in which order they are cut. We have thus for the domain wall entropy per unit length

$$S_s/k = (n_1+n_2)\ln(n_1+n_2) - n_1 \ln n_1 - n_2 \ln n_2 \qquad (12)$$

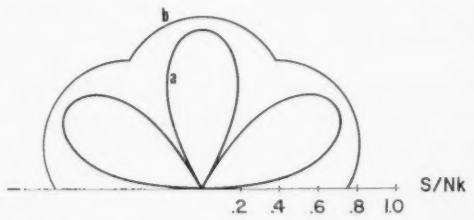

FIG. 10. Surface entropy of domain walls in the two-dimensional honeycomb net as a function of orientation: (a) entropy at absolute zero; (b) average entropy of the temperature range from absolute zero to the critical temperature.

where

$$n_1 = \frac{2}{\sqrt{(3)}b}\sin(30°-\theta)$$

$$n_2 = \frac{2}{\sqrt{(3)}b}\sin(30°+\theta).$$

The quantity S_s is compared with $E_s(0)/T$ in Fig. 10. Similar to the previous section this S_s is rigorous.

B. *Three-dimensional structures*

We have been able to formulate the calculation of the exact entropy of domain walls in three-dimensional structures as a combinatorial problem, which so far has eluded exact evaluation except for

certain orientations. It has been possible, however, to obtain good upper and lower estimates for the entropy for a variety of structures.

The technique for obtaining the formulation consists of describing the shape of the dividing surface by a contour map. The condition of minimum energy places restrictions on the contour lines. The number of different maps is related to the exact entropy.

The mappings are described by choosing a direction lying within an angle of 90° of every orientation enclosed by the solid angle bounded by planes normal to the bond directions and containing the domain wall orientation. The dividing surface is then projected onto a plane normal to the chosen direction and its height above the plane is used to describe its shape. Since a domain wall of minimum energy can have a dividing surface whose elements range over every orientation within one solid angle, choosing a projection direction within an angle of 90° insures that the height of the dividing surface will be a single-valued function of position on the projected plane.

We will first describe the combinatorial problems that arise from counting the number of different surfaces of lowest energy and then in the appendices give some methods of estimating the entropy. The formulations of entropy for any projection is exact, but we were unable to evaluate them exactly. Since some projections enabled us to obtain good upper estimates, while others gave good lower estimates, we will give several projections for each structure.

1. *Body-centered cubic.* With nearest-neighbor ⟨111⟩ interactions the unit sphere breaks into fourteen solid angles: six surrounding ⟨100⟩ and eight surrounding ⟨111⟩ (Types I and II respectively in Fig. 3). Two projections were found useful, one in the ⟨100⟩ direction for both Type I and II surfaces and another in the ⟨111⟩ direction for Type II.

(a) ⟨100⟩ *projection.* A body-centered cubic structure projects in the ⟨100⟩ direction into two interlocking two-dimensional square nets. We may specify the shape of the domain wall by associating with each lattice point the height of the dividing surface there in units of $a/2$, a being the cube edge of a unit cell. Then all numbers of one sublattice will be even, and those of the other sublattice odd. If the orientation of the domain wall lies within the solid angle surrounding the ⟨100⟩ direction (Type I), the rule of minimum energy places the following restriction on the numbers: *Nearest neighbors must differ by one.* The average domain wall orientation is specified by fixing the integers on the periphery of the net. The entropy is

$$S = k \ln W$$

where W is the number of ways one can create a square array of integers in which each integer differs from its neighbors by unity and in which the numbers on the periphery of the array are prescribed. For a Type II domain wall the rule for the square array of integers becomes:

In the horizontal direction, neighbors must differ by one; in the vertical direction, neighbors must differ by an odd integer and must form a monotonic increasing sequence.

(b) ⟨111⟩ *projection.* The body-centered cubic structure projects in the ⟨111⟩ direction into a two-dimensional triangular net. If we assign to each point of the triangular net the height of the domain wall in units of $a/2\sqrt{3}$, we obtain a set of integers of the form $3n$ for sublattice 1, $3n+1$ for sublattice 2 and $3n+2$ for sublattice 3, where n is an integer. If the domain wall orientation lies within the solid angle surrounding the ⟨111⟩ direction, the rule of minimum energy places the following restriction on the numbers: *Nearest neighbors must differ by either one or two.* The domain wall entropy is computed by finding the logarithm of the number of ways one can create a triangular net of integers which obey the above rule and in which the numbers on the periphery of the net are prescribed.

2. *Simple cubic.* With nearest-neighbor interaction the unit sphere breaks into eight equivalent solid angles each surrounding a ⟨111⟩ direction and bounded by {100} planes. Any projection direction will do. Two give simple formulations.

(a) ⟨111⟩ *projections.* These result in triangular nets, and if we assign the height in units of $a/\sqrt{3}$ (where a is the nearest neighbor distance), we obtain a rule identical to the one found for ⟨111⟩ projections of the body-centered cubic.

(b) ⟨100⟩ *projections.* These result in a square net and, if we assign height in units of a, we obtain the rule that the integers in this square net must monotonically increase or remain the same in

two directions (from top to bottom, and from left to right). Again, the average orientation of the surface is specified by the peripheral numbers.

C. *Non-stoichiometric crystals*

The above considerations apply to an ordered AB structure with $\mu_A - \mu_B = 0$. Creating the zero energy domain wall in non-stoichiometric structures does not require an energy change but does require an ordering of the excess atoms along the wall. This gives rise to a negative surface entropy which at low temperatures is the only source of surface tension.

If the composition is c ($c < 1/2$) the bulk ordered phase at absolute zero consists of one sublattice fully occupied by the major component, the other lattice containing a random mixture of the remaining atoms. The molar entropy of such a structure is then

$$S/Nk = -(1/2)[2c \ln (2c) + (1-2c) \ln (1-2c)],$$

$N/2$ being the number of lattice points in one sublattice. When an atom of the major species is changed into the minor species

$$\Delta S = -k \ln [2c/(1-2c)].$$

Since the creation of a unit area of surface in a closed system requires an excess N_s of the major species, the accompanying change in entropy of the bulk is $(kN_s/2) \ln [2c/(1-2c)]$. When c is close to 1/2, the magnitude of this entropy change is large compared to the entropy of position of the dividing surface and the latter may be neglected. We thus have for the entropy per unit length of a zero energy domain wall in a non-stoichiometric crystal:

$$S_s/N_s k = -(1/2) \ln [2c/(1-2c)].$$

This entropy is negative and at low temperatures gives rise to an increasing surface tension with increasing temperature. We thus find that the surface tension has a steep maximum (as a function of composition) at the stoichiometric point, which broadens with increasing temperature from a δ-function at the absolute zero. The width Δc of the maximum is approximately estimated by setting

$$-TS_s = \sigma_0$$

or

$$\Delta c = \exp [-2N_s \sigma_0 / kT].$$

IV. DISCUSSION

We have derived rigorous expressions for the energy and entropy of domain walls at absolute zero for several types of structures and as a function of orientation and composition. This is useful because rigorous results have not been obtained at non-zero temperatures, except for special orientations in two-dimensional structures.

The energy and entropy at absolute zero, together with the knowledge that the surface tension will vanish at the critical temperature if the transition is not of the first order, is usually adequate to estimate the surface tension at all temperatures. Thus the absolute-zero calculation is not only a guide for the non-zero temperature calculation but also permits estimates of many properties which we expect to find at non-zero temperatures. Among these are the anisotropy of surface tension, the composition effect, and the entropy of the boundary.

A. *Anisotropy of surface tension*

At absolute zero the surface energy as a function of orientation is given by segments of spheres. The junctions of these spherical segments are for orientations that are zones of bond directions and, for negative bond energies, are grooves in the polar plot of surface tension.

The surface entropy at absolute zero is a much stronger function of orientation. The entropy is zero and has a cusped minimum for those orientations for which the energy has a grooved minimum; for other orientations the entropy is large. We thus predict that the anisotropy of surface tension will diminish with increasing temperature.

The decrease in anisotropy is shown in Fig. 11, where we have plotted the surface tension as a function of temperature for the two dimensional square lattice for three orientations. The $\langle 10 \rangle$ orientation is the exact calculation of Onsager and corresponds to an orientation for which at absolute zero the surface tension has a grooved minimum and the entropy is zero. For the other two orientations we have plotted the limiting value of surface tension and its limiting slope at absolute zero as calculated in this paper. CAHN and HILLIARD[6] predicted that the surface tension would be isotropic at high temperatures and it seems that with this prediction the surface tension can be accurately

estimated for all temperatures and orientations for this structure.

A construction similar to that used in Fig. 11 may be used to estimate the low temperature behavior of surface tension in the body-centered cubic and β-brass structure for which the method of CAHN and HILLIARD predicts surface-tension anisotropy at high temperatures. For the AB_3 face-centered structure, where the method predicts the surface tension plot to approach a doughnut shape with circular cross section, a similar estimate may be made.

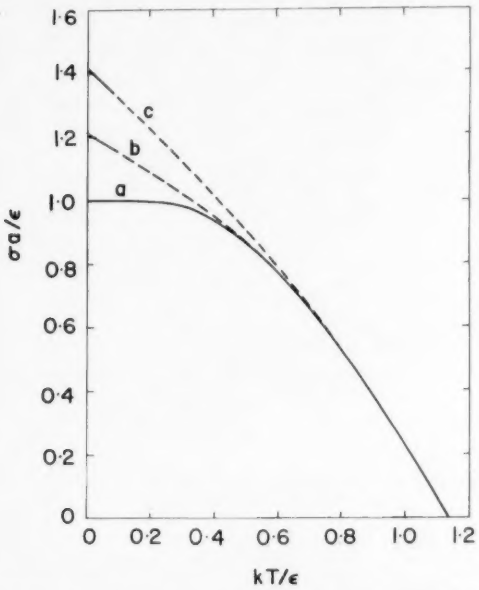

FIG. 11. The temperature dependence of domain wall surface tension for three orientations in the two-dimensional square net: (a) ⟨1 0⟩ from Onsager's exact calculation; (b) ⟨1 4⟩; (c) ⟨1 1⟩ based on low temperature results of present paper.

Of particular interest in the field of crystal growth[7] and crystal shape[8] is the question of whether grooved or pointed minima remain grooved or pointed at non-zero temperatures. If the energy rise away from orientations of minimum energy is linear, while the entropy rise from zero entropy has infinite slope, the minimum in surface tension becomes rounded at an infinitesimally small temperature. Therefore, for the two-dimensional structures the minima will become rounded; for the three-dimensional structures, comparison of (C.2) with (C.3) shows that while the grooves will become rounded, the pointed minima at the intersection of grooves will remain pointed at least at low temperatures. This is in agreement with the result of others.[7]

B. *The composition effect*

The possibility of a composition effect has been largely ignored in previous domain wall calculations. In the present calculations we predict that the surface tension as a function of composition will have a sharp maximum at the stoichiometric point and that with increasing temperature this maximum will broaden. We also suggest the possibility of a negative surface entropy, that is, a surface tension increasing with increasing temperature. This is indicated schematically in Fig. 12 for a ⟨11⟩ domain wall in the square net. The initial values are calculated exactly, but the high temperature values are estimated.

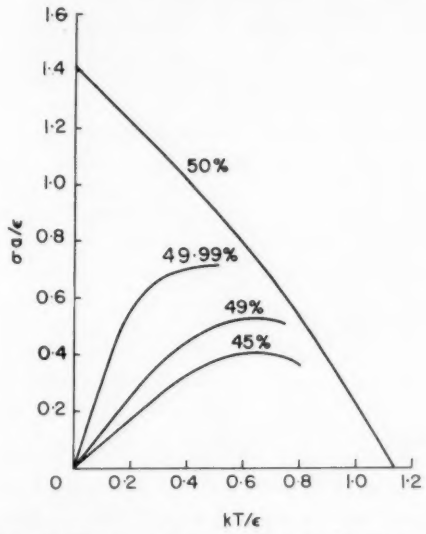

FIG. 12. The temperature dependence of surface tension for several compositions for a ⟨11⟩ domain wall in the two-dimensional square net.

C. *Domain wall entropy*

Except for the orientations for which the surface tension at absolute zero has a grooved minimum,

the dividing surface at absolute zero has considerable freedom to wander. There are many configurations of lowest energy. The surface entropy at absolute zero results from this ground state degeneracy.

This ground state degeneracy is the result of assuming pair-wise bonds of identical energy. In a real crystal this degeneracy will undoubtedly be destroyed by lattice relaxation in the vicinity of the domain wall, or by the presence of bonds which decrease in energy if they straddle a domain wall. We feel however that there is some justification in the calculation in these cases, for the existence of a large number of low energy configurations will give rise to the entropy we have calculated at a low temperature, if not at absolute zero.

The domain wall surface tensions at non-zero temperatures are usually obtained by minimizing the total free energy expressed as a sum of contributions from each plane of atoms or bonds parallel to the domain wall. It will be instructive to compare such a calculation and the present method.

For example, a {100} domain wall in the body-centered cubic structure in what we shall term the Bragg–Williams approximation will consist at absolute zero of one complete disordered {100} plane of atoms. It is easily seen that this is the lowest energy and corresponds to a dividing surface that is confined to zigzag only over the distance of only one interplanar distance normal to the domain wall. The result is that the Bragg–Williams calculation, while giving the correct surface energy at absolute zero, gives a surface entropy that is too small by a factor of 20 per cent. The relative error in surface entropy increases with decreasing coordination number. This comparison will be discussed in greater detail in the next paper.

We may take the surface entropy as a measure of the disorder introduced by the domain wall. Thus the entropy of the {11} domain wall in the two-dimensional square net at absolute zero corresponds to the entropy of two layers of atoms which are completely disordering; with increasing temperature the entropy corresponds to the entropy of an increasingly larger number of such planes for two reasons. Not only does the excess entropy due to the surface increase but also, since the homogeneous crystal now has some disorder, the entropy gain on disordering a layer decreases.

Acknowledgements—The authors wish to extend their thanks to many of their colleagues, especially to L. GUTTMAN and F. C. FRANK of Bristol University for many valuable discussions, and to J. S. KASPER for clarifications about crystallography.

REFERENCES

1. ONSAGER L., *Phys Rev.* **65,** 117 (1944).
2. HILLERT M., *A Theory of Nucleation for Solid Metallic Solutions*, D.Sc. thesis, Massachusetts Institute of Technology, Cambridge, Mass (1956).
3. BROWN N., *Phil. Mag.* **4,** 693 (1959).
4. FLINN P. A., *Trans. A.I.M.E.* **218,** 145 (1960).
5. HERRING C., *Phys. Rev.* **82,** 87 (1951).
6. CAHN J. W. and HILLIARD J. E., *J. Chem. Phys.* **28,** 258 (1958).
7. BURTON W. K., CABRERA N. and FRANK F. C., *Phil. Trans. Roy. Soc.* **243,** 299 (1951).
8. HERRING C., *Structure and Properties of Solid Surfaces*, p. 5. (edited by GOMER R. and SMITH C. S.) University of Chicago Press (1953).
9. KRAMERS H. A. and WANNIER G. H., *Phys. Rev.* **60,** 252 (1941); LASSETTRE E. N. and HOWE J. P., *J. Chem. Phys.* **9,** 747 (1941); MONTROLL E., *J. Chem. Phys.* **9,** 706 (1941); KUBO R., *Busseiron Kenkyu* **1,** 1 (1943).
10. KIKUCHI R., *J. Chem. Phys.* **24,** 861 (1956).

APPENDIX A

ENTROPY OF A (100) DOMAIN WALL IN A BODY-CENTERED CUBIC STRUCTURE AT 0°K

As was mentioned in Section III.B.1(a), the ⟨001⟩ projection of a Type I domain wall results in a square-net array of integers with a rule that *nearest neighbors must differ by one.* A Type I wall of any direction can be projected on a (100) plane, but in this appendix we limit ourselves to a (100) wall, and calculate the upper and lower limits of entropy by means of succesive approximations.

An example of a part of the projection is shown in Fig. A1. It should be noticed that in this example, all the numbers on the 0^{th} row are deliberately chosen as 0. The advantage of this choice will become evident later. The successive approximation starts from the evaluation of the entropy of a single row (i.e. the 0^{th} row) and proceeds to double rows (the 0^{th} and 1^{st} rows) and triple rows (the 0^{th}, 1^{st} and 2^{nd}) and so on.

It is clear that the entropy for the 0^{th} row of this example is zero:

$$S_0 = 0. \tag{A.1}$$

This is certainly the lower limit of entropy.

Next we examine the double rows composed of the 0^{th} and 1^{st}. On the 0^{th} row we have all 0's as before. Then on the 1^{st} row, both $+1$ and -1 are allowed on *each* point, leading to the entropy per unit section of

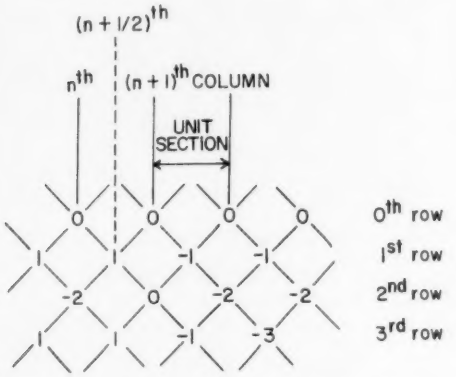

FIG. A1. An example of a part of the projection of a Type I wall on a (100) plane. The first row is deliberately chosen as 0–0–0–.

the double rows:

$$S_1 = k \ln 2. \tag{A.2}$$

The next approximation deals with the triple row, the 0^{th}, 1^{st} and 2^{nd}. The entropy of this triple row can be calculated by various methods, but here we use the matrix diagonalization technique.[1,9]

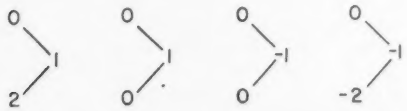

FIG. A2. The allowed configurations of a half unit in a (100) projection.

The possible configurations of the n^{th} column are (0,2), (0,0) and (0,−2). Those of the $(n+1/2)^{th}$ column are (+1) and (−1). Let us use $p_i^{(n)}(i = 2,0 \text{ and } -2)$ in denoting the number of ways of constructing the triple rows starting from a certain column far left of the picture proceeding towards right up to the n^{th} column with the end configuration $(0,i)$. The corresponding quantity for the $(n+1/2)^{th}$ column is written as $q_j^{(n+1/2)}(j = 1 \text{ and } -1)$. When we take into account the fact that the allowed configurations of a half unit are as shown in Fig. A2, the two sets of numbers $p_i^{(n)}$ and $q_j^{(n+1/2)}$ are connected by the following equation:

$$\boldsymbol{q}^{(n+1/2)} = \boldsymbol{T}\boldsymbol{p}^{(n)}. \tag{A.3}$$

Here $\boldsymbol{q}^{(n+1/2)}$ and $\boldsymbol{p}^{(n)}$ are vectors with components $[q_1^{(n+1/2)}, q_{-1}^{(n+1/2)}]$ and $[p_2^{(n)}, p_0^{(n)}, p_{-2}^{(n)}]$, respectively. $\boldsymbol{T}$ is a matrix:

$$\boldsymbol{T} = \begin{pmatrix} 1 & 1 & 0 \\ 0 & 1 & 1 \end{pmatrix}. \tag{A.4}$$

Also we see the relation

$$\boldsymbol{p}^{(n)} = \tilde{\boldsymbol{T}}\boldsymbol{q}^{(n-1/2)} \tag{A.5}$$

where $\tilde{\boldsymbol{T}}$ is the transposed matrix of $\boldsymbol{T}$.

The standard procedure of the matrix theory of cooperative phenomena tells that the entropy S per unit section is derived from the maximum eigenvalue λ of either the matrix $\boldsymbol{T}\tilde{\boldsymbol{T}}$ or $\tilde{\boldsymbol{T}}\boldsymbol{T}$ as

$$S_3 = k \ln \lambda, \tag{A.6}$$

Although $\boldsymbol{T}\tilde{\boldsymbol{T}}$ is a 2×2 matrix and $\tilde{\boldsymbol{T}}\boldsymbol{T}$ is a 3×3, the largest eigenvalues are identical and is $\lambda = 3$ so that

$$S_3 = k \ln 3. \tag{A.7}$$

When we compare (A.7) with (A.2),

$$S_3 - S_2 = k \ln (3/2) = 0{\cdot}4055k \tag{A.8}$$

is the entropy attributed to a lattice point of the 2^{nd} row.

Proceeding in the similar way, we treat more rows step by step. The results are summarized in Table A1. This table is interpreted as follows. As we increase ν, the difference $S_\nu - S_{\nu-1}$ approaches an asymptotic value, the choice of the initial row 0–0–0–0 affecting less and less. However, it should be noticed that $S_\nu - S_{\nu-1}$ is alternatively larger and smaller than the asymptotic value. This zigzag behavior is the consequence of the choice of the 0^{th} row. The best estimate of the asymptotic value of $S_\nu - S_{\nu-1}$, which is the entropy per atom on the projection, is $(0{\cdot}4363 \pm 0{\cdot}005)k$; hence

$$S_s = (0{\cdot}8726 \pm 0{\cdot}0010)k/a^2. \tag{A.9}$$

Strictly, the surfaces included in this evaluation are not only the (100) surface but all the surfaces containing a ⟨010⟩ direction, the row of zeros. We could have required not only that the first row be a row of zeros but also the last row be a row of zeros. The last column gives the result of such a calculation. This makes little difference in the entropy as the number of rows increases.

The reason it makes little difference is that the (100) orientation is the orientation with the largest entropy among all the orientations in the zone of the ⟨010⟩ direction. Thus the log of the total number of surfaces containing one ⟨010⟩ line is approximately equal to the log of the total number of surfaces constrained to the (100) orientation by two ⟨010⟩ lines. This is not true for the other orientations in the ⟨010⟩ zone; in general, the exact evaluation of the entropy of a surface by this method requires that two lines be specified. Obviously

Table A1. *Entropy of a* {100} *domain wall in a body-centered cubic structure*

Number of rows ν	λ_ν	$S_\nu/k = \ln \lambda\nu$	$(S_\nu - S_{\nu-1})/k$	$S'_\nu/k = \ln \lambda'_\nu$
0	1	0	0	0
1	2	0·6932	0·6932	0·6932
2	3	1·0986	0·4055	
3	$3+\sqrt{3}$	1·5540	0·4554	1·5358
4	7·2874	1·9861	0·4321	
5	11·312	2·4259	0·4398	

there is some freedom of choice, both with regard to direction of projection and direction of the lines which are specified. Some of these give more rapid convergence than others.

An alternate method of attack is to specify one line and the probabilities of a $+1$ and -1 change. For the (100) walls these probabilities were equal. For other orientations the specification of unequal probabilities will insure that the domain wall slopes at some angle to the projection direction.

APPENDIX B

ENTROPY OF A (111) DOMAIN WALL IN EITHER A SIMPLE CUBIC OR BODY-CENTERED CUBIC STRUCTURE AT 0°K

We have shown in Section III.B by using [111] projections that we obtain identical combinatorial problems for Type II orientations of the body-centered cubic structure and a corresponding orientation in the simple cubic structure. We shall make use of this and evaluate Type II domain walls of body-centered cubic by solving for the entropy in the simple cubic structure. This is most easily done by using the [100] projection.

Consider a (111) domain wall in the [001] projection. We may fix the domain wall orientation by specifying a $[11\bar{2}]$ line of the (111) surface and obtain as in the projection a row of integers $0, 2, 4, 6, \cdots\cdots 2n$.

An example of a part of this projection is shown in Fig. B1. The rule of building up this array is that each number is bounded by its two neighbors above. Proceeding as before, we obtain the results summarized in Table B1.

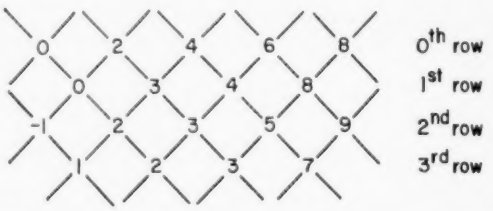

FIG. B1. An example of a part of the projection of a (111) wall in the ⟨110⟩ direction.

The same problem can be treated by using rows perpendicular to those used in Fig. B1. (In that case the initial row can be taken as made of all zeros and the final row all $2n$'s.) The asymptotic behavior of S_ν's is more or less the same and is given for comparison in the last column of Table B1.

The (111) domain wall can be projected on to a (111) plane to result in a triangular lattice as mentioned in Section III.B. We can calculate the wall entropy based

Table B1. {111}

Number of rows ν	λ_ν	$S_\nu/k = \ln \lambda_\nu$	$(S_\nu - S_{\nu-1})/k$	$S'_\nu/k = \ln \lambda'_\nu$
0	1	0		0
1	3	1·0986	1·0986	1·0986
2	8·2749	2·1132	1·0146	
3	22·3012	3·1046	0·9914	3·0180

Vol. 2
196

on this projection also. Two approximate calculations were made using the cluster-variation method[10] with a triangle and a hexagon as the basic figures. The entropies (converted for comparison to unit area of ⟨100⟩ projection) for these two calculations are

$$S/k = 0{\cdot}8631 \text{ (triangle)}$$
$$= 0{\cdot}9462 \text{ (hexagon).} \qquad \text{(B.1)}$$

It should be noticed that these are the lower limits of the true entropy whereas the numbers in Table B1 are upper limits.

Since these are entropies per unit area on the ⟨100⟩ projection, the entropy per unit true area is

$$S_s = 0{\cdot}98\sqrt{(3)}k/a^2 = 1{\cdot}70k/a^2. \qquad \text{(B.2)}$$

APPENDIX C

FIRST ORDER APPROXIMATIONS FOR OTHER ORIENTATIONS

It is possible to obtain by simple one or two row calculations expressions which are upper and lower bounds for all orientations. For some orientations convergence is rapid and the expressions are close to the correct limit. For simple cubic we have two expressions for the upper bound. For $h_1 \geqslant h_2 \geqslant h_3$,

$$Sa^2/k \leqslant h_3(h_1^2+h_2^2+h_3^2)^{-1/2} \ln [(h_1+h_2+h_3)/h_3], \qquad \text{(C.1)}$$

or

$$Sa^2/k \leqslant (h_1^2+h_2^2+h_3^2)^{-1/2}[(h_2+h_3) \ln (h_2+h_3) - h_2 \ln h_2 - h_3 \ln h_3]. \qquad \text{(C.2)}$$

The first expression is close to being an equality around $\{h_1, h_2, 0\}$; the latter is the better approximation around {111} but never is close to being an equality,

As a lower limit, for $h_1 > h_2 > h_3$ we obtain

$$Sa^2/k \geqslant h_3(h_1^2+h_2^2+h_3^2)^{-1/2} \ln [(h_2+h_3)/h_3]. \qquad \text{(C.3)}$$

Since this is close to the upper limit near {110}, we have a close bracketing of the true entropy there. With more effort these general expressions for upper and lower limit can be improved.

The body-centered cubic Type II boundaries of orientation (h_1, h_2, h_3) are combinatorially equivalent to the simple cubic boundary of orientation (k_1, k_2, k_3) where

$$k_1 = h_2+h_3-h_1$$
$$k_2 = h_3+h_1-h_2$$
$$k_3 = h_1+h_2-h_3. \qquad \text{(C.4)}$$

Therefore the entropy per unit area of a Type II boundary in body-centered cubic is given by

$$S_s(h_1, h_2, h_3)a^2(h_1^2+h_2^2+h_3^2)^{1/2} = S_s'(k_1, k_2, k_3)a'^2(k_1^2+k_2^2+k_3^2)^{1/2} \qquad \text{(C.5)}$$

where the S_s' is the entropy per unit area of the corresponding simple cubic boundary. For Type I boundaries we obtain as an upper limit

$$S_s a^2/k \leqq (h_1^2+h_2^2+h_3^2)^{-1}[2h_1 \ln (2h_1) - (h_1+h_2+h_3) \ln (h_1+h_2+h_3) - (h_1-h_2-h_3) \ln (h_1-h_2-h_3)] \qquad \text{(C.6)}$$

which is a good approximation around the {110} orientation.

J. Phys. Chem. Solids Pergamon Press 1961. Vol. 20, Nos. 1/2, pp. 110–121. Printed in Great Britain.

QUELQUES PROPRIETES PHYSIQUES DEPENDANT DE DEFAUTS DE STRUCTURE DANS L'OXYDE DE GERMANIUM PUR ET VITREUX

V. GARINO-CANINA

Centre de Recherches de la Compagnie de St. Gobain, Paris

(*Received* 20 *July* 1960; *revised* 28 *October* 1960)

Résumé—L'oxyde de germanium peut être obtenu sous forme vitreuse par refroidissement à partir de l'état fondu. Sa composition est alors, généralement, non stœchiométrique par suite de la décomposition thermique que l'oxyde subit aux températures élevées : un refroidissement rapide le fige dans cet état et la matière obtenue présente alors un défaut d'oxygène qui se manifeste par une bande absorbante à 2445 Å attribuée à des centres constitués par des lacunes d'oxygène contenant 2 électrons.

Par irradiation avec des longueurs d'onde comprises dans la région d'absorption cette bande peut être blanchie par suite de l'ionisation des centres et de la capture des électrons par des pièges. On peut la reformer, par recombinaison des centres ionisés avec les électrons, en faisant subir à l'échantillon un traitement thermique en atmosphère d'argon ou par irradiation avec des rayons X. Ces phénomènes correspondent uniquement à des déplacements d'électrons.

Par traitement thermique en présence d'oxygène la bande peut être diminuée ou éliminée par suite de la disparition des centres dûs au déficit anionique, ce dernier étant graduellement éliminé, dans ces conditions, jusqu'à l'obtention de l'oxyde stœchiométrique. Ce phénomène correspond à une diffusion d'oxygène dans la masse et semble être dû à un déplacement d'ions oxygène via des lacunes.

Des mesures qui ont été faites, on a déduit l'énergie d'activation pour la diffusion observée : la valeur déterminée est de 1,2 eV ($\pm$0,1).

On termine par des considérations générales tirées du rapprochement entre les structures cristallines et vitreuses et concernant le rôle qui peut être joué par les défauts de structure dans les corps sous l'état vitreux.

Abstract—Germanium oxide can be obtained in a vitreous state by cooling from the melt. It is generally non-stoichiometric, owing to the thermal dissociation of the oxide at high temperatures: by fast cooling, the state with too little oxygen is frozen in. This deficit in oxygen produces an absorption band at 2·445 Å, which is attributed to oxygen vacancies with two electrons.

This band can be bleached by irradiating with light of wave lengths in the absorption range; the absorption centres are then ionized, and their electrons captured by traps. The band can be reformed by recombining thermally the ionized centres with the electrons through heat treatment in an argon atmosphere or through irradiation by X-rays. Only electrons are displaced in these processes.

The band can be reduced or suppressed by heat treatment in oxygen. The centres disappear because, in these conditions, the anionic deficit is gradually eliminated to give the stoichiometric oxide. This process corresponds to a volume diffusion of oxygen ions, and seems to be due to a displacement via vacancies of oxygen ions. From these measurements the activation energy of this diffusion is 1·2 $\pm$ 0·1 eV.

Finally general considerations are deduced from a comparison between the crystalline and vitreous structures, about the possible role of structural defects in the vitreous state.

1. INTRODUCTION—FORMES CRISTALLISEES ET FORME VITREUSE DE L'OXYDE DE GERMANIUM

On connaît deux formes cristallisées de l'oxyde de germanium GeO_2[1] :

(1) Une forme tétragonale, de structure du type rutile, à germanium hexacoordonné,

Vol. 20
1961

ayant une densité de 6,239 à 25°C, pratiquement insoluble dans l'eau et pratiquement inattaquable par HF ou HCl : cette forme est thermodynamiquement stable à la température ambiante.

(2) Une forme hexagonale, de structure du type quartz, à germanium tétracoordonné, densité 4,228 à 25°C, soluble dans l'eau, facilement attaquable par HF ou HCl : cette forme est thermodynamiquement stable au dessus de 1033°C et fond à 1116°C.

Pratiquement, on obtient toujours, par précipitation de la solution ou par dévitrification de la forme vitreuse, la forme type quartz, dite forme soluble. Pour obtenir la forme type rutile, il est nécessaire de soumettre la forme type quartz à des traitements thermiques en présence de minéralisateurs.[1] L'oxyde de germanium subit une fusion pateuse : à une température à peine supérieure à 1116°C la matière est extrêmement visqueuse, cette viscosité diminue au fur et à mesure que la température augmente.

Par refroidissement relativement rapide de la matière fondue on obtient l'oxyde de germanium sous forme vitreuse[2], si le refroidissement est effectué très lentement on obtient la forme cristallisée, type quartz.

Pour obtenir un verre transparent il faut porter l'oxyde, pendant un certain temps, à une température supérieure à 1400°C.

Pour des températures inférieures à 1400°C la viscosité est trop grande et les bulles d'air ne peuvent pas monter en surface en un temps raisonnable : on obtient donc une matière blanche fortement diffusante à cause des nombreuses bulles d'air qu'elle contient.

On opère généralement à des températures entre 1400°C et 1550°C pendant quelques heures en utilisant un creuset de platine. Le refroidissement est effectué simplement en sortant à l'air libre le creuset avec son contenu. On obtient ainsi un verre parfaitement limpide et dépourvu de bulles.

Les propriétés de cette forme vitreuse de l'oxyde de germanium sont les suivantes : densité 3,637 à 25°C[2], très facilement attaquable par l'eau et les acides fluorhydrique et chlorhydrique. Le nombre de coordination du germanium, déterminé par l'étude de la diffraction des rayons X, est égal à 4 en moyenne. Le verre se transforme en oxyde cristallisé type quartz par traitement thermique à des températures comprises entre 700–800°C et la température de fusion (1116°C).

Les résultats exposés ci-dessous se réfèrent uniquement à cette forme vitreuse.

Dans la bibliographie nous indiquons les travaux les plus récents concernant les propriétés du verre GeO_2 (3–11).

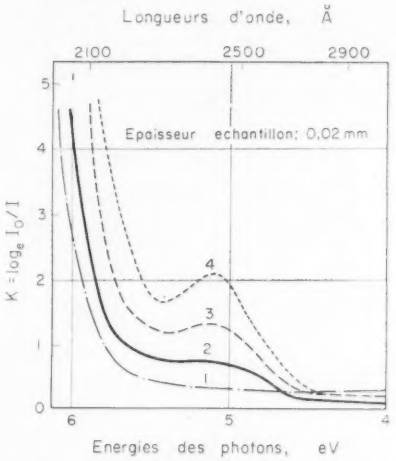

FIG. 1. Courbes d'absorption de verres d'oxyde de germanium pur sous une épaisseur de 0,02 mm.

(1°) Verre obtenu par fusion à 1.500°C traité, après fusion, à 1.200°C dans l'air pendant 72 h.
(2°) Verre obtenu par fusion à 1.420°C.
(3°) Verre obtenu par fusion à 1.460°C.
(4°) Verre obtenu par fusion à 1.500°C.

2. OXYDE DE GERMANIUM VITREUX A COMPOSITION NON STOECHIOMETRIQUE

Comme nous l'avons vu, il est possible d'obtenir un verre d'oxyde de germanium parfaitement limpide par fusion à des températures comprises entre 1400°C et 1550°C.

La fusion est effectuée dans un creuset de platine et la matière est laissée à la température maximum pendant un temps suffisant pour obtenir un verre dépourvu de bulles.

Nous avons porté dans la Fig. 1 les spectres d'absorption* des verres ainsi obtenus. Les temps

* Les mesures optiques ont été effectuées avec un spectrophotomètre enregistreur de la firme Optica.

Les courbes ont été construites en portant en abscisses les longueurs d'onde ou les énergies des photons, en ordonnées le coefficient d'absorption $K = \log_e I_0/I$, I_0 étant l'intensité incidente, I l'intensité transmise.

de séjour à la température maximum ont été chaque fois les mêmes ainsi que le refroidissement qui est obtenu simplement en sortant le creuset du four. On voit que la courbe d'absorption dépend de la température à laquelle la fusion a été effectuée ou des éventuels traitements thermiques que l'échantillon peut avoir subi par la suite.

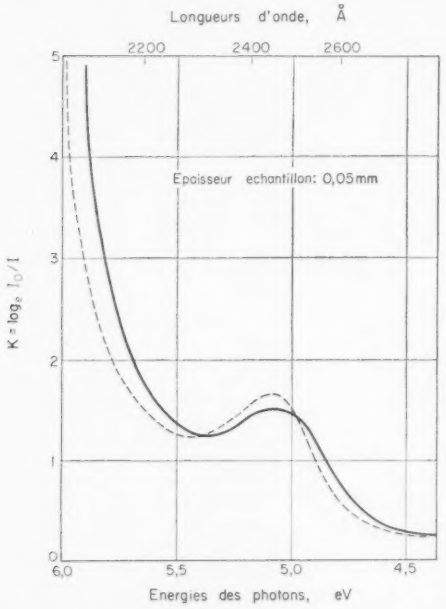

FIG. 2. Courbes d'absorption optique d'un verre d'oxyde de germanium pur obtenu par fusion à 1.460°C sous une épaisseur de 0,05 mm.

——— température ambiante
– – – (−180°C)

Deux particularités de ces courbes sont typiques :

(1) Un pic d'absorption vers 2445 Å (5,07 eV) dont la hauteur va en augmentant avec la température à laquelle on effectue la fusion. La largeur à mi-hauteur est de 0,45 eV à la température ambiante.

(2) Une montée rapide de la courbe d'absorption en-dessous de 2200 Å : l'importance de cette absorption dépend aussi de la température de fusion.

Aux basses températures (−180°C) le pic se déplace légèrement vers les courtes longueurs d'onde, sa hauteur augmente pendant que sa largeur diminue (Fig. 2). La queue d'absorption dans la région préfondamentale est considérablement réduite.

Il est possible, par des traitements thermiques à une température inférieure à celle à laquelle la fusion a été effectuée et dans une atmosphère contenant de l'oxygène, de réduire, ou d'éliminer, la bande d'absorption à 2445 Å. On obtient alors une matière présentant une courbe d'absorption comme la courbe 1 de la Fig. 1, ne présentant

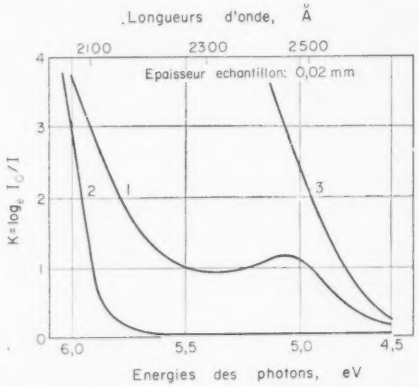

FIG. 3. Courbes d'absorption optique d'échantillons de verres d'oxyde de germanium ayant subi des traitements oxydants ou réducteurs. Epaisseur des échantillons 0,02 mm.

(1°) Verre GeO_2 obtenu par fusion à 1.470°C.

(2°) Verre GeO_2 obtenu par fusion à 1.470°C et blanchi ensuite par traitement à l'air.

(3°) Verre GeO_2 obtenu par fusion à 1.470°C et soumis ensuite à un traitement réducteur ménagé à l'hydrogène.

aucune trace de bande absorbante à 2445 Å. Ce résultat peut être obtenu (§ 4) en un temps qui dépend, d'une part, de l'épaisseur de l'échantillon et, d'autre part, de la température à laquelle l'essai est effectué. Les temps nécessaires pour un blanchiment total diminuent quand les épaisseurs utilisées diminuent et quand les températures de traitement augmentent à condition de ne pas dépasser 1200°C–1250°C. En effet, la bande absorbante commence à se reformer entre 1250° et 1300°C et son intensité va en croissant avec la température de traitement selon une loi sensiblement exponentielle.

Cet effet de blanchiment n'a pas lieu si les

Vol. 20
1961

traitements sont effectués en atmosphère d'argon ou d'azote purs. Il est, d'autre part, possible d'augmenter la hauteur du pic en soumettant les échantillons à des traitements réducteurs ménagés. Par exemple, par des traitements à l'hydrogène vers 400°C la hauteur du pic augmente avec la durée du traitement au point que, même pour des lamelles d'épaisseur inférieure à 20 μ on ne peut plus observer qu'un "cut off" apparent vers 2500 Å (Fig. 3). Ces traitements sont effectués généralement sur des échantillons très minces qui sont soumis, une fois le traitement réducteur à l'hydrogène terminé, à une longue recuisson à l'argon dans le but de réduire le gradient de concentration des centres absorbants.

Tous ces résultats nous indiquent que les centres absorbants à 2445 Å sont reliés à une réduction partielle de l'oxyde de germanium. L'oxyde subit une décomposition partielle avec perte d'oxygène lorsqu'il est porté à haute température.[4, 5, 7, 8] Cette décomposition semble commencer, quand le chauffage est effectué dans l'air à la pression atmosphèrique, vers 1300°C; elle croît très vite avec la température.

On peut utiliser la formule de SMAKULA[12] pour déterminer la concentration des centres absorbants.

$$fN_0 = 1{,}31 \times 10^{17} \frac{n}{(n^2+2)^2} K_{\max} H$$

en introduisant la valeur de l'indice de réfraction de l'oxyde de germanium vitreux ($n \simeq 1{,}7$) pour la région spectrale considérée nous avons $fN_0 \simeq 10^{16} K_{\max} H$ où $K_{\max}$ est le coefficient d'absorption au maximum et H la largeur à mi-hauteur exprimée en eV ($\sim 0{,}45$ eV)

N_0 est le nombre des centres absorbants par cm^3, f la force optique de la transition. Nous ne connaissons pas la valeur de f, mais nous savons qu'elle est toujours inférieure à 1, en général proche de l'unité.

Nous poserons $f = 1$ ce qui nous donnera une détermination de N_0 par défaut.

Dans les expériences que nous avons effectuées N_0 a pu varier entre des valeurs inférieures au seuil de détection et des valeurs supérieures à 10^{19} : il est difficile de mesurer la valeur du coefficient d'absorption au maximum quand celle-ci devient très grande à cause des limites pratiques dans l'obtention des lamelles minces (nous avons utilisé des lamelles obtenues par polissage jusqu'à des épaisseurs de 15μ).

Les concentrations qu'on peut atteindre par réduction ménagée à l'hydrogène sont sûrement supérieures à 10^{20} centres/cm^3.

Si nous admettons que chaque oxygène manquant produit un centre absorbant, nous pouvons déduire de ces mesures l'écart à la composition stœchiométrique qui peut donc se chiffrer à des valeurs allant jusqu'à 1 pour cent (ordre de grandeur) la composition de l'oxyde s'exprimerait donc par la formule Ge $O_{1.98}$: cette valeur n'est probablement pas à considérer comme une valeur maximum du défaut d'oxygène pouvant exister dans un verre GeO_2. Il serait intéressant de déterminer la valeur de l'écart à la stœchiométrie pour laquelle on peut encore avoir un verre.

3. BLANCHIMENT DE LA BANDE ABSORBANTE PAR IRRADIATION ULTRAVIOLETTE REFORMATION DES CENTRES PAR RECOMBINAISON THERMIQUE OU PAR IRRADIATION X.

COHEN[5] a montré que si on soumet un échantillon d'oxyde de germanium non stœchiométrique à une irradiation avec des ultraviolets d'énergie comprise dans la bande d'absorption (par exemple en utilisant une lampe à mercure basse pression dont l'émission est particulièrement intense à 2537 Å) on constate un blanchiment partiel de la bande absorbante.

Nous avons pu montrer[10] que la bande peut être entièrement reconstituée si, après irradiation, on chauffe l'échantillon à une température convenable et dans une atmosphère ne présentant pas une action chimique sur GeO_2 : nos traitements ont été effectués en atmosphère d'argon. Les traitements à l'air sont à proscrire à cause de l'interaction $Ge_nO_m (m/n < 2) \rightleftarrows$ oxygène, traitée au § 4.

Le blanchiment de la bande à 2445 Å est accompagné d'une augmentation de l'absorption vers 2200 Å. Tout revient à la situation de départ après traitement thermique.

Dans la Fig. 4, nous avons représenté quelques courbes qui montrent l'effet de blanchiment sous l'action de l'irradiation u.v. et la reformation progressive de la bande lors des traitements thermiques en atmosphère d'argon à une température de 200°C : pour des températures de traitements

plus élevées, la remontée du pic a lieu beaucoup plus vite.

Cet effet est à considérer comme purement électronique : les centres seraient vidés lors de l'irradiation u.v. : les électrons étant piégés à des endroits particuliers du réseau : les cations Ge^{IV}

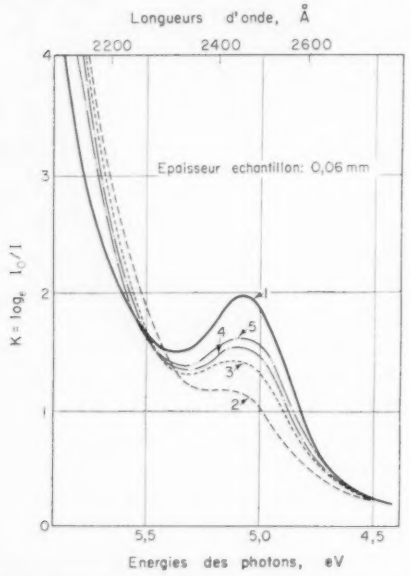

FIG. 4. Courbes d'absorption optique pour un échantillon de verre GeO_2 pur d'épaisseur 0,06 mm montrant le "blanchiment" de la bande à 2.455 Å après irradiation aux ultraviolets d'une lampe Hg basse pression et sa réformation lors d'un traitement thermique en atmosphère d'argon.

(1°) Avant irradiation.
(2°) Après une irradiation de 38 h aux ultraviolets d'une lampe Hg basse pression à 20°C.
(3°) Traitement de 1 h à 200°C dans une atmosphère d'argon.
(4°) Traitement de 17 h à 200°C dans une atmosphère d'argon.
(5°) Traitement de 128 h à 200°C dans une atmosphère d'argon.

(ou certains cations Ge^{IV}) pourraient peut être jouer le rôle de pièges. L'augmentation d'absorption vers 2200 Å qui accompagne ce blanchiment pourrait d'ailleurs s'expliquer par la perturbation produite par les germanium ayant piégé un électron sur les niveaux des oxygènes environnants.

Lors du chauffage, les pièges seraient vidés et les électrons réoccuperaient les centres, c'est-à-dire ils reviendraient à leurs positions stables.

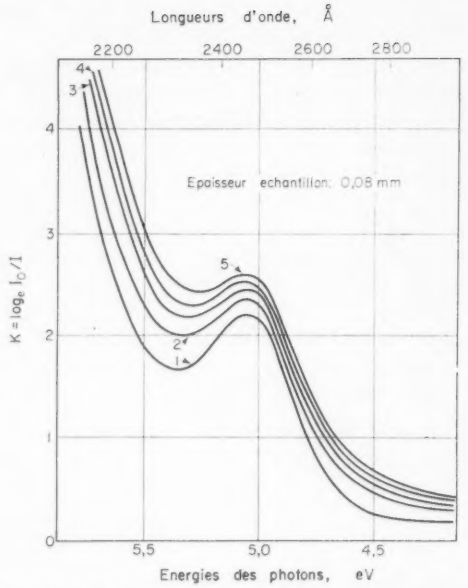

FIG. 5(a). Effet de l'irradiation aux rayons X (150 kV, 20 mA, anticathode tungstène) sur l'absorption optique d'un échantillon de verre GeO_2 pur ayant une épaisseur de 0,08 mm.

(1°) Courbe initiale.
(2°) Après irradiation aux rayons X pendant 1 h 10.
(3°) Après irradiation aux rayons X pendant 1 h 10 + 1 h 30 = 2 h 40.
(4°) Après irradiation aux rayons X pendant 2 h 40 + 2 h 00 = 4 h 40.
(5°) Après irradiation aux rayons X pendant 4 h 40 + 2 h 30 = 7 h 10.

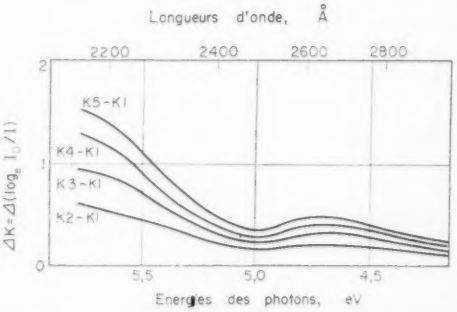

FIG. 5(b) Courbes représentant les différences entre les ordonnées des courbes 2, 3, 4, 5, et celles de la courbe 1 de la Fig. 5.

On peut aussi reconstituer les centres absorbants, après blanchiment par irradiation aux

Vol. 2
196

ultraviolets, en irradiant l'échantillon avec des rayons X à la température ambiante.

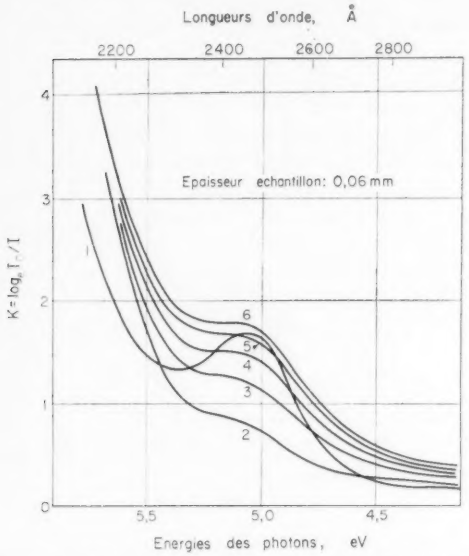

FIG. 6(a) Effet de l'irradiation aux rayons X (150 kV, 20 mA, anticathode tungstène) sur l'absorption optique d'un échantillon de verre GeO_2 pur ayant une épaisseur de 0,06 mm et préalablement blanchi aux ultraviolets.

(1°) Courbe initiale.
(2°) Aprés irradiation aux ultraviolets d'une lampe Hg basse pression pendant 64 h.
(3°) L'irradiation aux ultraviolets, dont les effets sont montrés par la courbe 2, est suivie d'une irradiation aux rayons X pendant 1 h 10.
(4°) Après irradiation aux ultraviolets puis aux rayons X pendant 1 h 10 + 1 h 30 = 2 h 40.
(5°) Après irradiation aux ultraviolets puis aux rayons X pendant 2 h 40 + 2 h 00 = 4 h 40.
(6°) Après irradiation aux ultraviolets puis aux rayons X pendant 4 h 40 + 2 h 30 = 7 h 10.

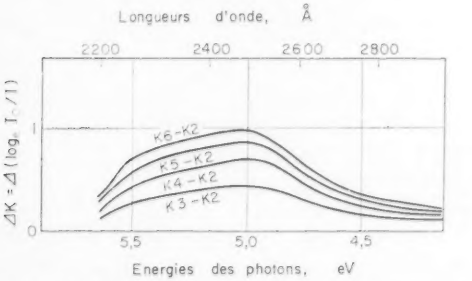

FIG. 6(b) Courbes représentant les différences entre les ordonnées des courbes 3, 4, 5, 6, et celles de la courbe 2 de la Fig. 6.

Dans les Figs. 5 et 6 on voit comme l'absorption optique croît sous l'action du rayonnement X (anticathode en tungstène 150 kV, 20 mA) pour un échantillon de GeO_2 blanchi préalablement aux ultraviolets (Fig. 6) ou non blanchi (Fig. 5). Un traitement thermique en atmosphère d'argon ramène l'échantillon à la situation de départ.

L'effet des rayons X est complexe. Il consiste en :

(1) formation d'une queue d'absorption dans la région préfondamentale ($\lambda > 2080$ Å) s'étendant jusqu'à 3000 Å environ.

(2) blanchiment partiel de la bande à 2445 Å ce qui produit en combinaison avec l'effet (1) une légère bande vers 2600 Å dans les courbes différences (Fig. 5 bis).

(3) Croissance de la bande à 2445 Å dans les échantillons où cette bande été précédemment blanchie par irradiation aux ultraviolets (Fig. 6 et 6 bis).

L'effet 3 peut être expliqué simplement par la capture d'une partie des électrons libérés par les rayons X dans le solide par les centres préalablement vidés par irradiation ultraviolette.

L'effet 1 pourrait être dû à la perturbation des niveaux des électrons de valence des oxygènes par les électrons libérés par les rayons X et piégés vraisemblablement sur les cations Ge^{IV} ou sur certains cations Ge^{IV} se trouvant au centre de tétraèdres déformés.

L'effet 2 est un effet banal dû au fait que les électrons responsables de l'absorption à 2445 Å contenus dans les centres ont une probabilité non nulle d'être excités sous l'action de l'irradiation X.

L'oxyde de germanium vitreux, qu'il soit sous forme stœchiométrique ou non stœchiométrique ne présente pas de résonance paramagnétique électronique.*† Les échantillons présentent par contre une résonance paramagnétique après irradiation aux rayons X ou aux ultraviolets.† Nous

* Communication personnelle du Dr. A. J. COHEN du Mellon Institute, Pittsburgh, U.S.A.

† Communication personnelle du Dr. J. S. VAN WIERINGEN du Philips Res. Lab., Eindhoven.

avons pu constater que le blanchiment progressif de la bande à 2445 Å lors de l'irradiation aux ultraviolets s'accompagne de la naissance d'une résonance paramagnétique caractérisée par un facteur g ayant une valeur inférieure à celle pour les électrons libres* : au fur et à mesure que l'absorption optique diminue, l'absorption pour les ondes centimétriques augmente ; de même, lorsque après blanchiment aux ultraviolets on soumet l'échantillon à un traitement thermique, on observe une remontée du pic d'absorption optique et une diminution des pics de résonance.

Le calcul du nombre de centres par voie optique et à partir des résultats de R.P.E. conduit à des valeurs de même ordre de grandeur. La résonance paramagnétique observée peut donc être attribuée aux électrons qui ont quitté les centres lors de l'irradiation ultraviolette et qui sont restés piégés à des sites actuellement mal identifiés. Une étude plus approfondie est évidemment nécessaire : elle est en cours actuellement.

Ces effets sont discutés plus longuement dans le § 5.

4. INTERACTION OXYDE DE GERMANIUM NON STŒCHIOMÉTRIQUE ⇄ OXYGENE-BLANCHIMENT DE LA BANDE ABSORBANTE A 2445Å

Nous avons étudié la cinétique d'après laquelle la bande absorbante d'un verre d'oxyde de germanium présentant un défaut d'oxygène s'atténue lors d'un traitement à l'air[9, 11]

Les essais sont effectués sur des échantillons d'épaisseur inférieure à 100μ afin que les temps nécessaires pour un blanchiment total soient raisonnables. Ces essais se font à des températures inférieures à 700°C. On est, en effet, obligé de travailler en-dessous de cette température si on veut éviter, d'une part, une dévitrification commençant aux faces, d'autre part, une déformation des échantillons.

Les résultats sont représentés (Fig. 7) en portant en ordonnées les logarithmes népériens du rapport entre le coefficient d'absorption à 2445 Å de l'échantillon après un temps t de traitement à une température donnée et le même coefficient d'absorption avant traitement et, en abscisses, les temps de traitement. Le rapport K_t/K_0 est d'ailleurs égal au rapport $\overline{C_t}/C_0$ entre la concentration moyenne en centres après un traitement de durée et la concentration initiale supposée uniforme ceci au moins pour les concentrations pas trop élevées.

Si nous admettons que la concentration en centres absorbants peut être identifiée à celle des oxygènes manquants, l'étude du blanchiment de la bande à 2445 Å pourra nous renseigner sur le mécanisme par lequel l'oxyde non stœchiométrique peut se saturer en oxygène.

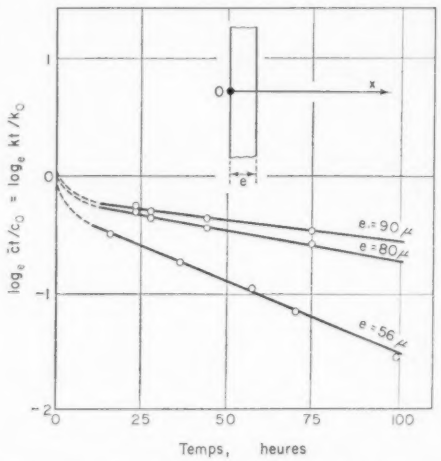

FIG. 7. Evolution de la concentration des centres absorbants à 2.445 Å, lors des traitements thermiques en présence d'oxygène à la température de 500°C pour 3 échantillons d'épaisseur 0,056, 0,080 et 0,090 mm.

Abscisses : Temps en heures.

Ordonnées : $\mathrm{Log}_e\ \bar{c}_t/c_0 = \mathrm{Log}_e\ k_t/k_0$ où c_0 et k_0 sont respectivement la concentration des centres et le coefficient d'absorption optique pour 2.445 Å au début de l'expérience ; $\bar{c}_t$ et k_t sont la concentration moyenne des centres et le coefficient d'absorption optique après un traitement de durée t.

Admettons qu'au début de l'expérience, l'échantillon présente une concentration uniforme de centres absorbants que nous appellerons C_0, se traduisant par un coefficient d'absorption K_0 à l'endroit du maximum ($K = {}^{X}C_0$) et identifions les centres absorbants à des germanium se trouvant sous un état de valence inférieure à 4. Il est logique d'admettre que, lors du traitement thermique, les centres absorbants vont disparaître d'abord en surface par recombinaison avec l'oxygène. Nous

* Les essais ont été effectués par les soins du Dr. ROCH de l'Ecole Normale Supérieure de St.-Cloud.

serons donc conduits à un gradient de concentration sous l'action duquel on pourra observer un phénomène de diffusion.

Ce problème se ramène, au point de vue mathématique, à trouver une solution de l'équation de Fick :

$$\frac{\partial c}{\partial t} = D\frac{\partial^2 c}{\partial x^2}$$

pour un système limité par deux faces planes, de dimensions très grandes par rapport à son épaisseur e et caractérisé par les conditions aux limites suivantes :

$C = C_0$ pour $0 \leqslant x \leqslant e$ et pour $t = 0$

$C = 0$ pour $X = 0$ et $x = e$ et pour $t > 0$

L'axe des X est normal aux faces de la lamelle, son origine est à l'intersection avec une des faces.

Il s'agit d'un problème classique qui conduit, si l'on admet que la concentration c en centres tend à une valeur nulle quand t tend vers l'infini, à l'expression suivante[13] :

$$\bar{c}(t) = \frac{1}{e}\int_0^e c(x,t)\,dx$$

$$= C_0\frac{8}{\pi^2}\sum_{v=0}^{v=\infty}\frac{1}{(2v+1)^2}\exp\left[-\frac{(2v+1)^2\pi^2}{e^2}Dt\right]$$

Pour des valeurs de t suffisamment grandes, le premier terme donne une approximation suffisante :

$$\bar{C}(t) = C_0\frac{8}{\pi^2}\exp\left[-\frac{\pi^2}{e^2}Dt\right]$$

De la pente des courbes de la Fig. 7 calculée dans la portion droite, on peut alors déduire la valeur du coefficient de diffusion D pour le phénomène étudié à une température donnée.

$$D = -\frac{e^2}{\pi^2}\frac{\Delta[\log \bar{C}(t)/C_0]}{\Delta t}\,(t > t^*)$$

t^* est le temps après lequel la courbe peut être considérée comme droite.

Une source importante d'erreurs dans la détermination de D tient à la mesure de l'épaisseur e de la lamelle qui intervient au carré.

Il est très difficile d'obtenir des lamelles à faces planes et parallèles pour des épaisseurs comprises entre 50 et 100μ.

Avec des échantillons sélectionnés avec soin, les valeurs de D, déterminées pour des lamelles d'épaisseurs différentes et pour une même température, peuvent concorder à mieux que 10 pour cent. Pour des lamelles normalement sélectionnées la dispersion sur les valeurs de D calculées a été de 20 pour cent environ.

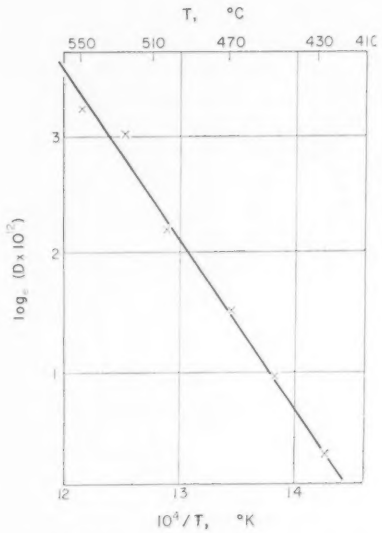

FIG. 8. Variation du logarithme du coefficient de diffusion en fonction de $10^4/T°K$.

Abscisses : Inverses des températures absolues multipliées par 10^4 ou températures en degrés centigrades.

Ordonnées : Logarithmes népériens des produits des coefficients de diffusion par 10^{12}.

Nous avons pris, comme valeur de D à une température donnée, la moyenne entre les valeurs calculées sur des échantillons d'épaisseurs différentes soumis au même traitement thermique, l'épaisseur étant mesurée au centre de la lamelle. On a ainsi déterminé la valeur de D à différentes températures comprises entre 400° et 700°C. Nous nous sommes limités à des températures supérieures à 400°C parce que, pour des températures inférieures à cette valeur, les temps nécessaires pour avoir un blanchiment, même partiel, sont extrêmement longs. D'autre part, ponr des températures

supérieures à 700°C les lamelles tendent à se déformer ou parfois à dévitrifier en surface.

Si on représente les résultats en portant en ordonnées les logarithmes népériens du coefficient de diffusion, en abscisses les inverses des températures absolues (Fig. 8) on obtient sensiblement une droite dont la pente nous permet le calcul de l'énergie d'activation.[11]

On a ainsi déterminé $W = 1{,}2$ eV ($\pm 0{,}1$) la valeur de D_0 qu'on peut calculer, est de l'ordre de 10^{-3} mais elle est déterminée avec une très mauvaise précision.

Les phénomènes décrits dans ce paragraphe sont à attribuer à une diffusion d'oxygène dans le réseau vitreux de l'oxyde de germanium. Une valeur si faible de l'énergie d'activation nous suggère un mécanisme de diffusion par déplacements d'oxygènes via des lacunes.

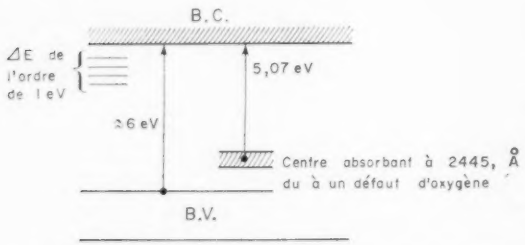

FIG. 9. Niveaux d'énergie dans l'oxyde de germanium pur et vitreux. Représentation schématique.

Nous avons vu qu'il est possible d'éliminer la bande absorbante à 2445 Å ainsi que la queue d'absorption vers les courtes longueurs d'onde par traitement thermique en présence d'oxygène. Ces traitements doivent être effectués à des températures inférieures à 1250°C environ car, en effet, c'est à cette température que les centres commencent à se reformer.

On obtient ainsi une matière caractérisée par une transmission totale jusqu'à 2300 Å environ. En dessous de cette longueur d'onde le coefficient d'absorption commence à monter de plus en plus rapidement et l'échantillon devient pratiquement opaque sous une épaisseur de 20μ en dessous de 2080 Å (6 eV). La matière ainsi obtenue n'est plus modifiée par des traitements oxydants ultérieurs : elle est à considérer comme caractérisée par une composition stœchiométrique. L'absorption très intense vers 6 eV peut être attribuée à l'absorption fondamentale due aux électrons de valence ($2p$) des ions oxygène. La séparation entre le niveau de valence et celui de conductivité (ou d'excitation) dans l'oxyde de germanium vitreux serait donc d'environ 6 eV (Fig. 9).

Nous rappellerons que dans la silice pure vitreuse dont la structure est analogue à celle de GeO_2, les mesures optiques indiquent une hauteur de région interdite d'environ 8 eV.[14, 15]

5. DISCUSSION DES RESULTATS ET CONCLUSIONS

Les résultats exposés dans le § 2 nous montrent clairement que l'oxyde de germanium, porté à température élevée (au-dessus de 1250°C environ) tend à perdre de l'oxygène. On doit admettre qu'à ces températures l'oxyde est thermodynamiquement plus stable sous forme non stœchiométrique.

Lors du refroidissement qui est, en général, effectué d'une façon relativement rapide, on fige pratiquement cette situation et on obtient un oxyde qui présente un écart à la stœchiométrie. L'oxyde passe, en effet, d'une température d'environ 1500°C à la température ambiante (où le coefficient de diffusion de l'oxygène dans l'oxyde est extrêmement faible) en un temps suffisamment court pour que la reprise d'oxygène par la matière n'intéresse que les parties périphériques de l'échantillon.

Le fait qu'il s'agisse bien d'une perte d'oxygène est prouvé par les expériences de blanchiment à l'air (§ 4) et par les résultats obtenus lors des traitements réducteurs à l'hydrogène (§ 2). La tendance à perdre de l'oxygène à une température plus ou moins élevée est d'ailleurs commune à tous les oxydes.

Dans le paragraphe 3 on a montré qu'une irradiation prolongée avec des ultraviolets de fréquence comprise dans la bande d'absorption produit un blanchiment du pic d'absorption à 2445 Å. Ceci démontre que la transition optique conduit l'électron de son état stable à un état non lié. En empruntant le langage de l'électronique des corps cristallisés, on dira que c'est une transition du centre absorbant à la bande de conductibilité ; l'électron serait rapidement capturé par des pièges (Fig. 9) sur la nature desquels il est difficile de faire des hypothèses précises. Il n'est

d'ailleurs que trop facile d'imaginer des pièges à électrons dans une matière à l'état vitreux. Les pièges en question semblent être relativement profonds si l'on juge par la vitesse à laquelle la bande se reforme par recombinaison thermique. On peut voir sur la Fig. 4 qu'il faut une centaine d'heures pour que, par traitement thermique à 200°C la bande augmente d'environ 50 pour cent de la valeur dont elle avait diminué lors de l'irradiation aux ultraviolets effectuée à la température ambiante.

Nous verrons plus loin qu'une hypothèse raisonnable sur la structure des centres absorbants consiste à admettre qu'ils sont formés de lacunes anioniques complètement neutralisées, autrement dit ayant piégé deux électrons. Lors du blanchiment aux ultraviolets un des deux électrons quitterait le centre qui resterait partiellement vide donc ionisé.

Les expériences décrites à la fin du § 3 sont en accord avec ce modèle. Les centres ne sont pas paramagnétiques : ceci s'explique par le fait qu'ils contiennent deux électrons à spins antiparallèles. On observe une résonance paramagnétique électronique aprés irradiation aux ultraviolets : les centres étant ionisés nous avons des électrons non couplés dans notre matière et nous pourrons observer une résonance. Il est évident qu'une étude plus approfondie est nécessaire qui permettrait probablement de séparer ce qui peut être dû à l'électron piégé de ce qui peut être dû à l'électron restant dans le centre ionisé.

Le blanchiment de la bande par irradiation est accompagné d'une augmentation de l'absorption dans la région spectrale de longueur d'onde inférieure à 2250 Å. Les deux phénomènes, diminution de l'absorption dans la bande, augmentation dans la région préfondamentale, vont de paire lors des irradiations aux ultraviolets. Ils vont encore de paire, mais dans l'autre sens, lors des traitements thermiques.

Cette augmentation de l'absorption en-dessous de 2250 Å peut être attribuée à la perturbation des niveaux des électrons de valence ($2p$) des oxygènes par les électrons capturés dans les pièges. Lors des traitements thermiques on a recombinaison électrons–centres : les pièges se vident, les centres se remplissent et on observe d'une part, la remontée du pic absorbant, d'autre part, la diminution de l'absorption dans la région préfondamentale.

Nous avons vu dans le § 3 que, si l'échantillon préalablement blanchi aux ultraviolets est irradié aux rayons X, l'absorption optique augmente partout mais plus particulièrement dans la région autour de 2445 Å comme le montrent bien les courbes de la Fig. 6. Ce résultat est facilement interprèté dans le cadre des idées exposées : des électrons libérés par l'irradiation X seraient capturés par les centres préalablement ionisés (ne contenant qu'un électron), les centres absorbants seraient ainsi reconstitués. La remontée du pic s'accompagne d'une augmentation de l'absorption vers les courtes longueurs d'onde : cet effet pourrait encore être interprèté en admettant que les électrons piégés perturbent les niveaux de valence des oxygènes.

Le problème qui se pose est celui de la nature des pièges à électrons dans le verre GeO_2 pur. Ceux-ci pourraient être constitués tout simplement par des cations Ge^{IV} ou par des cations Ge^{IV} se trouvant au centre de tétraèdres déformés ou encore par des cations ayant un nombre de coordination inférieur à 4.

Encore une fois, tout revient dans la situation d'origine après un traitement thermique effectué à une température et pendant un temps suffisants dans une atmosphère de gaz inerte.

Si les traitements thermiques sont effectués en présence d'oxygène les phénomènes décrits au § 3, et qui sont imputables uniquement à des déplacements électroniques, auront également lieu : mais un autre phénomène s'y superposera, celui décrit au § 4 consistant en une diminution de la concentration moyenne des centres par suite de l'action de l'oxygène sur l'oxyde non stœchiométrique. Nous rappelons ici qu'on n'observe aucun changement sensible dans la concentration des centres si le traitement est effectué en atmosphère d'argon.

Ce phénomène est donc à attribuer à une diffusion d'ions oxygène dans la matière. Les résultats décrits au § 4 ont permis de calculer la valeur de l'énergie d'activation pour la diffusion observée. Cette valeur paraît assez faible et conduit à interpréter cette diffusion comme ayant lieu via des lacunes d'oxygène. On est alors tenté d'admettre que les centres absorbants à 2445 Å sont constitués par des lacunes d'oxygène ayant piégé des électrons. Les résultats du § 3 discutés au début de ce paragraphe semblent nous indiquer

que ces lacunes auraient piégé deux électrons, autrement dit qu'elles seraient complètement neutralisées. Reste le problème de la répartition de la densité électronique dans le centre : le modèle le plus probable pour des raisons de symétrie consiste à admettre que les deux électrons se distribuent sur les deux cations environnant immédiatement la lacune ; les deux électrons auraient des spins antiparallèles ce qui expliquerait l'absence de paramagnétisme. Ce modèle n'est que l'image détaillée de la notion chimique de réduction partielle. Des ions oxygène sont remplacés par des électrons ; tout se passe comme si un certain nombre de cations Ge^{IV} passait à un état de valence inférieur à quatre.

Si on accepte ce modèle les phénomènes décrits au § 4 peuvent être interprétés aisément. Le mécanisme élémentaire de la diffusion observée consisterait en un échange de place d'un ion oxygène et des deux électrons piégés à la lacune voisine. Cet échange aurait lieu de proche en proche, les oxygènes se déplaçant selon la direction du gradient de concentration des germaniums à l'état réduit dans le réseau GeO_2, c'est-à-dire vers la surface de l'échantillon lors du traitement réducteur, vers l'intérieur lors du traitement oxydant. Ce phénomène peut évidemment être décrit en parlant d'un déplacement de lacunes anioniques vers l'intérieur ou vers la surface lors des traitements respectivement réducteurs ou oxydants. Les lacunes disparaîtraient à la surface en se recombinant avec l'oxygène de l'air.

Ceci peut être décrit par la réaction suivante :

$$[L_0]^{++} + 2e^- + \tfrac{1}{2}O_2 \rightarrow O_0$$

où L_0 représente une lacune d'oxygène et O_0 un ion oxygène à une place normale dans le réseau GeO_2.

Lors des traitements réducteurs le contraire se produirait d'après l'équation

$$O_0 + H_2 \rightarrow \overset{\nearrow}{H_2O} + [L_0]^{++} + 2e^-$$

Le système

$$[L_0]^{++} + 2e^-$$

représenterait une lacune neutralisée capable de diffuser dans la masse de la matière et constituant un centre de couleur absorbant à 2445 Å.

Quand la diffusion de l'oxygène est poussée à fond (ce qui peut être obtenu dans un temps raisonnable à une température de 400–600°C, pour des échantillons minces, ou vers 1200°C c'est à dire au-dessus du point de fusion, quand on veut blanchir des quantités importantes de substance) la matière obtenue est caractérisée par une transparence totale jusqu'à 2300 Å et une montée très rapide du coefficient d'absorption vers 2080 Å (6 eV) (Fig. 1 courbe 1). Nous pouvons en déduire une hauteur de région interdite qui sera d'environ 6 eV. Tous ces résultats peuvent nous conduire à un schéma pour les niveaux d'énergie dans l'oxyde de germanium pur et vitrifié (Fig. 9).

La notion de bande de conductivité dans une substance à l'état vitreux est à considérer évidemment avec précaution. Nous sommes dans une matière douée d'une structure caractérisée par l'absence d'ordre à grande distance mais où l'ordre à courte distance est à considérer comme approximativement réalisé. Les phénomènes localisés, tel que l'absorption optique, ne faisant intervenir que des petits domaines, de l'ordre de quelques unités Å auraient lieu d'une façon sensiblement identique dans les verres et dans les corps cristallisés.

Une deuxième question peut être soulevée lors du rapprochement, structures vitreuses–structures cristallines. Les résultats décrits dans un certain nombre de travaux ainsi que dans cet article montrent qu'il existe dans les verres—aussi bien que dans les cristaux—toute une série de propriétés physiques qui ne peuvent être interprètées que par l'idée de défaut de structure. L'introduction de cette idée pour les structures vitreuses exige quelques commentaires. La définition de défaut dans un corps cristallisé découle immédiatement de la notion même de réseau : tout écart à la structure périodique caractérisant un réseau cristallin représente un défaut.

Cette définition ne peut pas être adoptée sans modification pour les matières vitrifiées qui sont caractérisées justement par l'absence d'un réseau dans le sens que les cristallographes donnent à ce terme.

Une définition claire de ce qu'on doit entendre par défaut dans une structure vitreuse ne peut pas être donnée en une seule ligne, mais cette difficulté est, à notre avis, purement verbale. Elle tient essentiellement à la structure même des verres.

Vol. 2
196

Ce problème a été discuté par DEKEYSER[16] : nous pensons avec cet auteur, qu'il est parfaitement légitime d'admettre l'existence, dans les matières vitrifiées, de tous les défauts ponctuels qu'on a imaginés pour les cristaux : les lacunes, les interstitiels, les impuretés.

Le fait que ces différents types de défauts existent dans les verres, comme dans les cristaux, ne doit pas nous conduire à la conclusion que les effets qu'ils produisent sur les propriétés physiques d'un verre sont, dans chaque cas, analogues à ceux qu'ils produisent dans un corps cristallisé.

On peut prévoir, et on le constate que, sauf dans des cas particuliers, les corps vitreux seront beaucoup moins sensibles aux défauts que les cristaux. La perturbation qu'un défaut peut produire dans une structure vitreuse, donc fortement désordonnée, ne sera généralement pas comparable à celle qu'il produit dans une structure cristalline. Les structures vitreuses semblent pouvoir "accepter" beaucoup plus facilement les atomes étrangers ou, plus généralement, les écarts à la structure normale (en admettant que ce mot ait un sens). La raison profonde de cette différence entre les cristaux et les verres (surtout les verres complexes) peut tenir au fait que les positions des atomes sont données, pour les premiers, par une solution unique (aux défauts près) et que ceci n'est plus vrai pour les verres; pour ces derniers, le réseau peut aisément se réarranger localement autour d'une imperfection (défaut ou impureté).

Remerciements—Nous tenons à remercier très vivement le Docteur J. ROCH, de l'Ecole Normale Supérieure de Saint Cloud, pour les mesures de résonance paramagnétique électronique.

Nous voudrions aussi exprimer notre gratitude à Mlle J. DENONCIN, M. R. MORINEAU et Mme M. PRIQUELER, qui ont collaboré à ce travail.

BIBLIOGRAPHIE

1. LAUBENGAYER A. W. et MORTON D. S., *J. Amer. Chem. Soc.* **54,** 2303–20 (1932).
2. DENNIS L. M. et LAUBENGAYER A. W., *J. Phys. Chem.* **30,** 1510–16 (1926).
3. KREIDL N. J. et HENSLER J. R., *Congrès International du Verre, Paris* 1956, p. 367.
4. COHEN A. J., *Phys. Rev.* **105,** 1151–5 (1957).
5. COHEN A. J. et SMITH H. L., *J. Phys. Chem. Solids* **7,** 301–6 (1958).
6. KATS A., *Verres et Réfractaires.* Juillet–Août 1958, pp. 191–205.
7. GARINO-CANINA V., *C.R. Acad. Sci., Paris* **247,** 92–6 (1958).
8. GARINO-CANINA V., *Symposium sur la fusion du verre.* Bruxelles, 6–10 Octobre 1958.
9. GARINO-CANINA V., *C.R. Acad. Sci., Paris* **248,** 1319–22 (1959).
10. GARINO-CANINA V., *C.R. Acad. Sci., Paris* **248,** 1488–91 (1959).
11. DENONCIN J. et GARINO-CANINA V., *C.R. Acad. Sci., Paris* **250,** 1815–17 (1960).
12. SMAKULA A., *Z. Phys.* E. **59,** 603 (1930).
13. JOST W., *Diffusion in Solids, Liquids and Gases.* Academic Press, New York (1952).
14. TERRIEN J., *Rev. Opt. (théor. instrum.)* **15,** 258 (1936).
15. MITCHELL E. W. et PAIGE E. G. S., *Phil. Mag.* (ser. 8) **1,** 1085 (1956).
16. DEKEYSER W., *Silicates industr.* **21,** 61 (1956).

J. Phys. Chem. Solids Pergamon Press 1961. Vol. 20, Nos. 1/2, pp. 122–126. Printed in Great Britain.

INFRARED ABSORPTION IN MAGNESIUM SILICIDE AND MAGNESIUM GERMANIDE*

P. KOENIG,† D. W. LYNCH and G. C. DANIELSON

Institute for Atomic Research and Department of Physics, Iowa State University, Ames, Iowa

(*Received* 21 *September* 1960; *revised* 11 *January* 1961)

Abstract—Infrared absorption spectra of several *n*-type Mg_2Si and Mg_2Ge single crystals were obtained in the wavelength regions from 1–13 μ and 1–7 μ, respectively, over the temperature range from 85–370°K. Free carrier absorption occurred in Mg_2Si at the longer wavelengths. The absorption edges appeared to be due to indirect transitions and the shift of the optical energy gap with temperature is estimated to be -5×10^{-4} eV (°K)$^{-1}$ for Mg_2Si and $-6{\cdot}5\times10^{-4}$ eV (°K)$^{-1}$ for Mg_2Ge. No values for the gaps were determined from the present data but they can be seen to be approximately equal to the gaps determined by electrical measurements. An absorption peak at 0·40 eV in *n*-type Mg_2Si was observed and is discussed.

1. INTRODUCTION

MAGNESIUM silicide and magnesium germanide are semiconducting compounds which crystallize in the antifluorite structure. The temperature dependence of their electrical properties has been studied in some detail by WINKLER[1], MORRIS *et al.*[2,3] and NELSON[4]; but their infrared absorption spectra as functions of temperature have not been available. NELSON[4] obtained an infrared absorption spectrum of an *n*-type Mg_2Si single crystal at room temperature. The temperature dependence of the optical energy gap was not determined experimentally. By assuming spherically symmetric energy surfaces, non-degenerate carriers, acoustical mode scattering, and equal deformation potentials for electrons and holes, WINKLER[1] predicted a temperature coefficient of the energy gap of $-6{\cdot}4\times10^{-4}$ eV/°K for Mg_2Si and $-7{\cdot}6\times10^{-4}$ eV/°K for Mg_2Ge. The purpose of this research was to study the optical energy gaps in Mg_2Si and Mg_2Ge.

2. EXPERIMENTAL PROCEDURE

The crystals used in this investigation were taken from the same ingots as those used by MORRIS *et al.* The preparation of these crystals is described in their papers.[2,3] For most of the measurements the single crystal samples were ground to thin plates, approximately 6 mm by 6 mm by 0·3 mm, with silicon carbide paper. Final polishing with a suspension of powdered alumina in distilled water (Mg_2Si) or absolute alcohol (Mg_2Ge) was done on a rotating wheel covered with a short nap cloth.

The optical measurements on these samples were made with a Perkin Elmer Model 13 spectrometer equipped with a KBr or CaF_2 prism, and used in double beam operation in which data proportional to the optical density of the samples were obtained. The samples were mounted in an evacuated metal cryostat provided with NaCl windows. Engelhard CA 9R cement mixed with silver paste held the sample to the temperature bath without cracking due to differential thermal expansion.

Some thinner samples (0·10 to 0·18 mm) were prepared, but these usually broke into very small pieces during polishing. The largest piece of each crystal was mounted in a cryostat built to fit the stage of the microscope attachment of a Perkin Elmer model 112 spectrometer, used in single-beam operation with a quartz prism. These samples were used to obtain absolute values of the absorption coefficients.

The doping agents and the sample resistivities are given in Table 1. The resistivities were measured by the four probe method described by VALDES[5]. All of the samples were *n*-type semiconductors.

3. RESULTS

The absorption spectra of two Mg_2Si samples are shown in Figs. 1 and 2. The spectrum of

* Contribution No. 935. Work was performed in the Ames Laboratory of the U.S. Atomic Energy Commission.

† Present address: 21 Cordes Drive, Tonawanda, New York.

Table 1. *Doping agents and resistivities of samples*

	Sample number	Doping agent		Resistivity (ohm cm)
		element	per cent by weight	
Mg_2Si	23B01	silver	0·02	0·18
Mg_2Si	27B01	iron	0·023	0·45
Mg_2Si	28B04	aluminum	0·03	0·16
Mg_2Ge	13B1	none		~ 1

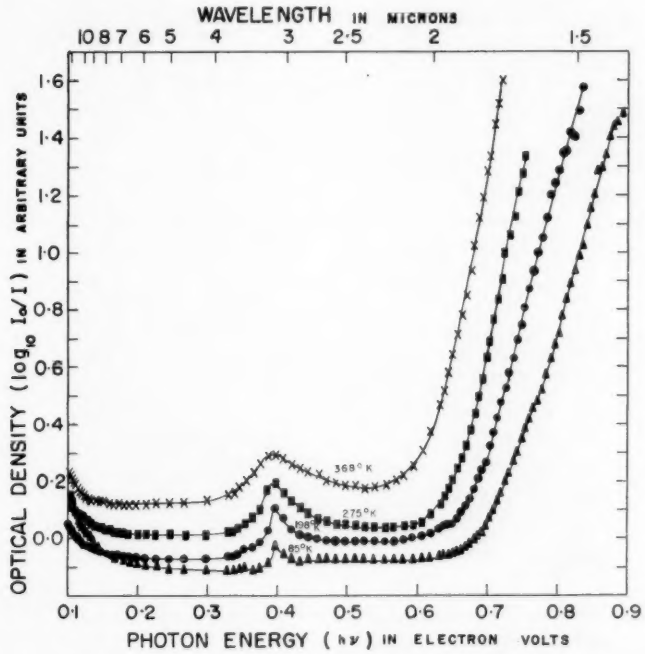

FIG. 1. Optical density vs. photon energy of Mg_2Si sample 27B01. The ordinates shown are for a temperature of 368°K; the other curves are displaced downward for clarity.

23B01 was similar to that of 28B04. At high photon energies each spectrum showed an absorption edge caused by electronic transitions across the band gap. At 0·40 eV a broad absorption band, which was observed in the spectra of all three Mg_2Si samples, decreased in height and width with decreasing temperature. It was less prominent in the sample of highest resistivity. At wavelengths beyond 8 μ, the absorption in each sample was proportional to the square of the wavelength, as predicted by the classical Drude theory for free charge carrier absorption.

The Mg_2Ge spectra exhibited an absorption edge at slightly longer wavelengths than the Mg_2Si edge. There was no absorption peak between the edge and 7 μ. Free carrier absorption was not observed for wavelengths shorter than 7 μ.

Figure 3 shows the absorption coefficient (α)

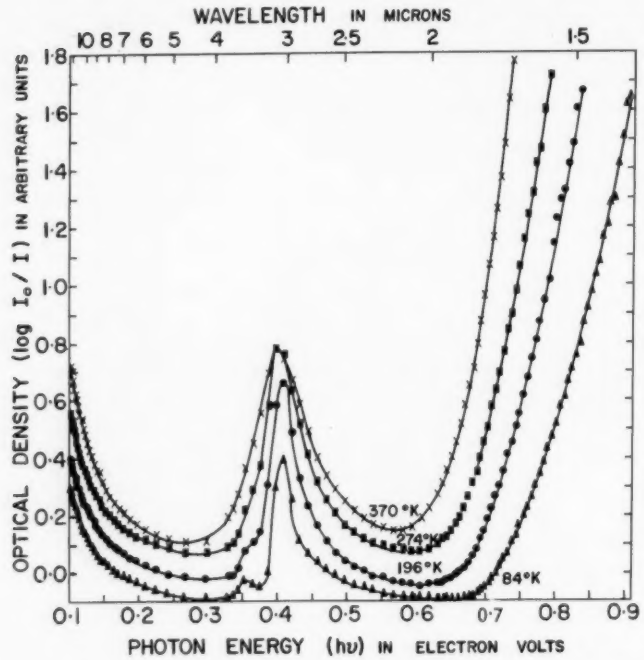

FIG. 2. Optical density vs. photon energy of Mg_2Si sample 28B04. The ordinates shown are for a temperature of 370°K; the other curves are shifted downward for clarity.

in the region of the absorption edge for Mg_2Ge 13B1 and Mg_2Si 27B01 at several temperatures. The absorption coefficients were obtained by applying the formula

$$\frac{I}{I_0} = \frac{(1-R)^2 \exp(-\alpha d)}{1-R^2 \exp(-2\alpha d)}$$

to the data taken on the thinnest samples with the microscope attachment, d is the sample thickness. R, the reflection coefficient, was found by applying the above formula to I/I_0 far from the absorption edge so that $\alpha d \sim 0$. This method could be used only on the purer samples which had less free-carrier absorption; and in the case of Mg_2Si, only when the peak around 0·40 eV was small. In these samples there was a wavelength region throughout which I/I_0 was constant. This region of maximum transmission was used to obtain R, which varied from 0·45 to 0·75. A series of spectra on different samples at room temperature gave nearly identical α vs. $h\nu$ curves even though R varied from sample to sample. It should be noted that the approximate expression, $I/I_0 = (1-R)^2 \exp(-\alpha d)$, is not always valid in the present work because of the large reflection coefficients. Thus the ordinates in Figs. 1 and 2 are not directly proportional to α for the smaller values of I_0/I.

4. DISCUSSION

The transitions in the edge appear to be indirect transitions involving the creation or destruction of a phonon in the absorption process. The participation of phonons is suggested by the temperature dependence of the shape of the absorption edge. The curves are not simply translated along the energy axis as the temperature varies. Indirect transitions are also inferred from plots of log α vs. $\log(h\nu - h\nu_t)$ where $h\nu_t$ is taken to be the photon energy at which the curve of I/I_0 vs. $h\nu$ begins to depart from a straight line, i.e. the low energy limit of edge transitions detectable in our samples. These plots were linear with slopes, n, in the range

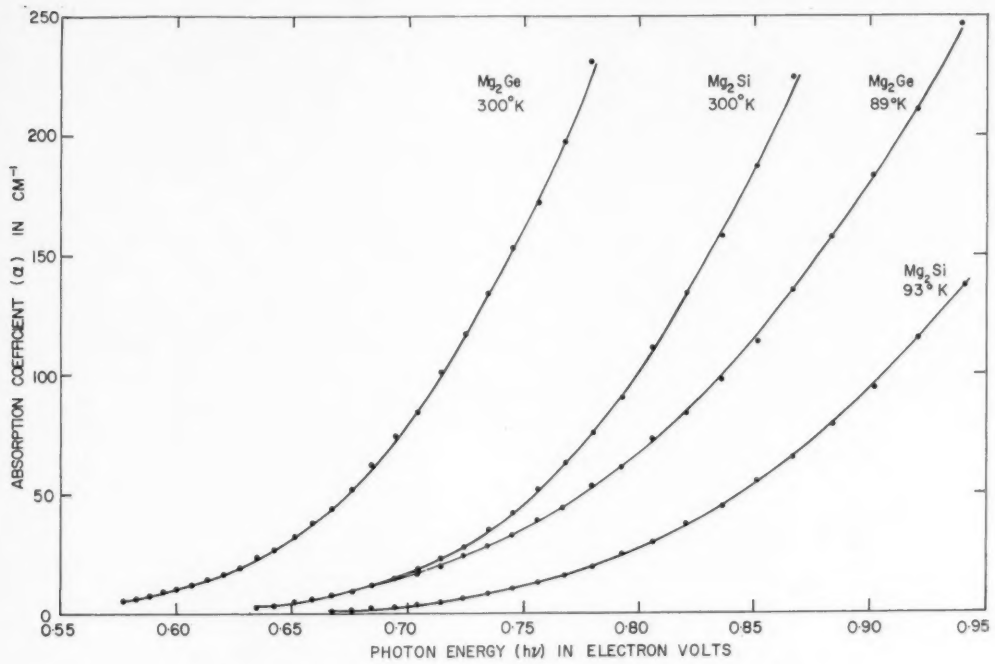

FIG. 3. Absorption edge of Mg_2Si and Mg_2Ge at 300° and 90°K.

2·5 to 3·5 for both compounds at all temperatures. The values of n obtained are sensitive to the choice of $h\nu_t$ but remain within the above limits for all reasonable values of $h\nu_t$. For direct transitions one expects n to be $\frac{1}{2}$ or $\frac{1}{3}$ while an n of 2 or 3 is expected for indirect transitions.[6]

It is difficult to associate a part of the absorption edge with the band gap. Our absorption coefficients in the beginning of the edge could be in error due to the imprecise knowledge of R and its unjustified extrapolation to shorter wavelengths. Better data for small absorption coefficients are needed before an analysis similar to that of MACFARLANE and ROBERTS[7] can be made. It is clear from Fig. 3 that the absorption edge at 90°K begins near the photon energies corresponding to the gaps at 0°K determined from electrical measurements by MORRIS *et al.*[2,3] 0·69 eV and 0·78 for Mg_2Ge and Mg_2Si, respectively.

The shift of the energy gap with temperature, $(\partial E_G/\partial T)_p$, is of interest in connection with the transport properties. One way to determine this shift is to use the displacement with temperature of a point on the edge having constant absorption coefficient.[8] This method is more reliable if the shift is the same for all values of α or if the absorption coefficient curves for various temperatures can be made to coincide by horizontal and vertical translations. The Mg_2Ge and Mg_2Si edges cannot be made to coincide by any such translations. If a value of $\alpha = 100\ \text{cm}^{-1}$ is chosen the resultant temperature shift of the corresponding point on the edge of each compound is linear between 90 and 370°K. The shifts are -5×10^{-4} eV/°K and $-6{\cdot}5\times10^{-4}$ eV/°K for Mg_2Si and Mg_2Ge respectively (see Fig. 4).

The broad absorption band at 0·40 eV in Mg_2Si appears to be due to indirect transitions from a conduction band minimum to a higher conduction band. Such transitions are believed to occur in n-type Si,[9] n-type GaAs,[10] and n-type AlSb.[11] This band appeared in all n-type Mg_2Si regardless of doping agent but not in a p-type sample doped with Cu. It appeared smaller in the sample of highest resistivity. The band shifts to higher energy as the sample is cooled, but the shifts vary from 0·012 eV (28B01) to 0·06 eV (23B01) for the interval from 370 to 84°K. Low temperature Hall

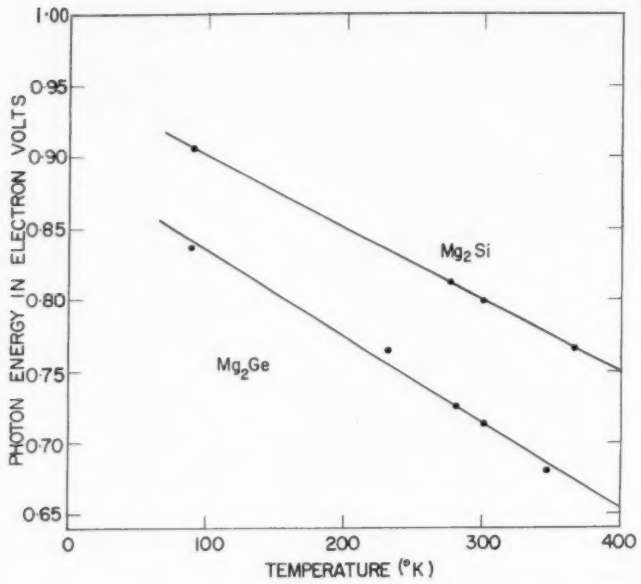

FIG. 4. Shift with temperature of the point on the absorption edge for which $\alpha = 100\ \text{cm}^{-1}$.

coefficients are not amenable to analysis for activation energies and do not seem to have the same general characteristics in the three samples.[2,12] Thus the shift of the 0·40 eV band upon cooling cannot be correlated yet with the capture of conduction electrons by donors.

The very small absorption maximum near 0·35 eV has not been positively identified. It may be caused by a trapping level whose absorption is masked at high temperatures by the increased width of the 0·40 eV absorption band.

Further work is being undertaken to obtain more reliable values of the absorption coefficient in the low energy part of the edge. Purer crystals are now available* and it is hoped that reflection coefficients can be measured. Photoconductivity measurements are also being undertaken to obtain information on the gap energy and the nature of the 0·40 eV peak in Mg_2Si.

* Room temperature resistivities of ~ 1 ohm cm for Mg_2Si and ~ 10 ohm cm for Mg_2Ge.[13]

REFERENCES

1. WINKLER U., *Helv. Phys. Acta* **28,** 633 (1955).
2. MORRIS R. G., REDIN R. D. and DANIELSON G. C., *Phys. Rev.* **109,** 1909 (1958).
3. REDIN R. D., MORRIS R. G. and DANIELSON G. C., *Phys. Rev.* **109,** 1916 (1958).
4. NELSON J. T., *Amer. J. Phys.* **23,** 390(A) (1959).
5. VALDES L. B., *Proc. Inst. Radio Engrs., N.Y.* **42,** 420 (1954).
6. HALL L. H., BARDEEN J. and BLATT F. J., *Photoconductivity Conference,* p. 146. John Wiley, New York (1956).
7. MACFARLANE G. C. and ROBERTS V., *Phys. Rev.* **97,** 1714 (1955).
8. FAN H. Y., SHEPHERD M. L. and SPITZER W., *Photoconductivity Conference,* p. 184. John Wiley, New York (1956).
9. SPITZER W. and FAN H. Y., *Phys. Rev.* **108,** 268 (1957).
10. SPITZER W. G. and WHELAN J. M., *Phys. Rev.* **114,** 59 (1959).
11. TURNER W. J. and REESE W. E., *Phys. Rev.* **117,** 1003 (1960).
12. MORRIS R. G., Thesis, Iowa State University (1958).
13. HELLER M. W., private communication.

J. Phys. Chem. Solids Pergamon Press 1961. Vol. 20, Nos. 1/2, pp. 127–133. Printed in Great Britain.

KNIGHT SHIFTS AND QUADRUPOLE EFFECTS IN Al ALLOYS*

M. B. WEBB

General Electric Research Laboratory, Schenectady, New York

(*Received* 16 *August* 1960)

Abstract—The Al^{27} nuclear resonance in AlZn and AlMg has been studied as a function of composition, temperature and applied magnetic field. At temperatures where the dipolar width is motionally narrowed but where the quadrupole splitting of the satellite lines is not, the second order quadrupole shift of the central transition is readily measureable. It is then possible to measure directly the average electric field gradient at the Al nuclei and the average Al Knight shift in the alloy. The measured gradients are essentially the same in AlMg and AlZn alloys consistent with the suggestion that the gradients arise from the electronic charge distribution about the solute and not from strain effects. The average gradients are of the order of 1×10^{23} cm^{-3}. The Al Knight shift in the alloys is equal to that in pure Al to within the experimental uncertainty. The results are compared with the previous experiments of ROWLAND and the theory of BLANDIN and FRIEDEL.

NUCLEAR resonance experiments are potentially useful for giving information about the electronic structure of alloys, since both the observable variations in the Knight shifts and effects of quadrupole interactions depend on the states of the conduction electrons.

The relatively large changes in the Knight shift with alloy composition have been the subject of several investigations[1,4] and it is generally found that the solvent shift is a linear function of the solute concentration through the whole terminal solid solution phase. This is particularly well established in AgCd and in the liquid alkali binary alloys and is at least nearly true in the other simple systems studied to date which contain no transition metal atoms. FRIEDEL and his coworkers[5] have suggested that these observations result from a long range damped, oscillatory component of the charge distribution surrounding the solute atoms in the alloy.

ROWLAND[6,7] and others[8,9] have investigated quadrupole effects in alloys of Al and of Cu. ROWLAND and BLOEMBERGEN find that in dilute Cu alloys the satellite (those transitions other than $m = 1/2 \rightarrow -1/2$) contributions to the resonance are broadened enough so that they do not contribute to the observed resonance and that the intensity of the remaining central transition ($m = 1/2 \rightarrow -1/2$) is proportional to $(1-c)^n$. This has been interpreted by assuming that, at the sites of the first n neighbors around an impurity atom the electric field gradient,† q, is great enough so that the central transition is broadened beyond observation and that at more distant sites q is so small that the resonance is unaffected. One may then assign limits to the possible values of q for which these conditions would be satisfied. From the correlation of n with the difference in valence ROWLAND concludes that the gradient arises from the charge distribution rather than from strain effects and that the gradient falls as the reciprocal of the third power of the distance from an impurity atom. In Al based alloys the satellite intensity is observed at small concentrations and it too falls as $(1-c)^n$. A similar explanation is invoked and limits to values of q are determined.

The oscillatory component of the charge distribution about a solute atom discussed by

* This research was supported by the Office of Naval Research.

† q is defined by $eq = \partial^2 v/\partial Z'^2 - \frac{1}{3}\nabla^2 v$ where the axis Z' is chosen in the direction of the maximum field gradient. Throughout the paper it is assumed that the field gradients in the alloys are axially symmetric.

FRIEDEL will produce field gradients at other nuclei. KOHN and VOSKO[10] and BLANDIN and FRIEDEL[11] have calculated these gradients and find semi-quantitative agreement with many of the experimental results.

This paper concerns n.m.r. experiments in AlZn and AlMg alloys at elevated temperatures where the equilibrium phase is a homogeneous solid solution and where the resonance lines are "motionally narrowed". From these experiments it is possible to measure directly both the r.m.s. value of the field gradients at the Al nuclei, by observing the second order quadrupole shift at the central transition, and the average value of the Al Knight shifts by extrapolating the results to infinite field where the quadrupole shift is absent. For these alloys there is a temperature range within which the dipolar contribution to the line width is narrowed but the first order quadrupole splitting of the satellite lines is not, so that small changes in the frequency of the central transition are readily measured.

EXPERIMENTAL

These experiments were done with a Varian 6 inch magnet and a Pound–Watkins spectrometer made by NUMR and considerably modified.[12] The oscillator frequency was measured with a Berkeley frequency meter. The furnace was contained in a brass can 4 in. long and 2 in. in diameter with copper cooling coils soldered on the outside and with fire brick liner. Pt wire furnace windings were wound on a mica insulated silver shield 3 in. long and 1 in. in diameter. A 3/8 in. o.d. ceramic tube passed axially through the furnace. The outer surface of the lower half of this tube was painted with heat resisting silver paint to form the outer conductor of the coaxial lead to the r.f. coil. The r.f. coil of Pyrex insulated Ag wire was wound in a slot machined on a ceramic tube. Even though the furnace was used several hundred degrees above the softening point of Pyrex the r.f. coil seldom shorted.

Samples were contained in thin walled Pyrex or quartz vials 1/2 in. long which were dropped into position in the ceramic tube. A plug in the top of the tube carried a Pt–PtRh thermocouple into the sample enclosure. The temperature calibration is made by comparing the e.m.f. of this thermocouple with that from a similar one embedded in a dummy sample. The temperature gradient over the sample was about 5° at the highest temperature and the temperatures were stable to ± 10°C during a day's operation.

In all cases, a sequence of resonances alternating between pure Al and the alloy was made during the day making it possible to recognize and correct for small drifts in the magnetic field. The final results are then averages of several such experiments. To improve the signal to noise ratio, the output of the spectrometer was integrated for 30 or 90 sec and ½ hr was generally used to traverse a given resonance. In all cases the resonances were symmetrical.* The zero of the derivatives was determined by tracing the recorded derivative curves, rotating the tracing by 180°, and shifting it along the frequency axis for the best fit with the original curve. Only differences in frequencies were important so errors due to the integration time were eliminated by measuring frequency relative to pure Al resonances taken under identical conditions. Because of small differences in the width of the Al and alloy resonances, this procedure was checked by scanning some resonances with both increasing and decreasing frequency. The applied field was modulated at 280 c/s with an amplitude which depended on the width of the resonance but which was always less than ¼ of the separation of extrema of the derivative curve and less than 1 gauss for the broadest resonances. The frequency difference between resonances in pure Al and in an alloy were uncertain by less than ± 50 c/s in the least favorable cases. The major contribution to the uncertainty in the frequency was due to the relatively poor signal to noise ratio, particularly at high temperatures.

The sample preparation was complicated by the fact that although the alloys are homogeneous solid solutions at the temperature of measurement they are two phase at room temperature. This of course required that, before filing the samples, any segregation of the two phases be on a scale small compared to the particle size of the powders needed for the resonance experiments. The samples were prepared from 99·99 per cent pure Al and commercially pure Zn and Mg. Ingots

* The AlMg data were taken at temperatures of 350°C and higher where the resonance lines had already begun to narrow and their shape was appreciably changed so that the asymmetry seen by ROWLAND was not observed.

were swagged, drawn into 30 mil wire, homogenized for 1 hr at 500°C and then quenched either into brine at −40°C or ice water. The wires were filed under liquid N_2 without having been warmed to room temperature. After drying the samples were sieved through 325 mesh screens and any iron particles removed with a magnet.

The powdered samples were sealed in thin wall quartz or Pyrex tubes under a rough vacuum. After extended use at higher temperatures there was visual evidence of a chemical reaction between the sample and the container walls. In the later experiments the inside walls of the vials were coated with aquadag which inhibited but did not completely stop the reaction. To insure that after extended use at high temperature the reaction had not proceeded far enough to alter the experimental results, the earliest experiments with each particular sample were repeated. The problem of the sample instability was more serious for the AlMg samples and it was difficult to obtain reliable data above about 450°C. It was possible to use AlZn samples even above the melting point for short times. The oxide layer formed during the preparation of the powders was sufficient to insulate the particles from one another and no serious sintering was encountered below 500°C.

RESULTS

The work consisted of observing the Al resonance in both AlZn and AlMg alloys as a function of concentration, applied magnetic field and temperature.

Motional narrowing

Resonances in pure Al and in several alloys containing from 2·5 to 12 per cent Zn were observed at temperatures between 200 and 500°C. In addition a few experiments were done at 700°C. Above 350°C the resonance lines narrowed and the line shape changed from Gaussian to nearly Lorentzian in the same way as has previously been reported by SPOKAS and SLICHTER for pure Al.[13] The "narrowing temperatures" defined in Ref. (13) were determined and found to be independent of Zn concentration and equal to 340 ± 10°C. This suggests that any effects of Zn on the self diffusion of Al are small.

Above about 450°C the width of the resonance in pure Al was nearly independent of temperature and equal to 760 ± 80 c/s measured between extrema of the recorded derivative curves. Field inhomogeneities, broadening due to the spin lattice relaxation, and the modulation amplitude account for roughly 500 c/s of this width leaving an unaccounted for contribution of ≈ 300 c/s in rough agreement with the observations of SPOKAS and SLICHTER.

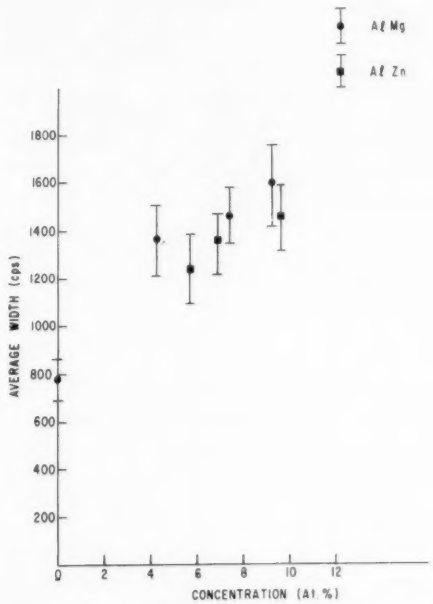

FIG. 1. Resonance line width measured between extrema of derivative curve for AlZn and AlMg alloys at 450°C. Error bars indicate mean deviation of several experiments.

Although there is considerable scatter in the data, the widths of the resonances in the alloys at 450° was several hundred c/s greater than in pure Al as shown in Fig. 1. Since, as is shown in the next paragraph, below 500° the entire observed resonance is due to the $1/2 \rightarrow -1/2$ transition, first order quadrupole broadening is not responsible for the additional width in the alloys. There was no apparent field dependence of this additional width, and for most concentrated alloys, the experimental accuracy is sufficient to eliminate possible 2nd order quadrupole effects as the major source of the broadening. At 700°C the extra

broadening had disappeared and the width was the same as in pure Al. More extensive investigation seems to be necessary to determine the source of the broadening.

Intensity

The relative intensities of the Al resonance in the alloys were measured at several temperatures with the aid of the calibration circuitry in the spectrometer. Because the shape of the resonance line was changing with temperature, the resonance curves were integrated over the whole frequency interval where there was an observable signal. For AlZn alloys at low temperatures the intensity as a function of concentration was just the same as that shown by ROWLAND[6]. The satellite contribution to the intensity disappears with addition of 3 or 4 at. per cent Zn and the intensity per Al nucleus is then constant to at least 12 at. per cent Zn and equal to that expected for the central transition. This dependence of intensity of concentration remains unchanged with increasing temperature to about 450°C. Above this temperature, the satellite intensity begins to reappear and at 700°C the intensity per nucleus is the same as in pure Al within the experimental error. Due to poor signal to noise ratio at the higher temperatures and the instability of the alloys, we have not determined the functional dependence of the intensity on temperature above 450°C.

It is reasonable to expect that the satellite intensity should reappear when the first order quadrupole shifts begin to be "motionally narrowed" or when

$$\tau\Delta\nu_q \approx 1$$

where τ is the average time a nucleus spends in a particular field gradient and $\Delta\nu_q$ is the mean absolute quadrupole shift of the satellite lines. In alloys as concentrated as those considered here, one or two lattice displacements will change the local environment of an atom appreciably so we may associate τ approximately with the jump time for diffusion. Using the Al diffusion data of SPOKAS and SLICHTER and an estimate of the average field gradient to be discussed later in this paper, this condition is satisfied at 425°C.

The data on AlMg samples are less extensive because phase boundaries limit available ranges of temperature and composition; however, it appears that the results are generally the same as for AlZn.

Frequency

From the results of the previous paragraph, it is concluded that the Al resonance in the alloys from $\approx$ 380°C to 450°C is motionally narrowed and is entirely due to the $m = 1/2 \rightarrow -1/2$ transition. In second order, the quadrupole interaction shifts the center of gravity of this central transition to lower frequencies by an amount[8]

$$\overline{\delta\nu} = -(8/15)Ah^{-1}$$

where

$$A = \left(\frac{9}{64}\right)\frac{2I+3}{4I^2(2I-1)} \times \frac{e^4Q^2q^2}{h\nu_0}$$

where all the symbols have their usual meaning, and where $I = 5/2$ and $Q = 0{\cdot}149 \times 10^{-24}$ cm^2 for Al^{27}. Then, if K and $K+\Delta K$ are the Knight shifts of the Al^{27} resonance in pure Al and in the alloy respectively, we may write

$$\frac{\nu_{\text{alloy}} - \nu_{\text{pure}}}{\nu_0} = \frac{\Delta\nu}{\nu_0} = \Delta K - \frac{C}{\nu_0^2}$$

where C is a constant.

Figure 2 shows $-\Delta\nu/\nu_0$ plotted vs. $1/\nu_0^2$ for several alloys at temperatures between 400 and 440°C and Table 1 gives values of $\langle\overline{q^2}\rangle^{1/2}$ calculated from the slopes of such plots. Each point is an average of from three to ten measurements and the error bars, for clarity shown only on a single curve, are a measure of the mean deviation of the several measurements. The uncertainty in the slope of the curves is surely less than 20 per cent and thus the uncertainty in $\langle\overline{q^2}\rangle^{1/2}$ less than 10 per cent.

The value of $\langle\overline{q^2}\rangle^{1/2}$ is independent of temperature within the experimental error below 450°C.

Table 1

Alloy	Composition (at. per cent)	$\langle\overline{q^2}\rangle^{1/2}$(cm^{-3})
AlZn	5·7	$1{\cdot}32 \times 10^{23}$
	6·9	$1{\cdot}43 \times 10^{23}$
	9·6	$1{\cdot}55 \times 10^{23}$
AlMg	5·0	$1{\cdot}13 \times 10^{23}$
	7·5	$1{\cdot}30 \times 10^{23}$
	11·0	$1{\cdot}75 \times 10^{23}$

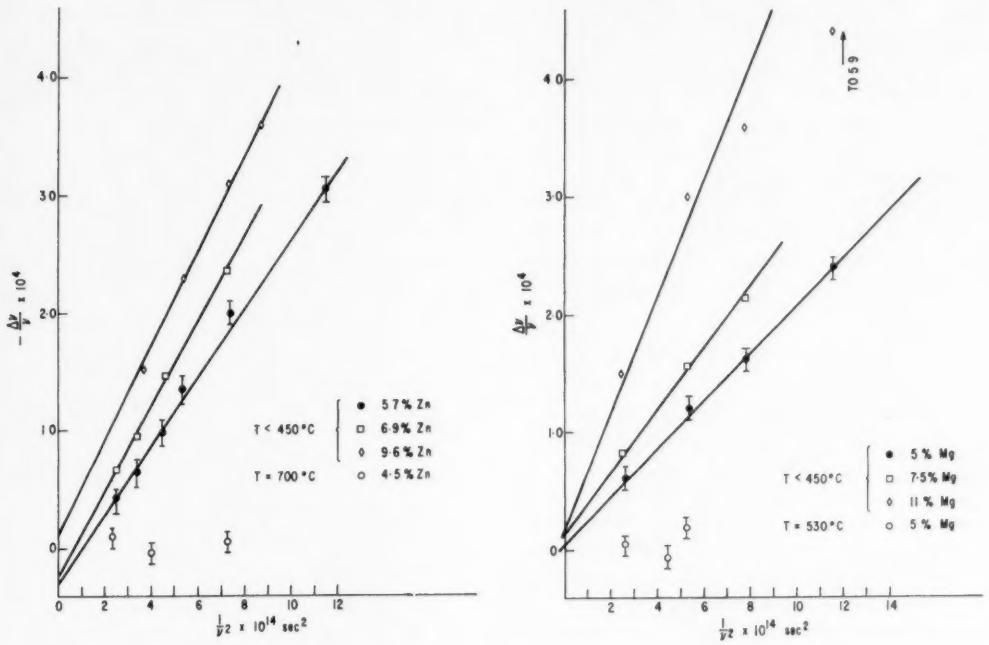

FIG. 2. $-\Delta\nu/\nu_0$ vs. $1/\nu_0^2$ where $\Delta\nu = \nu_{\text{alloy}} - \nu_{\text{pure}}$. (a) AlZn; (b) AlMg. Error bars, shown only for 5 per cent samples, indicate mean deviation of several experiments.

Above this temperature the apparent value of $\langle\overline{q^2}\rangle^{1/2}$ decreases becoming zero in the vicinity of 500°C. Thus the second order shift of the central transition disappears as the first order shift of the satellite components is motionally narrowed as might be expected. Included in Fig. 2 are some data at higher temperatures for the 5 per cent alloys. Between 450 and 500°C there is considerably more scatter in the experimental data presumably because the decrease of $\langle\overline{q^2}\rangle^{1/2}$ with temperature is rather abrupt and the temperature control in these experiments was relatively poor. It again was not possible to obtain reliably the temperature dependence of $\langle\overline{q^2}\rangle^{1/2}$ in this region.

The Al Knight shift in the alloys can be obtained from either the intercept of curves in Fig. 2 or from the frequency of the resonances at the higher temperature where quadrupole effects have disappeared. From the data given in Fig. 2 it seems that an upper limit of $\Delta\nu/\nu_0$ at infinite ν_0 for any of the alloys is 2×10^{-5} which is $\approx 1{\cdot}2$ per cent of the pure Al Knight shift. If one assumes that the Knight shift is a linear function of concentration, it follows that

$$\left|\frac{1}{c}\times\frac{\Delta K}{K}\right| < 0{\cdot}1$$

for AlMg and AlZn alloys.

DISCUSSION

It had earlier been widely thought that the electric field gradients in alloys were produced by the strains in the lattice surrounding the impurity atom. The present result indicates that this is not so since the strain associated with a Mg atom in the Al lattice is roughly four times that associated with a Zn atom and yet $\langle\overline{q^2}\rangle^{1/2}$ is essentially the same for the two systems.

This suggested that perturbations of the electronic charge density about the impurity are responsible for the observed gradients, even though it is easily shown that the Thomas–Fermi

screening of the impurity is not sufficient to account for the results. These conclusions are in agreement with the recent results for Cu alloys of CHAPMAN and SEYMOUR[9] and of ROWLAND[7] who also showed that the quadrupole effects are well correlated with the valence difference between the solvent and solute atoms.

The present experiments give a measure of q^2 averaged over all the Al^{27} nuclei in the sample and so it is necessary to compute this average from any theory which is to be compared with the experiments. We may write

$$\overline{q^2} = \sum_m q_m^2 P_m \qquad (1)$$

where q_m's are the various values of q which may occur each with probability P_m. Since the electric field gradient at a site due to an impurity atom in the vicinity decreases very rapidly with the distance from the impurity, we shall ignore all contributions to q from impurities other than the nearest and shall also assume that the gradient at a site equidistant from two or more impurities is equal to that due to one of them alone. These assumptions are the same as those CHAPMAN and SEYMOUR[9] used in computing the resonance line shapes in CuNi alloys and are reasonable approximations for the small concentrations. ROWLAND[6] has made further assumptions to account for some of the more complex configurations, but these refinements do not seem warranted here.

The probability, P_m, that the solute atom or atoms nearest the site in question will be in the m^{th} shell is given by

$$P_m = (1-c)^{N_{m-1}} - (1-c)^{N_m} \qquad (2)$$

where c is the atomic fraction of solute and N_m is the number of atoms in the first m shells.

Both the experimental work of ROWLAND[6] on Cu alloys and the calculations of FRIEDEL[11] and of KOHN and VOSKO[10] indicate that q falls roughly as $1/r^3$ where r is the distance from a solute atom. In Fig. 3 the solid line shows $\langle\overline{q^2}\rangle^{1/2}$ as a function of concentration calculated from equations (1) and (2) assuming that $q_m = b/r_m^3$ where b has been chosen so that $\langle\overline{q^2}\rangle^{1/2} = 1{\cdot}2\times10^{23}\,\text{cm}^{-3}$ at $c = 0{\cdot}05$. This would give a value q at the site of a nearest neighbor of a solute atom of $1{\cdot}7\times10^{23}\,\text{cm}^{-3}$.

Thus gradients determined in this work are about 50 per cent larger than those suggested by ROWLAND from intensity measurements in the same alloys. For AlZn, again assuming that $q \propto 1/r^3$, he obtains $q_1 \approx 1{\cdot}1\times10^{23}\,\text{cm}^3$ and he further suggests that if $q_1 \geqq 1{\cdot}2\times10^{-3}\,\text{cm}^3$ the second order quadrupole broadening of the central transition would be observable. He also finds that the gradients are somewhat larger in

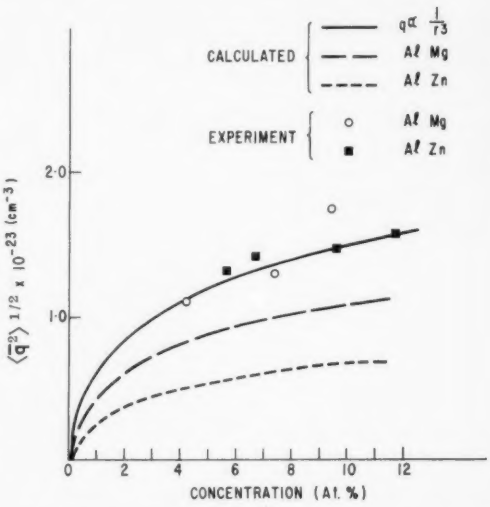

FIG. 3. Data points are experimental values of $\langle\overline{q^2}\rangle^{1/2}$. Solid curve is that calculated for $\langle\overline{q^2}\rangle^{1/2}$ from assuming that $q_m = b/r_m^3$ with b chosen so that $\langle\overline{q^2}\rangle^{1/2} = 1{\cdot}2\times10^{23}\,\text{cm}^{-3}$ at $c = 0{\cdot}05$. Dashed curves are for $\langle\overline{q^2}\rangle^{1/2}$ calculated from results of BLANDIN and FRIEDEL.

AlMg than in AlZn alloys, since the central transition is somewhat asymmetrically broadened and since in the expressions for the intensity

$$I = (1-c)^n$$

n equals 98 and 130 in the zinc and magnesium alloys respectively. This implies that q is the order of 20 per cent greater in AlMg. It is not clear if these discrepancies are real since the gradient is almost certainly not strictly proportional to $1/r^3$, and since the gradient at the nearest neighbors will depend strongly on small displacements of atoms around the impurity. Certainly the present work shows that the second order effects on the $m = 1/2 \rightarrow -1/2$ transition are appreciable although not readily observed in the rigid lattice.

It should be emphasized that measurements of the satellite intensity are sensitive to the gradients at large distances from the impurity (the 6th and 7th shells in AlZn and AlMg) while the present measurements weigh the gradients due to nearer neighbors more heavily. In spite of these possible small discrepancies, it is felt that there is good agreement between the present experiments and the gradients inferred from intensity measurements where the interpretation is perhaps less straightforward.

FRIEDEL and BLANDIN[11], considering the oscillating component of the electronic charge density about an impurity atom, have calculated the value of q at many lattice sites in the vicinity of solute atoms in AlMg and AlZn alloys. In this calculation, q depends on δ_l^F, the phase shifts of electrons as the Fermi surface scattered by the impurity atom, and a factor μ which depends on band structure of the host metal. They have used only $l = 0$ and $l = 1$ phase shifts chosen to satisfy the Friedel sum rule and to give the experimentally determined residual resistivity of the alloys. The sum rule was modified to take account of the size of the solute atom as done by HARRISON[14] and BLATT[15]. The factor μ was chosen to give agreement with ROWLAND's results.

$\langle \overline{q^2} \rangle^{1/2}$ calculated from equations (1) and (2) using the q_m's of BLANDIN and FRIEDEL are shown in Fig. 3. Again there is semi-quantitative agreement with the experimental results; however, the relative difference between the $\langle \overline{q^2} \rangle^{1/2}$'s for AlZn and AlMg predicted by the calculation is somewhat too large to be consistent with the experimental results and their estimated uncertainty.

An apparently more serious disagreement between the present work and these calculations is found in the Al Knight shifts. The proposed oscillating charge distribution about an impurity atom would change the average solvent Knight shift. We have computed the parameter $1/c \times \Delta K/K$ for the alloys from the results of Refs. (5) and (11) using the phase shifts from Ref. (11) with the result that $1/c \times \Delta K/K = -0{\cdot}29$ for AlZn and $-0{\cdot}43$ for AlMg which are to be compared to the experimental result that $|1/c \times \Delta K/K| < 0{\cdot}1$. For the 9 per cent alloys at high temperatures where the quadrupole shift is not present this calculated result would imply a frequency shift of more than 300 c/s at the highest fields used in these experiments and such a shift would certainly have been detected. Thus we conclude that, although the proposed charge distribution in alloys may give rise in many cases to field gradients and Knight shift changes of the order of magnitude of those observed, the calculations of the effects are not in quantitative agreement with experiment.

Acknowledgement—We gratefully acknowledge the assistance of R. J. WOLFF who assisted with these measurements.

REFERENCES

1. RIMAI L. and BLOEMBERGEN N., *Bull. Amer. Phys. Soc.* (ser. 2) **4,** 166 (1959).
2. DRAIN L. E., *Phil. Mag.* **4,** 484 (1959).
3. ROWLAND T. J., unpublished work.
4. WEBB M. B. and ORIANI R. A., to be published.
5. BLANDIN A. and DANIEL E., *J. Phys. Chem. Solids* **10,** 129 (1954); BLANDIN A., DANIEL E. and FRIEDEL J., *Phil. Mag.* **4,** 180 (1959).
6. ROWLAND T. J., *Acta. Met.* **3,** 74 (1955).
7. ROWLAND T. J., *Phys. Rev.* **119,** 900 (1960).
8. BLOEMBERGEN N. and ROWLAND T. J., *Acta. Met.* **1,** 731 (1953).
9. CHAPMAN A. C. and SEYMOUR E. F. W., *Proc. Phys. Soc. Lond.* **72,** 797 (1958).
10. KOHN W. and VOSKO S. H., *Phys. Rev.* **119,** 912 (1960).
11. FRIEDEL J. and BLANDIN A., to be published.
12. SILVER A. H., Ph.D. Thesis, Rensselaer Polytechnic Institute, 1958 (unpublished).
13. SPOKAS J. J. and SLICHTER C. P., *Phys. Rev.* **113,** 1462 (1959).
14. HARRISON W. A., *Phys. Rev.* **110,** 14 (1958).
15. BLATT F. J., *Phys. Rev.* **108,** 295 (1957).

ol. 20
1961

J. Phys. Chem. Solids Pergamon Press 1961. Vol. 20, Nos. 1/2, pp. 134–137. Printed in Great Britain.

THE PROBLEM OF EXCITON INDUCED PHOTOEMISSION FROM CdS

W. E. SPICER

RCA Laboratories, Princeton, N. J.

(*Received* 1 *February* 1961)

Abstract—SHUBA has found the velocity distribution of photoelectrons from CdS to be almost independent of photon energy. He assumes that this indicates that the photoemission is due to the ionization of defect levels by excitons. It is shown here that both the velocity and spectral distributions found by SHUBA can be explained by the assumption of an exponential distribution of states from which the photoelectrons are directly excited by the photons. It is concluded that a velocity distribution which is insensitive to photon energy is, in itself, not sufficient evidence for exciton induced photoemission.

I. INTRODUCTION

SHUBA[1] has observed photoemission from evaporated layers of CdS in the photon energy range 5·0–6·5 eV. He believes that this emission is due to the ionization of defect levels by excitons.*[2] For the model of SHUBA to hold, it would be necessary for the excitons involved to have the following, rather unexpected, properties:

(1) Exciton formation must be probable for photons with energies of over twice the band gap.

(2) Between 5·0 and 6·5 eV, there must be no appreciable structure in the exciton absorption.

(3) Irrespective of the energy of the exciting photon, all of the excitons must relax to a state of common energy before interacting with the defect levels. In this metastable state, the exciton must have an energy about one eV greater than the band gap energy.

(4) The probability for formation of an exciton which will produce an external electron through the ionization of a defect level must increase by 10^4 as the photon energy is increased from 5·0 to 6·5 eV.

Since the existence of excitons possessing these properties would be very important,† it is appropriate to see if there is an alternative explanation for the experimental results of SHUBA.

The evidence for exciton induced photoemission from CdS lies principally in the lack of dependence of the photoelectric velocity distribution on photon energy (see Fig. 1). SHUBA also found that the photoemission increased when the number of electrons in defect levels was increased. Both of these phenomena are characteristic of exciton induced photoemission.[2] However, it is our purpose to show here that there is an alternative explanation. This is based on the fact that the quantum yield from CdS increases quite rapidly with increasing photon energy (see Fig. 2). In such a case, it is likely that the number of slow electrons which are added to the velocity distribution by an increase in photon energy will be large compared to the number of electrons with increased energy. As a result, the slow electrons will dominate the velocity distribution causing it to be relatively insensitive to the energy of exciting

* By "defect" level we mean any energy level introduced into a semiconductor by an imperfection.

† This work of SHUBA has been used to support the position of LASKAREV who believes that excitons play a large part in photoconductivity. See: LASKAREV V. E. *et al.*, *Bull. Acad. Sci., Phys. Ser.* **16,** 81 (1952); LASKAREV V. E., *Abstracts International Conference on Semiconductor Physics*, p. 72 (1960); SHEINKMAN M. K., *Soviet Phys.—Solid State* **2,** 1046 (1960).

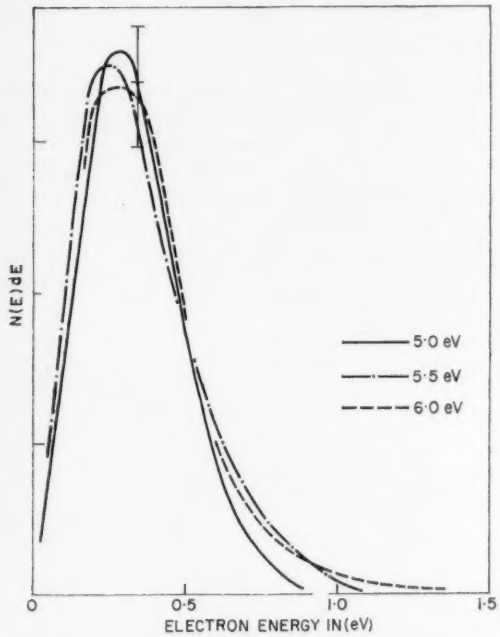

FIG. 1. The velocity distributions obtained by SHUBA (Ref. 1) from CdS.

photons. This will be developed quantitatively below.

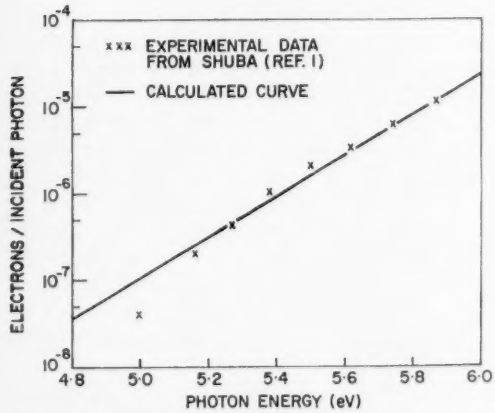

FIG. 2. The spectral distribution of photoemission from CdS. The data points are from SHUBA (Ref. 1). The solid line represents the calculated curve. This has been fitted vertically.

II. A MODEL FOR THE PHOTOEMISSION FROM CdS

There is no definitive theory of photoemission from semiconductors. However, there are certain generalizations which seem to hold.[3,4] It is our purpose here to propose a model for the photoemission from CdS which is consistent with these generalizations.

As is shown in Fig. 2, the most striking fact about the spectral distribution of the yield from CdS found by SHUBA[1] is its strong dependence on photon energy. The yield increases by almost a

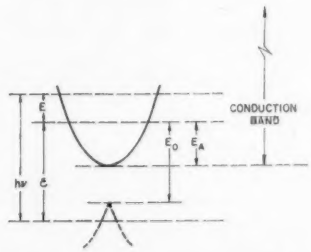

FIG. 3. Schematic of band structure used in this calculation. E_a is the electron affinity. All energies less than the vacuum level are measured with respect to the vacuum level and are designated by ϵ. All energies greater than the vacuum level are designated by E. All energies have been taken as positive numbers. The term "occupied states" is used to cover both filled valence band states and filled states due to defects.

factor of 10^4 as the photon energy increases from 5·0 to 6·5 eV. The dependence on photon energy is almost exponential. Any model of photoemission from this material must take this into account. Since there is usually a direct connection between the spectral distribution of photoemission and the probability for optical transitions into states above the vacuum level,[3] we will assume that the probability of exciting an electron from the states located at an energy ϵ below the vacuum level into a state above the vacuum level (see Fig. 3) is given by:*

$$P(\epsilon) = A \exp(\beta\epsilon) \quad \text{if } h\nu \geq \epsilon \qquad (1)$$

$$P(\epsilon) = 0 \qquad \text{if } h\nu < \epsilon \qquad (2)$$

* Evidence has been found for an exponential distribution of states in CdS (see ROSE A., *RCA Review* **12,** 362 (1951); ROSE A., *L'Onde Electrique* **34,** 645 (1954); NIEKISCH E. A., *Ann. Phys., Paris* **15,** 279 (1955); DEVORE H., *RCA Review* **20,** 79 (1959).

Here, A and β are constants.* If we assume that there are no filled states above an energy ϵ_0, this will place the additional condition:

$$P(\epsilon) = 0 \qquad \text{if } \epsilon < \epsilon_0 \tag{3}$$

on equation (1).

Up to this point, we have considered only the excitation process; it is also necessary to consider the energy of the photoelectrons and their escape probability. If we assume that the electrons which escape lose a negligible amount of energy before escaping,† the kinetic energy, E, of an external photoelectron excited from a state of energy, ϵ, by a photon of energy, $h\nu$, will be given by:

$$E(h\nu, \epsilon) = h\nu - \epsilon \tag{4}$$

However, for an electron to escape, it is not sufficient that its kinetic energy be greater than the surface barrier, i.e. the electron affinity; but the kinetic energy associated with the component of velocity directed perpendicular to the surface must be greater than the electron affinity.[3] Assuming an isotropic velocity distribution of excited electrons and that an electron strikes the surface only once with sufficient energy to escape,[3] it can be shown that the escape probability of electrons which approach the surface with kinetic energy $E+E_a$ (see Fig. 3) is:

$$F(E) = \frac{1}{2\pi} \arccos\left(\frac{E_a}{E_a+E}\right)^{1/2} \tag{5}$$

Although equation (5) is a reasonable expression for the escape probability, it should be emphasized that our results do not depend on the particular form taken for equation (5). Provided that the expression for the escape probability is a smooth function which goes to zero as E goes to zero, the results will not be affected in an essential manner by its choice.

III. CALCULATED VELOCITY AND SPECTRAL DISTRIBUTION CURVES

The velocity distribution for photon energy $h\nu$ is given by the probability of an electron being emitted with energy E by a photon of the energy $h\nu$. Using the approximations given above, this is just the product of the probability for exciting an electron into a state of energy E [see equations (1) and (4)] multiplied by the probability of escape for an electron with energy E equation (5). Thus the velocity distribution, $n(E, h\nu)$, is given by:

$$n(E, h\nu) = \frac{A}{2\pi} \exp[\beta(h\nu)] \exp(-\beta E) \times \arccos\left(\frac{E_a}{E+E_a}\right)^{1/2} \quad \text{for } h\nu - \epsilon_0 \geqslant E \geqslant 0. \tag{6}$$

$n(E, h\nu)$ is zero if E does not fall within the indicated limits. The limits follow from those given in equations (2) and (3). Since only the normalized velocity distribution curves are of interest, it is clear that the significant photon energy dependence of the velocity distribution is in the maximum energy given by the condition $E \leqslant h\nu - \epsilon_0$. The term $\exp[\beta(h\nu)]$ affects the magnitude of $n(E, h\nu)$ but not the shape of the $n(E, h\nu)$ curve.

To calculate specific velocity and spectral distribution curves, it is necessary to assume values for β, E_a, and ϵ_0. Since the best straight line which can be fitted to a semilogarithmic plot of the spectral distribution curve of SHUBA[1] has a slope of 5·3/eV, this value was chosen for β. (This gives a variation in the density of states of less than a thousand from the middle of the forbidden band to the valence band edge.) ϵ_0 and the work function should coincide since it is most probable that no filled states occur above ϵ_0 because the Fermi level lies at ϵ_0. Although SHUBA does not give any precise values for the work functions of his CdS layers, he does state that the work function of the majority of the layers did not exceed 4·1 eV. Since, presumably, 4·1 eV was close to the median work function, this was used for ϵ_0. A variation of a few tenths of a volt in the value used for ϵ_0 would not significantly change the results. The calculation is even less sensitive to E_a. 2·9 eV was chosen

* It should be noted that no detailed assumption is being made about the nature of the levels from which the photoelectrons originate. These may be associated with individual defects, defect bands, and/or a valence band which has been smeared out due to crystal imperfections. It should also be pointed out that the exponential absorption probability given by equation (1) is only a first approximation. Any real distribution of states could be expected to be more complicated.

† If the energy loss by an electron were assumed to be independent of the original energy of the electron, this calculation would be essentially unaffected.

Vol. 2
1961

for this parameter. Such a choice is based on the assumption that the Fermi level lies near the center of the forbidden band.

To obtain an expression for the spectral distribution of quantum yield, it is necessary to integrate equation (6) between the limits of $E = 0$ and $E = h\nu - \epsilon_0$. This has been accomplished with the use of a computer. A typical curve is included in Fig. 2. Since there is no way of evaluating the constant A in equation (6), the curve has been fitted vertically to SHUBA's data. The slope of the calculated curve is equal to β. Identical values were used for the parameters ϵ_0, E_a, and β as in calculating the velocity distribution curve (Fig. 4). The fit between SHUBA's data and the calculated curve is reasonable considering the rough assumptions used in the model.

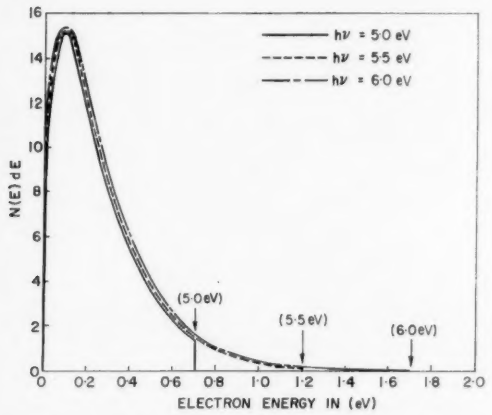

FIG. 4. The calculated velocity distributions for CdS. The arrows indicate the energies at which the velocity distributions become zero for the indicated values of photon energy.

IV. THE EFFECT OF BIASING RADIATION AND OF DOPING

SHUBA found that the photoemission near the threshold of response could be markedly increased by illuminating the CdS sample with photons of energy between that of the band gap and the threshold for photoemission.* Since this radiation could increase the number of electrons in higher lying defect levels, SHUBA felt that this result was confirmation of his exciton model. However, the effect can also be explained by the model suggested here. If the emission were due to direct excitation from defect levels, an increase in the population of higher lying levels would certainly greatly increase the photoemission in the threshold region.

The actual situation is probably more complicated than that suggested above. SHUBA observed that the apparent work function was decreased by the biasing light. This suggests a bending of the bands downward. Such a bending would lead to an enhanced emission in the threshold region.[3,5] The increase observed is probably due to both the effect of the filling of higher lying states and of band bending.

The increase of photoemission obtained by SHUBA when additional donors (Cu or excess Cd) were added to the CdS layers can be explained either on the basis of the exciton model or on the basis of the model presented here.

V. CONCLUSIONS

By means of a simple model, it has been shown that the principal features of the experimental data obtained by SHUBA[1] from CdS can be explained without assuming exciton induced photoemission.[2] The theory of photoemission is not so well founded that this can be taken as definitive proof for the absence of exciton induced photoemission in CdS; however, it does show that for CdS as well as for other materials a velocity distribution which is insensitive to photon energy is not *sufficient* evidence for exciton induced photoemission.

Acknowledgement—The useful suggestions of M. LAMPERT, R. PARMENTER, and other members of the staff of RCA Laboratories are gratefully acknowledged.

* Such radiation will be termed "biasing radiation".

REFERENCES

1. SHUBA Iu. A., *Soviet Phys. Tech. Phys.* **1,** 1104 (1956).
2. APKER L. and TAFT E. A., *Phys. Rev.* **79,** 964 (1950); **81,** 698 (1951); **82,** 814 (1951); PHILIPP H. R. and TAFT E. A., *Phys. Rev.* **106,** 671 (1957).
3. SPICER W. E., *J. Appl. Phys.* **31,** 2077 (1960).
4. TAFT E. A., PHILIPP H. R. and APKER L., *Phys. Rev.* **110,** 876 (1958).
5. SPICER W. E., *RCA Review* **19,** 555 (1958).

J. Phys. Chem. Solids Pergamon Press 1961. Vol. 20, Nos. 1/2, pp. 138–145. Printed in Great Britain.

DIE EINWIRKUNG ENERGIEREICHER IONEN AUF METALLOBERFLÄCHEN

M. BALARIN und F. HILBERT

Zentralinstitut für Kernphysik Rossendorf bei Dresden, Bereich Werkstoffe und Festkörper, Deutsche Demokratische Republik

(*Received* 2 *January* 1961)

Abstract—The investigation of a metallic surface, strongly sputtered with high-energy ions, shows that the sputtering of atoms can be understood only by a collision mechanism, but not by means of evaporation theory. It has been proposed for an approximate mathematical treatment, that the maximum impulse, transfered to an atom, moving parallel to the surface as a result of a single collision process, is a measure of the probability for the ejection of atoms out of the lattice. In accordance with the experiment the existence of an angle of incidence between 45° and 90° for the greatest sputtering yield can be shown. The samples have been investigated by light and electron microscopy. The furrows on the Cu-surface due to the bombardment with a monoenergetic, obliquely incident, parallel ion beam, show that the lattice ions have been ejected preferentially in the forward direction. An attempt is made to find a relation between the observed clods and furrows and the close-packed lattice planes.

Zusammenfassung—Die Untersuchung einer durch Ionenbeschuss stark geätzten Metalloberfläche ergibt bei Berücksichtigung der Beschussbedingungen eindeutig, dass die Abtragung von Atomen nur vermittels eines Stossmechanismus erklärt werden kann und nicht mit Hilfe der Verdampfungstheorie. Für eine überschlägige mathematische Behandlung wird der bei einem Stossprozess an ein Atom parallel zur Oberfläche maximal übertragene Impuls als Bezugsgrösse der Wahrscheinlichkeit für das Herausschlagen von Atomen aus dem Gitterverband angesetzt. Es kann dann in Übereinstimmung mit dem Experiment gezeigt werden, dass es einen Einfallwinkel zwischen 45° und 90° gibt, bei dem die grösste Abtragungsdichte erreicht wird. Licht- und elektronenmikroskopische Aufnahmen einer mit einem monoenergetischen, schräg einfallenden parallelen Ionenstrahl beschossenen Cu-Oberfläche zeigen durch die gebildeten Furchen, dass die Atome vorzugsweise in Vorwärtsrichtung abgetragen wurden. Es wird versucht, die beobachteten Schollen und Furchen mit den dichtestgepackten Gitterebenen in Beziehung zu bringen.

Vol. 20
1961

Der bei Ionenbeschuss im Vakuum an Festkörperoberflächen auftretende Abtragungseffekt ist hauptsächlich auf die Impulsübertragung an einzelne Atome des Metallgitters dieser Proben zurückzuführen, die danach aus dem Gitterverband herausfliegen können. Das lässt sich anhand von Aufnahmen einer beschossenen Metalloberfläche zeigen, deren typisches Aussehen bei den vorliegenden Versuchsbedingungen keinesfalls als Folge einer örtlichen Temperaturerhöhung und daraus resultierenden Verdampfung gedeutet werden kann.* In der vorliegenden Arbeit wird versucht, einen Beitrag zur mathematisch-physikalischen und zur experimentellen Klärung des aufgetretenen richtungsabhängigen Effektes bei der Abtragung zu geben.

1. DER PARALLEL ZUR OBERFLÄCHE ÜBERTRAGENE IMPULS

Experimentell wurde bereits mehrfach eine Abhängigkeit der Zerstäubungsrate vom Einfallwinkel festgestellt.[1–5] Gewöhnlich liegen die verwendeten Ionenenergien im Bereich von etwa 100 eV bis zu 50 keV. Alle Stösse zwischen den eingeschossenen Ionen und einzelnen Gitteratomen (Primärstösse) sowie Stösse zwischen den dabei aus ihren normalen Gitterlagen herausgeschlagenen Atomen (Primärteilchen) mit

* Eine Übersicht über die Verdampfung als Mechanismus beim kathodischen Ätzen findet man bei Massey H. S. W. und Burhop E. H. S., *Electronic and Ionic Impact Phenomena.* Oxford University Press (1956).

weiteren Gitteratomen (Sekundärstösse) können als Stösse zwischen harten Kugeln (hard-sphere-collision) behandelt werden.[6–9] Die sphärische Symmetrie der in Wechselwirkung tretenden Teilchen kann man als bestätigt ansehen.[10] Ausserdem kann angenommen werden, dass die einfallenden Teilchen in einer oberflächennahen Schicht vollständig abgebremst werden und dass die freie Weglänge aller Teilchen, d.h. auch der Stossprodukte, mit ihrer kinetischen Energie monoton abnimmt.[11–13] Alle einfallenden Ionen sollen die gleiche Richtung und gleiche Energie besitzen. Der Einfachheit halber wollen wir bei der theoretischen Behandlung ausschliesslich Teilchen gleicher Masse betrachten. (Beim Stoss von Teilchen ungleicher Masse verringert sich bekanntlich die maximal übertragbare Energie entsprechend einem vom Massenverhältnis bestimmten Faktor. Das ist aber nicht von prinzipiellen Einfluss auf das Ergebnis der nachfolgenden Betrachtungen.)

Um etwas über die Wirkung aussagen zu können, die das Ionenbombardement auf die Oberfläche ausübt, benötigen wir einen Massstab für die abtragende Wirkung. Von vornherein sind bei den Primärstössen keine Beschränkungen für die übertragene Energie E' zwischen Null und E_0 auferlegt (E_0 = Energie des einfallenden Ions). Diese Primärstösse erfolgen nach dem statistischen Stossgesetz :

$$g(E_0; E')\,dE' = \begin{cases} \dfrac{1}{E_0}\,dE'; & E' \leqslant E_0 \\ 0; & E' > E_0 \end{cases} \qquad (1)$$

Die Abtragung von Atomen kann über mehrere Mechanismen erfolgen. Ihre Beziehung zur realen mikroskopischen Oberfläche wird in Abschnitt 3 behandelt. Als einen Grenzfall zwischen Teilchen, die den Gitterverband ohne weitere Stösse und solchen, die den Kristall nicht direkt verlassen können, kann man die Atome ansehen, die sich im Ergebnis eines Stosses parallel zur Oberfläche bewegen. Unter diesen besitzen diejenigen, die sich gleichzeitig in der Einfallsebene weiterbewegen, den grössten Impuls, der als Bezugsgrösse der Wahrscheinlichkeit q für das Herausschlagen von Atomen aus der Oberfläche dienen soll. Das bedeutet bei der in Fig. 1 angegebenen Wahl des Einfallwinkels

$$q = c \cdot v_{\sigma_{max}}; \quad v_{\sigma_{max}} = v_0 \cdot \sin\beta \qquad (2)$$

Der aus Fig. 1 ersichtliche Vorgang entspricht einem von WEHNER[1] durchgeführten Versuch, bei dem polykristalline Metallkugeln mit Ionen beschossen wurden. Dabei bildeten sich gewisse quasistationäre Flächen heraus, deren Normale

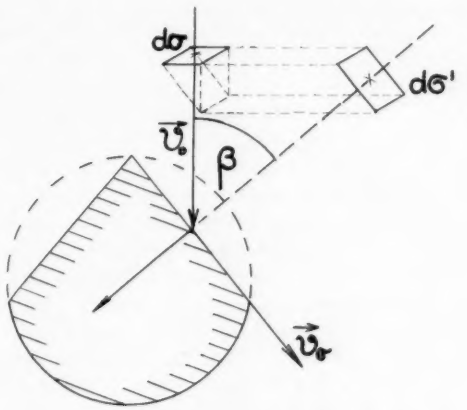

ABB. 1. Abtragungsschema nach WEHNER[1]. $\boldsymbol{v}_0$ = Impuls des einfallenden Ions; $\boldsymbol{v}_\sigma$ = Impuls des Sekundärteilchens parallel zur Kristalloberfläche; β = Einfallwinkel; $d\sigma$, $d\sigma'$ = Flächenelemente.

mit der Ionenstrahlrichtung den Winkel β einschloss. Um die Abtragung an verschiedenen Stellen der Oberfläche vergleichen zu können, muss ausser der Wahrscheinlichkeit q noch berücksichtigt werden, dass die Anzahl der abgetragenen Atome der Anzahl N der einfallenden Teilchen pro Flächenelement $d\sigma$ proportional ist. Dabei wollen wir nicht die absolute Abtragungsrate betrachten, sondern nur den winkelabhängigen Anteil S, der angibt, welcher Teil des Ausgangsimpulses v_0 für die Abtragung unter Berücksichtigung der eingeschossenen Teilchendichte wirksam wird :

$$S = \frac{v_{\sigma_{max}} \cdot \dfrac{dN}{d\sigma'}}{v_0 \cdot \dfrac{dN}{d\sigma}} = \sin\beta \cdot \cos\beta \qquad (3)$$

Hierbei setzen wir für unsere Überlegungen voraus: $\beta \gg 0$.

Die herausfliegenden Teilchen entstehen jedoch nicht nur bei Primärstössen und auch nicht nur direkt an der Oberfläche, und unter diesen Teilchen befinden sich sowohl reflektierte als auch neu ausgelagerte Atome. Aufeinanderfolgende Sekundärstösse sind wegen der symmetrisch-periodischen Anordnung der Gitteratome nicht mehr voneinander unabhängig ; es können daher u.a. auch "fokussierende" und "crowd-ion"-Stösse auftreten.[14–16] An Einkristallen wurde schon mehrfach beobachtet, dass die abgetragenen Atome bevorzugt in Richtungen fliegen, die als Verlängerung kristallographischer Gitterreihen aufgefasst werden können. Dies kann man jetzt nachträglich als das Ergebnis korrelativer Stossprozesse verstehen. Daraus kann man weiter schlussfolgern, dass der Ursprung der zu Grunde liegenden Stossketten mehrere Atomabstände unter der Oberfläche liegen muss. Da die Rechnung nur als Schema gedacht ist, setzen wir näherungsweise für die Aufsplitterung des Impulses bei einem zweiten Stoss bzw. einem Sekundärstoss den gleichen Winkel β ein, da die wirklich auftretenden Winkel schwer zu erfassen sind. Das gestattet die Durchführung einer wesentlich vereinfachten Rechnung. Wichtig ist lediglich, dass ein in ähnlicher Weise winkelabhängiger, verkleinernder Faktor hinzutritt. Nach diesem zweiten Stoss ist dann der winkelabhängige wirksame Impulsanteil multipliziert mit der Teilchendichte

$$S^{(2)} = \sin^2\beta \cdot \cos\beta \tag{4}$$

bzw. für den n-ten Stoss

$$S^{(n)} = \sin^n\beta \cdot \cos\beta \tag{5}$$

An der resultierenden Abtragung werden alle diese Stossprozesse mit einem bestimmten Prozentsatz α_n beteiligt sein, sodass wir erhalten :

$$S = \sum_{n=1}^{n'} \alpha_n \sin^n\beta \cdot \cos\beta;\ (\alpha_n \geqslant 0;\ \sum_{n=1}^{n'} \alpha_n = 1) \tag{6}$$

Die maximale Abtragung erhält man bei einem β_0, das folgender Bedingung genügt :

$$\sum_{n=1}^{n'} \alpha_n(n - \mathrm{tg}^2\beta_0) \cdot \sin^{(n-1)}\beta_0 = 0 \tag{7}$$

Hieraus ergibt sich, dass $45° \leqslant \beta_0 \leqslant 90°$ sein muss. Im Falle niedrigster Energie, wenn nur Einfachstösse an der Oberfläche erfolgen, erhält man wegen $\alpha_1 \to 1$, dass $\beta_0 \to 45°$ geht. Mit wachsender Energie der einfallenden Ionen steigt auch ihre Eindringtiefe sowie die Zahl der Mehrfachstösse. Als qualitatives Ergebnis wollen wir der Summe (7) nur entnehmen, dass damit auch der effektivste Winkel β_0 grösser wird. Diese Folgerung stimmt gut mit dem Ergebnis der bereits zitierten Arbeit von WEHNER überein. Bei den verschiedenen untersuchten Metallen und bei mittleren Ionenenergien (800–400 eV) liegt β_0 zwischen 65° und 50°. Bei kleinen Energien (200–125 eV) wird β_0

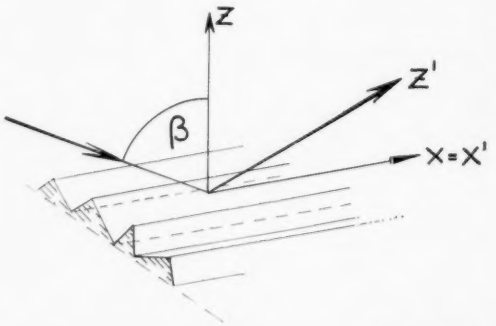

ABB. 2. Beschuss der Mikrofläche. z = Hauptnormale der Oberfläche; z' = Normale der Mikrofläche; β = Einfallswinkel zur Hauptnormalen; $x = x'$ = Richtung der Projektion des Ionenstrahles auf die Oberfläche.

ungefähr 45° und in den meisten Fällen tritt kein ausgeprägtes Maximum mehr auf. Es ist nur noch eine leichte Zunahme der Zerstäubungsrate mit wachsendem Einfallwinkel festzustellen.

Wie WEHNER in einer anderen Arbeit[2] nachweist, wird bei niedriger Energie die Strahlrichtung durch das Oberflächenpotential beeinflusst. Die Annahme eines homogenen verteilten Parallelstrahles ist dann nicht mehr erfüllt. Diesen Energiebereich und denjenigen in der Grössenordnung der Bindungsenergien der Atome im Gitter schliessen wir wegen des andersartigen Charakters der Wechselwirkung aus unseren Betrachtungen aus.[17–19]

* Bei WEHNER wird als Einfallwinkel der Ergänzungswinkel $(\pi/2 - \beta)$ zu unserem β angegeben.

Vol. 2
1961

2. GENEIGTE MIKROFLÄCHEN

Als nächstes soll der Einfluss von Unebenheiten der Kristalloberfläche auf die Abtragung berücksichtigt werden. Wir wollen dabei von einer Fläche ausgehen, die Furchen längs der Projektion der Strahlrichtung auf diese Fläche $[(x00) = (x'00)]$ enthält (Fig. 2). Die Neigung der Mikroflächen, d.h. der Furchenseiten $(00z')$ gegenüber der Probenfläche $(00z)$ sei durch den Winkel δ gegeben, wie das die Fig. 3 zeigt.

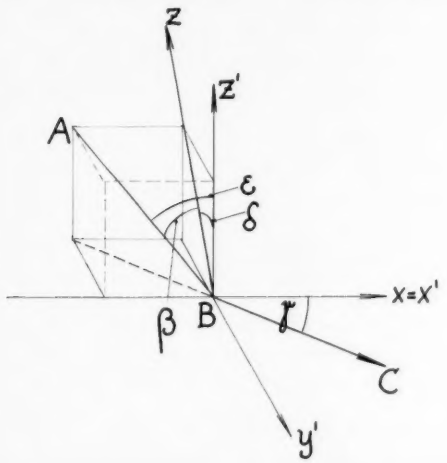

ABB. 3. Impulsübertragung in der Mikrofläche. Geometrische Darstellung zur Erklärung der Winkelbeziehungen zwischen ϵ, β, δ und γ.

Kommt der Ionenstrahl (Richtung $\overline{AB}$) unter einem Winkel β zur $(00z)$-Fläche an, so wird für die Impulsübertragung in der $(00z')$-Fläche ein dritter Winkel ϵ massgebend. Zwischen den Winkeln β, δ und ϵ besteht folgende Beziehung :

$$\cos\epsilon = \cos\beta \cdot \cos\delta; \quad \beta,\delta \leqslant \epsilon \leqslant (\beta+\delta) \qquad (8)$$

Das Verhältnis des maximal in der Mikrofläche in $\overline{BC}$-Richtung übertragenen Impulses zum Anfangsimpuls ist gleich $\sin\epsilon$. Für die Richtung $\overline{BC}$ gilt ferner

$$\operatorname{tg}\gamma = \sin\delta \cdot \operatorname{ctg}\beta; \quad 0° \leqslant \gamma \leqslant (90°-\beta) \qquad (9)$$

Das bedeutet, dass beim Abtragen der Mikrofläche die Furche nicht einfach eingeebnet wird. Besonders wichtig ist der Fall $\epsilon = \beta_0$. In diesem Falle bleiben bei einem vorgegebenen β' bestimmte Mikroflächen mit der entsprechenden Neigung δ' in ihrer Form erhalten. Nach starkem Beschuss müssten derartige Furchen immer wieder beobachtet werden. Es lässt sich zeigen, dass der Neigungswinkel δ' bei vorgegebenem Einfallwinkel β' innerhalb eines relativ grossen Intervalls liegen kann.

Das soll mit dem Vergleich der Abtragungsraten in der Makro- und in der Mikrofläche gezeigt werden :

$$S_z : S_{z'} = (v_{\sigma_{\max}} \cdot dN)_{\beta'} : (v_{\sigma_{\max}} \cdot dN)_{\epsilon}$$

wegen $dN_\epsilon/dN_{\beta'} = \cos\delta'$:

$$= \sin\beta' : \sin\epsilon \cdot \cos\delta'$$

$$= \sin\beta' \cdot \cos\beta' : \sin\epsilon \cdot \cos\epsilon \gtrless 1 \qquad (10)$$

Da ausserdem $\epsilon \geqslant \beta'$ ist, wird bei $\beta' < 45°$ in der Mikrofläche mehr abgetragen als in der $(00z)$-Fläche, wenn für diese $\beta' < \epsilon < (90°-\beta')$ ist. Betrachtet man Mehrfachstösse, so gibt es ebenfalls bestimmte Intervalle für ϵ, d.h. auch für $0 \leqslant \delta' \leqslant \delta'_{\max}$, bei denen die Abtragung in der Mikrofläche überwiegt, entsprechend

$$S_z^{(n)} : S_{z'}^{(n)} = (v_{\sigma_{\max}}^{(n)} \cdot dN)_{\beta'} : (v_{\sigma_{\max}}^{(n)} \cdot dN)_{\epsilon}$$

$$= \sin^n\beta' : \sin^n\epsilon \cdot \cos\delta'$$

$$= \sin^n\beta' \cdot \cos\beta' : \sin^n\epsilon \cdot \cos\epsilon \qquad (11)$$

Bei fixiertem β' wächst $\delta'_{\max}$ mit n.

3. DIE HERAUSBILDUNG DER MIKROFLÄCHEN UND IHRE BEZIEHUNG ZU DEN GITTEREBENEN

Im zweiten Abschnitt wurde die Abtragung von Mikroflächen behandelt, die bereits als Furchen in der Probenoberfläche vorhanden waren. Jetzt soll der Zusammenhang zwischen diesen Mikroflächen und den Gitterebenen sowie das Entstehen dieser Furchen geklärt werden.

Beim Stoss zweier Atome wird die Energie in Vorwärtsrichtung gestreut, d.h. sie wird auf 2 Teilchen aufgeteilt, die im allgemeinen eine von der ursprünglichen abweichende Richtung haben. Das wiederholt sich bei jeder weiteren Stossgeneration. Wie im Ergebnis einer Stosskaskade die Energie des eingeschossenen Teilchens aufgeteilt wird, hängt von der freien Weglänge aller beteiligten Stosspartner und der Energieaufspaltung bei jedem Stossprozess ab. Unterhalb bestimmter Energien wird die freie Weglänge dem

Gitterabstand vergleichbar.[9,11–13,16] Würde dabei die Energie jeweils auf die Stosspartner gleich verteilt werden, so wäre eine vollständige Abbremsung schnell erreicht, die Energie wäre innerhalb eines kleinen Gebietes auf viele Atome, die in alle Richtungen fliegen, verteilt. Bei solchen Stössen, ebenso wie bei den defokussierenden Stössen, werden Atome nur in der unmittelbaren Umgebung der Einschussstellen aus dem Gitter herausgeschlagen. Bei geringer werdender Energie setzt aber in den Richtungen dichtester Atompackung eine Fokussierung der Energieübertragung ein.[9,14–16] Dadurch, dass bei jedem dieser Stösse an das nächste Atom fast die gesamte Energie übertragen wird, wird über eine weite Strecke die Energie überwiegend durch jeweils nur ein Atom weitertransportiert. Das führt dazu, dass auch noch Atome aus ihren Gitterlagen herausgeschossen werden können, die wesentlich tiefer liegen als die mittlere Eindringtiefe der eingeschossenen Ionen beträgt, bzw. solche Atome, die von der Einschussstelle weiter entfernt sind. Endet solch eine Atomreihe, in der die Energie konzentriert übertragen wird, wieder an der Oberfläche, so wird das letzte Atom vollkommen aus dem Gitterverband herausgestossen. Die fokussierenden Stösse verlaufen jedoch nicht vollkommen längs einer Atomreihe wie eine mathematische Gerade, so dass das jeweils stossende Atom eine, wenn auch sehr geringe, kinetische Energie behält, die zum Teil an Atome benachbarter Atomreihen übertragen werden kann. Gehört ein solches Atom der äussersten Gitterebene an, so kann es unter Umständen ebenfalls aus dem Gitterverband herausgeschlagen werden. Nacheinander werden so alle weniger fest gebundenen Atome abgetragen. Während der Abtragung bilden sich stabilere Gitterebenen, und zwar dichtgepackte, in Übereinstimmung mit den oben behandelten Winkelbeziehungen, als quasistationäre Mikroflächen heraus. Dass die einzelnen Atome in ihnen stärker gekoppelt sind, zeigt das Herausbilden genau der gleichen Flächen an thermisch geätzten Proben.[20] Selbstverständlich sind diese Mikroflächen nur relativ stabiler. Einzelne Atome werden bei weiterem Beschuss auch aus diesen Flächen herausgestossen und danach setzt das Abtragen der obersten Gitterebene lawinenartig ein. Überhaupt setzt das Herausschlagen von Atomen aus dem Gitterverband wahrscheinlich besonders an solchen oberflächennahen Stellen ein, deren Homogenität von vornherein gestört war und in deren Umgebung die Atome weniger stark und unsymmetrisch gekoppelt sind. Darauf beruht das Sichtbarwerden der Mikrostruktur, bestimmter Korngrenzen, Gleitlinien, Versetzungen u.a. bei der entsprechenden Anwendung des Ionenbeschusses zur metallographischen Präparation.

Diese allgemeinen Betrachtungen über die Entstehung des Mikroreliefs einer mit Ionen beschossenen Kristalloberfläche wollen wir mit dem konkreten Beispiel eines kubisch-flächenzentrierten Materials abschliessen. Die dichtest gepackten Atomreihen, in denen vorzugsweise die fokussierte Energieübertragung stattfindet, sind die [110]-Reihen. Als Mikroflächen bilden sich die dichtgepackten Gitterebenen, insbesondere die (111)- sowie (100)-Flächen heraus. In diesen liegen gleichzeitig dichtgepackte Atomreihen. Es gibt also eine beschränkte Anzahl möglicher Mikroflächen und -kanten, die durch den Schnitt zweier derartiger Flächen entstehen. Für die genannten dichtest gepackten Flächen verlaufen diese Kanten in [100]- und [110]-Richtung. Die Mikroflächen werden sich immer so herausbilden, dass es eine Kante gibt, die mit der Projektion der Einschussrichtung annähernd übereinstimmt. Dem entspricht, dass die Kanten nicht immer vollkommen parallel verlaufen. Nach langandauerndem Beschuss müssten die Furchen in der Oberfläche dominieren, ohne dass die metallographische Struktur noch erkennbar ist. Bei kurzzeitigem Beschuss jedoch werden derartige Furchen sich nur über kleinere, von besonders vorstehenden Unebenheiten geglättete Gebiete ausbreiten.

4. EXPERIMENTELLER NACHWEIS

Als anschauliches Beweismaterial für die vorstehenden Überlegungen dienten uns die mikroskopischen Untersuchungsergebnisse am Ionenauffänger eines Massentrenners.* Mg^{24}-,

* Wir danken an dieser Stelle dem VEB Vakutronik, Dresden, dafür, dass er uns in freizügiger Weise den Auffänger des magnetischen Isotopentrenners als Untersuchungsobjekt mit Angabe der gewünschten Daten über die Ionen zur Verfügung stellt. Anmerkung bei der korrektur: ARDENNE M. v., JÄGER G., KÖHLER F. und PETTER G., *Kernenergie* **3**, 1177 (1960).

Vol. 2
196

ol. 20
1961

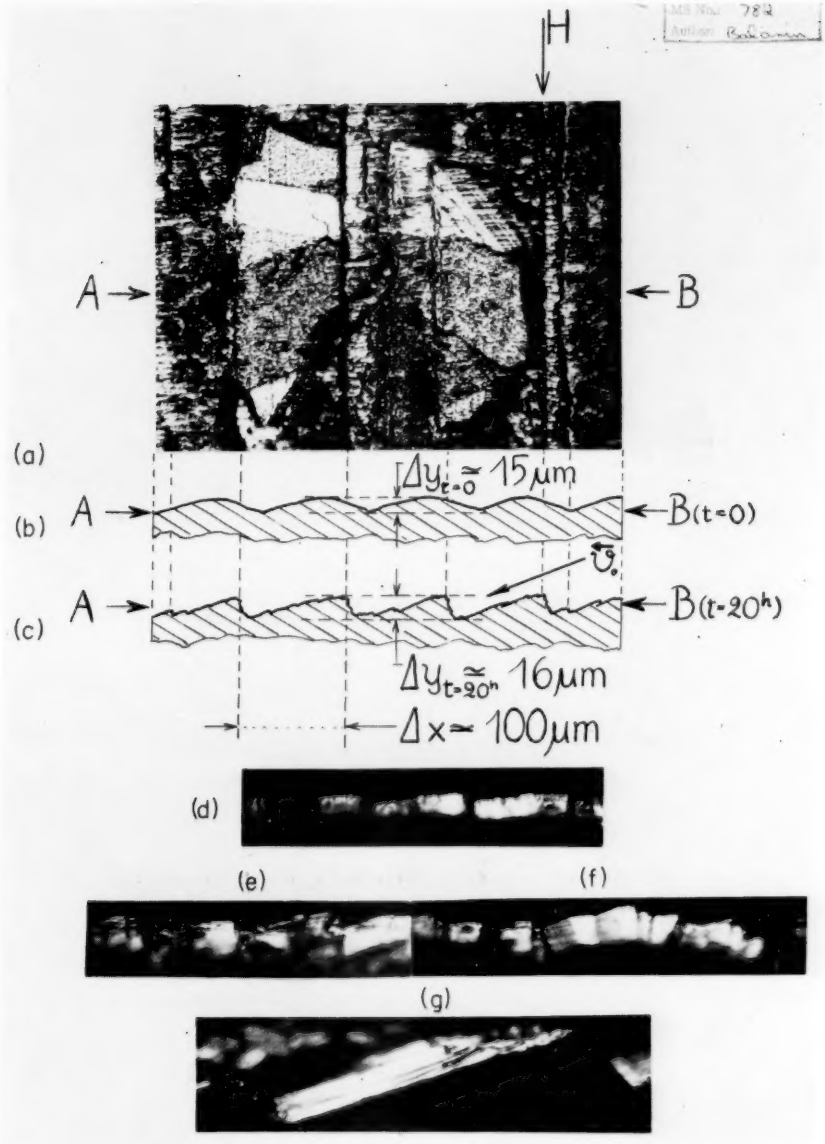

ABB. 4. Mikroskopische Deutung des Abtragungsvorganges. Lichtmikroskopische Aufnahme der Probenoberfläche (V = 180×; H = Richtung der Hobelrillen; v_0 = Beschussrichtung); (a) Probenoberfläche (Lackabdruck, Al-verspiegelt) nach 20-stündigem Beschuss der Probe bei 40 kV; (b) und (d) Oberflächenrauhigkeit der Probe vor Beschuss; (c), (e) und (f) Oberflächenrauhigkeit nach 20-stündigem Beschuss (V = 120×); (f) Störung der Schollensymmetrie durch grobe Körner (V = 120×); (g) Ausschnitt von (e) (V = 570×).

facing p. 142

Abb. 5

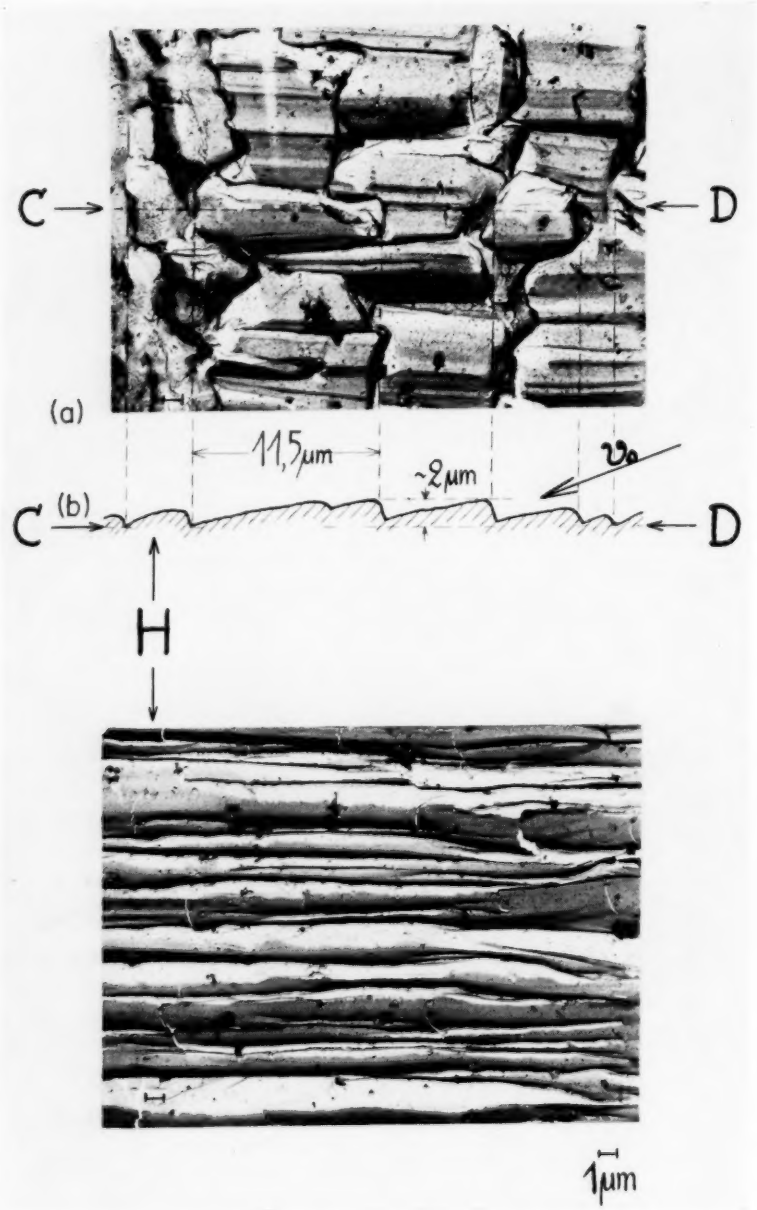

Abb. 6

Abb. 5. (a) Elektronenmikroskopische Aufnahme der Schollenoberfläche (H = Hobelrille, v_0 = Beschussrichtung, V = 2450×); (b) Schematischer Schnitt durch 5a).

Abb. 6. Elektronenmikroskopische Aufnahme der Schollenoberfläche (V = 2450×).

bzw. Mg^{25}-Ionen wurden unter einem Winkel von $\beta = 70°$ und mit einer Beschleunigungsspannung von $U_B \simeq 40$ kV auf einen wassergekühlten Kupferauffänger geschossen. Der Auffänger bestand aus grosskristallinem technischen Kupfer (mittlere Korngrösse 80 μm). Der Block war quer zur Beschussrichtung abgehobelt worden und hatte daher eine Rillenstruktur [0y0] rechtwinklig zum einfallenden Ionenstrahl (vgl. Fig. 4(a), 5(a) und 6 ; Hobelrichtung H senkrecht zur Beschussrichtung!). Die Rillentiefe dieser Oberflächenstruktur vor dem Beschuss betrug etwa 10–15 μm, der Rillenabstand etwa 100–130 μm. Diese Rillenstruktur hatte den Vorteil, dass stets eindeutig die Beschussrichtung festzulegen war. Die grosse Intensität, mit welcher der Kupferblock beschossen wurde, liess die untersuchten Effekte auch bei dieser grossen Oberflächenrauhigkeit deutlich sichtbar werden. Die Rillenstruktur gab zusätzlich die Möglichkeit, die von WEHNER[1] und von PLESCHIWZEW[4,5] gefundenen Gesetzmässigkeiten über die Abhängigkeit der Abtragung vom Einfallwinkel am Objekt detaillierter zu erkennen. Die Mikroaufnahmen der Fig. 4 und die zugehörigen zeichnerischen Darstellungen sollen den Abtragungsmechanismus unter Einwirkung des Ionenbeschusses erklären. Fig. 4(a) zeigt die lichtmikroskopische Aufnahme der Oberfläche des Kupferauffängers nach etwa 20-stündigem Beschuss mit Mg^{24}-Ionen.

Die Aufnahme wurde vermittels eines Al-verspiegelten Nitrozellulosefilmabdruckes hergestellt, ebenso die Aufnahmen 4(c), 4(f) und 4(g). Lediglich 4(d) zeigt direkt die Oberfläche des nicht beschossenen Kupfers. Das Ausmessen der Oberflächenrauhigkeit der Proben sowie die Herstellung der Aufnahmen 4(d), (e), (f) und (g) geschah mit Hilfe des "Oberflächenprüfgerätes nach Prof. Schmaltz", Fabrikat des VEB Carl Zeiss, Jena.

Deutlich sind auf dem Bild 4(a) die vom Hobeln des Blockes herrührenden Rillen und die senkrecht dazu durch den Ionenbeschuss hervorgerufene furchenartige Feinstruktur [00z'] zu erkennen. Fig. 4(b) und 4(c) geben in zeichnerischer Darstellung den Querschnitt der Probe in der Linie AB wieder. Durch den Beschuss tritt eine Umformung der welligen Probenoberfläche, eine Art Schollenbildung (00z) ein. Dies wird auch durch die fotografischen Aufnahmen 4(d), (e) und (f) bewiesen. 4(d) zeigt die Aufnahme der Probenoberflächenstruktur vor, 4(e) und 4(f) zeigen sie nach dem 20-stündigen Ionenbeschuss. 4(g) gibt eine vergrösserte Darstellung des Querschnittes einer dieser Schollenreihen aus Fig. 4(e) wieder. Die Beschussrichtung liegt, wie aus der Skizze ersichtlich, in der Bildebene. Es tritt in dem beobachteten Zeitraum also keine Einebnung der Oberflächenrauhigkeit, sondern eine geringe Vertiefung der ursprünglich vorhandenen Querrillen senkrecht zum Ionenstrahl, vor allen Dingen jedoch eine Bildung von Furchen parallel zum Ionenstrahl auf, wie dies in den Figuren 4(a), (e) und (f) bereits zu erkennen ist.

Damit bestätigen unsere Untersuchungen über den Beschuss von Metalloberflächen mit Ionen hoher Energie vollkommen diejenigen von CUNNINGHAM *et al.*[21] gefundenen Ergebnisse mit Ionen mittlerer Energie. In der Regel zeigte die Oberfläche eine schollenartige Form entsprechend der Aufnahme 4(e). Doch wurden auch Stellen gefunden, in denen die Symmetrie der Schollenbildung empfindlich gestört war, wie das in der Aufnahme 4(f) gezeigt wird. Wir neigen zu der Auffassung, dass in diesem abgebildeten Abschnitt das Zusammentreffen mehrerer unterschiedlich orientierter Körner die Ursache der Störung ist.

Auf den Oberflächen der einzelnen Schollen bilden sich Furchen parallel zur Einfallsrichtung der Ionenstrahlen, wie sie von HAYMANN[22–24] an verschiedenen Stellen beschrieben wurden. Wir haben im ersten und zweiten Teil dieser Arbeit versucht, ihre Entstehung aus der Impulsübertragung mathematisch-geometrisch zu erklären und stimmen damit vollkommen mit den zuletzt genannten Autoren überein, die den gesamten Prozess ebenfalls durch Impuls- und nicht durch Energieübertragungsprozesse deuten.

Besonders eindrucksvoll wird das durch die beiden elektronenmikroskopischen Aufnahmen Fig. 5(a) und 6 bestätigt, die Ausschnitte verschiedener Stellen der Schollenoberflächen zeigen.*

In Fig. 5(a) ist am linken Rand noch deutlich die Orientierung der vom Hobelprozess herrührenden Rille zu erkennen. Der Ionenbeschuss erfolgte senkrecht dazu und führte zur Herausarbeitung der Mikrofurchen und -flächen. Während es sich bei Fig. 5(a) um relativ kurze und breite Furchenbildung handelt (Schnittzeichnung Fig. 5b) ziehen sich in Fig. 6 die Furchen über weite Strecken hin.

In Übereinstimmung mit den bereits zitierten

* Die elektronenmikroskopischen Aufnahmen wurden mit unserem Elektronenmikroskop "El–Mi–D2" (Fabrikat VEB Carl Zeiss Jena) hergestellt. Die Präparation geschah vermittels Nitrozellulose-Filmabdruck und einer Platin–Kohle–Bedampfung nach SKATULLA[25].

Arbeiten von CUNNINGHAM *et al.* und HAYMANN muss man zu der Deutung gelangen, dass diese unterschiedliche Abtragungswirkung im wesentlichen von der Orientierung der beschossenen Kornfläche abhängt. Diese Ansicht dürfte bis zu einem gewissen Grade auch schon durch die lichtmikroskopische Aufnahme, Fig. 4(a), bestätigt werden.

5. DISKUSSION

Bisher wurde der Abhängigkeit von der Richtung des einfallenden Ionenstrahls in theoretischen Arbeiten, in denen die Abtragung von Festkörpern bei Ionenbeschuss vermittels eines Stossmechanismus behandelt wurde, keine Beachtung geschenkt. Die Annahme einer Ionenreflexion durch isotrope Vielfachstreuung[18,26] führt zu einer gleichen Massen- und Energieabhängigkeit, wie sie für die Reflexion von Neutronen experimentell gefunden wurde.[19] Aber gerade die in dieser Arbeit nachgewiesene Abhängigkeit von der Beschussrichtung mit schweren geladenen Teilchen beweist erneut eindeutig, dass die vielfach vertretene Verdampfungstheorie unzutreffend ist. Um das zu zeigen, wollen wir die Schlussfolgerungen sowohl der Stosstheorie als auch der Verdampfungstheorie mit dem experimentellen Befund vergleichen.

Bei der Verdampfungstheorie muss eine kurzzeitige Erwärmung vorausgesetzt werden, die zwar lokalisiert sein sollte, jedoch auf ein Gebiet, das eine Vielzahl von Atomen umfasst. Eine jeweils nur geringe Anzahl dieser Atome vermag in die Dampfphase überzugehen und zwar teilweise beeinflusst durch die Kristallstruktur und die Richtung des Ionenstrahles. Die Oberfläche sollte demzufolge ein andersartiges Aussehen als das der oben beschriebenen Furchen annehmen. Es sei dahingestellt, ob es dem Bild thermisch geätzter Proben ähnlich wäre. Entsprechende Untersuchungen an Kupfer, das bei 950–1075°C im Hochvakuum geglüht wurde,[20] zeigen an keiner Stelle die Bildung derartiger Furchen, wie sie von uns beobachtet wurden. Besonders zu bemerken ist, dass die Furchen an allen Stellen längs der Projektion der Ionenstrahlrichtung verlaufen. An den thermisch geätzten Proben bilden sich im Ergebnis der Verdampfung möglichst glatte, niedrig indizierte Oberflächen heraus. Auch bei etwas geringeren Temperaturen (700–950°C), bei denen die Verdampfung keinen wesentlichen Beitrag mehr gibt, wird eine Nivellierung von makroskopischen Oberflächenstörungen an polykristallinem Kupfer beobachtet,[27] die durch Diffusion in der Oberfläche bedingt ist. An mit Ionen beschossenen Oberflächen wird jedoch die Entstehung kantiger Furchen und nicht eine Glättung beobachtet, woraus zu schliessen ist, dass die Oberfläche nicht übermässig erwärmt wurde. Die Entstehung und Quasistabilität der Furchen, sowie ihre Form und Richtung sprechen deshalb für die Stosstheorie. An dieser Stelle kann man auch darauf hinweisen, dass trotz des sehr intensiven, lokalisierten Beschusses keine Anzeichen von solchen Umlagerungsgebieten (displacement spikes) vorliegen, wie sie mehrfach in der Theorie der Strahlenschäden von Festkörpern beschrieben wurden.

Die Energie verdampfter Ionen müsste im Durchschnitt recht gering sein und könnte gar nicht die Energie der einfallenden Ionen erreichen. Nachgewiesen ist jedoch ein härteres Energiespektrum, das kontinuierlich bis zu der nach der Stosstheorie an ein einzelnes Atom maximal übertragbaren Energie reicht.[17,28,29]

Infolge der maximalen Ionenstrahldichte sollte bei Verdampfung die maximale Abtragung bei senkrechtem Beschuss erfolgen, das ist aber nicht der Fall.

Von Einfluss auf die Abtragung ist sicher auch die Probentemperatur. Nach der Verdampfungstheorie wäre mit einer Temperaturerhöhung auch eine Zunahme der Abtragungsrate zu erwarten. Nach KEYWELL[30] ist das auch bei der Stosstheorie wegen einer Reduktion der Energie, die aufgebracht werden muss, um ein Atom von der Oberfläche zu entfernen, zu erwarten. Berücksichtigt man jedoch, dass die Kopplung bei höheren Temperaturen geringer ist, die thermischen Gitterschwingungen stärker werden und dass die Konzentration von Leerstellen und anderen Fehlordnungserscheinungen zunimmt, wodurch fokussierende Stösse in geringerem Masse stattfinden, so ergibt sich in Übereinstimmung mit dem Experiment,[31] dass die Abtragungsrate mit steigender Temperatur fällt.

Folgende allgemeine Bemerkungen sollen noch gemacht werden: Mit höheren Ionenenergien finden die Primärstösse tiefer statt. Daher ist

Vol. 2
196

bezogen auf eine gleiche Leistung eine Verringerung der Abtragung zu erwarten und das Verhältnis der Anzahl der aus dem Inneren neu herausgeschlagenen Ionen zu den reflektierten und den von der Oberfläche abgelösten Ionen müsste ansteigen.[32] Uns scheint, dass zur genaueren Untersuchung derartiger Fragen nur massenspektrometrische Methoden wegen ihrer hohen Empfindlichkeit und ihrer nach Elementen getrennten Aussage angewandt werden können.[28,31]

Weiterhin ist zu bemerken, dass die elektrische Ladung sowohl der eingeschossenen als auch der abgetragenen Teilchen im Prinzip keine Rolle für die genannten Abtragungseffekte zu spielen scheint. Die Energie wird entsprechend der Massenkonzentration zwischen den Atomschwerpunkten übertragen. Für die Änderung der Elektronenanzahl der Ionen, Neutralisierung und Umladung wird nur eine vernachlässigbar geringfügige Energie verbraucht.[33]

Zum Schluss wollen wir noch darauf hinweisen, dass beim Vorhandensein von Fremdstoffen in Form adsorbierter oder chemisch gebundener Schichten, oder durch Beschuss mit chemisch aktiven Ionen die reine Abtragung durch eine Reihe weiterer Faktoren in einem solchen Masse beeinflusst werden kann, dass die hier gegebenen einfachen Zuzammenhänge überdeckt werden. Die bewusste Ausnutzung dieser Effekte kann für die Anwendung des Ionenbeschusses zur metallographischen Ätzung von Metallschliffen von besonderem Vorteil sein.

Anerkennungen — Herrn Dr. K. FUCHS und Herrn Dr. F. THÜMMLER danken wir für die kritische Durchsicht dieser Arbeit und für die Aussprache. Herrn Dr. O. HAUSER sowie den Mitarbeitern der Abteilung Physik des Bereiches Werkstoffe und Festkörper danken wir für die vielen anregenden Diskussionen.

LITERATUR

1. WEHNER G., *J. Appl. Phys.* **30,** 1762 (1960).
2. WEHNER G., *Phys. Rev.* **102,** 690 (1956).
3. WEHNER G. und ROSENBERG D., *J. Appl. Phys.* **31,** 177 (1960).
4. JURASOWA V. E., PLESCHIWZEW N. V. und ORFANOW I. V., *Z. eksp. teor. fiz.* **37,** 966 (1959) (Auf russisch).
5. PLESCHIWZEW N. V., *Z. eksp. teor. fiz.* **37,** 1233 (1959) (Auf russisch).
6. BOHR N., *K. Danske Vidensk. Selsk.* **18,** 1 (1948).
7. BALARIN M. und HAUSER O., ZfK–WF3; *Kernenergie* **3,** 973 (1960).
8. HENSCHKE E. B., *J. Appl. Phys.* **28,** 411 (1957); *Phys. Rev.* **106,** 737 (1957).
9. GIBSON J. B., GOLAND A. N., MILGRAM M. und VINEYARD G., BNL–4871; *Phys. Rev.* **120,** 1229 (1960).
10. VAPNIK V. N., GURWITSCH L. G. und SINOWJEW H. V., *Izv. akad. nauk. SSSR*, (Ser. Phys). **24,** 685 (1960) (Auf russisch).
11. BRINKMANN J. A., *J. Appl. Phys.* **25,** 961 (1954).
12. BRINKMANN J. A., *Amer. J. Phys.* **24,** 246 (1956).
13. HOLMES D. K. und LEIBFRIED G., *J. Appl. Phys.* **31,** 1046 (1960).
14. LEIBFRIED G., *J. Appl. Phys.* **30,** 1388 (1959).
15. LEIBFRIED G., *J. Appl. Phys.* **31,** 117 (1960).
16. GONSER U., *J. Nucl. Mat.* **2,** 43 (1960).
17. ARIFOW U. A., AJUCHANOW A. CHR. und GRUITSCH D. D., *Izv. akad. nauk. SSSR* **24,** 710 (1960) (Auf russisch).
18. BRUNNEE C., *Z. Phys.* **147,** 161 (1957).
19. KOGAN A. M., PETROW G. G., TSCHUDOW L. A. und JAPOLSKI P. A., *Atomn. Energiya* **7,** 385 (1959) (Auf russisch).
20. YOUNG F. W. und GWATHMEY A. T., *J. Appl. Phys.* **31,** 225 (1960).
21. CUNNINGHAM R. L., HAYMANN P., LECOMTE C., MOORE W. und TRILLAT J. J., *J. Appl. Phys.* **31,** 839 (1960).
22. HAYMANN P., *C.R. Acad. Sci., Paris* **248,** 2472 (1959).
23. HAYMANN P., *C.R. Acad. Sci., Paris* **251,** 85 (1960).
24. HAYMANN P. und MIHAMA K., *Vortrag auf der European Regional Conference on Electron Microscopy, Delft* (1960).
25. SKATULLA W. und HORN L., *Exp. Tech. Phys.* **8,** 1 (1960).
26. ROOS O., *Z. Phys.* **147,** 184 (1957).
27. GEGUSIN JA. E. und OWTSCHARENKO N. N., *Fiz metal. i metalloved.* **9,** 569 (1960) (Auf russisch).
28. AJUCHANOW A. CHR. und ISCHAKOW G. I., *Izv. akad. nauk SSSR* (Ser. Phys.) **24,** 715 (1960) (Auf russisch).
29. WEHNER G., *Phys. Rev.* **114,** 1270 (1959); *J. Appl. Phys.* **31,** 1392 (1960).
30. KEYWELL F., *Phys. Rev.* **97,** 1611 (1955).
31. FOGEL JA.M., SLABOSPITZKI R. P. und KARNANCHOW I. M., *Z. tech. fiz.* **30,** 824 (1960) (Auf russisch).
32. YONTS O. C., NORMAND C. E. und HARRISON D. E., *J. Appl. Phys.* **31,** 447 (1960).
33. ARIFOW U. A. und CHADSCHIMUCHAMEDOW CHR. CHR., *Izv. akad. nauk SSSR* (Ser. Phys.) **24,** 705 (1960) (Auf russisch).

J. Phys. Chem. Solids Pergamon Press 1961. Vol. 20, Nos. 1/2, pp. 146–149. Printed in Great Britain.

THERMAL CONDUCTIVITY OF SILICON AT LOW TEMPERATURES*

J. C. THOMPSON and B. A. YOUNGLOVE†

The University of Texas, Austin 12, Texas

(*Received* 10 *February* 1961)

Abstract—The thermal conductivity of several single crystal silicon samples has been measured over the range 2–200°K. Conductivities as high as 35 watt/cm deg were observed. The concentration of the impurities (which were *p*-type in all but one sample) was varied from 10^{12} cm^{-3} to 10^{16} cm^{-3}. The thermal resistance for the purest samples is due to point defect (isotope) and boundary scattering. In the less pure samples an additional resistance is observed in qualitative agreement with the predicted effects of electron–phonon scattering. Comparisons are made with existing theories.

INTRODUCTION

EARLY measurements of the thermal conduction of silicon and germanium[1,2] failed to show the expected high conductivity in the region 10–50°K. More recent work on germanium[3,4,5] has shown that isotopic variety is the source of a large part of the thermal resistance in this region. However, boundary scattering does not account for all of the resistance in the low-temperature region where point defect scattering is small. This additional resistance has been ascribed,[3] in the case of germanium, to scattering by electrons in an "impurity band".

A series of measurements has been made on seven silicon crystals of varying impurity concentrations. As expected, the results are similar to those reported for germanium. The data have been analyzed by a scheme due to CALLAWAY[5].

EXPERIMENTAL

Seven single crystal silicon samples were measured over the range 2–200°K. Six of these were *p*-type, boron doped, with impurity concentrations ranging from 1×10^{13} to 3×10^{16} cm^{-3}. The seventh sample was *n*-type, arsenic doped. Descriptions are given in Table 1. Impurity concentrations were determined by comparison of resistivity data with that of MORIN and MAITA[6]. Oxygen content was measured by infrared absorption at 9μ.[7] Most of the samples were bars of dimensions $3\times3\times20$ mm.

The thermal conductivity was measured with a conventional "thermal potentiometer". Heat generated in a resistance heater flowed through the sample to the bath. Extraneous heat leaks were reduced by using manganin wire, long leads, a radiation shield, and high vacuum. Temperatures were determined by resistance thermometers attached at two points along the sample. Power supplied to the thermometers was less than 10^{-6} W. Temperature gradients were typically less than 1 per cent of the average temperature. Different thermometers were used for the high and low temperature regions. Below 70°K $\frac{1}{10}$ W carbon radio resistors were used; they were also used in some cases to 200°K. In most cases the range 60–200°K was covered using copper resistance thermometers as described by DAUPHINÉE[8]. Both potentiometric and electronic[9] techniques were used for resistance determinations. Calibration was at He, N_2, and room temperatures, with interpolated values computed from the usual Clement and Quinnell formula for carbon resistors. The thermometers were intercompared over the entire range to reduce errors in computed temperature differences.

* Supported in part by the Office of Naval Research.

† Texas Instruments Fellow in Physics. Now at NBS Cryogenic Laboratories, Boulder, Colorado.

Vol. 2
196

Table 1. Physical properties of all samples

Designation	ρ0°C (Ω-cm)	Impurity	Impurity concentration (cm^{-3})	O_2 concentration (cm^{-3})	k_{max} (W/cm deg)	L (mm)	A' ($10^{-44}sec^3$)	T^n(4°K)	T^n(140°K)
M-1[a]	2000	Boron	2×10^{12}	$<10^{17}$	28	3·54	0·133	+2·76	−1·6
E-2828[b]	2000	Boron	2×10^{12}	$<10^{17}$	33	0·67	0·133	+2·76	−1·6
E-2592[b]	12·0	Boron	5×10^{14}	—	17	0·70	0·78	—	−1·6
Q-20[b]	7·2	Boron	1×10^{15}	2×10^{17}	14·5	3·54	1·325	+2·44	−1·6
Q-18[b]	5·0	Boron	2×10^{15}	1×10^{17}	17	1·95	0·95	+2·74	−1·6
Q-22[b]	0·57	Boron	3×10^{16}	$<10^{17}$	10	3·54	1·82	+3·30	−1·45
Si-2[b]	18	Arsenic	5×10^{14}	—	18	3·05	0·715	+2·44	—

[a] Furnished through the courtesy of F. J. BOURASSA, Electronics Chemical Division, Merck and Co., Inc.

[b] Furnished through the courtesy of H. L. TAYLOR, Texas Instruments, Inc.

RESULTS AND DISCUSSION

Thermal conductivity data is shown in Fig. 1 for two typical samples; a summary of results is given in Table 1 for all samples. M-1 is the purest sample, Q-20 of relatively low purity. Relative values are good to 2 per cent, absolute values to 10 per cent. The lines represent theoretical expectations based on the phenomenological theory of CALLAWAY[5].

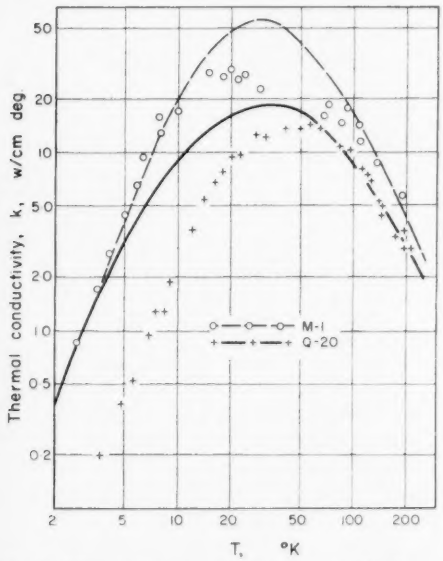

FIG. 1. Thermal conductivity for two single crystal silicon specimens. M-1 is of high purity (10^{12} imp./cm^3) and Q-20 of relatively low purity (10^{15} imp./cm^3). The solid and dashed curves include point defect and boundary scattering as described by CALLAWAY; the theory is matched to the data near 140°K.

CALLAWAY considers contributions to thermal resistance from boundary scattering, point defects (isotopes), and Umklapp processes. Normal scattering is included for its effect upon the phonon distribution. Rather than adding resistivities due to each process he adds reciprocal relaxation times and derives a net thermal resistance. Experimental data, at one fixed temperature (140°K), is used to fix the one arbitrary constant of the theory. It is also necessary to assume that, in the purest sample, isotope scattering dominates other point-defect scattering. The effect of isotopic scattering is obtained from the known isotopic abundances for silicon and a formula due to KLEMENS[10].

$$\tau_{iso}^{-1} = A\omega^4 = (V_0/4\pi c^3)\sum n_i(\Delta M_i/M)^2\omega^4$$

where τ is the relaxation time for isotope scattering, ω the phonon frequency, V_0 the volume per atom, c the velocity of sound, and n_i the fraction of atoms differing by ΔM_i from the average mass M.

In the purest samples CALLAWAY's approach yields a satisfactory fit of the data except in the region of the maximum where an overestimate is expected. In particular, the low-temperature conductivity is well described by boundary scattering plus some residual isotope scattering. In less pure samples deviations are observed below the maximum in which the theory predicts a conductivity much higher than that observed. A fit is forced

above 100°K by matching a new constant, A', to the data. A' differs from A by the inclusion of non-isotopic point defect scattering, though this is done empirically since both the concentration of non-ionizing impurities and the scattering power of any defect other than a mass difference are difficult to estimate.[12] The values obtained for A' are listed in Table 1. The additional thermal resistance below 20°K is presumed due to the scattering of phonons by electrons.[3,13,14] The electrons are either in impurity bands or are almost free and "hop" from one impurity center to another.

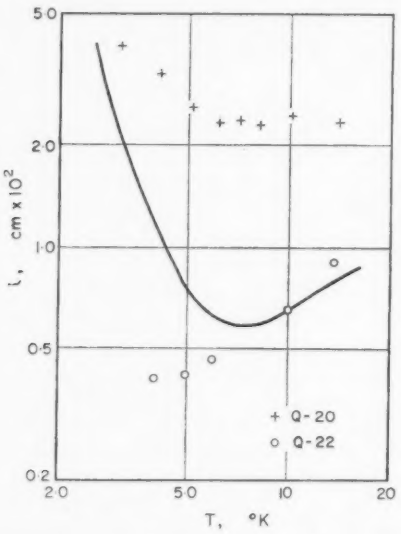

FIG. 2. Mean-free path associated with thermal resistance not attributal to point defect or boundary scattering. The solid line shows ZIMAN's theory for phonon–electron scattering with $m^*/m = 10$ and 10^{15} carriers/cm³.

ZIMAN[13] has predicted a mean free path due to this effect which is strongly dependent upon electron concentration. Variations in donor (acceptor) concentrations of only an order of magnitude can change the slope of the temperature dependence from negative to positive. Such sensitivity renders comparisons difficult.

Figure 2 shows the residual mean-free path for two samples of moderate purity. These curves were obtained by subtracting the boundary and isotope resistance from the experimental data, and using the kinetic formula

$$1/W = (\tfrac{1}{3})Ccl$$

where W is the residual thermal resistance, C the heat capacity (Debye), and l the desired mean-free path. The curves given by ZIMAN may be fitted by choosing m^*/m (the only adjustable parameter) to be approximately 10; the effective mass would be expected to be large for the low impurity concentrations used here. Agreement is at least qualitative.

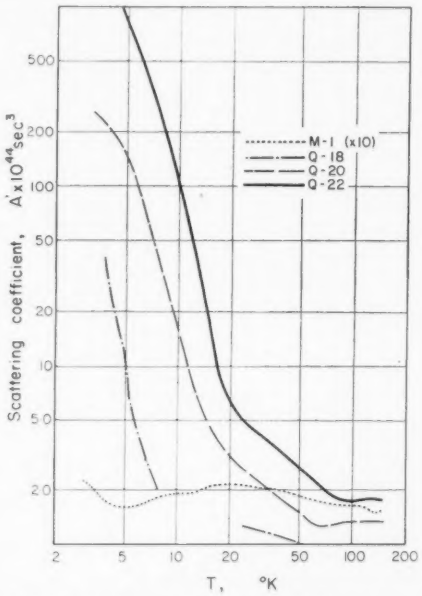

FIG. 3. Effective defect scattering coefficient vs. temperature. The coefficient is obtained by forcing the theoretical expression to fit the data. The rise at low temperatures may be ascribed to additional scattering produced by strains induced by the deionization of acceptors.

Neither temperature dependence nor magnitude of the extra thermal resistance is in agreement with that predicted from either static[12] or mobile[15] dislocation scattering. KEYES[14] has suggested that electrons bound to impurity centers would yield the resistance ascribed by ZIMAN to electrons in an impurity band. A detailed exposition is not available for comparison. However, qualitative comparisons can be made. Keyes assumes that the bound charges are effective scatterers at low temperatures only because the donors (or acceptors)

would be ionized at higher temperatures and because there are relatively fewer long wave phonons at higher temperatures. Where effective the strains scatter with a relaxation time depending on ω^4. This effect would then be included in the A' of CALLAWAY's phenomenological approach, with A' temperature dependent. We have computed the $A'(T)$ required to fit our data and obtained thereby Fig. 3. The increase in A' below 20°K cannot be matched to the increase of scatterers due to deionization of acceptors as the latter yields a much steeper curve. One may again infer a qualitative agreement with theory.

SUMMARY

The thermal conductivity of relatively pure silicon may be well described by Umklapp and isotope scattering at high temperatures and by boundary and electron scattering at low temperatures. The CALLAWAY analysis scheme, which lacks the phonon–electron scattering term, is satisfactory above the maximum in the thermal conduction. Below the maximum the decrease in observed conductivity may be qualitatively explained by either the electron–phonon scattering model due to ZIMAN, or by the strain scattering model due to KEYES.

Acknowledgements—The authors are indebted to Texas Instruments, Inc. for a grant in support of this work. Mr. L. DREHER rendered invaluable aid in programming the IBM 650 and CDC 1604 and Mr. W. B. WOLLET provided general technical aid.

REFERENCES

1. HULL G. W. and GEBALLE T. H., *Phys. Rev.* **96,** 846 (1954).
2. WHITE G. K. and WOODS S. B., *Phys. Rev.* **103,** 569 (1956).
3. CARRUTHERS J., GEBALLE T. H., ROSENBERG H. M. and ZIMAN J. M., *Proc. Roy. Soc.* A**238,** 502 (1957).
4. GEBALLE T. H. and HULL G. W., *Phys. Rev.* **110,** 773 (1958).
5. CALLAWAY J., *Phys. Rev.* **113,** 1046 (1959).
6. MORIN F. J. and MAITA J. P., *Phys. Rev.* **96,** 28 (1954).
7. KAISER W. and KECK P. H., *J. Appl. Phys.* **28,** 882 (1957).
8. DAUPHINÉE T. M. and PRESTON-THOMAS H., *Rev. Sci. Instrum.* **25,** 224 (1956).
9. SANDLIN B. J. and THOMPSON J. C., *Rev. Sci. Instrum.* **30,** 659 (1959).
10. CLEMENT J. R. and QUINNELL E. H., *Rev. Sci. Instrum.* **23,** 213 (1952).
11. KLEMENS P. G., *Proc. Phys. Soc. Lond.* **A68,** 1113 (1955).
12. KLEMENS P. G., *Handbuch der Physik* Vol. XIV, p. 198 (edited by FLÜGGE S.). Springer-Verlag, Berlin (1956); *Solid State Physics* Vol. VII, p. 1. (edited by SEITZ F. and TURNBULL D.). Academic Press, New York (1958).
13. ZIMAN J. M., *Phil. Mag.* **1,** 191 (1956).
14. KEYES R. W., *Bull. Amer. Phys. Soc.* (ser. 2) **5,** 264 (1960); Westinghouse Scientific Report 6–40602–P9 (1960).
15. GRANATO A., *Phys. Rev.* **111,** 740 (1958).

Vol. 20
1961

J. Phys. Chem. Solids Pergamon Press 1961. Vol. 20, Nos. 1/2, pp. 150–161. Printed in Great Britain.

MECHANICAL AND RADIATION INDUCED FAULTING IN SODIUM AZIDE*

D. T. KEATING

Brookhaven National Laboratory, Upton, New York

and

S. KRASNER†

Explosives Research Section, Picatinny Arsenal, Dover, New Jersey

(*Received* 15 *February* 1961)

Abstract—Sodium azide powders subjected to mechanical grinding, gamma irradiation, and pile irradiation have been examined by X-ray diffraction techniques. Faulting and strain are found in the ground samples with no indication of decomposition. Faulting and strain are also found in samples subjected to irradiation accompanied by signs of decomposition such as coloration, lowering of the ignition temperature, and a lattice contraction in the direction of the long dimension of the azide ion. Annealing removes some of the faults and strain both in the ground and irradiated samples, but in the latter cases a significant fraction of these imperfections are stable even at the ignition temperature. The two types of irradiation produce qualitatively similar results, and quantitative differences are ascribed to the more inhomogeneous decomposition induced by pile irradiation. In both cases a return to stoichiometry upon annealing is evidenced by a disappearance of the lattice contraction.

INTRODUCTION

SODIUM azide, which is chemically related to the explosive heavy metal azides, decomposes under irradiation. HEAL[1,2] has studied the decomposition of sodium azide exposed to X-rays by chemical analysis of the products formed upon dissolution. ROSENWASSER *et al.*[3] have attributed some of the observed optical absorption bands in gamma and pile irradiated sodium azide to decomposition. An investigation using X-ray diffraction techniques was undertaken to ascertain the effects, if any, of gamma and pile irradiation on the sodium azide structure.

Sodium azide is rhombohedral[4] with a rhombohedral angle, $\alpha = 38°43'$ and $a_0 = 5{\cdot}44$ Å. With α less than 60°, the structure is NaCl-like,[5] elongated along the body diagonal by the linear N_3^- ion. The stacking of layers in the direction of the long diagonal is that of an undistorted cubic close-packed alternating sequence of sodium and azide planes. Alternatively, a hexagonal cell[4] may be chosen with $A_1 = A_2 = 3{\cdot}637$ Å and $A_3 = 15{\cdot}209$ Å parallel to the azide ion. In this paper the cell chosen is that pictured in Fig. 1(a). It is uncertain whether the azide ion is centro-symmetric[6,7] or polar.[8,9] This question could not be settled from our powder patterns because of strong preferred orientation, numerous overlapping lines, uncertainty in temperature factors, nitrogen scattering factors for N_3^-, and the relatively weak scattering of nitrogen.

Preliminary examination of irradiated powders revealed the quite unexpected results of a systematic broadening of certain reflections, namely those for which $H-K \neq 3M$ (hexagonal indices, M integer). This is illustrated in Fig. 2(b). Such phenomena are usually associated with stacking disorders, and accordingly a sample of sodium azide was ground with the results shown in Fig. 2(a). Figs. 2(a) and 2(b) are strikingly similar

* Work performed primarily at Brookhaven National Laboratory and supported jointly by Picatinny Arsenal and the U.S. Atomic Energy Commission.

† Guest Scientist, Brookhaven National Laboratory.

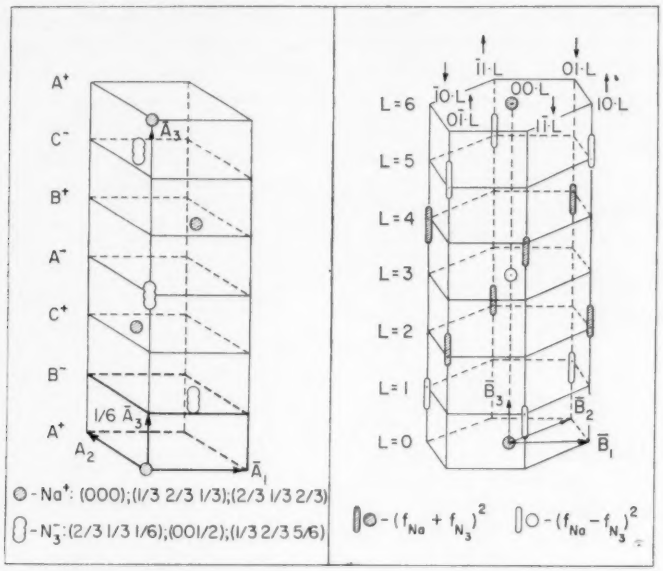

(a) (b)

FIG. 1. (a) Choice of hexagonal unit cell for sodium azide. (b) Interference function of sodium azide containing stacking faults.

Vol. 20
1961

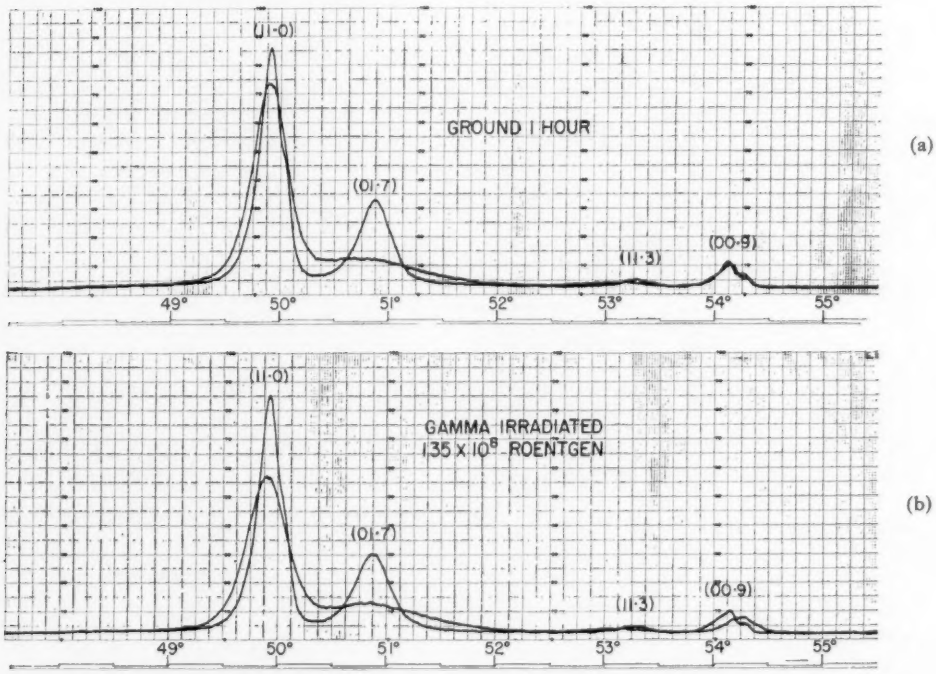

FIG. 2. X-ray diffraction patterns of (a) sample ground for one hour, and (b) sample γ-irradiated $1{\cdot}35 \times 10^8$r compared in each case with an undamaged sample.

except for the displacement of the (00·9) reflection for the irradiated case. It was concluded that the basic cause of line broadening in both cases was due to stacking disorders. In general the X-ray patterns agreed with faults in the cubic close-packed sequence of basal planes, except that the broadened peaks were not observed to shift. In addition to line broadening, faulting usually produces a small but measurable line shift.

DIFFRACTION THEORY

We consider the diffraction effects due to stacking faults occurring in a cubic close-packed sequence of two atomic species. A fault is assumed to extend throughout a crystallite, a condition probably not often met in fact. The analysis closely parallels that of WARREN and WAREKOIS[10] which is equivalent to PATERSON'S[11] method. Their results are extended to include the case of two different atomic species and six layers per cell. WAGNER[12] has given the results for the more general case of both deformation and twin faulting in a cubic close-packed sequence of one atomic species.[12]

Let $\boldsymbol{A}_1$, $\boldsymbol{A}_2$, and $\boldsymbol{A}_3$ be the translation vectors of the hexagonal unit cell, and $\boldsymbol{B}_1$, $\boldsymbol{B}_2$, and $\boldsymbol{B}_3$ be their reciprocal vector set. Let $\boldsymbol{r}_m$ be the vector to atom m_1m_2 in layer m_3, where

$$\boldsymbol{r}_m = m_1\boldsymbol{A}_1+m_2\boldsymbol{A}_2+\frac{m_3}{6}\boldsymbol{A}_3+\boldsymbol{\epsilon}(m_3).$$

The vector $\boldsymbol{\epsilon}(m_3)$ is in the $\boldsymbol{A}_1\boldsymbol{A}_2$ plane and defines the stacking sequence of the layers. The intensity from the crystallite in units of the scattering from a Thompson electron is

$$I = \sum_{-\infty}^{m=\infty}\sum_{-\infty}^{m'=\infty} f_m f_{m'}^{*} \exp 2\pi i\left(\frac{\boldsymbol{S}-\boldsymbol{S}_0}{\lambda}\right)(\boldsymbol{r}_m-\boldsymbol{r}_{m'}). \quad (1)$$

Here $\boldsymbol{S}$ and $\boldsymbol{S}_0$ are unit vectors in the direction of the scattered and incident beams, and λ is the X-ray wavelength. Let $(\boldsymbol{S}-\boldsymbol{S}_0)/\lambda = h_1\boldsymbol{B}_1+h_2\boldsymbol{B}_2+h_3\boldsymbol{B}_3$ be the diffraction vector in terms of the continuous variables h_1, h_2, and h_3.

Summing over m_1m_1' and m_2m_2',

$$I = N_1N_2\delta(h_1 = H)\delta(h_2 = K)$$
$$\times\sum_{-\infty}^{m_3=\infty}\sum_{-\infty}^{m_3'=\infty} f_{m_3}f_{m_3'}^{*}\exp 2\pi i[(m_3-m_3')h_3/6+(h_1\boldsymbol{B}_1+h_2\boldsymbol{B}_2)(\boldsymbol{\epsilon}(m_3)-\boldsymbol{\epsilon}(m'_3))]. \quad (2)$$

Here N_1N_2 is the number of atoms in a layer, and assuming the layers to be large it follows that the intensity differs significantly from zero only when h_1 and h_2 are closely equal to the integers H and K.

Let $m_3-m_3' = n$, and $\boldsymbol{\epsilon}(m_3)-\boldsymbol{\epsilon}(m_3') = \boldsymbol{\epsilon}(n)$. If N_n is the number of layers having an nth neighbor, the double sum can be replaced by the single sum over n,

$$I = N_1N_2\delta(h_1 = H)\delta(h_2 = K)$$
$$\times\left\{f_{\mathrm{Na}}\cdot f_{N_3}\sum_{\substack{-\infty\\ \text{odd}}}^{n=\infty} N_n\langle\exp 2\pi i(H\boldsymbol{B}_1+K\boldsymbol{B}_2)\cdot\boldsymbol{\epsilon}(n)\rangle\right.$$
$$\times\exp 2\pi in\frac{h_3}{6}+\tfrac{1}{2}(f_{\mathrm{Na}}^2+f_{N_3}^2)\sum_{\substack{-\infty\\ \text{even}}}^{n=\infty} N_n\langle\exp 2\pi i$$
$$\left.\times(H\boldsymbol{B}_1+K\boldsymbol{B}_2)\cdot\boldsymbol{\epsilon}(n)\rangle\exp 2\pi in\frac{h_3}{6}\right\}. \quad (3)$$

The sum over even and odd values of n takes into account the alternate layers of sodium and azide ions. The displacement, $\boldsymbol{\epsilon}(n)$, between nth layers is the sum of the displacements between each intermediate neighbor pair. In the normal cubic close-packed sequence this displacement, $\boldsymbol{\epsilon}(1)$, is $\frac{1}{3}(\boldsymbol{A}_2-\boldsymbol{A}_1)$ as in Fig. 1(a). If the layers are faulted $\boldsymbol{\epsilon}(1) = \frac{1}{3}(\boldsymbol{A}_1-\boldsymbol{A}_2)$. If we assume the probability of occurrence of a fault between any two nearest layers is α, independent of all other layers,

$$\langle\exp 2\pi i(H\boldsymbol{B}_1+K\boldsymbol{B}_2)\cdot\boldsymbol{\epsilon}(n)\rangle = [(1-\alpha)$$
$$\times\exp(2\pi i(K-H)/3)+\alpha\exp(2\pi i(H-K)/3)]^n.$$

If $H-K = 3M$, M integer, the effect of faulting drops out, and such a reflection is identical to that of an unfaulted crystal. However, for $H-K = 3M\pm 1$ we have for both positive and negative n,

$$\langle\exp 2\pi i(H\boldsymbol{B}_1+K\boldsymbol{B}_2)\cdot\boldsymbol{\epsilon}(n)\rangle = Z^{|n|}\exp 2\pi in\left(\frac{1}{2}\pm\frac{\gamma}{2\pi}\right).$$

Where $Z = [1-3\alpha(1-\alpha)]^{1/2}$ and $\tan\gamma = \sqrt{(3)}(1-2\alpha)$; $-\pi/3 \leqslant \gamma \leqslant \pi/3$. For $H-K = 3M\pm 1$ equation (3) becomes*

* We use the identities: $\frac{1}{2}(A^2+B^2)\cos 2\pi nx = \frac{1}{4}(A+B)^2\cos 2\pi nx+\frac{1}{4}(A-B)^2\cos 2\pi n(x+\frac{1}{2})$, n even; $AB\cos 2\pi nx = \frac{1}{4}(A+B)^2\cos 2\pi nx+\frac{1}{4}(A-B)^2\times\cos 2\pi n(x+\frac{1}{2})$, n odd.

Vol. 2
196

$$I = \tfrac{1}{4}N_1N_2N_3\delta(h_1 = H)\delta(h_2 = K)$$

$$\times\left\{(f_{Na}+f_{N_3})^2\sum_{-\infty}^{n=\infty}\frac{N_n}{N_3}Z^{|n|}\cos 2\pi n\left(\frac{h_3}{6}\pm\frac{\gamma}{2\pi}+\frac{1}{2}\right)\right.$$

$$\left.+(f_{Na}-f_{N_3})^2\sum_{-\infty}^{n=\infty}\frac{N_n}{N_3}Z^{|n|}\cos 2\pi n\left(\frac{h_3}{6}\pm\frac{\gamma}{2\pi}\right)\right\}. \quad (4)$$

The interference function of the faulted structure is depicted in Fig. 1(b). The reflections for $H-K = 3M$ are unaffected by faulting, and those for $H-K = 3M\pm 1$ are broadened symmetrically along the HK loci and shifted up or down according to $H-K = 3M\pm 1$. For small values of α the displacement, Δ, along an HK locus is given by $\Delta = \pm(3/2\pi)\sqrt{(3)}\alpha$. The integral breadth, β, defined as the peak area divided by the peak height, is given for large particle size ($N_n \simeq N_3$, $n \gg 1$) by $\beta = 6(1-Z)/(1+Z)$.

The powder pattern is considerably simpler than that of the face-centered cubic metals; since there is a unique slip plane, no correction is needed for a multiplicity of slip planes. In a powder pattern the shifts and breadths along the H, K loci are related to the scattering angle, 2θ, by

$$\frac{2\sin\theta}{\lambda} = |B_3|\left[(H^2+K^2+HK)\left|\frac{B_1}{B_3}\right|^2+h_3^2\right]^{1/2}.$$

For $h_3 \simeq L$, an integer,

$$\Delta(2\theta^0) = \frac{360}{\pi}\tan\theta\frac{L\Delta(h_3)}{4/3(H^2+K^2+HK)|A_3/A_1|^2+L^2} \quad (5)$$

where $\Delta(h_3)$ represents Δ or β.

For the reflections unaffected by faulting, we assume that any observed broadening is due to strain only. WARREN[13] has shown that a Fourier series may be used to represent a reflection in terms of the scattering angle 2θ as

$$P(2\theta) = \sum_m A_m^a(l)\exp 2\pi imx,$$

where $P(2\theta)$ is the line profile as a function of the dimensionless variable

$$x = \frac{2a}{\lambda}(\sin\theta-\sin\theta_0)$$

for a peak centered at θ_0. The unit of distance, a, is determined from the choice of Fourier interval by

$$a = \frac{\lambda}{2}(\sin\theta_{max}-\sin\theta_{min})^{-1}.$$

The order of the reflection from the planes of spacing d is denoted by l. For strain broadening only,

$$A_m^a(l) = \langle\cos 2\pi l(\Delta L)_L/d\rangle$$
$$\simeq \exp-2\pi^2l^2\langle(\Delta L)_L^2\rangle/d^2$$

for small arguments. Here ΔL is the displacement between planes a distance $L = ma$ apart. The root-mean-square strain,

$$\langle\xi^2\rangle^{1/2} = \frac{\langle(\Delta L)_L^2\rangle^{1/2}}{L},$$

may then be determined as a function of L from

$$\langle\xi^2\rangle^{1/2} = \frac{1}{\pi ml}\left(\frac{d}{a}\right)(-\tfrac{1}{2}\ln A_m)^{1/2}. \quad (6)$$

EXPERIMENT

The sodium azide powders were prepared by triple-fractional crystallization from aqueous solution by precipitation with acetone. A saturated water solution was prepared from reagent-purity sodium azide and filtered to remove insoluble matter. About 10 per cent of the azide in the filtrate was precipitated with acetone and discarded. An additional 80 per cent of the azide remaining in the filtrate was then precipitated, washed with acetone, and dried. Examination showed the powder to be crystallites of about 8μ in size sufficiently large that particle size broadening could be neglected. However, X-ray patterns of this powder did not show the resolution expected because of the faults and strains initially present, nor did subsequent annealing improve the pattern. Thus the powder as prepared was used in the study.

Samples were ground in a motor-driven mortar and pestle; to prevent caking this was done under an atmosphere of dry nitrogen. It was found necessary to grind about two grams of powder each time to insure reproducible results. Annealing studies were done on hand ground material. Deliquescence was always a problem and samples were stored in vacuum desiccators at all times.

ol. 20
1961

Table 1. *Stacking fault probability from the* (10·2), (01·4), *and* (10·5) *reflections; root-mean-square strain at* 80 Å *from the* (11·0) *reflection; and mean lattice strain from the* (00·9) *reflection; for ground, γ-irradiated, and neutron irradiated samples*

Condition	α			$\langle \xi^2 \rangle^{1/2}$ 80Å	$-(\Delta c/c)$
	(10·2)	(01·4)	(10·5)	(11·0)	(00·9)
Initial values	0·010	0·010	0·008	0·0014	0·0000
Ground 10 min	0·021	0·025	0·022	0·0019	0·0000
Ground 30 min	0·031	0·045	0·036	0·0020	0·0000
Ground 120 min	0·035	0·046	0·041	0·0027	0·0000
γ-irr. $1{\cdot}20 \times 10^7$r	0·018	0·024	0·020	0·0018	0·0011
γ-irr. $1{\cdot}35 \times 10^8$r	0·033	0·046	0·038	0·0026	0·0019
γ-irr. $2{\cdot}48 \times 10^8$r	0·040	0·054	0·044	0·0036	0·0029
γ-irr. $5{\cdot}01 \times 10^8$r	0·046	0·064	0·057	0·0045	0·0067
n-irr. $2{\cdot}3 \times 10^{16}$nvt	0·014	0·014	0·012	0·0022	0·0011
n-irr. $6{\cdot}9 \times 10^{16}$nvt	0·025	0·032	0·027	0·0033	0·0022
n-irr. $1{\cdot}89 \times 10^{17}$nvt	0·046	0·065	0·050	0·0048	0·0041
n-irr. $2{\cdot}30 \times 10^{17}$nvt	—	—	0·058	0·0055	0·0046

All irradiations were performed at about 30°C. Gamma irradiations were done in the Co^{60} irradiation facility at Brookhaven. The samples were either sealed in evacuated quartz tubes of sufficient volume to contain gases evolved in irradiation* or kept in tubes provided with a small capillary bleed, which allowed escape of evolved gas without exposure to excessive moisture. Similar precautions were taken with the neutron irradiations done in the air-cooled hole, (W-24), of the Brookhaven reactor. Examination of these samples was delayed until the Na^{24} activity decayed to convenient levels.

The diffraction patterns were taken with a Philips diffractometer with specimen spinner and pulse height discriminator. All patterns were recorded with a copper tube run at 38 kV and 20 mA using a nickel filter and 1° divergence, scatter, and 0·006 in. receiver slits. A scanning speed of $\frac{1}{8}$°/min and chart speed of 30 in./hr were used. A Fourier interval of 6° in 2θ with ordinates spaced at every 0·025° in 2θ was chosen for all reflections. The instrumental broadening at 30·54° in 2θ was determined from the (020) reflection of tin, at 36·22° from the lead (111) reflection, at 40·48° from the molybdenum (110) reflection, and at 50·41° from the copper (200) reflection. The additional instrumental broadening due to the low absorption of sodium azide was computed[14] and applied as an additional broadening affect on the tin, lead, molybdenum, and copper reflections. The reflections used in the analysis of faulting and root-mean-square strain were STOKES[15] corrected for these instrumental affects. Transforms were computed and corrected coefficients found by machine computation on a small punch-card computer.

The integral breadths in scattering angle, 2θ, were transformed into β along $\boldsymbol{B}_3$ by equation (5) and the faulting probability, α, determined accordingly. As mentioned previously, within the limits of experimental error, line shifts of the expected magnitude were not observed. The (10·2), (01·4), and (10·5) reflections were used to determine α. The root mean square strains normal to the (11·0) planes were determined from the (11·0) reflection by equation (6), and in the irradiated cases the lattice contraction from the (00·9) reflection. This choice of reflections was governed by the fact that they were relatively intense and free of overlap with other reflections. These conditions, in particular the lack of well resolved reflections of

* A positive pressure was observed after irradiation indicating some diffusion of nitrogen which might possibly have affected HEAL's[2] gas analysis.

Vol. 2
196

multiple order, severely limited the analysis for strains. However, it can be said that the root mean-square strains normal to the (00·L) planes were always smaller than in the (00·L) planes since the (00·L) reflections were the least broadened. While strain would affect the faulting parameter, α, as determined from a breadth measurement (the value thus determined would be too large), it is probably not a large error. Table 1 lists the faulting probability, α, for a number of cases as determined from the (10·2), (01·4), and (10·5) reflections; the root-mean-square strain perpendicular to the (11·0) planes at 80 Å; and the mean lattice strain (contraction) as determined from the (00·9) reflection. As strain becomes a more effective broadening agent with increasing scattering angle, the faulting parameter, if severly in error due to strains, should increase in magnitude in going from the (10·2) to the (10·5) reflections in the table. Such a trend is not discernible within the accuracy of the data.

RESULTS AND DISCUSSION

Table 1 summarizes the effects of the various methods of damaging sodium azide. The material as initially prepared contained a small amount of faulting and strain. We are not prepared to say whether this faulting is due to deformation faults (stacking faults) or growth faulting (twin faults), although in principle there is detectable X-ray difference.[12] Fig. 3 shows the increase in fault probability and strain as a function of mechanical deformation (grinding time). The initial rapid increase in faulting indicates large initial susceptibility of the structure to faulting which later shows a strong tendency to saturate. In all graphs the stacking fault probability is that from the (10·5) reflection and the root-mean-square strain the value at 80 Å as found from the (11·0) reflection. There are no signs of decomposition such as coloration, lattice contraction, and lowering of the ignition temperature in the mechanically deformed specimens. These results are taken to indicate that faulting is a major imperfection in sodium azide. Here it appears that a structure derived from the NaCl structure can contain stacking faults. FRANK[16] has stated that stacking faults should not be observed in a NaCl structure. In the NaCl structure faulting is energetically not favorable since a fault shortens second neighbor bonds (similar charges) by 18·4 per cent. However, in sodium azide this distance is decreased only 7·7 per cent by a fault.

The effects of gamma and reactor irradiation upon the diffraction pattern of sodium azide are similar and resemble those of grinding, as can be

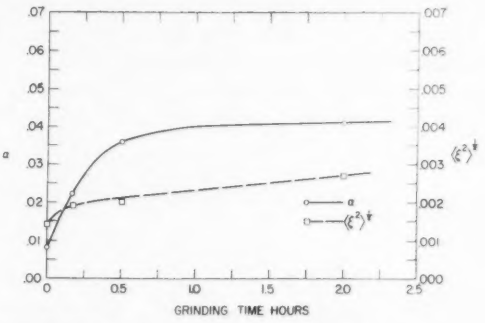

FIG. 3. Stacking fault probability and root-mean-square strain against grinding time in hours.

seen in examining Figs. 2(a) and (b); the most significant difference is the displacement of the (00·9) reflection. The (00·L) reflections were always observed to shift upon irradiation indicating

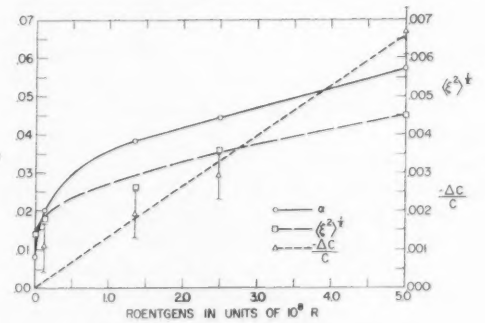

FIG. 4. Stacking fault probability, root-mean-square strain, and mean lattice strain against γ-ray dosage in roentgens.

a shrinkage in the A_3 direction. Since the long dimension of the azide ion extends in this direction, decomposition of the ion by ionization from the irradiation correlates with this observation. A decreased layer spacing, coloration, and lower ignition temperature, indicative of decomposition,

were always found in the irradiated specimens. In Fig. 4 the faulting probability, root-mean-square strain, and mean lattice strain, $\Delta c/c$, are plotted against γ-ray dosage in roentgens. Again there is a rapid initial increase in faulting and root-mean-square strain, which tend to saturate, while the new feature, the mean lattice strain (contraction), is proportional to dosage. The root-mean-square strains, both in and normal to the basal planes, tend to be larger than in the ground samples for the same faulting probability [not plotted, the $(00\cdot L)$ reflections showed broadening not observed in the ground samples]. These parameters are plotted in Fig. 5 for the neutron-irradiated specimens against total integrated neutron flux, nvt. The results are qualitatively similar, but quantitative differences are evident.

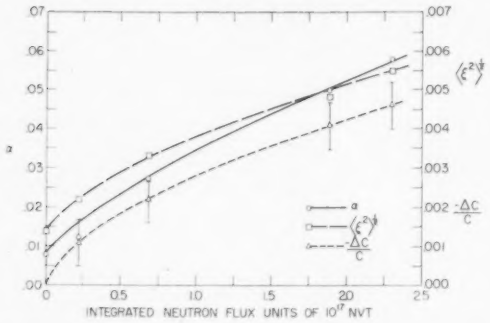

FIG. 5. Stacking fault probability, root-mean-square strain, and mean lattice strain against total integrated neutron flux.

The production of stacking faults in the ground specimens is likely governed by the motion of SHOCKLEY[17] partial dislocations or twinning[18] dislocations along the basal planes under the influence of complicated stress fields induced by grinding. If under the application of a stress a partial dislocation in the form of a ring expands over the slip plane the faulted region expands, and similarly as a partial dislocation anchored at a point sweeps over the slip plane there is an increase in the faulted region. If a succession of rings or spirals are generated at the same place and spread outward one after another, the net effect is that of slip, but with the additional feature that as the dislocation lines come to rest they delineate alternate bands of faulted and unfaulted material. Such Frank–Read sources[19] probably abound in the virgin material since it initially contained faults and strain. Certain complete dislocations may split into partial dislocations[17]: e.g. $[11\cdot0] \rightarrow \frac{1}{3}[21\cdot0] + \frac{1}{3}[12\cdot0]$. As the two partials separate, a sheet of stacking fault is formed between them. These Shockley partial dislocations have Burgers vectors in the basal planes, as a consequence there is little component of strain normal to the basal planes which is in agreement with the observed sharpness of the $(00\cdot L)$ reflections and broadening of the $(11\cdot0)$ reflection in the ground cases. This argument can be used to rule out the presence of a large number of dislocations of the type with Burgers vectors having components normal to the basal planes in the virgin or ground samples, e.g. FRANK[20] sessile type dislocations.

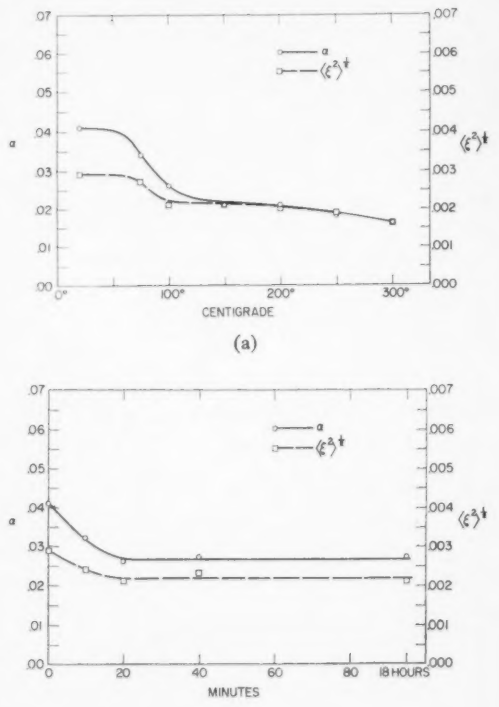

FIG. 6. Stacking fault probability, and root-mean-square strain for a sample ground one hour (a) annealed isochronally 20 min each point, (b) annealed isothermally at 100°C each point.

Vol. 2
196

In Fig. 6(a) the faulting probability and root-mean-square strain for a sample ground one hour are plotted as a function of annealing temperature ($t = 20$ min). Near 100°C approximately 40 per cent of the faults are removed, accompanied by considerable strain relief. A larger recovery is observed at higher temperatures, but some of the faults and strain remain in excess of the virgin material even at 300°C. In Fig. 6(b) these parameters are plotted for an isothermal anneal at 100°C. From analysis of our annealing data it was concluded that the removal of the faults is not a single activation process. Those faults readily removed around 100°C may terminate in partial dislocations which, upon increasing the available thermal energy, are able to move by glide in such a way as to reduce the faulting and strain energy. Some of the faults remaining after annealing may extend throughout the crystallite. Such faults do not terminate at high stress concentrations and would be the most stable since their energy is of the order of a twin boundary. However, since the remaining root-mean-square strains are also significantly higher than for the virgin material, it is more probable that a locking mechanism is present which reduces the ease of glide of some of the partial dislocations associated with faults. A likely locking mechanism is the jogs[17] introduced by cross slip. It is possible that $\frac{1}{3}[12\cdot1]$ slip on $(2\bar{1}\cdot0)$ planes occurs, since this is the slip direction and plane in the NaCl structure from which sodium azide can be derived. Such a locking mechanism would explain the saturation phenomenon of the faulting and strain. Dislocation jogs could conceivably cover a spectrum of activation energies accounting for the observed absence of a single activation energy. However COTTRELL and AYTEKIN[21] have shown formally that even for a single type mechanism the activation energy for recovery can increase with decreasing (internal) stress.

Calculations have been made for the effectiveness of the X-rays employed in diffraction, the Co^{60} source and the reactor in producing decomposition. At 30°C approximately 0·033 decomposition is produced per electron volt absorbed.[2] The X-ray diffraction unit produced about 0·0003 per cent decomposition per hour, or a negligible decomposition in a normal run. The Co^{60} source caused 9×10^{-11} decomposition per roentgen or a 4·5 per cent decomposition in the $5\cdot01\times10^{8}$r sample. The reactor produced about $1\cdot44\times10^{-20}$ decomposition per nvt, or a 3·3 per cent decomposition in the $2\cdot3\times10^{17}$ nvt sample. Although the Co^{60} and pile irradiations are both equivalent to charged particle irradiations, there is a vast difference in the density of ionization along the paths of the ionizing particles produced by the two sources. The Co^{60} source produces Compton electrons of a mean energy around 0·56 MeV. These Compton electrons then ionize the sample along their paths. In the reactor, the pile γ-flux and the 1·39 MeV electrons from the $Na^{24}(\beta\gamma)Mg^{24}$ decay produce electrons of similar energies amounting to only 19 per cent of the total decomposition. However, the major part of the decomposition (81 per cent) in the reactor is produced by heavy charged particles from the "knock-ons" produced by fast neutrons and the $N^{14}(n, p)C^{14}$ reaction (both mechanisms are about equally effective*). These heavy particles produce dense columnar ionization some thousands of times more intense than the electrons over much shorter paths.

In light of the difference in these processes the Co^{60} irradiation would be expected to produce a more homogeneous decomposition in the crystal, whereas the reactor would be expected to produce patches of heavy decomposition interspersed by relatively undamaged material. The strain associated with decomposition, the shrinkage in the A_3 direction, will vary with the degree of decomposition of any region of the crystal and internal stresses must develop since these regions are joined so that each constrains the other to an unnatural size or shape. Such stresses must then cause dislocation movement and faulting. The more inhomogeneous the decomposition, the larger these types of internal stresses.

The internal stresses induced by decomposition and the external stresses from grinding probably produce dislocations with Burgers vectors having components normal to the basal planes. However, such dislocations can produce faults. COTTRELL and BILBY[22] have proposed a dissociation whereby a

* The number of displacements produced by these two processes is about $1\cdot6\times10^{-21}$ per nvt per NaN_3 molecule, the $N^{14}(n, p)C^{14}$ process producing about 75 per cent of the displacements. For the sample irradiated to $2\cdot3\times10^{17}$ nvt this amounts to 0·00037 displacements per NaN_3 molecule, an amount negligible compared to the number of decomposition products.

complete dislocation can split into two partials viz: $\frac{1}{3}[12\cdot1] \rightarrow \frac{1}{3}[00\cdot1]+\frac{1}{3}[12\cdot0]$. The $\frac{1}{3}[00\cdot1]$ is a sessile dislocation lying in (00·1) and along with the $\frac{1}{3}[12\cdot1]$ forms a pole for the $\frac{1}{3}[12\cdot0]$ Shockley partial to sweep in (00·1). In one revolution the $\frac{1}{3}[12\cdot0]$ must meet the sessile $\frac{1}{3}[00\cdot1]$, and only one revolution can occur and only a monolayer of stacking fault is formed. In sodium azide a dislocation like $\frac{1}{3}[00\cdot1]$ involves two layers of opposite charge.

It is possible that decomposition produces vacancy clusters lying on (00·1) planes. Such a cluster would in view of charge considerations involve two (00·1) planes. The disk-like region can form either a complete dislocation e.g. $\frac{1}{3}[12\cdot1]$ of the *R*-type discussed by WILSDORF[23] or the sessile $\frac{1}{3}[00\cdot1]$ and a stacking fault. The latter probably would compete with the former since the Burgers vector is smaller.

The quantitative differences between the Co^{60} and reactor irradiations are clearly evident in Figs. 4 and 5. The initial rapid increase in faulting is less conspicuous in the neutron irradiated specimens, and the faulting and root-mean-square strains are more proportional to the mean lattice strain than in the gamma irradiated specimens. There is clearly a difference in the isochronal annealing of the gamma and neutron irradiated specimens as is evident in Figs. 7(a) and 8(a). Annealing the neutron irradiated specimens causes a large increase in mean strain as the temperature is raised before a decrease in mean strain sets in, and

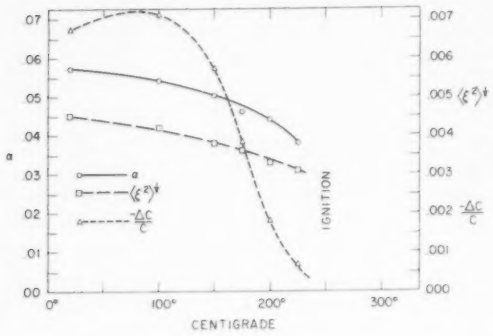

FIG. 7. Stacking fault probability, root-mean-square strain, and mean lattice strain for a sample γ-irradiated to $5\cdot01\times10^{8}$r (a) annealed isochronally 20 min each point, (b) annealed isothermally 200°C each point.

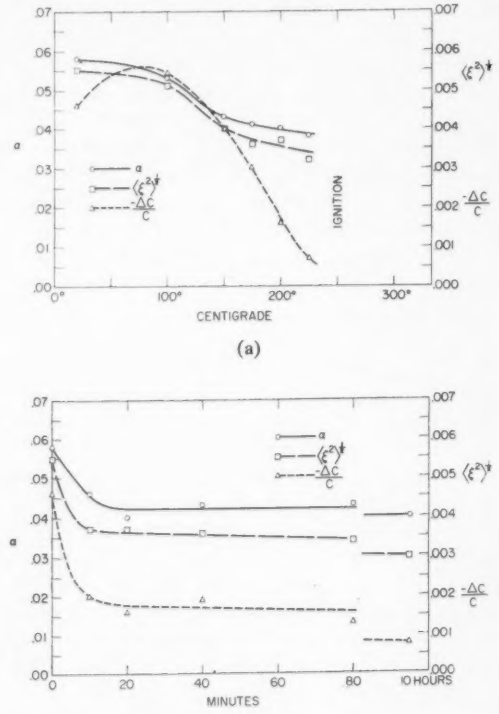

FIG. 8. Stacking fault probability, root-mean-square strain, and mean lattice strain for a sample neutron-irradiated to $2\cdot3\times10^{17}$ nvt (a) annealed isochronally 20 min each point, (b) annealed isothermally 200°C each point.

Vol. 2
196

there is a decrease in root-mean-square strain and faulting at about 120°C reminiscent of the decrease in these quantities at about 75°C for the ground case. This seems to be entirely absent in the gamma irradiated specimens, and the mean strain overshoot is considerably less.

In any explanation of the observed differences in the effects of gamma and pile irradiations, one must recognize that to an appreciable extent effects characterizing the gamma irradiation are also present in the neutron irradiation. However, certain differences may be explained.

The gamma irradiation produces a homogeneous decomposition with a uniform distribution of decomposition products and vacancies. There is a shrinkage of the structure in the A_3 direction (parallel to the azide ion) since the azide ion vacancies are more effective in producing contraction than decomposition products are in producing dilation. The internal stresses developed by a uniform distribution of defects are very efficient in producing slip and faulting accompanied by root-mean-square strains in the basal planes. Additional root-mean-square strains in and normal to the basal planes arise from defects of decomposition. As the irradiation proceeds, dislocation movement becomes more restricted by the development of jogs and the increased number of defects. The increased number of defects increases the effectiveness of pinning by the development of COTTRELL[24] atmospheres. Thus faulting and root-mean-square strains in the basal planes begin to saturate with gamma dose.

In contrast to the gamma irradiation, neutron irradiation produces heterogeneous decomposition or small dense patches of decomposition products and vacancies in a relatively undamaged matrix. There is a shrinkage of the lattice in the A_3 direction, but the imperfections when clustered are less effective than a uniform distribution in producing a mean strain. Internal stresses of constraint develop between the small heavily damaged region and the less damaged matrix, causing larger root-mean-square strains in and normal to the basal planes than in the gamma case. Slip and faulting are induced by these stresses in the less damaged matrix, and along with root-mean-square strain are proportional to the number of such decomposed regions, which in turn is proportional to neutron dose.

In the early stages of annealing the gamma irradiated specimens, the decomposition products are removed first.* The removal of such centers of dilation causes a further small lattice contraction, but little change in root-mean-square strain and faulting. As the temperature is raised, vacancy removal starts decreasing the mean strain. The increase in diffusion decreases the effectiveness of locking mechanisms, and faulting and root-mean-square strains decrease. These processes accelerate with increasing temperature. Stoichiometry is restored as indicated by the small residual mean strain, but a considerable number of faults and accompanying root-mean-square strains remain. Carbonates of sodium are detectable.

In the early stages of annealing the neutron irradiated specimens, decomposition products and vacancies migrate away from the badly decomposed regions. Removal of decomposition products (centers of dilation) and especially the dispersion of azide ion vacancies cause a larger increase in mean strain than in the gamma case. The mean strains of the decomposed and less damaged regions are made more equal by the dispersion of vacancies with a reduction in the stresses of constraint. It is reasonable to expect the vacancies to be more effective in producing contraction when dispersed in a less damaged matrix, than when concentrated in a less coherent region of high damage. ESHELBY[25] has shown (for an elastically isotropic sphere) that the X-ray lattice parameter can depend strongly on the (non-uniform) distribution of point defects, so that again a redistribution of such defects accounts for the large overshoot in mean strain. At higher temperatures vacancy removal reduces the mean strain and pinning; the more uniform dispersion of vacancies reduces the stresses of constraint, allowing a quasi reversible slip which reduces faulting and root-mean-square strain in a manner similar to the ground case. At higher temperatures the reduction in mean strain, faulting, and root-mean-square strains is accelerated much as in the gamma case. When stoichiometry is achieved, the gamma and neutron specimens show

* All well annealed irradiated samples showed weak extra reflections traceable to carbonates of sodium. However, it was impossible to check at what stage of annealing sodium diffusion occurred, since annealing may have been necessary for a detectable (well crystallized) compound to form.

Table 2. Chronology of damage to sodium azide induced by mechanical deformation (grinding), gamma irradiation, and neutron irradiation; and effects of annealing these damaged structures

Mechanical deformation	Gamma irradiation	Neutron irradiation
(1) No decomposition.	(1) Homogeneous decomposition produces a more uniform distribution of decomposition products and vacancies.	(1) Heterogeneous decomposition produces small dense patches of decomposition products and vacancies in relatively undamaged matrix.
(2) No mean strain observed.	(2) Vacancies (especially azide ions) are more effective in producing mean strain (contraction) than decomposition products (dilation). Lattice starts contracting in A_3 direction. Uniform distribution of defects is most effective in producing mean strain.	(2) Same as γ-case, except that imperfection clusters are less effective than uniform distribution in producing mean strain.
(3) Externally applied stresses introduce dislocations and dislocation movement generating stacking faults with r.m.s. strain in basal planes, due to faults. Little r.m.s. strain observed normal to basal planes.	(3) Internal stresses developed by random point defects generate faults with r.m.s. strain in basal planes. Additional r.m.s strain in and normal to basal planes due to decomposition.	(3) Internal stresses of constraint develop between small heavily damaged regions and larger less damaged regions, causing large r.m.s. strains in and normal to basal planes and slip and faulting (in less damaged regions).
(4) Dislocation motion becomes more restricted by introduction of cross slip and jogs. Faulting and r.m.s. strain tend to saturate.	(4) Same as ground case, except that increased number of defects increases effectiveness of pinning by Cottrell atmosphere. Faulting and r.m.s. strain in basal plane show saturation with increasing γ-dose.	(4) Faulting (in less damaged region) and r.m.s. strains proportional to number of highly decomposed regions, which in turn is proportional to neutron dose.
Annealing mechanical deformation	**Annealing γ-ray damage**	**Annealing neutron damage**
(1) Thermal energy activates dislocation motion, allowing quasi reversible slip with precipitous reduction in faulting and r.m.s. strain.	(1) Removal of decomposition products (centers of dilation) causes further small increase in mean strain (contraction) with little decrease in faulting and r.m.s. strains.	(1) Decomposition products and vacancies migrate away from badly decomposed regions. Removal of decomposition products (centers of dilation) and especially dispersion of azide ion vacancies causes a large increase in mean strain. Mean strain of decomposed and less damaged regions start to equilibrate.
(2) Little change.	(2) Vacancy removal starts decreasing mean strain. Diffusion processes decrease effectiveness of locking mechanisms (Cottrell atmosphere and jogs.) Faulting and r.m.s. strain decrease slowly.	(2) Vacancy removal starts reducing mean strain, and further dispersion of vacancies reduces stresses of constraint, allowing quasi reversible slip with large reduction in faulting and r.m.s. strain.
(3) Higher temperatures increase diffusion processes which decrease effectiveness of locking mechanisms reducing faulting and r.m.s. strains.	(3) Higher temperatures hasten vacancy removal, with accompanying rapid decrease in mean strain. Diffusion processes cause locking mechanisms to become less effective than at lower temperatures. Faulting and r.m.s. strains decrease.	(3) Same.
(4) Some faults and r.m.s. strains still present in excess of virgin material. No carbonates of sodium observed.	(4) Stoichiometry is nearly restored (almost all vacancies and decomposition products removed). Mean strain is very small, but considerable faulting, and r.m.s. strain remain locked in. Carbonates of sodium now detectable.	(4) Same.

identical features. The chronology of inducing damage in sodium azide by grinding, gamma irradiation, and neutron irradiation as well as the effects of annealing is summarized in Table 2.

Both the gamma and neutron irradiated specimens ignited at 250°C and burned (the annealing was done in air). It is tempting to postulate that the stored energy release was so rapid that ignition occurred. However, it is likely that a decomposition product, e.g. colloidal sodium, may have been ignited, or acted as a catalytic agent.

Since the irradiated samples show a much larger retained faulting and strain after annealing, it is likely that in addition to dislocation jogs there is additional pinning of dislocations by the Cottrell atmospheres of decomposition products. Further, it seems likely that sessile dislocations with stacking faults form in the irradiated cases. In any case diffusion is required to remove these imperfections, which would account for the slower and less effective recovery of the irradiated samples.

SUMMARY

Mechanical deformation produces faulting in sodium azide which probably results from the motion of dislocations under externally applied stresses. There are no signs of decomposition, and strain and faulting can be effectively reduced by annealing. γ-ray and reactor irradiations produce decomposition, faulting, and strain, the faulting probably resulting from the motion of dislocations under internal stresses resulting from decomposition. The two irradiations produce qualitatively similar results, but differ quantitatively probably due to the greater inhomogeneity of decomposition in reactor irradiation. Stoichiometry is apparently achieved upon sufficient annealing of the irradiated specimens, as evidenced by the disappearance of the mean strain, but faulting and root-mean-square strain do not anneal out as readily as in the ground cases. Such evidence is taken to indicate pinning by some of the decomposition products and the presence of sessile dislocations with stacking faults.

Acknowledgements—The authors are indebted to Dr. J. V. R. KAUFMAN of Picatinny Arsenal for the initiation of this program and to Dr. G. J. DIENES of the Solid State Group at Brookhaven National Laboratory whose support and interest made this work possible. The authors would like to thank the members of the Solid State Group at Brookhaven for their many valuable discussions.

REFERENCES

1. HEAL H. G., *Canad. J. Chem.* **31,** 1153 (1953).
2. HEAL H. G., *Trans. Faraday Soc.* **53,** 210 (1957).
3. ROSENWASSER H., DREYFUS R. W. and LEVY P. W., *J. Chem. Phys.* **24,** 184 (1956).
4. WYCKOFF R. W. G., *Crystal Structures* Vol. II, Chapter 6, table, p. 7. Interscience, New York (1957).
5. WYCKOFF R. W. G., *Crystal Structures* Vol. II, Chapter 6, p. 7. Interscience, New York (1957).
6. HENDRICKS S. B. and PAULING L., *J. Amer. Chem. Soc.* **47,** 2904 (1925).
7. FREVEL L. K., *J. Amer. Chem. Soc.* **58,** 779 (1936).
8. BASSIÈRE M., *J. Chim. Phys.* **36,** 71 (1939).
9. BASSIÈRE M., *C.R. Acad. Sci., Paris* **208,** 659 (1939).
10. WARREN B. E. and WAREKOIS E. P., *Acta Met.* **3,** 473 (1955).
11. PATERSON M. S., *J. Appl. Phys.* **23,** 805 (1952).
12. WAGNER C. N. J., *Acta Met.* **5,** 427 (1957).
13. WARREN B. E., *Acta Cryst., Camb.* **8,** 483 (1955).
14. KEATING D. T. and WARREN B. E., *Rev. Sci. Instrum.* **23,** 519 (1952).
15. STOKES A. R., *Proc. Phys. Soc. Lond.* **61,** 382 (1948).
16. FRANK F. C. and NICHOLAS J. F., *Phil. Mag.* **44,** 1213 (1953).
17. HEIDENREICH R. D. and SHOCKLEY W., *Report of a Conference on the Strength of Solids, University of Bristol, England,* p. 57. Physical Society, London (1948).
18. HALL E. O., *Twinning* Chapter 6, p. 115. Butterworths, London (1954).
19. FRANK F. C. and READ W. T., *Phys. Rev.* **79,** 722 (1950).
20. FRANK F. C., *Proc. Phys. Soc. Lond.* **A62,** 202 (1949).
21. COTTRELL A. H. and AYTEKIN V., *J. Inst. Met.* **77,** 389 (1950).
22. COTTRELL A. H. and BILBY B. A., *Phil. Mag.* **42,** 573 (1951).
23. WILSDORF D., *Phil. Mag.* **3,** (8), 125 (1958).
24. COTTRELL A. H., *Report of a Conference on the Strength of Solids, University of Bristol, England,* p. 30. Physical Society, London (1948).
25. ESHELBY J. D., *J. Appl. Phys.* **25,** 255 (1954).

LETTERS TO THE EDITOR

The effect of magnetic anisotropy in cobalt ferromagnetic thin films

(*Received* 25 *July* 1960; *revised* 7 *November* 1960)

THIN ferromagnetic films, with a thickness smaller than approximately 10^{-5} cm are single domains, magnetized in a direction parallel to the surface of the thin film.[1] In this paper we shall deal with cobalt thin films, with a few monatomic layers, crystallized in hexagonal close packed lattice, with the axis (0001) perpendicular to the surface of the film, We shall assume that the axis (0001) is also the easy direction of magnetization (the magnetic anisotropy axis). Theoretical studies of single domain thin films are due to KLEIN *et al.*[2,3], VALENTA[4], CORCIOVEI[5]. The theory of KLEIN *et al.* is based on the Block spin wave approach, whereas the latter two scientists have applied Heisenberg's theory. VALENTA has obtained ferromagnetism even for monatomic thin film, but CORCIOVEI, in the second approximation, has obtained that thin films can support ferromagnetism only if the number q of monatomic layers of the film is equal or greater than two.

VALENTA and CORCIOVEI have obtained for a given thickness a greater Curie temperature than the experimental results of DRIGO[6] and COLOMBANI[7]. According to these works the saturation magnetization of films thinner than about 100 Å decreases much more rapidly with increasing temperature, than that of the bulk material, thus the Curie temperature for such films is lower than the Curie temperature of the bulk material. More recently, NEUGEBAUER[8], from his experimental results for nickel, concluded that thin films less than 100 Å thick have a Curie temperature equal to that of bulk nickel at least down to a thickness of 27 Å. But below 27 Å it is very possible that the Curie temperature decreases with decreasing thickness. Such a situation can be easily explained by the theory of VALENTA and it is no more necessary the hypothesis of superparamagnetic particles of NEUGEBAUER.

In the quoted theoretical papers (KLEIN, VALENTA, CORCIOVEI), the anisotropy term in the Hamiltonian is not taken into account. In this paper we shall try to introduce an anisotropy term, and to see what are the theoretical consequences concerning magnetic properties. We shall write the Hamiltonian in the form

$$H = H^{\text{ex}} + H^{\text{anis}} \tag{1}$$

where H^{ex} is the common exchange term, and H^{anis} is written in the form:

$$H^{\text{anis}} = -K_0 \sum_k S_k^{(a)2} - 2K \sum_{(k,k')} S_k^{(a)} S_{k'}^{(a)} \tag{2}$$

where K_0 and K are positive anisotropy constants, $S_k^{(a)}$ is the operator of projection on the anisotropy axis of the spin (supposed of $\frac{1}{2}$ value) of the k atom, and the summation

$$\sum_{(k,k')}$$

is performed only on the distinct pairs of nearest neighbours k and k'. We shall develop Heisenberg's traces method in second approximation. The form (2) of the anisotropy term, is an improved form of the ordinarily used one

$$-K_0 \sum_k S_k^{(a)2},$$

which cannot be used in our case, because it gives insignificant, constant contributions in the traces. The form (2) agrees with the general considerations concerning magnetic anisotropy.

A quantum state of the system is determined by giving the projections of all atomic spins on to the magnetization axis (situated in the plane of the film). By calculating the matrix elements of the Hamiltonian between the quantum states, we can then obtain the traces of the Hamiltonian. The diagonal matrix elements of H^{anis} are constant and equal to $-(K_0/4)Nq$, where N is the number of atoms in a monatomic layer. The nondiagonal matrix elements of H^{anis} are nonvanishing only between two states which differ by the reversing of spins of two nearest neighbours. In such a case the matrix element is $-K/2$.

We denote by y_i the relative magnetization of layer i (i.e. the ratio between the actual magnetization and the saturation magnetization of the

i layer). A thermodynamic state m of the system can be characterized by the set of all y_i ($i = 1, \ldots, q$). In view of calculating the partition function for a thermodynamic state m, we shall apply the formula

$$Z(m) = f(m) \exp\left(-\frac{\overline{E_m}}{kT}\right) \exp \frac{\overline{\Delta E_m^2}}{2(kT)^2} \quad (3)$$

where $f(m)$ is the number of quantum states corresponding to the thermodynamic state m, and $\overline{E_m}$, $\overline{\Delta E_m^2}$ are mean values in the thermodynamic state m of the energy and respectively of $(E_m - \overline{E_m})^2$. Let us denote by H_m the submatrix of the Hamiltonian which contains all the elements between two quantum states corresponding to the same thermodynamic state m, and denote by $(H^2)_m$ the submatrix of H^2, where the elements of H^2 are restricted in the same manner. We have

$$\overline{E_m} = \frac{1}{f} \operatorname{tr} H_m, \quad \overline{\Delta E_m^2} = \frac{1}{f} \operatorname{tr} (H^2)_m - \left(\frac{1}{f} \operatorname{tr} H_m\right)^2 \quad (4)$$

The calculation can be performed in the same manner as by CORCIOVEI[5] and the differences arise from the anisotropy term (2). One obtains significant contributions only for $\overline{\Delta E_m^2}$. In order to find the equations at thermodynamic equilibrium for the quantities y_i it is necessary to equate to zero the expressions $\partial \log Z_m / \partial y_i$ ($i = 1, \ldots, q$). One obtains the following system of implicit equations:

$$y_i = \operatorname{th}\{\tfrac{1}{2}\beta \sum_{j=1}^{q} z_{ij} y_j + \tfrac{1}{4}\beta^2 \sum_{j=1}^{q} [-z_{ij}(y_i + y_j + \alpha y_j) + z_{ij} y_i y_j^2]\} \quad (i = 1, \ldots, q) \quad (5)$$

where $\beta = A/(kT)$, $\alpha = K/A$ and z_{ij} is the number of nearest neighbours situated in layer j of any atom belonging to the layer i, A being the exchange integral between two nearest neighbours. The equations (5) are the same as equation (20) from Ref. (5) if $\alpha = 0$, i.e. if $K = 0$. One sees also that K_0 does not appear in (5), i.e. the ordinary anisotropy term

$$-K_0 \sum_k S_k^{(a)2}$$

does not contribute to (5).

The relative magnetization of the entire film is given by

$$y = \frac{1}{q} \sum_{i=1}^{q} y_i \quad (6)$$

In principle it is possible to obtain from (5) and (6) the dependence $y = y(T, q, \alpha)$ and also the Curie temperature T_c as a function of q and α. To obtain T_c one considers the system of equations

$$y_i = \tfrac{1}{2}\beta \sum_{j=1}^{q} z_{ij} y_j + \tfrac{1}{4}\beta^2 \sum_{j=1}^{q} [-z_{ij}(y_i + y_j + \alpha y_j)] \quad (i = 1, \ldots q) \quad (7)$$

which result from (5) by series expansions and by retaining only the first degree terms containing y_i, and requires the conditions that this system has non-vanishing solutions, i.e. the determinant of coefficients be equal to zero. In Fig. 1 we have selected some of the results obtained for T_c of cobalt thin film, using the electronic computer. We have traced $x = T_c/T_c^{(\infty)}$ (where $T_c^{(\infty)}$ is Curie temperature for a solid cobalt with $\alpha = 0$) as a function of q until $q = 10$ for different α. The solutions for $q \to \infty$ are represented as horizontal asymptotes. The given results are situated in a region where the experimental results are not certain ($q < 10$). It is well known the disaccord between the experimental results of DRIGO[6] COLOMBANI[7] and NEUGEBAUER[8]. The theory predicts that T_c must be lower (T_c decreases also when α increases) for very thin films ($q < 10$) as for bulk material. It is possible that α be not negligible for very thin films. In such a case ferromagnetism can appear only for q greater than a $q_{\min}$ (which depends on α). This is not in disaccord with HERRING and KITTEL[9], because they deal with an easy axis of magnetization parallel with the magnetization, and in our case the two axes are perpendicular.

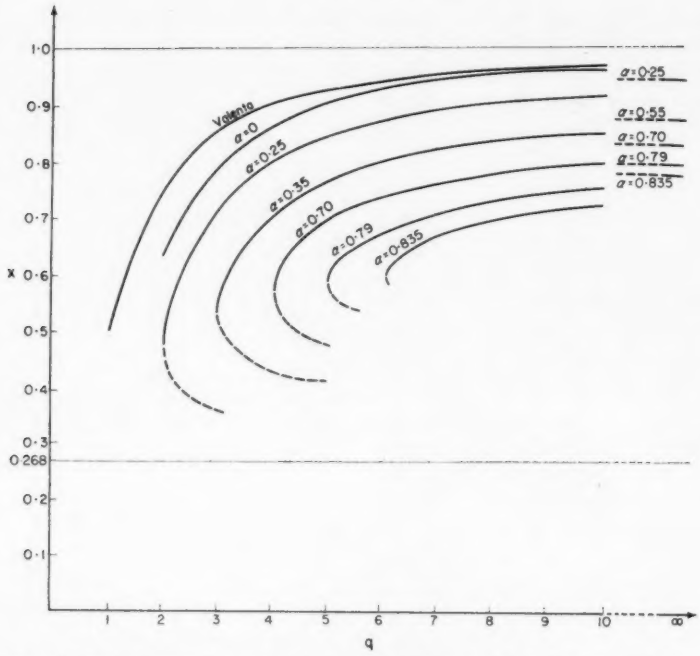

FIG. 1. Curie temperature as a function of thickness of thin film, for different values of the coefficient α.

In this paper we have given only a theoretical study for ferromagnetic thin films, taking also account of an anisotropy term in the Hamiltonian. It will be a pleasure for us if experimental works would clarify the magnetic properties to such thin films ($q < 10$). Further details are appearing in *Czech. J. Phys.*

Institute for Atomic Physics A. CORCIOVEI
Bucharest

References

1. KITTEL Ch., *Phys. Rev.* **70,** 965 (1946).
2. KLEIN M. J. and SMITH R. S., *Phys. Rev.* **81,** 378 (1951).
3. GLASS S. J. and KLEIN M. J., *Phys. Rev.* **109,** 288 (1958).
4. VALENTA L., *Czech. J. Phys.* **7,** 127 (1957); **7,** 136 (1957).
5. CORCIOVEI A., *Czech. J. Phys.* **10,** 568 (1960).
6. DRIGO A., *Nuovo Cim.* **8,** 498 (1951).
7. COLOMBANI A., GOUREAUX G. and HUET P., *J. Phys. Radium* **20,** 303 (1959).
8. NEUGEBAUER C. A., *Phys. Rev.* **116,** 1441 (1959).
9. HERRING G. and KITTEL Ch., *Phys. Rev.* **81,** 869 (1951).

Electron mobility in indium arsenide

(*Received* 21 *December* 1960)

THE NATURE and quantity of the residual impurities in high quality indium arsenide have been determined[1] using a mass spectrometric solid analysis method. The samples all showed electron type conduction and the analyses suggested that no appreciable compensation existed in any of the specimens examined. The room temperature electron mobility of all samples lay between 22×10^3 and 25×10^3 cm^2/V sec, while at 77°K, where ionized impurity scattering is dominant, a much wider spread in mobility was observed. In Fig. 1, the Hall mobilities ($R\sigma$) of these specimens and others have been plotted against Hall coefficient (R). The material of low Hall coefficient was obtained by deliberate doping with sulphur.

With one or two exceptions the spread in mobility for material of given Hall coefficient is not greater than about 25 per cent. Sufficient information exists regarding the properties and band structure of indium arsenide to permit a

theoretical estimate of the electron mobility and its dependence on impurity concentration. By this means it may be possible to check the analytical conclusions regarding the absence of compensation in the samples measured.

EHRENREICH[2] has discussed the importance of polar optical mode scattering in indium antimonide and shown that this, and not deformation potential scattering, is the main limitation to the rate of electron transport. Theoretical values for mobility between 200°K and 500°K show good agreement with experimental results. Indium arsenide is more strongly polar than indium antimonide and it is to be expected that polar scattering should again be the prime mechanism. A value of 22×10^3 cm^2/V sec at room temperature is obtained[3, 4] for the polar limited electron mobility in InAs and this is in excellent agreement with the experimental values for pure samples.

The expression given by EHRENREICH for polar limited mobility reduces to

$$\mu_{OPT} = 3{\cdot}1 \times 10^{31} \times \left(\frac{T}{300}\right)^{1/2} \times \left(\frac{e}{e^*}\right)^2 \times \left[\frac{m}{m^*}\right]^{3/2} M a^3 \nu [\exp(h\nu/kT) - 1] Y \qquad (1)$$

where e^* is an effective ionic charge obtained from restrahlen data and equal to $0{\cdot}22e$ for InAs. M is the reduced mass of the indium and arsenic atoms, a the lattice constant and ν the fundamental optical frequency. Y is a function of $h\nu/kT$ and the electron plasma frequency and may be estimated from data given by EHRENREICH[5]. m^*/m is the effective electron mass ratio which at room temperature for InAs is, by general consent, equal to 0·03, but at low temperatures may fall to 0·025.[6]

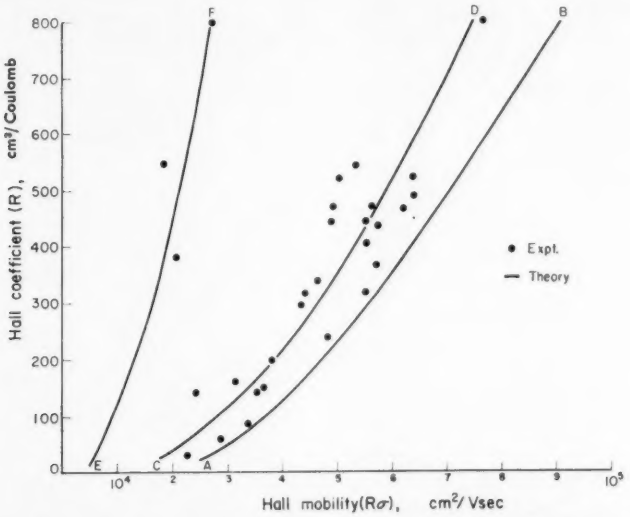

FIG. 1. Hall mobility of electrons in InAs at 77°K vs. Hall coefficient. Theoretical curves AB ($m^*/m = 0{\cdot}025$); CD ($m^*/m = 0{\cdot}03$); EF ($m^*/m = 0{\cdot}03$) compensated as in text.

Substitution in (1) for a temperature of 77°K and electron concentration of 10^{16}/cm^3 gives values for the mobility.

$$\mu_{OPT} = 8{\cdot}7 \times 10^5 \text{ cm}^2/\text{V sec for } \frac{m^*}{m} = 0{\cdot}025$$

$$\mu_{OPT} = 6{\cdot}7 \times 10^5 \text{ cm}^2/\text{V sec for } \frac{m^*}{m} = 0{\cdot}03.$$

Owing to the low effective mass some degree of degeneracy will exist in even the purest samples and the mobility due to ionized impurity scattering has therefore been calculated using the method detailed by MANSFIELD[7]. The combination of lattice and impurity mobility has been carried out

using a simple combination of the kind

$$\frac{1}{\mu} = \frac{1}{\mu_{OPT}} + \frac{1}{\mu_{IMP}} \qquad (2)$$

The combined theoretical values are given in Fig. 1 curve AB ($m^*/m = 0{\cdot}025$) and curve CD ($m^*/m = 0{\cdot}03$). If it is assumed that the samples are compensated and contain twice as many donors as acceptors so that the total ionized impurity concentration = 3 × free electron concentration, then curve EF is obtained. The assumption of a fixed number of acceptors and proportion of impurity scattering. It would, therefore, have been more correct to compare $R\sigma/r$ with the theoretical results. The effect of this would be to move the experimental points to the left in Fig. 1 so that they would relate more closely to curve CD. The main conclusions would still be unaffected.

In Fig. 2 a theoretical estimate of the temperature dependence of mobility has been made for the purest sample measured using a value for $m^*/m = 0{\cdot}03$. The results are compared with the measured values of mobility ($R\sigma/r$) and it is seen that the agreement is fair.

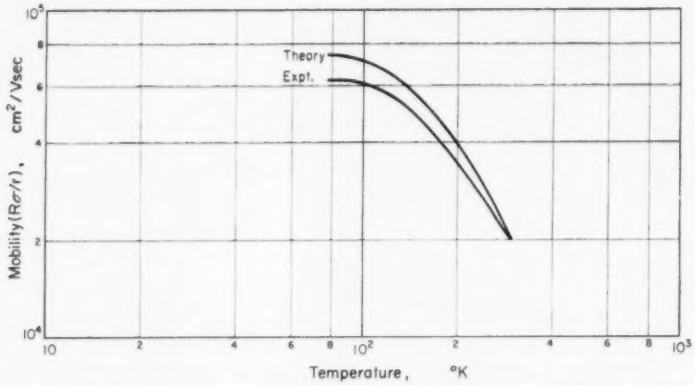

FIG. 2. Experimental and theoretical values of electron mobility in InAs vs. temperature.

$= 10^{16}/\text{cm}^3$ would produce a curve approximately given by a straight line joining F to C.

It can be seen that the experimental points scatter well around the theoretical curves. Since the ionized impurity mobility corresponding to point D is $8{\cdot}4 \times 10^4$ cm²/V sec the adjustment due to combination with the optical lattice mobility is not negligible and suggests that the calculated lattice value is of the correct order. With few exceptions the experimental spread is small compared with the effect of even a modest degree of compensation and confirms the analytical observation that few acceptor type impurities exist in these samples.

In performing the calculations the electron concentration (n) has been deduced from the Hall coefficient (R) using the expression $R = r/ne$. Values for r ranging from 1 to 1·2 have been used roughly estimated from the degree of degeneracy

Acknowledgements—Thanks are due to my colleagues for the electrical data and to Sir WILLIS JACKSON, F.R.S., Director of Research and Education, Associated Electrical Industries (Manchester) Ltd., for permission to publish.

Research Laboratories R. P. CHASMAR
A.E.I.
Manchester

References

1. EFFER D., *J. Electrochem. Soc.*, in press.
2. EHRENREICH H., *J. Phys. Chem. Solids* **2,** 131 (1957); **9,** 129 (1959).
3. EHRENREICH H., *J. Phys. Chem. Solids* **12,** 97 (1959).
4. HILSUM C., *Proc. Phys. Soc. Lond.* **76,** 414 (1959).
5. EHRENREICH H., *J. Phys. Chem. Solids* **8,** 130 (1959).
6. ANTELL G. R., CHASMAR R. P., CHAMPNESS C. H. and COHEN E., Meeting of British Physical Society, Rugby, 1956, p. 99.
7. MANSFIELD R., *Proc. Phys. Soc. Lond.* B**69,** 76 (1956).

To the existence of tetragonally distorted $Mn^{3+}O_6^{2-}$ octahedra in cubic $MnFe_2O_4$

(*Received* 5 *December* 1960)

As HASTINGS and CORLISS[1] have proved by neutron diffraction, the cubic manganese ferrite $MnFe_2O_4$ is of an almost normal type having about 0·8 Mn per formula unit in tetrahedral sites. There are some indications[2,3,4] that the remaining manganese ions occupying the octahedral positions are present as Mn^{3+}.

It is known, on the other hand, that a sufficient quantity of Mn^{3+} ions in octahedral sites leads to macroscopic tetragonal distortion of the cubic lattice.[5] The origin of tetragonal symmetry is supposed to be the result of cooperative Jahn–Teller distortion of Mn^{3+}-occupied octahedra which in sufficient concentration leads to their long-range order.[6,7,8] The question now arises as to whether Mn^{3+}-occupied octahedra remain tetragonally distorted or undertake cubic symmetry if the concentration of Mn^{3+} ions is not sufficient to create macroscopic distortion, the over-all symmetry of the crystal remaining cubic, as in the $MnFe_2O_4$ case.

It seems that the X-ray diffraction might be a suitable method to elucidate this question. It is known that displacements of atoms from equilibrium positions due to local distortions lead to a decrease of integrated intensities in more or less the same way as thermal vibrations do. When we measure the integrated intensities we can determine the total mean-square amplitude $\overline{u^2}$ of the atom, which is the sum of the mean-square amplitude of thermal vibrations $\overline{u_T^2}$ and the mean-square static displacement $\overline{u_D^2}$. To estimate the mean value of local lattice distortions a separation of those two components is necessary.

To get an orientation concerning the magnitude of $\overline{u^2}$ in different ferrospinels we have performed X-ray measurements on typical representatives listed in Table 1. Measurements were carried out with Mn-filtered Fe-radiation on flat powder samples using semifocusing method and film technique. Measured relative intensities corrected for usual factors were divided by theoretical values of $|F_{hkl}|^2$—the squared moduli of the structure factor. The logarithmic plot of the latter values against $\sin^2\theta/\lambda^2$ yielded a straight line from the slope of which $\overline{u^2}$ were determined. The accuracy of values obtained was estimated to be about $\pm 0{\cdot}01$ Å.

The results are summarized in the following table:

Table 1

Composition	Type	$\sqrt{\overline{u^2}}$(Å)
$MnFe_2O_4$	intermediate, almost normal	0·31
$NiFe_2O_4$	inverse	0·27
$MgFe_2O_4$	intermediate	0·26
$ZnFe_2O_4$	normal	0·25

As was to be expected, the lowest value for $\overline{u^2}$ was found for $ZnFe_2O_4$, the structure of which, being of the normal type, shows no irregularities.

From the table it is further apparent that the values $\overline{u^2}$ for Zn-, Mg- and Ni-ferrite increase with their increasing degree of inversion. This seems to be consistent with the idea that the gradual occupation of equivalent crystallographic sites by ions of unequal sizes increases the probability of ionic displacements from regular positions. $MnFe_2O_4$, for which the highest value $\overline{u^2}$ was found, does not follow this succession, in spite of being an almost normal spinel. The difference in $\overline{u^2}$, in contrast to other studied spinels, is so great that it could hardly be explained by mere size effect. Thus we believe that the most natural explanation can be given on the basis of the existence of local distortions in the crystal lattice which originate in the presence of tetragonally deformed Mn^{3+}-occupied octahedra.

To consider the plausibility of this conception we may use the following simple model. Let us suppose that the Mn^{3+}-occupied octahedra are tetragonally deformed in the same way as in Mn_3O_4, which has $c/a = 1{\cdot}16$. First of all let us consider such an isolated $Mn^{3+}O_6^{2-}$ group. If we presume that the volumes of the cubic and the tetragonally distorted octahedra are equal, we can easily compute that the r.m.s. displacement of the oxygen anion in the cubic-to-tetragonal transformation amounts to about 0·14 Å. The mean displacement of an arbitrary ion may then be deduced as $\approx 0{\cdot}06$ Å by taking into account that there exist 0·2 Mn-occupied octahedra per formula unit of

$MnFe_2O_4$ embedded in the lattice. We can further suppose that in normal spinel $ZnFe_2O_4$ is $\overline{u_D^2} = 0$, so that in this case the measured value $\sqrt{\overline{u^2}} = 0{\cdot}25$ Å is due to lattice vibrations only. If we take this value as an approximate numerical estimate for the amplitude of thermal vibrations in other studied ferrites, too, we get for $MnFe_2O_4$ $\sqrt{\overline{u_D^2}} \approx 0{\cdot}06$ Å. This value is thus consistent with what we can expect from our simplified model.

Although our results support the idea about the existence of tetragonally deformed octahedra and thus also the conception of the existence of Mn^{3+} ions in $MnFe_2O_4$ they are to be considered only as preliminary ones. A more detailed study of the Mn-containing spinels including the measurements of the scattered intensities at different temperatures is in progress.

Acknowledgement—We are greatly indebted to our colleague K. Závěta C.Sc., for helpful discussions.

Institute of Technical Physics
Czechoslovak Academy of Sciences
Prague

L. Červinka
S. Krupička
V. Syneček

References

1. Hastings J. M. and Corliss L. M., *Phys. Rev.* **104,** 328 (1956).
2. Harrison F. W., Osmond W. P. and Teale R. W., *Phys. Rev.* **106,** 865 (1957).
3. Krupička S. and Závěta K., *Czech. J. Phys.* **9,** 324 (1959).
4. Miller A., *J. Appl. Phys.* **31,** 261S (1960).
5. Goodenough J. B. and Loeb A. L., *Phys. Rev.* **98,** 391 (1955); Goodenough J. B., *J. Phys. Radium* **20,** 155 (1959).
6. Dunitz J. D. and Orgel L. E., *J. Phys. Chem. Solids* **3,** 20, 318 (1957).
7. McClure D. S., *J. Phys. Chem. Solids* **3,** 311 (1957).
8. Wickham D. G. and Croft W. J., *J. Phys. Chem. Solids* **7,** 351 (1958).

The effective mass of holes in bismuth

(*Received* 23 *September* 1960; *revised* 1 *December* 1960)

Over the past few years there has arisen a considerable discrepancy in experimental data involving the Fermi energy and effective mass parameters of holes in bismuth. It is the purpose of this note to perhaps alleviate this discrepancy through a reinterpretation of the data based on a new model of the Fermi surface.

The model of the Fermi surface for holes which has been used to date consists of one (or two) ellipsoids of revolution in k-space. This model was first proposed by Jones[1] and is given by

$$E_h = (\hbar^2/2m_0)(\beta_{11}k_1^2+\beta_{22}k_2^2+\beta_{33}k_3^2) \qquad (1)$$

where E_h is the Fermi energy for holes, β_{ij} are components of the inverse effective mass tensor, and 1, 2, and 3 refer to the dyad, bisectrix and trigonal axes respectively. The number of holes N_h equals the number of electrons N_e and the parameters for the electrons have been well determined.* A short history of the experimental results for holes follows.

Heine[2] first proposed parameters for the hole band on the basis of a density of states of 0·0165 eV atom calculated from the effect of alloying on the de Haas–van Alphen effect. Using a single sphere model and $N_h = N_e = 1{\cdot}5\times10^{-5}$ atom, he obtained an effective mass of $m_h = 1{\cdot}5\ m_0$, where $m_h = m_0/(\beta_{11}^2\beta_{33})^{1/3}$. Aubrey and Chambers[4] combined Heine's results with a ratio of $\beta_{11}/\beta_{33} = 3{\cdot}7$ obtained from galvanomagnetic experiments[5] to quote values of $\beta_{11} = 0{\cdot}71$, $\beta_{33} = 0{\cdot}19$ and a Fermi energy of $E_h = 0{\cdot}0007$ eV. Measurements of the specific heat to 0·3°K were made by Kalinkina and Strelkov[6] from which they obtained a value for the temperature coefficient of the electronic contribution of $\gamma = 6{\cdot}7\times10^{-5}$ joule/mole deg^2. Using Shoenberg's[3] electron parameters, they calculate a density of states for holes to be $2{\cdot}72\times10^{-2}$ eV atom and an effective mass of $2{\cdot}5\ m_0$ assuming a single sphere model. Anomalous skin effect measurements[7] which measure β_{ij}/E_h were used in conjunction with the specific heat data to yield $\beta_{11} = 1{\cdot}7$, $\beta_{22} = 0{\cdot}13$ ($m_h = 1{\cdot}4\ m_0$) and $E_h = 1{\cdot}2\times10^{-3}$ eV. The analysis was based on a two equivalent ellipsoid model. The real discrepancy arose when hole parameters from cyclotron resonance data[8] were found to be $\beta_{11} = 14{\cdot}7$ and $\beta_{22} = 1{\cdot}07$ giving $m_h = 0{\cdot}16\ m_0$, a factor of ten lower than previous values. Furthermore, there has been no indication of any other hole resonances for masses up to at least

* For a summary of experimental results, see Ref. (7).

$5\ m_0$[9] which argues against the possibility of two hole bands. Recently, specific heat measurements by PHILLIPS[10] to 0·1°K yielded a value of $\gamma = 2{\cdot}1 \times 10^{-5}$ joule/mole deg^2, a value three times smaller than the previous one quoted above. This was interpreted on the basis of a one ellipsoid model to give $m_h = 0{\cdot}90\ m_0$ and $E_h = 1{\cdot}6 \times 10^{-3}$ eV. It will be assumed here, because of the greater temperature range, that the above value of γ is more reliable than that quoted by KALINKINA and STRELKOV.

To bring the last three experiments into agreement, we will now assume a six ellipsoid model for the hole band, one of which is of the form

$$E_h = (\hbar^2/2m_0)(\beta_{11}k_1^2 + \beta_{22}k_2^2 + \beta_{33}k_3^2 + 2\beta_{23}k_2k_3) \tag{2}$$

the other five being generated by rotations of $\pm 120°$ about the trigonal axis and by inversion. It has been shown, however, that to within the experimental error of data obtained on the symmetry of the band,[5,7,8] (2) may be approximated by (1). As stated above, the electron parameters are relatively well determined and representative values of $N_h = N_e = 5{\cdot}5 \times 10^{17}$ cm^{-3} and $E_e = 0{\cdot}0177$ eV will be used. Putting γ in a form

$$\gamma = \frac{\pi^2 k^2}{2}(N_e/E_e + N_h/E_h) \tag{3}$$

which is independent of the multiplicity of the ellipsoids, one then obtains $E_h = 4{\cdot}05 \times 10^{-3}$ eV from PHILLIPS' data. With the six ellipsoid model, the total number of holes is given by

$$N_h = 6\frac{8\pi}{3h^3}(2m_hE_h)^{3/2} \tag{4}$$

from which one can now calculate $m_h = 0{\cdot}18\ m_0$.* The anomalous skin effect data can also be reinterpreted on the basis of a six ellipsoid model to give $\beta_{11}/E_h = 2{\cdot}56 \times 10^3$ eV and $\beta_{33}/E_h = 0{\cdot}46 \times 10^3$ eV. Using $E_h = 4{\cdot}05 \times 10^{-3}$ eV from specific heat data one obtains $\beta_{11} = 10{\cdot}8$ and $\beta_{33} = 1{\cdot}86$ or $m_h = 0{\cdot}17\ m_0$. It should also be noted that using GALT's $m_h = 0{\cdot}16\ m_0$ and $N_e = N_h = 5{\cdot}5 \times 10^{17}$ cm^3 in (4), one obtains $E_h = 4{\cdot}6 \times 10^{-3}$ eV. It is in view of the closer agreement in the three sets of data that the six ellipsoid model is chosen. This view is supported in a band structure calculation by MASE[11] which points to the probable existence of six equivalent maxima in the valence band.

In measuring the de Haas–van Alphen effect at 0·07°K, BRANDT[12] has seen a new set of oscillations which are attributed to a single hole ellipsoid of revolution. Values of $\beta_{11} = 20$, $\beta_{33} = 1{\cdot}4$ and $E_h = 16 \times 10^{-3}$ eV are obtained. The mean effective mass ($m_h = 0{\cdot}12\ m_0$) is in fair agreement with the above model but there is a factor of four discrepancy in the Fermi energy which remains unexplained. One possibility is the existence of two hole bands as suggested by BRANDT[12].

Acknowledgement—The author is indebted to P. HAMILTON for carrying out the recalculation of the anomalous skin effect data.

Bell Telephone Laboratories G. E. SMITH
Murray Hill
New Jersey
U.S.A.

* KALINKINA and STRELKOV's value of γ, when corrected for the nuclear quadrupole term found by PHILLIPS, gives $E_h = 1{\cdot}9 \times 10^{-3}$ eV and $m_h = 0{\cdot}40\ m_0$.

References

1. JONES H., *Proc. Roy. Soc.* **A147,** 396 (1934); **A155,** 653 (1936).
2. HEINE V., *Proc. Phys. Soc. Lond.* **A69,** 513, 505 (1956).
3. SHOENBERG D., *Proc. Roy. Soc.* **A170,** 341 (1939); *Phil. Trans.* **A245,** 1 (1952); DHILLON J. S. and SHOENBERG D., *Phil. Trans.* **A248,** 1 (1955).
4. AUBREY J. E. and CHAMBERS R. G., *J. Phys. Chem. Solids* **3,** 128 (1957).
5. ABELES B. and MEIBOOM S., *Phys. Rev.* **101,** 544 (1956).
6. KALINKINA I. N. and STRELKOV P. G., *Zh. eksp. teor. fiz.* **34,** 616 (1958); translation: *Soviet Physics, JETP* **34(7),** 426 (1958).
7. SMITH G. E., *Phys. Rev.* **115,** 1561 (1959).
8. GALT J. K., YAGER W. A., MERRITT F. R., CETLIN B. B. and BRAILSFORD A. R., *Phys. Rev.* **114,** 1396 (1959).
9. GALT J. K., private communication.
10. PHILLIPS N. E., *Phys. Rev.* **118,** 644 (1960).
11. MASE S., *J. Phys. Soc. Japan* **14,** 584 (1959).
12. BRANDT N. B., DUBROUSKAYA A. E. and KYTIN S. A., *Soviet Physics, JETP* **9,** 405 (1960); BRANDT N. B., *Zh. eksp. teor. fiz.* **38,** 1355 (1960).

Enhanced nonequilibrium diffusion in plastically deformed AgZn*

(*Received* 15 *February* 1961)

MOTION of dislocations through a solid during plastic deformation is expected to produce a considerable excess of vacancies and interstitials.[1] At sufficiently high temperatures these defects will be mobile and can be removed by diffusion to surfaces and dislocations, by recombination, and by aggregation into immobile multiplets. During their lifetime, the excess defects should cause an enhancement in the rate of various diffusion-limited processes.

While the general features of this process are qualitatively understood, quantitative information about the rate of production of the defects and of their lifetimes is almost entirely lacking. Several investigators,[2–6] using radioactive tracer techniques, have studied diffusion in specimens undergoing large simultaneous plastic deformation at elevated temperatures, with conflicting results. In some cases diffusion rates are apparently increased by several orders of magnitude;[2–4] in other cases, under almost identical conditions, no enhancement is found.[5, 6] Large transient increases in ionic conductivity have been reported for alkali[7] and silver halides[8] immediately following plastic strain at low temperatures.

In all of these experiments, large plastic strains are involved, and there are serious questions regarding the extent to which the enhancement, when observed, can be related to an increase in the bulk diffusivity as contrasted to effects resulting mainly from large increases in the dislocation density. The interpretation of the experiments depends critically on assumptions made regarding the effective diffusion mechanism and the lifetime of the defects. If the experiments are interpreted in terms of a simple vacancy mechanism, the vacancy lifetimes derived span a range of 10^4–10^{12} jump times.

The use of anelastic relaxation in these studies obviates a number of these difficulties. This phenomenon has been well correlated with bulk diffusion in alpha-phase alloys,[9, 10] and, since it occurs at low temperatures, it can be used to study diffusion under nonequilibrium conditions. Moreover, since the effect is determined by changes in local order of atoms throughout the bulk of the solid, it should be relatively insensitive to diffusion occurring only near dislocations, if the dislocation density is not excessive.

In the present experiment, deformation enhanced diffusion has been studied in AgZn by following the rate of anelastic relaxation as a function of time immediately following a very small plastic strain ($\sim 0{\cdot}005$). The diffusion process can then be studied continuously under nonequilibrium conditions, as the strained specimen approaches equilibrium. In this way it is possible to examine the kinetics of the annealing process in detail, and to determine directly the lifetimes of the excess defects as they migrate to various sinks. These results may be readily compared to other cases in which excess defects are introduced by other means, as by quenching or radiation damage.

Specimens used in the present investigation were in the form of wires of an AgZn alloy, containing 22 atomic per cent Zn, prepared by swaging and drawing vacuum-melted ingots comprised of silver of 99·99 per cent purity and zinc of 99·999 per cent purity. The specimens were about 18 cm in length and 0·06 cm in diameter. Anelastic relaxation measurements were made with a conventional torsion pendulum arrangement[9] by studying anelastic strain induced by a constant applied torque sufficient to produce an elastic strain of 3×10^{-5}. Measurements were carried out with well-annealed specimens and on specimens in which nonequilibrium excess concentrations of defects were initially introduced by plastic deformation or by rapid quenching from 400°C.

Initial deformation was accomplished by extending the annealed specimen by 1 mm against a stop, with the specimen mounted in the torsion apparatus. Immediately following the plastic extensional strain, the specimen was deformed elastically in torsion and the strain measured as a function of time, permitting the specimen to relax to a fraction of its final value, and then reversing the applied torsional stress. The use of an alternating torsional stress effectively eliminates any effects arising from dislocation relaxation during the anneal. Since the specimens were deformed *in situ*, with the apparatus previously in thermal

* Supported in part by the United States Atomic Energy Commission.

equilibrium, the relaxation rate could be determined within a very short time (1–2 min) following plastic deformation.

For comparison, quenched specimens were prepared in a manner similar to that previously used by NOWICK[11], by quickly withdrawing a specimen from a furnace maintained at 400°C and plunging it into a bath of water containing 10 per cent $CaCl_2$ at room temperature. The quenched specimen was then mounted in the torsion apparatus, and the relaxation followed by the same

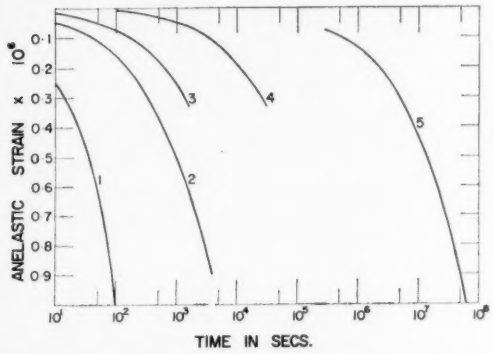

FIG. 1. Typical curves of strain at constant stress at 59°C, for various times following plastic deformation (D) or quench (Q): 1. 70 sec ($D2$); 2. 9100 sec ($Q1$); 3. 5200 sec ($D3$); 4. 97,000 sec ($Q2$). Curve 5 was made under equilibrium conditions at 146°C and referred to 59°C using the measured activation energy of 35 kcal/mole. The total anelastic relaxation at this strain is about 2×10^{-6}; the elastic strain is 3×10^{-5}.

methods used for the deformed specimens. However, in this case, several minutes were required to bring the specimen into equilibrium at the measurement temperature, and the initial relaxation rates could only be determined by extrapolation.

Typical relaxation curves for deformed and quenched specimens are shown in Fig. 1, together with a relaxation curve for a well-annealed specimen extrapolated to the measuring temperature of 59°C. As can be seen from the figure, the shape of the relaxation curve is essentially the same in all cases, except for a shift in the time scale, implying that the same diffusion-limited process is operative in all cases. This conclusion is also attested by the fact that the total anelastic relaxation (~6 per cent of the elastic strain) is identical for deformed, quenched, and equilibrated specimens. The relaxation rate is strongly time dependent, since the excess defects are being removed in times of the same order of magnitude as the relaxation time. For this reason the relaxation was not followed to the inflection point between alternations of the torsional stress, but only for an amount sufficient to determine the relaxation rate. If a single defect diffusion mechanism is operative for the relaxation process, the concentration of defects present as a function of time can be determined from the relation

$$d\epsilon_a/dt = f(\epsilon_a)c_d g(T)$$

in which ϵ_a is the anelastic strain, $f(\epsilon_a)$ is a function of the anelastic strain, ϵ_a (probably nearly linear in ϵ_a), c_d is the relative concentration of diffusing defects, and $g(T)$ is a function (probably of the form $\exp -E_m/kT$) which describes the temperature dependence of the mobility of the defects.

The relative excess defect concentration at any time can then be determined from the ratio of $d\epsilon_a/dt$ for a nonequilibrium specimen to that of a well-equilibrated specimen for the same applied stress and anelastic strain, extrapolated to the same temperature. By extrapolating to $t = 0$, the initial relative defect concentrations can then be determined. These are shown in Table 1 for a number of deformed and quenched specimens.

Table 1. *Relative initial defect concentration and half-life for quenched and deformed* AgZn *at* 59°C.

Run	$c_d(0)/c_d$ equil.	τ ½sec
Deformation D_1	6×10^4	200
Deformation D_2	5×10^5	200
Deformation D_3	2×10^5	200
Quench Q_1	2×10^5	700
Quench Q_2	2×10^5	1600

This table also shows the time required for half the initial excess defects to be removed. The original defect concentrations are all of the order of 10^5 times the equilibrium concentrations at 59°C. However, since, as noted earlier, a considerable extrapolation is required to determine $c_d(0)$ for the

quenched specimens, these values are much more uncertain than those given for the deformed specimens. The latter are probably accurate to within a factor of two. The times required for half the excess defects to be removed are of the order of 3×10^3 jump times at 59°C for deformation runs and 2×10^4 for quenched runs.

The kinetics of the annealing of the excess defects is shown in Fig. 2. Except for the case of one quenched specimen, the annealing process is apparently almost exactly *second order* over several orders of magnitude. This somewhat surprising

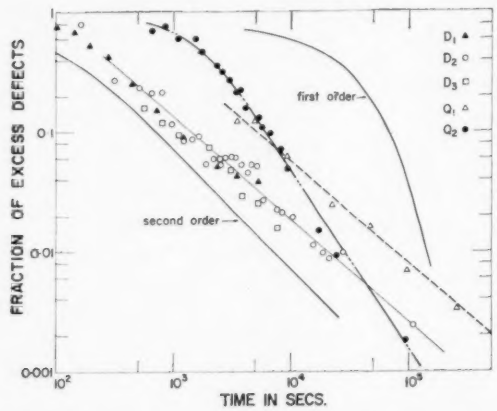

FIG. 2. Fraction of excess defects remaining as a function of time.

result shows that the enhanced diffusion cannot be explained solely in terms of excess vacancies migrating to fixed sinks, since such a model would give first-order kinetics. The present results for quenched specimens are consistent with those previously reported by NOWICK[11].

If the relaxation process is in fact governed by a vacancy diffusion mechanism, then, using NOWICK's value for the formation energy of vacancies of 0·5 eV, the initial vacancy concentrations in the quenched and deformed specimens may have been as large as 10^{-3}. Under such conditions it is highly likely that vacancy multiplets would form before the vacancies could migrate to fixed sinks. In this case the predominant mechanism for removal of the excess vacancies would presumably be by aggregation into immobile multiplets rather than by motion to dislocations. While such a model is appealing in the light of the present results, it would require the further assumption that divacancies formed during the annealing are either immobile or do not contribute to the anelastic relaxation, which is somewhat improbable. In addition, in the one case ($Q2$) in which the annealing was not exactly second order, the specimen had been previously given an exceptionally thorough high temperature anneal prior to quenching (120 hr at 645°C, while for other specimens the prior anneal was only about 4 hr at 600°C). For this specimen the initial dislocation density was probably appreciably lower than that for the other specimens, a fact which should have encouraged, rather than discouraged, the formation of vacancy multiplets. Further studies will obviously be required to clarify the details of the process.

Department of Physics C. H. NEUMAN
University of Illinois D. LAZARUS
Urbana D. B. FITCHEN
Illinois, U.S.A.

References

1. SEITZ F., *Phil. Mag.* **1,** 43S (1952).
2. BUFFINGTON F. S. and COHEN J., *J. Metals N.Y.*, **4,** 859 (1952).
3. LEE C. H. and MADDIN R., *Trans. AIME* **215,** 397 (1959).
4. FORESTIERI A. F. and GIRIFALCO L. A., *J. Phys. Chem. Solids* **10,** 99 (1959).
5. DARBY J. B., TOMIZUKA C. T. and BALLUFFI R. W., *J. Appl. Phys.* **30,** 104 (1959).
6. BLACKBURN D. A. and BROWN A. F., *Proc. IAEA Conference* (Copenhagen, 1960), to be published.
7. GYULAI Z. and HARTLY D., *Z. Phys.* **51,** 378 (1928); FISCHBACH D. B. and NOWICK A. S., *J. Phys. Chem. Solids* **5,** 302 (1958).
8. LAYER H. P. and SLIFKIN L., *Bull. Amer. Phys. Soc.* (Ser. II) **5,** 446 (1960).
9. NOWICK A. S., *Phys. Rev.* **88,** 925 (1952).
10. LAZARUS D. and TOMIZUKA C. T., *J. Appl. Phys.* **25,** 1443 (1954).
11. NOWICK A. S. and SLADEK R. J., *Acta. Met.* **1,** 131 (1953).

Vol. 2
1961

J. Phys. Chem. Solids Pergamon Press 1961. Vol. 20, Nos. 3/4, pp. 173–176. Printed in Great Britain.

THE ENERGY OF ELECTRON–HOLE PAIR FORMATION BY X-RAYS IN PbO

F. LAPPE

Laboratories RCA Ltd., Zurich, Switzerland

(*Received* 23 *February* 1961)

Abstract—Single crystals of yellow PbO were grown and irradiated by CuKα radiation. By comparing the X-ray induced photocurrents with the light induced photocurrents the average energy necessary to produce an electron–hole pair in PbO by X-ray was determined to be 8 eV.

1. INTRODUCTION

Two properties of single crystals of yellow PbO make it a promising material as a sensitive X-ray detector. First, PbO is a sensitive photoconductor since "undoped" PbO crystals show photoconductive gains as high as 100 at 550mμ. Second, the high atomic weight of Pb yields a high X-ray absorption. Below the K-absorption edge of Pb at 0·141 Å the absorption in PbO is higher than in CdS by a factor of ten almost (Fig. 1). Assuming a comparable gain for the X-ray induced electron–hole pairs in both materials PbO might therefore be superior to CdS as a X-ray sensitive photoconductor. Evaporated layers of PbO already are used as X-ray sensitive photoconductors in television pick-up tubes of the Vidicon type.[1,2]

2. EXPERIMENTAL

PbO crystals were obtained as yellow transparent plates with an area of some 10 mm^2 and a thickness of some 10 microns, by cooling down molten PbO in an aluminium oxide boat (m.p. 890°C). Gold electrodes 1 mm apart were evaporated on the crystals. The crystals were irradiated with a narrow beam of CuKα radiation (Ni-filter) just large enough to illuminate the crystal surface. This way the ionization of air in the neighbourhood of the crystal electrodes could be kept at a minimum. The position of the crystal in the X-ray beam was controlled by a luminescent screen. Intensity measurements of the X-ray beam were carried out with a small cylindrical ionization chamber in place of the crystal. The number a of X-ray quanta passing the chamber per cm^2 sec was obtained from

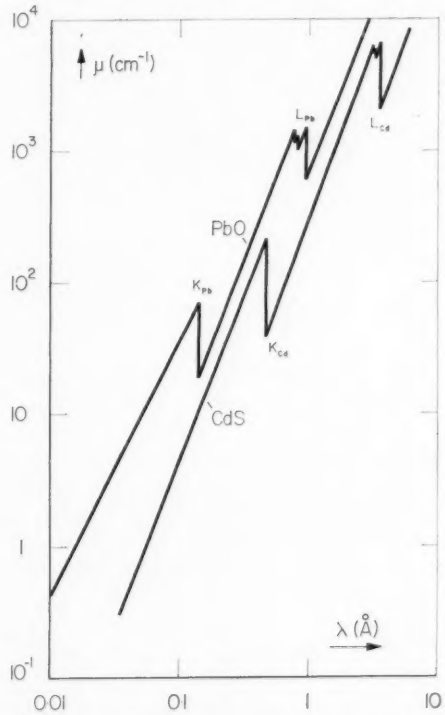

FIG. 1. X-ray absorption coefficient of PbO and CdS vs. wavelength [From *Handbook of Chemistry and Physics*. (42nd Ed.). Chemical Rubber Publishing Co., Cleveland (1960–1961)].

the measured ionization current by

$$a = \frac{iW}{e\mu v\, h\nu} \qquad (1)$$

where i = ionization current; $W = 32{\cdot}5$ eV = medium ionization energy of air; e = charge of electron; μ = absorption coefficient of air for CuKα radiation corrected for the actual air density; v = volume of the beam between the condenser plates of the ionization chamber and $h\nu$ = energy of one CuKα quantum $= 8{\cdot}06 \times 10^3$ eV.

3. RESULTS

Figure 2 shows the dependence of the X-ray induced photocurrent $\Delta\, i$ vs. the number a of absorbed X-ray quanta per cm^2 sec. The

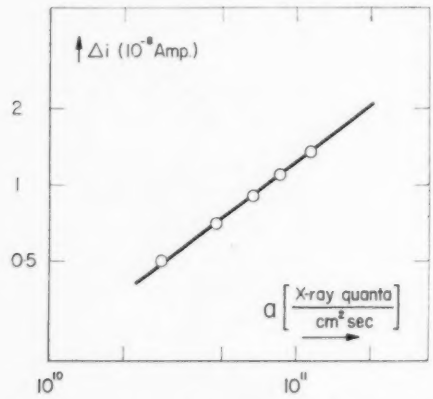

FIG. 2. X-ray induced photocurrent $\Delta i = i - i_{dark}$ vs. number of CuKα quanta per cm^2 sec.

applied field at the crystal was 10^4 V/cm. Due to its high energy one X-ray quantum produces many primary electron–hole pairs each of which contributes to the photocurrent by a factor given by the normal gain G in photoconductors. One therefore can write

$$\Delta i = eaF \times \frac{h\nu}{W_I} \times G \qquad (2)$$

with W_I = medium energy, necessary to produce one electron–hole pair, F = illuminated surface area of the crystal between the electrodes. The two factors $h\nu/W_I$ and G can be determined separately

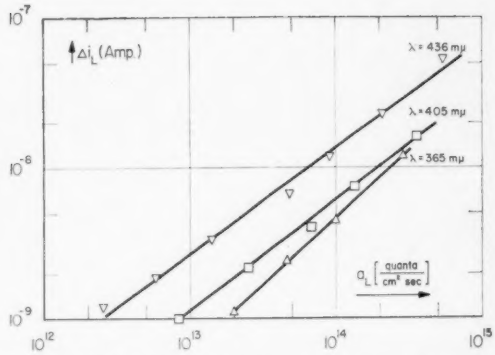

FIG. 3. Light induced photocurrent $\Delta i_L = i - i_{dark}$ vs. number of quanta per cm^2 sec. Parameter = wavelength of applied light.

by comparing the curve in Fig. 2 with the analogous curve taken by illumination with light of suitable wavelength (Fig. 3). If a quantum efficiency of one is assumed for the primary process of electron–hole pair production by light quanta, one can write an equation similar to (2):

$$\Delta i_L = ea_L FG \qquad (3)$$

with Δi_L = light induced photocurrent, a_L = number of light quanta per cm^2 sec entering the crystal surface and the same gain G. The

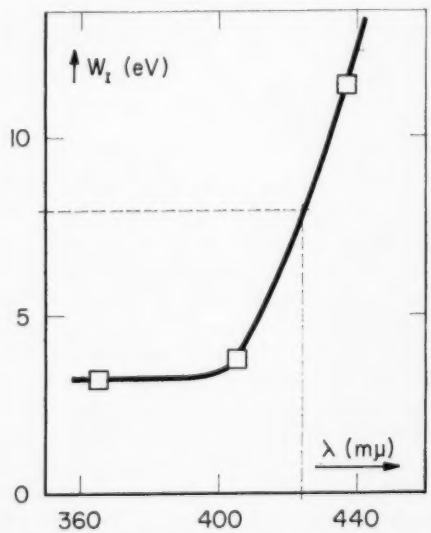

FIG. 4. Ionization energy vs. wavelength obtained from the comparison of the curves given in Fig. 2 and Fig. 3.

Vol. 2
196

comparison of equations (2) and (3) immediately gives $h\nu/W_I$ and W_I. Since the curves Δi vs. a and Δi_L vs. a_L have the same slope, the ratio of equations (2) and (3) always gives the same value, independent of a and a_L. However, this comparison is valid only if the absorption coefficient of the light used is the same as the absorption coefficient of the X-rays. The reason for this is that a stronger recombination in the surface causes a lower gain for strongly absorbed light. The energy W_I obtained in the way described above thus depends on the wavelength of the light used for the comparison as shown in Fig. 4. The absorption coefficient of PbO for CuKα radiation ($\lambda = 1{\cdot}54$ Å) is $2{\cdot}0\times10^3$ cm^{-1} (Fig. 1). The absorption of PbO vs. wavelength, measured on the same crystal as used for the photocurrent measurements, is given in Fig. 5. It shows that an absorption coefficient of $2{\cdot}0\times10^3$ cm^{-1} is obtained at a wavelength of 420 mμ. The correct value of W_I is therefore obtained by taking the photoconducting properties at 420 mμ. The value obtained this way is

$$W_I = 8\ \text{eV}$$

This value appears to be in line with the values obtained in other materials by completely other methods (see table below). Values for the energy W_I necessary to produce an electron–hole pair by fast electrons or by α-particles in Ge, Si, GaAs and CdS can be found in the literature. W_I always turns out to be about three times larger than the band gap. Older measurements on Ge and Si[8,9] yielded a higher value of W_I than the ones reported in Refs. (3) and (4). The new values appear to be more reliable because of an improved method. The listed value of W_I in GaAs is probably too high for the same reason. It therefore appears that a factor of about three between ionization energy W_I and energy gap ΔE might have a very general meaning.

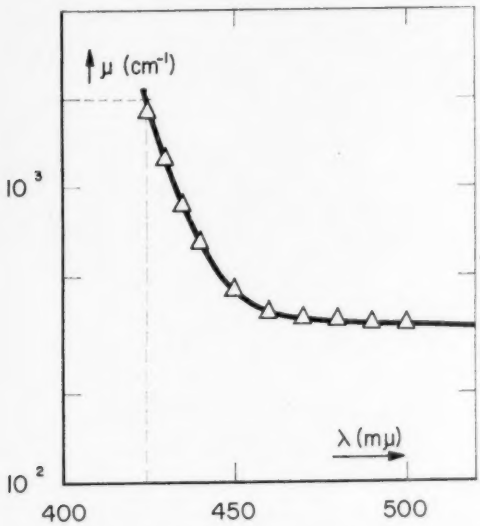

FIG. 5. Absorption coefficient of PbO vs. wavelength.

4. DISCUSSION OF THE ERROR IN W_I

The errors in the intensity and current scales of Figs. 2 and 3 determine the error of W_I in Fig. 4. The intensity of light was measured with a calibrated phototube. The error of the calibration is estimated to be ± 10 per cent. Due to the high refractive index of PbO ($n = 2{\cdot}7$) a large fraction $(n-1/n+1)^2 = 21$ per cent of the incident light is reflected from the crystal surface. This correction is already taken into account in Fig. 4. For the

Table 1

	Ge	Si	GaAs	CdS	PbO
Band gap ΔE	0·72	1·03	1·35	2·5	3·0
W_I	2·1[4]	3·1[3]	6·3[6]	7·3[5] 9·3[7]	8 present work
$W_I/\Delta E$	2·9	3·0	4·6	2·9/3·7	2·7

Vol. 20
1961

intensity scale of Fig. 2 an error of 5 per cent was found. It is due to the uncertainty in the determination of the beam volume between the condenser plates in the ionization chamber. An error in the current scales is likely since the crystal can change its properties in the time between the measurements of the curves of Figs. 2 and 3. This is very probable since the high absorption coefficient of PbO for the applied radiations causes the photocurrent to flow in the easily affected crystal surface. In order to obtain reproducible results the measurements have therefore to be performed in a high-vacuum chamber with an X-ray and light transparent window. The total error of W_I in Fig. 4 which depends on the errors of a and a_L amounts to about 15 per cent. Compared to these uncertainties the error due to the comparison of the two absorption coefficients is negligible.

REFERENCES

1. Heijne L., Schagen P. and Bruining H., *Nature, Lond.* **173,** 220 (1954).
2. Jacobs J. and Berger H., *Electr. Engng. N.Y.* **75,** 158 (1956).
3. Baldinger E., Czaja W. and Faroogi A. Z., *Helv. Phys. Acta* **33,** 551 (1960).
4. Baldinger E. and Czaja W., *Nucl. Instrum. Methods* Vol. 9, (1961), in press.
5. van Heerden P. J., *Phys. Rev.* **106,** 468 (1957).
6. Pfister H., *Z. Naturf.* **12a,** 217 (1957).
7. Lappe F., *Z. Phys.* **154,** 267 (1959).
8. McKay K. G. and McAffe K. B., *Phys. Rev.* **31,** 1079 (1953).
9. Rappaport P., *Phys. Rev.* **93,** 246 (1954).

Vol. 2
196

J. Phys. Chem. Solids Pergamon Press 1961. Vol. 20, Nos. 3/4, pp. 177–186. Printed in Great Britain.

ELECTRICAL RESISTIVITY, HALL EFFECT AND SUPERCONDUCTIVITY OF SOME b.c.c. TITANIUM–MOLYBDENUM ALLOYS*

R. R. HAKE, D. H. LESLIE and T. G. BERLINCOURT

Atomics International, A Division of North American Aviation, Inc., Canoga Park, California

(*Received* 22 *November* 1960)

Abstract—The electrical resistivities and the Hall coefficients of a series of body centered cubic Ti–Mo alloys have been measured between 1·1°K and room temperature, in magnetic fields up to 30 kG, and for concentrations of Mo between 7 and 24 atomic per cent. For the lower Mo concentration alloys the resistivities are high (≈ 140 microhm cm), and are slightly *larger* at 4·2°K than at 300°K. The resistivities *decrease* with increase of Mo over the entire range of alloy concentrations studied. The Hall coefficients are positive and are appreciably concentration and temperature dependent only below solute concentrations of about 12 atomic per cent Mo. The alloys are all superconducting at liquid helium temperatures, their resistive superconducting transition temperatures increasing with increase of Mo. Atomic ordering and structural transformation, concentration and temperature dependent electronic factors, and spin-disorder scattering are considered as possible explanations for the anomalous concentration and temperature dependence of the resistivity.

1. INTRODUCTION

CONSIDERABLE attention has recently been directed toward the temperature dependence of the electrical resistivities of metals and alloys which display magnetic ordering.[1,2,3] In many cases a large and temperature independent contribution to the resistivity appears to exist above the Curie or Néel point. It appears likely that in some cases this extra electronic scattering is due to an exchange interaction between conduction electron spins and disordered spins of electrons localized on particular atoms of the lattice. In a survey of the experimental literature on spin-disorder effects in the resistivities of metals and alloys, COLES[1] has pointed out that the resistivity of the body centered cubic form of Ti (stable at temperatures in excess of ~ 1156°K) appears to contain a large and temperature independent term (~ 150 microhm cm), as do the resistivities of Ti-rich b.c.c. Ti–Nb alloys at temperatures down to 77°K.[4] The resistivities of the alloys actually decrease as solute is added, and extrapolation to zero Nb content suggests a value for the temperature independent resistivity of pure b.c.c. Ti of, again, about 150 microhm cm.

It would appear from resistivity and resistance data on b.c.c. Ti–V[5,6] and Ti–Mo[7] above 77°K, that unusual resistivity behavior (not due to atomic ordering or structural transformation) may be characteristic of Ti-rich b.c.c. alloys. A study of the electronic properties of such alloys down to 1°K is of interest. If the high and temperature insensitive resistivity were indeed due to spin-disorder scattering, then magnetic ordering with consequent effects on the resistivity might be expected at lower temperatures. On the other hand, if especially temperature and concentration dependent "electronic factors" (e.g. the numbers and effective masses of current carriers in various bands or the density of electronic states into which they can be scattered) were responsible for the resistive anomalies, then the influence of such factors might be reflected in measured values of Hall coefficient and electronic specific heat. In this paper we discuss some electrical resistivity and

* This research was supported by the U.S. Atomic Energy Commission.

Hall effect measurements on a series of b.c.c. Ti-rich Ti–Mo alloys.[8] In a succeeding paper[9] the results of liquid helium temperature calorimetric measurements on these alloys will be reported.

2. SPECIMENS

(a) *The β phase of* Ti–Mo

The b.c.c. (β) phase of Ti is stable from the melting point down to about 1156°K, at which point it transforms to the low temperature stable h.c.p. (α) phase. The transformation is of the martensitic type and the β phase cannot be retained at low temperatures by rapid quenching. However, such retention is possible in many Ti-rich, binary, transition metal alloys beyond certain critical concentrations of solute, generally in the range of four to twenty atomic per cent.[10] Thermal arrest measurements[11,12] on such Ti alloys containing low solute concentrations have shown that for a given alloy composition the temperature, M_s, at the start of the β to martensitic α (commonly designated α') transformation upon cooling is virtually independent of quenching rate, even up to rates of 10⁴°C/sec. In addition these measurements show that the amount of material transforming and the M_s temperature decrease with increasing solute concentration.

For Ti–Mo alloys, the thermal arrest measurements[11] as well as metallographic and X-ray analyses have indicated complete β phase retention at room temperature for alloys quenched from the β phase field and containing Mo concentrations in excess of 5·3–6·4 atomic per cent (a/o).[13] Extrapolation of the M_s curve determined by DUWEZ (Fig. 1) suggests that the martensitic transformation is completely suppressed for Mo concentrations greater than 7 a/o. Up to concentrations of about 35 a/o the β phase is metastable at room temperature and will transform slowly at elevated temperatures to the equilibrium $\alpha+\beta$ phases (Fig. 1). At solute concentrations near those just sufficient to stabilize the β phase upon quenching, a pre-precipitation stage of α, coherent with the parent β phase and invisible under the light microscope, may be rejected from the solid solution at rather low temperatures (apparently as low as room temperature in some cases[5]). Studies of the growth of this so-called ω phase in quenched and then annealed Ti–Mo[14,15] and Ti–V[5,6] alloys have shown that formation of the ω phase produces extreme hardness (diamond pyramid hardness numbers (DPH) of 400–550[5,15]) and a lowering of the high electrical resistivity which is characteristic of the pure β phase.

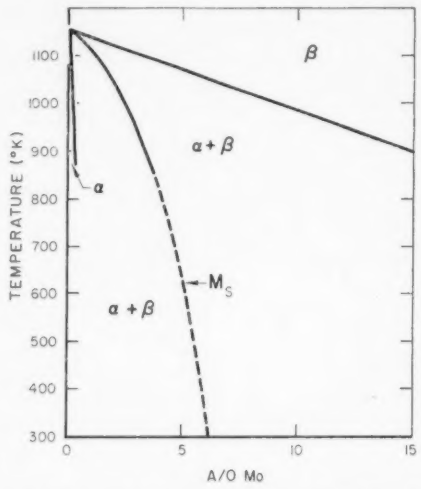

FIG. 1. The partial phase diagram of Ti–Mo[13] showing the M_s (temperature at the start of the martensitic transformation upon quenching) curve as determined by DUWEZ[11] (———— from thermal arrest measurements, – – – – – from microscopic examination of quenched specimens).

(b) *Preparation and analyses of samples*

Crystal bar, iodide process Ti, obtained from the Foote Mineral Company, was used in this study. A purity of about 99·92 per cent is claimed by the manufacturer for this type of Ti. Typical impurities in parts per million (p.p.m.) by weight are given as: Zr—500 p.p.m.; Si and Al—50 p.p.m.; Mg, Mn, Ca—30 p.p.m.; and Cr, Fe, O_2, N_2—20 p.p.m. Since the measurements reported here are all on relatively high concentration alloys (greater than 7 a/o) it is unlikely that such metallic impurity levels seriously affect the results. It is believed that the effects of interstitial gaseous impurities, while possibly significant, are much the same for all specimens measured and do not greatly influence the relative values of resistivity or Hall coefficient. The Mo used was obtained from A. D. MacKay, Inc., in the form of pellets of nominal purity 99·9 per cent by weight.

The alloys were made by arc melting together weighed amounts of Ti and Mo in a laboratory arc furnace utilizing an argon atmosphere, a water-cooled copper hearth and a tungsten electrode. A Ti "getter" button was melted prior to alloy melting as a precaution against O_2 and N_2 contamination. Each of the alloys was turned over and remelted at least six times to promote homogeneity.

Vol. 2
1961

Weight loss of the specimens during melting was in all cases less than 0·2 per cent so that alloy composition could be adequately determined from the starting weights of the materials melted. Upon breaking the arc a rapid quenching of the melt, in contact with the water-cooled copper hearth, occurred. Sections were cut from the arc melted button and ground and polished to a form (approximately 1 in. × 0·12 in. × 0·010 in.) suitable for Hall coefficient and resistivity measurements. Surface layers were removed by etching prior to measurement.

Sections of the buttons adjacent to the resistivity and Hall coefficient specimens were given hardness tests and examined via microscopy and X-ray diffraction. This work indicated that the β phase had been fully retained, and the measured lattice parameters (Table 1) are in reasonable accord with the determinations of HANSEN *et al.*[16] No extra diffraction lines indicative of ordering (in agreement with HANSEN *et al.*[16])* or of the presence of ω, α, or α' phases were observed. The hardness values (Table 1) are considerably lower than those normally

Table 1. *Compositions, lattice parameters, and hardness values for b.c.c.* Ti–Mo *alloy specimens*

Specimen	a/o Mo*	Lattice parameter† (Å)	DPH or Vickers hardness numbers (400 gm load, range of 7 measurements)
M	7·08	3·264	182–252
H	9·05	3·260	185–262
N	9·05	3·263	239–252
I	12·15	3·253	224–248
J	15·55	3·248	231–271
J3C	15·55	3·247	185–196
K	16·33	3·248	239–271
L	23·27	3·223	262–266

* Determined from weights of starting materials.

† From room temperature solid surface back reflection data taken with a Norelco diffractometer. The accuracy is approximately ±0·005 Å.

associated with the presence of ω phase.[5,6,15] Although no α' was observed microscopically, some coring was apparent. All microscopic evidence for coring was removed from one specimen (J3C) by severe cold working, subsequent annealing above the α–β boundary, and then quenching; however, no significant departures from the usual resistivity, Hall effect, or superconducting behavior were observed after this treatment.

As a control on the mode of specimen preparation a sample of pure Ti (iodide crystal bar) was arc melted, cut and polished to shape, and measured. All procedures were identical to those used in the alloy work. The measured ice-point resistivity of this Ti specimen was 41 microhm cm and the ratio of the ice-point to 4·2°K resistivity [$\rho(273)/\rho(4{\cdot}2)$] was 44, comparable to that of the highest purity specimens of Ti measured by BERLINCOURT[17] [$\rho(273)/\rho(4{\cdot}2) = 31$], and by WHITE and WOODS[18] [$\rho(295)/\rho(4{\cdot}2) = 22$]. The Hall coefficient, measured at 77°K, was $-4{\cdot}5 \times 10^{-5}$ cm³/C, very close to the 77°K value reported for the specimen with the resistivity ratio of 31.[17] The hardness of the arc melted and fabricated specimen (DPH ≈ 87) showed no increase over that of the original crystal bar (DPH ≈ 101).

3. APPARATUS AND METHOD

The cryogenic, magnetic, and electrical equipment used in this experiment, as well as the measuring method, have, for the most part, been described elsewhere[17,19] so that only a brief description is required. The potential and Hall leads were pressed tightly against the specimens with beryllium–copper spring clips, and indium coated current leads were clamped to the ends of the specimens. Measuring currents of about 0·5 amp were normally employed. Resistive voltages (≈ 6000 μV) were measured to 0·1 μV with a Leeds and Northrup type K-3 potentiometer, and thermal voltages were eliminated in the usual fashion. Resistivity measurements were made from 1·1 to 4·2°K in liquid helium, at 77°K in liquid nitrogen, at 195°K in a dry-ice–acetone bath, at 273°K in an ice-bath, and at room temperature. Relative values of resistivity as a function of temperature for a given specimen are accurate to about ±0·5 per cent, (including the error due to non-correction for thermal expansion), while absolute values of resistivity may be in error by ±3 per cent due primarily to uncertainties in specimen dimensions.

Transverse, isothermal Hall voltages (≈ 0·6 μV at 30 kG) were measured at 4·2°K, 77°K, and room temperature with a Rubicon microvolt potentiometer and photoelectric galvanometer such that readings could be made to 10^{-3} μV. Hall voltages were separated from the thermal voltages present by taking the difference between the voltages read with the field in the positive and negative directions. Four or five sets of voltage readings were normally taken at each measuring field (usually 10, 20, and 30 kG). The scatter in these points taken at a given field value averaged about 2 per cent. In all cases the dependence of the Hall voltage on field

* HANSEN *et al.* did observe some low angle lines foreign to the b.c.c. structure for concentrations of Mo above 40 a/o.

appeared to be linear and the Hall coefficient was determined from the slope of the best fit Hall voltage vs. field plot.

4. EXPERIMENTAL RESULTS

(a) *Electrical resistivity*

Figure 2 shows the resistivity vs. temperature curves measured for b.c.c. Ti–Mo alloys of different Mo concentrations between 7 and 24 a/o. For the lower Mo concentration alloys the resistivities are high (≈ 140 microhm cm) and *increase* slightly in going from room temperature to 4·2°K.* As Mo concentration is increased the resistivities *decrease*† and the temperature coefficients assume more normal positive values. There is no rapid decrease in the resistivity at low temperatures, such as might be indicative of magnetic ordering, for any of the alloys. At 4·2°K the higher concentration alloys were superconducting, and normal state resistivities were measured in magnetic fields of 30 kG.

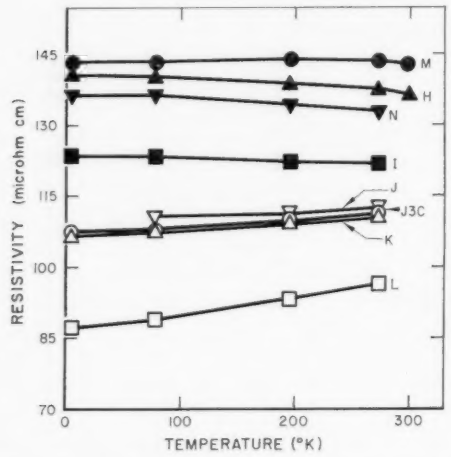

FIG. 2. Electrical resistivity vs. temperature curves for b.c.c. Ti–Mo alloys containing between 7·1 a/o Mo (specimen M) and 23·3 a/o Mo (specimen L). For Mo concentrations of the other specimens see Table 1.

Several specimens were examined for transverse magnetoresistive effects at room temperature and at liquid nitrogen temperature. Liquid helium temperature magnetoresistance measurements were not considered reliable, since the field dependence of the resistivity could be influenced by the presence of minute superconducting inclusions. For the measured specimens (M and I at room temperature, and M, I, N, and K at liquid nitrogen temperature) it was found that $[\rho(H = 30\text{ kG}) - \rho(H = 10\text{ kG})]/\rho(H = 10\text{ kG}) < 2 \times 10^{-4}$.

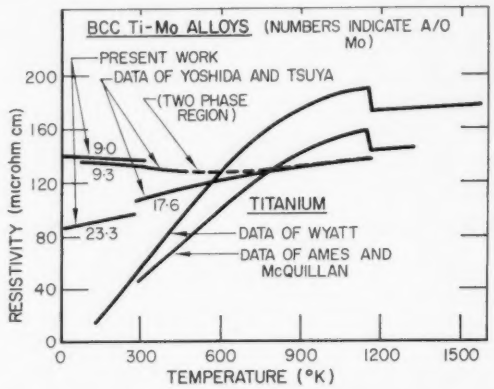

FIG. 3. Electrical resistivity vs. temperature for pure Ti as determined by WYATT[24] and by AMES and McQUILLAN[4], and for some b.c.c. Ti–Mo alloys as determined by the present measurements and those of YOSHIDA and TSUYA[7] (their *resistance* data have been normalized so as to be consistent with the measured ice point *resistivities* of the present study).

According to the work of YOSHIDA and TSUYA[7], the unusual resistive behavior of b.c.c. Ti–Mo alloys continues up to temperatures of ≈ 1100°K. The resistivity–temperature curves for two representative alloys of their study are shown in Fig. 3. These curves were obtained by normalizing their *resistance* data so as to be consistent with the ice point *resistivity* values measured in the present work. For b.c.c. Ti–6·4 a/o Mo and Ti–7·5 a/o Mo alloys YOSHIDA and TSUYA observed slight maxima in the resistances above 77°K. Also shown in Fig. 3

* Such anomalous increases in resistivity in going from 300°K to 4·2°K have also been observed in the b.c.c. U-rich alloys U–Mo and U–Nb,[20,21,22] and in the b.c.c. alloys Ti–28·7 a/o V, Ti–9·11 a/o Fe, Ti–11·85 a/o Fe, Hf–12·21 a/o Mo, and Zr–8·57 a/o Mo.[23] All of these alloys were also found to be superconducting at liquid helium temperatures. Negative temperature coefficients of resistivity have also been observed in b.c.c. Ti–Mo alloys[7] and b.c.c. Ti–Nb alloys[4] above 77°K.

† Such anomalous concentration dependence of resistivity has been previously observed above 77°K for series of b.c.c. Ti–Nb,[4] Ti–V,[5] and Zr–Mo[23] alloys.

Vol. 20
1961

are two resistivity–temperature curves for alloys of the present study. For comparison, the resistivity–temperature curves for pure Ti (high purity iodide process) as determined by WYATT[24] and by AMES and MCQUILLAN[4] are shown. The difference in these two sets of measurements could be due to differences in specimen purity, although a large deviation from Matthiessen's rule would also be required to explain the data if this were the case. The resistivity of pure Ti is relatively high and the departure of the resistivity vs. temperature curve from linearity above 800°K is more pronounced than that observed at high temperatures in some other transition metals such as Pd and Pt.[25] The

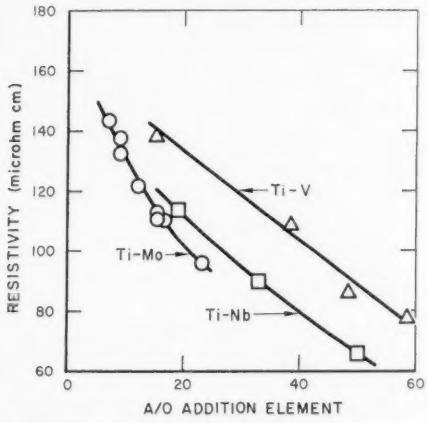

FIG. 4. Electrical resistivity vs. atomic per cent of addition element for b.c.c. Ti–Mo alloys as measured at 273°K in this study, and for b.c.c. Ti–Nb alloys (AMES and MCQUILLAN[4]) and b.c.c. Ti–V alloys (ADENSTEDT *et al.*[5]) measured at room temperature.

sharp break in the resistivity curve at ≈ 1156°K is due to the h.c.p. to b.c.c. phase transformation. As indicated above, the resistivity of the b.c.c. phase can be interpreted as consisting of a large temperature independent part plus a small lattice vibrational contribution linear in temperature ($d\rho/dT \approx 1{\cdot}2 \times 10^{-3}$ microhm cm/°K, according to WYATT's[24] measurements).

Figure 4 shows the 273°K resistivities measured for b.c.c. Ti–Mo alloys plotted as a function of Mo concentration. In addition, room temperature data are shown for some other b.c.c. Ti alloys measured by other investigators.[4,5] The unusual concentration dependence appears to be a common property of such Ti alloys. The concentration dependence of the 4·2°K resistivity is shown in Fig. 5 and is discussed below.

(b) *Hall coefficients*

Although there are recognized difficulties in the interpretation of the Hall effect,[17] it is probably correct to regard the Hall coefficient as being more a function of purely electronic factors than is the resistivity.* Fig. 5 shows the concentration dependence of the Hall coefficient for a series of b.c.c. Ti–Mo alloys. The Hall coefficients are positive, indicating a predominance of hole conduction, and are only weakly concentration and temperature

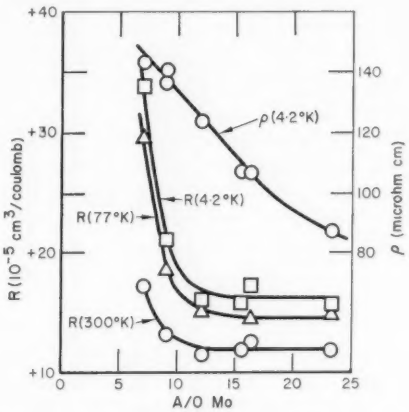

FIG. 5. Hall coefficients (R) vs. atomic per cent Mo for b.c.c. Ti–Mo alloys measured at 4·2°K, 77°K and room temperature ≈ 300°K. Also shown is the electrical resistivity (ρ) at 4·2°K vs. atomic per cent Mo.

dependent for alloys with Mo concentrations above 12 a/o. The concentration dependence of the resistivity is still markedly anomalous above 12 a/o Mo, however, as also shown in Fig. 5, where the 4·2°K

* For a single band model, assuming that the relaxation time τ is a function of energy E only, the expression for the low field Hall coefficient consists of integrals of derivatives of E with respect to the wave number k taken over the Fermi surface, with no dependence upon τ. For a two band model, assuming spherical energy surfaces and characterizing each band by an average τ and effective mass, the expression for the Hall coefficient involves the numbers of current carriers in the two bands and the *ratios* of their relaxation times and their effective masses.[26]

resistivity is plotted against concentration. The residual resistivities (ρ_0) of metallic random solid solutions are almost always found to obey, at least qualitatively, the Nordheim relation $\rho_0 \propto x(1-x)$, where x is the atomic fraction of solute.[25] Large changes in electronic parameters as a function of alloying could account for the complete failure of the Nordheim relation in the present instance, but if such is the case it would seem that the Hall coefficient should be strongly concentration dependent over the entire range of Mo concentrations studied. The marked concentration dependence of the Hall coefficients for solute concentrations below 12 a/o Mo could be due to rapidly changing electronic zone overlap conditions such as might be expected to occur at alloy concentrations approaching a region of crystalline phase instability.* In such a situation electronic parameters such as effective masses and the density of states might well be highly energy dependent. A temperature dependence of the effective values of electronic parameters might then result due to the varying thermal spread of the electronic energy distribution over a region of kT at the Fermi surface, the temperature dependence of the Fermi level, and shifts in energy band structure concomitant with thermal expansion. In accordance with this viewpoint the Hall coefficients are observed to be quite temperature dependent for the low Mo concentration alloys (Fig. 6). Similarly, the anomalous negative temperature coefficients of resistivity are observed only in the low Mo concentration alloys (Fig. 2) and might well be due to temperature dependent electronic factors. Judging by the form of the Hall coefficient vs. concentration curve (Fig. 5), the electronic sensitivity is much reduced for alloys containing more than 12 a/o Mo and, consistent with the foregoing interpretation, this condition is reflected in their less temperature dependent Hall coefficients and their more normal temperature coefficients of resistivity.

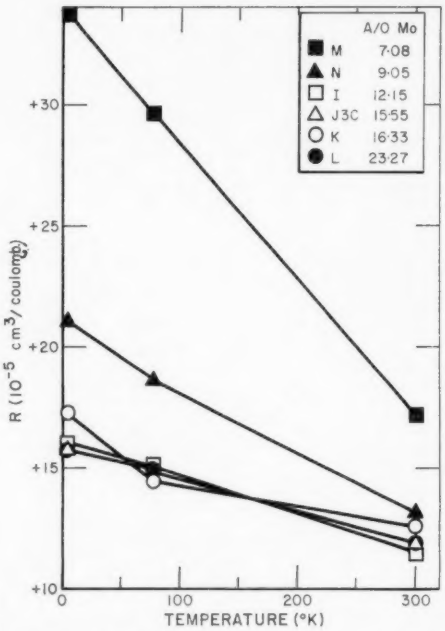

FIG. 6. Hall coefficients (R) vs. temperature for b.c.c. Ti–Mo alloys.

(c) *Superconductivity*

At temperatures in the vicinity of 4°K the resistivities of these alloys dropped rapidly to zero, indicating the presence of superconductivity. Fig. 7 shows the resistive superconducting transitions measured for five different alloy specimens. The resistive transitions are relatively broad and occur at higher temperatures the higher the Mo concentration. This increase of transition temperature is consistent with MATTHIAS' regularities[27] in that as Mo is added to these alloys the average number of "valence" electrons per atom moves closer to 5. MATTHIAS *et al.*[28] have recently observed that addition of Cr, Mn, Fe, or Co to b.c.c. Ti produces increasing transition temperatures up to average

* That electronic conditions are markedly concentration dependent in the low Mo concentration region is also suggested by direct calorimetric measurements of the electronic specific heat coefficient for b.c.c. Ti–Mo alloys containing low Mo concentrations.[9] These measurements indicate that the density of states at the Fermi level, $N(E_F)$, increases linearly by about 18 per cent as Mo concentration is increased from 6·25 to 8·60 a/o. A rigid band model interpretation of these results (to be considered only as suggestive) gives $N(E) = A \exp(BE)$, with $d \ln N/dE = B \approx +9\ (\text{eV})^{-1}$. It would, of course, be desirable to extend the calorimetric measurements to higher Mo concentration alloys but this is experimentally difficult due to the high magnetic fields required for adequate suppression of superconductivity in the desirable temperature range of measurement below 4°K.

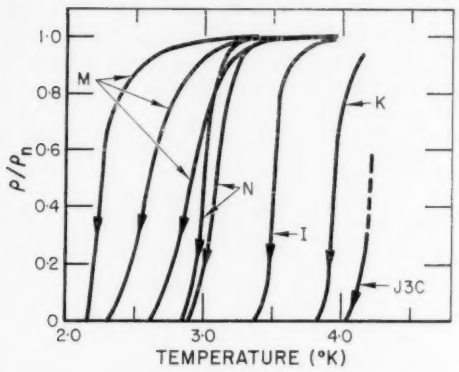

FIG. 7. Superconducting resistive transitions for b.c.c. Ti–Mo alloys containing between 7·1 a/o Mo (specimen M) and 16·3 a/o Mo (specimen K). From left to right the measuring current densities in A/cm² are: M(132, 44, 5·5), N(48, 5·9), I(49), K(48), and J3C(53). ρ_n is the resistivity in the normal state at a temperature just above the start of the superconducting transition.

valence electrons per atom concentrations of 4·4 to 4·7.

Figure 8 shows some typical magnetic field induced resistive transitions. The extremely high fields required to suppress superconductivity and the sensitivity of the resistive transition to the magnitude of the measuring current suggest that the transitions are of a filamentary type, the bulk of the sample being in the normal state during the transition. The resistance of specimen K was zero within the limits of measurement ($\approx 2\times10^{-7}$ ohms) at 1·23°K and 22 kG with a measuring current density of 48 A/cm² (0·4 A). The magnetic field induced resistive transitions for specimen J3C (15·55 a/o Mo), in which all microscopic evidence of coring was removed, were very similar to those of specimen K(16·33 a/o Mo).

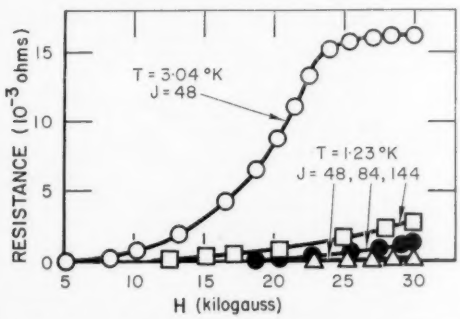

FIG. 8. Magnetic field induced superconducting resistive transitions for specimen K (b.c.c. Ti–16·3 a/o Mo), at two different temperatures and for different measuring current densities J in A/cm². All the transitions were taken in decreasing magnetic fields which were perpendicular to the plane of the specimen. These transitions are typical of all those measured for the different samples.

The resistivity (ρ) vs. temperature transitions shown in Fig. 7 are also probably not well representative of the bulk material transitions. This is shown by the high sensitivity of the transitions to the measuring current density (J) and by the fact that transitions measured for specimen M at $J = 44$ A/cm², in and out of the residual field of the magnet ($H \approx 200$ G), were nearly identical. Calorimetric measurements[9] indicate that typical zero field bulk material transitions are rather broad (about 0·4°K), and that the transition midpoints probably occur close to the intercepts of the $\rho = 0$ axis with a straight line extrapolation from the steep linear portion of the ρ vs. T curve. It is interesting to note the sharpening of the resistive transition (Fig. 7) as measuring current is increased. Such an effect can be explained as due to the current quenching of thin filament superconducting regions occurring at magnetic fields or temperatures somewhat above the bulk material transition.[29,30,31]

5. DISCUSSION

The uncertainty in interpreting Hall effect and resistivity data for transition metal alloys in terms of the usual electronic and scattering parameters of transport theory is considerable. Nevertheless, such data are valuable in indicating the gross characteristics of electronic behavior, and in some cases, suggesting more definitive experiments. The measurements reported in this paper and elsewhere show that many b.c.c. Ti alloys and some b.c.c. U[20,21,22], Hf[23], and Zr[23] alloys display marked anomalies of similar character in their resistive behavior. In the case of b.c.c. U–Mo and U–Nb alloys it has been pointed out[22] that the lack of appreciable temperature dependence of the Hall coefficients casts some doubt on the explanations which have been advanced by CHANDRASEKHAR and HULM[20] and by LOASBY[21] to account for the negative temperature coefficients of resistivity observed for these alloys, since the

temperature dependent electronic conditions which they envisage would most likely produce markedly temperature dependent Hall coefficients. For the case of the b.c.c. Ti–Mo alloys, although it seems possible to attribute the anomalous negative temperature coefficients of resistivity to temperature dependent electronic factors, the weak concentration dependence of the Hall coefficients for alloys of Mo concentration between 12 and 24 a/o would argue against attributing the anomalous concentration dependence of the resistivity to concentration dependent electronic factors. It might be mentioned that according to the two band *s–d* type model proposed by CHANDRASEKHAR and HULM[20] the anomalous concentration dependence of the resistivity observed here would be accounted for by a density of electronic states at the Fermi level, $N(E_F)$, which decreased rapidly with increase of Mo concentration. However, the concentration dependence of the superconducting transition temperature, as well as more direct calorimetric evidence,[9] indicates that $N(E_F)$ for these alloys is actually an increasing function of Mo concentration.*

A feature which is common to all the b.c.c. Ti, U, and Zr alloys mentioned above is that they are metastable at room temperature. In addition, if their solute concentrations were to be somewhat reduced they would undergo some degree of martensitic transformation upon being quenched to room temperature. Varying degrees of undetected structural transformation during quenching, for a series of alloys, or martensitic transformation below room temperature might lead, then, to the observation of anomalous concentration and temperature dependence in the resistivity. For the case of Ti–Mo alloys, however, it seems unlikely that such effects could seriously influence the results.

That the unusual temperature or concentration dependence of the resistivity could be accounted for by martensitic transformation is improbable because:

(1) anomalous temperature and concentration dependence is observed at temperatures and compositions well outside the area enclosed by the M_s curve as determined by DUWEZ or any reasonable extrapolation of this curve to lower temperatures;

(2) no temperature hysteresis was observed in the resistivities of Ti–Mo alloys below 300°K;

(3) the anomalous concentration dependence of the resistivity was observed at room temperature where direct micrographic and X-ray examination indicated that no α' was present. It also seems unlikely that the anomalous resistive behavior could be caused by the presence of ω phase because:

(a) hardness and X-ray measurements failed to indicate the presence of ω phase;

(b) previous work on Ti–V[5,6] and Ti–Mo[14] alloys has shown that formation of the ω phase occurs more readily the lower the solute concentration and results in a more nearly normal type of resistivity behavior, i.e. a resistivity lower in magnitude with a more positive temperature coefficient;

(c) resistivity measurements on specimens M and L taken one year apart were the same within experimental accuracy, so that there were apparently no room temperature aging effects due to ω phase formation such as have occasionally been detected.[5]

High and temperature insensitive resistivity is characteristic of magnetic metals above their magnetic ordering temperatures and this has been attributed to spin-disorder scattering in some[1] or nearly all[2] cases. That spin-disorder scattering could exist in any of the above mentioned b.c.c. alloys is somewhat difficult to believe, however, because none of them (except for b.c.c. Ti–Fe) contains any of the known anti- or ferromagnetic transition metals (Cr, Mn, Fe, Co, and Ni).

* As discussed by PINES[32], the dependences of $N(E_F)$ values and the superconducting transition temperatures, T_C, on the average number of valence electrons per atom are, for transition metals, rather similar. This is in accord with the BARDEEN *et al.*[33] expression for T_C [$T_C \propto \theta_D \exp -(1/N(E_F)V)$] providing that V, the electron–electron interaction parameter, is much the same for the different transition metals. That V is a relatively slowly varying function of concentration for b.c.c. Ti–Mo alloys is indicated by the calorimetric measurements.[9] Judging, then, from the present T_C measurements and those of BUCHER *et al.*[39] on b.c.c. Ti–Mo alloys containing more than 30 a/o Mo ($T_C \approx 3$°K for b.c.c. Ti–30 a/o Mo) it would appear that the marked increase of T_C and $N(E_F)$ with Mo concentration for alloys below 9 a/o Mo[9] must cease at slightly higher concentrations, as is implied by the form of the Hall coefficient vs. concentration curve (Fig. 5).

Nevertheless the compounds $ZrZn_2$[34] and UH_3[35] are known to be ferromagnetic, and MOTT and STEVENS[36] have argued that localized or non-conducting *d*-electron spin states can occur in b.c.c. transition metals (e.g. Fe). Spin-disorder effects are large and could easily swamp out the atomic disorder contribution to the resistivity. They depend in a complex way upon the solute concentration, since this concentration might well be expected to affect both the degree of spatial and orientational order (if any) in the spin system as well as the number of electrons per unit volume in localized spin states. Of course no clear cut indication of any magnetic ordering appears in the resistivities of these alloys even down to temperatures just above their superconducting transitions and there is no calorimetric sign of any magnetic ordering between 1·1°K and 4·3°K.[9] The alloys are, however, atomically disordered so that considerable spin-disorder scattering would be expected even if localized spins were completely ordered in orientation. Then, too, it is not completely obvious that magnetic orientational ordering must occur at or above liquid helium temperatures and in this regard it is significant that unannealed α-Mn has apparently been observed to display an appreciable spin-disorder resistivity contribution at 4·2°K.[37,1] It would appear that neutron diffraction experiments might be the most direct method of investigating possible localized spin states in the b.c.c. alloys discussed here. Added interest is attached to such studies because of current concern with the effects of localized spin states on superconducting transition temperatures.[38]

6. SUMMARY

The present measurements show that b.c.c. Ti-rich Ti–Mo alloys are superconducting at liquid helium temperatures. Above their resistive superconducting transitions the alloys display high electrical resistivities which are anomalous in both their concentration and temperature dependence. It is unlikely that the anomalies are due to atomic ordering or structural transformation. The form of the concentration dependence of the Hall coefficients, considered in conjunction with superconductivity and electronic specific heat data, appears to preclude any simple interpretation of the concentration dependence of the resistivity on the basis of concentration dependent electronic factors such as the numbers and effective masses of current carriers in various bands or the density of states into which they can be scattered. The existence of spin-disorder scattering in these alloys might account for the resistive anomalies although the present measurements provide no definitive evidence for its presence.

Notes added in proof: (1) In a recent paper, BLATT (*J. Phys. Chem. Solids* **17,** 177 (1961)) has attempted a *quantitative* application of the MOTT–JONES two band *s–d* type model to the data of CHANDRASEKHAR and HULM[20], BERLINCOURT[22], and GOODMAN *et al.*[40] (specific heat) on b.c.c. U–rich U–Mo alloys. These alloys display electronic properties rather similar to those exhibited by the b.c.c. Ti–Mo alloys considered above. BLATT concludes that "all available data are consistent with a reasonable density of states curve", even though his analysis as applied to the resistivity and Hall effect data yields "unreasonable magnitudes for the derivatives of $N(E_F)$". For the case of the presently considered Ti-rich b.c.c. Ti–Mo alloys, the solute concentration dependence of the resistivity (considering the specific heat data, see Section 5 above), as well as the temperature dependence of the Hall coefficients, is in a direction opposite to that predicted by BLATT's analysis.

(2) Recent measurements of resistivity (ρ), Hall coefficient (R), and resistive superconducting transitions on two b.c.c. Ti–6·25 a/o Mo specimens (cut from the specimen which was measured calorimetrically[9]) are in excellent agreement with extrapolations of the present data to the 6·25 a/o Mo concentration. The data for the two specimens are nearly identical. The values measured for one specimen (Q1) are: $\rho(\sim 293°K) = 149{\cdot}0$, $\rho(273°K) = 149{\cdot}5$, $\rho(195°K) = 149{\cdot}6$, $\rho(77°K) = 148{\cdot}1$, $\rho(4{\cdot}2°K) = 147{\cdot}9$, all in microhm cm; and $R(\sim 293°K) = +22{\cdot}4$, $R(77°K) = +39{\cdot}8$, $R(4{\cdot}2°K) = +43{\cdot}3$, all in 10^{-5} cm^3/C.

Acknowledgements—We wish to acknowledge the valuable contributions of C. G. RHODES who carried out the micrographic and hardness examinations, of P. C. ROMO and F. M. FARRAH who provided the X-ray diffraction analyses, and of P. W. BICKEL who assisted in making the electrical measurements.

REFERENCES

1. COLES B. R., *Advanc. Phys.* **7,** 40 (1958).
2. WEISS R. J. and MAROTTA A. S., *J. Phys. Chem. Solids* **9,** 302 (1959).
3. ANDERSON G. S. and LEGVOLD S., *Phys. Rev. Letters* **1,** 322 (1958).
4. AMES S. L. and MCQUILLAN A. D., *Acta Met.* **2,** 831 (1954).
5. ADENSTEDT H. K., PEQUIGNOT J. R. and RAYMER J. M., *Trans. Amer. Soc. Metals* **44,** 990 (1952).

6. BROTZEN F. R., HARMON E. L. and TROIANO A. R., *Trans. AIME* **203,** 413 (1955).
7. YOSHIDA S. and TSUYA Y., *J. Phys. Soc. Japan* **11,** 1206 (1956).
8. For a preliminary account of this work see HAKE R. R., LESLIE D. H. and BERLINCOURT T. G., *Bull. Amer. Phys. Soc.* (Ser. II) **4,** 362 (1959).
9. For an abbreviated account of this work see HAKE R. R., *Proceedings of the VIIth International Conference on Low Temperature Physics* (Toronto, 1960), to be published.
10. For a recent review of the physical metallurgy of Ti alloys see JAFFEE R. I., *Progress in Metal Physics* Vol. VII, p. 65 Pergamon Press, London (1958).
11. DUWEZ P., *Trans. AIME* **191,** 765 (1951).
12. DUWEZ P., *Trans. Amer. Soc. Metals* **45,** 934 (1953).
13. For a review of the pertinent literature see HANSEN M., *Constitution of Binary Alloys*, p. 976. McGraw-Hill, New York (1958).
14. SPACHNER S. A. and ROSTOKER W., *Trans. AIME* **212,** 765 (1958).
15. HOLDEN F. C., OGDEN H. R. and JAFFEE R. I., *J. Metals N.Y.* **8,** 1388 (1956).
16. HANSEN M., KAMEN E. L., KESSLER H. D. and MCPHERSON D. J., *Trans. AIME* **191,** 881 (1951).
17. BERLINCOURT T. G., *Phys. Rev.* **114,** 969 (1959).
18. WHITE G. K. and WOODS S. B., *Phil. Trans.* **251,** 273 (1959).
19. BERLINCOURT T. G., *Phys. Rev.* **112,** 381 (1958).
20. CHANDRASEKHAR B. S. and HULM J. K., *J. Phys. Chem. Solids* **7,** 259 (1958).
21. LOASBY R. G., *Proc. Phys. Soc. Lond.* **72,** 425 (1958).
22. BERLINCOURT T. G., *J. Phys. Chem. Solids* **11,** 12 (1959).
23. HAKE R. R., LESLIE D. H. and BERLINCOURT T. G., unpublished work.
24. WYATT J. L., *Trans. AIME* **197,** 903 (1953).
25. See, for example, MOTT N. F. and JONES H., *Theory of Properties of Metals and Alloys*, pp. 240–314. Clarendon Press, Oxford (1936); reprinted by Dover Publications, Inc., New York (1958).
26. For a discussion see JONES H., *Encyclopedia of Physics* (edited by FLÜGGE S.) Vol. 19, p. 298. Springer, Berlin (1956).
27. MATTHIAS B. T., *Progress in Low Temperature Physics* (edited by GORTER C. J.) Vol. 2, p. 138. Interscience, New York (1957).
28. MATTHIAS B., COMPTON V. B., SUHL H. and CORENZWIT E., *Phys. Rev.* **115,** 1597 (1959).
29. SERAPHIM D. P. and CONNELL R. A., *Phys. Rev.* **116,** 606 (1959).
30. REEBER M. D., *Phys. Rev.* **117,** 1476 (1960).
31. SHAW R. W. and MAPOTHER D. E., *Phys. Rev.* **118,** 1474 (1960).
32. PINES D., *Phys. Rev.* **109,** 280 (1958).
33. BARDEEN J., COOPER L. N. and SCHRIEFFER J. R., *Phys. Rev.* **108,** 1175 (1957).
34. MATTHIAS B. T. and BOZORTH R. M., *Phys. Rev.* **109,** 604 (1958).
35. WILKINSON M. K., SHULL C. G. and RUNDLE R. E., *Phys. Rev.* **99,** 627 (1955).
36. MOTT N. F. and STEVENS K. W. H., *Phil. Mag.* **2,** 1364 (1957).
37. WHITE G. K. and WOODS S. B., *Canad. J. Phys.* **35,** 346 (1957).
38. MATTHIAS B., *J. Appl. Phys.* **31,** 23S (1960).
39. BUCHER E., BUSCH G. and MÜLLER J., *Helv. Phys. Acta* **32,** 318 (1959).
40. GOODMAN B. B., HILLAIRET J., VEYSSIÉ J. J. and WEIL L., *Proceedings of the VIIth International Conference on Low Temperature Physics*. Univ. of Toronto Press, Toronto (1960).

J. Phys. Chem. Solids Pergamon Press 1961. Vol. 20, Nos. 3/4, pp. 187–189. Printed in Great Britain.

ELECTRON SPIN RESONANCE OF IRRADIATED FERROELECTRIC TRI-GLYCINE SULFATE

R. BLINC, S. DETONI, I. LEVSTEK, M. PINTAR, S. POBERAJ and M. SCHARA

J. Stefan Institute, Ljubljana, and Ljubljana University, Ljubljana, Yugoslavia.

(*Received* 24 *January* 1961)

Abstract—A preliminary analysis of the electron spin resonance spectra of ferroelectric tri-glycine sulfate single crystals, which were subjected to γ-ray damage indicated that:

(a) the principal stable radical produced by γ-ray damage is $NH_3\dot{C}H$—;
(b) the orientations of the radicals are fixed in the crystal lattice;
(c) the approximate values of the $H_{(c)}$, the three $H_{(N)}$, and the N Fermi coupling constants are 21·0, 14·5 and 3·2 G respectively;
(d) the NH_3 group is rotating in the ferroelectric phase.

INTRODUCTION

TRI-GLYCINE sulfate (TGS) is one of the few crystals exhibiting ferroelectricity at room temperature. It is a ferroelectric with low coercive field and simple domain structure and therefore appears to be a promising material for use in memory devices of computers. Exposure to ionizing radiation produces striking changes in its electrical properties.[1] The mechanism of these effects is not yet fully understood. Recently it was reported that although the infrared spectrum of TGS is only slightly affected by radiation, drastic changes are found in the ultraviolet spectrum.[2] These changes cannot be due to color centers, for they decay neither with time nor with application of heat.

In order to elucidate the radiation damage in this crystal the electron spin resonance spectrum of a γ-irradiated single crystal of TGS was studied. The object of this paper is to report some preliminary results of the room temperature measurements.

EXPERIMENTAL

The irradiations of the TGS crystals were carried out at room temperature with a Co^{60} γ-ray source ($0{\cdot}6 \times 10^6 r$). The electron magnetic resonance spectra were observed with a home built spectrometer working at 9100 Mc/s with recorder presentation of the derivative of the absorption curve. The klystron was frequency modulated with 35 Mc/s. The circulator instead of the magic T was used for automatic frequency stabilization. By this method the sensitivity is increased by a factor $2\sqrt{2}$.[3] Spectroscopic splitting factors were measured in the x, y, and z directions by comparing the position of the centre of the radical spectrum with that of DPPH.

RESULTS AND DISCUSSION

The results of the present work show that stable free radicals are formed in irradiated TGS. The spectra immediately after irradiation and the spectra of an irradiated crystal, aged for two months at room temperature, are exactly the same. The spectroscopic splitting factors are very close to the free spin value. The small asymmetry of the spectra (Fig. 1) with respect to their own centers demonstrates the occurrence of two or more differently oriented radicals in the unit cell with slightly anisotropic g-factors.

The orientation dependence of the spectra (Fig. 1) shows that the radicals are fixed in the crystal lattice. The hyperfine splitting thus arises from combined effects of the isotropic Fermi contact interactions and the anisotropic electron–nuclear dipolar interaction.

In order to identify the radicals the line shape

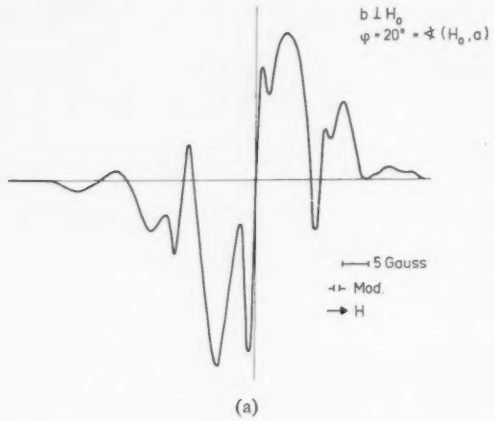

(a)

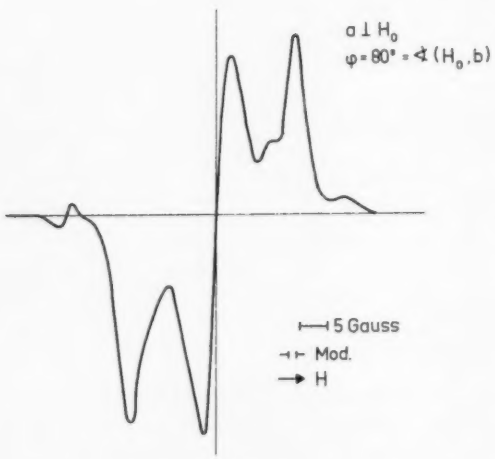

(b)

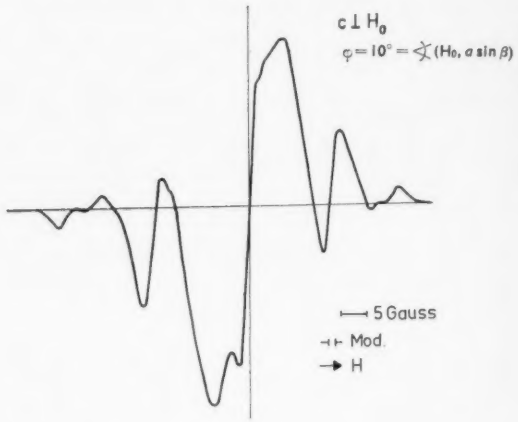

(c)

FIG. 1. Derivatives of the electron spin resonance absorption lines for a gamma-irradiated single crystal of TGS at 9·1 kMcs.

(a) $b \perp H_0$, $\varphi = 20°$ ($\varphi \sphericalangle a, H_0$);
(b) $a \perp H_0$, $\varphi = 80°$ ($\varphi \sphericalangle b, H_0$);
(c) $c \perp H_0$, $\varphi = 10°$ ($\varphi \sphericalangle a \sin \beta, H_0$).

should be, at least approximately, evaluated. The well known spin Hamiltonian for an oriented free radical can be written as a sum of the electronic Zeeman coupling, the isotropic and anisotropic hyperfine interactions, and the nuclear Zeeman coupling. In the present case, the nuclear Zeeman coupling is negligible in comparison with the hyperfine terms. The strong field and isotropic g-factor approximation can be applied as well. Further the spectra seem to indicate that the isotropic part of the hyperfine interaction always exceeds the anisotropic part. For the purpose of identifying the radicals thus only the isotropic hyperfine coupling has to be considered. In this approximation, it seems to be possible to fit the isotropic part of the spectra to the following spin Hamiltonian:

$$\mathcal{H}_0 = g\beta H_0 S_z + (a_1 I_{1z} + a_2 I_{2z} + a_3 I_{3z}) S_z, \quad (1)$$

with $I_1 = \frac{1}{2}$, $I_2 = \frac{3}{2}$, $I_3 = 1$, and $a_1 = 21{\cdot}0$, $a_2 = 14{\cdot}5$ and $a_3 = 3{\cdot}2$ G. Using the selection rules $\Delta M_s = \pm 1$ and $\Delta M_I = 0$, twenty-four transitions have non-zero intensity. The calculated spectrum, assuming Gaussian line shapes with $\sigma = 1{\cdot}6$ G, is reproduced in Fig. 2.

The present results seem to show that it is

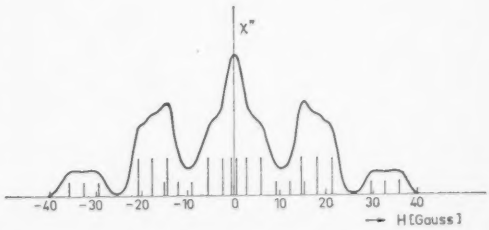

FIG. 2. Isotropic part of the $NH_3\dot{C}H$— absorption spectrum calculated from $\mathcal{H}_0 = g\beta H_0 S_z + (a_1 I_{1z} + a_2 I_{2z} + a_3 I_{3z}) S_z$ using the assumption of Gaussian line shapes with $\sigma = 1{\cdot}6$ G.

Vol. 2
1961

possible to interpret the spectra as resulting from a $NH_3\dot{C}H$— radical. This radical is produced from the parent molecule by the destruction of one of the C—H bonds in the CH_2 group, as found in α-glycine[4] and N-acetylglycine.[5] The a_1 Fermi coupling constant is identified as the coupling with $H_{(C)}$, a_2 is identified as the coupling with the three $H_{(N)}$, and a_3 is the N coupling constant. The numerical values of these constants, however, must be treated with some caution as they can be in error by as much as twenty per cent. The equivalence of the coupling of the electron to the three NH_3 protons requires rapid reorientation of the NH_3 group in the ferroelectric phase just below the Curie point as found in an earlier nuclear magnetic resonance study.[6]

Acknowledgements—The authors are very grateful to Dr. R. NITSCHE, RCA Laboratories, Zürich for a gift of the TGS single crystals and to Professor I. KUŠČER for a critical reading of the manuscript.

REFERENCES

1. CHYNOWETH A. G., *Phys. Rev.* **113,** 159 (1959).
2. DODD D. M., *Spectrochim. Acta* **15,** 1072 (1959); **16,** 113 (1960).
3. POBERAJ S., Thesis, University of Ljubljana (1959).
4. GHOSH D. K. and WHIFFEN D. H., *Mol. Phys.* **2,** 285 (1959).
5. MIYAGAWA I., KURITA Y. and GORDY W., *J. Chem. Phys.* **33,** 1599 (1960).
6. BLINC R., DETONI S. and PINTAR M., to be published.

ol. 20
1961

J. Phys. Chem. Solids Pergamon Press 1961. Vol. 20, Nos. 3/4, pp. 190–192. Printed in Great Britain.

OPTICAL INVESTIGATION OF THE BAND STRUCTURE OF Ge–Si ALLOYS

J. TAUC and A. ABRAHÁM

Institute of Technical Physics, Czechoslovak Academy of Sciences, Prague, Czechoslovakia.

(*Received* 6 *March* 1961)

Abstract—The reflection spectra of Ge–Si alloys have been measured at room temperature in the photon energy range 2–5 eV. The curve giving the dependence of the energy of the first characteristic peak in the reflection spectrum on the composition of the alloy shows a break at about 79 at. per cent of Si. The consequences of this observation for the band structure are discussed.

MEASUREMENTS of the dependence of the absorption edge in Ge–Si alloys on composition made it possible to draw important conclusions about the band structure of this system.[1, 2, 3] A study of the reflection spectra reported here allowed us to find analogous results for the band structure in the higher energy range.

EXPERIMENTAL

The measurements were performed with a double-prism monochromator using a 1 P 28 photomultiplier with a galvanometer. It was possible to measure either the absolute value of the reflectivity with a moving detector or the reflection spectrum relative to an aluminium mirror. The samples were coarsely polycrystalline and were polished and etched before measurement. It was generally impossible to obtain reliable absolute values for the reflectivity with etched samples, however, the position of the peaks could be much better determined than with polished samples. The reproducibility of the position of the peaks on different samples of the same composition was within about $\pm 0{\cdot}02$ eV. The composition was determined by X-ray methods using the data by JOHNSON and CHRISTIAN[1]. The powder necessary for the X-ray analysis was scratched directly from the surface of the samples after the optical measurements were finished. The precision of the method and the homogeneity of the samples were such that their composition was determined with an error of about ± 1 at. per cent.

The first peak in the curve giving reflectivity vs. photon energy was observed in germanium near 2 eV[4, 5, 6]; it has been shown later[7, 8] that it is split, even at room temperature, into two peaks (a) at 2·1 eV and (b) at 2·3 eV. (See Fig. 1). If Si is added to Ge the general features of the reflection spectrum remain the same for the whole composition range including pure silicon; the peaks (a) and (b) move towards higher energies. The peak (b) is always smaller than (a) and progressively less and less distinct as the content of Si is increased; starting at about 35 atomic per cent of Si it was not observable at all at room temperature. The first peak in Si has been found[9] at 3·4 eV.

DISCUSSION

The question how much information on the optical constants can be deduced from a measurement of the reflection spectrum in a restricted photon-energy range has been discussed by VELICKÝ[10]. Using his results, we can confidently assume that the peaks in the reflection spectra of Ge–Si alloys are related to the characteristic features of the absorption spectrum in an analogous way as in Ge and Si, in which this relation has been explicitly found by PHILIPP and TAFT[6, 9]. On this assumption are based our deductions concerning the band structure.

PHILLIPS[11] gave two independent reasons to ascribe the first peak in germanium to the transition $L_3' \rightarrow L_1$. His suggestion was later confirmed[7] by the observation that this peak is a double peak

Vol. 2
196

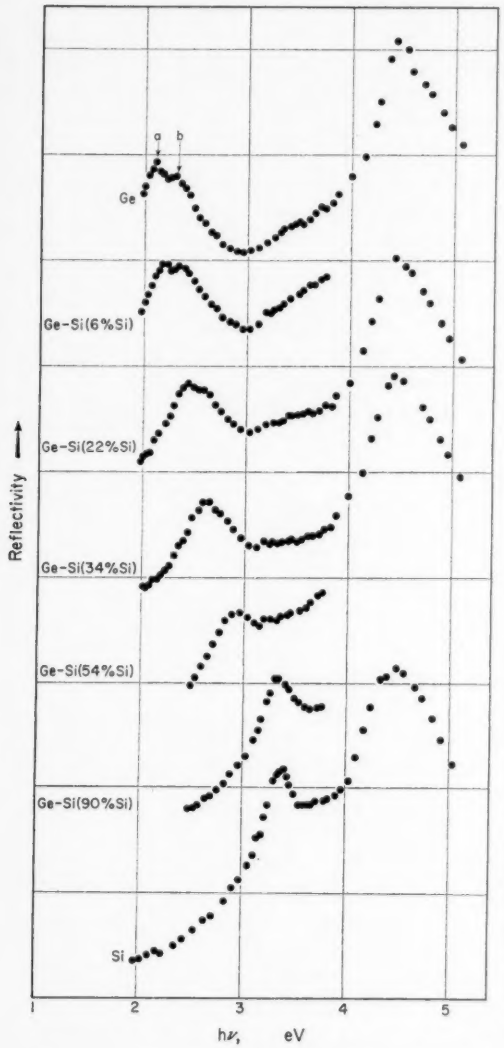

FIG. 1. Reflection spectra of Ge–Si alloys at 300°K. The reflectivity in the first peak is in the neighbourhood of 50 per cent for all samples; the difference between two horizontal lines corresponds to 10 per cent.

as there are theoretical reasons to expect that the state L_3' must be split by spin–orbit interaction.[12] In silicon, recent theoretical work has shown that in the conduction band the state L_3 has a lower energy than L_1.[13, 14] The first peak in the reflection spectrum of Si should then correspond to a different transition than in germanium. If the dependence of the energy difference involved in this transition on the composition is different from that of $L_3' \rightarrow L_1$, a break in the curve giving the position of the first peak vs. composition is to be expected.

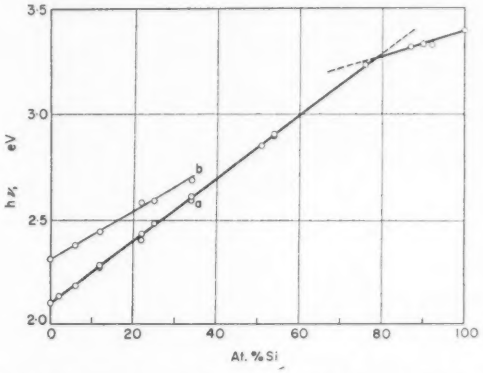

FIG. 2. Dependence of the energy of the peaks (a) and (b) in the reflection spectrum of Ge–Si alloys on composition.

This was actually confirmed by our measurements as seen in Fig. 2: at the composition of about 79 atomic per cent of Si a break is distinctly apparent.

This proves that in Si the first peak corresponds to another transition than in Ge; it is difficult, however, to be sure with the presently known experimental and theoretical facts which this transition should be. The most simple possibility is to assume that it corresponds to the transition $L_3' \rightarrow L_3$. The second peak in the reflection spectrum which has in the whole composition range an almost constant position near 4·5 eV may correspond to the transition $X_4 \rightarrow X_1$ as has been suggested for germanium by PHILLIPS[11]. With this assumption the band structure of the Ge–Si system is suggested in Fig. 3. We used here the results of the absorption measurements near the edge[3] and a linear extrapolation of the curves involved. The energy levels were referred to the state Γ_{25}', arbitrarily assumed constant in the whole composition range.

The assumption that in silicon the transition $X_4 \rightarrow X_1$ corresponds to a higher energy than

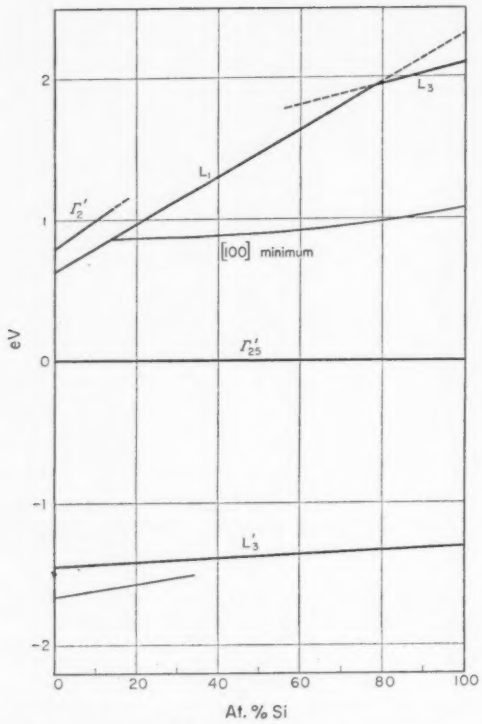

FIG. 3. Suggested band structure of Ge–Si alloys.

$L_3' \rightarrow L_3$ contradicts the results of the recent calculations on silicon,[13, 14] which suggest that the contrary may be true. However, as Dr. PHILLIPS kindly pointed out to us, the precision of this part of the computations is, in view of the comparatively small energy difference between both transitions, not high enough to make the statement definitive.

Acknowledgements—We thank Dr. Z. TROUSIL for the preparation of the samples, Dr. K. TOMAN for the determination of their composition and Dr. E. ANTONČÍK for helpful discussions.

REFERENCES

1. JOHNSON E. R. and CHRISTIAN S. M., *Phys. Rev.* **95,** 560 (1954).
2. HERMAN F., *Phys. Rev.* **95,** 847 (1954).
3. BRAUNSTEIN R., MOORE A. R. and HERMAN F., *Phys. Rev.* **109,** 695 (1958).
4. AVERY D. G., *Proc. Phys. Soc. Lond.* B**66,** 512 (1953).
5. KOC S., *Czech. J. Phys.* **7,** 91 (1957).
6. PHILIPP H. R. and TAFT E. A., *Phys. Rev.* **113,** 1002 (1959).
7. TAUC J. and ANTONČÍK E., *Phys. Rev. Letters* **5,** 253 (1960).
8. TAUC J. and ABRAHÁM A., *Proceedings of the Conference on Semiconductor Physics, Prague* 1960 (in press).
9. PHILIPP H. R. and TAFT E. A., *Phys. Rev.* **120,** 37 (1960).
10. VELICKÝ B., *Czech. J. Phys.* (in press).
11. PHILLIPS J. C., *J. Phys. Chem. Solids* **12,** 208 (1960).
12. ROTH L. M. and LAX B., *Phys. Rev. Letters* **3,** 217 (1959).
13. BASSANI F., *Nuovo Cim.* **13,** 244 (1959).
14. KLEINMAN L. and PHILLIPS J. C., *Phys. Rev.* **118,** 1153 (1960).

J. Phys. Chem. Solids Pergamon Press 1961. Vol. 20, Nos. 3/4, pp. 193–196. Printed in Great Britain.

ON THE DIELECTRIC LOSS AND THERMAL BLEACHING OF CALCITE IRRADIATED BY X-RAYS

K. V. RAO

Department of Physics, Indian Institute of Technology, Kharagpur, India.

(*Received* 27 *February* 1961)

Abstract—The changes produced by X-ray irradiation in the dielectric and optical properties of calcite crystals are reported. At ordinary temperatures, the dielectric constant as well as the dielectric loss of the uncoloured crystal remains practically unchanged in the frequency region of 10 kc/s–15 Mc/s. It has been found that the temperature variation of its dielectric loss can be represented by an equation $\tan\delta = A + Be^{-0.4/kT}$ where A and B are constants; this is attributed to the movement of vacancies in the crystal.

On irradiation by X-rays, calcite exhibits pronounced optical absorption in the ultraviolet region beyond 400 mμ; the dielectric loss of calcite also increases considerably on colouration. The thermoluminescence shows a very strong glow peak at 85°C with minor ones at higher temperatures. During thermal bleaching, the dielectric loss of the coloured crystal shows a prominent maximum in the temperature range 70–120°C and beyond 230°C, it varies in the same way as in the case of the uncoloured crystal. The correspondence between the change in dielectric loss and the first glow peak is possibly due to thermal release of trapped electrons. The optical absorption disappears when the crystal is heated to 350°C and on cooling to room temperature, its dielectric loss returns to its original value before colouration.

INTRODUCTION

THE colouration of alkali halides by X-ray irradiation and the corresponding changes in their electronic properties have been extensively studied;[1–4] such investigations have yielded valuable information about the defects and electronic processes that take place inside an ionic crystal. But similar investigations on other substances have as yet received limited attention.

Natural calcite is available in the form of comparatively large single crystals, which are transparent in the near visible region. Also these crystals show an extraordinary long period afterglow extending to 10 hr. As such these crystals are quite suitable for the investigation of the effect of X-ray irradiation on their optical and dielectric properties.

Several workers[5–10] have investigated the effect of radium as well as X-ray irradiation on the optical absorption and thermoluminescence of both natural and artificial calcite crystals. In the present work, the effects of irradiation on the dielectric constant and loss of calcite have been studied; the dielectric changes during the process of thermal bleaching have also been measured. Along with this, the optical absorption and the thermoluminescence of the crystal have been studied.

EXPERIMENTAL

The optical absorption spectra in the visible and ultra-violet region were measured with a Beckmann (DU Model/2400) Spectrophotometer. The thermoluminescence of the samples was studied with the conventional experimental arrangement. The changes in the dielectric loss and constant were measured with Marconi Circuit Magnification Meter Type TF329G using the resonance curve principle as was done by GARLICK and GIBSON[11].

The present investigations were carried out with cleaved crystals of natural calcite of good optical quality, and in the final form, these had dimensions of about $20 \times 20 \times 1$ mm. These were exposed to X-rays at a distance of 2 cm from the tungsten target of a Machlett tube run at 50 kV

and 20 mA for about 12 hr. The samples after colouration were kept in the dark and all measurements were made at room temperature (about 25°C).

RESULTS

The dielectric constant of calcite at room temperature is 8·0 and the dielectric loss is below $\tan\delta = 0{\cdot}0001$, the values being practically independent of frequency in the region of 10 kc/s–15 Mc/s. No relaxation peak is observed in this frequency range. On colouration with X-rays, the dielectric constant remains unchanged within the limits of accuracy of the present measurement (0·1 per cent). The dielectric loss of the coloured calcite is increased to about $\tan\delta = 0{\cdot}001$ after irradiation. On bleaching the crystal by heating it to a temperature of 350°C and then cooling to room temperature, the dielectric loss reduces to its original value. In the coloured calcite also, no relaxation peak could be detected in the frequency range mentioned above.

The dielectric loss of calcite before exposure to X-rays, remains below $\tan\delta = 0{\cdot}0001$ up to a temperature of 150°C; above this temperature, it is found to increase rapidly (Fig. 1). The dielectric loss of irradiated calcite during thermal bleaching, also shown in Fig. 1, passes through a maximum in the temperature range 40–130°C, which agrees with that of the most prominent glow peak of thermoluminescence; above 130°C, it decreases up to a temperature of about 230°C beyond which it again shows an increase. This part is the same as that of an uncoloured crystal. The temperature variation of the dielectric loss of bleached crystal is practically identical with that of a virgin crystal.

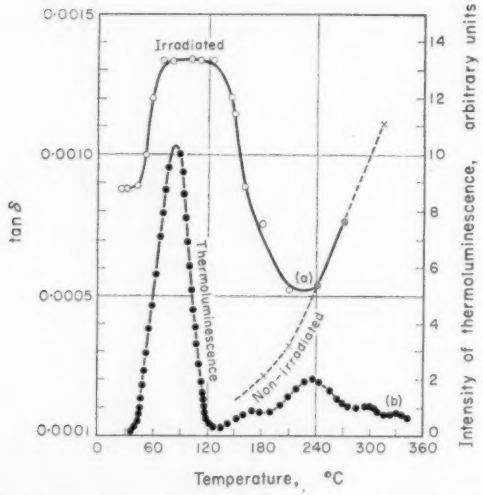

FIG. 1(a) Dielectric loss of calcite as a function of temperature before and after X-ray irradiation. The sample is exposed for 12 hr to tungsten radiation at 50 kV and 20 mA.

(b) Thermoluminescence curve of calcite crystal; rate of heating is about 1·5°C/sec, the dosage of irradiation being approximately the same as above.

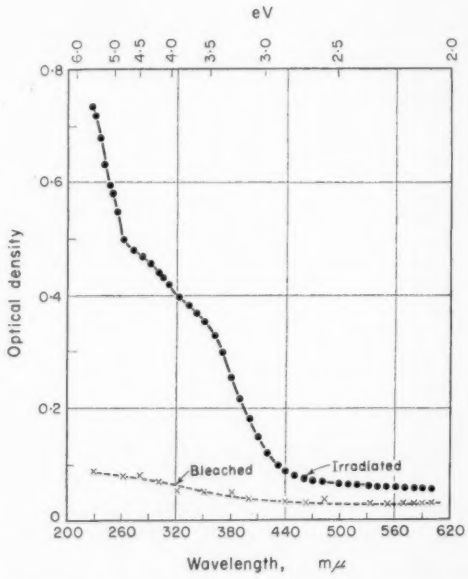

FIG. 2. The absorption spectra of X-ray irradiated calcite crystal before and after thermal bleaching. Measurements pertain to the same sample as for Fig. 1.

The absorption spectrum of calcite, on colouration by X-rays, is shown in Fig. 2. It shows the extra absorption induced in the crystal by X-rays in the region beyond 440 mμ; absorption peaks appear to be present at 290 mμ and 350 mμ. This induced absorption is wiped away by heating the crystal to a temperature of 350°C; there is

however an increase in the general level of optical absorption beyond 400 mμ towards the ultraviolet region. This might be due to increased scattering of light by the bleached crystal.

The thermoluminescence pattern of calcite, excited by X-rays, is shown in Fig. 1. It has five peaks at temperatures of 85°C, 171°C, 234°C, 299°C and 329°C. The exact spectral nature of emission at different stages of thermoluminescence is not known, but the measurements of the thermoluminescence for different spectral regions, isolated by red, blue and Wood's filters, indicate that (a) the emission during thermoluminescence is mostly confined to the visible range, and (b) the relative intensity of emission in different spectral regions is not the same for all the glow peaks. The trap depths obtained for the glow peaks are 0·67 eV, 0·82 eV, 0·93 eV, 1·14 eV and 1·22 eV respectively, calculated using the relation $E = 21\,kT_g$.

Calcite after X-ray excitation shows a very long period afterglow at room temperature. The afterglow emission is mostly in the red–yellow region and it persists over ten hours.

DISCUSSION

The absorption spectrum of the coloured calcite does not have well defined bands (like the absorption bands of the alkali halides); it has rather the appearance of the long wavelength tail of the fundamental absorption of solids. The logarithm of the absorption coefficient of the coloured calcite is plotted against $\log(E - V_0)$ in Fig. 3. The slope of the straight line near the origin is found to be nearly 0·5. Thus, the absorption band appears to be due to a transition from the defect centres to the conduction band of the crystal.[12]

The thermoluminescence measurements show that about 90 per cent of the stored-up energy is released by the coloured crystal in the temperature range of 30–120°C.

The difference between the dielectric losses of the crystal before and after colouration, i.e. $\Delta \tan \delta$, for different stages of thermal bleaching shows a pronounced peak around 90°C which bears a general resemblance to the thermoluminescence curve for the sample. This indicates the identical nature of the mechanism involved in the two cases. It may therefore be presumed that the trapped electrons are thermally raised to the conduction band and produce thermoluminescence in the process of recombination with the holes initially created by X-rays. The increase in conductivity of the crystal at this stage is due to such electrons in the conduction band.

The temperature variation of the dielectric loss of calcite before X-ray irradiation, can be represented by the sum of a constant part and an exponential part, e.g. $\tan \delta = 7{\cdot}0 \times 10^{-5} + 3{\cdot}14 \exp(-0{\cdot}4/kT)$.

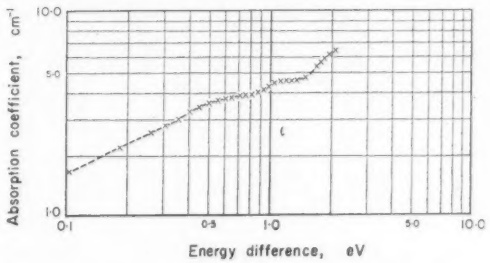

FIG. 3. Absorption coefficient of coloured calcite as a function of energy difference $(E - V_0)$ where V_0 is taken as the energy corresponding to 412 mμ.

The results indicate that the lattice vacancies become comparatively mobile above about 150°C; the activation energy for such mobility is 0·4 eV. The constant part may be due to other mechanism for which the activation energy is much higher.

Acknowledgements—The author is indebted to Prof. H. N. BOSE for suggesting the problem and guiding him throughout the work. He is thankful to Dr. J. SHARMA for helpful discussions and to Prof. S. GUPTA for providing the facilities of work and encouragement.

REFERENCES

1. DUTTON D. and MAURER R., *Phys. Rev.* **90,** 126 (1953).
2. ISHIGURO M., ODA F. and FUJINO T., *Phys. Rev.* **95,** 1347 (1954).
3. CHRISTY R. W. and HARTE W. E., *Phys. Rev.* **109,** 710 (1958).
4. KALABUKOV N. P., *Zh. Eksp. Teor. Fiz.* **27,** 347 (1954); *Sci. Abstr.* 5088 (1955).
5. PRZIBRAM K., *Phys. Z.* **25,** 640 (1924).
6. HEADDEN W. P., *Amer. J. Sci.* **5,** 301 (1906).

7. GROGER L., *Schr. Balkankomm. Akad. Wiss. Wien* IIa, **135,** 705 (1926).
8. STEINMETZ H., *Fortschr. Min.* **20,** 58 (1936).
9. HAYAKAWA N., *Technol. Rep. Tôhoku Univ.* **22,** 187 (1958).
10. DEBENEDETTI H., *Nuovo Cim.* **7,** 251 (1958).
11. GARLICK G. F. J. and GIBSON A. F., *Proc. Roy. Soc.* **188**A, 485 (1947).
12. DEXTER D. L., *Nuovo Cim. Suppl.* **7,** 245 (1958).

Vol. 2
196

J. Phys. Chem. Solids Pergamon Press 1961. Vol. 20, Nos. 3/4, pp. 197–203. Printed in Great Britain.

MEASUREMENT AND ANALYSIS OF THE INFRARED REFLECTION SPECTRUM OF SEMICONDUCTING SnS

C. HAAS and M. M. G. CORBEY

Philips' Research Laboratories, N.V. Philips' Gloeilampenfabrieken, Eindhoven, The Netherlands

(*Received* 23 *February* 1961)

Abstract—The infrared reflection spectrum of p-type SnS single crystals was measured between 2 and 25μ. The observed dispersion was ascribed to the combined effects of lattice vibrations and free holes. An analysis gave for the index of refraction $n_0 = 3{\cdot}6 \pm 0{\cdot}1$, the dielectric constant $\epsilon = 19{\cdot}5 \pm 2$, and the effective charge on the atoms $e^* = 0{\cdot}7e_0$.

The effective mass of holes is isotropic in the plane perpendicular to the c-axis, with $m_\perp^* = 0{\cdot}20m_0$; the effective mass parallel to the c-axis is much larger: $m^* \simeq m_0$.

1. INTRODUCTION

VARIOUS processes give rise to absorption in semiconducting crystals. In the first place transitions of electrons over the forbidden gap cause a very strong intrinsic absorption at photon energies larger than the bandgap E_G. Secondly transitions of electrons from the valence or conduction band to localized impurity levels give rise to absorption bands at smaller photon energies. The presence of free carriers results in an absorption which strongly increases with wavelength. Finally, in the case of polar crystals a very strong absorption band in the infrared is due to lattice vibrations.

In this paper we consider the reflection of SnS at rather long wavelenghs. This means, we investigate the region $h\nu \ll E_G$, where the effect of intrinsic band-to-band transitions has disappeared. The strength of transitions to impurity levels is usually not sufficient to have any marked influence on the reflection. Therefore the measurements of the infrared reflection spectrum of a polar semiconductor such as SnS in the frequency region $h\nu < E_G$ will give information only on the lattice vibrations and on the properties of the free carriers.

Optical properties are conveniently described by a complex refractive index $n-ik$, where n is the (real) refractive index, and k the absorption index. The contribution of lattice vibrations for a polar crystal AB (with only one absorption band at a frequency ν_0) to this complex index of refraction at frequency ν is:

$$(n-ik)^2 = n_0^2 + \left(\frac{n_0^2+2}{3}\right)^2 \times \frac{N_0 e^{*2}}{\pi M[\nu_0^2 - \nu^2 + (i\nu/2\pi\tau_0)]} \qquad (1)$$

where N_0 is the number of atom pairs AB per cm^3, e^* the effective charge of these atoms, M the reduced mass ($1/M = 1/M_A + 1/M_B$), ν_0 the vibration frequency of atoms A with respect to B, and τ_0 a relaxation time related to the damping of the vibrations.[1]

The presence of free carriers, say holes, with a concentration p per cm^3, also contributes to $(n-ik)^2$. According to the Drude–Zener theory[2] this contribution is:

$$-\frac{pe^2}{\pi m^*} \times \frac{1}{\nu^2 - (i\nu/2\pi\tau)} \qquad (2)$$

where m^* is the effective mass of the holes, and τ a relaxation time describing the scattering of holes from one state to another in the same valence band.

The complete equation for the index of refraction

for a polar semiconductor containing p holes per cm^3 is:

$$(n-ik)^2 = n_0^2+\left(\frac{n_0^2+2}{3}\right)^2 \frac{N_0 e^{*2}}{\pi M(\nu_0^2-\nu^2+i\nu/2\pi\tau_0)} - \frac{pe^2}{\pi m^*}\frac{1}{(\nu^2-i\nu/2\pi\tau)}. \quad (3)$$

In a cubic crystal one (complex) index of refraction is sufficient to describe the optical properties. In a rhombic crystal, such as SnS, there are three, mutually perpendicular crystallographic axes a, b and c, and to each axis corresponds an equation (3), with in general different values of n_0, e^*, ν_0, m^*, τ and τ_0 for the three axes.

For light polarized parallel to the a-axis, for instance, one should use equation (3) for the a-axis (with n_a, k_a, n_{0a}, e_a^* etc.).

At sufficiently high frequencies of the light ($\nu\tau \gg 1$ and $\nu\tau_0 \gg 1$) the imaginary part of equation (3) becomes small, and we have approximately:

$$n^2 = n_0^2+\left(\frac{n_0^2+2}{3}\right)^2 \frac{N_0 e^{*2}}{\pi M(\nu_0^2-\nu^2)} - \frac{pe^2}{\pi m^*\nu^2} \quad (4)$$

In this case the absorption index k is small, and the reflection coefficient for normal incidence

$$R = \frac{(n-1)^2+k^2}{(n+1)^2+k^2} \quad (5)$$

becomes approximately equal to $(n-1)^2/(n+1)^2$. The reflection then depends only on dispersion, and a measurement of R gives us directly the value of n.

2. EXPERIMENTAL

We have measured the reflection coefficient for approximately normal incidence of SnS single crystals between 2 and 25 μ, using a conventional infrared spectrometer with NaCl and KBr prisms. In a number of cases measurements were done with light, polarized by an infrared polarizer consisting of AgCl sheets set at the Brewster angle.

SnS crystallizes in a pseudotetragonal, rhombic crystal structure.[3] The single crystals used were grown by zone-levelling.[4] The crystals were cut out in such a way that the reflecting surface was perpendicular to one of the crystallographic axes. The surface was polished in a conventional way. We were not able to obtain optically good surfaces in this way; at shorter wavelengths ($\lambda < 3\mu$) scattering at the surface was appreciable, but at long wavelengths this scattering was of little importance.

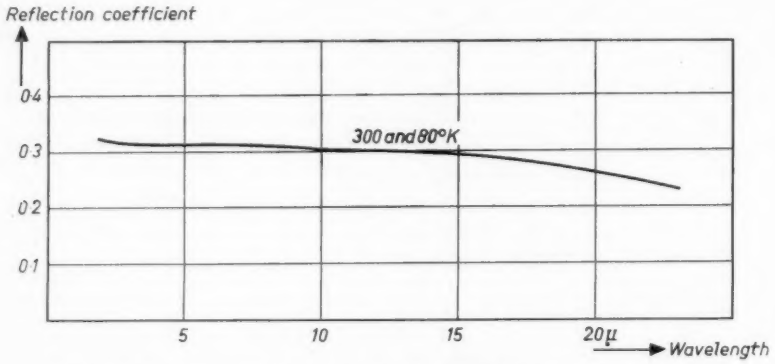

FIG. 1. Reflection coefficient (unpolarized light falling on a surface $\perp$ c-axis) for an undoped SnS crystal, containing 4×10^{17} holes per cm^3.

Undoped SnS is always p-type (presumably due to the presence of Sn-vacancies), with a carrier concentration of about 5×10^{17} cm^{-3}.[4] We also used crystals doped with Ag; these crystals have hole concentrations up to 10^{19} cm^{-3}. Finally some experiments were done on crystals doped with Sb, having a very low carrier density ($<10^{14}$ cm^{-3}).

In Fig. 1 the reflection coefficient as a function

of wavelength is shown for an undoped SnS crystal, with a carrier concentration of $p = 4\times10^{17}$; we note a slow decrease of the reflection coefficient at long wavelength. Approximately the same result was found for this crystal at 300°K and 80°K.

In Fig. 2 the reflection coefficient of an Ag-doped crystal with a much larger hole concentration is shown (at 80°K: $p = 1{\cdot}06\times10^{19}$ cm^{-3}; the carrier concentration in undoped and in Ag-doped SnS crystals varies only slightly between 80 and 300°K). At 80°K we see a deep minimum in the reflection curve at 16μ; at 300°K the minimum is still present but less pronounced. The reflection

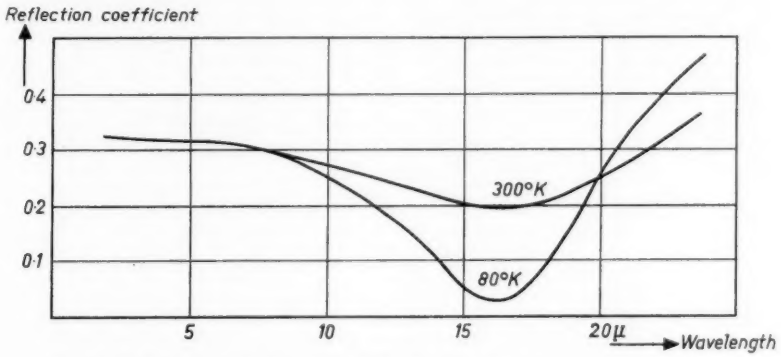

FIG. 2. Reflection coefficient (unpolarized light falling on a surface $\perp c$) for an Ag-doped SnS crystal at 300°K and 80°K; hole concentration at 80°K: $p = 1{\cdot}06\times10^{19}$ cm^{-3}.

curves shown in Figs. 1 and 2 were measured with unpolarized light falling on a SnS-surface perpendicular to the c-axis.

3. LATTICE VIBRATIONS

The fundamental lattice absorption frequency ν_0 of SnS is not known; however this is the only quantity in equation (1) for which a reasonable estimate can be made. In fact, by comparing the values of ν_0 for a number of compounds such as ZnS, CdS, CdSe etc.,[5] we find that ν_0 is roughly proportional to $M^{-1/2}$, as expected. Because SnS has about the same value of M as CdS, whereas the force constant for the vibration probably does not differ too much between SnS and CdS, we think that the value of ν_0 for SnS will be about the same as for CdS, that is $\tilde{\nu}_0 = c\nu_0 = 260$ cm^{-1}.

The damping of lattice vibrations is usually very small (for ZnS for example $2\pi\nu_0\tau_0 = 20$),[6] so that for $\tilde{\nu} > 400$ cm^{-1} we can neglect $i\nu/2\pi\tau_0$ with respect to $\nu_0^2-\nu^2$ in equation (3).

One can easily show that if free carriers give rise to a very deep minimum in the reflection curve, the influence of absorption on the reflection must be small at frequencies higher than the frequency of the minimum. From Fig. 2 we therefore conclude that the relaxation time τ at 80°K is apparently sufficiently large to make the approximate equation (4) valid at $\lambda<15\mu$ and at 80°K.

Comparing Fig. 2 with Fig. 1 we see that the decrease of R with λ in a crystal with $p = 10^{19}$ cm^{-3} is mainly due to the free carriers. We may obtain a provisional value for the effect of free carriers by calculating from Fig. 2 at $\lambda<10\mu$ n^2 from $R = (n-1)^2/(n+1)^2$; a plot of n^2 vs. $1/\nu^2$ gives $e^2/\pi m$.*

This provisional value of $e^2/\pi m^*$ can then be used to calculate the contribution of the free carriers in crystals containing only a small hole concentration. In this way we find $n^2+(pe^2/\pi m^*\nu^2)$; this quantity contains, apart from n_0^2, only the contribution of the lattice vibrations to the dispersion. A plot of $n^2+(pe^2/\pi m^*\nu^2)$ as a function of $(\nu_0^2-\nu^2)^{-1}$ will give a straight line of slope $[(n_0^2+2)/3]^2(N_0e^{*2}/\pi M)$. We followed this procedure for a number of undoped crystals, as well as for an Sb-doped crystal. In this way we found $n_0^2 = 13{\cdot}0\pm0{\cdot}5$, or $n_0 = 3{\cdot}6\pm0{\cdot}1$, and for the

effective charge $e^* = 0{\cdot}7\ e_0$ (e_0 is the charge of an electron).

The values of n_0 and e^* were found to be essentially the same for the three principal axes in the crystal (measurements with polarized light). Apparently SnS is a cubic crystal as far as the fundamental lattice absorption is concerned. In SnS each Sn-atom is surrounded by three S-atoms at short distance (2·66 Å), and three S-atoms at a somewhat longer distance (3·30 Å). The lines connecting Sn with the first group of S-atoms are approximately mutually perpendicular; the same is true for the second group of S atoms. The oscillator strength of an Sn–S vibration which makes an angle ϕ with the direction of polarization of the light is proportional to $\cos^2\phi$; three mutually perpendicular Sn–S vibrations give $\cos^2\phi_1 + \cos^2\phi_2 + \cos^2\phi_3 = 1$, which makes the oscillator strength independent of the direction of polarization. Therefore the observed isotropy of the lattice vibration is in agreement with the expectation based on the crystal structure.

From the values of n_0 and e^* we are able to calculate the dielectric constant $\epsilon = n^2$ ($\nu = 0$), and find $\epsilon = 19{\cdot}5 \pm 2$. (This result is in good agreement with $\epsilon = 19 \pm 1$ found by electrical measurements by HOFMAN†.) Further we may calculate the frequency of longitudinal waves ν_1 from $(\nu_1/\nu_0)^2 = \epsilon/n_0^2$[7], and find $\tilde{\nu}_1 = c\nu_1 = 320\ \text{cm}^{-1}$.

We have also measured the refractive index of Sb-doped SnS between 4 and 10μ from interference fringes in thin cleavage plates; in this way too a value of $3{\cdot}6 \pm 0{\cdot}1$ was found.

As to the value of $e^* = 0{\cdot}7\ e_0$ we remark that e^* is a dynamic quantity related to the vibration of the atoms, and not necessarily equal to the static charge on the atoms at rest.[8] The value found for SnS is somewhat smaller than that for ZnS ($e^* = 0{\cdot}88\ e_0$),[1] indicating a more covalent character of SnS.

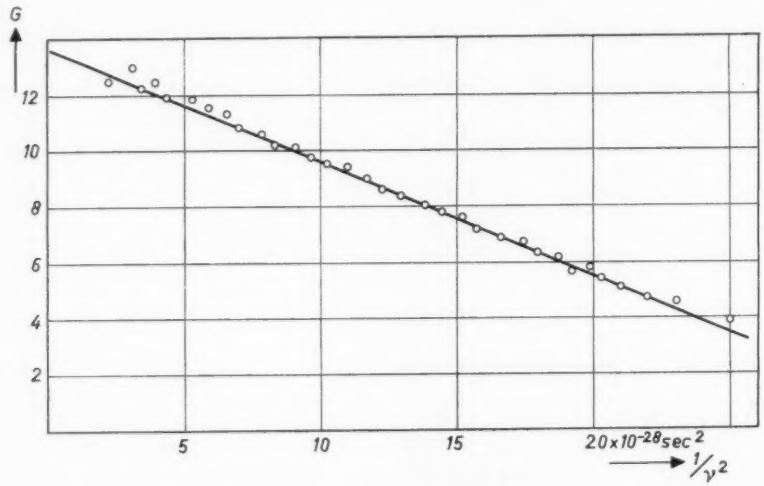

FIG. 3. Free carrier contribution (= constant + G) to the square of the refractive index as a function of $1/\nu^2$ at 80°K for a crystal containing $1{\cdot}06 \times 10^{19}$ holes per cm^3.

4. FREE CARRIERS

After having calculated the effect of lattice vibrations on the dispersion, we are now in a position to determine the influence of free carriers. In order to calculate the effective mass from the observed reflection curves, we use the experimental data taken at 80°K, because only at this temperature do we know that for $\lambda < \lambda_{\min}$ the condition $\nu\tau \gg 1$ is fulfilled, so that we may use

† D. HOFMAN, private communication.

equation (4). To separate the effect of free carriers, we calculated n^2 from $R = (n-1)^2/(n+1)^2$, and plotted

$$G = n^2 - \left(\frac{n_0^2+2}{3}\right)^2 \frac{N_0 e^{*2}}{\pi M(\nu_0^2-\nu^2)}$$

as a function of $1/\nu^2$ (using the values of n_0, e^* and ν_0 given in Section 3). For $\nu > \nu_{\min}$ a straight line of slope $pe^2/\pi m^*$ is obtained (Fig. 3); from the slope, together with the hole concentration obtained from Hall measurements, the value of m^* we calculated $m_\perp^* = 0{\cdot}20 m_0$ (m_0 is the mass of an electron).

If the reflection minimum is sufficiently deep, one can also calculate the effective mass directly from the position of the minimum:

$$m^* = \frac{pe^2}{\pi \nu_{\min}^2 (n_1^2-1)};$$

$$n_1^2 = n_0^2 + \left(\frac{n_0^2+2}{3}\right)^2 \frac{N_0 e^{*2}}{\pi M(\nu_0^2-\nu_{\min}^2)} \qquad (6)$$

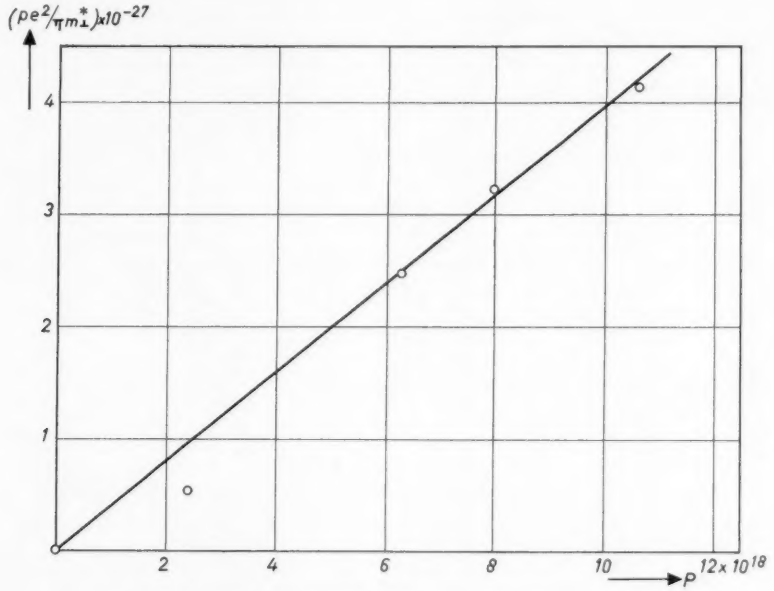

FIG. 4. Slope ($pe^2/\pi m_\perp^*$) of the straight line G vs. $1/\nu^2$, plotted here for crystals with different carrier concentrations.

was calculated. This procedure was followed for a number of crystals containing different hole concentrations, and using light polarized parallel to the crystallographic a, b and c axes. It was found that no significant difference (the difference found was smaller than 10 per cent) exists between a and b axes, so that the effective mass in the plane perpendicular to the c-axis is isotropic: $m_\perp^* = m_a^* = m_b^*$. Therefore most experiments were done with unpolarized light on crystal plates $\perp c$. The value of $pe^2/\pi m_\perp^*$, found for various crystals, is plotted as a function of p (Fig. 4); from this plot in this way we find from Fig. 2 a value of $m_\perp^* = 0{\cdot}21\, m_0$.

The values of m^* calculated above are independent of any assumptions about the scattering mechanism of the holes. Because the scattering mechanism is not taken into account in the proper way, values of m^* deduced from absorption data using the Drude–Zener theory are not reliable. Therefore the value $m_\perp^* = 0{\cdot}20\, m_0$ is more reliable than the value of $0{\cdot}4\, m_0$ calculated recently from absorption data.[4]

A measurement with light polarized parallel to

the c-axis revealed a much smaller dispersion; in this case no pronounced reflection minimum was found. Although the dispersion in this case was hardly larger than for lattice vibrations only, and although we are not very certain whether the condition $\nu\tau \gg 1$ is still fulfilled here (τ may also be anisotropic), we made a rough estimate of the effective mass parallel to the c-axis: $m_{\parallel}^* \sim m_0$.

Having sufficient information about the lattice vibrations, we are able to calculate polaron effects

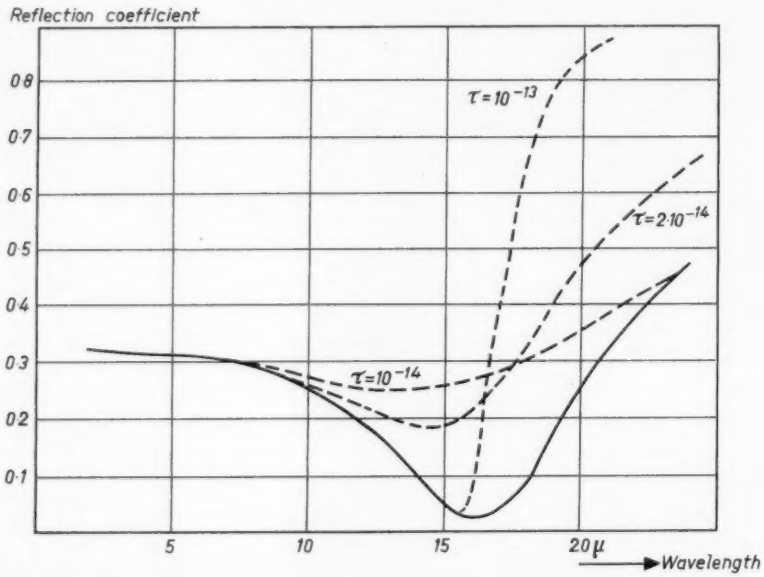

FIG. 5. Calculated reflection curves (dotted lines) for various values of τ for a crystal having $p = 1{\cdot}06 \times 10^{19}$ cm^{-3} and $m_{\perp}^* = 0{\cdot}20\, m_0$. For comparison the measured reflection curve of Fig. 2 (solid line) is also given.

of the free holes. It is known[9] that for $\nu > \nu_1$ the bare electron mass m^* should be used, but that for low frequency phenomena $\nu < \nu_1$, the polaron mass $m_p = m^*(1+\alpha/6)$ is the relevant quantity. α is the constant of coupling of the holes with phonons, given by:

$$\alpha = \frac{e^2}{\hbar}\left(\frac{m^*}{2h\nu_1}\right)^{1/2}\left(\frac{\epsilon - n_0^2}{n_0^2}\right) \qquad (7)$$

We find $\alpha_{\perp} = 0{\cdot}2$ and $m_{p\perp}^* = 1{\cdot}03\, m_{\perp}^*$. Therefore polaron effects are small in SnS; the polaron mass is almost equal to the bare electron mass.

Using the complete equations for n^2 and R we have tried to reproduce the reflection curve of Fig. 2 taken at 80°K also in the region $\nu < \nu_{\min}$. We calculated the reflection curve from equations (3) and (5) for various values of τ (see Fig. 5); a value of $\tau = 3 \times 10^{-14}$ sec corresponds to the observed mobility of 350 cm^2/V sec at 80°K. We see from Fig. 5 that the experimental curve is in agreement with theory only if τ increases with increasing frequency. A discrepancy of the same kind (the impossibility of describing the reflection curve with a constant relaxation time) has also been observed for ZnO.[10]

This phenomenon can be explained qualitatively in the following way; it is well known that impurity scattering is less effective for fast electrons. For optical absorption in the region $h\nu > kT$, the energy of the electron in the final state (after absorption) will play the role of the kinetic energy of the electron in normal d.c. conduction.[11] As a result we expect that for impurity scattering τ will increase with ν. Because in the Ag-doped crystals impurity scattering predominates at 80°K, as shown by the μ–T curve (at 300, 150, 100 and

80°K $\mu_\perp$ is respectively 80, 240, 380 and 350 cm^2/V sec), this prediction is in agreement with the experimental reflection curve.

It is difficult to treat the effect just mentioned in a quantitative way, firstly because the influence of the carriers on the optical properties is so large (large change of n and k) that a simple perturbation treatment as used by MEYER[12] is not valid, and secondly because at these large carrier concentrations screening of the Coulomb field of the charged impurities by the carriers will be of importance. In the FAN[11] or MEYER[12] treatment screening is neglected because $\kappa^2 \gg (1/l_D)^2$ in the cases these authors discuss, where l_D is the Debye-length given by $(1/l_D)^2 = 4\pi pe^2/\epsilon kT$, and κ the wave-vector of the final state. In our case, however, with $p = 10^{19}\,cm^{-3}$, $l_D = 10^{-7}$ cm, κ for $\lambda = 10\mu$ is about $10^7\,cm^{-1}$ (from $\hbar^2\kappa^2/2m^* \simeq h\nu$), so that screening cannot be neglected here.

REFERENCES

1. SZIGETI B., *Trans. Faraday Soc.* **45,** 155 (1949).
2. MOSS T. S., *Optical Properties of Semiconductors* Butterworths, London (1959).
3. HOFMANN W., *Z. Kristallogr.* **92,** 161 (1935).
4. ALBERS W., HAAS C. and VAN DER MAESEN F., *J. Phys. Chem. Solids* **15,** 306 (1960).
5. MITSUISHI A., YOSHINAGA H. and FUJITA S., *J. Phys. Soc. Japan* **13,** 1235 (1958).
6. HAAS C. and MATHIEU J. P., *J. Phys. Radium* **15,** 492 (1954).
7. FRÖLICH H., *The Theory of Dielectrics*, Oxford University Press, London (1949).
8. HOOGE F. N., *Z. Phys. Chem.* **21,** 298 (1959).
9. LEE T. D., LOW F. E. and PINES D., *Phys. Rev.* **90,** 297 (1953).
10. COLLINS R. J. and KLEINMAN D. A., *J. Phys. Chem. Solids* **11,** 190 (1959).
11. FAN H. Y., SPITZER W. and COLLINS R. J., *Phys. Rev.* **101,** 566 (1956).
12. MEYER H. J. G., *Phys. Rev.* **112,** 298 (1958).

Vol. 20
1961

J. Phys. Chem. Solids Pergamon Press 1961. Vol. 20, Nos. 3/4, pp. 204–221. Printed in Great Britain.

A HIGH TEMPERATURE X-RAY STUDY OF ORDERING IN IRON–ALUMINIUM ALLOYS

A. LAWLEY* and R. W. CAHN

Department of Physical Metallurgy, University of Birmingham, Birmingham 15

(*Received* 27 *January* 1961; *revised* 14 *March* 1961)

Abstract—The variation with temperature of long-range order in iron–aluminium solid solutions was studied using a high temperature diffractometer, and short-range order was studied at room temperature by measuring diffusely scattered X-rays. Compositions in the range 19–50 at. per cent† aluminium were investigated. The atomic configurations discovered by BRADLEY and JAY were largely confirmed, including the structural discontinuity at the stoichiometric Fe_3Al composition. The Fe_3Al-type superlattice exists over the range 23–35 per cent Al approximately, and the order disappears gradually during heating, with no sudden drop at the critical temperature T_c. The degree of order at a given temperature below T_c depends on the thermal history by which that temperature was approached. This anomaly is explained in terms of a competition between directional order, of ferromagnetic origin, and long-range order; this model is also used to interpret certain anomalous magnetic properties at high temperature.

Alloys with less than 23 per cent aluminium possess various kinds of short-range order. An alloy containing 20·5 per cent aluminium has a structure which is unaffected by heat treatment, but all the other alloys investigated are sensitive to heat treatment. A tentative equilibrium diagram is proposed.

INTRODUCTION

BRADLEY and JAY[1] first showed that the iron-rich solid solutions in the iron–aluminium system, extending from pure iron to just over 50 per cent aluminium, are liable to a somewhat complex type of crystallographic ordering. In the approximate range 20–35 per cent aluminium, alloys are ordered at low temperatures but progressively disorder on heating; beyond 25 per cent aluminium exactly, order is never entirely lost, even near the melting point. In the range 20–25 per cent aluminium, the published evidence on physical properties as a function of temperature suggested that order disappears progressively up to the critical temperature T_c, without a discontinuous jump at T_c. This feature made the alloy particularly attractive for the study of mechanical properties as a function of degree of long-range order. The present detailed study, by X-ray diffraction at temperature, of the ordering behaviour of this alloy series was undertaken as a preliminary to studies of creep rate,[2] flow stress[3] and mechanical twinning[4] of alloys heat-treated to give different degrees of order. Anomalies which were discovered in the course of the X-ray studies led to a further series of investigations of the electrical resistivity[5–7] and of induced magnetic anisotropies.[8] In the present paper, the implications of all these studies for the constitution of the alloy system will be examined, but the main concern here will be with the results of the X-ray investigation.

On the basis of BRADLEY and JAY's X-ray work, HANSEN and ANDERKO[9] proposed the phase diagram of Fig. 1. In the phase field α'' a DO_3 superlattice based on stoichiometric Fe_3Al exists while in phase field α' there is a B2 superlattice based on stoichiometric FeAl. These structures are shown in Fig. 2. Elsewhere, the structure is crystallographically random. The sharp structural discontinuity across the vertical boundary AB at 25 per cent aluminium is the most singular feature of this diagram.

Recently TAYLOR and JONES[10] made precision

* Present address: Franklin Institute, Research Laboratories, Philadelphia, U.S.A.

† All compositions are given in atomic per cent.

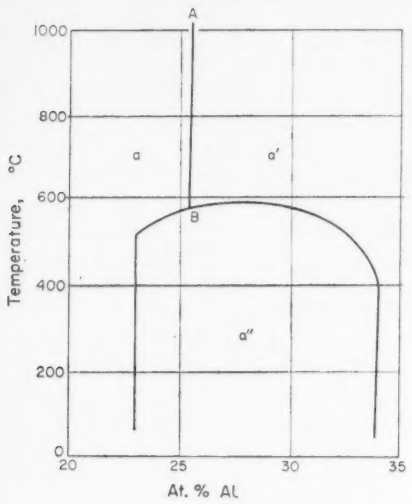

FIG. 1. Iron–aluminium equilibrium diagram (after HANSEN and ANDERKO[9]).

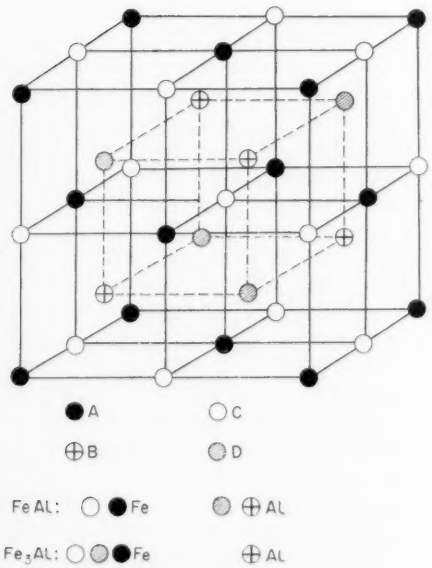

FIG. 2. Fe_3Al (DO_3) and "pseudo-FeAl" (B2) superlattices.

measurements of lattice parameters at high temperatures, and deduced phase boundaries from discontinuities in the slopes of isothermal plots of lattice parameter vs. composition. McQUEEN and KUCZYNSKI[11] obtained a series of peaks on differential dilatometric heating curves of several alloys. Fig. 3 indicates the phase limits deduced by these investigators. The main feature of disagreement between Figs. 1 and 3 is that the vertical boundary at 25 per cent has been replaced by a sloping boundary, which intersects the upper boundary of the α'' field at less than 25 per cent aluminium.

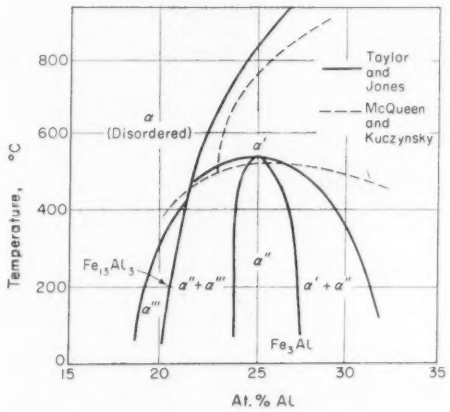

FIG. 3. Revised iron–aluminium equilibrium diagram, based on recently published work.[10,11]

TAYLOR and JONES' experimental technique was of exceptionally high quality and there can be no doubt that their results are more reliable than BRADLEY and JAY's older work. However, they made no intensity measurements on superlattice lines to check those made by the earlier investigators. It has been the main purpose of the present work to make such measurements, using a Geiger counter diffractometer operating at high temperatures, in an attempt fo find the origin of the differences between the various extant phase diagrams. Experiments were also performed to define the conditions under which a face-centered cubic phase, not shown by the phase diagram, can precipitate from the alloys.

EXPERIMENTAL METHODS

Preparation of alloys

Alloys were either melted and chill-cast in vacuum or prepared in an arc-furnace. The alloys were subsequently hot-rolled except for those with high aluminium content, which were brittle. A list of alloy compositions and the corresponding source is given in Table 1. Accurate chemical analysis of iron–aluminium alloys is not easy, and all analyses were therefore made in quadruplicate,

Table 1. *Analysis of alloys used*

Alloy no.	Wt. % Al.	At. % Al.	Source and preparation
1	10·35	19·3	A, C.C.V.
2	11·1	20·5	A, C.C.V.
3	11·5	21·2	A, C.C.V.
4	12·0	22·2	A, C.C.V.
5	12·5	22·9	B, A.M.
6	12·9	23·5	C, C.C.V.
7	13·7	24·8	C, C.C.V.
8	13·9	25·0	A, C.C.V.
9	14·1	25·5	C, C.C.V.
10	14·8	26·5	A, C.C.V.
11	15·7	27·8	A, C.C.V.
12	17·1	29·9	D, A. M.
13	20·5	34·8	D, A.M.
14	24·6	40·3	D, A.M.
15	32·6	50·0	C, C.C.V.

Code: A: U.S. Naval Ordnance Lab., Maryland.
B: University of Birmingham, England.
C: Philips Research Lab., Eindhoven.
D: Edwards High Vacuum, England.
C.C.V.: Chill-cast in vacuum.
A.M.: Arc-melted.

by a specially devised method giving an accuracy of $\pm 0{\cdot}2$ at. per cent. Filings were prepared using a non-magnetic tungsten carbide file. The sieved filings were cleaned, degreased, and hot-pressed at 450°C in a steel die[12] into the form of disc specimens 28 mm in diameter and 1 mm thick. All discs were annealed for 5 hr at 800°C in a vacuum better than 10^{-4} mm of mercury, and quenched *in vacuo* into silicone oil, to obtain a strain-free, disordered structure. Subsequent heat treatments were carried out in the diffractometer itself.

The diffractometer

The instrument used has been designed and described by WILLIAMSON and MOORE[12]. The specimen is fixed in a sealed chamber filled with purified helium, which is kept in forced circulation over a heating coil and past the specimen. It is possible to heat the specimen rapidly to any temperature up to 610°C (this limit is set by the use of aluminium foil to make gas baffles capable of transmitting X-rays), and then to maintain the temperature constant and uniform throughout the irradiated volume of the specimen, to ± 1°C. The heating chamber was mounted on the specimen table of an X-ray spectrometer base, allowing the usual Bragg–Brentano focussing arrangement. Cobalt radiation, monochromated by a bent quartz crystal, was used so as to achieve a good line-to-background ratio for the weak superlattice diffraction lines.

Three kinds of measurement were carried out:

(a) The intensities of two superlattice lines, (111) and (200),* and one fundamental line, (220), were measured at a fixed temperature and also during cooling at a fixed rate using a wide slit, subtending 1° in 2θ, in front of the Geiger counter. This was more than wide enough to take in a whole line, and only two measurements were required to get the value of the integrated intensity of a line: one with the slit straddling a line, and one to measure the background level just to one side of the line.

Counts of one minute duration were used throughout. For such a count, the probable error of the integrated intensity of a superlattice line of fully ordered Fe_3Al, duly corrected for background, was about ± 4 per cent.

(b) At intervals during heating or cooling sequences, the profiles of the (400) and (422) fundamental lines were determined by scanning with a narrow slit subtending 8 minutes of arc in 2θ; these profiles were used to determine the lattice parameter and half-breadth. In a few cases, profiles of a superlattice line were also taken; this required long counting times to get adequate statistical precision.

(c) The diffractometer was also used at room temperature, with the chamber evacuated, to take measurements of X-ray scattering from *solid*

* All Miller indices, whether for ordered or for disordered alloys, are referred to the *large* unit cell of Fig. 2.

Vol. 2
1961

polycrystalline discs. The purpose was to get a qualitative measure of line intensities and also of diffuse scattering between lines; the inevitable presence of some preferred orientation meant that the line intensities found had no absolute significance. To achieve the highest sensitivity in measuring the very weak diffuse scattering, an argon-filled proportional counter was used in conjunction with a single channel pulse height analyser. This allowed the background count to be reduced to only 4 counts/min.

Computation of atomic distribution

Results from the main investigation {method (a)} are expressed in the form of the ratio:

$$\frac{\text{integrated intensity of a superlattice line at } T°\text{C}}{\text{integrated intensity of the (220) fundamental line at } T°\text{C.}}$$

In this way, variations of the X-ray tube output were compensated; moreover, since the lines concerned did not differ greatly in Bragg angle, the change with temperature of the Debye–Waller factor of each line was also almost exactly compensated.

It was necessary to study both the (111) and the (200) superlattice lines because the intensities of these two lines convey two distinct kinds of information. The (200) line is sensitive only to the distribution of aluminium atoms between the centres and corners of the *small* unit cells (containing 2 atoms apiece); the (200) line responds to the "pseudo-FeAl" type of order pictured in Fig. 2,* irrespective of whether or not the "Fe_3Al" type of order is superimposed upon it. The (111) line is sensitive only to the distribution of the aluminium atoms among 4 of the 8 cube centres of each group of 8 small cells which make up the large unit cell of the "Fe_3Al" superstructure of Fig. 2. The Fe_3Al superstructure presupposes the presence of "pseudo-FeAl", of which it is a further development. It is impossible, therefore, to have a finite (111) intensity without also having a finite (200) intensity, but the converse is not true.

From the observed ratio I_{200}/I_{220} the values $(a+c)$ and $(b+d)$ can be calculated, where a, b, c, d, are the mean scattering powers of the atoms at the sites marked A, B, C, D in Fig. 2. The value of F_{111} is calculated from the observed ratio I_{111}/I_{220} where:

$$|F_{111}|^2 = 16[(a-c)^2+(b-d)^2].$$

Thus only the sum of the atomic fractions of aluminium on the A and C, and B and D sublattices is uniquely determined from the X-ray data. Two special cases arise whereby further statements concerning the values of a, b, c, d, can be made. When the reflections of odd indices are absent, $(a-c)^2+(b-d)^2 = 0$ which allows solution for a, b, c and d; also if $a+c \simeq 0$, b and d can be approximately determined. Otherwise it must be assumed that $a = c$ in order to solve for a, b, c and d. Experimentally, it is found that the A and C sublattices are almost wholly occupied by iron in Fe_3Al $(a+c \simeq 0)$ and by assuming a = c, the distribution of iron and aluminium atoms on the A, B, C, D sublattices was computed. Corrections to the intensity ratios were made for the variation of atomic scattering factor with angle, for counting losses, and for polarization; a dispersion correction[13] was applied to the published values of atomic scattering factors.

EXPERIMENTAL RESULTS—I. HIGH TEMPERATURE MEASUREMENTS

Intensity measurements

The effect of continuous heating and cooling at various rates on the build-up of the "Fe_3Al" superlattice was first examined. Sample discs, quenched from 800°C *in vacuo*, were rapidly heated to 600°C in the diffractometer. The temperature was then reduced at the rate of 5°C/min,

* This type of order is here referred to as "pseudo-FeAl" type, since for the more dilute alloys investigated the atoms at cube centres have a definite probability, less than unity, of being aluminium; only in stoichiometric FeAl is this probability actually unity. However, this configuration is not identical with the *imperfect* "FeAl" order which can result from increasing temperature. As the temperature rises, aluminium becomes distributed progressively on the cube corners as well as cube centres, whereas in "pseudo-FeAl" order, at low temperature at least, the atoms at cube corners are very nearly 100 per cent iron.

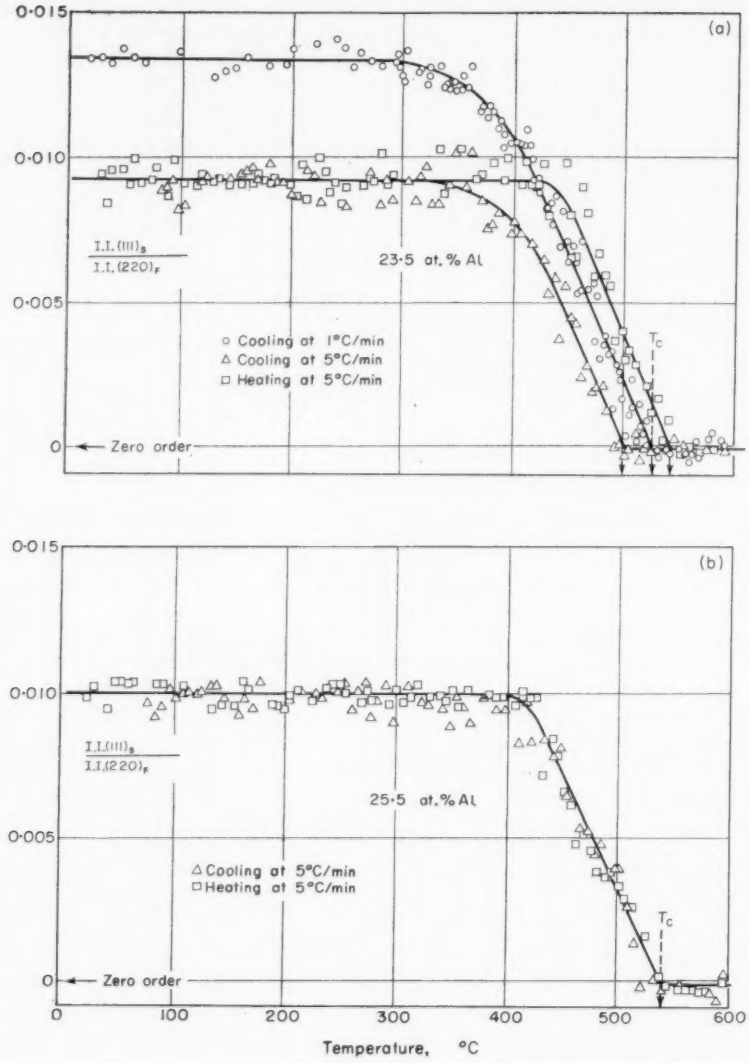

FIG. 4. High temperature X-ray diffraction data [(111) superlattice] for the 23·5 and 25·5 per cent Al alloys, heated and cooled at various rates.

and alternate measurements of (111) and (220) intensities were made. (The variation of superlattice line intensity, *during* each count, due to the concomitant fall in temperature, was roughly equal to the probable error of the measured intensity.) After reaching room temperature, the sample was re-heated at the same rate to 600°C. Thereafter it was cooled at 1°C/min. In each case, intensity measurements were made at short intervals.

In a separate series of experiments, using the

same set of samples, the equilibrium order for each temperature was determined by heating to 600°C in the diffractometer, and then cooling at 1°C/min in small steps, with long isothermal anneals after each cooling step. Intensities were measured at intervals during each isothermal anneal, which was prolonged until the intensity of the superlattice line had become invariant for some hours.

(ii) Alloys containing less than 25 per cent aluminium evince a pronounced hysteresis; the heating and cooling curves for 5°C/min do not coincide and the critical temperatures are substantially different. Alloys with more than 25 per cent aluminium show no form of hysteresis.

(iii) A comparison of the curves obtained at 1°C/min with the equilibrium curves shows that 1°C/min is a sufficiently slow cooling rate to main-

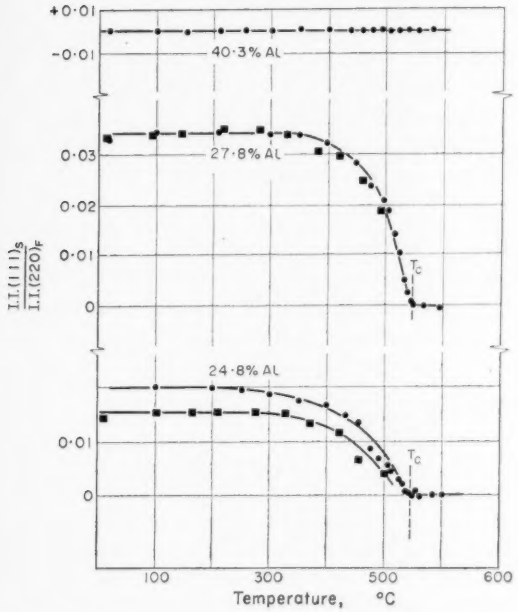

FIG. 5. High temperature X-ray diffraction data [(111) superlattice line] for the 24·8, 27·8 and 40·3 per cent alloys. ● equilibrium values, ■ after transcritical fast cool.

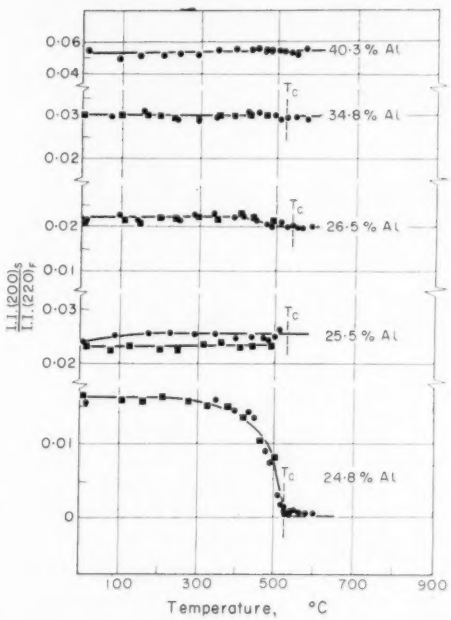

FIG. 6. High temperature X-ray diffraction data [(200) superlattice line] for the 24·8, 25·5, 26·5, 34·8 and 40·3 per cent alloys. ● equilibrium values, ■ after transcritical fast cool.

Results representative of the various alloys are given in Figs. 4–6. (At this stage the square symbols in Figs. 5 and 6 should be ignored.) Alloys containing 21·2, 22·2 and 22·9 per cent aluminium gave no detectable superlattice intensity even with very slow cooling. The following conclusions can be drawn for alloys in the range 23·5–34·8 per cent Al:

(i) Cooling at 5°C/min is not sufficiently slow to produce equilibrium order in any of the alloys.

tain equilibrium order at all temperatures down to 300°C.

(iv) Comparison of Figs. 5 and 6 shows that there is indeed a discontinuous change in behaviour of the alloys at 25 per cent aluminium, as first discovered by BRADLEY and JAY. In the alloys containing less than 25 per cent, the (200) and (111) lines disappear *together* at T_c; in the more concentrated alloys, the (200) intensity remains almost constant during heating up to 600°C.

Small changes in (200) intensity between 400°C and 500°C in the 26·5, 27·8 and 29·9 per cent alloys appear to coincide with the Curie points of the alloys. In Table 2, the critical temperatures found for the various alloys are listed and compared with values from earlier work.

Table 2. Critical temperatures for the disappearance of "Fe_3Al" order

Present work		Sykes and Evans[33] (Specific heat measurements)	
At. % Al	$T_c \pm 3$°C	At. % Al	T_c
23·5	527°C	23·7	550°C
24·8	540°C	24·3	546, 548°C
—	—	24·8	542°C
—	—	25·0	537, 538, 540°C
25·5	542°C	25·4	553, 556°C
26·5	548°C	—	—
27·8	550°C	27·6	545, 554°C
29·9	547°C	29·8	518°C
34·8	528°C	—	—

Thermal memory

An interesting anomaly was found to result from a more drastic form of heat treatment. Thus, each alloy, after being tested as described above, was re-heated to a temperature T_c+50°C, and then cooled rapidly down to T_c-50°C by switching off the furnace heaters. (Cooling rate 45°C/min.) This treatment is hereafter referred to as a *transcritical fast cool*. Thereafter slow cooling with prolonged isothermal steps was resumed, as before. The data so obtained are included as squares in Figs. 5 and 6. In some cases, the superlattice intensities after a transcritical fast cool are found to be significantly *lower* than the equilibrium intensities.* Thus, in spite of the fact that the transcritically fast cooled samples were subsequently given adequate time to reach equilibrium, they nevertheless did not do so. These alloys therefore preserve *thermal memories*, as it were, of their past heat treatment.

An alloy containing 24·8 per cent Al, which had been transcritically fast cooled and then slow cooled in steps as described above, was re-heated in the diffractometer to 600°C (i.e. a temperature well above T_c), held 2 hr, then cooled at 1°C/min back to room temperature. Measurements of (111) and (200) superlattice intensities gave values identical to those obtained after the previous transcritical fast cool, i.e. those indicated by the squares at 20°C in Figs. 5 and 6. A similar result was obtained when the experiment was repeated with the 25·5 per cent alloy. Finally, each of these alloys was heated in the vacuum furnace to 800°C for 5 hr, quenched, re-heated in the diffractometer to 600°C, held 1 hr and then cooled at 1°C/min to room temperature.† The resulting (111) and (200) superlattice intensities at 20°C had now returned to the equilibrium values shown by the circles in Figs. 5 and 6. A temperature of 800°C thus suffices to remove the thermal memory; 600°C does not.

Several alloys were heated to 600°C in the diffractometer and cooled at 5°C/min, and then re-heated to 400°C for 1 hr. In all cases, the superlattice intensities thereupon increased to the equilibrium values for 400°C indicating that there is no thermal memory effect with this slower rate of cooling.

Computations from intensity measurements

Using only intensity data from alloys which had been slow cooled, with interposed isothermal anneals, equilibrium atomic distributions were computed. These distributions are plotted as a function of composition in Fig. 7. Bradley and Jay's distributions, computed from their photographic data, are included for comparison; the agreement in most parts of the diagram is close.

Figure 8 shows similar distributions computed from intensity data obtained from alloys quenched from 800°C into silicone oil *in vacuo*. Bradley and Jay's data, included here, refer to water-quenched alloys. Oil quenching evidently is not fast enough to prevent all atomic rearrangement during cooling. A comparison between the distributions on either side of the stoichiometric Fe_3Al composition will show the distinction between "ideal" pseudo-FeAl order (Al > 25 per cent) and the same kind of order partially destroyed

* The (111) intensity is lower for the 24·8, 25·5 and 26·5 per cent Al alloys and the (200) intensity is lower for the 25·5 per cent alloy.

† It would have been clearer and simpler to re-heat to 800°C in the diffractometer and slow cool all the way to room temperature, but the instrument's limitations precluded this.

by high temperature (Al < 25 per cent). The important difference is that for the former case, only atoms on the B and D sublattices (Fig. 2) are disordered by heating, while A and C sublattices remain almost wholly populated by iron atoms;

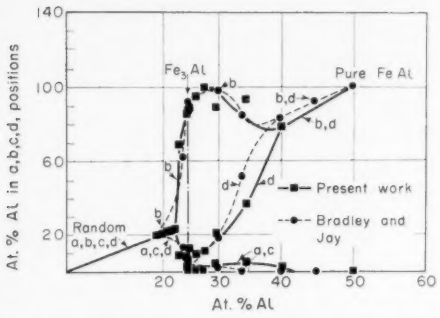

FIG. 7. Distribution of iron and aluminium atoms on the four sublattices of Fig. 2; slow-cooled condition.

whereas alloys containing less than 25 per cent Al disorder uniformly, in the sense that all four sublattices disorder together as the alloy is heated. One would therefore expect the order/temperature

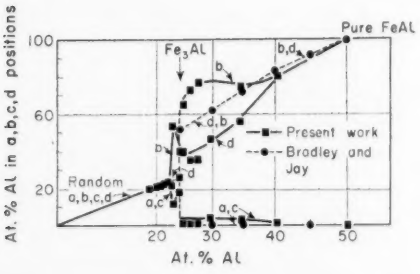

FIG. 8. Distribution of iron and aluminium atoms. Oil quenched from 800°C.

relationship to differ in the two cases. A hyper-stoichiometric alloy (> 25 per cent Al) resembles an equiatomic "AB" alloy such as B-brass in its thermodynamic behaviour, because half the iron atoms (those on the A and C sublattices) can be discounted, leaving *equal numbers* of iron and aluminium atoms actually participating in the ordering reaction. The hypo-stoichiometric alloy corresponds more nearly to the Cu_3Au case; yet it does not disorder discontinuously at T_c, as that alloy does.

In Fig. 9, theoretical curves are plotted of the Bragg–Williams order parameter S as a function of temperature. These curves are all computed for the AB case, and should in theory apply to hyper-stoichiometric alloys only. BRAGG and WILLIAMS' curve[14] is based on classical co-operative theory; COWLEY's curve[15] is based on the concept of

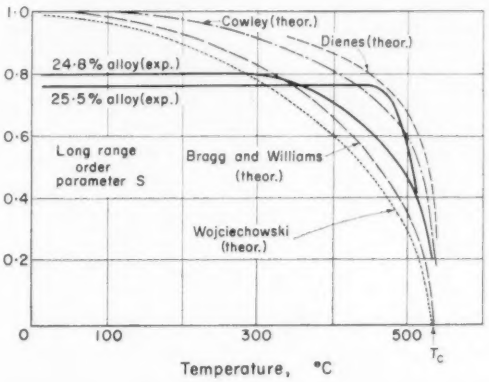

FIG. 9. Order–temperature relationship for 24·8 and 25·5 per cent alloys, compared with four theoretically predicted relationships.

short-range order among groups of neighbouring atoms; DIENES'[16] curve is a recent refinement of BRAGG and WILLIAMS' theory, in which the inter-atomic bond energies are no longer a linear function of S. WOJCIECHOWSKI's[17] calculation refers specifically to Fe_3Al.

S/T curves have also been computed from the experimental values of the I_{111}/I_{220} ratio for the alloys containing 24·8 and 25·5 per cent Al, Fig. 9. If the very small aluminium contents of the A and C sublattices in the fully ordered alloy are left out of account, one can compute S from the observed fractional aluminium population f^{B}_{Al} of the B sublattice. $f^{B}_{Al} \approx 1$ for the fully ordered alloy in each case; in the disordered alloy, $f^{B}_{Al} \approx 0{\cdot}25$ in the

slightly hypo-stoichiometric case and 0·50 in the slightly hyper-stoichiometric case. Then we write $S = 2f_{Al}^{B} - 1$ in the former case, and $(4f_{Al}^{B} - 1)/3$ in the latter case. It is readily shown, analogously to the case of other ordering alloys, that if S is defined in this way then $I_{111} \propto S^2$. Neither alloy becomes fully ordered; $S_{max} \sim 0{\cdot}8$ for the 24·8 per cent alloy and 0·75 for the 25·5 per cent alloy. (Fig. 7 shows that the 25·5 per cent alloy is actually slightly more ordered than the 24·8 per cent; the fact that S_{max} as computed here is slightly greater for the 24·8 per cent alloy reflects the element of arbitrariness in the definition of the Bragg–Williams order parameter.)

Fair agreement exists between DIENES' theoretical curve for an equiatomic alloy and the experimental curve for the 25·5 per cent alloy (which should behave like an equiatomic alloy); but below a certain temperature, the experimental curve suddenly veers away and flattens out. The hypo-stoichiometric alloy shows no sudden jump in S at the critical temperature (and therefore differs from other AB_3 alloys such as $AuCu_3$). A possible reason for this flattening out of the S/T curves will be suggested below.

High temperature lattice parameters and line widths

Values of lattice parameter as a function of temperature were obtained during isothermal pauses in the course of slow cooling for all the alloys studied. The estimated relative accuracy of parameters derived from (400) and (422) profiles was about 1 in 5000; when (220) profiles were used, the accuracy was rather lower. In spite of the lower accuracy as compared with TAYLOR and JONES',[10] some results are included here (Fig. 10) in view of the fact that the thermal history was more rigorously controlled and because the compositions used were somewhat different in the two studies.

Comparison with the intensity data in earlier figures reveals that the slope of the lattice parameter–temperature plots increases steeply in the regions where order is changing rapidly. However, contrary to TAYLOR and JONES' assumption, anomalies of the slopes of the parameter plots are no sure indication of the establishment of *long-range* order. Both the 22·2 per cent and the 40·3 per cent alloys have slope anomalies yet in the former no detectable long-range order is formed while the latter possesses order which is invariant with temperature. The slope anomalies of the other alloys are not simply related to the critical temperatures for ordering (T_c) or ferromagnetism (θ_c).

Minor discrepancies apart, the curves of Fig. 10 agree with the precision dilatometric results obtained by MCQUEEN and KUCZYNSKI[11]. The 24·8 per cent alloy is an exception; a dilatometric

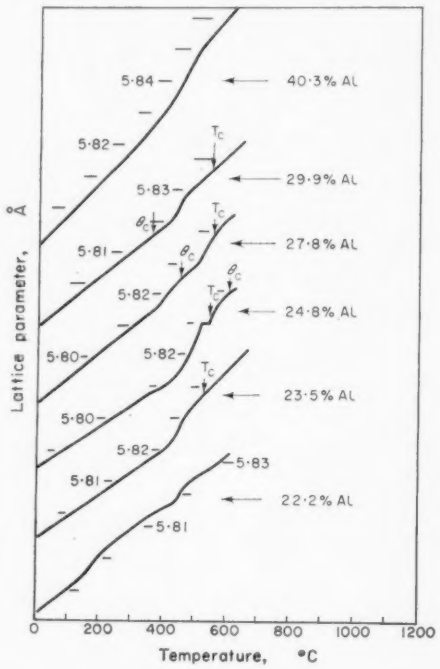

FIG. 10. Selected X-ray thermal expansion data.

curve kindly prepared by Dr. P. LEHR, using a piece of solid metal with 24·8 per cent aluminium, deviates from the X-ray plot in the range 300–550°C, but agrees fairly well with MCQUEEN and KUCZYNSKI's curve. The origin of this X-ray anomaly is not known.

Line widths of fundamental lines did not vary significantly as a function of temperature, except for the 27·8 per cent alloy, which shows a pronounced increase in line width in the vicinity of

the critical temperature. In the case of the 24·8 per cent alloy, the profile of the (111) superlattice line was taken at intervals during the determination of the equilibrium order–temperature relation. At all temperatures below T_c the lines were sharp; the width was always sensibly the same as that of the neighbouring fundamental line. This shows that antiphase domains had grown quickly to a size at which they no longer determined the line width.

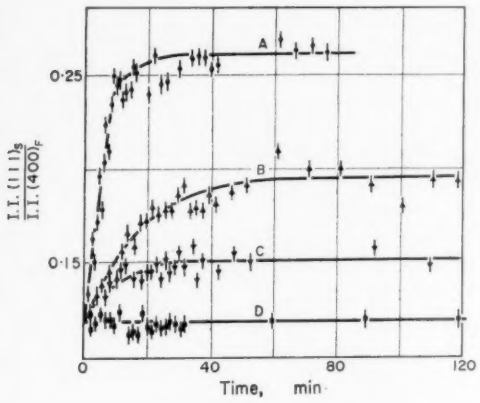

FIG. 11. Isothermal kinetics of ordering of the 24·8 per cent alloy, as shown by time-change of the (111) superlattice line intensity.

A: Ordering at 400°C.
B: Ordering at 500°C.
C: Ordering at 522°C.
D: Ordering at 537°C.

The first two experiments were done by rapidly heating the quenched sample to temperature; the others, by cooling the sample rapidly to temperature from 600°C.

Ordering kinetics—24·8 per cent alloy

The experimental procedure was to either heat a previously quenched (externally) sample rapidly to temperature in the diffractometer, or to cool the sample rapidly to temperature from 600°C in the diffractometer. At temperature, the (111) superlattice line intensity was measured at frequent time intervals and compared to the (400) fundamental line intensity measured before and after each run. Results are plotted, without background correction, in Fig. 11.

It is striking that ordering is much more rapid at 400°C than at 500°C, but is slower at 500°C than 522°C. While these results are consistent with the observed kinetics of build-up of coercive force (see below), they do not agree with kinetic data obtained by resistivity measurements in this temperature range. McQUEEN and KUCZYNSKI[11] find equal ordering rates at 400°C and 500°C, with a minimum rate at 450°C, and RODE[18] finds a steady decrease in ordering rate as the temperature falls below T_c. The origin of this multiple discrepancy remains to be explored. It is however noteworthy that McQUEEN and KUCZYNSKI did not prolong their tests at 400–500°C beyond a few minutes, so that any slow but persistent decreases in resistivity may have been missed.

EXPERIMENTAL RESULTS—II. MEASUREMENTS ON WATER-QUENCHED ALLOYS*

Since earlier experiments had shown that oil quenching was too slow to preserve the high temperature condition perfectly, the alloys were quenched into water. The vacuum annealing furnace was fitted with a vacuum-tight plastic membrane at the bottom, through which the sample pierced on its way into the water-bath. Solid sheet samples were used since with porous sintered samples, there was risk of surface oxidation during the water quench. Tests were made at room temperature, using a proportional counter in the diffractometer, on alloys of the following compositions: 20·5, 21·2, 22·2 and 22·9 per cent Al. None of these had shown any long-range order in earlier tests with powder compacts. Each specimen was examined as quenched from 800°C; or after slow cooling (800–600°C at 1°C/min, 600–250°C at 7–8°C/hr). Fig. 12 shows the results, plotted in terms of an arbitrary intensity scale. No corrections have been applied for extraneous sources of scattering such as Compton scattering; these will be identical, for any one alloy, in both states of heat treatment.

The 22·9 per cent alloy (which had shown no order when previously examined in the form of sintered filings) surprisingly had a pronounced though broad (200) line when slow-cooled; this betokens the presence of pseudo-FeAl order.

* The experiments described in this sub-section were performed by Dr. R. G. DAVIES.

There is also a very weak (111) line, indicative of slight Fe_3Al-type order. The quenched alloy is disordered.

The 22·2 per cent alloy, which again had shown no trace of long-range order when the sintered compact had been used, had no long-range order in the solid sample either. The slow cooled solid sample, however, showed pronounced short-range order. A single, very broad peak, centered at $2\theta = 29°$, is approximately in the correct position according to the theory of diffraction from solid solutions with strong short-range order.[19] The same alloy when quenched had only feeble short-range order. The 21·2 per cent alloy showed very weak long-range order with very broad lines when slow cooled, whereas the quenched alloy had only short-range order. Finally, the 20·5 per cent alloy was notable in that its condition, of pronounced short-range order, was exactly the same in the slow cooled and quenched conditions.

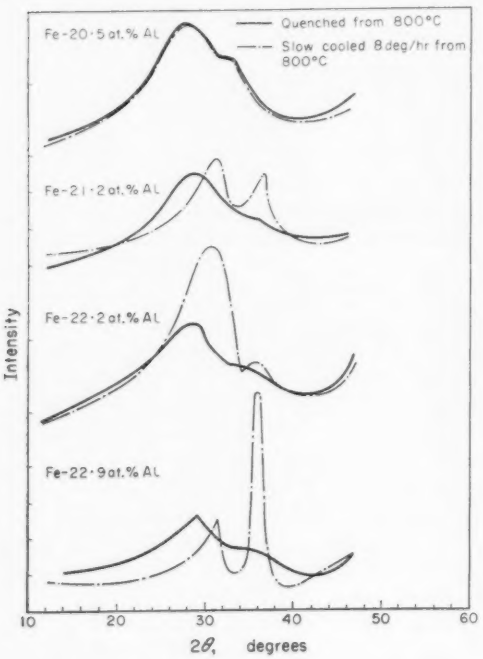

FIG. 12. Diffuse X-ray scattering data from solid 20·5. 21·2, 22·22 and 22·9 per cent alloys in quenched (solid line) and slow-cooled (broken line) conditions. Arbitrary intensity scale.

A rigorous interpretation of short-range order scattering curves, in terms of order parameters in successive co-ordinate shells was not carried out. The shape of the short-range order peaks suggests, that both first- and second-nearest neighbour ordering exists. The further the peak is displaced towards small angles, the greater the component of short-range ordering of second-nearest neighbours. A detailed analysis of the order, which evidently varies greatly from one alloy to the next, calls for a separate investigation.

A sintered powder sample of the 19·3 per cent alloy was examined after oil quenching from 800°C and after slow cooling to room temperature over a period of 5 days. The quenched sample had no short-range order peak but in the slow cooled state there was substantial short-range order. Since the peak shape is that expected for strong first-neighbour ordering, a rough estimate was made of the coefficient α_1.[19] It was estimated that $\alpha_1 \simeq -0{\cdot}10$. With perfect order, the short-range order parameters α_1, α_2, α_3 for the first, second and third nearest neighbour shells are $-0{\cdot}33$, $+1{\cdot}00$ and $-0{\cdot}33$ respectively. For complete disorder, $\alpha_i = 0 (i = 1, 2, 3)$.

EXPERIMENTAL RESULTS—III. THE FACE-CENTERED CUBIC PHASE

The presence of an unexpected f.c.c. phase with a lattice parameter of about 3·7 Å was first reported by BRADLEY and TAYLOR[20] and it has recently been studied by TAYLOR and JONES[10].

Micrographs of quenched Fe_3Al had sometimes shown the precipitation of an unknown phase along straight traces, presumed to be due to slip generated by quenching stresses. This phenomenon was systematically investigated (in co-operation with Dr. A. BERGHEZAN). It was found that quenching alone, even from as high as 1200°C, did not generate the new phase, but if the alloy was first quenched from 1200°C and then annealed in the range 400–650°C, the new phase was precipitated in some grains, Fig. 13. Quenching from 800°C did not introduce enough strain to cause precipitation on subsequent annealing at 500°C. Precipitation often, but not always, took place along slip traces, and a narrow zone at the grain boundary was often devoid of precipitate. Some

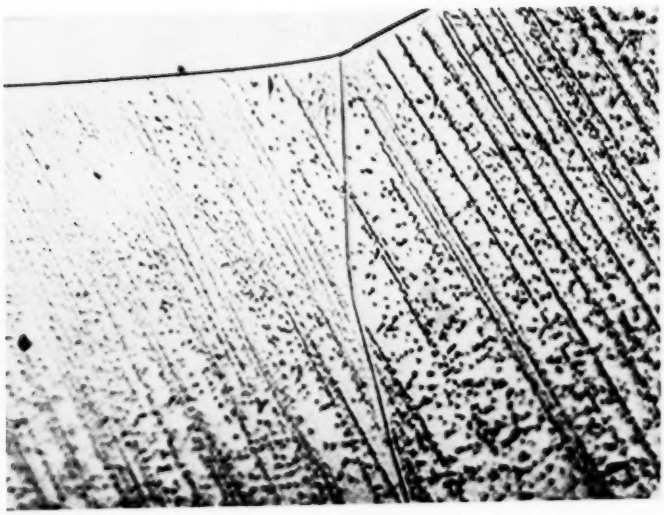

FIG. 13. 24·7 per cent alloy, water-quenched from 1200°C and annealed 18 hr at 500°C. Electrolytically polished and etched. ×940.

[*facing p.* 214

BLANK
PAGE

Vol. 2
196

samples were highly deformed by bending *instead* of being quenched from 1200°C, and subsequently were annealed at 500°C. These also precipitated the f.c.c. phase. These micrographic experiments show that the heat treatment used in the experiments described in the preceding pages cannot have produced any f.c.c. phase, and therefore cannot have led to any consequential change in the composition of the b.c.c. matrix.

X-ray diffraction photographs were made of powders which had been quenched in evacuated silica quills from 1200°C and annealed *in vacuo* at various lower temperatures. In all cases, four diffraction lines due to an f.c.c. structure with a lattice parameter (extrapolated to $\theta = 90°$) in the range 3·750–3·761° Å were found. This range of parameters agrees with those quoted by TAYLOR and JONES. They attributed the phase to nucleation by the double carbide Fe_3AlC. However, GENGNAGEL[21] specifically excludes Fe_3AlC. The possibility also exists that the phase is based on Fe_4N (a = 3·787 Å).[22]

DISCUSSION OF OBSERVATIONS

Comparison with published diffraction data, with special reference to the composition range 22–25 *per cent* Al

The computed atomic distributions assembled in Figs. 7 and 8 agree well with the classical results due to BRADLEY and JAY[1], subject to the limitations introduced by the use of an oil quench. The main difference is the more rapid falling away of order in the slow-cooled alloys below 25 per cent aluminium, as compared with BRADLEY and JAY's estimate. However, they had no alloy in the crucial composition range, so that the difference is reduced to a matter of curve drawing. The *most startling result of their work, the brusque discontinuity in behaviour at* 25 *per cent, is fully borne out by the present high temperature data*. The reality of the brusque discontinuity in ordering behaviour at 25 per cent is further borne out by the observations on heating and cooling at 5°C/min, of which some results were shown in Fig. 4. For alloys containing less than 25 per cent aluminium, this rate of heating and cooling results in a substantial hysteresis of the critical temperature T_c, up to ±20°C from equilibrium. More concentrated alloys showed no hysteresis. Alloys with less than 25 per cent solute disorder completely on heating, as regards both first and second nearest neighbours, and therefore the required atomic rearrangement is more elaborate than in the case of the alloys with more than 25 per cent solute, in which only second nearest neighbour ordering decreases on heating. This less elaborate rearrangement can, apparently, take place readily even during comparatively fast heating and cooling.

The problem therefore arises: What is the reason for the difference between these high temperature data and BRADLEY and JAY's data on the one hand, which lead to a phase diagram approximately as in Fig. 1, and the dilatometric and X-ray parameter data, and our own results on quenched solid samples, which suggest that there is no discontinuity at 25 per cent and which imply a diagram of the approximate form of Fig. 3?

Three interpretations present themselves: (i) there may be an intrinsic difference in behaviour between powder and massive material of the same composition, or (ii) our powder samples, and those of BRADLEY and JAY, may have become contaminated by oxygen or nitrogen and thus changed in composition, or (iii) quenching (even in water) of alloys with less than 25 per cent Al, from above T_c, is not fast enough to prevent ordering entirely.

The first alternative is consistent with most of the available results, except, at first sight, with the phase boundaries deduced by TAYLOR and JONES from their lattice parameter data. However, when critically examined, it is seen that in the crucial composition range, 22–25 per cent aluminium, TAYLOR and JONES' X-ray powder data are just as consistent with the phase diagram of Fig. 1 as with that of Fig. 3. The second alternative, that the composition of the alloys was changed by contamination, cannot be ruled out; contamination might have taken place during hot pressing of the diffractometer samples at 450°C. However, the sample was tightly enclosed in a well-fitting die, and appeared perfectly clean after withdrawal. Also, this hypothesis requires an explanation for the brusque discontinuity in ordering behaviour at 25 per cent. It is impossible to see how a smooth transition in ordering behaviour as implied by Fig. 3 could be turned into the behaviour expressed by Figs. 1 and 8, merely by a change in the mean aluminium content of the filings.

The weight of the evidence is in favour of the

view that *powders* containing less than 25 per cent aluminium disorder in a different way, when they are heated, than do *solid* samples of the corresponding composition. GOLDMAN and ARROTT[23] also reached this conclusion for Fe–Ti alloys by comparing magnetic properties of a series of Fe–Ti solid solutions in both powdered and solid form. They attributed the difference to the high dislocation concentration present in the filings *before* annealing.

SELISSKY[24] made precision measurements, by the powder method, of the room temperature lattice parameter of a 24·3 per cent alloy as a function of quenching temperature. The lattice parameter continues to increase substantially as the quenching temperature is raised above T_c (540°C), suggesting that there is a further loss of order *above* T_c and up to about 750°C. These values agree closely with those for the 24·3 per cent published by TAYLOR and JONES.

Recently, LIHL and STICKLER[25] reported measurements on lattice parameters of rapidly quenched Fe–Al alloys. Above 23 per cent Al, even quenching of fine powders at up to 900°C/sec was not fast enough to prevent some ordering during the quench, as evinced by the persistence of superlattice lines on their films. SELISSKY's lattice parameter data is therefore subject to this limitation.

The above observations suggest the possibility that conclusions drawn from alloys in the approximate composition range 22·5–25 per cent, which have been quenched from high temperatures may be misleading because of the impossibility of quenching fast enough (alternative (iii) above). This is in accord with TAYLOR and JONES'[10] claim, on the basis of measurements of magnetic saturation, that at and above 24 per cent Al even a rapidly quenched alloy is not entirely disordered.

Whatever the nature of the alloy structure in the disputed range (22·5–25 *per cent* Al, *above* 540°C), *it is clear from* MCQUEEN *and* KUCZYNSKI's *dilatometric data that some change is taking place in these alloys* (*in massive form*) *at temperatures in the range* 600–800°C. The uncertainties of interpretation discussed in the preceding section do not detract from this conclusion, which is reinforced by the discovery of pronounced discontinuities in creep resistance of 23·5 and 24·8 per cent alloys at similar temperatures as for the dilatometric singularities.[2]

If FeAl-type order does indeed persist above ~ 540°C in this composition range, then the singularities referred to correspond to the disappearance of this order. If such order does not persist even in massive material, then the singularities must be due to the disappearance of short-range order; in the case of alloys near 19 per cent this is certainly so.

It is concluded that

(i) Powdered alloys with 22·5–25 per cent Al lose all long-range order at T_c, but retain some short-range order above this temperature. When quenched from above T_c, these alloys acquire some long-range order, no matter how drastic the quench.

(ii) Solid alloys in this composition range probably retain pseudo-FeAl type order above T_c.

Interpretation of the thermal memory effect—directional order

The reduced degree of order which had been obtained when alloys were rapidly cooled through the critical temperature T_c, and then annealed below T_c, calls for an explanation. It is proposed that this effect can be interpreted in terms of the phenomenon of *directional order*.

The concept of directional order was originally introduced to account for the effect of annealing certain ferromagnetic solid solutions in a magnetic field. This leaves behind a "memory" in the form of an induced magnetic anisotropy; this also happens when iron–aluminium alloys are field-annealed.[8] The concept was introduced by SNOEK[26] in connection with the behaviour of the interstitial solution of carbon in iron, and extended by NÉEL[27] and TANIGUCHI[28] to the case of substitutional solid solutions. The whole topic has been admirably reviewed by GRAHAM[29].

When a large field is applied below the Curie temperature, the magnetization vectors in all domains line up parallel to the field vector. While the temperature is still high enough for diffusion to occur, the atoms of the alloy tend to arrange themselves in such a way that there are unequal numbers of solvent–solute atom pairs parallel to, and perpendicular to, the magnetization vector; this is *directional order*. The atoms become

"frozen" into their positions on cooling, and the anisotropic atomic arrangement is then responsible for the observed magnetic anisotropy. *It is important to recognize that directional order will arise irrespective of whether an external field is applied or not.* In the absence of a field the axis of the directional order (which coincides with the magnetization vector) will vary from one magnetic domain to the next, so that no macroscopic anisotropy can then be detected. However, on a microscopic scale the anisotropy is still there.

*In a ferromagnetic alloy, the tendency to form directional order is in competition with the tendency, if that exists, to form normal (or isotropic) short-range or long-range order.** Each tendency will vary with temperature in a different way, and the balance between the two kinds of order will depend on the relative value of the critical ordering temperature T_c and the Curie temperature θ_c (which is in effect the critical temperature for directional ordering). If the present interpretation is correct, then the balance depends also on the thermal history.

The degree of directional order established at any temperature will depend upon the magnitude of the saturation intensity of magnetization I_s *at that temperature.* It is well established[17,30,31,32] that, just below T_c, the partly ordered alloy has a lower I_s than has the disordered alloy (though the opinion[33] that the partly ordered alloy just below T_c is non-magnetic is incorrect). It follows that, immediately after a transcritical fast cool to (T_c-50)°C, an alloy will be more highly magnetic, and therefore possess more directional order, than when the alloy has been slowly cooled to this same temperature. This should reduce the degree of isotropic order induced in the former condition, as compared with the latter. This reduction of order should, moreover, be persistent, because there is a two-way interaction between order and magnetism (in the sense that a high degree of magnetism depresses the degree of isotropic order, and *vice versa*). *This model also accounts for the fact that as soon as the Curie temperature dips* below T_c (26 *per cent* Al *approx.*), *the thermal memory effect disappears.*

GENGNAGEL[21] has shown that an iron carbide (probably containing some aluminium, but not Fe_3AlC), is precipitated when a carbon-containing iron–aluminium alloy is heat-treated in the temperature range 400–650°C. This increases the mean aluminium content of the matrix and thus affects the degree of order. If it be postulated that, after transcritical fast cooling, the degree of carbide precipitation is different than after slow cooling, then the thermal memory effects might in principle be explained. However, it is hard to see how anomalies of the type described in the section on thermal memory could be readily interpreted in this way. Further, the present alloys had a low carbon content and under the experimental conditions described, precipitation did not occur in solid samples (Section III above). With sintered powders no carbide X-ray diffraction lines were recorded.

It is not possible to attribute the thermal memory effect to an enhanced vacancy concentration resulting from the transcritical cooling, since this would alter only the rate of ordering, not the final degree of order. There is the possibility that directional order may be present to a limited extent in slowly cooled or equilibrium samples, and that this is responsible for the abnormal levelling off of the experimental S–T curves below T_c (Fig. 9).

THE DIAGRAM OF STATE

On the basis of the results obtained in this and previous research the tentative diagram of state of Fig. 14 is proposed. The available information is not sufficiently clear-cut to warrant the term "equilibrium diagram".

The ordering temperatures (ABC) are taken directly from the high temperature diffractometer plots (Table 2). The temperatures are about 25°C higher than those derived from dilatometric curves by MCQUEEN and KUCZYNSKI[11]. The maximum critical temperature is found not at the stoichiometric Fe_3Al composition but at $\sim$ 28 per cent aluminium. This is also the composition at which the most complete state of order is achieved (Fig. 7). This displacement of maximum order and ordering temperature from the stoichiometric composition is like that found in the nickel–iron system[9,34] near the composition Ni_3Fe; LYASHCHENKO *et al.*[34] suggest that the displacement is due to a postulated magnetic component

*Normal order is termed *isotropic* since if $S = 1$, the number of AB bonds must be accurately the same in all directions.

ol. 20
1961

in the ordering "force", in conjunction with a Curie temperature that varies rapidly with composition. A similar interpretation might apply in the present instance.

The ambiguity concerning the loci AB and AD as alternative temperatures for the loss of FeAl-type order has been discussed above. The locus

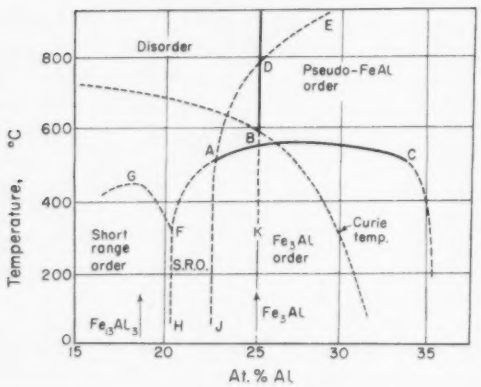

FIG. 14. Proposed diagram of state for iron–aluminium solid solutions.

AD must be included since some structural discontinuity certainly takes place at these temperatures, as shown by dilatometric[11] and creep[2] data. Equally the X-ray evidence is unambiguous that the discontinuity along BD is genuine.

AJ (at a composition near 23 per cent Al) marks the limit of Fe_3Al-type ordering. In the present analysis no long-range order was found in a 22·9 per cent alloy; nevertheless there was a considerable difference in resistivity between quenched and slow-cooled forms of this alloy.[7] It is therefore possible that the boundary AJ should be nearer to 22·5 than 23 per cent.

The area enclosed by the lines AJHF, in the range 20·5–22·5 (or 23) per cent Al, represents compositions which show pronounced short-range order when slow cooled, and a smaller amount of such order when quenched from 800°C. The upper boundary AF is based on dilatometric data[11] and on measurements of resistivity as a function of quenching temperature,[35] and no doubt corresponds to temperatures at which short-range order is disappearing rapidly.

The behaviour of alloys with about 22 per cent Al is subject to some disagreement. No X-ray or resistometric[7] sign of long-range order was found in the present work for the 22·2 per cent alloy, whereas MASUMOTO and SAITO[35] find a large difference in resistivity between quenched and slow-cooled states in a 22·0 per cent alloy, and THOMAS[36] found the same for a 21·4 per cent alloy. Moreover, VLASOVA[37] reported the existence of a form of order intermediate between long- and short-range order, in a 22 per cent alloy. SEYBOLT[38] suggested on the basis of the resistivity–temperature relationship that the 22 per cent alloy, between 400°C and 500°C, consists of a mixture of ordered and disordered phases. The present X-ray results do not bear this out.

Possibly, the structure of the alloys near 20 per cent Al, irrespective of heat treatment, undergo brusque changes for slight changes of composition. This is seen most clearly from the behaviour of the Young's modulus in this composition range.[39] The field AJHF can perhaps be denoted as a kind of transition region. The present X-ray data, and MASUMOTO and SAITO's resistivity measurements,[35] show that the 20·5 per cent alloy is a special case in that its structure is unaffected by heat-treatment. The short-range order is appreciable but is not altered by slow cooling (Fig. 11), and the resistivity is virtually the same for different quenching temperatures. This composition thus constitutes the boundary between two fields.

In the field GFH (the left-hand boundary of which is indefinite) we have short-range order in the slow cooled alloy, and less or more in the quenched alloy. The maximum order appears to be present in the composition range 18·5–19·5 per cent.* This assertion is based on the careful resistometric study by THOMAS[36]. In this field the resistivity is *raised* by ordering, which is not uncommon in the case of short-range order. The temperatures of the upper boundary GF, at which short-range order has substantially disappeared

* The composition 18·75 per cent Al corresponds to a formula, $Fe_{13}Al_3$, which TAYLOR and JONES[10] have proposed as the stoichiometric composition of a distinct superlattice type. Perhaps the field GFH (Fig. 14) represents an attempt to form this superlattice.

(there can be no exactly defined critical temperatures) are estimated from data on resistivity[36,35,40] dilatometry[11] and saturation magnetization.[41]

Alloys in the range 19–21 per cent Al have an unusually strong directional order effect. This is clearly shown by studies of anisotropies induced by annealing in a field or, especially, annealing under load,[8] by internal friction measurements,[42] and by data on magnetic saturation.[41] This strong directional order leads to pronounced forms of thermal memory; the effects of this, as disclosed by electrical resistivity, are currently under study.

A single locus of Curie temperatures is included in Fig. 14. The second locus hitherto included below ABC, and identified as representing Curie temperatures of the ordered alloys, is misleading, because it is based on SYKES and EVANS'[33] low-field permeability measurements which have mistakenly been taken to imply the absence of ferromagnetism just below the ordering temperatures, ABC.

Detailed investigation will be required to set the entire diagram of state on a firm footing; this applies especially to the fields AJHF and ABD. It is also a matter for discussion whether it is justifiable to include in the diagram a boundary such as GF which corresponds to the substantial disappearance of a state of short-range order, for which there cannot be any sharp critical temperature.

Vol. 20
1961

THE COERCIVE FORCE OF IRON–ALUMINIUM ALLOYS

Iron–aluminium solid solutions have a number of unusual magnetic properties, some of which will be briefly reviewed because the present study casts fresh light upon their interpretation.

BENNETT[32] discovered that for alloys in the range 23–27 per cent Al (compositions that showed thermal memory effects in the present study), the coercive force was anomalously high, up to 12 Oe, between ~ 450°C and the Curie temperature. This high coercive force was only observed *at temperature*; alloys quenched from the corresponding temperatures had the normal coercive force of less than one oersted. Further, in the range 450–500°C, the full coercive force took several hours to build up; below 450°C, where the coercive force was low, its final value became established very quickly. Recent work by IVANOVSKY[43] has shown that BENNETT greatly underestimated the true magnitude of the high-temperature coercive force due to limiting test fields below 25 Oe which were insufficient to saturate his samples. IVANOVSKY, using larger field strengths, found that the 25 per cent alloy built up a coercive force as high as 200 Oe at 480°C. However, the time required was about 2 hr at 480°C—rather less than the 2 days reported by BENNETT. This temperature seems to be that of maximum "magnetic viscosity". IVANOVSKY confirmed that even after "critical" heat treatment, the room temperature coercive force was small.

SHIRAKAWA *et al.*[44] determined indirectly the high temperature magnetostriction by means of the Wiedemann effect, and found that in Fe_3Al magnetostriction almost disappeared between 400°C and 500°C, well below the Curie temperature.

It is suggested that these various observations are connected with the directional order effect and its competition with long-range order. In fact, the X-ray kinetic results reported above (Fig. 11) showed that long-range order, like the coercive force, took almost one hour to build up at 500°C, but only a few minutes at 400°C; unfortunately no data were obtained at 480°C.

Why should times of this magnitude be required for the establishment of equilibrium between directional and long-range order above 450°C? One possibility is that the morphology of the magnetic domains is important here.* YAMAMOTO *et al.*[45] have shown experimentally that an alloy in the directionally ordered state is apt to have unusually small magnetic domains arranged in a complicated pattern. It may be that Fe_3Al above 450°C has exceedingly fine magnetic domains. The presence of large numbers of domain walls would account, in terms of the ideas of YAMAMOTO *et al.* for the very small initial permeability of Fe_3Al at high temperatures. If the domains were small enough, this might also account for the observed absence of magnetostriction. As the

* GENGNAGEL[21] has proposed that the anomalous high temperature coercive force, which builds up on annealing near 480°C, is due to the precipitation of a very fine carbide. If this were so, then the high coercive force should be apparent at room temperature. This is not the case.

magnetic domain structure grows during holding at constant temperature, the directional order in the region through which domain walls migrate must be destroyed and re-established in a fresh pattern; this respite will allow more long-range order to form while domain walls are moving. One consequence of such a process would be to form, gradually, a chequerwork of regions of greater and lesser long-range order, according to the accident of domain growth. The more highly ordered regions will be less magnetic, and *vice versa*. Such a fine-scale pattern of regions of different magnetization will have a high coercive force,[46] as observed. When the alloy is quenched, the coercive force diminishes sharply, because at room temperature the regions of different order have almost identical degrees of magnetization.[10, 47]

It is not suggested that the alloy is divided into tiny adjacent regions of large S and zero S; if this were so, it would be inconsistent with the observation that both fundamental and superlattice lines remain sharp right up to T_c. Long-range order is presumably substantial everywhere, and the proposed fine-scale structure is a local perturbation of this uniform state of order. The above model for the establishment of a high coercive force can also help to account for IVANOVSKY's remarkable discovery that the application of a small magnetic field during heat treatment prevents the generation of a high coercive force. The field would be expected to coarsen the domain structure[45] and thus prevent the operation of the mechanism described.

Acknowledgements—We are grateful to the following: Professor G. V. RAYNOR for the provision of laboratory facilities and for his encouragement; Professor J. D. FAST and Dr. J. F. NACHMAN for the provision of vacuum-cast alloys; Dr. A. BERGHEZAN and Mr. E. FELLOWS for experimental assistance; Mr. C. SERGEANT for the chemical analyses; Dr. P. LEHR for carrying out dilatometric tests; H.M. Department of Scientific and Industrial Research which provided financial support for A. L.

REFERENCES

1. BRADLEY A. J. and JAY A. H., *Proc. Roy. Soc.* **A136,** 210 (1932).
2. LAWLEY A., COLL J. A. and CAHN R. W., *Trans. A.I.M.E.* **218,** 166 (1960).
3. LAWLEY A., VIDOZ E. A. and CAHN R. W., *Acta Met.* **9,** 287 (1960).
4. CAHN R. W. and COLL J. A. *Acta Met.* **9,** 138 (1961).
5. FEDER R. and CAHN R. W., *Phil. Mag.* **5,** 343 (1960).
6. CAHN R. W. and FEDER R., *Phil. Mag.* **5,** 451 (1960).
7. FEDER R., THORNTON P. H. and CAHN R. W., *Phil. Mag.* (in press).
8. BIRKENBEIL H. J. and CAHN R. W., *J. Appl. Phys.* **32,** 362S (1961).
9. HANSEN M. and ANDERKO K., *Constitution of Binary Alloys*, McGraw-Hill, New York (1958).
10. TAYLOR A. and JONES R. M., *J. Phys. Chem. Solids* **6,** 16 (1968).
11. MCQUEEN H. J. and KUCZYNSKI G. C., *Trans. A.I.M.E.* **215,** 619 (1959).
12. WILLIAMSON G. K. and MOORE A., *J. Sci. Instr.* **33,** 107 (1956).
13. JAMES R. W., *The Optical Principles of the Diffraction of X-rays*. Bell, London (1950).
14. BRAGG W. L. and WILLIAMS E. J., *Proc. Roy.* **A145,** 699 (1934); **151,** 540 (1935).
15. COWLEY J., *Phys. Rev.* **77,** 669 (1950).
16. DIENES G. J., *Acta Met.* **3,** 544 (1955).
17. WOJCIECHOWSKI K. F., *Acta Phys. Polon.* **18,** 15 (1959).
18. RODE V. E., *Izv. Akad. Nauk SSSR, Ser. Fiz.* **21,** 1234 (1957).
19. WARREN B. E. and AVERBACH B. L., *Modern Research Techniques in Physical Metallurgy*, American Society of Metals, Cleveland (1954).
20. BRADLEY A. J. and TAYLOR A., *Proc. Roy. Soc.* **A166,** 353 (1938).
21. GENGNAGEL H., *Berichte der Arbeitsgemeinschaft Ferromagnetismus* (1958); Dr. Riederer-Verlag, Stuttgart, 127 (1960).
22. JACK K. H., *Proc. Roy. Soc.* **A195,** 34 (1948).
23. GOLDMAN J. E. and ARROTT A., *Magnetic Properties of Metals and Alloys*, p. 93, American Society of Metals, Cleveland (1959).
24. SELISSKY Ya. P., *Fiz. Metal. Metalloved.* **4,** 191 (1957); **7,** 534 (1959).
25. LIHL F. and STICKLER R., *Arch. Eisenhettünw* **31,** 47 (1960).
26. SNOEK J. L., *Physica*, **5,** 663 (1938); **6,** 161, 591, 797 (1939).
27. NÉEL L., *J. Phys. Rad.* **15,** 225 (1954).
28. TANIGUCHI S., *Sci. Rep. Res. Inst. Tôhoko Univ.* **7A,** 269 (1955).
29. GRAHAM C. D., *Magnetic Properties of Metals and Alloys*, p. 288, American Society of Metals, Cleveland (1959).
30. CRANGLE J., private communication.
31. IVANOVSKY V. I. and DENISOV P. P., *Fiz. Metal. Metalloved.* **4,** 550 (1957).
32. BENNETT W. D., *J. Iron St. Inst.* **171,** 372 (1952).
33. SYKES C. and EVANS H., *J. Iron St. Inst.* **131,** 225 (1933).
34. LYASCHENKO B. G., LITVIN D. F., PUZEI I. M. and ABOV YU G., *Kristallografiya* **2,** 64 (1957).
35. MASUMOTO H. and SAITO H., *Sci. Rep. Rec. Inst. Tôhoko Univ.* **4A,** 321 (1952).
36. THOMAS H., *Z. Metallk.* **41,** 185 (1950).
37. VLASOVA E. N., *Izv. Akad. Nauk. SSSR, Ser. Fiz.* **23,** 655 (1959).

38. SEYBOLT A. U., *Trans. A.I.M.E.* **218,** 570 (1960).
39. YAMAMOTO M. and TANIGUCHI S., *Sci. Rep. Res. Inst. Tôhoko Univ.* **8**A, 193 (1956).
40. GRIGORIEV A. T. and GRUZDENA N. M., *Izv. Sek. Fiz.-Khim. Anal. Inst. Obstachei Neorg. Akad. Nauk. SSSR* **14,** 245 (1941).
41. PARSONS D., SUCKSMITH W. and THOMPSON J. E. *Phil. Mag.* **3,** 1174 (1958).
42. SHYNE J. C. and SINNOT M. J., *Trans. A.I.M.E.* **218,** 861 (1960).
43. IVANOVSKY V. I., *Fiz. Metal. Metalloved.* **4,** 70 (1957).
44. SHIRAKAWA Y., OHARA T. and ABE T., *Sci. Rep. Res. Inst. Tôhoko Univ.* **10**A, 211 (1958).
45. YAMAMOTO M., TANIGUCHI S. and AOYAGI K., *Phys. Rev.* **102,** 1295 (1956); *Sci. Rep. Res. Inst. Tôhoko Univ.* **10**A, 20 (1958).
46. NÉEL L., *Ann. Univ. Grenoble* **22,** 299 (1946).
47. ARROTT A. and SATO H., *Phys. Rev.* **114,** 1420 (1959).

Vol. 20
1961

J. Phys. Chem. Solids Pergamon Press 1961. Vol. 20, Nos. 3/4, pp. 222–229. Printed in Great Britain.

ATOMIC CONFIGURATIONS IN IDEALLY FLAT SURFACES—I

CONSTRUCTION OF MODELS OF SURFACES IN FACE-CENTRED AND BODY-CENTRED CUBIC CRYSTALS

A. J. W. MOORE and J. F. NICHOLAS

Division of Tribophysics, C.S.I.R.O., University of Melbourne, Australia

(*Received* 23 *January* 1961)

Abstract—A method is described for constructing ball models of atomically flat surfaces of any orientation in face-centred and body-centred cubic crystals.

1. INTRODUCTION

IN RECENT years, models of crystal structures have been constructed from small hard spheres in order to help the understanding of problems in field emission, adsorption, and catalysis. For example, models, with external surfaces as close to spherical as the size of the spheres and the crystal structure permit, have been constructed by BECKER[1] for a body-centred cubic structure and by WORTMAN *et al.*[2] for a face-centred cubic structure. An inspection of such models shows that the surfaces consist of flat areas (some quite large) separated by well-defined monatomic steps, and suggests that the surface of any crystal could be described in terms of such areas and steps. The field ion patterns found by MÜLLER[3] provide experimental evidence for the existence of such monatomic steps. It was, therefore, felt worthwhile to evolve a simple technique for constructing ball models of atomically flat surfaces of various orientations.

Clearly, the first problem is to stack the balls together in the required crystal structure. Since any crystal having a simple structure, i.e. one which can be described in terms of a unit cell containing only one atom, can be considered as a set of identical parallel planes of atoms, the stacking can be carried out by building up the structure in layers. Suppose that a model of one such plane has been constructed from balls fixed rigidly with respect to each other, then a model of the next plane can be built by resting balls on this array provided each atom of the new plane is linked to three or four atoms in the first plane by nearest-neighbour bonds. By continuing in this way a model of the crystal can be built up, the model being stable under gravitational forces provided the layers are set horizontally and the side surfaces are not too steep.

The construction of the first layer is considerably simplified if the atoms within this plane are linked by nearest-neighbour bonds, i.e. if some close-packed directions lie in the plane. It is then sufficient to pack the balls together on a flat sheet and surround them by suitably placed barriers. For a face-centred cubic crystal, it is simple to construct models based on either (100) or (111) planes since these planes contain two or three distinct close-packed directions and an atom in one plane is linked to four or three nearest neighbours in each adjacent plane. For a body-centred cubic crystal, the only planes which have sufficient nearest-neighbour links *between* planes are of {100} or {111} type. Since no close-packed directions (the ⟨111⟩ directions for this structure) can lie in such planes, the first layer must be carefully constructed by, for example, partly embedding the balls in a suitably arranged set of holes drilled in a flat slab.

The model of an atomically flat surface can, in

principle, be constructed by drawing an imaginary surface through the crystal model and then removing all the balls to one side of this surface. It is clear that when the imaginary surface makes a small angle with the layers, such a model will consist of areas of successive layers separated by steps. A similar picture can, in fact, be used for a surface of any orientation. Furthermore, the translational symmetry of the crystal structure ensures that, for a given flat surface, the edges of all layers are crystallographically identical, i.e. one can be found from another by a pure translation. Therefore, a crystal surface can be described by first describing a typical edge and then describing the stacking of the edges. A model of a given surface can thus be built up by constructing layers with the correct type of edge and then correctly locating the edges relative to one another.

In this paper, the construction of a model of any atomically flat surface in a face-centred or body-centred cubic crystal will be described. In Section 2, where the surface of a face-centred cubic crystal is described in terms of (100) layers, all necessary results are derived in an elementary though somewhat inelegant fashion. In Sections 3 and 4, some results are quoted without proof since, in Part II,[4] the method of description is extended to cover any crystal structure and the general formulae developed there can be applied simply to the cases discussed here.

2. SURFACES IN A FACE-CENTRED CUBIC CRYSTAL DESCRIBED IN TERMS OF (100) LAYERS

Models of a face-centred cubic crystal can be constructed based on (100) planes, the configuration of balls in any layer being as shown in Fig. 1. The discussion in this paper will be restricted to surfaces, (*hkl*) say, having normals lying within the unit stereographic triangle in which $h \geqslant k \geqslant l \geqslant 0$ (see Fig. 2). Because of cubic symmetry, this restriction on (*hkl*) still allows a complete range of typical surfaces to be considered but ensures that all models will be stable under gravitational forces provided the (100) planes are kept horizontal. It is convenient at this stage to choose a particular orientation for the two crystal axes that ie in the (100) plane. This choice is shown in Fig. 1 together with the two close-packed directions that will be used in the next sub-section.

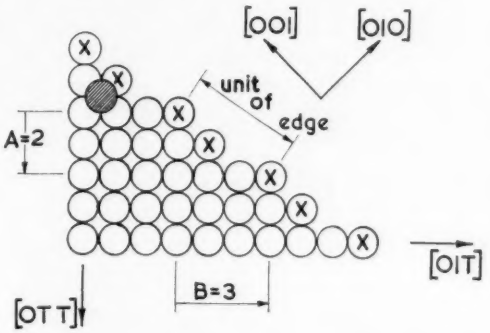

FIG. 1. Arrangement of balls in a (100) plane of the face-centred cubic model. The edge shown corresponds to $A = 2$, $B = 3$, and balls marked with a cross represent kink atoms. The shaded circle shows the position in the layer above of the ball separated from the adjoining kink atom by the chosen inter-layer translation [see Section 2(b)].

(a) *Description of the edge of a layer*

From Fig. 1, it is clear that the edge of a layer, i.e. the intersection of the (*hkl*) plane with a (100) plane, can be described as a sequence of displacements in the two perpendicular directions, $[0\bar{1}\bar{1}]$ and $[01\bar{1}]$, the size of all displacements being one atomic diameter. Further, if the surface has rational indices, the sequence must be periodic, one repeat distance of the edge (unit of edge) containing, say, A displacements along $[0\bar{1}\bar{1}]$ and B along $[01\bar{1}]$, where A and B have no common factor.

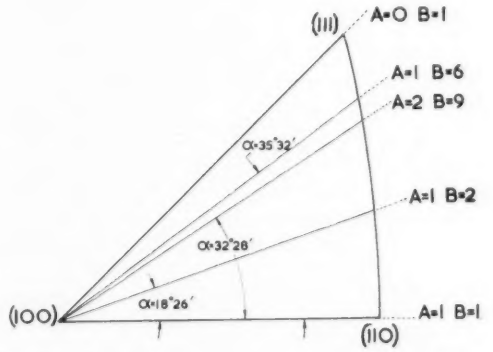

FIG. 2. Orientation of the unit stereographic triangle containing the normals to the surfaces considered. The lines through (100) indicate zones each of which contains the normals to all surfaces with a given type of edge.

The determination of A and B in terms of the indices of the surface, follows from the fact that the indices of the mean direction of the edge must be proportional to the three numbers 0, $-A+B$, $-A-B$. Therefore, since this direction lies in the (hkl) plane, then

$$k(-A+B)+l(-A-B) = 0, \qquad (1)$$

$$\text{i.e. } A(k+l) = B(k-l). \qquad (2)$$

Thus A, B must be the smallest positive integers satisfying equation (2). Within the unit stereographic triangle, the condition $k \geqslant l$ implies that $B \geqslant A$. In fact, B/A varies from 1 when $l = 0$, i.e. along the (100)–(110) side of the triangle, to ∞ when $k = l$, i.e. along the (100)–(111) side.

An interesting feature of equation (2) is that the index h does not appear. This implies that a whole set of surfaces will have edges of the type given by B/A. In fact the set of surfaces consists of all surfaces whose normals lie in a definite zone through [100]. This zone can be specified either by its crystallographic axis, namely $[0\bar{l}k]$, or by specifying the angle α between the line representing the zone and the (100)–(110) side of the triangle. It is easily shown that α is given by

$$\tan\alpha = l/k = (B-A)/(B+A). \qquad (3)$$

Fig. 2 shows plots of some zones for simple values of A, B.

In order to specify an edge completely, it is necessary to specify the order in which the $[0\bar{1}\bar{1}]$ and $[01\bar{1}]$ displacements occur. The criterion governing this order is that the edge should be atomically straight. This means that the sequence of displacements should be so arranged that if a straight-edge is set parallel to the mean edge direction and moved up until it touches some balls along the edge then there should be no spaces between the balls and the straight-edge large enough to accommodate an extra ball. It will be shown[4] that this implies that all displacements parallel to $[0\bar{1}\bar{1}]$ occur one at a time and that the displacements parallel to $[01\bar{1}]$ occur in groups of I or $I+1$, where I is the integral part of B/A.

If $B/A = I+R/A$ with $0 \leqslant R < A$, then it is easily shown that any repeat distance will contain $A-R$ groups of length I and R groups of length $I+1$. The order in which these groups occur is usually obvious but, in doubtful cases, use of the straight-edge criterion is the simplest practical method (a strict specification of the order is given in Part II). As an example, Figs. 3(a) and 3(b) show the construction of two repeat distances of edge for the case $B/A = 7/3 = 2+1/3$. This edge corresponds to $k/l = 5/2$.

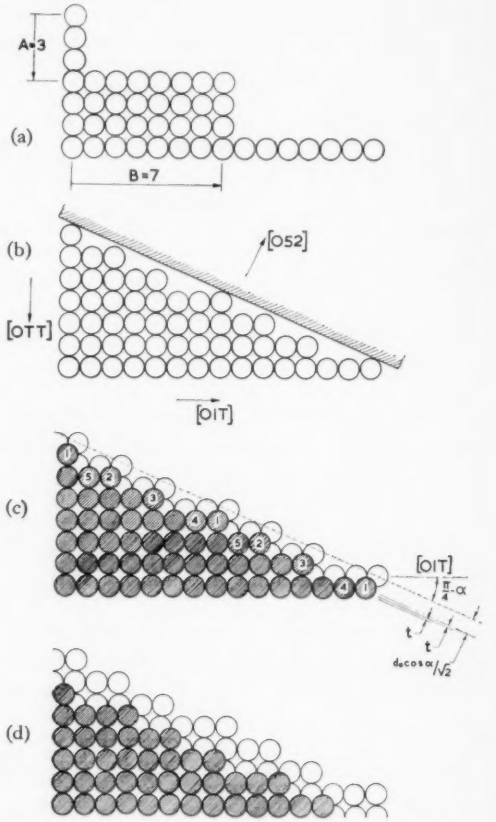

FIG. 3. (a) and (b) Stages in the construction of an edge of a layer for which $A = 3$, $B = 7$.

(c) The dotted line represents the ideal edge and its relationship to α is shown. The shaded circles represent the positions of balls in the layer above when the ideal edge has been displaced by the inter-layer translation only. The numbered circles represent kink-atoms in the edge of the upper layer, the number increasing with distance from the ideal edge. Their successive removal gives a succession of t-displacements of the ideal edge.

(d) A later stage in the construction of a model of a (28 15 6) surface.

Vol. 2
1961

If a kink-atom is defined as an atom in the edge which is preceded by a $[01\bar{1}]$ displacement and followed by a $[0\bar{1}\bar{1}]$ displacement, it is clear that there are A kink-atoms in one repeat distance of edge. This result will be used in Section 2(b). The kink-atoms in Fig. 1 are marked with a cross.

(b) *The stacking of the edges to form a surface*

Since all edges in a given surface are identical a description of the translations necessary to position each edge relative to the preceding one effectively completes the description of the surface. In this section, which describes these translations, the structure of the edge will in general be neglected and consideration will be restricted to the ideal edge, i.e. the straight line which passes through the centres of the outermost balls. This means that only the displacement of the line perpendicular to itself need be calculated and any component of displacement parallel to the edge can be ignored.

The position of an edge in a new layer relative to an existing edge in the layer below can be described in terms of two translations. The first, the inter-layer translation, is any translation which can carry a ball from an atomic site in one layer to an atomic site in the layer above. There are, of course, an infinite number of such translations possible but in this paper the translation shown in Fig. 1 will be used. This corresponds to a displacement of one atomic diameter in the $[1\bar{1}0]$ direction. Physically, if two layers are built up as in Fig. 3(c) with their edges separated by this translation, then the edges are as close together as gravitational stability allows. Further, Fig. 3(c) shows that such a translation corresponds to moving the ideal edge up a distance $d_0/\sqrt{2}$ and backward by

$$(d_0/\sqrt{2})\cos\alpha = kd_0/[2(k^2+l^2)]^{1/2}$$
$$= \tfrac{1}{2}(A+B)d_0/(A^2+B^2)^{1/2},$$

where d_0 is the diameter of a ball (atom).

The second part of the translation corresponds to a movement of the ideal edge in the plane of the layer. The discreteness and symmetry of the atomic arrangement show that this translation can only occur by discrete amounts, each of a given magnitude, say t, measured perpendicular to the ideal edge. In fact, if the arrangement in the (100) layer is taken as defining a square net with parameter d_0, then t is just the spacing between (AB) lines in that net and can be calculated from standard crystallographic theory. However, it is instructive to calculate t from movements of balls in a model. In order to displace a given edge by t, balls representing the outermost kink-atoms [those marked 1 in Fig. 3(c)] must be removed from the edge. This removal makes some other kink-atoms [those marked 2 in Fig. 3(c)] the outermost in the new edge and removal of these balls as well will cause a total translation of $2t$. If this process is continued until all the kink-atoms in the original edge have been removed, the total translation will be At. However, it is clear that the net effect of removing the A kink-atoms is equivalent to a displacement of the whole edge back by a distance d_0 parallel to $[01\bar{1}]$, i.e. at an angle $(\pi/4+\alpha)$ to the normal to the ideal edge. Therefore,

$$At = d_0\cos(\pi/4+\alpha),$$
$$\text{i.e. } t = (k-l)d_0/A\,[2(k^2+l^2)]^{1/2}$$
$$= d_0/(A^2+B^2)^{1/2}. \qquad (4)$$

Thus, as predicted, t is the interlineal spacing between (AB) lines in a square net.

The movement from one edge to that in the layer above must contain one inter-layer translation, i.e. one step in the surface, together with some number (possibly zero) of t-translations, these latter representing the widths of the treads of the steps on the surface. Therefore, a sequence of edges is related by a sequence of such combinations of translations, and this sequence is periodic if the surface has rational indices. Suppose now that one period of this sequence contains a total of C t-translations and a total of D inter-layer movements. Then the total horizontal translation is

$$[C(k-l)d_0/A + Dk\,d_0]/[2(k^2+l^2)]^{1/2}$$

and the total vertical movement is

$$Dd_0/\sqrt{2}.$$

Thus, if β is the angle which the surface makes with [100], i.e. the vertical direction, then

$$\cot\beta = [C(k-l)/AD+k]/(k^2+l^2)^{1/2}. \qquad (5)$$

However, since the surface is an (hkl) plane,

$$\cos\beta = h/(h^2+k^2+l^2)^{1/2} \qquad (6)$$

and combining equations (5) and (6) leads to

$$\frac{C}{D} = A\left(\frac{h-k}{k-l}\right) = B\left(\frac{h-k}{k+l}\right). \quad (7)$$

Since C and D describe a period in the sequence of edges, they must be integers without a common factor, and equation (7) is sufficient to define both of them.*

Clearly, the distribution of the C t-translations over the D layers in the repeat unit of edges is an analogous problem to the distribution of the B $[01\bar{1}]$-displacements among the A $[0\bar{1}\bar{1}]$-displacements in a repeat distance of one edge. In fact, if $C/D = J+S/D$ with $0 \leqslant S < D$ and J an integer, then the sequence of edges consists of $D-S$ steps each followed by J t-translations and S steps each followed by $J+1$ t-translations. One distinction from the previous discussion is that J may be zero. This does not affect the general argument. The order in which these groups of translations occur is usually obvious but in cases of doubt the simplest procedure is to set out an edge of D $[0\bar{1}\bar{1}]$-displacements and C $[01\bar{1}]$-displacements and apply the straight-edge criterion to this. The required sequence of translations is identical with the sequence of displacements found in this way.

(c) *Construction of a model of the* (28 15 6) *surface*

To construct a ball model of a given surface a square array of balls of uniform size is packed into a shallow rectangular tray in which opposite sides are separated by a multiple of the ball diameter. This array corresponds to the arrangement of atoms in a (100) plane of a face-centred cubic crystal and balls stacked onto this base will form a face-centred cubic array.

For the surface chosen, namely (28 15 6), equation (2) gives $21A = 9B$, so that $A = 3$ and $B = 7$. The edge, therefore, is that already shown in Fig. 3(b). Further, equation (7) shows that $C/D = 7\times 13/21 = 4\frac{1}{3}$. Thus, a repeat unit in the sequence of edges consists of one step followed by 5 t-translations and two steps each followed by 4 t-translations.

To build the model, a first layer is set out on the base array with an edge conforming to Fig. 3(b). A second layer is then added with its edge separated from the first edge by only the inter-layer translation [see Fig. 3(c)]. The balls at the outermost kinks of this new edge, i.e. those marked 1, are removed and then those marked 2, 3, 4, 5 as they progressively become the outermost kinks. This gives the arrangement shown in Fig. 3(d), the two edges being separated by an inter-layer translation plus 5 t-translations. Two more edges on successive planes are then set up by removing the balls corresponding to 1, 2, 3, 4 from edges which have been constructed with only the inter-layer translation. This produces two unit cells of the surface (since the length of edge chosen contains two repeat distances). Fig. 4 shows a model constructed in this way.

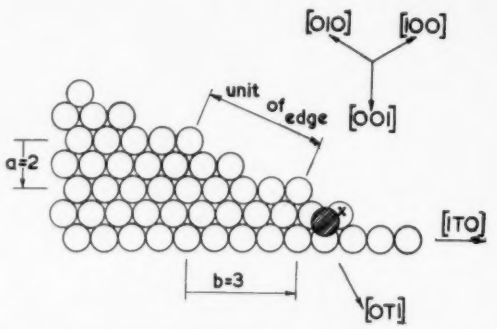

FIG. 5. Arrangement of the balls in a (111) plane of the face-centred cubic model. The edge shown corresponds to $a = 2$, $b = 3$. The three cubic axes project as shown but are inclined upwards 19° 28′ from the plane of the paper. The shaded circle shows the position in the layer above of the ball separated from the ball marked X by the chosen inter-layer translation. Notice that the three circles overlapped by the shaded circle have the ∇ configuration.

3. SURFACES IN A FACE-CENTRED CUBIC CRYSTAL DESCRIBED IN TERMS OF (111) LAYERS

The procedure given in Section 2 can be adapted very simply to the construction of surfaces based on (111) layers. In this case, the configuration of

* For a surface whose orientation is given in terms of α and β, estimates of A, B, C and D can be obtained from equations (2) and (7) by noting that $h : k : l = \cos\beta : \cos\alpha \sin\beta : \sin\alpha \sin\beta$.

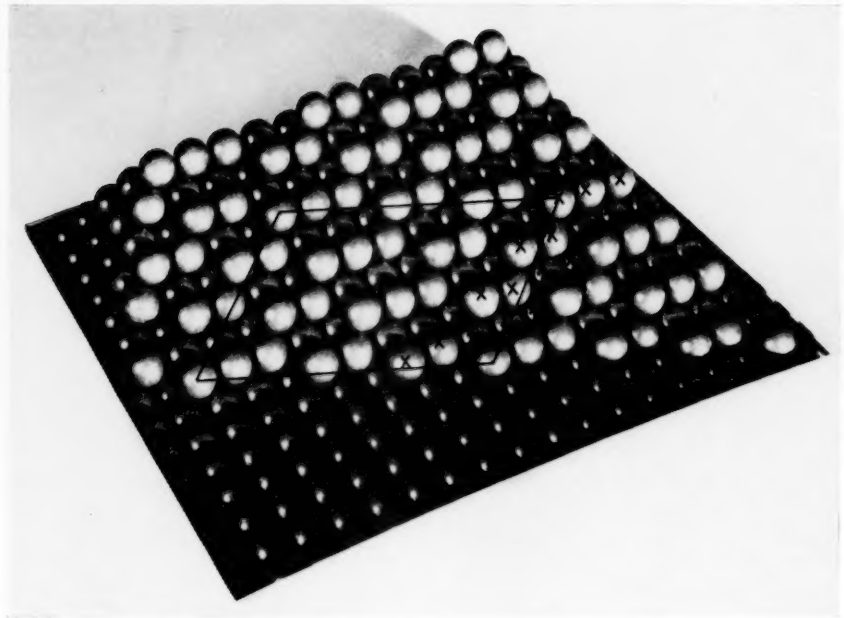

FIG. 4. Model of the (28 15 6) surface of a face-centred cubic crystal based on (100) layers. The balls marked with a cross lie on a (111) plane (compare with Fig. 6). The parallelogram encloses one unit cell of the surface.

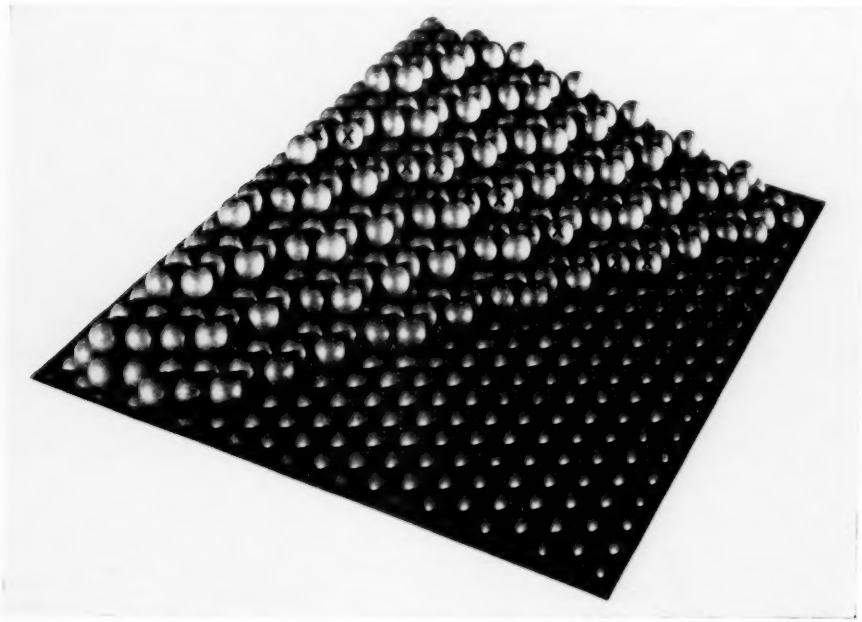

FIG. 6. Model of the (28 15 6) surface of a face-centred cubic crystal based on (111) planes. The balls marked with a cross lie on a (100) plane (compare with Fig. 4).

[*facing p.* 226

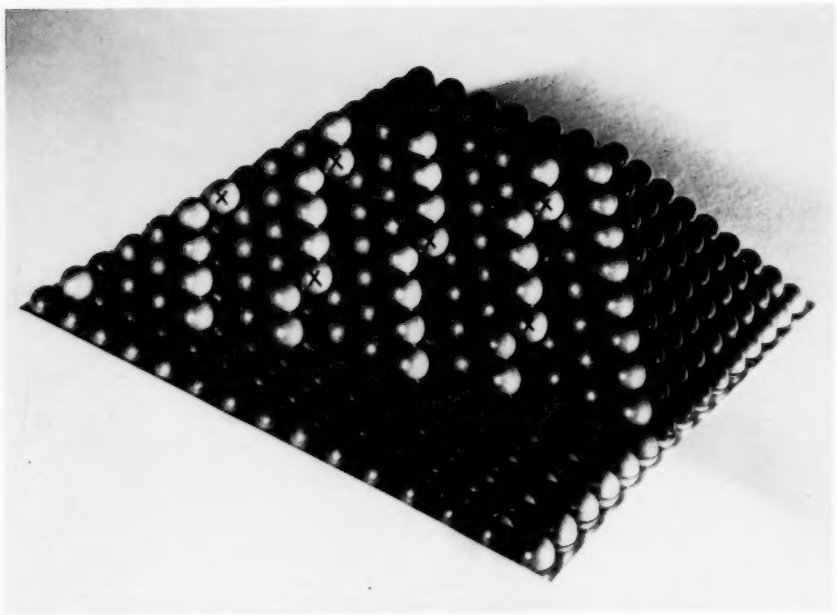

FIG. 10. Model of the (652) surface of a body-centred cubic crystal [based on (100) planes]. Balls marked with a cross are unstable when [100] is vertical.

balls in any layer is as shown in Fig. 5, and an edge consists of displacements parallel to either $[0\bar{1}1]$ or $[1\bar{1}0]$, there being say a and b of each type in a repeat distance. Therefore, for an (hkl) surface, the equation

$$hb+k(-a-b)+la = 0,$$

$$\text{i.e. } a(k-l) = b(h-k), \tag{8}$$

serves to define a and b for any surface (hkl). In this case the ratio b/a, which defines the edge, can have any value between 0 and ∞. Therefore, there are edges in which the $[0\bar{1}1]$ displacements occur individually ($a \leqslant b$) and edges in which the $[1\bar{1}0]$ displacements occur individually ($a \geqslant b$).

When the second layer is stacked on the first there is the well-known ambiguity of placement of the balls. With the layers oriented as in Fig. 5, cubic close-packing consistent with the quoted directions is achieved by placing all balls on triangles of balls of orientation ∇ (see Fig. 5). The inter-layer translation chosen will be that shown in Fig. 5. This corresponds to a movement of one atomic diameter in the [011] direction, and as before represents the smallest possible translation in which the new edge is gravitationally stable. The t-translations can again be considered as successive removals of the balls at the outermost kinks of the edge and for c t-translations combined with d inter-layer translations, it is found that

$$\frac{c}{d} = a\left(\frac{k+l}{h-k}\right) = b\left(\frac{k+l}{k-l}\right). \tag{9}$$

For the plane considered previously, (28 15 6), equations (8) and (9) give $a = 13$, $b = 9$, $c = 21$, $d = 1$. Therefore, the edge consists of 13 displacements along $[0\bar{1}1]$ interspersed with 9 displacements along $[1\bar{1}0]$. Further, every edge is displaced from the one below by the inter-layer translation plus 21 t–displacements. Fig. 6 shows a model of this surface built up on (111) planes. The surface is, of course, identical with that shown in Fig. 5 but is viewed from a different aspect.

At times, it may be convenient to specify a particular surface in terms of two angles comparable to the α and β used in Section 2. A pair of suitable angles are α_1 and β_1 where α_1 is the angle between the zone through (111) and (hkl) and the zone through (111) and (210) and β_1 is the angle between (111) and (hkl). The sense of α_1, as shown in Fig. 7, should be noted since it can be either positive or negative. A given value of α_1 defines a zone of planes all of which have the same type of edge. It is easily shown that

$$\tan \alpha_1 = \frac{h-2k+l}{\sqrt{3}(h-l)} = \frac{a-b}{\sqrt{3}(a+b)}, \tag{10}$$

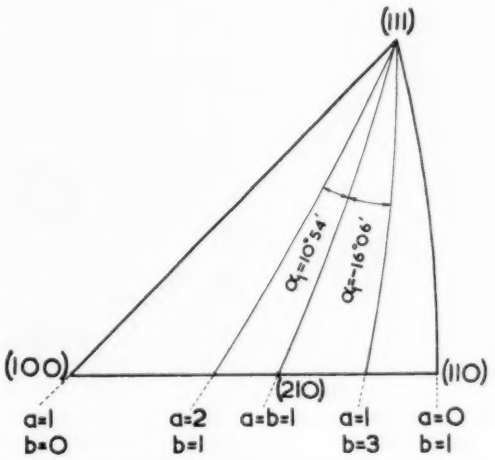

FIG. 7. Stereographic triangle showing zones corresponding to some given types of edge on (111) planes.

$$\text{and } \tan \beta_1 = \frac{\sqrt{(2)}(h^2+k^2+l^2-hk-kl-lh)^{1/2}}{h+k+l} = \frac{2\sqrt{(2)}d(a^2+ab+b^2)^{1/2}}{3c+(2a+b)d}. \tag{11}$$

4. SURFACES IN A BODY-CENTRED CUBIC CRYSTAL DESCRIBED IN TERMS OF (100) LAYERS

The above discussion for the face-centred cubic crystal (Section 2) can be applied to the body-centred cubic crystal very simply. As far as edges are concerned, the basic pattern of atoms in the layer is identical in the two cases except that the atoms are separated by more than an atomic diameter. Thus the balls in the first layer have to be fixed in a position individually, without relying on their neighbours to hold them. A suitable method of doing this is to drill a square array of holes in a sheet of metal, the spacing between the

holes being $(2d_0/\sqrt{3})$ for balls of diameter d_0, and rest the balls in the holes.

An edge in the body-centred cubic crystal can again be treated as a sequence of displacements in two perpendicular directions, these directions being now of $\langle 100 \rangle$ type. If discussion is again restricted to planes within the unit triangle for which $h \geqslant k \geqslant l \geqslant 0$, the orientations of the displacements are $[00\bar{1}]$ and [010] (see Fig. 8).

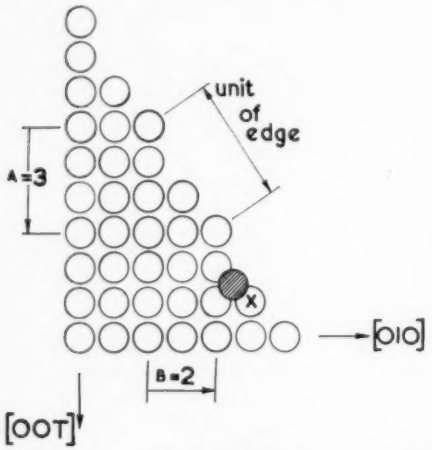

FIG. 8. Arrangement of balls in a (100) plane of the body-centred cubic model. The edge shown corresponds to A = 3, B = 2. The shaded circle shows the position in the layer above of the ball separated from the ball marked X by the chosen inter-layer translation.

Edges can now be constructed from A displacements in the $[00\bar{1}]$ direction and B displacements along [010], the magnitude of each displacement being $(2d_0/\sqrt{3})$. Therefore, for an (hkl) surface,

$$Al = Bk \tag{12}$$

with A, B being the smallest positive integers satisfying equation (12).

The construction of such an edge follows exactly as for the face-centred cubic case and one edge corresponds to all surfaces with orientations in a given zone through [100], the angle α between the line representing this zone and the (100)–(110) side of the stereographic triangle (see Fig. 2) being given by

$$\tan \alpha = \frac{l}{k} = \frac{B}{A}. \tag{13}$$

Since $k \geqslant l$ within the unit triangle, it follows that $A \geqslant B$ and hence the number of kinks in any repeat distance is B.

The inter-layer translation in this case will be taken as a movement of one atomic diameter in the $[1\bar{1}1]$ direction, i.e. to the position shown in Fig. 8. The t-translations within a layer will then be similar to those described in Section 2(b) and since the square array now has a parameter $2d_0/\sqrt{3}$,

$$t = (2d_0/\sqrt{3})/(A^2+B^2)^{1/2}. \tag{14}$$

If one period of the sequence of edges contains a total of C t-translations distributed over D layers,

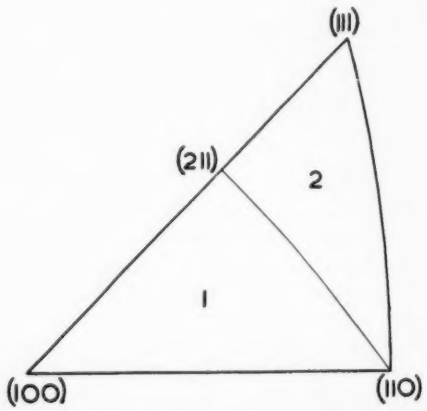

FIG. 9. Subdivision of the unit stereographic triangle into region 1 where $h \geqslant k+l$ and region 2 where $h < k+l$. Models of surfaces with normals in region 2 are stable only when the (100) layers are suitably tilted.

it can be shown that β, the angle between [100] and the normal to the plane, is given by

$$\tan \beta = D(A^2+B^2)^{1/2}/[2C+(A-B)D]. \tag{15}$$

Thence, by use of equations (6) and (13), the ratio C/D which defines the sequence of edges in the surface is found to be

$$\begin{aligned} C/D &= A(h-k+l)/2k \\ &= B(h-k+l)/2l. \end{aligned} \tag{16}$$

Thus any surface can be built up by a procedure analogous to that used previously. However, there is one distinction concerned with the gravitational stability of the model. If the (100) layers are placed horizontally, then any ball moved up from a kink

site on an edge by only the inter-layer translation will be in a position of unstable equilibrium. Therefore, fully stable models can only be produced for surfaces in which there are sufficient t-translations between each edge to move such balls on to stable sites. Clearly, this occurs as soon as the total t-translation is equivalent to the removal of all the kink atoms from the original edge, i.e. after B unit t-translations. This occurs for all edges in which C/D $\geqslant$ B and from equation (16) this condition is equivalent to the condition $h \geqslant k + l$. The region of the stereographic triangle satisfying this condition is shown in Fig. 9 as region 1. For surfaces with orientations in the upper region of the triangle, i.e. region 2, stable models can easily be produced by slightly tilting the base plate on which the model is being constructed.

A model of a (652) surface in a body-centred cubic crystal is shown in Fig. 10 where the unstable atoms are marked with a cross.

5. MODELS OF CUBIC CRYSTALS BASED ON OTHER PLANES

It is possible to construct models of face-centred and body-centred cubic crystals from layers of planes other than those considered above. In all such cases, the first layer has to be constructed carefully (e.g. as described in Section 4) but for only a few planes are there sufficient nearest-neighbour links between atoms in adjacent layers to allow a model to be built up after only this first layer has been constructed. These cases are (110), (311) or (210) planes for face-centred cubic and (111) planes for body-centred cubic crystals. With all such models, except face-centred cubic on (110) planes, there is an ambiguity in the choice of sites on which succeeding layers are built (cf. Section 3) and some care has to be exercised.

In principle, it is possible to construct a hard-sphere model for any simple crystal provided that (1) the crystal structure can be described in terms of a triclinic unit cell with equal axes, (2) these axes actually correspond to nearest-neighbour bonds, and (3) the layer planes are chosen to be (111) relative to this basis. The cases quoted above conform to these restrictions.

6. CONCLUSIONS

The above method enables models of quite complicated surfaces to be constructed simply and quickly so that particular features can be discerned in them. By counting, the concentration of atoms of a given co-ordination number in a particular surface can be determined and rules can be devised which give these concentrations in terms of the parameters A, B, C, D (or their equivalents). However, these results are more simply found by a different procedure that will be described in a later paper.[5]

REFERENCES

1. BECKER J. A., *Advances in Catalysis*, Vol. VII, p. 135. Academic Press, New York (1955).
2. WORTMAN R., GOMER R. and LUNDY R., *J. Chem. Phys.* **27,** 1099 (1957).
3. MÜLLER E. W., *Z. Phys.* **156,** 399 (1959).
4. NICHOLAS J. F., *J. Phys. Chem. Solids* **20,** 230 (1961). (Following paper).
5. MACKENZIE J. K., MOORE A. J. W. and NICHOLAS J. F., to be published.

J. Phys. Chem. Solids Pergamon Press 1961. Vol. 20, Nos. 3/4, pp. 230–237. Printed in Great Britain.

ATOMIC CONFIGURATIONS IN IDEALLY FLAT SURFACES—II

DESCRIPTION OF SURFACE FOR AN ARBITRARY CRYSTAL STRUCTURE

J. F. NICHOLAS

Division of Tribophysics, C.S.I.R.O., University of Melbourne, Australia

(*Received* 23 *January* 1961)

Abstract—An atomically-flat surface in a crystal of arbitrary structure is described in terms of the intersections of the surface with a set of parallel planes. It is shown how this description enables a model of such a surface to be constructed. The theory is applied to develop some of the formulae used in the preceding paper for constructing models of surfaces in face-centred cubic crystals. Details are also given for constructing models of surfaces in a crystal with a hexagonal close-packed structure.

1. INTRODUCTION

IN THIS paper, we consider a crystal consisting of a motif of s atoms arranged around the points of a space lattice, the lattice being described in terms of base-vectors $\boldsymbol{a}_1$, $\boldsymbol{a}_2$, $\boldsymbol{a}_3$, where the unit cell defined by $\boldsymbol{a}_i$ is not necessarily primitive.

If we choose a rational plane with normal $\boldsymbol{h} = (hkl)$, where h, k and l are the Miller indices of the plane, and consider the semi-infinite crystal consisting of those atoms whose position vectors $\boldsymbol{x}$ satisfy

$$\boldsymbol{h} \cdot \boldsymbol{x} \leqslant \delta, \tag{1}$$

where δ is some constant, then this semi-infinite crystal can be said to possess an atomically-flat $\boldsymbol{h}$ surface. The structure of such a surface will be described in this paper.

In Section 2, we will describe the arrangement of lattice points near the surface and thence, in Section 3, describe the positions of the atoms near the surface. These results will be used in Section 4 to give a set of rules for constructing a model of an atomically-flat surface. In Section 5, these will be applied to produce some of the results on cubic crystals found in Part I[1] and in Section 6, models of hexagonal close-packed structures will be discussed.

The description will be based on the intersections of the surface with a set of layer-planes, called L-planes. These L-planes can be any set of parallel rational crystallographic planes and we use them to define a new set of base-vectors, $\boldsymbol{b}_i$, for the lattice in the following way. In a given L-plane through lattice points we choose any pair of lattice vectors that define a primitive unit cell in the plane and call them $\boldsymbol{b}_1$, $\boldsymbol{b}_2$. We then select another L-plane through lattice points as close as possible to the first plane and choose $\boldsymbol{b}_3$ as any vector joining a lattice point in one plane to a lattice point in the other. The set $\boldsymbol{b}_i$, chosen in this way, defines a primitive unit cell in the lattice so that any lattice vector can be written in the form

$$\boldsymbol{x} = X\boldsymbol{b}_1 + Y\boldsymbol{b}_2 + Z\boldsymbol{b}_3 \tag{2}$$

with X, Y, Z integral. Throughout this paper, we assume that the arrangement of lattice points in an L-plane is known.

For convenience, we will adopt the convention that a variable denoted by a capital letter can take only integral values. Further, since we will frequently need to consider the integers above and below a given value, possibly non-integral, we will adopt the notation:

$$[y] = \text{the greatest integer} \leqslant y,$$

$$\text{and } [y]^+ = -[-y] = \text{the least integer} \geqslant y.$$

2. ARRANGEMENT OF LATTICE POINTS NEAR THE h SURFACE

When we consider lattice points, the arrangement near the surface is independent of δ [see Section 2 (d)], i.e. the arrangement for one value of δ can be carried into that for another δ by a pure translation. We will, therefore, put $\delta = 0$ in Sections 2 (a), (b), (c). Furthermore, if we consider, in two L-planes, the sets of lattice points for which $\boldsymbol{h} \cdot \boldsymbol{x} \leqslant 0$, then the two sets of points are congruent. Therefore, the description of the surface can be carried out in two steps:

(a) describe the arrangement of lattice points near the intersection of the surface with the L-plane through the origin and

(b) describe the set of translations necessary to carry this arrangement into all other L-planes.

At this stage, it is convenient to express $\boldsymbol{h}$ in terms of the vectors $\boldsymbol{b}_i^*$ reciprocal to the $\boldsymbol{b}_i$. Thus, we have

$$\begin{aligned} \boldsymbol{h} &= \boldsymbol{h}\cdot\boldsymbol{b}_1\,\boldsymbol{b}_1^* + \boldsymbol{h}\cdot\boldsymbol{b}_2\,\boldsymbol{b}_2^* + \boldsymbol{h}\cdot\boldsymbol{b}_3\,\boldsymbol{b}_3^* \\ &= (H\boldsymbol{b}_1^* + K\boldsymbol{b}_2^* + L\boldsymbol{b}_3^*)/Q, \end{aligned} \tag{3}$$

where H, K, L are the Miller indices of the surface relative to the base-vectors $\boldsymbol{b}_i^*$ and Q is a positive integer. If the $\boldsymbol{a}_i$ define a primitive unit cell in the lattice then the $\boldsymbol{h} \cdot \boldsymbol{b}_i$ are a set of integers without a common factor and are, therefore, the required Miller indices H, K, L, i.e. $Q = 1$. However, if the $\boldsymbol{a}_i$ define a unit cell containing q lattice points then the $\boldsymbol{h} \cdot \boldsymbol{b}_i$ may be non-integral; if so, they must be multiplied by some integer Q to produce the Miller indices H, K, L. It is easily seen that Q is a divisor of q and that its value depends on $\boldsymbol{h}$. For example, if the lattice is described in terms of a face-centred unit cell, i.e. $q = 4$, then $Q = 1$ when h, k, l are all odd and $Q = 2$ otherwise.

(a) *Intersection of the $\boldsymbol{h}$ surface with an L-plane*

Let us consider the vector

$$K\boldsymbol{b}_1 - H\boldsymbol{b}_2$$

which is perpendicular to $\boldsymbol{h}$ and lies in an L-plane. This vector is therefore parallel to the edge of that part of the L-plane that lies within the half-crystal considered. If D (>0) is the highest common factor of H and K, the vector can be written as

$$D\boldsymbol{c}_1 = D(A\boldsymbol{b}_1 + B\boldsymbol{b}_2),$$

where A, B are a pair of co-prime integers. Then, the shortest lattice vector in the intersection of the L-plane with the $\boldsymbol{h}$ surface is

$$\boldsymbol{c}_1 = A\boldsymbol{b}_1 + B\boldsymbol{b}_2, \tag{4}$$

where

$$\left.\begin{aligned} A &= K/D, \\ B &= -H/D, \end{aligned}\right\} \tag{5}$$

and D = h.c.f. of H and K.

In the next sub-section, we will discuss the detailed arrangement of lattice points in the section of the edge of the L-plane spanned by $\boldsymbol{c}_1$. This suffices to describe the whole edge since the translational symmetry of the lattice ensures that the complete edge consists of a repetition of this section, which we therefore term a unit of edge.

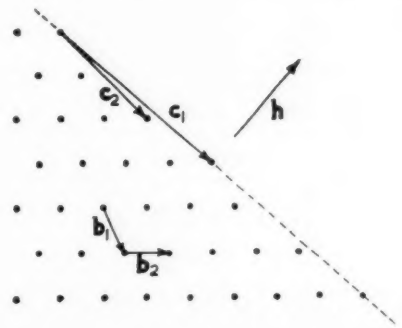

FIG. 1. Arrangement of lattice points in an L-plane with $\boldsymbol{b}_1, \boldsymbol{b}_2$ so oriented that $0 \leqslant -\boldsymbol{h}\cdot\boldsymbol{b}_1 \leqslant \boldsymbol{h}\cdot\boldsymbol{b}_2$. The vector $\boldsymbol{c}_2$ is explained in Section 2(c). Note that $\boldsymbol{b}_1, \boldsymbol{b}_2, \boldsymbol{c}_1, \boldsymbol{c}_2$ are in the plane of the paper but, in general, $\boldsymbol{h}$ is not. The ideal edge is shown as a dashed line and corresponds to $A = 3$, $B = 2$.

(b) *Detailed description of a unit of edge*

Various cases can arise depending on the signs and relative magnitudes of H and K. We will treat in detail the case $A > B > 0$, i.e. the case for which $0 \leqslant -\boldsymbol{h}\cdot\boldsymbol{b}_1 \leqslant \boldsymbol{h}\cdot\boldsymbol{b}_2$, (see Fig. 1). The results for all cases are given in Table 1.

Figure 1 shows that we can trace out an edge in the L-plane as a sequence of $\boldsymbol{b}_1$ and $\boldsymbol{b}_2$-displacements, using the following criterion. At any point in the edge, the next displacement should be $\boldsymbol{b}_2$ if this is possible within the half-crystal considered but $\boldsymbol{b}_1$ otherwise.

For simplicity, we will take the origin of the position vectors $\boldsymbol{x}$ to be one of the edge points that lies *in* the $\boldsymbol{h}$ surface. Then for all points in this L-plane $Z = 0$ and we can specify a point simply as X, Y relative to $\boldsymbol{b}_1$, $\boldsymbol{b}_2$. Thus the first point of the edge is 0, 0 and after A $\boldsymbol{b}_1$-displacements and B $\boldsymbol{b}_2$-displacements we reach the point

A, B which also lies *in* the surface. Therefore, the unit of edge spanned by $\boldsymbol{c}_1$ includes $A+B$ edge points.

Now relations (1), (2) and (3) show that all points in the half-crystal must satisfy

$$HX+KY = D(-BX+AY) \leqslant 0,$$
$$\text{i.e. } X \geqslant (A/B)\ Y. \tag{6}$$

Therefore, for a given Y, say Y_0, the least value of X is $[Y_0\ A/B]^+$, i.e. of all lattice points in the half L-plane which have this value of Y, the point lying closest to the surface has co-ordinates $[Y_0\ A/B]^+,\ Y_0$ and this is clearly an edge point. Similarly for $Y = Y_0+1$, the edge point lying closest to the surface has co-ordinates $[Y_0\ A/B+A/B]^+,\ Y_0+1$. It is easily seen that the difference between the two X co-ordinates must be either $[A/B]$ or $[A/B]^+$. Therefore, between these two edge points there must be either $[A/B]$ or $[A/B]^+$ $\boldsymbol{b}_1$-displacements followed by a single $\boldsymbol{b}_2$-displacement. Since $A > B$, $[A/B] > 0$ so that in fact all $\boldsymbol{b}_2$-displacements must occur separately. Therefore, the edge consists of groups of $[A/B]$ or $[A/B]^+$ $\boldsymbol{b}_1$-displacements separated by single $\boldsymbol{b}_2$-displacements.

At this stage it is convenient to define a "kink" as a point in the edge which is closer to the surface than either of the adjacent edge points. Then, under the present restrictions on the signs of A and B, a kink must be preceded by a $\boldsymbol{b}_2$-displacement and followed by a $\boldsymbol{b}_1$-displacement. Thus, kinks occur at the beginning of each group of $\mathbf{b}_1$-displacements, i.e. within the unit of edge, at the points $[YA/B]^+,\ Y$ for $Y = 1, 2, \ldots, B$. It is easily seen that an edge is completely specified as soon as the position of every kink is known, so that this result completes the description of the edge. Table 1 lists the positions of kinks in the edge for all signs and relative magnitudes of H and K.

A little consideration of the criterion for choosing successive displacements shows that we have defined as edge points all points lying within $\boldsymbol{b}_2-\boldsymbol{b}_1$ of the surface. Two features of this definition should be noted. Firstly, it is clear that the designation of a point as an edge point is not absolute but depends on the choice of $\boldsymbol{b}_1$, $\boldsymbol{b}_2$. Secondly, it can be shown that the co-ordinates of an edge point must, in the general case, satisfy the inequalities

$$0 \geqslant HX+KY > -(|H|+|K|). \tag{7}$$

A tedious but straightforward manipulation of these inequalities provides an alternative derivation of the results in Table 1.

Table 1. *Positions of kinks in a unit of edge. In all cases,* $X = 0, \pm1, \pm2, \ldots, A$ *or* $Y = 0, \pm1, \pm2, \ldots, B$, *the upper or lower sign being chosen according as* A *(or* B*) is positive or negative.*

Sign of			Positions of kinks:	
			$\lvert H\rvert < \lvert K\rvert$	$\lvert H\rvert > \lvert K\rvert$
H	K and A	B	i.e. $\lvert A\rvert > \lvert B\rvert$	i.e. $\lvert A\rvert < \lvert B\rvert$
+	+	−	$[YA/B],\ Y$	$X,\ [XB/A]$
+	−	−	$[YA/B],\ Y$	$X,\ [XB/A]^+$
−	−	+	$[YA/B]^+,\ Y$	$X,\ [XB/A]^+$
−	+	+	$[YA/B]^+,\ Y$	$X,\ [XB/A]$

Alternative description of edge. The above argument has specified all the kinks in a unit of edge but, for large A and B, the calculation of a whole set of integers such as $[YA/B]^+$ can be laborious and an alternative description is desirable. For the case of $A > B > 0$ the edge can be considered as made up of, say, A' displacements of total vector $\boldsymbol{b}_1'$ and B' displacements of total vector $\boldsymbol{b}_2'$ where

$$\boldsymbol{b}_1' = [A/B]^+\boldsymbol{b}_1+\boldsymbol{b}_2, \tag{8a}$$
$$\boldsymbol{b}_2' = [A/B]\boldsymbol{b}_1+\boldsymbol{b}_2, \tag{8b}$$
$$A' = B\{A/B\}_{\mathrm{fr}}, \tag{9a}$$
and
$$B' = B(1-\{A/B\}_{\mathrm{fr}}). \tag{9b}$$

Equations (8) arise in an obvious way from the previous discussion while equations (9) are found by setting $A'\,\boldsymbol{b}_1'+B'\,\boldsymbol{b}_2' = A\,\boldsymbol{b}_1+B\,\boldsymbol{b}_2 = \boldsymbol{c}_1$ and writing $\{y\}_{\mathrm{fr}} = y-[y]$ = fractional part of y. It is easily shown that $\boldsymbol{h}\cdot\boldsymbol{b}_1' \leqslant 0 \leqslant \boldsymbol{h}\cdot\boldsymbol{b}_2'$ and that, except when $B = 1$, $\boldsymbol{b}_1'\times\boldsymbol{b}_2' = \boldsymbol{b}_1\times\boldsymbol{b}_2$. Thus, unless $B = 1$, $\boldsymbol{b}_1'$ and $\boldsymbol{b}_2'$ are a pair of primitive lattice vectors in the L-plane, satisfying the conditions imposed on $\boldsymbol{b}_1, \boldsymbol{b}_2$. For the case $B > A > 0$, we can obtain analogous expressions by simply interchanging A and B and the subscripts on the vectors throughout equations (8) and (9). Therefore, in all cases except $A = 1$ or $B = 1$, these larger displacements can be grouped together to form still larger units. This process of grouping can be continued until the equivalent of A or B becomes unity. At this stage each of the next pair of $\boldsymbol{b}$-vectors is equal to $\boldsymbol{c}_1$ so that the edge is completely defined. The number of groupings necessary appears to be approximately equal to the number of convergents found when A/B is expressed as a continued fraction.

Figure 2 shows the edge of a typical L-plane with the successive groupings of displacements marked in.

(c) *Stacking of edges to form the* $\boldsymbol{h}$ *surface*

Since all the L-planes in the lattice have edges which are congruent, we can describe the edge of a plane not through the origin simply by the vector to a typical point of the edge from a corresponding point in the edge through the origin. When such vectors are known we can, in principle, stack the edges together to form the $\boldsymbol{h}$ surface.

In discussing the stacking of these edges, it is convenient to ignore their detailed structure and refer only to the "ideal edge" in a particular L-plane, i.e. the straight line parallel to $\boldsymbol{c}_1$ joining

Vol. 2
1961

the outermost points of the edge in that plane. In a particular L-plane, the lattice points can now be considered as defining a set of lattice lines parallel to $\boldsymbol{c}_1$.

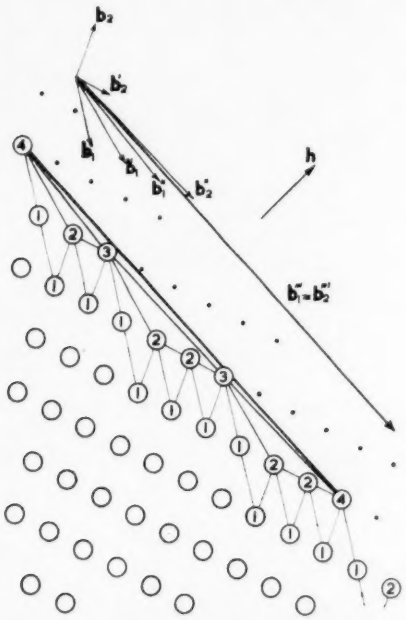

FIG. 2. An L-plane containing an oblique net of lattice points: circles represent lattice points within the half-crystal considered, dots represent those outside it. With $\boldsymbol{b}_1$, $\boldsymbol{b}_2$ as base vectors in the plane, the edge corresponds to $A = 11$, $B = 8$ and the edge-points are those numbered 1, 2, 3 or 4. Table 1 shows that the kinks occur at $[Y\ 11/8]^+$, Y for $Y = 0, 1, \ldots, 8$ and such points are numbered 2, 3 or 4. The first grouping of displacements leads to vectors $\boldsymbol{b}_1'$, $\boldsymbol{b}_2'$ and the edge then consists only of the points 2, 3 and 4, with 3 and 4 representing kinks. The second grouping introduces $\boldsymbol{b}_1''$, $\boldsymbol{b}_2''$ and a third leads to $\boldsymbol{b}_1''' = \boldsymbol{b}_2''' = \boldsymbol{c}_1$.

Now suppose the vector

$$\boldsymbol{c}_2 = F\boldsymbol{b}_1 + G\boldsymbol{b}_2 \tag{10}$$

is a vector joining a lattice point to one on an adjacent lattice line further into the crystal (see Fig. 1). Then $\boldsymbol{c}_1$, $\boldsymbol{c}_2$ define a primitive unit cell in the L-plane, i.e. $\boldsymbol{c}_2 \times \boldsymbol{c}_1 = \boldsymbol{b}_1 \times \boldsymbol{b}_2$ (the reversal of subscripts in this equation arises from the choice of sense for $\boldsymbol{c}_2$). This implies that

$$FB - GA = 1. \tag{11}$$

Since A, B are co-prime integers, equation (11) always has solutions for F, G (see any text book on number theory) but in this paper we are never concerned with evaluating such solutions.

If we now consider a section through the lattice perpendicular to these lattice lines, i.e. perpendicular to $\boldsymbol{c}_1$, the projections of the lattice lines will give a diagram such as is shown in Fig. 3. The obvious analogy between Figs. 1 and 3 shows that the arrangement of lattice lines near the surface can be treated in the same way as the arrangement of

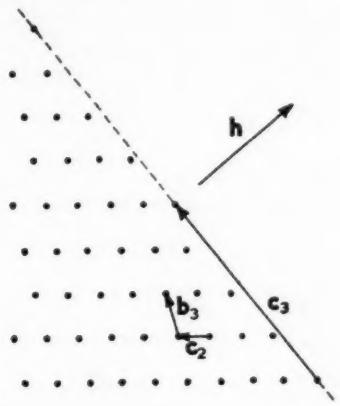

FIG. 3. Section through the lattice perpendicular to $\boldsymbol{c}_1$ with dots representing the projections of lattice lines parallel to $\boldsymbol{c}_1$. The vector $\boldsymbol{h}$ lies in the plane of the diagram but, in general, $\boldsymbol{b}_2$, $\boldsymbol{c}_2$, $\boldsymbol{c}_3$ do not. The surface corresponds to $C = 3$, $D = 5$.

points in the edge of the L-plane. Since we are ignoring the positions of the lattice points along the lattice lines, the fact that $\boldsymbol{c}_2$ and $\boldsymbol{b}_3$ are not in the plane of the diagram of Fig. 3 is of no consequence.

By analogy with the discussion in Section 2(a), the first problem is to define a lattice vector, $\boldsymbol{c}_3$, joining adjacent lattice lines *in* the $\boldsymbol{h}$ surface. Such a vector must be perpendicular to $\boldsymbol{h}$ and together with $\boldsymbol{c}_1$ must define a primitive unit cell in the surface, i.e. with Q as defined by equation (3), we must have

$$\boldsymbol{c}_3 \times \boldsymbol{c}_1/\Omega = Q\boldsymbol{h}, \tag{12}$$

where Ω is the volume of a primitive unit cell in the lattice. If we write

$$\boldsymbol{c}_3 = C\boldsymbol{c}_2 + D'\boldsymbol{b}_3 \tag{13}$$

with C, D' a pair of co-prime integers, we have

$$\begin{aligned} Q\boldsymbol{h} &= H\boldsymbol{b}_1^* + K\boldsymbol{b}_2^* + L\boldsymbol{b}_3^* \\ &= (CF\boldsymbol{b}_1 + CG\boldsymbol{b}_2 + D'\boldsymbol{b}_3) \times (A\boldsymbol{b}_1 + B\boldsymbol{b}_2)/\Omega \\ &= -D'B\boldsymbol{b}_1^* + D'A\boldsymbol{b}_2^* + C(FB - GA)\boldsymbol{b}_3^*. \end{aligned} \tag{14}$$

By comparing coefficients in the first and third lines of equation (14) and using equations (5) and (11), we find

$$C = L, \quad D' = D. \tag{15}$$

Then, arguments similar to those used in Section 2(b) show that one lattice point in the ideal edge of the Z'th layer has position vector $W_Z\boldsymbol{c}_2 + Z\boldsymbol{b}_3$ where

$$W_Z = [ZC/D]^+, \tag{16}$$

a result which is independent of the sign of C. This vector corresponds to translating the ideal edge into the Z'th layer plane by Z $\boldsymbol{b}_3$-displacements and then moving inwards through W_Z lattice lines in that layer.

We may note in passing that $\boldsymbol{c}_2$, $\boldsymbol{c}_1$, $\boldsymbol{c}_3$ define in the lattice a unit cell containing D lattice points.

(d) *Consideration of various values of* δ

Up to this stage we have considered only surfaces with $\delta = 0$. Clearly the treatment is identical if δ takes any other integral value. Therefore, let us consider the change in the surface as δ varies from 0 to 1, i.e. consider what happens as the surface moves away from the origin. Since the $\boldsymbol{h}$ surface can intersect lattice points only when δ is a multiple of $1/Q$, as δ increases from 0 to $1/Q$ the $\boldsymbol{h}$ surface sweeps through a volume free of lattice points and the surface structure is identical with that for $\delta = 0$ except that all lattice points have become further away from the surface itself. When $\delta = 1/Q$, the surface intersects new lattice points but the symmetry of the lattice ensures that the set intersected is congruent with the set intersected by the surface through 0, i.e. we have a new set of lattice points comprising the surface but its structure is identical with that described before. We can proceed in this way from $\delta = 1/Q$ to $\delta = 2/Q$ and so on up to $\delta = 1$ and clearly only one type of surface can appear.

A variation of δ can thus produce nothing new when a lattice array is being considered. However, for crystal structures in which the primitive unit cell of the lattice contains more than one atom, a variation of δ can produce different effects (see latter part of Section 3).

3. ARRANGEMENT OF ATOMS NEAR THE $\boldsymbol{h}$ SURFACE

The discussion of lattice points in Section 2 is easily extended to crystal structures. We suppose that, relative to a given lattice point, the atoms in a motif have vectors $\boldsymbol{d}_r$ ($r = 0, 1, \ldots, s-1$) and consider first the r'th subset of atoms, i.e. the set having a given $\boldsymbol{d}_r$. Then such atoms have position vectors

$$\boldsymbol{x} = X\boldsymbol{b}_1 + Y\boldsymbol{b}_2 + Z\boldsymbol{b}_3 + \boldsymbol{d}_r. \tag{17}$$

We now construct a series of L-planes through these atoms and consider one plane, defined by a given Z. The atoms in this plane will define a net in the plane and the edge of the net will be congruent to the edge described in Sections 2(a) and (b). Therefore, to define the edge, we need only specify the position of the row of atoms which is parallel to $\boldsymbol{c}_1$ and is as close as possible to the $\boldsymbol{h}$ surface.

For this purpose, it is convenient to write equation (17) as

$$\boldsymbol{x} = W_Z\boldsymbol{c}_2 + Z\boldsymbol{b}_3 + \boldsymbol{d}_r, \tag{18}$$

where W_Z is an index for the row of atoms parallel to $\boldsymbol{c}_1$ and in the Z'th plane. Thence by use of relations (1), (10), (3), (5), (11), and (15) we find

$$-W_ZD + ZC \leqslant Q(\delta - \boldsymbol{h} \cdot \boldsymbol{d}_r). \tag{19}$$

Manipulation of the inequality (19) shows that for the row of atoms closest to the $\boldsymbol{h}$ surface

$$W_Z = [(\boldsymbol{h} \cdot \boldsymbol{d}_r - \delta)Q/D + ZC/D]^+, \tag{20}$$

a result consistent with equation (16) when $\boldsymbol{h} \cdot \boldsymbol{d}_r = \delta = 0$.

If we let Z run through the sequence 0, 1, ..., D we can use equation (20) to define the positions of a set of ideal atomic edges in the L-planes through the particular r'th subset of atoms chosen.* By

* The set of displacements between the integers in the sequence defined by equation (20) must be congruent with the set of displacements between the integers in the sequence $[ZC/D]^+$, though it is not simple to specify the change of origin necessary to make the two sets coincide.

Vol. 2
196

using the structure of a unit of edge as specified for the lattice we can then describe the positions of the atoms of the given subset which lie near the surface.

The whole surface can be described by considering in turn the s subsets of atoms. This process is simplified if we choose the $\boldsymbol{d}_r$ to lie within the unit cell defined by $\boldsymbol{b}_1$, $\boldsymbol{b}_2$, $\boldsymbol{b}_3$, and then order the subsets so that the $\boldsymbol{d}_r \cdot \boldsymbol{b}_3^*$ form a monotonically increasing sequence for $r = 0, 1, \ldots, s-1$. Clearly, all such products will lie between 0 and $\boldsymbol{b}_3 \cdot \boldsymbol{b}_3^* = 1$. If we now consider the array of all L-planes that contain atoms, we find a periodic sequence of planes. Where all $\boldsymbol{d}_r \cdot \boldsymbol{b}_3^*$ are distinct, the repeat unit in this sequence consists of s planes, the r'th plane passing through atoms of the r'th subset, i.e. we can consider an ordered stacking of L-planes to form the whole crystal. If two or more of the $\boldsymbol{d}_r \cdot \boldsymbol{b}_3^*$ are equal, this can be treated as a degeneracy of the previous case and the L-planes can still be ordered although some planes will now contain atoms from more than one subset.

The complete surface for a crystal where $s > 1$ may depend on the value of δ chosen. A very simple example is the (111) surface in a crystal of NaCl type where the array of atoms closest to the surface may consist of either sodium or of chlorine depending on the precise position of the surface.

In order to consider all possible types of surface for a given $\boldsymbol{h}$ we need to consider all δ in the range $0 \leqslant \delta < 1/Q$. If the surface for $\delta = 0$ is known we can develop the other types from this by allowing δ to increase towards $1/Q$. Clearly the type of surface can change only at those values of δ, called "critical values", for which new atoms are added to the half-crystal that we are considering. Equation (20) shows that the critical values of δ must be those for which

$$(\boldsymbol{h} \cdot \boldsymbol{d}_r - \delta)Q/D + ZC/D = M_1, \qquad (21)$$

where M_1 is an integer. On rearrangement equation (21) gives

$$\begin{aligned} \delta &= \boldsymbol{h} \cdot \boldsymbol{d}_r + (ZC - M_1 D)/Q \\ &= \boldsymbol{h} \cdot \boldsymbol{d}_r + M_2/Q, \end{aligned} \qquad (22)$$

where M_2 is an integer which can assume any value by appropriate choice of M_1 and Z (since C and D are co-prime integers). Thus, for any given $\boldsymbol{d}_r$, there is one and only one critical value of δ in the range $0 \leqslant \delta < 1/Q$ and we can calculate all possible critical values by using equation (22) for the s possible values of $\boldsymbol{d}_r$.

4. PRACTICAL PROCEDURE FOR MODELLING AN *h* SURFACE

The results of Sections 2 and 3 showed how a surface could be described. This is of particular use when a model of such a surface is to be constructed. In this section, the steps necessary for constructing such a model will be summarized. They will be seen to parallel the method used in Part I to construct models of cubic crystals (in fact, all notation is consistent between the papers). In this paper no special symmetry is attributed to the lattice at any stage so that the results can be applied to any crystal structure. However, no account is taken of the method by which the "atoms" are to be fixed in position since such positioning will obviously vary with the structure considered.

The general procedure can be summarized as follows:

(i) Choose a convenient set of base-vectors $\boldsymbol{a}_i$ and suppose that $\boldsymbol{h}$ and δ are given.

(ii) Choose any convenient set of L-planes and a right-handed set of vectors $\boldsymbol{b}_i$. Any set of $\boldsymbol{b}_i$ defining a primitive cell in the lattice can be chosen but the following are desirable criteria for $\boldsymbol{b}_1$, $\boldsymbol{b}_2$: (a) the L-planes defined by $\boldsymbol{b}_1$, $\boldsymbol{b}_2$ should be reasonably simple and of some physical significance, e.g. densely packed planes, (b) $\boldsymbol{b}_1$, $\boldsymbol{b}_2$ should have some physical significance, e.g. nearest-neighbour vectors in the lattice or in the L-plane, (c) $\boldsymbol{h} \cdot \boldsymbol{b}_1$ and $\boldsymbol{h} \cdot \boldsymbol{b}_2$ should be small, and (d) if possible, $\boldsymbol{h} \cdot \boldsymbol{b}_1 \leqslant 0 \leqslant \boldsymbol{h} \cdot \boldsymbol{b}_2$. Then $\boldsymbol{b}_3$ should be chosen so that $\boldsymbol{h} \cdot \boldsymbol{b}_3$ is as small as possible in magnitude but preferably positive.

(iii) Choose the $\boldsymbol{d}_r$ to lie within the unit cell defined by the $\boldsymbol{b}_i$ and arrange these in order so that

$$0 \leqslant \boldsymbol{d}_0 \cdot \boldsymbol{b}_3^* \leqslant \boldsymbol{d}_1 \cdot \boldsymbol{b}_3^* \leqslant \ldots \leqslant \boldsymbol{d}_{s-1} \cdot \boldsymbol{b}_3^* < 1.$$

(iv) Calculate H, K, L, and Q from equation (3).

(v) Calculate A, B, C, D from equations (4) and (15).

(vi) Construct a half L-plane having one unit of edge with kinks arranged as in Table 1.

(vii) For the given δ, calculate the array of integers

$$W_{Z,r} = [(\boldsymbol{h}\cdot\boldsymbol{d}_r-\delta)Q/D+ZC/D]^+ \quad (20')$$

for $Z = 0, 1, \ldots, D-1$ and $r = 0, 1, \ldots, s-1$.

(viii) Place a half L-plane of $\boldsymbol{d}_0$-"atoms", constructed as in (vi), with an extreme "atom" displaced $\boldsymbol{d}_0$ from the origin; then remove the $W_{0,0}$ outermost "atoms" (a negative W implies that rows should be added to the edge).

(ix) Repeat (viii) for $\boldsymbol{d}_1$-"atoms" removing the $W_{0,1}$ outermost "atoms" and continue this process for each of the s types of "atom".

(x) Repeat (viii) and (ix) with L-planes displaced $\boldsymbol{d}_r+\boldsymbol{b}_3$ from 0, moving the edges back by $W_{1,r}$ "atoms".

(xi) Repeat (x) for displacements of $\boldsymbol{d}_r+Z\boldsymbol{b}_3$ and removals of $W_{Z,r}$ "atoms" for $Z = 2, \ldots, D-1$.

(xii) Set in place a plane of $\boldsymbol{d}_0$-"atoms" displaced $\boldsymbol{d}_0+D\boldsymbol{b}_3$ from the origin and remove the $W_{D,0} = W_{0,0}+C$ outermost "atoms". A complete unit of surface will then have been constructed.

It may be noted that the first three steps are common to a whole series of $\boldsymbol{h}$ surfaces, the next three can only be carried out when a definite $\boldsymbol{h}$ has been chosen and the last six depend on the value of δ.

5. APPLICATION TO CUBIC STRUCTURES

The above theory can be readily applied to the cubic structures discussed in Part I. The $\boldsymbol{a}_i$ are parallel to the cubic axes and we can restrict $\boldsymbol{h}$ to satisfy $h \geqslant k \geqslant l \geqslant 0$.

For the face-centred cubic structure described in terms of (100) layers, all the desirable criteria for $\boldsymbol{b}_i$ can be satisfied by taking $\boldsymbol{b}_1 = \frac{1}{2}[0\bar{1}\bar{1}]$; $\boldsymbol{b}_2 = \frac{1}{2}[01\bar{1}]$; $\boldsymbol{b}_3 = \frac{1}{2}[1\bar{1}0]$.

Then

$$\begin{aligned} \boldsymbol{h}\cdot\boldsymbol{b}_1 &= -DB/Q = -\tfrac{1}{2}(k+l), \\ \boldsymbol{h}\cdot\boldsymbol{b}_2 &= DA/Q = \tfrac{1}{2}(k-l), \end{aligned}$$

and

$$\boldsymbol{h}\cdot\boldsymbol{b}_3 = C/Q = \tfrac{1}{2}(h-k).$$

Therefore,

$$\left.\begin{aligned} A:B &= (k-l):(k+l) \\ \text{and} \\ C:DA &= (h-k):(k-l), \end{aligned}\right\} \quad (23)$$

as found in Part I.

6. MODELS OF SURFACES IN A HEXAGONAL CLOSE-PACKED STRUCTURE

In this section, the procedure outlined in Section 4 will be applied to construct models of surfaces in a hexagonal close-packed structure. Models of this structure are simple to construct since, if balls are used to represent the atoms, the positions of the balls are determined by the conditions of close-packing.

(i) We will choose $\boldsymbol{a}_1$, $\boldsymbol{a}_2$ as two nearest-neighbour vectors in a basal plane and inclined at 120° to each other and $\boldsymbol{a}_3$ as a vector perpendicular to $\boldsymbol{a}_1$ and $\boldsymbol{a}_2$ and of magnitude $(8/3)^{1/2}\times$ (nearest-neighbour distance). This gives a monoclinic primitive unit cell for the lattice and h, k, l are the first, second, and fourth indices of the conventional four-index notation. A complete set of typical surfaces can be obtained within the restrictions $h \geqslant k \geqslant 0$ and $l \geqslant 0$.

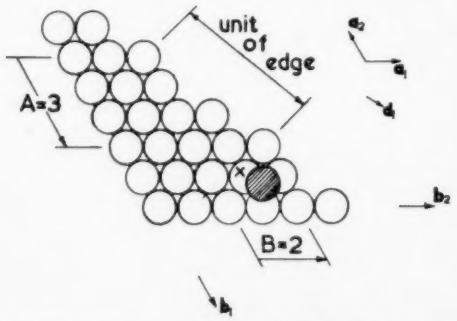

FIG. 4. Arrangement of balls in an L-plane of $\boldsymbol{d}_0$-"atoms" in the hexagonal close-packed structure. The edge shown corresponds to $A = 3$, $B = 2$. The shaded circle represents the position of a ball (corresponding to a $\boldsymbol{d}_1$-atom) displaced $\boldsymbol{d}_1$ from the ball marked X. The vector $\boldsymbol{d}_1$ has a component perpendicular to the paper whereas all other vectors shown lie in the plane.

(ii) The convenient choice for the L-planes are basal planes. All the desirable criteria for the $\boldsymbol{b}_i$ are satisfied by taking $\boldsymbol{b}_1 = -\boldsymbol{a}_2$, $\boldsymbol{b}_2 = \boldsymbol{a}_1$, and $\boldsymbol{b}_3 = \boldsymbol{a}_3$. Clearly, L-planes can be modelled by balls packed closely in a hexagonal array (Fig. 4).

(iii) The unit cell contains two atoms which can be conveniently located at $\boldsymbol{d}_0 = [000]$ and $\boldsymbol{d}_1 = \frac{1}{6}[2\bar{2}3]$ (relative to the $\boldsymbol{a}_i$). Then $\boldsymbol{d}_0\cdot\boldsymbol{b}_3^* = 0$ and $\boldsymbol{d}_1\cdot\boldsymbol{b}_3^* = \frac{1}{2}$. Thus the $\boldsymbol{d}_1$-atoms form L-planes half-way between the L-planes of the $\boldsymbol{d}_0$-atoms,

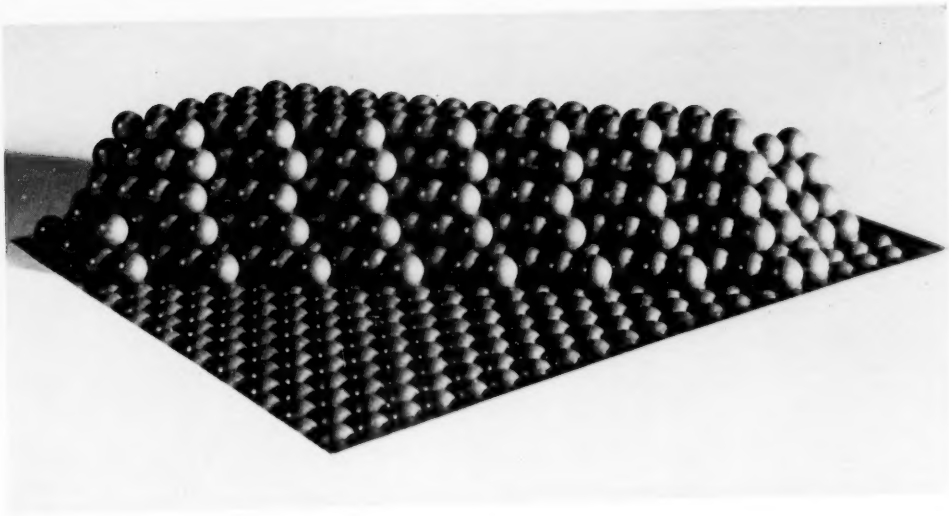

(a)

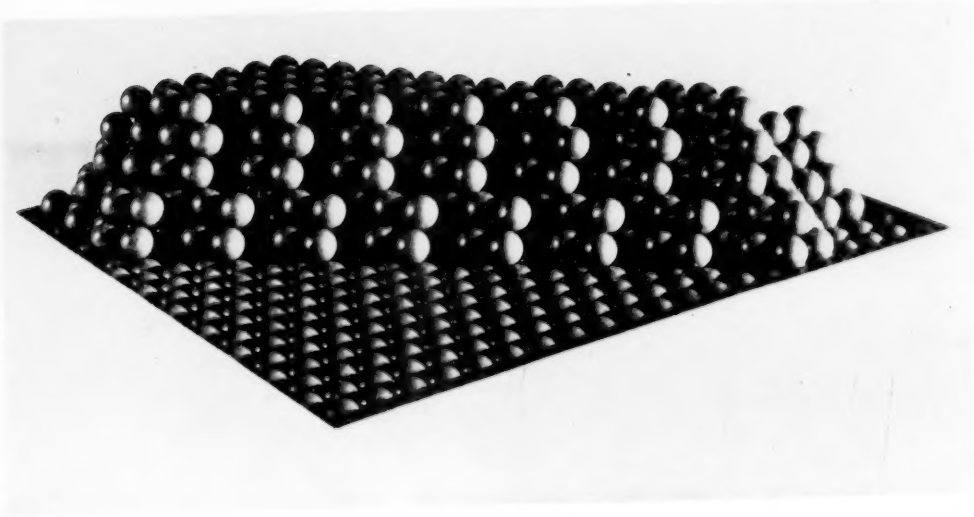

(b)

FIG. 6. Models of a (427) surface in the hexagonal close-packed structure: (a) for $0 \leq \delta < \frac{1}{6}$, (b) for $\frac{1}{6} \leq \delta < 1$.

[*facing p.* 236

BLANK
PAGE

Vol. 2
196

i.e. alternate layers consist of $\boldsymbol{d}_0$ and $\boldsymbol{d}_1$-atoms. It can be seen that if the model is oriented as in Fig. 4, $\boldsymbol{d}_1$-atoms are placed on a ∇ of $\boldsymbol{d}_0$-atoms. Further, since $\boldsymbol{a}_3$ is perpendicular to the L-planes, the next layer of $\boldsymbol{d}_0$-atoms lies directly above the first such layer, i.e. on a Δ of $\boldsymbol{d}_1$-atoms.

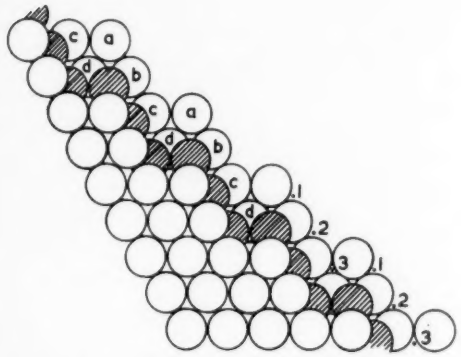

FIG. 5. The first two $\boldsymbol{d}_0$-layers (open circles) and the first $\boldsymbol{d}_1$-layer (shaded circles) of a model of a (427) surface in the hexagonal close-packed structure for $0 \leqslant \delta < \frac{1}{6}$. The points marked 1, 2, 3 (and the corresponding points in the upper part of the figure) are the points from which $\boldsymbol{d}_1$-"atoms" have been removed to give the correct position of the edge. The circles lettered a, b, c, d (and the corresponding circles in the lower part of the figure) show where $\boldsymbol{d}_0$-"atoms" have been removed from the upper $\boldsymbol{d}_0$-layer to give $W_{1,0} = 4$.

(iv) Since the $\boldsymbol{a}_i$ define a primitive cell in the lattice, $Q = 1$. Therefore $H = -k$, $K = h$, $L = l$.

(v) By using the results in (iv) we find the general relation $(hkl) = (DA\,DB\,C)$.

At this stage, it may be noted that the model we are building is that for the "ideal" hexagonal close-packed structure with an axial ratio of $(8/3)^{1/2}$. Structures with smaller axial ratios can be modelled in exactly the same way as is outlined here provided the balls in the first layer are suitably separated from each other (cf. the procedure given in Part I for constructing models of a body-centred cubic structure). For axial ratios greater than $(8/3)^{1/2}$, no such simple procedure is available since there are now no true nearest-neighbour links between the atoms in adjacent L-planes.

(a) *Model of* (427) *surface*

For the (427) surface [corresponding to $(42\bar{6}7)$ in four-index notation] we have $A = 2$, $B = 1$, $C = 7$, $D = 2$; $\boldsymbol{h} \cdot \boldsymbol{d}_0 = 0$, $\boldsymbol{h} \cdot \boldsymbol{d}_1 = 4\frac{1}{6}$. The critical values of δ are 0 and $\frac{1}{6}$.

For $0 \leqslant \delta < \frac{1}{6}$, $W_{0,0} = 0$, $W_{0,1} = 3$, $W_{1,0} = 4$, $W_{1,1} = 6$, and $W_{2,0} = 7$. Fig. 5 shows the initial L-plane of $\boldsymbol{d}_0$-"atoms" together with the first plane of $\boldsymbol{d}_1$-"atoms" and the succeeding plane of $\boldsymbol{d}_0$-"atoms", while Fig. 6(a) shows a completed model of this surface.

For $\frac{1}{6} \leqslant \delta < 1$, the $W_{Z,r}$ are unchanged except that $W_{0,1} = 2$. Thus the only change in the surface as δ increases through $\frac{1}{6}$ is that the edge of the first L-plane of $\boldsymbol{d}_1$-"atoms" comes further forward so that there are $\boldsymbol{d}_1$-"atoms" at the positions marked 3 in Fig. 5. Fig. 6(b) shows a model of the surface for values of δ in this range.

Acknowledgement—I am indebted to Dr. J. K. MACKENZIE for much helpful discussion and many useful suggestions.

REFERENCE

1. MOORE A. J. W. and NICHOLAS J. F., *J. Phys. Chem. Solids* **20,** 222 (1961), (preceding paper).

J. Phys. Chem. Solids Pergamon Press 1961. Vol. 20, Nos. 3/4, pp. 238–240. Printed in Great Britain.

THE SUSCEPTIBILITY OF NO IN β-QUINOL CLATHRATES

H. MEYER*

The Clarendon Laboratory, Oxford University

(*Received* 20 *March* 1961)

Abstract—Susceptibility measurements on polycrystalline samples of NO in β-quinol clathrates between 1°K and room temperature are described. The results show in particular that below 200°K the susceptibility becomes systematically larger than that expected for a free gas and that within an experimental error of about 5 per cent the susceptibility tends to a constant value of $13{\cdot}9 \times 10^{-5}$ e.m.u./g NO below about 15°K. The presence of a $1/T$ term at low temperatures suggested by VAN VLECK could not be detected. These results are compared to those obtained by COOKE and DUFFUS, which show an appreciable temperature dependence of the susceptibility even below 30°K. The discrepancy is attributed to paramagnetic impurities in the earlier sample.

THE MAGNETIC properties of NO in its gaseous form have been predicted theoretically by VAN VLECK[1] and there have been several measurements of the magnetic susceptibility of this gas between room temperature and its condensation point.[2] Measurements on NO in its condensed state cannot readily be compared to VAN VLECK's theory, because of the magnetic interaction between the molecules which are now much closer together. On the other hand, it is possible to keep the NO molecules separated by trapping them in β-quinol clathrates.[3] In this compound, the gas is kept in regularly spaced cages which contain no more than one trapped molecule, and since these molecules are separated by an average distance of about 8 Å, they interact only very weakly. It was shown by EVANS and RICHARDS[4] that at room temperature the NO in this compound has very nearly the same susceptibility as the free gas and the same was found to be true for oxygen in the clathrate. At low temperatures, however, the susceptibility results as obtained by COOKE and DUFFUS[5] down to 10°K no longer agreed with those predicted by VAN VLECK for the free gas. In particular, the susceptibility was still changing rapidly below 30°K, while from the theory one expects it to reach a constant value below that temperature region. Although a certain alteration of the susceptibility was to be expected because of the interaction between the orbital moment of the NO molecule and the electric field of the cage, the qualitative discrepancy between theory and experiment was rather surprising. Since there was a possibility that the specimen of COOKE and DUFFUS contained some paramagnetic impurities which might be responsible for the steady increase of the susceptibility at the lowest temperatures, it was decided to make a new series of measurements with freshly prepared NO clathrates between 1°K and room temperature. This paper gives a short account of these measurements, the interpretation of which will be given in the following paper by VAN VLECK[6].

EXPERIMENTAL

The NO clathrates were prepared the same way as described by EVANS and RICHARDS[4], except that a small pressure cylinder filled with NO provided a controlled pressure of 70 atm during a 5-day-long crystallization of the clathrates in the NO atmosphere.

There are several difficulties associated with the susceptibility measurements on this compound. Contrary to some other clathrates such as those of

* Now at the Department of Physics, Duke University, Durham, North Carolina.

N_2 and O_2, it is chemically not very stable. The NO which diffuses out of the cages is transformed on contact with air into NO_2 which attacks the lattice. The crystals were therefore carefully dried and sealed in a thin soda-glass tube under helium atmosphere, and kept most of the time at 80°K. Even with these precautions, the specimen slowly decomposed over a period of two weeks. Moreover, at temperatures above 100°K, the paramagnetic susceptibility of NO becomes small enough to be of the same order of magnitude as the diamagnetic susceptibility of the clathrate compound and of the thin glass tube. Consequently the accuracy of our results should be only about ± 5 per cent.

For the measurements between 20°K and room temperature, the GOUY method was used. Eight grammes of NO clathrates crystals, randomly oriented, were sealed in a tube of soda-glass 16 cm long filled with helium gas and the specimen was then suspended by a cotton thread on a semi-automatic Stanton balance. The magnetic field used for the measurements was about 5000 G and was supplied by a small Tickford electromagnet. The cryostat surrounding the specimen consisted of a large copper block with an axial hole in which the specimen was suspended. The helium atmosphere above the specimen was continuously flushed by a small stream of helium, in order to prevent diffusion of air to the specimen and subsequent condensation on it at temperatures below 80°K. Experiment showed that the slow flushing had no effect on the temperature of the sample.

The apparatus was first cooled to 20·6°K with liquid hydrogen, and once susceptibility measurements had been taken at this temperature, the hydrogen was boiled away and the cryostat warmed up in a time long enough to allow a sufficient amount of data to be taken. At temperatures above 70°K, a heater was used between the susceptibility measurements.

The temperature of the sample was measured using a platinum thermometer made up with Johnson and Matthey "thermopure" wire. This thermometer was calibrated by measuring the susceptibility between 20·6°K and room temperature of powdered copper ammonium sulphate, whose paramagnetic susceptibility obeys Curie's law over the whole temperature range. Between 75°K and 90°K, the platinum resistance was further calibrated using an oxygen vapour pressure thermometer and the pressure–temperature relation obtained by HOGE[7]. Susceptibility measurements with identical empty glass tubes were also made to account for the effect of the glass on the total susceptibility. At temperatures below 40°K this correction became quite appreciable.

The nitric oxide content of the sample could not be analyzed after the measurements, because as the glass tube was unsealed, the clathrate decomposed very quickly in the air. After subtracting the diamagnetic susceptibility of the quinol, $1{\cdot}99 \times 10^{-4}$ e.m.u./mole, and the effect of the glass tube, the susceptibility of NO, in arbitrary units, was fitted at 293°K to the value for the free gas, $4{\cdot}77 \times 10^{-5}$ e.m.u./gm NO given by VAN VLECK. From this fitting it was found that 36·6 per cent of the cages in the quinol were filled with NO. The experimental curve is shown to follow closely the calculated one for the free gas down to about 150°K, below which a systematic departure occurs.

The measurements below 20°K were made using an A. C. Hartshorn mutual inductance bridge as described by BENZIE and COOKE[8] and by WOLF[9]. Measurements were made between 9°K and 20°K and between 1°K and 4°K. The sample consisted of 2·8 g of clathrates, enclosed in a small Perspex (plexiglas) container. On this sample, the NO content could be analyzed chemically and it was found that 41·5 per cent of the cages in the quinol were filled. Our measurements showed that within experimental error, the susceptibility of NO did not change by more than 7×10^{-6} e.m.u./g below 20°K, tending towards a value of $13{\cdot}9 \times 10^{-5}$ e.m.u./g NO at 1°K. In particular, no contribution to the susceptibility varying as $1/T$ could be detected below 4°K within the experimental error of about 5 per cent. The consequences of the absence of this contribution will be discussed in the next paper by VAN VLECK[6]. The experimental points of our measurements are plotted in Fig. 1 together with those of COOKE and DUFFUS. The disagreement is particularly marked at temperatures below 100°K, where our new values are much lower. This seems to confirm the possibility of paramagnetic impurities in the early sample.

Smoothed values of our results are presented in Table 1. It is also instructive to compare the experimental results to the values expected for the free gas from VAN VLECK's theory. The calculated

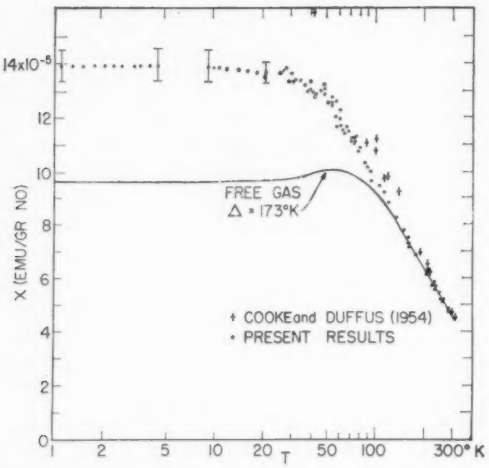

FIG. 1. The paramagnetic susceptibility of NO in randomly oriented clathrate crystals ● present results; + results by COOKE and DUFFUS. The susceptibility measured by these authors at 10°K is 23×10^{-5} e.m.u./g NO.

Table 1. *The magnetic susceptibility* χ *of* NO *in* β*-quinol clathrates, in* e.m.u./g NO.

T (°K)	χ	T	χ
1	$13{\cdot}9 \times 10^{-5}$	140	$8{\cdot}3 \times 10^{-5}$
10	$13{\cdot}9 \times 10^{-5}$	160	$7{\cdot}6 \times 10^{-5}$
20	$13{\cdot}6 \times 10^{-5}$	180	$7{\cdot}0 \times 10^{-5}$
30	$13{\cdot}4 \times 10^{-5}$	200	$6{\cdot}5 \times 10^{-5}$
40	$13{\cdot}1 \times 10^{-5}$	220	$6{\cdot}0 \times 10^{-5}$
50	$12{\cdot}6 \times 10^{-5}$	240	$5{\cdot}6 \times 10^{-5}$
60	$12{\cdot}0 \times 10^{-5}$	260	$5{\cdot}2 \times 10^{-5}$
80	$10{\cdot}8 \times 10^{-5}$	280	$4{\cdot}9 \times 10^{-5}$
100	$9{\cdot}6 \times 10^{-5}$	300	$4{\cdot}65 \times 10^{-5}$
120	$8{\cdot}9 \times 10^{-5}$		

susceptibility is

$$\chi = \frac{4}{3}\frac{N\beta^2}{kT} \times \frac{(1-e^{-x}+xe^{-x})}{(x+xe^{-x})} \frac{\text{e.m.u.}}{\text{mole}}$$

where β is the Bohr magneton, N is Avogadro's number and $x = A/kT$ with $A/k = 173$°K corresponding to the splitting between the $^2\Pi_{3/2}$ and $^2\Pi_{1/2}$ doublets. As can be seen in Fig. 1, the temperature dependence is qualitatively the same for the free gas and for NO in the clathrate compound, and practically disappears at temperatures below 20°K.

More accurate susceptibility measurements are planned in the temperature range between 0·4 and 4°K, using, if possible, single crystals, with the hope of detecting the $1/T$ contribution to the susceptibility which VAN VLECK predicts should occur unless the spin–lattice relaxation time is very long or the crystalline potential very peculiar. Spin resonance experiments, as discussed by VAN VLECK, are also planned for the near future.

Acknowledgements—This work was carried out during the tenure of a Nuffield fellowship for which acknowledgement is made. The author is very grateful to Dr. A. H. COOKE for his help during the experiments. He is also indebted to Dr. R. E. RICHARDS for his advice on the preparation of the clathrates.

REFERENCES

1. VAN VLECK J. H., *The Theory of Electric and Magnetic Susceptibilities*, Oxford University Press (1932).
2. BURRIS A. and HAUSE C. D., *J. Chem. Phys.* **11,** 442 (1943). For a list of papers before 1932, cf. VAN VLECK's book, Ref. (1), Chapter 10.
3. POWELL H. M., *J. Chem. Soc.* 61 (1948).
4. EVANS D. F. and RICHARDS R. E., *J. Chem. Soc.* 3295 (1952).
5. COOKE A. H. and DUFFUS H. J., *Proc. Phys. Soc. Lond.* **A57,** 525 (1954); DUFFUS H. J., Thesis, Oxford 1953.
6. VAN VLECK J. H., *J. Phys. Chem. Solids* **20,** 241 (1960), (following paper).
7. HOGE H. J., *J. Res. Nat. Bureau Stand.* **44,** 321 (1950).
8. BENZIE R. J. and COOKE A. H., *Proc. Phys. Soc. Lond.* **A63,** 213 (1950).
9. WOLF W. P., Thesis, Oxford, 1955.

J. Phys. Chem. Solids Pergamon Press 1961. Vol. 20, Nos. 3/4, pp. 241–254. Printed in Great Britain.

THEORY OF THE MAGNETIC SUSCEPTIBILITY OF THE NITRIC OXIDE CLATHRATE

J. H. VAN VLECK

Lyman Laboratory of Physics, Harvard University, Cambridge, Massachusetts

(*Received* 20 *March* 1961)

Abstract—The magnetic properties of the nitric oxide clathrate are studied with the hindered rotation model such as was successfully employed in the much simpler problem of the O_2 clathrate. MEYER's experimental measurements in the preceding paper show that the susceptibility at low temperatures is about 40 per cent higher than for the free molecule and is practically independent of temperature below about 20°K. This behavior is hard to explain since NO is an odd molecule, and hence in most crystalline potentials its susceptibility has a term in $1/T$ arising from the Kramers doublet. The best results are achieved by using a crystalline potential of trigonal symmetry, in accord with the crystallographic symmetry of the clathrates. By proper, though arbitrary, combination of matrix elements of the crystalline potential of the form $\Delta m = \pm 3$ and $\Delta m = 0$, we obtain the requisite 40 per cent increase in the susceptibility, but we have not been entirely successful in suppressing the $1/T$ term, which we estimate to be about 6 per cent of the main term at 1°K. Conceivably the spin-lattice relaxation time is so long that this term would not be detected in MEYER's experiments made at 175 c/s. Further experimentation is highly desirable to guide and clarify the theory.

Vol. 20
1961

INTRODUCTION

A SO-CALLED clathrate compound, β-quinol, has large holes in which gaseous molecules can be trapped. The magnetic susceptibilities of the two common paramagnetic gases, viz. O_2 and NO, have hence been measured in clathrate compounds down to low temperatures at Oxford. Such experiments have the advantage that the magnetic behavior of O_2 or NO molecules can be studied in the nearly free state even at fairly low temperatures, whereas in pure liquid or solid O_2 or NO, the intermolecular magnetic coupling is so large that the theory for free molecules is not even approximated. At room temperatures, the susceptibilities of both the O_2 and NO clathrates are in accord with the corresponding theory for the free molecule. However, in the O_2 clathrate there are pronounced deviations at helium temperatures, while in the NO compound they begin to appear even at liquid air temperatures, becoming more pronounced as the temperature is lowered. These deviations are caused by the hampering of the free rotation of the O_2 or NO molecule by the forces exerted by the non-magnetic atoms of the β-quinol. The magnetic atoms themselves are so far separated that any coupling between their magnetic moments is of minor importance. The appropriate theory for the magnetic behavior of the O_2 clathrate at low temperatures was given in an article by MEYER *et al.*[1]. The theory is confirmed, not merely by the measurements of susceptibilities, but especially by subsequent experiments on magnetic resonance made at the Lincoln Laboratory by FONER *et al.*[2]. It is the purpose of the present paper to treat the case of NO.

The theory for O_2 is characterized by simplicity, and, alas, that for NO by complexity. The calculations for the latter are complicated because there is orbital as well as spin magnetic moment and because, furthermore, the spin multiplet is so large that the coupling of the spin to the molecular axis cannot be neglected in comparison to kT, even at room temperatures. The salient experimental fact is that the susceptibility of the NO clathrate is independent of T at low temperatures, having a value approximately 40 per cent higher than for the free molecule. This fact poses a challenge to the theorist, for NO is an odd

molecule and so has Kramers doublets. With most models of a crystalline potential, the doublet inhabited at low temperatures carries an appreciable magnetic moment, and so leads to a $1/T$ term in the susceptibility, contrary to experiment. As we see at the very end, we have not been quite successful in suppressing the term in $1/T$, and it is just possible that MEYER's failure[3] to detect it is to be attributed to absence of thermal equilibrium at his frequency of 175 c/s.

We may mention parenthetically that in principle the general type of theory which we develop should be capable of adaptation to the measurements by SOLBAKKEN and REYERSON[4] on the susceptibility of nitric oxide adsorbed on silica gel. Presumably the adsorbed NO molecules are in some sort of crystalline field, which constrains their rotation, as in the clathrate, but of different symmetry and magnitude. It is, however, difficult to obtain appropriate magnetic data at low temperatures because of dimerization.

We assume the reader to be familiar with the basic theory of the magnetism of the free NO molecule.[5] The salient fact is that the ground state is $^2\Pi_{\frac{1}{2}}$ and $^2\Pi_{\frac{3}{2}}$, with the $\frac{1}{2}$ component 124 cm^{-1} below the $\frac{3}{2}$. The magnetic moment arises from the component of spin and orbital angular momentum parallel to the figure axis and also from the perpendicular spin component.

NOTATION AND HAMILTONIAN FUNCTION

The notation which we commonly employ is as follows:

θ, ϕ, polar coordinates of the molecular axis relative to an axis fixed in space;

r_i, θ_i, ϕ_i or x_i, y_i, z_i: polar or Cartesian coordinates of a particle (electronic or nuclear) relative to fixed axes. The origin is at the center of gravity. This may not quite coincide with the center of rotation, since the NO molecule is not symmetrical. However, the masses of the N and O nuclei are sufficiently similar that the wobbles about the center of gravity are unimportant for our problem;

r_i, θ_i', ϕ_i' or x_i', y_i', z_i' are polar or Cartesian coordinates such that the $\theta' = 0$ or z'-axis coincides with that of the molecule. The nodal line $\phi_i' = 0$ or $y_i' = z_i' = 0$ is to be taken perpendicular to the axis $\theta = 0$;

$Y_{lm}(\theta,\phi_i) = P_l^m(\theta_i)\ e^{im\phi_i}$ denotes a tesseral harmonic normalized to unity;

e_i = charge of particle i;

S = spin angular momentum, measured in multiplets of $h/2\pi$. A similar unit of measures is used for the molecular angular momenta p_θ, p_ϕ conjugate to θ, ϕ. The value of S for NO is $\frac{1}{2}$;

Λ = orbital angular momentum about the molecular axis; eigenvalues for our problem are ± 1;

Σ = spin angular momentum about this axis; eigenvalues $\pm\frac{1}{2}$ (not to be confused with summation signs, Σ_i, $\Sigma_\pm$ etc., which always carry subscripts indicating nature of summation);

$\Omega = \Lambda + \Sigma$ = total angular momentum about this axis;

β = Bohr magneton;

λ = spin–orbit constant, the same as the interval $^2\Pi_{\frac{3}{2}} - {}^2\Pi_{\frac{1}{2}}$ ($\lambda/k = 173°$ for NO);

$B = h^2/8\pi^2 I$ ($B/k = 2{\cdot}46°$);

ν = rotation–vibration frequency (doubly degenerate) for small oscillations of the NO molecule about equilibrium orientation;

R_Ω, R_Λ, R_Σ are operators reversing the sign of the angular momentum indicated in subscript. Note that $R_\Omega = R_\Lambda R_\Sigma$ and that $S_{x'} \mp iS_{y'} = R_\Sigma \delta_\Sigma^{\pm\frac{1}{2}}$;

b_0, b_3 are coefficients proportional to the axial and trigonal parts of the crystalline potential; see equations (18) and (12).

The Hamiltonian function can now be written as

$$\mathcal{H} = \lambda\Lambda\Sigma + B \operatorname{cosec}\theta(p_\theta - S_{x'}) \sin\theta(p_\theta - S_{x'})$$
$$+ B \operatorname{cosec}^2\theta(p_\phi - \Omega\cos\theta - S_{y'}\sin\theta)^2$$
$$+ 2\beta \boldsymbol{S}\cdot\boldsymbol{H} + \Lambda\beta H_z\cos\theta$$
$$+ \sum_i \sum_{l,m} e_i a_{lm} r_i^l Y_{lm}(\theta_i,\phi_i). \qquad (1)$$

The last member of (1) is the usual expansion of the crystalline potential, with the reality condition $a_{lm} = a_{l-m}{}^*$. The B or kinetic energy part of (1) is similar to that used in the theory of diatomic molecular spectra for treating such subjects as Λ-type doubling, etc. The term in $\Omega\cos\theta$ represents the gyroscopic effect of the electronic angular momentum about the figure axis, which makes the molecule behave dynamically like a symmetrical top. The terms in the kinetic energy involving $S_{x'}$, $S_{y'}$ arise from the spin angular momentum perpendicular to the molecular axis

and are those which potentially can cause decoupling of the spin, i.e. deviations from Hund's case (a) (very small in NO, whereas complete decoupling could be assumed in the MEYER, O'BRIEN and VAN VLECK theory for O_2). We originally carried through our calculation retaining these terms to the end, but their effect on the susceptibility proves to be inconsequential, and so in the interest of simplicity we will hence omit them. Because of the high energy of excited orbital states, the component of orbital angular momentum perpendicular to the figure axis has a negligible effect both in the kinetic and Zeeman energy, and so the corresponding terms have not been included even at the beginning in (1). On the other hand, it is essential to retain the perpendicular component of S in the Zeeman energy $2\beta \boldsymbol{H}\cdot\boldsymbol{S}$.

TRANSFORMATION OF AXES AND RE-GAUGING

We now transform to a system in which the coordinates of the individual particles are referred to axes mounted on the molecule rather than fixed in space. This is done by means of the transformation theorem for tesseral harmonics

$$Y_{lm}(\theta_i,\phi_i) = \sum_{m'} D^{(l)}_{m'm}(\theta,\phi) Y_{lm'}(\theta'_i,\phi'_i). \tag{2}$$

Only terms of the type $m' = 0$ and $m' = \pm 2$ are of interest for us. Those with $m' = 0$ give the usual potential energy interfering with the free rotation of the molecule. Those with $m' = \pm 2$ can convert $\Lambda = \mp 1$ into $\Lambda = \pm 1$, and these are the members which give rise to the perturbing effect of the crystalline field on the susceptibility.

In the kinetic and Zeeman energies, we now make the approximation that the angle θ is small. We do not yet make the small angle approximation for the crystalline potential because, as we shall see later, the convergence of the expansion of the representation coefficients is much poorer than that of the angular factors in the kinetic and Zeeman energies. For our purposes we are interested only in matrix elements interior to the ground $^2\Pi$ doublet. With the approximations which we have described, the Hamiltonian operator can consequently be taken to be

$$\mathscr{H} = \lambda\Lambda\Sigma + B[\theta^{-1}p_\theta\theta p_\theta + \theta^{-2}(p_\phi-\Omega)^2]$$
$$+\beta R_\Sigma \sum_{\pm} \delta^{\pm\frac{1}{2}}_{\Sigma} (H_x \pm iH_y) e^{\mp i\phi}$$
$$+\beta H_z(\Lambda+2\Sigma) + f(\theta,\phi) + R_\Lambda \delta^{1}_{\Lambda} g(\theta,\phi)$$
$$+ R_\Lambda \delta^{1}_{\Lambda} g^*(\theta,\phi), \tag{3}$$

where

$$f(\theta,\phi) = \sum_{l,m} \{a_{lm} \langle \sum_i e_i r_i^l \, Y_{l0} \rangle_{\Lambda\Sigma} D^{(l)}_{0m}(\theta,\phi)\}, \tag{4}$$

$$g(\theta,\phi) = -e \sum_{l,m} a_{lm} I_l D^{l)}_{2m}(\theta,\phi) \tag{5}$$

with

$$I_l = \int \psi^*_{\pi+} \, r_1^l Y_{l2}(\theta'_1,\phi'_1) \psi_{\pi-} \, d\tau'_1. \tag{6}$$

The symbol $\Sigma_\pm$ means a summation over both sign possibilities, δ^i_j is the usual Kronecker δ, and the meaning of the reversal operators R is explained above in the glossary of notation. The average in (4) is the usual expectation value, i.e. the average over the charge density of all the particles. The integration in (6) is only over the odd unpaired electron, which we call particle 1. This is the only one which can have its angular momentum reversed without excitation. Its wave function is denoted by $\psi_{\pi\pm}$ for $\Lambda = \pm 1$. We for simplicity suppose that the wave function of this electron can be isolated from that of the other electrons, as in a Hartree approximation, so that it can be classed as a π electron in molecular orbital notation. This assumption is, however, not really necessary if the integration is taken over configuration space rather than the coordinates of one electron.

It is convenient to make the transformation $\Psi_\Omega \to \Psi_\Omega \exp(i\Omega\phi)$ or in other words shift the origin of p_ϕ by an amount Ω. When this re-gauging is effected, and it is noted that the operators R_Σ and R_Λ involve respectively one and two unit changes in Ω, it is seen that equation (3) becomes

$$\mathscr{H} =$$
$$\lambda\Lambda\Sigma + B[\theta^{-1}p_\theta\theta p_\theta + \theta^{-2}p_\phi^2] + \beta R_\Sigma \sum_{\pm} \delta^{\pm\frac{1}{2}}_{\Sigma} (H_x \pm H_y)$$
$$+\beta H_z(\Lambda+2\Sigma) + f(\theta,\phi) + R_\Lambda \delta^{-1}_{\Lambda} e^{-2i\phi} g(\theta,\phi)$$
$$+ R_\Lambda \delta^{1}_{\Lambda} e^{2i\phi} g^*(\theta,\phi). \tag{7}$$

ELIMINATION OF THE UPPER STATE—THE EFFECTIVE HAMILTONIAN

The terms in (7) involving R operators generate transitions between the two components of the $^2\Pi$

doublet. This interval (173°) is moderately large compared to the spacing of the vibrational energy intervals, presumably of the same order of magnitude as in the O_2 or N_2 clathrates (25° or 75°). With a fair degree of approximation, we can therefore eliminate these "high frequency" terms by a standard procedure of perturbation theory, which tells us that we can omit the "high frequency" (jj') part of the Hamiltonian if instead we add to the low frequency (jj) portion a new member

$$(ji|\mathscr{H}_{\text{new}}|ji'') = \sum_{j'i'} \left\{ \frac{(ij|\mathscr{H}|j'i')(j'i'|\mathscr{H}|ji'')}{h\nu_{jj'}} \right\}. \quad (8)$$

If, as we do, we neglect the rotation–vibrational modulation of the multiplet intervals, the frequency denominator in (8) is merely λ. We treat θ, ϕ as constant parameters in the high frequency part of the problem, in much the same way as the spin variables are so treated in deriving the so-called spin Hamiltonian in paramagnetic resonance when the orbital spacings are large compared with spin–orbit energy. By use of (8) we are led to an effective Hamiltonian

$$\mathscr{H} = -\tfrac{1}{2}\lambda + B[\theta^{-1}p_\theta\theta p_\theta + \theta^{-2}p_\phi^2] + V(\theta,\phi) + \beta H_z(\Lambda + 2\Sigma) - \lambda^{-1}\beta^2[H_x^2 + H_y^2] + \mathscr{H}_{\text{per}} \quad (9)$$

where

$$V(\theta,\phi) = f - \lambda^{-1}|g|^2 \quad (10)$$

$$\mathscr{H}_{\text{per}} = -2\lambda^{-1}\beta R_\Omega[\delta_\Lambda^{-1}e^{-2i\phi}(H_x + iH_y)g(\theta,\phi) + \delta_\Lambda^1 e^{2i\phi}(H_x - iH_y)g^*(\theta,\phi)]. \quad (11)$$

Equations (9), (10), and (11) as they stand apply to the $^2\Pi_{\frac{1}{2}}$ state. The corresponding formulas for $^2\Pi_{\frac{3}{2}}$ are obtained by reversing the sign of λ in all three of these relations, and of H_y in (11).

The term $V(\theta,\phi)$ is the effective potential for the oscillation problem. If we neglect $\mathscr{H}_{\text{per}}$, the magnetic terms in (9) yield the same formula for the powder susceptibility as the conventional one for the free NO molecule. The member $\mathscr{H}_{\text{per}}$ gives rise to vibration–rotation modulation of the susceptibility and is of particular interest for us. We now note that the Taylor's expansion of $D^{(l)}_{m'm}$ begins with $\theta^{|m-m'|}$. The crystalline potential hence cannot contain terms of the form $m = 1$, as then $\theta = 0$ would not be a position of static equilibrium for $V(\theta,\phi)$. It is imperative that (11) should not contain any members diagonal with respect to the oscillation quantum numbers, for then there are matrix elements connecting two components $\Omega = \pm\frac{1}{2}$ of a Kramers doublet, leading to a very large $1/T$ term in the susceptibility at low temperatures, contrary to experiment. In order for the corrections to the free-molecule susceptibility to be not of the $1/T$ type but still fairly large, as required by experiment, it is essential that the development of (11) in θ start with terms of low but non-zero order, presumably first or second order in θ. Referring to (5), we see that this development will start with the first power if $m = 3$, and with the second if $m = 0$ or $m = 4$. In view of the appreciable modifications of the susceptibility found experimentally, *we conclude from the magnetic data that the local field about the* NO *molecule in the clathrates has trigonal symmetry*. (A purely axial term, apart from being of higher order, by itself gives the wrong variation with temperature, as we shall see later.) It is, indeed, known from X-ray analysis that the symmetry is trigonal, but the writer did not realize this fact at the time of his original calculations and reached the same conclusion by magnetic reasoning. A term of the type $m = 4$ seems incompatible with what is known about the crystal structure, and would not be particularly effective.

To simplify the problem and make it more concrete, we shall assume that the crystalline potential has a center of symmetry, making l even, and we shall retain only the harmonics of lowest order, viz. $l = 2$ and $l = 4$ respectively for axial and trigonal symmetry. Then the crystalline potential, in so far as the odd magnetic electron responsible for the magnetism is concerned, can be taken to be

$$V = a_{20}Y_{20}(\theta) + a_{43}Y_{43}(\theta,\phi) + a_{43}^*Y_{4-3}(\theta,\phi). \quad (12)$$

Actually, because of the unequal masses and especially the different electron distributions of the N and O atoms, there certainly is not rigorously a center of symmetry, so $l = 3$ is not *a priori* excluded. Also higher order terms in l may not be negligible.

We shall henceforth call the first and second parts of (12) respectively the axial and trigonal potentials. It is, of course, to be understood that in any actual trigonal field normally occurring,

there are members of the axial type $m = 0$ as well as what we term the "trigonal" type $m = \pm 3$. The axial portion is, of course, always the important part for determining the frequency of oscillation of the molecular axis about its equilibrium position.

THE HARMONIC OSCILLATOR AND OTHER SMALL ANGLE APPROXIMATIONS

At low temperatures, the oscillations of the molecule about its equilibrium position are presumably small, and so, as in the corresponding theory of the O_2 and N_2 clathrates, we take

$$V(\theta,\phi) = \tfrac{1}{2}\alpha\theta^2. \tag{13}$$

If we neglect magnetic terms, the Hamiltonian (9) is then simply that of a two-dimensional harmonic oscillator in polar coordinates, with θ playing the role of a radius vector. The corresponding eigenvalues of the energy are

$$E = -\tfrac{1}{2}\lambda + (n_1+n_2+1)h\nu, \quad h\nu = (2\alpha B)^{1/2}, \tag{14}$$

where n_1, n_2 are oscillation quantum numbers and ν is the oscillation frequency connected with small vibrations or rotations of the molecule about its equilibrium position. When the crystalline potential has the form (12), the representation coefficients which we need in connection with (5) are

$$D^{(4)}_{23} = (7/32)^{1/2}(1+\cos\theta)^2 \sin\theta\,(2\cos\theta - 1)e^{3i\phi},$$
$$D^{(2)}_{20} = (3/8)^{1/2}\sin^2\theta, \tag{15}$$

as one finds from the ξ, η spinor calculus, or otherwise.[6] Their Taylor's developments are

$$D^{(4)}_{23} = (\tfrac{7}{8})^{1/2}[\theta - (\tfrac{11}{6})\theta^3 + \ldots]e^{3i\phi}, \tag{16}$$
$$D^{(2)}_{20} = (\tfrac{3}{8})^{1/2}[\theta^2 - \tfrac{1}{3}\theta^4 + \ldots].$$

If we keep only the first term in each case, the perturbing potential (11) reduces to

$$\mathscr{H}_{\text{per}} = -2\lambda^{-1}\beta R_\Omega[\delta^{-1}_\Lambda(H_x + iH_y)(b_3\theta e^{i\phi} + b_0\theta^2 e^{-2i\phi}) + \delta^1_\Lambda(H_x - iH_y)(b^*_3\theta e^{-i\phi} + b_0\theta^2 e^{2i\phi})] \tag{17}$$

where the operator R_Ω reverses the sign of both Λ, Σ, and

$$b_3 = -(\tfrac{7}{8})^{1/2}I_4 e a_{43}, \quad b_0 = -(\tfrac{3}{8})^{1/2}I_2 e a_{20}. \tag{18}$$

The integral I_l is defined in (6).

We shall henceforth assume b_3 to be real. This condition can always be met by proper choice of the origin for ϕ. Also, in computing the $\perp$ susceptibility, we can without loss of generality take $H_x = H_\perp$, $H_y = H_z = 0$, since with axial or trigonal symmetry the susceptibility is the same for all directions of the field perpendicular to the axis of figure.

It is now convenient to make the "Wang"[7] transformation $\Psi_\pm = (\Psi_\Omega \pm \Psi_{-\Omega})/\sqrt{2}$ in the spin–orbit wave functions, and to introduce Cartesian vibrational coordinates $x \pm iy = \theta e^{\pm i\phi}$. (This transformation spoils the diagonalization of the $H_\parallel$ part of the Zeeman energy, but this is immaterial as $\chi_\parallel$, $\chi_\perp$ can be computed independently.) In a perpendicular field then (9) becomes

$$\mathscr{H} = -\tfrac{1}{2}\lambda + B(p_x^2+p_y^2) + \tfrac{1}{2}\alpha(x^2+y^2) - \lambda^{-1}\beta^2 H_\perp^2 - 2\lambda^{-1}\beta H_\perp[b_3 x + b_0(x^2-y^2) \pm iR_\pm(b_3 y - 2b_0 xy)]. \tag{19}$$

where the operator $R_\pm$ reverses the component of the Wang doublet. The upper and lower signs apply to the two components of this degenerate doublet (not to be confused with the $^2\Pi_{\frac{1}{2},\frac{3}{2}}$ doublet).

It can be shown that the roots of the secular equation connected with (19) are precisely the same as though we omitted the troublesome factor $\pm R_\Omega$, except that each root occurs twice as often. The problem of computing the eigenvalues is hence reduced to the elementary one of the harmonic oscillator. (To prove this, we first note that if n_2 be the vibrational quantum number associated with the y coordinate, the perturbation (19) links states of even n_2 to states of even n_2 of the same Wang parity, and to states of odd n_2 of opposite parity. If we re-phase all of the wave functions of odd n_2 and one given parity by a factor i, the effect is the same on the secular determinant as though we removed the factor $\pm iR_\pm$.)

To terms of the second order in $H_\perp$, the eigenvalues of (19) are thus found to be

$$E = (n_1+n_2+1)h\nu - \tfrac{1}{2}\lambda - \lambda^{-1}\beta^2 H_\perp^2 - 8b_3^2(B/h^2\nu^2\lambda^2)\beta^2 H_\perp^2 - 4\sqrt{2}b_0(B/h\nu\lambda)\beta H_\perp(n_1-n_2) - 16b_0^2(n_1+n_2+1)(B^2/h^3\nu^3\lambda^2)\beta^2 H_\perp^2. \tag{20}$$

Through terms of the second order in b_0, b_3, the expressions for the susceptibility perpendicular and parallel to the trigonal axis of the crystal are

$$\chi_\perp = \chi_\perp^0 + \Delta\chi_\perp, \quad \chi_\parallel = \chi_\parallel^0 + \Delta\chi_\parallel, \tag{21}$$

$$\chi_\perp^0 = \frac{2N\beta^2}{\lambda}\tanh\left(\frac{\lambda}{2kT}\right),$$
$$\chi_\parallel^0 = \frac{2N\beta^2}{kT}\frac{\exp(-\lambda/2kT)}{\cosh(\lambda/2kT)}, \tag{22}$$

$$\Delta\chi_\perp = \frac{16N\beta^2B}{\lambda^2h\nu}\left[b_3^2\left(\frac{1}{h\nu}-\frac{\phi_1}{\lambda}\tanh\frac{\lambda}{2kT}\right)\right.$$
$$\left.+\frac{2b_0^2B}{h\nu}\left(\frac{\phi_1}{h\nu}+\frac{\phi_2-1}{2kT}-\frac{2\phi_2}{\lambda}\tanh\frac{\lambda}{2kT}\right)\right]$$
$$+\frac{4}{\lambda}\frac{\partial\chi_\perp}{\partial\lambda}\frac{B}{h\nu}\left(b_3^2\phi_1+\frac{4b_0^2B}{h\nu}\phi_2\right), \tag{23}$$

$$\Delta\chi_\parallel = \left[b_3^2\phi_1+\frac{4b_0^2\phi_2B}{h\nu}\right]\left[\frac{B}{h\nu}\right]$$
$$\times\left[\frac{8\chi_\perp^0-4\chi_\parallel^0}{\lambda^2}+\frac{4}{\lambda}\frac{\partial\chi_\parallel^0}{\partial\lambda}\right], \tag{24}$$

where ϕ_1, ϕ_2 are functions of the temperature given by

$$\phi_1 = 1+\frac{2}{\exp(h\nu/kT)-1}, \quad \phi_2 = 1+\frac{4\exp(h\nu/kT)}{[\exp(h\nu/kT)-1]^2}.$$

The expressions $\chi_\perp^0$, $\chi_\parallel^0$ given in (22) are the susceptibilities for a molecule completely frozen with molecular axis parallel to the axis of the crystalline field, and $\chi^0 = \frac{1}{3}\chi_\parallel^0 + \frac{2}{3}\chi_\perp^0$ is the usual formula for the susceptibility of gaseous NO, which we shall henceforth refer to as the "conventional" susceptibility. It is not quite right to call χ^0 the susceptibility of free NO, for at very low temperatures, where the rotational energy intervals are comparable to kT, there are corrections to χ^0 which are not usually considered and which would be of only academic interest since NO condenses long before $B/kT = 1$.

Equations (23) and (24) give the corrections to the "frozen" model caused by oscillation about the equilibrium axis, the primary concern of the present paper. Only the leading terms of (23) are obtained if one simply uses the eigenvalues (20) in the usual expression

$$M = NkT\partial[\log\sum_i \exp(-E_i/kT)]/\partial H \tag{25}$$

for the magnetic moment M. Instead we have included in (23) and (24) certain additional terms which are necessary if we are not to omit any significant part of the susceptibility of the order b_3^2 or b_0^2. These extra members arise because the Hamiltonian (19) only contains terms internal to the one of the $^2\Pi$ doublets. In making the transformation which generates (19), the matrix elements of the Zeeman energy have been created which are interior to the ground state, but the conservation of "line strength" requires corresponding depletion of the off-diagonal elements of s_x, s_y connecting $^2\Pi_{\frac{1}{2}}$ and $^2\Pi_{\frac{3}{2}}$. Similarly in the case of $\chi_\parallel$, a weak off-diagonal element of s_z joining $^2\Pi_{\frac{1}{2}}$ and $^2\Pi_{\frac{3}{2}}$ is created at the expense of the diagonal Zeeman energy for the upper $^2\Pi_{\frac{3}{2}}$ state. We do not give the details of the perturbation theory, but it is quite straightforward. The extra terms we henceforth for brevity call the depletion corrections. They are of secondary, but by no means negligible, importance at very low temperatures, as they are of the order $h\nu/\lambda$ compared with the main terms yielded by (20) and (25). Also the interaction (12) spreads apart the energy levels $^2\Pi_{\frac{1}{2}}$, $^2\Pi_{\frac{3}{2}}$ making the effective multiplet interval greater than λ. The corresponding contribution to (23) and (24) is that involving $\partial\chi/\partial\lambda$. The additional terms are quite necessary at higher temperatures comparable with λ, in order to make the susceptibility flow into the conventional formula and vanish as $1/T$ as the temperature is raised. Even when they are included, the coefficient of $1/T$ in the limit $T\to\infty$ differs by terms of the order $(B^2b_0^2/h^4\nu^4)N\beta^2$ from the conventional value $4N\beta^2/3$. This state of affairs, however, is to be expected, as the vibrational modulation becomes more and more important as the temperature is raised, and the usual conditions for the derivation of the Langevin–Debye formula are not met. This difference is only academic, for long before the high temperature limit is reached, the assumption that θ^2 is small ceases to be valid.

Before we proceed to display the results of

Vol. 2
1961

calculations based on (23) and (24), it is perhaps well to discuss qualitatively and physically the nature of the effects. The modulation caused by the molecular oscillations transfers some of the Zeeman line strength from transitions connecting $^2\Pi_{\frac{1}{2}}$ and $^2\Pi_{\frac{3}{2}}$ to transitions between different vibrational or rotational components of the ground state. The susceptibility will be increased, since the perturbation denominators become of the order $h\nu$ rather than λ, and furthermore the susceptibility will be independent of temperature as long as $kT \ll h\nu$. This is just the type of behavior required to explain MEYER's experimental results. To explain his data it is, however, necessary that χ remain approximately constant even when $h\nu$ is comparable with kT (unless $h\nu$ is unreasonably large), though not when the Boltzmann factor $e^{-\lambda/kT}$ becomes appreciable, i.e. the $^2\Pi_{\frac{3}{2}}$ state excited. This criterion is more nearly satisfied with the trigonal field b_3 than the axial one b_0. In fact, if one includes only the leading terms arising from b_3, i.e. those obtained from (20) and (25), (or in other words the b_3 part of (23) not having a ϕ factor), the susceptibility would be constant as long as $kT/\lambda \gg 1$. This is because the b_3 contribution to (20) is independent of n_1, n_2, a manifestation of the fact that the trigonal potential gives a linear perturbing potential in (19), and it is well known that addition to a harmonic oscillator of a perturbation linear in the displacement yields an energy shift or polarizability which is independent of the stationary state. The independence of temperature is, however, spoiled by the extra terms arising from the depletion of the off-diagonal elements, and other corrections explained in the preceding paragraph. As a result, even with a trigonal field, the susceptibility decreases slightly when excited vibrational states come into play. With an axial potential, the variation of χ with temperature because of oscillation effects is much more pronounced, as the b_0 part of (20) depends on n_1,n_2. In particular, there is a linear Zeeman term in (20) except for the ground vibrational level $n_1 = n_2 = 0$, and correspondingly there is a $1/T$ term in the susceptibility when $b_0 \neq 0$, which disappears when $T = 0$.

THE TROUBLESOME ANHARMONIC TERMS

If we content ourselves with the expressions which we have derived for the susceptibility, we find that the observed susceptibility can be pretty well represented by (23) and (24) with a purely trigonal term b_3. However, there is a serious difficulty, which the writer was not aware of when he first reported the results of his calculations at the Leiden Low Temperature Conference of 1958. The coefficient $-11/6$ of the anharmonic term proportional to θ in (16) is quite large, so that the approximation (17) on which equations (23) and (24) are founded is not really warranted. (The corresponding axial term has a smaller anharmonic correction, and it will be disregarded.) There are other corrections which should be included in our approximate corrections to our small angle approximation, e.g. the angular dependence of the Zeeman members of (1), also terms in θ^5 in the development (16), but the θ^3 member of (16) is by far the most important one. (Actually these other corrections slightly offset the effect of the θ^3 term, and to allow for this fact, we base our numerical calculations on a slightly smaller coefficient, $-3/2$ of θ^3 rather than $-11/6$.) We will not give the formulas resulting from these anharmonic corrections, which are quite cumbersome, and which it is feasible to use only for the first few oscillational states. These corrections have been made only approximately; only the elements of θ^3 of the form $\Delta n_1, \Delta n_2 = \pm 1$ have been included, as they are by far the most important, since they enter additively to the harmonic matrix elements and materially modify the square of the latter. We will exhibit graphically later the effect of the anharmonic corrections in a particular case, and suffice it to say for the present that they materially lower $\Delta\chi$ at low temperatures, and make $\Delta\chi$ depend much more on temperature for a trigonal field than without the correction.

SEMICLASSICAL APPROXIMATION

It is clear that at high temperatures, the convergence of a series development of the representation coefficients in θ is poor, and another approach is indicated. This consists in eliminating the low-frequency denominators in the formulas for the perturbed energy by means of a pairing of terms which is valid when $k\nu \ll kT$, and which gives denominators of the order kT rather than $h\nu$. Then the oscillation problem is treated classically rather than quantum mechanically, so that in place of a summation over the oscillation states, we have

ol. 20
1961

an integration over solid angle. The resulting formulas for $\Delta\chi$ are

$$\Delta\chi_{\parallel} = Q(T)[2\chi_{\perp}^{0} - \chi_{\parallel}^{0} + \lambda\partial\chi_{\parallel}^{0}/\partial\lambda] \quad (26)$$

$$\Delta\chi_{\perp} = Q(T)[(2N\beta^2/kT) - 2\chi_{\perp}^{0} + \lambda\partial\chi_{\perp}^{0}/\partial\lambda] \quad (27)$$

where

$$Q(T) = \frac{2}{\lambda^2} \times \frac{\iint\{(8/7)b_3^2|D_{23}^{(4)}|^2 + (8/7)b_3^2|D_{-23}^{(4)}|^2 + (8/3)b_0^2|D_{20}^{(2)}|^2\} - \exp(V/kT)d\omega}{\iint \exp(-V/kT)\, d\omega}. \quad (28)$$

As before, we suppose that only the members of (12) are present in the crystalline potential in so far as the magnetic problem is concerned. If we assume that the exponent in the Boltzmann factor is $-\alpha\sin^2\theta/2kT$ rather than $-\alpha\theta^2/2kT$, something within our limits of accuracy, the integrals can be evaluated in an elementary way in terms of probability integrals. The resulting formula is longish and will not be given here, as this whole approach has only asymptotic validity for our problem.

We call the method based on equations (26) and (27) a semiclassical one, as the oscillation problem has been treated as a continuum, whereas the problem of interaction between the $^2\Pi_{\frac{1}{2}}$ and $^2\Pi_{\frac{3}{2}}$ states is treated rigorously by means of quantum mechanics. In other words, it is assumed that the oscillation quantum $h\nu$, but not the spin–orbit quantum λ, is small compared to kT. This semiclassical method begins to be valid only at liquid air temperatures and above, as it assumes $h\nu \ll kT$. In this region, the deviations of χ from χ^0 are small anyway, and we use the method mainly as a control on our results in the medium temperature region.

GRAPHICAL DISPLAY OF SOME RESULTS

Results of numerical calculations based on our various methods of approximation are displayed in Figs. 1 and 2. For these graphs we have assumed

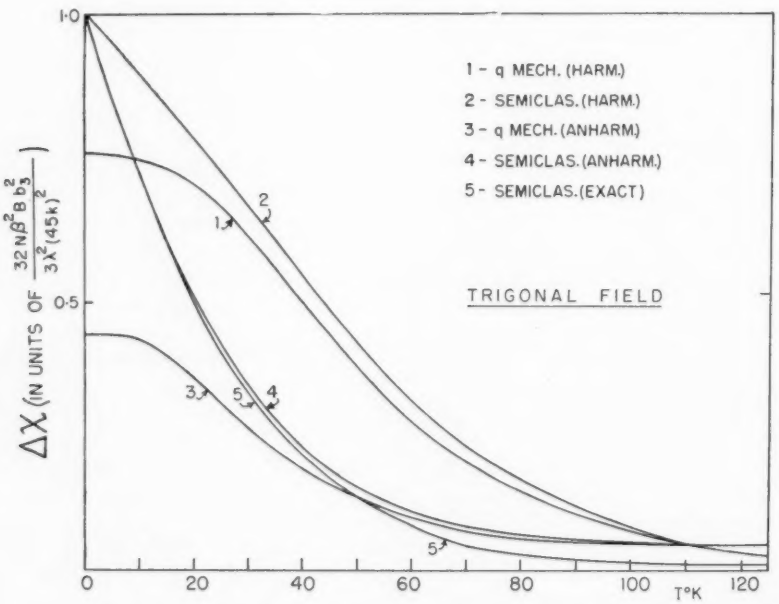

FIG. 1. Alteration in susceptibility caused by a trigonal field of type Y_{43} when $h\nu/k = 45°$.

that $h\nu/k = 45°$. This is to be compared with the values of about 25° and 75° respectively furnished by magnetic experiments on the O_2 and N_2 clathrates.[1,2,8] Because of the different molecular quadrupole moments (not to mention the dipole moment of NO), there is no reason that the molecular frequency of vibration should be the same in the different clathrates except for rough orders of magnitude. It is perhaps not unreasonable that ν for NO has a value intermediate between that for N_2 and O_2.

appropriately weighted some of the $\Delta\chi$s given by Figs. 1 and 2. The absolute value of $\Delta\chi$ can be scaled to any desired size by proper choice of b_3 or b_0.

In Fig. 1, curve 1 is constructed by means of the quantum mechanical formulas (23) and (24) in which only the linear or harmonic term of the first relation of (16) is retained. In curve 3, the corrections for higher order terms in θ are allowed for by including a cubic term in θ (with the coefficient 11/6 replaced by 3/2 for reasons previously

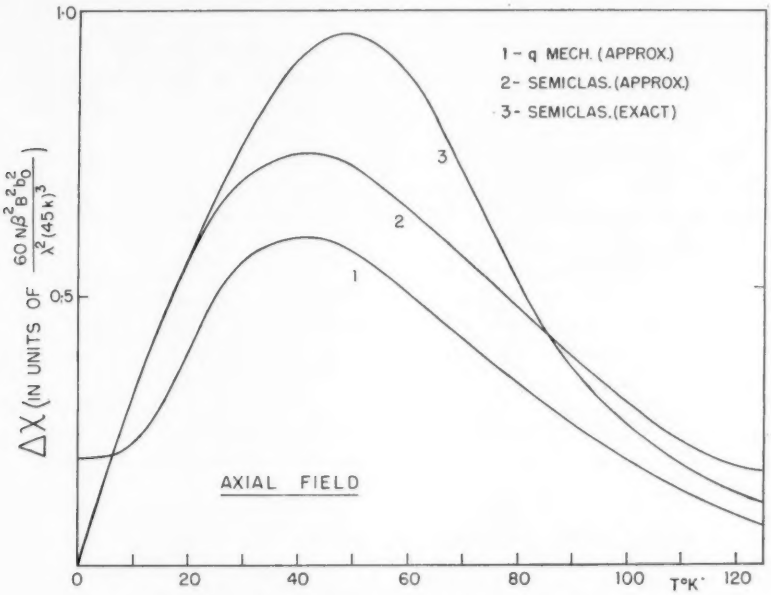

FIG. 2. Alteration in susceptibility caused by an axial field of type Y_{20} when $h\nu/k = 45°$.

In both Figs. 1 and 2, we plot against temperature the excess $\Delta\chi = \frac{2}{3}\Delta\chi_\perp + \frac{1}{3}\Delta\chi_\parallel$ of the powder susceptibility over that given by the conventional formula for the free molecule. In Figs. 1 and 2 it is assumed that $\Delta\chi$ is caused respectively only by the trigonal and axial members of the perturbing potential. In other words, Fig. 1 assumes $b_3 \neq 0$, $b_0 = 0$, and Fig. 2 the reverse. To our degree of approximation, the axial and trigonal contributions to the susceptibility are additive so if one has both $b_3 \neq 0$, $b_0 \neq 0$, doubtless the case physically, one has

described). Curve 2 is constructed by means of the semiclassical formulas (26) and (27), but with the "harmonic" approximation that only the linear term of $D_{23}^{(4)}$ is retained. In curve 4, the cubic approximation (16) to $D_{23}^{(4)}$ is used, while in curve 5 the accurate formula (15) is employed. In curve 5 of Fig. 1 and also curve 3 of Fig. 2, the potential governing the oscillations of the molecular axis about equilibrium is supposed proportional to $\sin^2\theta$, as previously described, while in the remaining curves it is taken proportional to θ^2. Curves 1 and 2 of Fig. 1 are thus the exact quantum

mechanical and semiclassical approximations for one and the same approximate model. The same is also true of curves 3 and 4. Comparison of curves 1 and 2 or 3 and 4 exhibits the failure of the semiclassical approximation at low temperatures. Comparison of curves 4 and 5 gives us an idea of the amount of error involved in the cubic approximation to the representation coefficients. It is seen not to be serious in most of the temperature region in which we are interested. In this connection it is to be noted that at $T = 0$, the classical amplitudes are infinitesimal, so that any anharmonic corrections are unimportant, but around 45° comparison of the two curves should show roughly the amount of error involved in the cubic approximation in a quantum mechanical treatment. If we did not allow for the depletion effect in the terms of $\chi_\perp$ non-diagonal in Ω, and creation of small off-diagonal elements for $\chi_\parallel$, as discussed following equation (25), and thus included only the leading members of (23), (24), or (26), (27), both the quantum and semiclassical curves 1 and 2 for the harmonic model would be horizontal lines coincident with the top boundary of Fig. 1. It is for this reason that the quantum and classical approximations agree better for the harmonic trigonal model than for any of the other cases displayed in Figs. 1 and 2.

In Fig. 2, curves 1 and 2 are based on the approximation $D^{(2)}_{20} \sim \theta^2$ whereas in curve 3 the exact formula for $D^{(2)}_{20}$ is used. (Most of the difference between curves 2 and 3, however, is caused not by the approximation to $D^{(2)}_{20}$ but by use in constructing curve 3 of a potential $\frac{1}{2}\alpha \sin^2\theta$ rather than $\frac{1}{2}\alpha\theta^2$.)

COMPARISON WITH EXPERIMENT

The experimental work of MEYER shows that χ remains constant at low temperatures, but above about 25° falls off gradually to zero. A purely axial field thus fails completely to give the observed behavior. The trigonal model fits much better, but falls off too rapidly as the temperature is raised. In making comparison with experiment, we use curve 3 up to about 45°, and then curve 5 as being the most reliable approximations. The difficulty of the too rapid fall-off can be averted, though in a somewhat forced fashion, by taking a properly weighted combination of axial and trigonal potentials, in which about 90 per cent of the observed $\Delta\chi$ at $T = 0$ is ascribed to a trigonal and 10 per cent to an axial field.

By taking the sum of curve 3 of Fig. 1 and curve 1 of Fig. 2 respectively normalized to intercepts $\Delta\chi = 0{\cdot}40\chi^0$ and $\Delta\chi = 0{\cdot}04\chi^6$ at $T = 0$, continued at the right of the figure by corresponding curves 5 and 3 made with the semiclassical approximations, the experimental results shown by MEYER in Fig. 1 of the preceding paper can be reproduced within the experimental error. The corresponding values of the constants b_3 and b_0 defined in (18) are $b_3/k = 130°$, $b_0/k = 115°$, which are not unreasonable as regards orders of magnitude. (Although the axial contribution to $\Delta\chi$ is smaller than the trigonal in this combination, b_0 is comparable with b_3 because the trigonal term influences the susceptibility in lower order in $B/h\nu$ than does the axial.) We do not, however, give a separate figure to advertise the comparison of theory with experiment, since any such curve is exclusive of the troublesome $1/T$ correction which we now discuss.

THEORETICAL EXISTENCE OF A SMALL TERM IN $1/T$ AT LOW TEMPERATURES

So far, we have given the impression that the susceptibility contains no term in $1/T$ at low temperatures as long as the crystalline field has axial or trigonal symmetry. Unfortunately, this is not true when one goes to higher approximations than we have in our previous calculation. We have consistently discarded terms in the partition function or susceptibility involving terms of higher than the second order in the crystalline potential, which we now symbolize by U. In other words we have computed the first and second order Zeeman coefficients $E^{(1)}$, $E^{(2)}$ respectively to the approximations U and U^2, since the contribution to the susceptibility χ of a state of energy $E = E^{(0)} + E^{(1)}H + E^{(2)}H^2$ is proportional to $[2E^{(2)} - E^{(1)2}/kT]$. However, when we compute χ through terms in U^4, there is a term proportional to $1/T$ at low temperatures. This term is of the order $\Delta\chi_\perp(U^2h\nu/\lambda^2kT)$ and so is presumably of importance only in the helium region; but here it gives trouble, as no such term is revealed by MEYER's measurements.

It is easy to see how this term comes in. Let $\psi_{\Omega,v}$ denote the wave functions of a state of electronic angular momentum and oscillation

quantum numbers Ω,v ($v \sim n, n_2$) in the absence of the actual terms in the crystalline potential which are of the form $\Delta\Omega = \pm 2$, and which are basically the origin of the alteration $\Delta\chi$ in the susceptibility as compared with the conventional value. The matrix elements of U are of the form $\Delta\Omega = \pm 2$, $\Delta v = \pm n$, and we consider only the pair of states $(\frac{1}{2}, 0)$, $(-\frac{3}{2}, n)$ or $(-\frac{1}{2}, 0)$, $(\frac{3}{2}, n)$, and thereby neglect the higher vibrational states $2n$, $3n$ of relatively minor importance at low temperatures. The wave functions, exclusive of the applied magnetic field, then become of the form

$$\psi = (1-a^2)^{1/2}\,\psi_{\pm\frac{1}{2},0} + a\psi_{\mp\frac{3}{2},n}, \qquad (29)$$

where in first approximation,

$$a = \langle \pm\tfrac{1}{2}0|\,U\,|\mp\tfrac{3}{2}n\rangle/\lambda.$$

Since

$$\langle \mp\tfrac{3}{2}n|(2S_{z'}+L_{z'})|\mp\tfrac{3}{2}n\rangle = \mp 2,$$

we see that when squares of a are considered, the diagonal elements of the magnetic moment are no longer zero, and correspondingly there is a term in $\Delta\chi_\parallel$ of magnitude $4N\beta^2a^4/kT$. The main part of $\Delta\chi_\perp$, that which we have previously considered, comes from the matrix elements of S_x, or S_y, connecting $\pm\frac{1}{2}$, 0 and $\pm\frac{1}{2}$,n. At very low temperatures, where only the state $v = 0$ is inhabited, the leading terms of the expressions which we have previously derived for $\Delta\chi$ ($= \frac{2}{3}\Delta\chi_\perp$) can be written as $\Delta\chi = 16Na^2\beta^2/3nh\nu$, where n is 1 or 2 according as the field is trigonal or axial. The contributions of the two types of fields both to our original $\Delta\chi$ and to our new $1/T$ term are readily shown to be additive. We thus find that at low temperatures the powder susceptibility should behave in the fashion

$$\chi = (\chi^0+\Delta\chi)\left(1+\frac{\tau}{T}\right), \qquad (30)$$

where

$$\chi^0 = 4N\beta^2/3\lambda$$

and

$$\tau = \frac{(\Delta\chi)^2}{16\chi^{(0)}}\,\frac{h^2\nu^2}{k(\chi^{(0)}+\Delta\chi)\lambda}\,(f_1+2f_2)^2. \qquad (31)$$

Here f_1, f_2 denote the fractions of $\Delta\chi$ which result from the trigonal and axial parts of the crystalline field. Formula (31) as it stands assumes that the mixture coefficients, a, in (29) are unchanged if we interchange 0 and n; actually they are slightly different because vibrational modulation makes the energy intervals $\lambda \pm nh\nu$ rather than just the spin–orbit constant λ. When allowance is made for this fact, and also for the "depletion effect" discussed following equation (25), it is found after some calculation that we should instead define τ as

$$\tau = \frac{(\Delta\chi)^2}{16k\chi^{(0)}} \times \frac{h^2\nu^2\lambda}{(\chi^0+\Delta\chi)}\left(\frac{f_1}{\lambda+h\nu}+\frac{2f_2}{\lambda+2h\nu}\right)^2. \qquad (32)$$

The corrections involved in the substitution of (31) for (30) are accurate only to the approximation $1/(\lambda+h\nu) = (1/\lambda)-h\nu/\lambda^2$ etc., as it is tacitly assumed that the vibrational energy is small compared to λ.

We have written the formula for τ in such a way that the coefficients of the crystalline potential are eliminated, and as a result τ depends mainly on known quantities. Virtually the only disposable constant in the formula (31) or (32) for τ, is the oscillation frequency ν, for λ is known from spectroscopy, and MEYER's measurements show that $\Delta\chi/\chi^0 = 0{\cdot}45$. The sum f_1+f_2 is unity, and we know that f_2 is small compared to f_1 since the only kind of field that will give any accord with MEYER's data is one that is mainly trigonal rather than axial, as far as its contribution to the susceptibility is concerned. Incidentally, a purely axial field would make the situation as regards the $1/T$ term even worse than for a trigonal one, since a purely axial field gives a value of τ approximately 4 times as large as for a purely trigonal one.

If we use the choice of constants cited in the preceding section, viz. $h\nu/k = 45°$, $f_1 = 0{\cdot}9$, $f_2 = 0{\cdot}1$, the coefficient τ is 0·06. (The situation has been helped somewhat by the use of (31) rather than (30); otherwise τ would be 0·10.)

A value of τ as large as 0·06 would probably have been detected in MEYER's experiments, but the effect is very close to the limit of sensitivity of his mutual inductance bridge, which is only able to measure the susceptibility of NO within about 5 per cent (private communication). Further experimentation is obviously indicated. If it should turn out, as appears likely, that a value of τ as large as 0·06 or thereabouts does not exist, there is obviously a dilemma. What are the ways of escaping it? The possible ways out, as we see it, are the following.

(1) The most obvious suggestion is that the value of the vibration frequency which we have used, viz. $h\nu/k = 45°$, is too large. The constant τ is approximately proportional to ν^2, and so use of a value $h\nu/k = 25°$, the same as that in the O_2 clathrate, will reduce τ to 0·02, a value which might well have escaped detection. However, there are serious objections to use of such a low value of ν. Among molecules, O_2 is rather exceptional for its low quadrupole moment, and it is doubtful if this quality, which is presumably responsible for the low ν in O_2, carries over to NO. If anything, NO is probably more like N_2; the N_2 clathrate has $h\nu/k = 75°$. This type of argument, however, is rather uncertain, and a more straightforward argument is that any reduction in ν impairs the constancy of $\Delta\chi$ (exclusive of the $1/T$ term) as the temperature is raised. This can be seen physically from the fact that in order to make $\Delta\chi$ constant over an appreciable temperature range, it is necessary that all states with appreciable Boltzmann factors have very nearly the same polarizability. The moment we reduce ν, the temperature interval is reduced over which constancy can be secured by proper blending of trigonal and axial fields. We have already used about as low a value of ν as can be successfully employed to reproduce MEYER's curves. As already mentioned, it is the anharmonic or θ^3 part of (16) that is responsible for the drop-off in the curve 3 of Fig. 1. It should, however, be mentioned that if the potential is of the type Y_{33} rather than Y_{43}, the development D^3_{23} replacing (16) is proportional to $\theta - \frac{2}{3}\theta^3$. With the lower anharmonic term, it is possible to use a value of $h\nu/k$ as low as 30° or so and still fit the data if a small amount of axial term is intermixed. Since the two ends of the NO molecule are not the same, there is no reason that it be symmetrically located in the cavity, and so a term of the form Y_{33} can exist. It is, however, doubtful whether it could over-shadow a term in Y_{43}, even though it is of lower order in the ratio of molecular to cavity diameter.

(2) It is barely conceivable that if $h\nu/k$ is large, say 75° or so, the convergence of the developments in θ is so bad that even the qualitative validity of our formulas is impaired. However, the expression (30) or (31) is rather the most general of any of our results, and it is hard to believe that τ could be reduced by increasing ν.

(3) Incorrect calibration. If actually the susceptibility were only about 20 rather than 40 per cent higher than the conventional value, the $1/T$ difficulty would disappear, as (31) or (32) shows that then τ is reduced by about a factor 4. Such an adjustment would require that the interatomic forces in the clathrate make the susceptibility about 20 per cent higher than the gaseous value at room temperatures, for MEYER's measurements on the susceptibility were calibrated on the assumption that the susceptibility had the conventional value at ambient temperatures. This possibility does not seem likely, especially since the use of the smaller crystalline potentials implied by the smaller $\Delta\chi$ diminishes the deviations of the susceptibility from that for free molecules.

(4) Finally, there is the possibility that the MEYER experiments did not detect the $1/T$ term simply because he made his measurements with an alternating field of 175 c/s. The derivation of the term in $1/T$ assumes that there is thermal equilibrium at each instant of time, so that the distribution between the states $\frac{1}{2}$, 0 and $-\frac{1}{2}$, 0 is given by the Boltzmann factor. However, if the time involved for a switch between these two states is long compared with 1/175 sec, there will not be the proper adjustment of population between the two states, and the $1/T$ term will not be detected. We are therefore led to examine in the next section the magnitude of the relaxation time. We will mention in advance that this discussion seems to indicate that it is just possible that the relaxation time is long enough to inhibit the $1/T$ term when the frequency has as high a value as that used by MEYER.

RELAXATION PROCESSES AT LOW TEMPERATURES

We must distinguish between two different relaxation processes which can be operative in the NO clathrate.

(1) Spin–lattice relaxation. Reversal of the electronic angular momentum $\Omega = \Lambda + \Sigma$ requires that one turn over both the orbital and spin angular momentum. Our crystalline potential furnishes a mechanism for reversing Λ, but not Σ. This is because we have included only the diagonal part $\lambda\Lambda\Sigma$ of the spin–orbit interaction $\lambda L \cdot S$. A reversal mechanism for both Λ and Σ is provided when we include in addition to the crystalline potential the matrix elements of the part

$\lambda(L_{x'}S_{x'}+L_{y'}S_{y'})$ of the spin–orbit interaction which is non-diagonal in both Λ and Σ, and which joins the ground state with excited electronic states. Because of the Kramers degeneracy, the resulting relaxation processes can only be of non-adiabetic variety and are presumably of the Raman type as in titanium alum. (The direct processes are negligible because of the weak magnetic fields employed experimentally and also for other reasons.) The theoretical relaxation time varies inversely as the sixth power of the distance to excited electronic levels,[9] which is about 100 times as great as in titanium alum. The observed relaxation time of about 10^{-9} sec in titanium alum at helium temperatures thus corresponds to a relaxation time of about 10^3 sec in NO, even not allowing for the smaller spin–orbit parameter of NO or for the fact that the crystalline fields are smaller in clathrates than in alums. We thus believe this type of mechanism to be unimportant. Another type of process is caused by uncoupling of the spin from the molecular axis by the vibrations of the molecule about its equilibrium position. This effect can give matrix elements non-diagonal Σ, and combination of it with the crystalline potential perhaps provides a mechanism for reversing both Λ and Σ. Because of the smallness of the value of B and of the crystalline potential, we believe this relaxation process to be inconsequential, but further study is desirable.

(2) Spin–spin interaction. Our model as it stands is incapable of yielding resonance or cross-relaxation, as $\Delta\Sigma = \pm 1$, $\Delta\Lambda = \mp 2$ is a magnetically forbidden transition. However, this is not true when one includes the perturbing effect of the spin–orbit interaction connecting the ground state with excited electronic states, which mixes a little $^2\Sigma$ into the $^2\Pi$ ground level. The amount of this mixing can be determined from the observed Λ-doubling in the NO molecule, as the writer will discuss elsewhere, and one finds that in consequence the magnetic moment is like that of a fictitious spin $\frac{1}{2}$ with $g_\perp = 0{\cdot}35 \times 10^{-2}$. The corresponding contribution to $g_\parallel$ is negligible. However, a small $g_\parallel$ is generated by the crystalline field, because of the mechanism that gives the τ term in equation (30). The resulting value of $g_\parallel$ is $0{\cdot}36\tau^{\frac{1}{2}}$.

The question now arises whether even if spin–lattice coupling is too slow to give equilibrium at 175 c/s, the spin–spin heat capacity due to dipolar interaction is so large that the adiabatic susceptibility is substantially equivalent to the isothermal, and at the same time the cross-examination is sufficiently powerful that the adiabetic rather than isolated susceptibility is achieved. Otherwise, the $1/T$ term is diminished or suppressed. The specific heat is caused mainly by $g_\parallel$ and has approximately the value $(N\beta^2 g_\parallel{}^2/12kT^2)(H^2+H_0^2)$, where H_0, the internal field caused by dipolar interaction, has roughly the value 5 G. In this connection, one should note that N is 36 per cent of the number of cavities, as this is the fraction filled in MEYER's experiment. As MEYER used fields of only 2 G peak, the condition $H^2 \ll H_0^2$ is satisfied, and the isothermal and adiabatic susceptibilities are sufficiently equal. The spin–spin relaxation frequency $1/t_{ss}$ is of the order* $10^{-1}(g_\perp^2/g_\parallel)\beta H_0$. The resulting value of $1/t_{ss}$ is of the order 10^2 sec^{-1}. Substantially, the same value is obtained if instead of using orders of magnitude considerations, one employs the Kronig–Bouwkamp model based on a Gaussian distribution of internal fields. As the achievement of adiabatic equilibrium in an applied field of frequency ν_0 begins to be inhibited when $2\pi\nu_0 \sim 1/t_{ss}$, one sees that 175 c/s (MEYER's frequency) is in the frequency region where it is conceivable that relaxation effects should begin to manifest themselves.

All this discussion of spin–spin relaxation neglects the interaction of the spin with the nuclear spin of the nitrogen nucleus. Since this interaction conserves the total angular momentum about the molecular axis, it presumably does not ameliorate the relaxation process except in so far as the nuclear moment is, *ipse sui*, a faster relaxer because of interaction of its quadrupole moment with the crystalline field, etc.

It is clear that the questions of relaxation and resonance connected with the small $g_\perp$, and also the synthetic $g_\parallel$ created by the crystalline field are of interest and deserve further study. The magnetic moments involved are somewhat unusual

* The relaxation frequency is taken proportional to $g_\perp{}^2/g_\parallel$ rather than $g_\perp$ to allow for the spectral width of the dipolar field arising from $g_\parallel$. The extra power 10^{-1} is included because the two nearest neighbors of a given molecule are located along the trigonal axis, and so coupling to such molecules is incapable of reversing the angular momentum about the molecular axis.

in that they are intermediate between the usual nuclear and electronic cases in magnitude. Molecular beam experiments on $g_\perp$ in the gas (there is no appreciable $g_\parallel$ here) are in progress at Ramsey's laboratory at Harvard.

NEED FOR FURTHER MEASUREMENTS

Further experimental data on the NO clathrates are much to be desired since the theory seems to involve so many ambiguities and difficulties. The following possibilities are suggested.

(1) Measurements on single crystals, that will isolate $\chi_\parallel$ and $\chi_\perp$. Our troublesome $1/T$ arises from $\chi_\parallel$.

(2) Relaxation experiments where χ is measured at a variety of frequencies. A constant field parallel to the molecular axis could be added to study the difference between the isothermal and adiabatic susceptibilities.

(3) Resonance experiments. Although in the usual approximation $\Lambda = \pm 1$, $\Sigma = \mp \frac{1}{2}$, there is no activity, we have already called attention to the fact that in higher approximations there is a small $g_\perp$ and probably a somewhat larger $g_\parallel$. The resonance pattern should be interesting because it is complicated by interaction with the magnetic moment of the nitrogen nucleus.

(4) Measurements on samples with varying amounts of magnetic dilution, possibly by changing the amount of dissolved NO or using other materials, such as zeolites, or NO trapped in ordinary solids where its rotation is frozen out more completely.

REFERENCES

1. MEYER H., O'BRIEN M. and VAN VLECK J. H., *Proc. Roy. Soc.* **243A,** 414 (1957).
2. FONER S., MEYER H. and KLEINER W. H., *J. Phys. Chem. Solids* **18,** 273 (1961).
3. MEYER H., *J. Phys. Chem. Solids* **20,** 238 (1960).
4. SOLBAKKEN A. and REYERSON L. H., *J. Phys. Chem.* **63,** 1622 (1959).
5. VAN VLECK J. H., *The Theory of Electric and Magnetic Susceptibilities*, Section 67. Oxford University Press, London (1932).
6. Cf., for instance, WIGNER E. P., *Group Theory*, Chapter XV, John Wiley, New York (1959) (or original German edition).
7. WANG S. C., *Phys. Rev.* **34,** 249 (1929); our mathematical formalism also shows considerable resemblance to that in the Renner effect, RENNER R., *Z. Phys.* **92,** 172 (1934) or in the dynamical Jahn–Teller effect [e.g. HOBEY W. D. and MCLAEHLAN A. D., *J. Chem. Phys.* **33,** 1699 (1960)].
8. MEYER H. and SCOTT T. A., *J. Phys. Chem. Solids* **11,** 215 (1959).
9. VAN VLECK J. H., *Phys. Rev.* **57,** 436 (1940).

J. Phys. Chem. Solids Pergamon Press 1961. Vol. 20, Nos. 3/4, pp. 255–267. Printed in Great Britain.

PHOTOCONDUCTIVITY AND CHEMISORPTION KINETICS IN SINTERED ZINC OXIDE SEMICONDUCTOR*

D. B. MEDVED

Physics Section, Convair Division of General Dynamics Corporation, San Diego, California

and

Department of Physics, University of Pennsylvania, Philadelphia, Pennsylvania.

(*Received* 9 *May* 1960; *revised* 7 *November* 1960)

Abstract—Decay kinetics of the photoconductivity of zinc oxide are measured as a function of previous intensity of illumination and ambient oxygen pressure. The analysis of the measured kinetics is carried out in terms of a model wherein the basic process is the penetration of a surface barrier by the photoconduction electrons and the consequent formation of adions. The model is used to derive a generalized Elovich equation.

1. INTRODUCTION AND SUMMARY OF PREVIOUS WORK

ZINC oxide (ZnO) has been extensively reported in the literature as a typical *n*-type metal oxide semiconductor.[1, 2] ZnO is obtainable as a very pure white powder of small particle size† (approximately 1μ in diameter); the powder exhibits negligible conductivity. If this powder is compressed and then sintered at temperatures in the neighborhood of 1000°C, it becomes a semiconductor without admixture of foreign impurity atoms. The change in the conducting properties and the corresponding *n*-type behavior have usually been considered to originate from the formation of interstitial zinc atoms which act as donor centers (the zinc excess is formed during the sintering process as oxygen leaves the lattice).[1, 2, 3] THOMAS[4] has investigated the question of interstitial zinc in single crystals of ZnO grown by the Scharowsky method. From this work he concludes that unless the oxide undergoes special treatment, e.g. rapid quenching from an atmosphere of nearly saturated zinc vapor, it will contain very little interstitial zinc. Infrared absorption measurements[5] in the region 6–9μ have shown that for the "undoped" single crystal there are donor levels at the appropriate energy below the conduction band, which before the work of THOMAS were assumed to be those associated with interstitial zinc. It is the intent of this paper to show that the measurement of photoconductance decay kinetics in sintered ZnO is consistent with the interpretation and derivation of the Elovich equation of chemisorption; thus, the identity and origin of the donor system is not essential to the ensuing discussion. In either case, the assumption of the existence of a donor system which is effectively ionized at room temperature is sufficient.

The use of polycrystalline ZnO for the study of the influence of ambient atmosphere on the photoconductance brings out features which are not evident from the work on single crystals.‡ The large surface-to-volume ratio of the grains and grain boundaries (about 10^5 cm^{-1}) in the sintered medium is about two orders of magnitude greater than for the single crystal specimens used. In

* Supported in part by AF19(604)–5554 ARPA Order 42–59, and in part by AF33(616)–78.

† From the New Jersey Zinc Co., available as their LP grade.

‡ The photoconductivity of single crystals has been studied by COLLINS and THOMAS[7]. Unfortunately, no data on the kinetics of the "slow effect" rise and decay have appeared in this literature.

addition, the wavelength dependence of photoconductance is considerably different than that of the single crystals.[6] Great care must be exercised in any attempt to apply models constructed on the basis of single crystal observations to the sintered medium and conversely. In particular, the photoconductance here measured is essentially due to radiation in the visible region (4000–8000 Å) whereas with single crystals such photoconductance has not been reported. The photoconductance of ZnO has been observed by MELNICK[8] on sintered specimens, by MOLLWO[9] on evaporated thin films, by PAPASIAN *et al.*[10] on powders, and by THOMAS and co-workers[7, 11] at the Bell Telephone Laboratories in single crystals. MOLLWO treats the photoconductive process as a bulk phenomenon wherein the incident light causes second ionization of the singly ionized interstitial zinc. MELNICK,[8] on the other hand, has applied the theory of chemisorption as developed by MORRISON[3] who explained his experimental results on the dark conductivity of ZnO at various temperatures in terms of the effect of ambient oxygen atmosphere.

MELNICK considers that light in the vicinity of the fundamental absorption edge forms hole–electron pairs, the hole migrating toward the surface under the influence of the field of chemisorbed O^-. The oxygen ion when neutralized by the hole, becomes physically adsorbed and hence is in equilibrium with the ambient atmosphere. The electron remains to contribute to the photoconductivity. When the light is turned off, the electrons decay through a surface potential barrier to the physically adsorbed species which now act as surface traps or acceptor sites. The basic rate limiting process proposed is a form of the empirical Elovich equation[12]

$$\frac{dq}{dt} = ae^{-bq} \qquad (1)$$

where q is the surface concentration of chemisorbate and a, b are pressure and temperature dependent parameters. Equation (1) states that the rate of the chemisorption process slows down exponentially with chemisorbate concentration. It was used in an empirical manner by ELOVICH *et al.* to describe observable chemisorption rates of H_2 on ZnO and H_2 on $Cr_2O_3 \cdot MO_3$. TAYLOR and THON[13] extended the applicability of this equation beyond that of the Russian school to many additional cases of chemisorption. MELNICK showed that one is led to the derivation of the Elovich equation by means of the mechanism described above, i.e. the rate limiting process being the transfer of conduction electrons through the surface barrier field. It is necessary to postulate a one-to-one correspondence between loss of a conduction electron and formation of a chemisorbed oxygen ion.

Unfortunately, the interpretation of his experimental data was considerably complicated by his choice of sample geometry. Since the sample is photoconducting, it also is absorbing the incident radiation and considerable variation of intensity with depth into the sample occurs. A continuous spectrum of time constants associated with the photoconductivity rates results and hence the basic processes are rather thoroughly masked when one studies the experimental rise and decay curves obtained with the "thick" sample. Consequently, only indirect methods could be utilized to study the rise and decay kinetics in terms of the suggested theory (cf. Fig. 11, Ref. 8).

It is the purpose of this paper to show that direct verification of the Elovich decay process can be obtained by working with ultra-thin sintered specimens of zinc oxide. In addition, the saturation of the photocurrent during the rise is discussed and it is shown that this may be achieved in seconds or minutes with a thin sample, whereas in the previous work saturation could not be approached with equivalent intensity even after one month. Finally the limitations of the Elovich equation are examined. It is shown that its integral is an approximation to a more general form which results when depletion of conduction electrons during the chemisorption process is taken into account. Prediction and observation of photodesorption effects has been discussed in other reports and papers.[14, 15]

2. PHOTOCONDUCTIVITY IN THIN SAMPLES

(a) *Preparation of samples and apparatus used*

A typical thin sintered specimen of zinc oxide is prepared in the following manner. Spectroscopically pure zinc oxide is compressed in a steel die at 15,000 p.s.i. and then sintered at 1000°C for a period of approximately 1 hr. The pellet is mounted on a wooden block with Duco cement and sliced on a diamond saw to a size of $2 \times 3 \times 12$ mm. Attempts to fabricate thinner samples

Vol. 2
1961

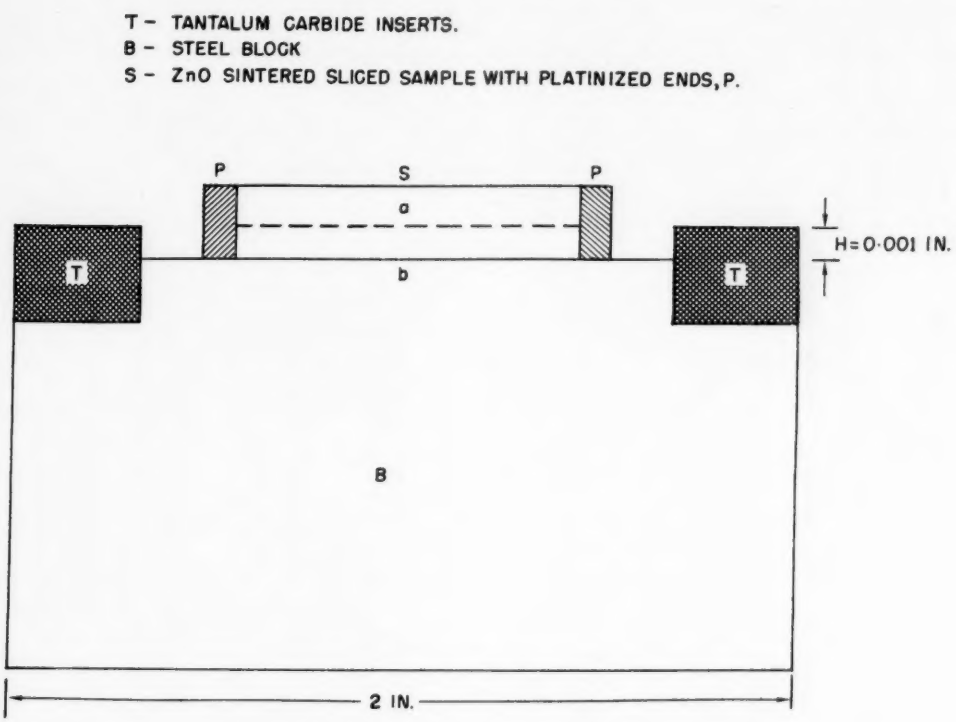

FIG. 1. Mounting system used for preparing thin specimens.

by this method of direct slicing were not successful due to splintering and cracking of the sintered material and hence an alternative technique was developed.

An intact sample of the above dimensions was mounted with a thin layer of Duco cement on the block whose construction is illustrated in Fig. 1. The parts marked (T) are tantalum carbide sections precisely welded into a steel base (B). The surfaces of (T) are 0·001 in. above that of (B). With careful positioning and hand grinding on an optical plate, the 2 mm thickness can be reduced to approximately 0·001 in. Platinum electrodes are then applied to the sample ends P and the sample subsequently mounted in the vacuum-optical system shown in Fig. 2.

The conductance measuring circuit is shown in Fig. 3. In order to amplify the scale of the photoconductance a bucking voltage is applied from a commercial potentiometer in the circuit as shown. Thus, an accurately calibrated voltage to give an arbitrary dark current beading on the recorder was readily available.

To achieve uniform illumination, a special light source using a tungsten strip ribbon filament was employed. The filament operates at 6 V and draws 20 A. The area of the filament was somewhat larger than the sample so that the image could be brought to a sharp focus at the sample by the optical system and still provide uniform coverage. To reduce both ultraviolet which is highly absorbed and infrared as a heating source, a water cell and glass heat filter were incorporated into the optical system. Two transmission grey filters were inserted as needed. These grey filters were perforated metal screens with flat transmissions of 14 and 3 per cent respectively. The radiation falling on the sample is thus essentially in the 4000–8000 Å region where there is very little absorption but still measureable photoconductance. The variation of photoconductance with wavelength in this interval is shown as Fig. 4.

(b) *Background discussion*

Figure 4(a) shows a typical photoconductivity rise and decay curve obtained with a thin sample of sintered zinc oxide mounted in the system of Fig. 2 (Fig. 4(a) also serves as a means of defining our terms and symbols for the following discussion). The rise is characterized by a rapid approach to saturation in a matter of minutes or seconds depending on the intensity of the illumination, whereas rise curves in MELNICK's work, e.g.

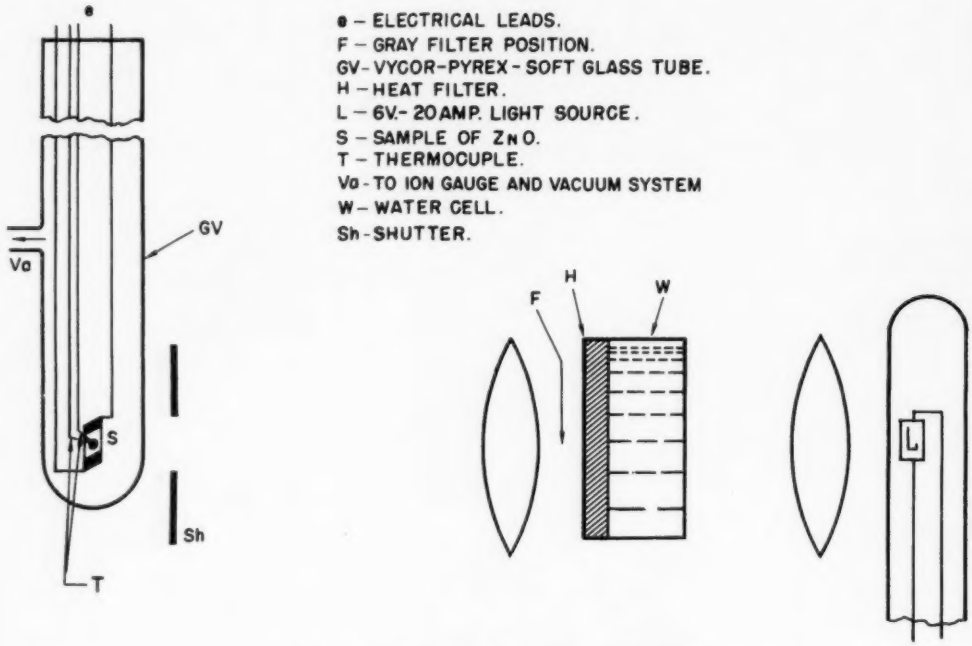

FIG. 2. Optical system and mounted ZnO sample.

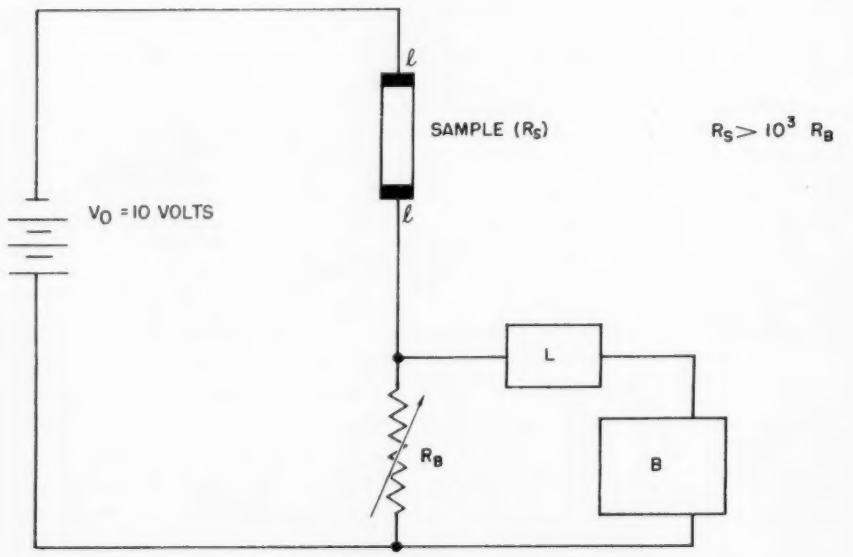

L – LEEDS & NORTHRUP POTENTIOMETER.
B – BROWN "ELECTRONIK."

FIG. 3. Conductance circuit.

Fig. 2 of Ref. (8), were nonsaturating even after seven decades in time. The decays from a value ΔG_s in the runs typified by Fig. 4(a) were essentially a unique function of the photoconductance ΔG, independent of how ΔG is achieved, in sharp contrast to the different decay modes observed previously in the thick samples (see Fig. 9 of Ref. 8).

Thus, the use of the thin sample has effectively reduced the multiplicity of time constant processes previously associated with the rise and decay rates of the photoconductivity.* A discussion of directly extracted experimental results in terms of the consequences of the Elovich equation (1) is now pertinent.

The observed macroscopic photoconductance, ΔG, is considered to be proportional to changes in concentration of conduction electrons, Δn in the

* In practice, even our thinnest samples were still less than 10 per cent transmitting and there is consequently at least a decade spread in the time constant spectrum. However, the effect of the surface being irradiated is amplified when measuring the over-all sample photoconductance for the thin specimens. The approximation to a single lamina with its unique time constant characterization is correspondingly better than for the 2 mm thick samples previously investigated.

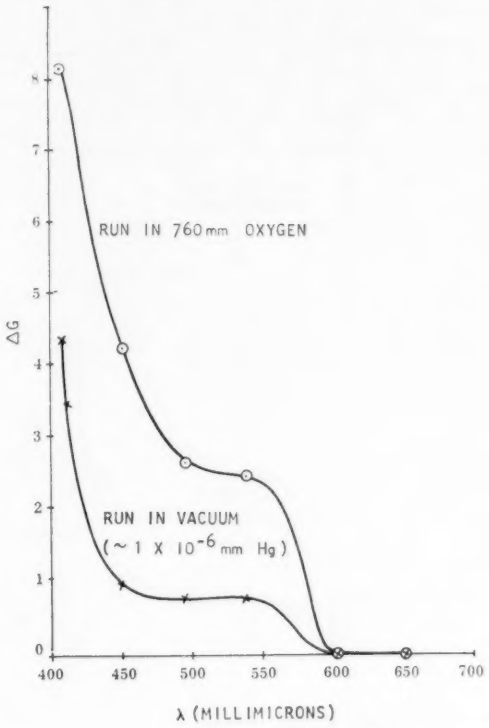

FIG. 4. Photoconductance, ΔG vs. λ for sintered ZnO.

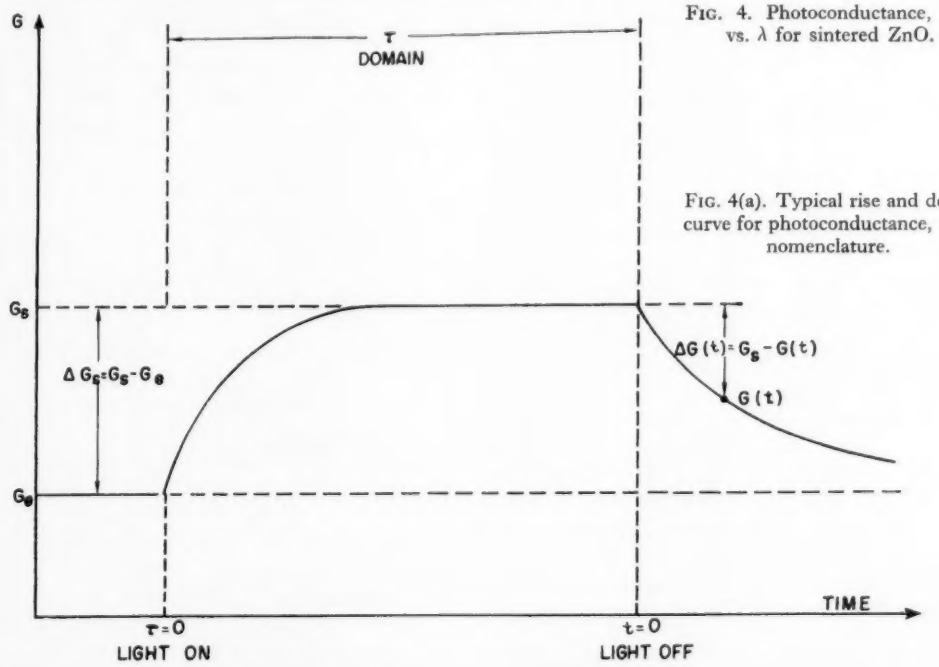

FIG. 4(a). Typical rise and decay curve for photoconductance, and nomenclature.

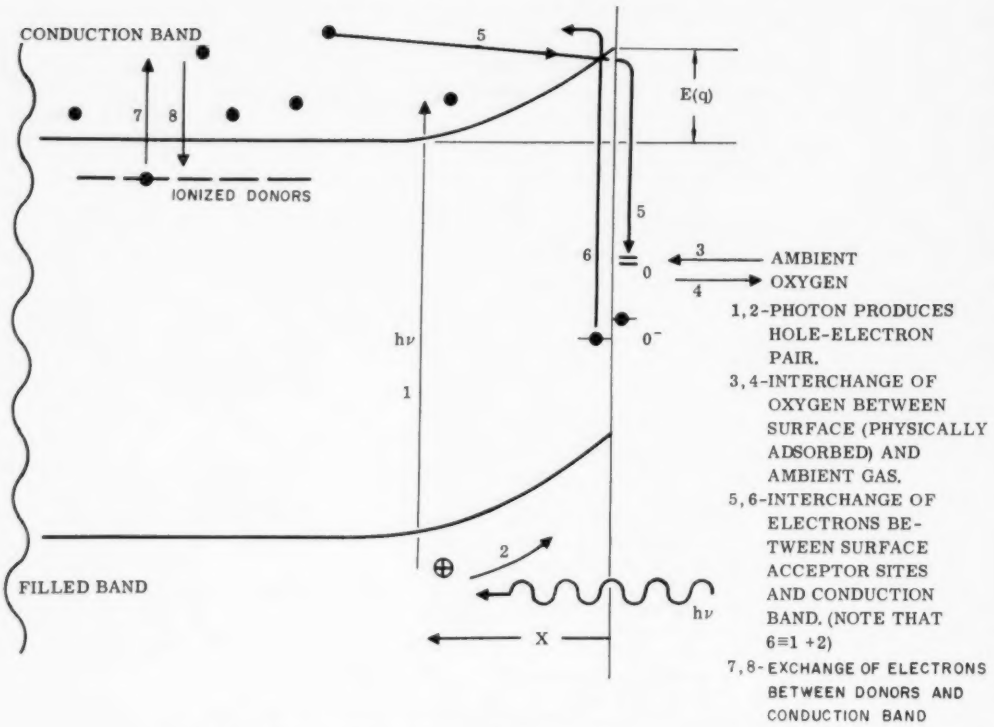

FIG. 5. Model for setting up the rate equations for photoconductivity in ZnO.

"necks" or grain boundaries of the sintered sample. The analysis is performed in terms of conduction electron concentrations, but observable phenomena are described in terms of G, etc. However, we shall generally maintain the same notation for observable parameters as applied to the single grain model. An arbitrary conductance unit (a.c.u.) is used in order to reduce computational work in transferring data from the recorder paper. All the parameters discussed will then be appropriate combinations of an (a.c.u.) with cgs units.†

The Elovich equation (1) is transformed to the more relevant n-language by means of the following argument. It is assumed that during photoconductance rise, every conduction electron added represents a desorbed oxygen and conversely, loss of a conduction electron implies formation of a chemisorbed oxygen ion. Then:

$$\Delta N = +\Delta Q \tag{2}$$

where ΔN represents the change in the number of conduction electrons and ΔQ represents the corresponding change in the number of chemisorbed ions. These and associated processes are shown in terms of a band model in Fig. 5, full description of which is deferred until Section 3. Throughout the following discussion, we neglect a spontaneous desorption term, $S(q)$, corresponding to process 6 in Fig. 5, excited thermally. It is assumed that in the neighborhood of room temperature and below, the contribution of $S(q)$ to the relevant rate processes is negligible ($\Delta E \gg kT$) except near the beginning of the rise or the termination of the decay, i.e. only near equilibrium in the dark (Fig. 4a), where $S(q)$ is evidently necessary for establishment of same, do we need consider it in the rate equations.

† To convert the a.c.u. of the samples described in this work to conductance values in mhos, multiply by 5×10^{-7}.

We have:

$$\Delta N = V\Delta n = V(n_s - n)$$
$$\Delta Q = A\Delta q = A(q - q_s) \tag{3}$$

where subscript (s) signifies values at saturation (see Fig. 4a), V and A are the effective volume and surface area of the grain boundary and n and q are the concentrations of electrons and chemisorbate respectively. Since equation (1) applies only to the decay process (there is no source term), we shall limit this discussion to that region and thus n, q, etc. are considered as functions of t, with $t = 0$ corresponding to commencement of decay from saturation. The time parameter for the rise kinetics will be denoted by τ with $\tau = 0$ being the initiation of the photoconductivity experiment. The desired transformation equation is then

$$q = q_m - x_0 n \tag{4}$$

with $x_0 = V/A$ and $q_m = q_s + x_0 n_s$. It is seen that q_m corresponds to the maximum concentration of chemisorbate attainable.* In terms of the photoconductance decay rate then, equation (1) becomes

$$\frac{d}{dt}(\Delta n) = +Ae^{-B\Delta n} \tag{5}$$

with

$$A = ax_0^{-1} \exp[-bq_s] \tag{5a}$$

$$B = bx_0 \tag{5b}$$

$$\Delta n(t) = n_s - n(t).$$

The integral of equation (5) is

$$\Delta n(t) = \frac{1}{B} \ln(t/t_d + 1) \tag{6}$$

with

$$t_d = \frac{1}{BA} = \frac{\exp(bq_s)}{ab}. \tag{6a}$$

For $t \gg t_d$, Δn becomes a logarithmic function of the time and thus t_d may be designated as the "time constant" of equation (6).† It is seen from equation (6a) that t_d is some inverse function of the intensity of illumination, I, producing the original rise, since one expects lower values of q_s, i.e. cleaner surfaces at saturation, for increasing flux densities of the incident light. The explicit dependence of t_d on I is found in the following manner.

Consider the kinetics of rise; we wish to write the appropriate differential equation in the time domain τ (Fig. 4a). Consistent with our previous discussion, it is assumed that the basic rate limiting process during rise is the penetration of the surface barrier by conduction electrons returning to emptied oxygen sites physically adsorbed on the surface (process 5 of Fig. 5); all other processes are considered essentially as instantaneous adjusting to equilibrium relative to this one. Thus, the desorption process or equivalently, the formation of conduction electrons *vis-à-vis* the photon absorption, is assumed to proceed at a constant rate, L, directly proportional to the light intensity, I, for a given wavelength. The rate equation during the rise is consequently written as a combination of the term L with the decay back into the adsorption sites as characterized by equation (1):

$$\frac{dq}{d\tau} = ae^{-bq} - L. \tag{7}$$

Of interest here is the value of q, $q = q_s$.

At saturation, $dq/d\tau = 0$.

From equation (7)

$$q_s = \frac{1}{b} \ln \frac{a}{L} \tag{8}$$

from which (6a) reduces to:

$$t_d = \frac{1}{bL} \tag{6b}$$

or the time constant of the decay is inversely proportional to the prior intensity of the illumination.

As a final result of the simple theory, we shall calculate the percentage of the decay $\rho(t) = \Delta n(t)/\Delta n_s \times 100$ wherein Δn_s represents the net

* The value $n_m = n_s + x_0^{-1} q_s$ corresponds to the maximum number of electrons available for chemisorption. In the model of Fig. 5, this can be identified with the concentration of donor atoms.

† Perhaps a term such as "characteristic time" would be more appropriate but for the purposes of this report we maintain prior nomenclature.

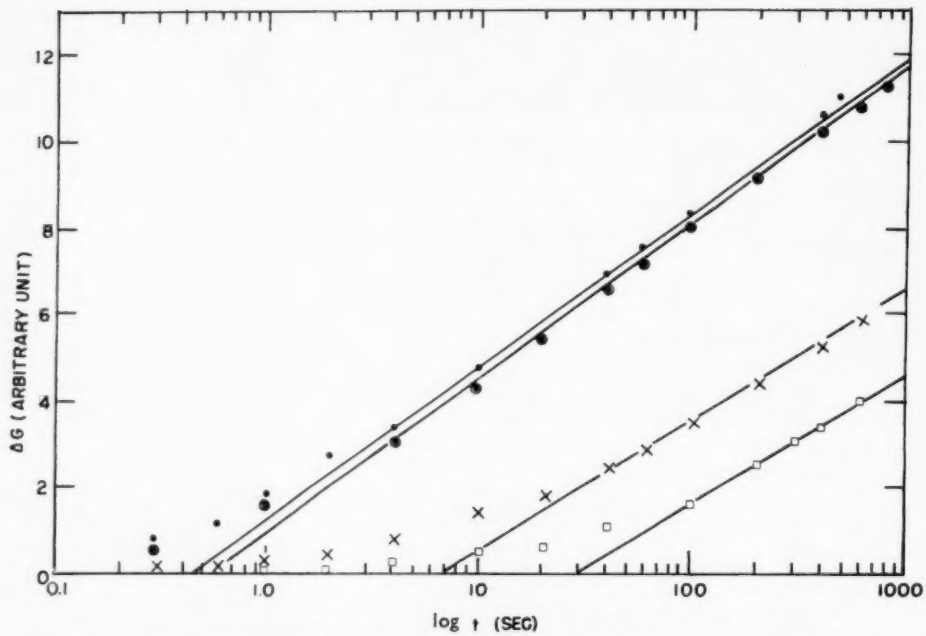

FIG. 6. Photoconductivity decay from saturation (ΔG) as a function of log t for sintered ZnO; 0·001 in. thick.

● P = 760 mm, L = 100 ● P = 2×10^{-2} mm, L = 100
× P = 760 mm, L = 14 □ P = 760 mm, L = 3

increase of the photoconductance from equilibrium in the dark to saturation. By an argument similar to that used in deriving equation (8),

$$\Delta n_s = \frac{1}{B} \ln \frac{L}{A_e} \tag{9}$$

wherein $A_e = a x_0^{-1} e^{-b q_e}$ and we have excluded the term for spontaneous desorption. The expression for $\rho(t)$ is then

$$\rho(t) = \frac{\ln [t/t_d + 1]}{\ln L/A_e}. \tag{10}$$

The equations (6), (6b), (9) and (10) are to be used in the following sections for the interpretation of the experimental data, and as such they become the key criteria for testing the validity of the rate model herein described. In particular it is to be expected that:

1. Plots of ΔG vs. log t should be linear for times $t \gg t_d$.
2. Onset of linearity should consequently be inversely proportional to the intensity of illumination during the rise.
3. Slopes of $\Delta G(\log t)$ should be independent of previous intensity and pressure of ambient.
4. Plots of $\rho(t)$ should be linear but nonparallel for different intensities on log time scale. Nonequal slopes for different pressures are also to be expected since A_e is a pressure dependent factor. Explicit pressure dependence of a, A, and A_e can be calculated using the methods to be discussed in Section 3. However, even without the specifics one may particularize from equation (10) that: (a) the slope of $\rho(t)$ for intensity constant should increase as the pressure increases and (b) the slope of $\rho(t)$ for pressure fixed, should decrease for increase of prior intensity of illumination.

(c) *Experimental results*

Figures 6 through 8 summarize the results of a series of experiments in which the total photoconductance ΔG_s did not exceed 10 per cent of the

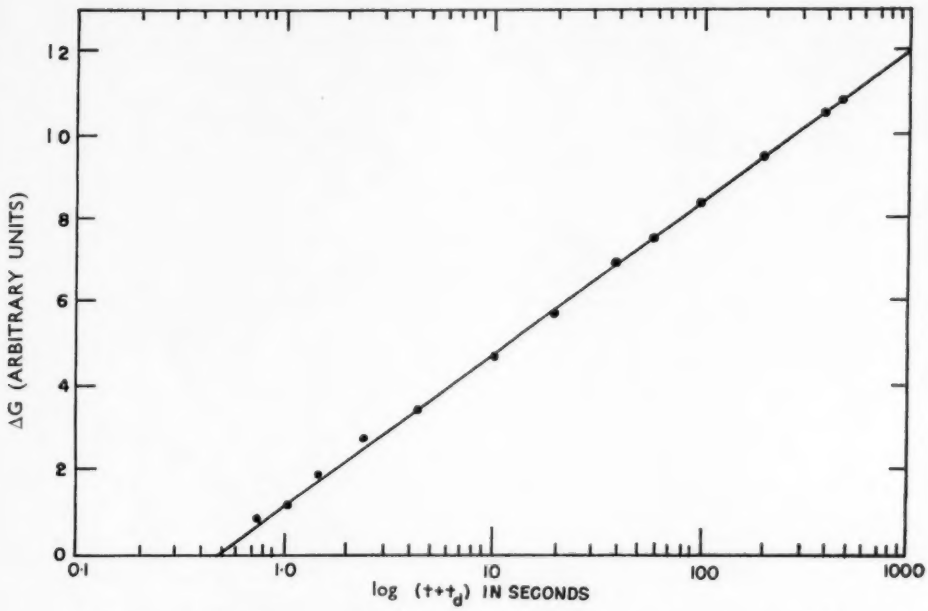

FIG. 7. Decay of photoconductivity ΔG vs. log $(t+t_d)$ for t_d (trial) = 0·45; $L = 100$; $P = 760$ mm.

dark conductance. The reasons for this ceiling on ΔG_s are discussed at length in Section 3; essentially it turns out that the validity of theory discussed above is limited to cases where $\Delta G/G_s$ is considerably less than unity. Intensities are given in terms of percentage transmission of the particular grey filter used.

In Fig. 6, ΔG vs. log t is plotted for the decay of the photoconductance for three intensities at the same pressure and for two pressures at a given intensity. Predictions 1, 2, and 3 which are consequences of equations (6) and (6b) are seen to be followed up to four decades in time. Data of the form shown in Fig. 6 may be displayed more significantly in a ΔG vs. log $(t+t_d)$ plot as shown in Fig. 7. Fig. 6 is considered merely as an exploratory plotting in which the decay is tested for onset of the "Elovich behavior" and an approximate value obtained for t_d. Several trial values of t_d in the neighborhood of the approximate value

Table 1. *Summary of data derived from Figs.* 6–8. *Comparison saturation photoconductance* (ΔG_s) *as measured in the rise curve with* ΔG_s *as calculated from the decay curve parameters*

Relative intensity, L	Pressure P (mm)	Decay time constant, t_d (sec)	Pressure factor, A (a.c.u./sec)	Temperature factor, B (a.c.u.$^{-1}$)	ΔG_s (a.c.u.), measured	ΔG_s (a.c.u.), calculated
100	760	0·46	16	0·70	11·8	10·8
14	760	6·0	16	0·70	6·20	7·1
3	760	25·0	17	0·67	4·0	4·6
100	2×10^{-2}	0·55	10	0·61	12·4	13·2
100	1×10^{-6}	0·85	4·3	0·59	20·0	15·2

$$\rho(t) = 100 \times \frac{\Delta G}{\Delta G_S} = \frac{\ln\left(\frac{t}{t_d} + 1\right)}{\ln\left(\frac{L}{A_e}\right)}$$

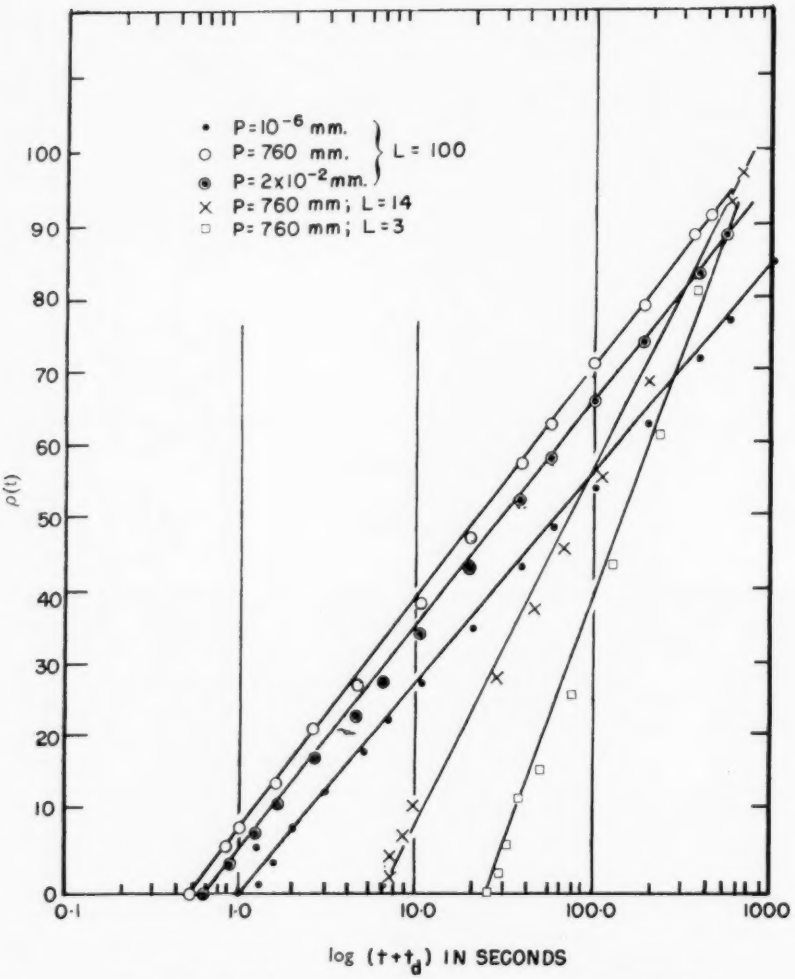

FIG. 8. Per cent decay of the saturation photocurrent vs. log $(t+t_d)$.

result in the best fit being plotted as in Fig. 7. Tabulated values of the "best" t_d are given in column 3 of Table 1.

In Fig. 8, we have plotted $\rho(t)$ as a function of $\log(t+t_d)$, t_d having been obtained in the manner described above. Three pressures for a given intensity and three intensities at a given pressure are displayed as parameters in the curves. It is seen that the change in slopes follows along the general conclusions expressed in Item 4 of the discussion in Section 2(b) relating to equation (10).

A quantitative comparison of the data in Figs. 6–8 and the equations (6), (6b), (9) and (10) is summarized in Table 1. The constancy of B and A,

as calculated from the decay curve characteristics, with intensity of previous illumination, L, and of B with pressure, is noted. The shift in t_d with L is in fair agreement with equation (6b). Finally, the comparison of the saturation photoconductance calculated from decay curve parameters according to equation (9) with the measured values for ΔG_s obtained for rise shows good agreement and an internal consistency of the rate model for rise and decay.

3. THEORETICAL DERIVATION OF THE ELOVICH EQUATION AND THE CHEMISORPTION KINETICS

(a) *Formulation of the differential equations*

The model illustrated in Fig. 5 is used as the basis for discussion of the phenomena at a single grain boundary. In using this model we make the following simplifying assumptions:

1. The only shallow traps are the volume traps associated with the ionized donors. The equilibrium between processes 7 and 8, i.e. the interchange of electrons between the conduction band and the donor states, is established in times short compared to the long times involved in the return of electrons to the surface acceptors. At room temperatures and above, we assume that these donors are all ionized.
2. Small percentage changes in the concentration of surface populations produce relatively large percentage changes in volume concentrations of conduction electrons $\Delta n/n \gg \Delta q/q$.
3. The effect of light is to cause a constant rate of electron excitation or oxygen desorption by either (a) the production of hole–electron pairs (processes 1 and 2) when the sample is exposed to u.v. or (b) direct ionization (process 6) which is assumed to be connected with the photoconductance in the 4000–6000 Å region (Fig. 4). In case (a), the hole moves under the influence of the electric field produced by the surface charge. The rate of electron excitation is proportional to the capture cross-section of a filled band electron for an incident photon and the intensity of illumination, I. In order to analytically obtain the rate of desorption which is after all the rate of the net electron transfer to the conduction band, it would be necessary to set up simultaneous differential equations involving recombination rates of holes and electrons, the equation of motion of the hole in the electric field which itself is a function of q, etc. However, as discussed below we will consider that either the hole recombines with a conduction electron or migrates to the surface instantaneously relative to the basic rate limiting process, the decay of conduction electrons to the surface sites. The contribution of the hole–electron pairs to the photoconductivity is thus neglected. (In effect then this is a fourth assumption.)

   The treatment of case (b) would proceed somewhat differently. The electrons from the adsorbed ions are excited directly into the conduction band by incident photons (process 6). This essentially constitutes a bimolecular process involving the light intensity, the capture cross section of a surface adion for the incident photons and the concentration of these chemisorbed species, q_c. (Even though this is a bimolecular process, case (b) cannot be distinguished from case (a) in this work, where time effects are measured in seconds or minutes. Experiments using pulse techniques should lead to a resolution of this question.)

The rate equations for concentration changes of physically adsorbed species and chemisorbate are written within the framework of Fig. 5 and these assumptions in the following manner:

$$\frac{dq_p}{dt} = \eta\left(1-\frac{q_p}{q_{po}}\right) - \zeta_p q_p - \frac{dq_c}{dt} \qquad (11)$$

(3) (4)

$$\frac{dq_c}{dt} = \sigma q_p \eta_e^* - \zeta_c q_c - L \qquad (12)$$

(5) (6) (1+2)

wherein

q_p = concentration of physically adsorbed species
q_c = concentration of chemisorbed species
η = number of molecules of ambient striking each cm^2 of surface per sec

η_e^* = number of conduction electrons penetrating each cm^2 of surface
σ = capture cross section of physically adsorbed atoms for an electron on the surface
ζ = rate of desorption due to thermal excitation
L = rate of photodesorption.

The numbers written under each term correspond to the processes of Fig. 5. Process 3 (first term) of equation (11) is written for a Langmuir monolayer adsorption isotherm wherein q_{po} represents the maximum number of available sites for physical adsorption. Process 5 (first term) of equation (12) will be seen to be the equivalent of the basic rate-limiting phenomenon which is expressed by equation (1). In the form given (equation 12), it represents a "bimolecular" surface reaction between the electrons per cm^2 sec^{-1} penetrating the surface barrier and the physically adsorbed species. η_e^* is found in a manner analogous to the derivation of the Richardson–Dushman equation for thermionic emission, i.e.

$$\eta_e^* \simeq nv(T) \exp[-E(q_c)/kT]$$

wherein n is the volume concentration of conduction electrons, $v(T)$ is the thermal velocity and $E(q_c)$ represents the energy height of the surface barrier for electrons which is a function of the chemisorbate concentration.

The fourth assumption is now applied; the rate processes governing physical adsorption are fast, relative to process 5 ($\dot{q}_p \gg \dot{q}_c$), and hence in the absence of light ($L = 0$), the system of equations (11) and (12) reduces to:

$$\frac{dq_c}{dt} = \sigma q_p n v \exp[-E(q_c)/kT] - \zeta_c q_c. \quad (13)$$

Some additional assumptions are now needed. Consider the second term of equation (13) which represents the spontaneous desorption of chemisorbed species. It may be written as

$$\zeta_c q_c = \nu_s(T) \exp[-E_c/kT]\, q_c$$

where ν_s is the thermal vibration frequency (the number of jumps per sec) and E_c the binding energy of chemisorption assumed to be in the neighborhood of 1–3 eV. Note that $E_c \neq E(q_c)$; in fact $E_c \gg E(q)$ for all values of q and during a major portion of the decay, the first term of (13) is dominant.

$$\therefore \frac{dq}{dt} \simeq a'(P,T)\, n \exp[-E(q)/kT] \quad (13a)$$

wherein $a'(P,T) = \sigma(T)\ \bar{v}(T)\ q_p(T,P)$ and subscript c has been omitted. Correspondence with equation (1) is then achieved by invoking the second assumption, namely, small changes in q produce large changes in n such that

$$E(q) \simeq e^2 q / C_a$$

wherein C_a is the capacitance of the surface barrier independent of q^*,† and where n is assumed constant in the coefficient of the exponential.

Then:

$$a \geqslant \sigma v q_p n$$

$$b \geqslant \frac{e^2}{C_a kT}$$

and

$$\frac{dq}{dt} = a e^{-bq}.$$

Since a and hence A (in the equation transformed to the n-language) is now a function of n, the integral of equation (5) is no longer straightforward. If $y = \Delta n / n_s$ then equations (4), (5), (13a) and (13b) give:

$$\frac{dy}{dt} = A'(1-y)\, e^{-\beta y}$$

with

$$A' \equiv a' \exp[-bq_s/x_0]$$

$$\beta \equiv bx_0 n_s = Bn_s.$$

† The assumption of constant capacitance is equivalent to linearizing $E(q)$. Let $E(q) = E(q+\Delta q)$ and expand about q_s. Then

$$E(q_s+\Delta q) = E(q_s) + \left[\frac{\partial E}{\partial(\Delta q)}\right]_{q_s} \Delta q + \ldots$$

and the rate equation is written

$$\frac{d}{dt}(\Delta q) = A' n \exp[-E(q_s)/kT] \times \exp\left\{[-\partial E/\partial(\Delta q)]_{q_s} \frac{\Delta q}{kT}\right\}.$$

The integration then gives:

$$J = \int_0^y \frac{e^{\beta y}\, dy}{1-y} = \int_0^t A'\, dt = A't$$

and J is evaluated by expansions for $y < 1$ as

$$J = \frac{1}{\beta} \sum_{p=0}^{\infty} \frac{(\beta y)^{p+1}}{(p+1)!} + \text{terms of order } y^2$$

and one obtains the equation

$$\beta A't = (e^{\beta y} - 1) + 0(y^2) \tag{15}$$

which reduces to

$$\Delta n = \frac{1}{B} \ln \left(\frac{t}{t_d} + 1 \right) \tag{16}$$

for $y \ll 1$, wherein t_d is defined as

$$t_d \equiv \frac{1}{B(n_s A')}. \tag{16a}$$

Correspondence of equations (16) and (16a) with equations (6) and (6a) is obtained by defining $A = n_s A'$; thus, one can recover the original Elovich expression by using the saturation value of conduction electron concentration instead of $n(t)$ in the coefficient of the exponential.

It should be noted that the first correction terms are of order y^2; in all of the experimental work reported here $\Delta n/n_s$ was less than 10 per cent. In fact, decays from photoconductance obtained with higher intensities of illumination have shown marked deviations from linear behavior on log time scale.

4. CONCLUSIONS

Photoconductance measurements on sintered samples of ZnO become meaningful and readily interpreted if the sample thicknesses are made small relative to the reciprocal of the absorption coefficient. Rapid saturation of photoconductance is observed in minutes or seconds and the decay kinetics are directly comparable with the predictions of the rate equations for chemisorption as given by ELOVICH, CHARACHORIN and others. Considerable work remains to be done in cleaning up the question of the surface energetics (i.e. the type and binding energy of the adsorbed species which is assumed to be interacting with the bulk electrons); experimentation of the type described in this report concomitant with photodesorption measurements as a function of wavelength (monochromatic instead of white light) appears to be a promising approach in general for the elucidation of the energetics and kinetics of chemisorption processes.

Acknowledgements—The author wishes to acknowledge the assistance of R. D. MOORE of the Convair-San Diego Physics Section in obtaining corroborating data of the decay kinetics and for the work on the wavelength dependence of the photoconductance.

I wish to thank P. H. MILLER, formerly of the University of Pennsylvania, now with the General Atomic Division of General Dynamics, for his interest in this work.

REFERENCES

1. FRITSCH O., *Ann. Phys. Lpz.* **22,** 375 (1935).
2. HAHN E. E., *J. Appl. Phys.* **22,** 855 (1951).
3. MORRISON S. R., *Advanc. Catalys.* **7,** 249 (1957).
4. THOMAS D. G., *J. Phys. Chem. Solids* **3,** 229 (1957).
5. THOMAS D. G., *J. Phys. Chem. Solids* **10,** 47 (1959).
6. MOORE R. D., Convair Physics Section Report ZPh–050, p. II–506 (1959).
7. COLLINS R. J. and THOMAS D. G., *Phys. Rev.* **112,** 388 (1958).
8. MELNICK D. A., *J. Chem. Phys.* **26,** 1136 (1957).
9. MOLLWO E., *Ann. Phys. Lpz.* **3,** 240 (1948).
10. PAPASIAN H. A., FLINN P. A. and TRIVICH D., *J. Electrochem. Soc.* **104,** 84 (1957).
11. THOMAS D. G. and LANDER J. J., *J. Phys. Chem. Solids* **2,** 318 (1957).
12. CHARACHORIN F. and ELOVICH S., *Acta Physicochim, USSR* **20,** 227 (1945).
13. TAYLOR H. A. and THON N., *J. Amer. Chem. Soc.* **74,** 4169 (1952).
14. MEDVED D. B., Semi-Annual Report No. 7 on Semiconductor Research, University of Pennsylvania, June 1954.
15. MEDVED D. B., *J. Chem. Phys.* **28,** 870 (1958).

J. Phys. Chem. Solids Pergamon Press 1961. Vol. 20, Nos. 3/4, pp. 268–273. Printed in Great Britain.

A RELATION BETWEEN THE BINDING ENERGY AND THE BAND-GAP ENERGY IN SEMICONDUCTORS OF DIAMOND OR ZINC-BLENDE STRUCTURE

P. MANCA

Istituto di Fisica dell'Università di Cagliari, Cagliari, Italy

(*Received* 14 *December* 1960; *revised* 16 *March* 1961)

Abstract—From an empirical calculation of bond energy, of semiconductors of diamond and zinc-blende structures, and of some wurtzite-type, it is revealed that between the gap energy (E_g) and single-bond energy (E_s) there exists a linear correlation which, for the different series of binary semiconductors of tetrahedral coordination taken into consideration here, can be expressed by a relation of the type:

$$E_g = a(E_s - b)$$

where a and b are characteristic constants of the series $A^{IV}A^{IV}$, $A^{III}B^{V}$, $A^{II}B^{VI}$. The correlations found for the said semiconductors are not valid for the compounds $A^{I}B^{VII}$ of zinc-blende type structure and for the two oxides ZnO, CdO of wurtzite-type structure. This fact is attributed to the almost completely ionic character of the bond in these compounds, because of which the localization of the electrons along the valence bonds is negligible.

1. INTRODUCTION

ACCORDING to WELKER's postulate,[1] the gap energy depends on the binding energy and the effective charge of atoms, the gap energy being related to a great number of parameters[2–11] that are directly or indirectly connected with the binding energy or the lattice energy. Of these, the bond length, taken into consideration by GOODMAN[12], leads to a linear relation between $\sqrt{E_g}$ and $10/d^2$, where E_g is the gap energy and d the bond length, in diamond-type structures. According to PAULING[13] in fact, the covalent bond energy, between two equally shared electrons at the minimum bond distance, is related to the reciprocal of the bond length so that the gap energy, of the pure covalent semiconductors of diamond-type structure, should exhibit a similar relationship as a function of bond strength or bond length. In a recent paper, SUCHET[14], after a study of the importance of the covalent coordination and of the structure type in the prediction of the semiconductivity of inorganic compounds, relates the atomic and structural results to the value of the energy gap by means of empirical formulae allowing the computation of the homopolar and heteropolar contributions to this value.

The object of this paper is to calculate, according to PAULING's principle of additivity of bond, the single-bond energy of the semiconductors of diamond and zinc-blende type structure, and to study the relationship found between the gap energy and the bond strength.

2. CALCULATION OF SINGLE-BOND ENERGY

According to the criterion of PAULING[15], the single-bond energy of the binary semiconductors being taken into consideration here, may be represented as the sum of a non-polar contribution D_{np}(A–B) and polar contribution D_p(A–B). The former is taken here to be the geometric mean of the non-polar bond energy of the two atoms:

$$D_{np}(A\text{–}B) = [D(\text{A–A})\, D(\text{B–B})]^{1/2} \qquad (1)$$

and the latter to be proportional to the square of the difference between the electronegativity, X_A and X_B respectively, of the atoms in question:

$$D_p(\text{A–B}) = (X_A - X_B)^2. \qquad (2)$$

Table 1

Compounds	E_s	Ref.	Elements	E_s	Ref.
Si–I	50·9	(15)	C–C(dia)	84·5	(18)
Ge–I	48·1	(19)	Cl–Cl	58·0	(15)
Sn–Cl	76	(20)	Br–Br	46·1	(15)
B–Br	94·6	(21)	I–I	36·1	(15)
Al–Br	99·2	(22)	N–N	38·4	(15)
Ga–I	66·9	(22)	P–P	51·3	(15)
In–Br	76·1	(21)	As–As	35	(20)
Zn–S	101·4	(21)	Sb–Sb	30·2	(15)
Cd–Se	73·8	(22)	S–S	63	(23)
Hg–S	64·6	(22)	Se–Se	50	(23)
			Te–Te	49	(23)

In this way the single-bond energies of the semiconducting elements of group IV have been calculated, starting with experimental values of the bond energies of their compounds, the results being in agreement with the values given by PAULING[15]. Similarly the bond energies of the elements of groups IIIb and IIb have been calculated in order to obtain the bond energies of $A^{III}B^{V}$ and $A^{II}B^{VI}$ semiconductors. The polar contribution D_p(A–B) was calculated using the values of GORDY and THOMAS[16] for the electronegativities of atoms, except for Te, for which the value (2·25) recently proposed by CLIFFORD[17] was used. Table 1 contains the single-bond energy (E_s kcal/mole) of compounds and elements, used in our calculation; in each case the calculation was carried out using the formula involving the geometric mean.

3. RESULTS

The results are gathered in the following tables, where next to each element the electronic configuration of the valence ground state is indicated, thus permitting the variation of the bond energy to be followed as one passes to interatomic bonds with valence levels of gradually increasing total quantum number. The upper numbers represent the calculated single-bond energies (kcal/mole) and the lower numbers the optical gap energies (eV) at 300°K.

Figure 1 indicates schematically the process of formation of the semiconducting compounds

Table 2. *Single-bond and gap energies of the* $A^{IV}A^{IV}$ *and* $A^{IV}B^{IV}$ *semiconductors*

	C $2(s^2p^2)$	Si $3(s^2p^2)$	Ge $4(s^2p^2)$	Sn $5(s^2p^2)$
C $2(s^2p^2)$	84·5 5·2	72·0 2·86	— —	— —
Si $3(s^2p^2)$	72·0 2·86	43·4 1·12	40·3 0·89*	37·0 0·59*
Ge $4(s^2p^2)$	—	40·3 0·89	37·5 0·66	34·5 0·40*
Sn $5(s^2p^2)$	—	37·0 0·59	34·5 0·40	31·6 0·08

* Values deduced from $E_g = f(E_s)$.

Table 3. Single-bond and gap energies of $A^{III}B^{V}$ semiconducting compounds

	N $2(s^2p^3)$	P $3(s^2p^3)$	As $4(s^2p^3)$	Sb $5(s^2p^3)$
B $2(s^2p)$	95·8 ~ 5·0	84·4 4·2*	69·5 3·0*	64·6 2·6*
Al $3(s^2p)$	106·8 4·0*	71·8 3·1	58·2 2·16	50·8 1·52
Ga $4(s^2p)$	97·1 3·3	60·6 2·24	49·0 1·35	42·2 0·71
In $5(s^2p)$	85·8 2·5*	47·5 1·25	38·0 0·35	32·2 0·16

* The values ~5·0 and 3·3 eV for the gap energy of BN and GaN are quoted from WRIGHT[24].

Table 4. Single-bond and gap energies of $A^{II}B^{VI}$ semiconducting compounds

	S $3(s^2p^4)$	Se $4(s^2p^4)$	Te $5(s^2p^4)$
Zn $4(s^2)$	101·4 3·6	88·5 2·6	81·8 2·2
Cd $5(s^2)$	84·9 2·5	73·8 1·7	67·6 1·41
Hg $6(s^2)$	64·6 0·97*	55·8 0·32*	51·6 0·02

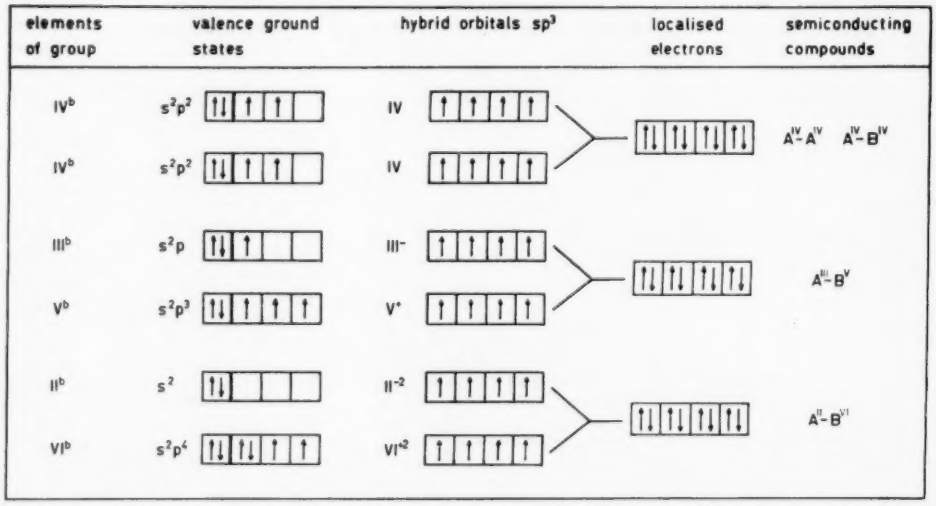

FIG. 1. Schematic process of bond formation in $A^{IV}A^{IV}$, $A^{III}B^{V}$ and $A^{II}B^{VI}$ semiconductors.

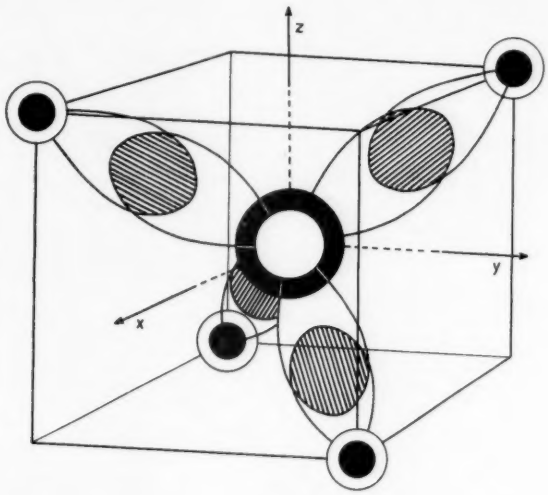

FIG. 2. Angular distribution and overlapping of the sp^3 hybrid wave function in bond formation of semiconductors with tetrahedral coordination.

Vol. 20
1961

considered here, starting from the ground states of the isolated atoms. For the $A^{IV}A^{IV}$ and $A^{IV}B^{IV}$ semiconductors the processes of formation of bond are fundamentally identical, the only difference being, that the hybrid orbital is formed by the simple transition $s^2p^2 \rightarrow sp^3$ without the transfer of electrons from one atom to the other. Fig. 2 illustrates empirically the angular distribution and the overlapping of the hybrid sp^3 wave function which leads to the tetrahedral geometry and the localization of the bonding electrons, characteristic of the diamond, the zinc-blende and the wurtzite-type structure. In Fig. 3 the gap energy is plotted as a function of the bond energy; three straight lines are found to represent the behaviour of almost all the compounds of the series so far considered.

From Fig. 3 we have then the following expressions for the width of the forbidden energy band as a function of the bond energy in $A^{IV}A^{IV}$, $A^{III}B^{V}$ and $A^{II}B^{VI}$ semiconductors: (values in eV)

$$A^{IV}A^{IV} \quad E_g = 2{\cdot}17\ (E_s - 1{\cdot}34) \qquad (3)$$

$$A^{III}B^{V} \quad E_g = 1{\cdot}88\ (E_s - 1{\cdot}43) \qquad (4)$$

$$A^{II}B^{VI} \quad E_g = 1{\cdot}65\ (E_s - 2{\cdot}23). \qquad (5)$$

4. DISCUSSION

Tables 2–4 and the graph in Fig. 3 show that the width of the forbidden band in the semiconductors of diamond and zinc-blende type structures, and in some wurtzite-type ones, increases with the increasing of the bond energy. This fact may be interpreted, in accordance with GOODMAN[12], in the sense that an increase of the bond energy produces, in the pure covalent semiconductors, a lowering of the valence band, while the conduction band is only slightly modified, as SERAPHIN[25] has shown from the analysis of a simplified model of the diamond-type lattice, with the result that there is an increase in the width of the forbidden band.

The agreement between the width of the forbidden band, calculated from equation (3) for SiGe (0·89 eV) and that found[26] (0·92 eV), makes us think that also for SiSn, GeSn, there exists an analogous correlation with that established for the semiconductors $A^{IV}A^{IV}$. This supposition is strengthened by the fact that Si, Ge, Sn have the same value of the electronegativity (1·8), and the bond, in such compounds, can be considered purely covalent. For SiSn and GeSn a value should therefore be found of the width of the forbidden band of 0·59 and 0·40 eV

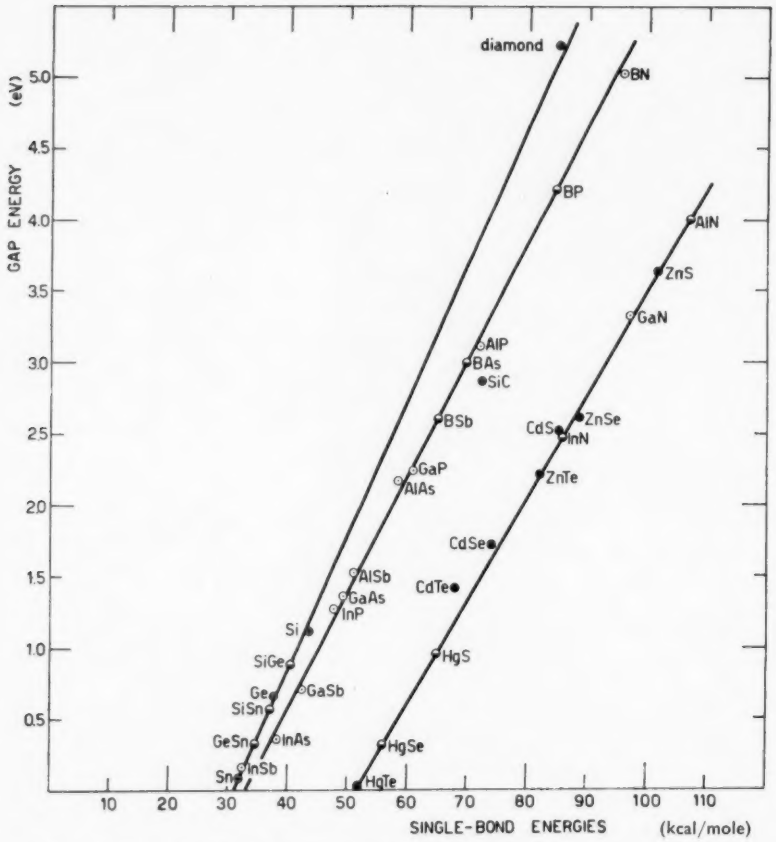

FIG. 3. Dependence of the gap energy on the single-bond energy: ⊕ $A^{IV}A^{IV}$, $A^{IV}B^{IV}$; ○ $A^{III}B^{V}$; ● $A^{II}B^{VI}$ semiconductors; half-filled circle, semiconductors for which the gap energy is unknown or uncertain.*

respectively. SiC, on the contrary, departs from the said linear correlation; in fact, the electronegativity difference of 0·7 between C and Si gives this bond 13 per cent of ionic character.† KOBAYASI[28] considers this solid as the transition term, in regard to the behaviour of the valence electrons, between the mono-atomic diamond-type crystals and the zinc-blende type compounds and attributes a number of electrons of about $-3e$ and $-5e$ to Si and C respectively.

In the $A^{III}B^{V}$ semiconductors, as is schematically indicated in Fig. 1, the bond is stabilized by transferring one electron from atom B^{V} to atom A^{III}; these solids have a certain polar character of the bond, which increases the bond energy. From Si, for example, a pure covalent semiconductor with a width of the forbidden band of 1·12 eV, one passes to the isoelectronic AlP compound with a band gap of 3·1 eV; the difference of the bond energy between the two semiconductors is about 28·4 kcal/mole, analogous to the Ge and Sn isoelectronic series.

* For the gap energy of HgSe, as far as is known, the works of reference do not report concordant values. WRIGHT[24] gives a value ~ 0·2 eV, BUBE, Ref. (8) p. 223, gives instead 0·6 eV.

† The percentage of ionic character has been calculated with the criterion of HANNAY and SMYTH[27].

The slopes of the straight lines relative to the semiconductors $A^{III}B^{V}$ and $A^{II}B^{VI}$ vary from 2·17 to 1·88 and 1·65 respectively. This can be attributed to ionic character of the bond, and in part to an effect of polarization of the component atoms, in agreement with FOLBERT and WELKER[7], who suppose that all the compounds $A^{III}B^{V}$ have, in the first approximation, the same polarization. As can be seen from Fig. 3, GaN is in the linear sequence of the compounds $A^{II}B^{VI}$ rather than $A^{III}B^{V}$. This fact may be justified by thinking of the strong percentage of ionic character in the Ga–N bond (32 per cent); in the same sequence AlN and InN should be found, which have the same percentage of ionic character and the same crystal structure (wurtzite-type) as GaN.

The state of semiconductors $A^{II}B^{VI}$ can be considered as an intermediate between the totally ionic one $(B^{VI})^{-2}$ (s^2p^6), $(A^{II})^{+2}$ (d^{10}) and (Fig. 1) the totally covalent one $(B^{VI})^{+2}$, $(A^{II})^{-2}$. The considerations made for the semiconductors $A^{III}B^{V}$ are generally valid for the semiconductors $A^{II}B^{VI}$ in which, because of the greater ionic character of the bond, there is less localization of the electrons along the direction of the bond.

For the $A^{I}B^{VII}$ compounds of zinc-blende type structure and for the two ZnO, CdO oxides of wurtzite-type structure, the linear correlation between E_g and E_s is no longer there: this is probably due to the fact that the bond, in these compounds, is prevalently ionic for which reason the localization of the electrons along the direction of the bond should be negligible.

It may also be interesting to note that, as can be seen in Fig. 3, in agreement with the bond-energy, the width of the forbidden band is greatest in the purely covalent semiconductors, and diminishes with increasing ionic character of the bond. In agreement with the bond-energy, in fact, the state of localization of the electrons in the molecular orbitals is greatest in the purely covalent semiconductors.

Acknowledgements—I would like to express my gratitude to Prof. G. FRONGIA, Director of the Institute, for introducing me to this new field and sincere thanks to Prof. J. FRIEDEL for his interest and constructive criticism of the work.

REFERENCES

1. WELKER H., *Z. Naturf.* **7a,** 744 (1952); **8a,** 248 (1953).
2. GOODMAN C. H. L., *Proc. Phys. Soc. Lond.* B**67,** 258 (1954).
3. WOLFF G. A., TOMAN L. Jr., FIELD N. J. and CLARK J. C., *Proceedings of the* 1956 *International Colloquium on Semiconductors and Phosphors.* Interscience, New York (1958).
4. MIYAUCHI T., *J. Phys. Soc. Japan* **12,** 308 (1957).
5. KOLM C., KULIN S. A. and AVERBACH B. L., *Phys. Rev.* **108,** 965 (1957).
6. FOLBERT O. G., *Z. Naturf.* **13a,** 856 (1958).
7. FOLBERT O. G. and WELKER H., *J. Phys. Chem. Solids* **8,** 14 (1959).
8. BUBE R. H., *Photoconductivity of Solids.* John Wiley, New York (1960).
9. MOSS T. S., *Optical Properties of Semiconductors.* Butterworths, London (1959).
10. PEARSON W. B., *Canad. J. Chem.* **37,** 1191 (1959); Abstract R14 of *International Conference on Semiconductor Physics, Prague* (1960).
11. HOOGE F. N., *Z. Phys. Chem.* **24,** 275 (1960).
12. GOODMAN C. H. L., *J. Electronics* **1,** 115 (1955).
13. PAULING L., *J. Phys. Chem.* **58,** 662 (1954).
14. SUCHET J. P., *J. Phys. Chem. Solids* **16,** 265 (1960); **12,** 74 (1959).
15. PAULING L., *The Nature of the Chemical Bond,* (3rd Ed.) Cornell University Press, New York (1960).
16. GORDY W. and THOMAS W. J. O., *J. Chem. Phys.* **24,** 439 (1956).
17. CLIFFORD A. F., *J. Phys. Chem.* **63,** 1227 (1959).
18. GLOCKLER G., *J. Chem. Phys.* **19,** 124 (1951).
19. EVANS D. F. and RICHARDS R. E., *J. Chem. Soc.* 1292 (1952).
20. COTTRELL T. L., *The Strengths of the Chemical Bond.* Butterworths, London (1954).
21. HERZBERG G., *Molecular Spectra and Molecular Structure,* Vol. I. *Spectra of Diatomic Molecules.* Van Nostrand, New York (1950).
22. GAYDON A. G., *Dissociation Energies and Spectra of Diatomic Molecules.* Chapman-Hall, London (1953).
23. PITZER K. S., *J. Amer. Chem. Soc.* **70,** 2140 (1948).
24. WRIGHT D. A., *Elect. Engng.* **31,** No. 381 (1959).
25. SERAPHIN B., *Z. Naturf.* **9a,** 450 (1954).
26. BRAUNSTEIN R., MOORE A. R. and HERMAN F., *Phys. Rev.* **109,** 695 (1958).
27. HANNAY N. B. and SMYTH C. P., *J. Amer. Chem. Soc.* **68,** 171 (1946).
28. KOBAYASI S., *J. Phys. Soc. Japan* **13,** 261 (1958).

Vol. 20
1961

J. Phys. Chem. Solids Pergamon Press 1961. Vol. 20, Nos. 3/4, pp. 274–280. Printed in Great Britain.

THE ADSORPTION OF CHLORINE ON CLEAN GERMANIUM SURFACES

MINO GREEN* and K. H. MAXWELL

Zenith Radio Corporation, Chicago 39, Illinois

(*Received* 10 *October* 1960; *revised* 11 *January* 1961)

Abstract—The adsorption of chlorine on clean germanium surfaces was studied in an all-glass system by crushing a single crystal disc of germanium in the presence of the gas and following the pressure changes. Surface areas of the powders were measured by the B.E.T. method using krypton at liquid nitrogen temperature. The experimental techniques evolved for working with chlorine are described. Chlorine was found to adsorb on germanium to monolayer coverage at room temperature and at −78°C. A slow desorption of a fraction of the adsorbed chlorine followed the rapid adsorption. The nature of the adsorption bond and a possible explanation for the slow desorption are discussed.

INTRODUCTION

THERE now exists a considerable amount of information about the adsorptive properties of the clean germanium surface and it has become clear that this element is quite specific in the surface reactions it will undergo.[1–12] For example, substances containing —OH or >NH groups in the molecule (water, alcohols, amines) adsorb rapidly at room temperature to approximately monolayer coverage by what is probably an electrostatic interaction between the permanent charge distributions of adsorbate and adsorbent.[1] This form of interaction can be described as a type of hydrogen bond and the concept of an adsorption site is retained.

A number of common gases, such as carbon monoxide, nitrogen and hydrogen (molecular) do not chemisorb on a clean germanium surface at room temperature.[1,2] However, hydrogen does appear to adsorb at elevated temperatures.[13] The adsorption of *atomic* hydrogen on a germanium surface, while superficially a straightforward reaction, shows features not readily explained on the basis of a simple bond between the hydrogen and the germanium surface atom.[12,14]

Finally, there is the unique case of the interaction of oxygen with a germanium surface,[2–5,9–11] which has been discussed in detail by GREEN[15]. This reaction exhibits an extensive take-up of oxygen beyond monolayer coverage, leading to the formation of a hyper-thin oxide similar to that found with a number of metals.[16] The adsorption of oxygen up to monolayer coverage has been studied by SCHLIER and FARNSWORTH[10] and their results re-interpreted by GREEN[15]. The very large heat of adsorption of oxygen[3,17] is the strongest single piece of evidence showing that the binding of the initial oxygen layer to the germanium must be by a covalent bond.

Chlorine is of interest as a potential adsorbate due to the variety shown in the types of bonds that exist between germanium and the different classes of adsorbates outlined above. While the interaction of chlorine with an etched germanium surface to form $GeCl_4$ has been studied over the temperature range 175–250°C,[18] no adsorption work appears to have been done using clean surfaces. Accordingly, this paper presents some results for chlorine adsorption on clean germanium surfaces at room temperature and at −78C°.

EXPERIMENTAL METHODS

(a) *Vacuum system*

The vacuum system was a conventional one, consisting of a rotary oil pump, a mercury diffusion pump and two traps which could be immersed in

* Present address: John Harrison Laboratory for Chemistry, University of Pennsylvania, Philadelphia, Pennsylvania.

Vol. 2
1961

liquid nitrogen. After the apparatus had been baked out for several hours at 300°C, a pressure of 2×10^{-7} mm Hg was attained readily.

(b) *Adsorption apparatus*

Two types of all-Pyrex adsorption cells were used, both of which have been described in previous papers.[1,3] In the so called "single chamber" apparatus a disc of germanium was crushed by a magnetically-operated, glass-encased iron drop-hammer in the presence of a known quantity of chlorine and the pressure decrease measured. The "double chamber" apparatus consisted, essentially, of two compartments separated from one another by a break-seal. The upper chamber contained the chlorine together with the pressure gauge, while the germanium disc and the crushing hammer were in the lower chamber. In this apparatus the germanium disc was crushed under high vacuum in the lower chamber and, at some later time, the break-seal was broken to admit the chlorine from the upper chamber. Typical volumes were: upper chamber 20 cm^3; lower chamber 25 cm^3; single chamber apparatus 30 cm^3.

(c) *Materials*

The germanium discs used in this work were cut from a single crystal of intrinsic germanium and were approximately 1 cm in diameter and 0·04 cm thick. The chlorine was cylinder gas with a claimed purity of 99·9 per cent. After being admitted to the all-Pyrex gas reservoir on the apparatus the chlorine was distilled back and forth several times between two points in the apparatus. While frozen out with liquid nitrogen between distillations the solid chlorine was pumped under 10^{-6} mm Hg vacuum. This procedure removed any impurities more volatile than the chlorine.

(d) *Pressure measurement and calibration*

Pressures were measured using a glass-coated thermistor bead as a non-linear Pirani gauge. The thermistor gauge circuit has been described elsewhere.[19] The thermistor was calibrated for chlorine by means of the apparatus shown diagrammatically in Fig. 1. The silver chloride "stopcocks", A and B, were devised by the authors for the vacuum manipulation of chlorine.[20] The bulbs a, b ... i, j, of known volumes, were joined to

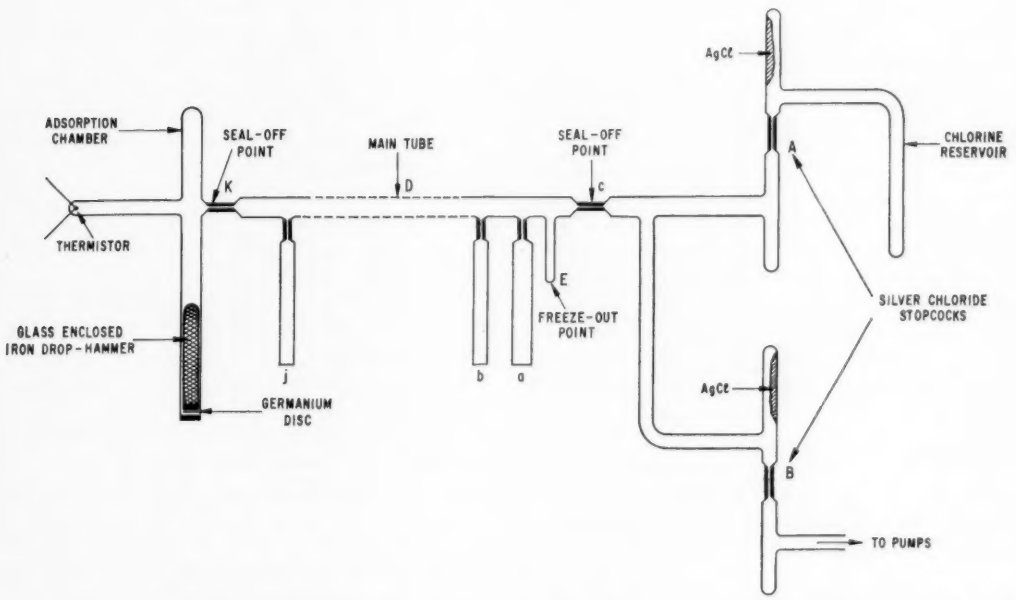

FIG. 1. Adsorption apparatus and the arrangement for calibration of chlorine pressure measuring gauge (thermistor).

the main tube D by 2 cm lengths of 1 mm diameter capillary tubing. The volumes of all parts of the system to the left of the point C in Fig. 1 were known accurately. The apparatus was thoroughly pumped and outgassed with A closed. B was then closed, A was opened and the chlorine reservoir tube immersed in a stirred bath of melting ethyl chloride contained in a Dewar flask. The temperature of the ethyl chloride bath was measured with a calibrated copper–constantan thermocouple and found to be $-137{\cdot}4$°C. At this temperature the saturation vapor pressure of chlorine is 48μ Hg[21] and thus the whole system was filled with chlorine at this pressure. After equilibrium was attained, the point C was sealed. The chlorine was then frozen out by immersing the point E in liquid nitrogen and, when the thermistor showed zero pressure in the apparatus, the bulb "a" was sealed off and the chlorine allowed to expand into the new volume. Knowing the amount of chlorine in the system and the volumes of the component parts, the chlorine pressure at the thermistor could be raised in known increments by successively removing the bulbs b, c ... i, j and allowing the chlorine to expand into progressively smaller volumes. Eleven calibration points were obtained, approximately equally spaced, in the pressure range 48μ Hg to about 550μ Hg. The complete calibration sequence was performed twice and the calibration curve drawn through the twenty-two points.

(e) *Experimental procedure*

When carrying out an actual experiment the apparatus was the same as shown in Fig. 1 except that the tube D and the bulbs a, b ... i, j were omitted. Around the chlorine reservoir tube was placed a Dewar containing stirred ethyl chloride, previously cooled to near its freezing point. The ethyl chloride bath was allowed to warm up slowly and the chlorine pressure increased accordingly. When the chlorine pressure reached the desired value, as shown by the thermistor, the point K was sealed to isolate the adsorption chamber from the rest of the apparatus. After equilibrium was established in the adsorption chamber, the germanium disc was crushed and the pressure recorded as a function of time.

(f) *Surface area measurements*

The B.E.T. apparatus for measuring surface areas was essentially the same as that described by ROSENBERG[19]. The krypton was reagent grade gas with a claimed purity of 99·995 per cent. Each crushing experiment produced 200–300 cm^2 of fresh germanium surface.

(g) *Accuracy*

The accuracy with which the total take-up of chlorine could be determined was governed by the accuracy of the pressure calibration which, in turn, relied on the accuracy of the vapor pressure data for chlorine.[21] These vapor pressure data are only good to ± 10 per cent. The other source of significant error is in the surface area measurements. The reproducibility of a particular B.E.T. determination was about ± 2–3 per cent but the absolute error is probably of the order of ± 10 per cent. Thus, the adsorption results, expressed in terms of amount adsorbed per unit surface area of adsorbent, could be in error by about ± 15 per cent, assuming that the contributing errors were random.

(h) *Cleanness of the germanium surfaces*

It is vital in adsorption studies, particularly where chemisorption dominates, that the adsorbent surface be clean. The reasons for believing that surfaces produced by the crushing technique were clean and the experiments substantiating this belief have been detailed in previous papers.[3,22] Briefly, the success of the crushing method in producing really clean surfaces results from the very favorable ratio of adsorbent surface area to the volume of the cell. The amount of gas available for contamination is very small and can cover only a minute fraction of the total surface.

RESULTS

The results of four experiments are given in Table 1. For each run the surface area of the germanium powder is given together with the final equilibrium pressure of chlorine in the adsorption cell at the end of the experiment. The amount of chlorine adsorbed is expressed in two ways, as *atoms* of chlorine adsorbed per cm^2 of surface (n) and also as units of coverage (θ). The conversion from n to θ was made assuming that there were $7{\cdot}7 \times 10^{14}$ sites per cm^2 of germanium surface.[3] All the adsorptions shown in Table 1 were carried out at room temperature, i.e. 23 ± 1°C.

After the room temperature adsorption had been

Table 1. *Results of chlorine adsorption on clean germanium surfaces*

Run No.	Surface area germanium (cm^2)	Final chlorine pressure (μ Hg)	Final amount adsorbed (n) (atoms Cl per cm^2)	Final coverage (θ)
1	280	178	$8{\cdot}01 \times 10^{14}$	1·04
2	252	307	$8{\cdot}32 \times 10^{14}$	1·08
3*	201	242	$7{\cdot}81 \times 10^{14}$	1·01
4	284	101	$8{\cdot}24 \times 10^{14}$	1·07

* This result also applied to the system after heating at 100°C for 1 hr.

followed in Run No. 3 for about 30 hr and the pressure was unchanged, the adsorption chamber was heated at 100°C for 1 hr. No further adsorption or desorption of chlorine was found to occur and, when the chamber cooled down to room temperature, the pressure reverted to the equilibrium value.

The adsorption of chlorine on germanium at room temperature showed the following features. There was an immediate and extensive take-up of gas when fresh surface was exposed to chlorine. The pressure in the adsorption cell had reached a minimum value by the time the first reading was made (usually 1 min after crushing was stopped). There followed a slow *increase* in the pressure which continued, at a decreasing rate, for about 20–30 min. The pressure then remained constant for as long as measurements were made (24 hr). It was this final equilibrium chlorine pressure which was used to calculate the values of n and θ shown in Table 1. Assuming that the slow pressure increase was caused by the desorption of chlorine,

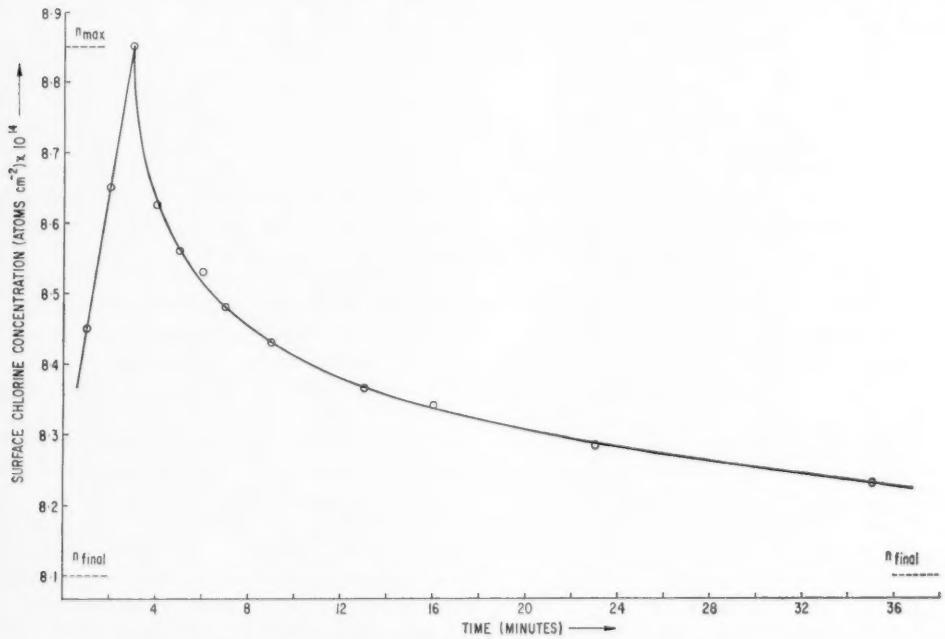

FIG. 2. Kinetics of the slow desorption of chlorine. The amount of chlorine adsorbed per cm^2 of germanium surface is plotted against the time.

the total amount of desorption observed corresponded to about 5×10^{13} *atoms* of chlorine per cm^2 of germanium surface.

The slow desorption of chlorine, which followed the initial large adsorption, was most easily followed at −78°C. For the low temperature experiment a double chamber procedure was followed. After the germanium disc was crushed, the bottom end of the lower chamber was immersed to a depth of about 2 cm in an acetone–CO_2 bath at −78°C. The result of a typical run is shown in Fig. 2. At this temperature a maximum in the amount adsorbed was found. The rate of the desorption reaction appeared to be independent of the chlorine pressure, as was found with the room temperature desorptions.

Some additional experiments were carried out in which oxygen was admitted to a germanium surface already covered with a monolayer of chlorine. This technique has been employed by the authors[12] previously to gain additional information about the bonding of an adsorbate to germanium. The double chamber procedure was employed and the germanium disc was crushed in the lower chamber in the presence of an excess of chlorine. After a time lapse sufficient to ensure complete equilibration the remaining chlorine was removed from the gas phase by freezing it out in a side arm cooled in liquid nitrogen. Oxygen was then admitted from the upper chamber and it was found some adsorption occurred; this adsorption was instantaneous and no further reaction took place over a period of 24 hr. The results of two experiments are given in Table 2.

Table 2. Results of oxygen adsorption on chlorine-covered germanium surfaces

Run No.	Surface area germanium (cm^2)	Oxygen adsorbed (micron cm^3 at 24°C)	Oxygen adsorbed (atoms per cm^2 Ge)
1	279	826	$1{\cdot}92 \times 10^{14}$
2	305	846	$1{\cdot}80 \times 10^{14}$

DISCUSSION

The results reported above show that chlorine chemisorbs on clean germanium surfaces to an extent equivalent to about one chlorine atom per surface germanium atom. Strong binding, i.e. chemisorption, is indicated by the fact that the final extent of adsorption is independent of temperature and pressure (over the ranges −78 to 100°C and 100–300μ Hg respectively). Since under most conditions of chemical reaction chlorine behaves as a monovalent species, it seems reasonable to assume that, for the large part, we are dealing with a monolayer of chemisorbed chlorine atoms. A calculation of the heat of adsorption of chlorine on germanium using the relation proposed by STEVENSON[23] yields a value consistent with strong adsorption of chlorine atoms, i.e. ΔH is −111 kcal mole^{-1} Cl_2. The germanium/chlorine bond would be expected to be dominantly covalent, using the over-all chemistry of germanium as a guide, c.f. PEARSON and WOLFF[24] and GUALTIERI *et al.*[25], who arrive at the same conclusion regarding the germanium/chlorine surface bond.

For the sake of simplicity, we consider the germanium powder produced by crushing to have exposed surfaces which are a mixture of the major crystal planes of low index, i.e. (100), (110) and (111). It is then apparent that for the (100) plane of germanium it is not reasonable to postulate a simple two electron bond for an adsorbed chlorine atom. The atoms on the (100) surface of germanium have two "free" bonds per surface atom but, on steric grounds, only one chlorine atom can bond to each germanium atom. In this case the surface germanium/chlorine complex might be expected to be a structure where a chlorine atom was bonded equally to two germanium atoms and the complex would have a free-radical character. Furthermore, it would be expected that the bonding in the (100) surface would be weaker than on the two other planes mentioned, since the germanium/chlorine bonds would be distorted. GUALTIERI *et al.*[25] concluded from experiments on

the etching of germanium with hot chlorine gas that chlorine bonding on the (100) plane was weaker than on the (111) plane.

The results of the study of oxygen adsorption on an already chlorinated germanium surface are consistent with the above conclusions regarding the nature of the adsorbent–adsorbate complex. The chief features of oxygen interaction were: fast adsorption with no subsequent long time kinetics (contrast this with oxygen–germanium systems[3]), and an amount of adsorption equal to about 3μ Hg ml of O_2 per cm^2 Ge, i.e. about 25 per cent of a monolayer of oxygen *atoms*. Since no long time oxygen adsorption kinetics were observed, there cannot have been any bare patches of germanium surface and the chlorine cannot have been displaced from the germanium surface. This fact, coupled with the small amount of oxygen adsorption leads us to suggest that oxygen adsorbs on the germanium/chlorine surface complexes that have a residual free valence giving rise to a complex of the kind,

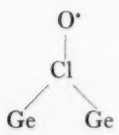

The slow desorption of a fraction of the adsorbed chlorine is a rather unusual observation, particularly for a strong chemisorption reaction such as this. The following explanation is offered and is based on the assumption that the final equilibrium chlorine coverage is a full monolayer of chlorine atoms: Cl_2 molecules are taken up on the Ge surface as Cl atoms whenever the molecule makes a successful collision with an adjacent pair of Ge surface atoms. The Ge–Cl species so formed are considered to be immobile, whereupon, as ROBERTS[26] and ROBERTS and MILLER[27] have shown, there will be approximately 8 per cent single uncovered Ge surface sites (holes) left in the otherwise chlorine covered surface. Chlorine molecules are then assumed to adsorb in these holes comparatively slowly and probably in the form of a weak charge transfer complex; the θ_{max} would be 1·08. There is assumed to be subsequent dissociation of the Cl_2 molecules, so that one chlorine atom of the molecule remains in the hole covalently bound and the other chlorine atom diffuses over the surface where it will combine with another chlorine atom and desorb as Cl_2. In terms of coverage, we have a good fit to the experimental data, i.e. $(\theta_{max}/\theta_{final})$ theory = 1·08 and $(\theta_{max}/\theta_{final})$ expt. = 1·09. The final surface configuration is a monolayer of covalently bound chlorine atoms.

If the above picture of the desorption process is the correct one, the kinetics should be controlled either by the slow dissociation of chlorine molecules or by slow chlorine atom recombination. In the first case we would have,

$$x = a[1-\exp(-k_1 t)] \qquad (1)$$

where x is the amount of chlorine desorbed (expressed in atoms of chlorine/cm^2) at time t, while a and k_1 are the initial number of chlorine molecules bound on the surface/cm^2 and the first order rate constant respectively. If first order kinetics were obeyed then a plot of $\ln(a-x)$ vs. t would be a straight line with a slope of $-k_1$. The slow recombination can be expressed by

$$x = a\left(1-\frac{1}{1+k_2 a t}\right) \qquad (2)$$

where a has the same value as above but is here the initial number of surface atoms available for recombination while k_2 is the second order rate constant. When such plots were made it was found that second order kinetics [equation (2)] represented the data quite well. Therefore, the indication is that the rate controlling step in the desorption reaction involves the slow recombination of chlorine atoms on the chlorine-covered germanium surface.

CONCLUSIONS

(1) Chlorine chemisorbs rapidly on a clean germanium surface with a final equilibrium take-up equivalent to about monolayer coverage.

(2) The chemical bond between chlorine and germanium, for the strongly bound monolayer, is dominantly covalent.

(3) The maximum amount of chlorine adsorbed is greater than the final amount by about 9 per cent and this excess chlorine is slowly desorbed. This can be explained in terms of molecular adsorption of Cl_2 in holes in the monolayer, followed by molecular dissociation and the recombination of chlorine atoms on the surface.

(4) The kinetics of the slow desorption are best fitted when the recombination of chlorine atoms is taken as the rate-determining stage.

REFERENCES

1. GREEN M. and MAXWELL K. H., *J. Phys. Chem. Solids* **11,** 195 (1959).
2. DELL R. M., *J. Phys. Chem.* **61,** 1584 (1957).
3. GREEN M., KAFALAS J. A. and ROBINSON P. H., *Semiconductor Surface Physics* (Edited by KINGSTON R. H.) p. 349. University of Pennsylvania Press (1957).
4. GREEN M., *Semiconductor Surface Physics* (Edited by KINGSTON R. H.) p. 362. University of Pennsylvania Press (1957).
5. WOLSKY S. P., *J. Phys. Chem. Solids* **8,** 114 (1959).
6. LAW J. T., *J. Phys. Chem.* **59,** 543 (1955).
7. LAW J. T., *J. Phys. Chem.* **59,** 67 (1955).
8. LAW J. T. and MEIGS P. S., *Semiconductor Surface Physics* (Edited by KINGSTON R. H.) p. 383. University of Pennsylvania Press (1957).
9. ROSENBERG A. J., ROBINSON P. H. and GATOS H. C., *J. Appl. Phys.* **29,** 771 (1958).
10. SCHLIER R. E. and FARNSWORTH H. E., *Semiconductor Surface Physics* (Edited by KINGSTON R. H.) p. 3. University of Pennsylvania Press (1957).
11. SANDLER Y. L. and GAZITH M., *J. Phys. Chem.* **63,** 1095 (1959).
12. MAXWELL K. H. and GREEN M., *J. Phys. Chem. Solids* **14,** 94 (1960).
13. TAMARU K., *J. Phys. Chem.* **61,** 647 (1957).
14. HEILAND G. and HANDLER P., *J. Appl. Phys.* **30,** 446 (1959).
15. GREEN M., *Progress in Semiconductors* Vol. 4, p. 37. Heywood, London (1959).
16. LANYON M. A. H. and TRAPNELL B. M. W., *Proc. Roy. Soc.* A**227,** 387 (1954).
17. BRENNAN D., HAYWARD D. O. and TRAPNELL B. M. W., *J. Phys. Chem. Solids* **14,** 117 (1960).
18. CARASSO J. I. and STELZER I., *J. Chem. Soc.* 1797 (1960).
19. ROSENBERG A. J., *J. Amer. Chem. Soc.* **78,** 2929 (1956).
20. GREEN M. and MAXWELL K. H., *J. Sci. Instrum.* **37,** 303 (1960).
21. *International Critical Tables* Vol. 3, p. 201. McGraw-Hill, New York (1928).
22. GREEN M. and MAXWELL K. H., *J. Phys. Chem. Solids* **13,** 145 (1960).
23. STEVENSON D. P., *J. Chem. Phys.* **23,** 203 (1955).
24. PEARSON W. B. and WOLFF G. A., *Disc. Faraday Soc.*, No. 28, p. 142 (1959).
25. GUALTIERI J. G., KATZ M. J. and WOLFF G. A., *Z. Kristallogr.* **114,** 9 (1960).
26. ROBERTS J. K., *Proc. Camb. Phil. Soc.* **34,** 399 (1938).
27. ROBERTS J. K. and MILLER A. R., *Proc. Camb. Phil. Soc.* **35,** 293 (1939).

J. Phys. Chem. Solids Pergamon Press 1961. Vol. 20, Nos. 3/4, pp. 281–288. Printed in Great Britain.

CYCLOTRON RESONANCE MEASUREMENTS OF THE ENERGY BAND PARAMETERS OF GERMANIUM

B. W. LEVINGER and D. R. FRANKL

General Telephone and Electronics Laboratories, Inc., Bayside Laboratories, Bayside, New York

(*Received* 13 *March* 1961)

Abstract—The energy band parameters of germanium have been remeasured by cyclotron resonance at 24 kMc. Results are in general agreement with previous authors, though greater precision has been attained.

INTRODUCTION

CYCLOTRON resonance measurements of the effective masses of electrons and holes in germanium have been reported by DRESSELHAUS *et al.*[1], DEXTER *et al.*[2], and FLETCHER *et al.*[3]. This work led to a quantitative description of the energy band edges, and has been of inestimable value in furthering the detailed understanding of this material. There were, however, sizable discrepancies between the values of the valence band parameters A, $|B|$, and $|C|$ obtained by D.K.K.[1] and D.Z.L.,[2] owing to the limitations of experimental resolution. The work of F.Y.M.,[3] though achieving considerably higher resolution, did not remove this discrepancy, since it was concerned primarily with the "quantum effects", i.e. the unequal spacing of the lower Landau levels in the valence band.

In recent work in these laboratories,[4] resolution comparable to that of F.Y.M. has been obtained, and it was, therefore, deemed worthwhile to redetermine the valence band parameters in order to resolve the remaining discrepancy.

EXPERIMENTAL PROCEDURE

The measurements were made at a frequency of 24 kMc, using a microwave bridge circuit similar to that of D.Z.L. However, the sample was placed in a shorted waveguide rather than in a cavity. This was done to reduce the electric field strength in the sample, in order to minimize line broadening due to carrier heating, while maintaining sufficient microwave power for good sensitivity. This arrangement is inherently less sensitive than a cavity, but the loss can readily be overcome by using a larger sample, which is permissible because of the large bandwidth of the circuit. The frequency was stabilized to an external reference cavity.

The sample used was cut from a highly purified germanium crystal in the shape of a rod $0{\cdot}6 \times 0{\cdot}6 \times 4$ mm along the [110] direction. The rod projected across the waveguide through the middle of the broad face one-quarter guide-wavelength from the termination, and could be rotated about its axis. The sample was maintained at 1·35–1·4°K by pumping on the liquid helium. Carriers were generated by infra-red radiation from a tungsten source and Corning 2540 filter, incident on the end of the sample through a small hole in the guide.

The most critical part of the work was the magnetic field measurement. Since no magnet large enough to accommodate both the Dewar and a gaussmeter probe simultaneously was available, it was necessary to make separate calibrating and measuring runs. A four-inch Varian magnet with Varian V–2301 A current regulator was used. The current was measured by the voltage drop across an ammeter shunt inserted in series with the magnet coils, and the magnetic field strength was measured with a Nuclear Magnetics Model M–2 proton resonance gaussmeter. Hysteresis effects were overcome by driving the magnet through a prescribed sequence of currents in both directions before each run. Calibration

runs were than reproducible to better than 0·1 per cent.

For the measuring runs, the magnetic field was slowly increased by manual operation of the fine control of the current regulator. The absorption curve was displayed on an X–Y recorder and the magnet current was measured at intervals on a potentiometer.

The magnetic field was oriented with respect to the crystal axes by rotating the crystal and the magnet about roughly perpendicular axes. The orientation can, in general, be determined entirely from the ratios of the four electron effective masses, as will be described later. For principal directions, the simpler procedure of merging electron peaks gave accuracies of a few tenths of a degree at worst.

RESULTS AND ANALYSIS FOR CONDUCTION BAND

The constant energy surfaces near the conduction band edge in germanium comprise four ellipsoids of revolution about the [111] directions. The cyclotron resonance effective mass for any of these is given[1] in terms of the principal masses m_l (longitudinal) and m_t (transverse) by

$$m_i = m_t \left[\frac{\kappa}{1+(\kappa-1)\cos^2\theta_i} \right]^{1/2} \quad (i = 1, 2, 3, 4) \quad (1)$$

where $\kappa = m_l/m_t$, θ_i = angle between magnetic field and major axis of i^{th} ellipsoid.

These relations can be used to determine the direction of H purely from the ratios of the electron effective masses. In terms of the direction cosines α, β, γ of the magnetic field with respect to the cubic axes, the θ_i are given by

$$\cos\theta_i = (\alpha \pm \beta \pm \gamma)/\sqrt{3}. \quad (2)$$

Inserting this into (1), we find

$$\begin{aligned} \alpha\beta &= L(1+\mu_2-\mu_3-\mu_4)/(1+\mu_2+\mu_3+\mu_4) \\ \beta\gamma &= L(1-\mu_2-\mu_3+\mu_4)/(1+\mu_2+\mu_3+\mu_4) \\ \gamma\alpha &= L(1-\mu_2+\mu_3-\mu_4)/(1+\mu_2+\mu_3+\mu_4) \end{aligned} \quad (3)$$

where

$$L = (\kappa+2)/2(\kappa-1) \quad (3a)$$

$$\mu_i = (m_l/m_t)^2 \quad (i = 2, 3, 4). \quad (3b)$$

Equations (3), together with the relation $\alpha^2+\beta^2+\gamma^2 = 1$ can be solved for α, β, γ, and L. Accuracies of a few tenths of a degree were obtained for the direction angles.

The measured effective masses for the principal directions and the calculated principal masses are listed in Table 1 and compared with previous results. Errors quoted for the present work in this and subsequent tables are the mean square deviations of at least six measurements. The electron resonances were measured at power levels of $< 10^{-7}$ W, and $\omega\tau$ values of about 80 were obtained. Hence the complex free electron conductivity may be represented with sufficient accuracy by

$$\sigma \propto [1+i(\omega-\omega_c)\tau]^{-1} \quad \omega_c = eH/mc \quad (4)$$

as in the case of circularly polarized microwaves. The real part of σ is then a symmetrical peak centered at $\omega_c = \omega$. In a bridge measurement, however, the signal will, in general, contain some

Table 1. *Conduction band effective masses (in units of* m_0)

Direction of H	D.K.K. (Ref. 1)	D.Z.L. (Ref. 2)	F.Y.M. (Ref. 3)	Present work
m (100)		0·164 ±0·001	0·1341	0·1346 ± 0·0001
m_1 (111)		0·0819 ± 0·0003	0·0814	0·08152 ± 0·00008
m_2 (111)		0·208 ±0·001	0·206	0·2057 ± 0·0004
m_1 (110)		0·138 ±0·001	0·0983	0·09875 ± 0·00011
m_2 (110)		0·368 ±0·005	0·361	0·3598 ± 0·0003
m_t	0·082 ± 0·001	0·0819 ± 0·0003	0·0813 ± 0·0002*	0·08152 ± 0·00008
m_t	1·58 ± 0·04	1·64 ±0·03	1·600 ± 0·008	1·588 ± 0·005

* This error is stated as 0·002 in the reference, but we presume this to be a misprint.

Vol. 2
196

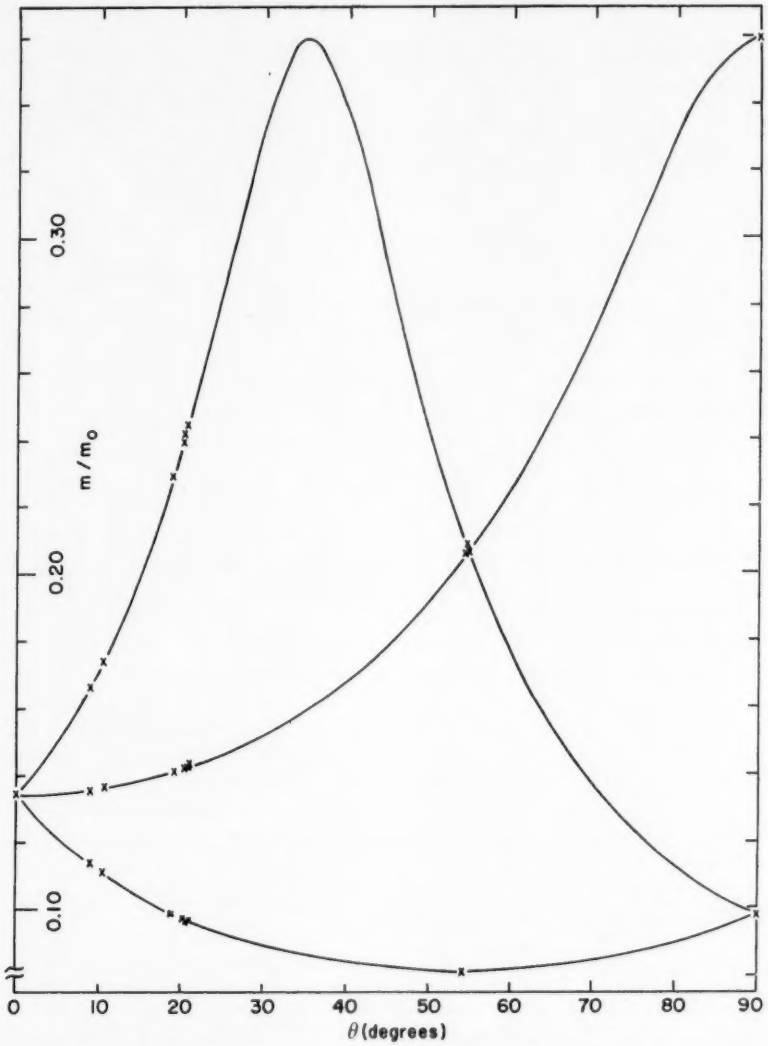

FIG. 1. Electron effective masses for H in (110) plane, as function of angle between H and [001]. Curves calculated from equation (1) with $m_t = 0{\cdot}08152\ m_0$, $m_0.m_l = 1{\cdot}588\ m_0$.

contribution from the (antisymmetric) imaginary part of σ. Our procedure was to adjust the bridge for zero signal at zero field, which usually resulted in very nearly symmetrical electron peaks. In cases where slight asymmetry was evident, a correction based on equation (4) was applied to the measured peak position.

The transverse mass m_t is equal to the smaller mass with H along [111], and the longitudinal mass m_l was obtained, using equation (1), from the larger mass with H along [110], since this point gives the greatest accuracy in m_l. A plot of the effective masses for H in the (110) plane is shown in Fig. 1.

RESULTS AND ANALYSIS FOR VALENCE BAND

The valence band of germanium consists of two warped spherical bands degenerate at $k = 0$ with the carrier energy given by

$$E(k) = -\frac{\hbar^2 k^2}{2m_0}\{A \pm [B^2 + C^2(f + \tfrac{1}{6})]^{1/2}\} \quad (5)$$

where m_0 = free electron mass and

$$f = k^{-4}(k_x^2 k_y^2 + k_y^2 k_z^2 + k_z^2 k_x^2) - \tfrac{1}{6}$$

so that

$$-\tfrac{1}{6} \leqslant f \leqslant \tfrac{1}{6}.$$

The experimental results will be interpreted by both classical and quantum theories. We follow previous authors[1, 2] in analyzing our results on the basis of two assumptions.

1. The transitions giving rise to the measured absorption take place principally at large quantum numbers, so that classical theory is applicable. The validity of this assumption will be discussed later.
2. The principal contribution to the resonance absorption peak comes from carriers with $k_H \approx 0$. This assumption is supported by classical calculations,[5] which show that the peak shift due to carriers with $k_H \neq 0$ is small and decreases rapidly with increasing $\omega\tau$.

Under these assumptions the classical effective mass is given by[1]

$$m/m_0 = \left(\hbar^2/2\pi m_0\right) \oint \frac{\rho \, d\phi}{\partial E/\partial \rho} \quad (6)$$

where ρ, ϕ, k_H are cylindrical coordinates in k-space.

The integral (6) can be evaluated exactly for H in a [111] direction, giving

$$m_0/m = A \pm (B^2 + C^2/4)^{1/2} \quad (7)$$

so that

$$A = \tfrac{1}{2}[(m_0/m_{111}^+) + (m_0/m_{111}^-)] \quad (7a)$$

$$K \equiv (B^2 + C^2/4)^{1/2} = \tfrac{1}{2}[(m_0/m_{111}^+) - (m_0/m_{111}^-)] \quad (7b)$$

where m^+ and m^- are, respectively, the light and heavy hole effective masses.

For other directions of H, the integrand of equation (6) is expanded in powers of f, giving

$$\frac{m^\pm}{m_0} = \frac{2}{\pi}\frac{1}{A \pm (B^2 + C^2/6)^{1/2}} \int_0^{2\pi} [1 \mp \frac{D^\pm}{2} f + \frac{D^\pm}{8}(2D^\pm \pm \beta) f^2 + \ldots] \, d\phi \quad (8)$$

where

$$D^\pm = C^2/\{[A \pm (B^2 + C^2/6)^{1/2}]\,[B^2 + C^2/6]^{1/2}\} \quad (8a)$$

$$\beta = C^2/(B^2 + C^2/6). \quad (8b)$$

For directions far from [111], this series converges more rapidly than does the series given by D.K.K. For the light holes (m^+), the three terms shown leave a remainder less than 0·1 per cent, though for the heavy holes, seven terms are required to achieve comparable convergence.

The quantum theory of LUTTINGER[6] gives expressions for the energy levels with the magnetic field in a (110) plane and $k_H = 0$, accurate to first order in the warping of the bands. In the limit of high quantum numbers, the results are

$$m^\pm = [\gamma_1 \pm (\gamma'^2 + 3\gamma''^2)^{1/2}]^{-1} \quad (9)$$

where

$$\gamma' = \gamma_3 + (\gamma_2 - \gamma_3)\,(3\cos^2\theta - 1)/4$$
$$\gamma'' = \tfrac{1}{3}(\gamma_2 + 2\gamma_3) + \tfrac{1}{6}(\gamma_2 - \gamma_3)\,(3\cos^2\theta - 1)/4 \quad (9a)$$

$$\gamma_1 = A$$
$$\gamma_2 = -\tfrac{1}{2}B$$
$$\gamma_3 = -\tfrac{1}{2}(B^2 + C^2/3)^{1/2} \quad (9b)$$

θ = angle between H and [001].

From (9) we obtain

$$\gamma_1 = \frac{1}{2}\left(\frac{m_0}{m^+} + \frac{m_0}{m^-}\right)$$
$$\gamma'^2 + 3\gamma''^2 = \frac{1}{4}\left(\frac{m_0}{m^+} - \frac{m_0}{m^-}\right)^2. \quad (10)$$

Table 2. Valence band effective masses (in units of m_0)

Direction of H	D.Z.L. (Ref. 2)	F.Y.M. (Ref. 3)	Present work
m^+ (100)	$0{\cdot}0438 \pm 0{\cdot}003$	0·0437	$0{\cdot}04368 \pm 0{\cdot}00008$
m^+ (111)	$0{\cdot}0426 \pm 0{\cdot}002$	0·0421	$0{\cdot}04187 \pm 0{\cdot}00005$
m^+ (110)	$0{\cdot}0430 \pm 0{\cdot}003$	0·0425	$0{\cdot}04236 \pm 0{\cdot}00005$
m^- (100)	$0{\cdot}284 \pm 0{\cdot}001$	0·284*	$0{\cdot}2825 \pm 0{\cdot}0006$
m^- (111)	$0{\cdot}376 \pm 0{\cdot}001$	0·376*	$0{\cdot}377 \pm 0{\cdot}002$
m^- (110)	$0{\cdot}352 \pm 0{\cdot}004$	0·368*	

* 4·2°K values.

Thus (10) and (9a) can be used to determine the parameters γ_1, γ_2, γ_3 directly from the measured effective masses. We note that the sum of the inverse masses is independent of the magnetic field direction according to the quantum theory, but not according to the classical theory, equation (8).

The measured effective masses for H in the principal directions are listed in Table 2 and compared with previous results. The values given for the light holes were measured at microwave power levels below 10^{-6} W, and the line widths and positions were found to be independent of power up to about 10^{-5} W, with $\omega\tau$ about 50.

For the heavy holes, on the other hand, the line widths and shapes were markedly power-dependent. Below about 10^{-5} W, the quantum lines were resolved. With increasing power the subsidiary peaks disappeared, and the main peak first became higher and *narrower* and then broadened again. The minimum line width, at about 10^{-4} W, corresponded to $\omega\tau \sim 25$. For H in the [111] direction, the peak position was independent of power over a considerable range about the minimum width. This is the only heavy-hole effective mass used in evaluating the band parameters. In the [100] direction, the peak shifted with power,[4] and the effective mass listed in Table 2 is that at the minimum width. No measurements were made on the heavy holes for any other direction of H.

Table 3. Valence band parameters

(a)

	D.K.K. (Ref. 1)	D.Z.L. (Ref. 2)	Present work
A	$13{\cdot}0 \pm 0{\cdot}2$	$13{\cdot}1 \pm 0{\cdot}4$	$13{\cdot}27 \pm 0{\cdot}025$
$K \equiv (B^2+C^2/4)^{1/2}$			$10{\cdot}62 \pm 0{\cdot}025$
$\lvert B\rvert$	$8{\cdot}9 \pm 0{\cdot}1$	$8{\cdot}3 \pm 0{\cdot}6$	$8{\cdot}63 \pm 0{\cdot}12$
$\lvert C\rvert$	$10{\cdot}3 \pm 0{\cdot}2$	$12{\cdot}5 \pm 0{\cdot}5$	$12{\cdot}4 \pm 0{\cdot}25$

(b)

	From equation (10)	From equation (9b)	Ref. (7)
γ_1	13·24	$13{\cdot}27 \pm 0{\cdot}025$	13·245
$\lvert\gamma_2\rvert$	4·36	$4{\cdot}32 \pm 0{\cdot}06$	4·20
$\lvert\gamma_3\rvert$	5·61	$5{\cdot}60 \pm 0{\cdot}03$	5·56

Table 3 lists the values of the band parameters obtained from the measured effective masses. The values in Table 3(a) were obtained from the classical theory based on equation (6). A and K were obtained directly from equation (7). Since $m^-/m^+ \sim 10$, the errors in these parameters are dominated by the error in measurement of the light hole mass. From these two parameters, the effective masses for any direction of H can be plotted as a function of C, using equation (8). The value of C listed in Table 3 was obtained by fitting the light hole effective mass for H along [100], since this point gives the best precision. The errors quoted for B and C were assigned on the basis of this fit assuming $A = 13{\cdot}27$ and $K = 10{\cdot}62$ exactly. Since the effective masses are considerably more sensitive to A and K than to B and C, the uncertainties in the latter two parameters are relatively large. In Table 3(b) we list the values of the parameters γ_1, γ_2, γ_3 derived from equation (10) using the measured effective masses from H in the [100] and [111] directions. These are compared with the values used by ROTH *et al.*[7] to fit their magneto-absorption data and with the values obtained from equation (9b).

As a check, measurements of the light-hole effective mass were made in several orientations in the (110) plane. Fig. 2 shows a comparison of these values with curves calculated from equations (8) and (10). Fig. 3 is a similar comparison for the heavy holes. With the band parameters known to the accuracies quoted in Table 3(a), equation (8) gives the light hole masses to within 0·3 per cent and the heavy hole masses to within 3 per cent. Thus the agreement with experiment is satisfactory. The rather large disagreement between the two calculated curves for the heavy holes is probably due to the use of first order perturbation theory in the quantum calculation. To first order in f, which is a measure of the warping, the classical expression (8) agrees quite well with the quantum result.

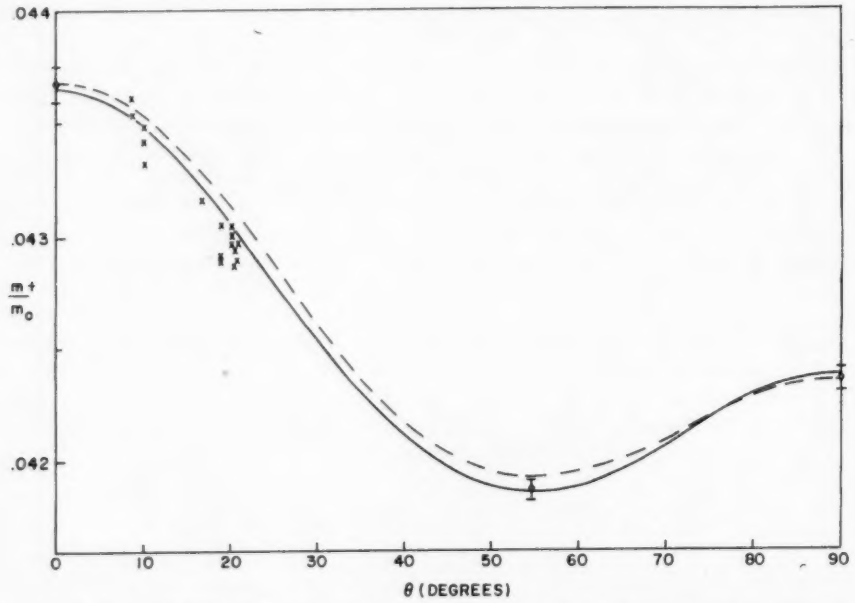

FIG. 2. Light hole effective masses for H in (110) plane, as function of angle between H and [001]. Solid curve calculated from equation (8) with $A = 13{\cdot}27$, $|B| = 8{\cdot}63$, $|C| = 12{\cdot}4$. Dashed curve calculated from equation (10) with $\gamma_1 = 13{\cdot}27$, $|\gamma_2| = 4{\cdot}32$, $|\gamma_3| = 5{\cdot}60$.

We now return to the question of the validity of the classical analysis for the valence band measurements. For the heavy holes, the changes in line shape with power and the disappearance of subsidiary peaks clearly demonstrate the transition from the quantum to the classical regime. This corresponds to a shift of population to the higher Landau levels as the carriers are heated. There is no problem of line shift accompanying this heating, since the analysis makes use of the heavy hole effective mass only for the [111] direction, where no shift was observed.

For the light holes, on the other hand, no evidence of quantum effects was observed down to the lowest power levels used. Since the Landau levels approach equal spacing more rapidly for the light than for the heavy holes[6], and since the heating is greater for the light holes, it seems reasonable to conclude that these carriers are in the classical regime at all power levels used.

There is one final point concerning the shapes of the light hole resonances. In the [111] and [110] directions, these were decidedly asymmetrical, the half-width at the half-power point being about 50 per cent greater on the high-field side. In the [100] direction, the peak was approximately symmetrical, though with perhaps a slight broadening on the low-field side. These asymmetries are probably due to carriers with non-zero k_H, as suggested by the calculations of D.K.K. The $\omega\tau$ values quoted above were based on the full observed widths. No attempt was made to apply corrections to the peak positions.

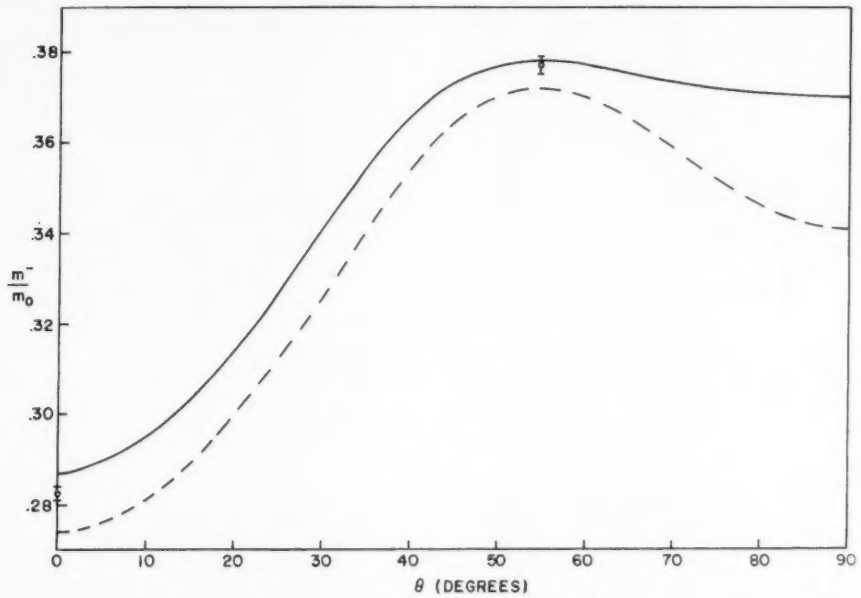

FIG. 3. Heavy hole effective masses for H in (110) plane as function of angle between H and [001]. Curves calculated as in Fig. 2.

Acknowledgements—Thanks are due to J. C. KUGLER for his able assistance in the experimental work. The germanium sample was prepared by K. M. ARNOLD and Miss M. G. TILTON, and oriented by G. H. SCHWUTTKE. G. E. WEIBEL, R. I. HARRISON, H. MALAMUD, and C. FALLIER gave much assistance in the design and construction of the apparatus, and W. R. WATSON suggested the magnet calibration procedure.

REFERENCES

1. DRESSELHAUS G., KIP A. F. and KITTEL C., *Phys. Rev.* **98,** 368 (1955). Denoted D.K.K.

Vol. 20
1961

2. DEXTER R. N., ZEIGER H. J. and LAX B., *Phys. Rev.* **104,** 637 (1956). Denoted D.Z.L.
3. FLETCHER R. C., YAGER W. A. and MERRITT R. F., *Phys. Rev.* **100,** 747 (1955). Denoted F.Y.M.
4. LEVINGER B. and FRANKL D. R., *Phys. Rev. Letters* **5,** 12 (1960).
5. LUTTINGER J. M. and GOODMAN R. R., *Phys. Rev.* **100,** 673 (1955); ZEIGER H. J., LAX B. and DEXTER R. N., *Phys. Rev.* **105,** 495 (1957).
6. LUTTINGER J. M., *Phys. Rev.* **102,** 1030 (1956).
7. ROTH L. M., LAX B. and ZWERDLING S., *Phys. Rev.* **114,** 90 (1959).

Vol.
196

J. Phys. Chem. Solids Pergamon Press 1961. Vol. 20, Nos. 3/4, pp. 289–293. Printed in Great Britain.

SPECIFIC HEAT AND SPIN SUSCEPTIBILITY OF DILUTE ALLOYS*

A. HOUGHTON†

University of California, La Jolla, California

(*Received* 22 *August* 1960; *revised* 21 *December* 1960)

Abstract—The change in the specific heat and spin susceptibility of a metal of valence Z due to the introduction of a small number of impurity atoms with valence $(Z+q)$ is calculated by the Thomas–Fermi method. It is shown that in the case of copper an exact Thomas–Fermi calculation accounts approximately for the seemingly linear behaviour of the change in C_v and χ from $q = 1$ to $q = 3$ observed in recent experiments by RAYNE. It does not, however, account for absolute values. In an appendix a check on the validity of the Thomas–Fermi theory is made for $q < 1$ by recalculating the specific heat and spin susceptibility by means of the techniques of many-body perturbation theory. The different methods give essentially the same results.

1. INTRODUCTION

IN THIS paper we will discuss the effect on the thermal and magnetic properties of a metal with valence Z of the introduction of an impurity atom with valence $Z+q$; particular reference will be made to the case of copper base alloys. This problem was first considered by MOTT[1], who used a linearized Thomas–Fermi model. It was found that the potential surrounding the impurity atom was of the screened Coulomb type with a screening radius independent of the valence of the impurity, and that the density of states varied linearly with q. FRIEDEL[2] has extended the method and calculated the screened Coulomb potential to second order in q. The above procedures are only valid in the small q limit and certainly do not apply to alloys where $q > 1$. Recently, ALFRED and MARCH[3] have solved the Thomas–Fermi equation exactly, for the case of copper, by direct numerical integration. They determine, within the framework of the Thomas–Fermi model, the exact potential around an impurity atom for all q.

Recently, new experiments on copper alloys have been carried out; in particular RAYNE[4,5] has determined the specific heat of copper–zinc and copper–germanium alloys, and work has been done by GUTHRIE[6] on the heat capacity of pseudo-copper. We feel that one of the most striking features of RAYNE's results is the approximate linearity in the variation of the specific heat with q between $q = 1$ and $q = 3$. This is somewhat surprising as $q = 3$ represents a large perturbation.

In this paper we will investigate this effect by means of the Thomas–Fermi method as this is the only non-perturbative approach available. As the validity of the Thomas–Fermi method is not well established we check the theory for small q by calculating the change in specific heat and spin susceptibility of an interacting electron gas due to the introduction of a positive charge q. This calculation, which appears in the appendix, was carried out by means of the standard techniques of many-body perturbation theory.

In Section 2 we give a brief outline of the Thomas–Fermi method. In Section 3 we calculate the density of states, and hence the specific heat and spin susceptibility of copper alloys by means of the exact Thomas–Fermi theory. These results are then compared with the experimental results and also with the predictions of a linear Thomas–Fermi theory.

2. THE THOMAS–FERMI EQUATION FOR THE POTENTIAL AROUND AN IMPURITY

In this section we assume following MOTT[1] that the solvent atom has valence Z whereas the solute

* Supported in part by the Office of Naval Research.

† Now at McMaster University, Hamilton, Ontario, Canada.

atom has $(Z+q)$ valence electrons. Then, adopting the free electron gas approximation we have the usual relation between the electronic density $\rho_0(r)$ and the maximum momentum. (Atomic units will be used throughout.)

$$\rho_0(r) = \frac{p_F^3(r)}{3\pi^2}. \tag{2.1}$$

The Fermi energy is given in terms of p_F by

$$E_F = \frac{p_F^2(r)}{2}. \tag{2.2}$$

By making this approximation we of course neglect exchange and correlation effects due to the mutual Coulomb repulsion of the electrons.

If we now write down the classical energy equation for an electron at the Fermi surface when an impurity is introduced:

$$E_F = \frac{p_F^2(r)}{2} - V(r, q) \tag{2.3}$$

and then substitute in equation (2.1) we obtain

$$\rho(r) = \frac{1}{3\pi^2}[2(E_F + V(r, q))]^{3/2} \tag{2.4}$$

where $V(r, q)$ is the electrostatic potential between the electron and the impurity. The requirement of self-consistency namely that the electrostatic potential $V(r, q)$ is due to the electron cloud of density $\rho(r)$ and the impurity can now be expressed by means of Poisson's equation

$$\Delta V(r, q) = 4\pi[\rho(r, q) - \rho_0(r)]. \tag{2.5}$$

With the help of equations (2.3) and (2.4) we arrive at the Thomas–Fermi equation

$$\Delta V(r, q) = \frac{4}{3\pi}(2E_F)^{3/2}\left[\left(1 + \frac{V(r, q)}{E_F}\right)^{3/2} - 1\right]. \tag{2.6}$$

We now adopt the usual method of finding a self consistent solution for the potential $V(r, q)$. That is, we assume q small, then on expanding both sides of equation (2.6) in powers of q and equating coefficients $V(r, q)$ can be determined to first and second order.

From the linear terms in q we find:

$$V^{(1)}(r, q) = q\frac{e^{-\lambda r}}{r} \tag{2.7}$$

where the inverse screening radius λ is given by

$$\lambda = \left[\frac{2^{5/2}E_F^{1/2}}{\pi}\right]^{1/2}. \tag{2.8}$$

Then putting this value for $V^{(1)}(r, q)$ back in the equation and equating quadratic terms in q we find

$$V^2(r, q) = \frac{-\lambda q^2}{8E_F}\left[\frac{e^{-\lambda r}}{r}\left(\ln 3 - \int_r^\infty \frac{e^{-\lambda\xi}}{\xi}\,d\xi\right) + \frac{e^{\lambda r}}{r}\int_r^\infty \frac{e^{-3\lambda\xi}}{\xi}\,d\xi\right]. \tag{2.9}$$

Therefore to second order in q, $V(r, q)$ is given by

$$V(r, q) = q\frac{e^{-\lambda r}}{r}\left[1 - \frac{\lambda q}{8E_F}\left(\ln 3 - \int_r^\infty \frac{e^{-\lambda\xi}}{\xi}\,d\xi\right)\right] + \frac{e^{\lambda r}}{r}\frac{\lambda q^2}{8E_F}\int_r^\infty \frac{e^{-3\lambda\xi}}{\xi}\,d\xi. \tag{2.10}$$

Finally a numerical solution of the Thomas–Fermi equation has been given by ALFRED and MARCH[3] who used a relaxation method. The equation has to be solved separately for each solvent metal; they give results for copper. The values of q investigated were $q = 1, 2, 3$ and 4. It was found that the screening radius is in general smaller than predicted by the linear treatment, and that the potential falls off more rapidly with r.

3. THE SPECIFIC HEAT AND SPIN SUSCEPTIBILITY

In this section we will use the results of Section 2 to determine the thermal and magnetic properties of our system. It is well known that in the independent electron model of a metal the specific heat and spin susceptibility are given in terms of

the density of states at the Fermi surface by the following formulae:

$$\left.\begin{aligned} C_v^{(0)} &= \frac{\pi^2}{3}k(kT)n(E_F) \\ \chi^0 &= \mu^2 n(E_F) \end{aligned}\right\} \tag{3.1}$$

where k is Boltzmann's constant, μ is the magnetic moment per electron, and

$$n(E_F) = \int \rho'(E_F, r)\, d^3r \tag{3.2}$$

where

$$\rho'(E_F,r) = \frac{d\rho(E_F,r)}{dE_F}. \tag{3.3}$$

Within the framework of the Thomas–Fermi model illustrated in the last section, we see that on the introduction of a static impurity of charge q the change in density of states at the Fermi surface is given by

$$\delta n(E_F) = \int \{\rho'[E_F + V(r, q)] - \rho_0'(E_F)\}\, d^3r. \tag{3.4}$$

Therefore, using equation (3.1) the corresponding changes in the specific heat and susceptibility are

$$\left.\begin{aligned} C_v^q &= \frac{1}{3\pi^2}\frac{C_v^{(0)}}{N}(2E_F)^{3/2}I(q) \\ \chi^q &= \frac{1}{3\pi^2}\frac{\chi^0}{N}(2E_F)^{3/2}I(q) \end{aligned}\right\} \tag{3.5}$$

where

$$I(q) = \int \left[\left(1 + \frac{V(r, q)}{E_F}\right)^{1/2} - 1\right] d^3r. \tag{3.6}$$

These formulae give the change in specific heat and spin susceptibility on the introduction of one impurity atom. If we now introduce a small but finite number of impurities "n" into the metal, with the restriction that the impurity density is so small that they don't interact, then it is obvious that the only change in equations (3.5) is that $(1/N)$ is replaced by (n/N).

By substituting the value of $V(r, q)$, given by equation (2.10) into equations (3.5), we find that to second order in q

$$\left.\begin{aligned} C_v^q &= \frac{C_v^0}{3}\left(\frac{qn}{N}\right)\left[1 - \frac{q}{\pi^{1/2}(2E_F)^{3/4}}\right] \\ \chi^q &= \frac{\chi^0}{3}\left(\frac{qn}{N}\right)\left[1 - \frac{q}{\pi^{1/2}(2E_F)^{3/4}}\right]. \end{aligned}\right\} \tag{3.7}$$

Incidentally the results of equation (3.7) are also obtained by making use of the much simpler solution for $V(r, q)$ given by FRIEDEL[2].

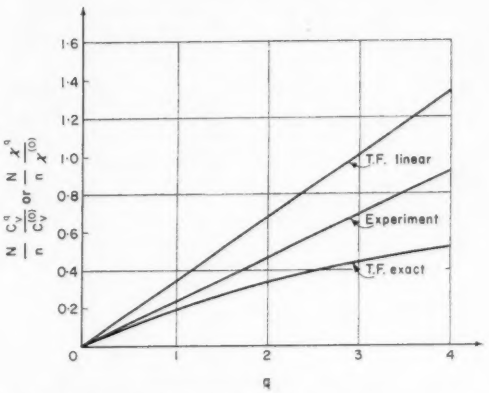

FIG. 1. Variation of specific heat and spin susceptibility with valence difference q for $(n/N) = 0{\cdot}005$.

Second order Thomas–Fermi theory

The linear term in equation (3.7) is the effect of adding qn extra electrons to our system. The quadratic term in q is due to the static polarization of the electron gas by the positive charge q. The change in this term due to electron correlations will be discussed in the Appendix.

Exact Thomas–Fermi theory

The exact q dependence of C_v^q and χ^q was found by using the results of ALFRED and MARCH[3] to evaluate $I(q)$ numerically. In Fig. 1 we compare the exact q dependence of C_v^q and χ^q with the results of RAYNE's experiments and also with the strict linear Thomas–Fermi theory. We have chosen $n/N = 0{\cdot}005$, for which value our theory should be accurate. We find that while at $q = 3$ the deviation from the linear theory is about a

factor of 2·3, nevertheless

$$\frac{C_v(q=5)}{C_v(q=1)} = 2{\cdot}5$$

is not so far off the value

$$\frac{C_v(q=3)}{C_v(q=1)} = 2{\cdot}9$$

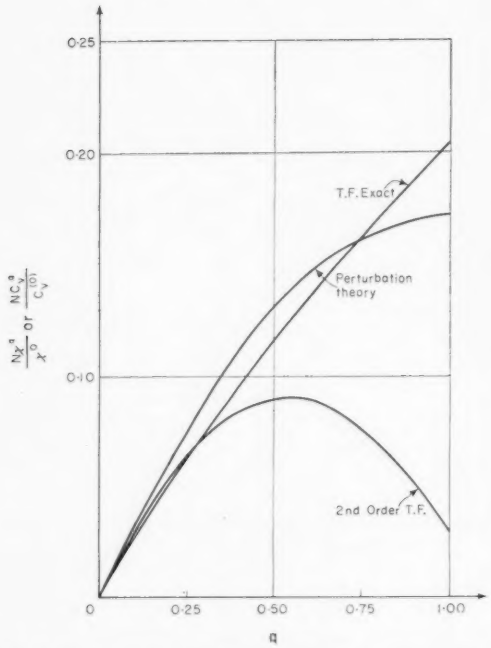

FIG. 2. Variation of specific heat and spin susceptibility with q for $q < 1$.

given by RAYNE's experiments. However, the disagreement with RAYNE's absolute value at $q = 3$ is large, the value of

$$\frac{N}{n} \times \frac{C_v^q}{C_v^{(0)}}$$

being 50 per cent greater than that predicted by the Thomas–Fermi theory. This disagreement is probably due largely to the omission of the periodic potential from our considerations. It has in fact been remarked by HEINE and COHEN[7] that even if q is very small, there will be a change in the band structure and hence in the functional form of the density of states at the Fermi surface. This statement is further reinforced by the comparison in Fig. 2 of the results obtained by many-body perturbation theory with the results of the exact Thomas–Fermi theory. It is seen that for small $q(q < 1)$ the predictions of the two theories are almost identical.

We conclude then, that the Thomas–Fermi theory accounts approximately for the seemingly linear behaviour of C_v^q for $q = 1$ and 3, although it disagrees with the strict linear theory by a factor of 2·3 at $q = 3$. It does not account for absolute values.

APPENDIX

Many-body perturbation theory approach

In this appendix we will consider the more physical model of our system, that is, an interacting electron gas. The effect on the free energy and hence the specific heat and spin susceptibility due to the polarization of the system by a static impurity of charge q, will be calculated to second order in q by means of the techniques of many-body perturbation theory developed by BLOCH and DE DOMINICIS[8]. We will consider only the contributions of the so-called Pair graphs. (Exchange terms will again be neglected.) It is just these graphs which GELL-MANN and BRUECKNER[9] have shown to give the leading contribution to the correlation energy in the limit of very high density.

The resulting correction to the free energy is:

$$F(q, T) = \frac{1}{2\Omega} \times \sum_k \frac{\left(\frac{4\pi q^2}{k^2}\right) \cdot 4\pi \int W_B(k, p) \frac{df(p)}{dp} \cdot dp}{\left[k^2 - 4\pi \int W_B(k, p) \frac{df(p)}{dp} \cdot dp\right]} \tag{A.1}$$

where $f(p)$ is the Fermi distribution function for an electron with wave vector p.

$$f(p) = \frac{1}{1 + \exp(E_p - E_F)/kT} \tag{A.2}$$

and

$$4\pi W_B(k, p) = -\frac{2p}{\pi}\left[1 + \frac{1}{k_p}\left(p^2 - \frac{k^2}{4}\right) \ln\left|\frac{k+2p}{k-2p}\right|\right]. \tag{A.3}$$

At zero temperature equation (A.1) reduces to the result derived by LANGER and VOSKO[10]. That is:

$$F(q,0) = E(q) = \frac{1}{2\Omega}\sum_k \left(\frac{4\pi q^2}{k^2}\right)\frac{4\pi W_B(k, p_F)}{[k^2 - 4\pi W_B(k, p_F)]}. \tag{A.4}$$

If we now switch on a magnetic field H the ground state of our system $E(q)$ becomes:

$$E(q,H) = \frac{1}{2\Omega}\sum_k \left(\frac{4\pi q^2}{k^2}\right)\frac{4\pi W'_B(k, p_F, H)}{[k^2 - 4\pi W'_B(k, p_F, H)]} \tag{A.5}$$

where

$$W'_B(k, p_F, H) = \tfrac{1}{2}[W_B(k, E_F+\mu H) + W_B(k, E_F-\mu H)]. \tag{A.6}$$

Finally for T and H small, equations (A.1) and (A.4) can be expanded in powers of (kT/E_F) and $(\mu H/E_F)$ respectively.

On making use of the well known formulae

$$\left.\begin{aligned} C_v^0 &= -\frac{1}{T}\frac{d^2F(T)}{dT^2} \\ \text{and} \\ \chi^0 &= -\frac{1}{H}\frac{d[E(H)]}{dH} \end{aligned}\right\} \tag{A.7}$$

we find the correction to the specific heat and spin susceptibility due to the polarization of the electron gas is given by:

$$\left.\begin{aligned} C_v^q &= -q^2\frac{C_v^{(0)}}{N}\frac{I(x)}{6\pi^3} \\ \chi q &= -q^2\frac{\chi^0}{N}\frac{I(x)}{6\pi^3} \end{aligned}\right\} \tag{A.8}$$

where

$$I(x) = \int d^3x \frac{\left[\frac{1}{x}\ln\left|\frac{x+2}{x-2}\right| - \frac{4}{(x-2)(x+2)}\right]}{\left[x^2 + \xi\left(1+\frac{1}{x}\right)\left(1-\frac{x^2}{4}\right)\ln\left|\frac{x+2}{x-2}\right|\right]^2} \tag{A.9}$$

with $k/k_F = x$, and $\xi = 0{\cdot}3317 r_s$. $I(x)$ was evaluated numerically.

The results of equation (A.8) are shown in Fig. 2. It is seen that within the range of validity of the theory outlined above, that is $q \ll 1$, the results obtained support the exact Thomas–Fermi theory; whereas the second order Thomas–Fermi theory is not a good approximation for $q > 0{\cdot}5$.

Acknowledgement—It is a pleasure to thank Professor W. KOHN for suggesting this problem and for many valuable discussions.

REFERENCES

1. MOTT N. F., *Proc. Camb. Phil. Soc.* **32,** 281 (1936).
2. FRIEDEL J., *Advanc. Phys.* **3,** 44 (1954).
3. ALFRED L. C. R. and MARCH N. H., *Phil. Mag.* **46,** 759 (1955).
4. RAYNE J. A., *Phys. Rev.* **108,** 22 (1957).
5. RAYNE J. A., *Phys. Rev.* **110,** 606 (1958).
6. GUTHRIE G. L., *Phys. Rev.* **113,** 793 (1959).
7. HEINE V. and COHEN M. H., *Advanc. Phys.* **7,** 396 (1958).
8. BLOCH C. and DE DOMINICIS C., *Nuclear Phys.* **10,** 181 (1959).
9. GELL-MANN M. and BRUECKNER K., *Phys. Rev.* **106,** 364 (1957).
10. LANGER J. S. and VOSKO S. H., *J. Phys. Chem. Solids* **12,** 196 (1959).

J. Phys. Chem. Solids Pergamon Press 1961. Vol. 20, Nos. 3/4, pp. 294–306. Printed in Great Britain.

A THEORY OF FUSION OF MOLECULAR CRYSTALS—II

PHASE DIAGRAMS AND RELATIONS WITH SOLID STATE TRANSITIONS

F. E. KARASZ and J. A. POPLE

National Physical Laboratory, Teddington, Middlesex, England

(*Received* 28 *December* 1960)

Abstract—The theory of melting of molecular crystals with orientational degrees of freedom developed in a previous paper[1] is extended to cover disordering solid–solid transitions and complete phase diagrams for transitions under pressure. It is predicted that solid–solid and melting transitions should become second-order under certain conditions and also that a solid transition may appear at high pressures in some materials which show only a melting transition at zero pressure. The theory is compared with available experimental data.

1. INTRODUCTION

In a previous paper[1] (Part I), a statistical theory of fusion of molecular crystals was developed, taking into account the possibilities of long-range disorder in both the positions and orientations of the molecules. This was based on a model in which molecules could take up two possible orientations on two possible kinds of site. By introducing suitable energies for various relative configurations, a theory was obtained which brought together the features of the original theory of rotational disorder in solids[2] and the treatment of melting due to Lennard-Jones and Devonshire[3]. This theory reproduced some of the trends in the experimental data on the thermodynamics of melting in terms of a single non-dimensional parameter associated with the ratio of energies involved in orientational and translational defects in a crystal lattice. For small values of this parameter, the model gives a solid-state rotational transition as well as the ordinary melting point. For larger values, however, the two transitions coalesce and there is a single transition with a larger entropy change, as observed experimentally.

In this paper, we shall extend the calculations on the melting transition (reported in Part I) to the predicted thermodynamic features of the solid state transition, where this is separate. We shall also consider the predictions of the theory for the transition temperatures at higher pressures, leading to a set of phase diagrams which can be compared directly with experimental data. The theory also makes some predictions about conditions under which both transitions change from first to second order.

2. THE STATISTICAL MODEL

The statistical model on which the theory was based was fully described in Part I and we shall only give a brief summary here to indicate the additional features needed for calculations on solid-state transitions. Following the original theory of melting of monatomic substances due to Lennard-Jones and Devonshire[3], each of the N molecules in the crystal is supposed to be placed on one of two interpenetrating lattices of N-sites, referred to as α- and β-sites. Further each may take one of two orientations 1 or 2, so that there are four possibilities (α_1, α_2, β_1 and β_2) in all.

Apart from a partition function f^N associated with the vibration of each molecule in its cell, the effects of misplacement and misorientation are allowed for by an energy $W(>0)$ associated with each pair of molecules on neighbouring α- and β-sites and by another energy $W'(>0)$ associated with each pair on neighbouring α- (or neighbouring

β-) sites with unlike orientation (e.g. $\alpha_1\,\alpha_2$ or $\beta_1\,\beta_2$). The lowest energy configuration of such an assembly is clearly one in which all particles are on the same kind of site with the same kind of orientation. W and W' are then energies associated with positional and orientational defects in such a structure. No additional energy is associated with molecules in unlike orientations on neighbouring α- and β-sites to allow for the destabilization of the lattice caused by an orientational defect. The complete partition function then has the form

$$Z = f^N\,\Omega = f^N \sum \exp[-(N_{\alpha\beta}W + N_{\alpha_1\alpha_2}W' + N_{\beta_1\beta_2}W')/kT] \qquad (2.1)$$

where the summation is over all arrangements and orientations of molecules and $N_{\alpha\beta}$, $N_{\alpha_1\alpha_2}$, $N_{\beta_1\beta_2}$ are the numbers of pairs associated with energies W and W'.

To solve the statistical problem, two long-range order parameters are introduced. Q represents the fraction of particles on α-sites and S the fraction in 1-orientations. The partition function Ω is written in the form

$$\Omega = \sum_{Q,S} \Omega(Q,S) \qquad (2.2)$$

where $\Omega\,(Q,S)$ is the corresponding sum in (2.1) for given values of Q and S. The sum is replaced by its largest term, given the corresponding values of Q and S. These depend only on the two parameters

$$\kappa = zW/kT \qquad (2.3)$$

$$\nu = z'W'/zW \qquad (2.4)$$

where z is the number of β-sites immediately surrounding any α-site and z' is the coordination number of the α-lattice itself (the number of α-sites closest to any one α-site). Some values of Q and S obtained in this way are listed in the Appendix.

For small values of ν, long-range order first disappears in the rotational coordinates (S becomes $\frac{1}{2}$) as the temperature increases from zero. Positional disorder (Q becoming $\frac{1}{2}$) occurs for smaller κ (higher temperature). To investigate how these transitions show up thermodynamically, it is necessary to examine isotherms associated with the total free energy

$$A = A' + A'' \qquad (2.5)$$

$$A'/NkT = -\log f \qquad (2.6)$$

$$A''/NkT = -N^{-1}\log\Omega(Q,S) \qquad (2.7)$$

as described in Part I. The pressure associated with the cell partition function f was that based on the 6–12 potential

$$u(r) = 4\epsilon[(r_0/r)^{12} - (r_0/r)^6] \qquad (2.8)$$

and the three-shell spherically smoothed cell fields tabulated by WENTORF *et al.*[4] (To study the solid-state transitions adequately, it is necessary to know the thermodynamic functions for lower temperatures than those tabulated by these authors. These were obtained by interpolating between the values actually tabulated and the known behaviour in the limit of zero temperature.) In addition it is necessary to specify the volume dependence of W and W'. Following LENNARD-JONES and DEVONSHIRE[3] and the extension proposed in Part I, we take W'/W to be independent of volume and

$$W = W_0\,(v_0/v)^4 \qquad (2.9)$$

$$W_0/\epsilon = 0{\cdot}977 \qquad (2.10)$$

where v_0 is the volume if the molecules are placed on a face-centred cubic lattice where the distance between nearest neighbours is equal to the distance minimizing $u(r)$, that is $2^{1/6}\,r_0$.

The thermodynamic behaviour predicted by the model depends on the value of the parameter ν. It has already been noted[1] that there is a critical value of ν (0·325) below which two separate transitions may be distinguished, corresponding to a rotational disordering in the solid and melting. If ν is greater than 0·325, the two transitions merge into one first-order transition with correspondingly larger entropy and volume changes. (For much larger values of ν, the two transitions separate again, but the model is then less realistic and we shall not consider this aspect further.)

3. THEORETICAL PREDICTIONS FOR SOLID STATE TRANSITION

In this section we are concerned with the predictions about the solid-state transition at zero

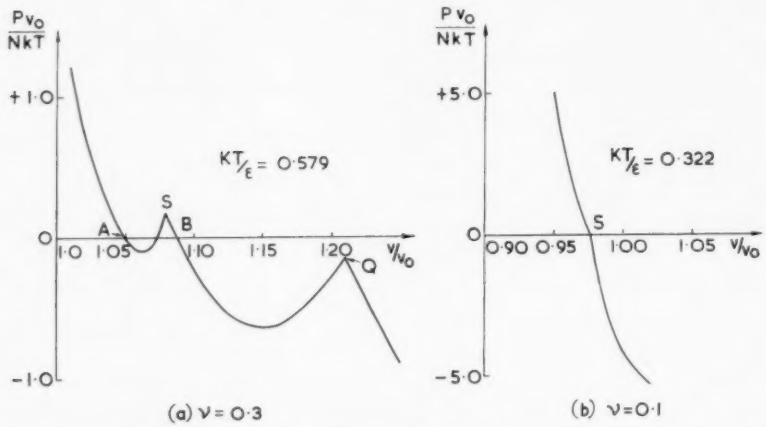

FIG. 1. Theoretical isotherms for solid-transition temperatures (a) $\nu = 0{\cdot}3$, (b) $\nu = 0{\cdot}1$.

pressure in the region where the two transitions are separate. If ν is not too far below the critical value of 0·325, the solid transition is found to be first-order, as is the melting transition. Fig. 1(a) shows a typical isotherm for the solid-state transition temperature in this region ($\nu = 0{\cdot}3$). The points marked S and Q indicate volumes at which orientational and positional order disappear. The two areas cut off by the line AB are equal so that phases corresponding to these points may exist in equilibrium with each other. For the phase B, the value of S is $\frac{1}{2}$ but Q still differs from $\frac{1}{2}$ so that

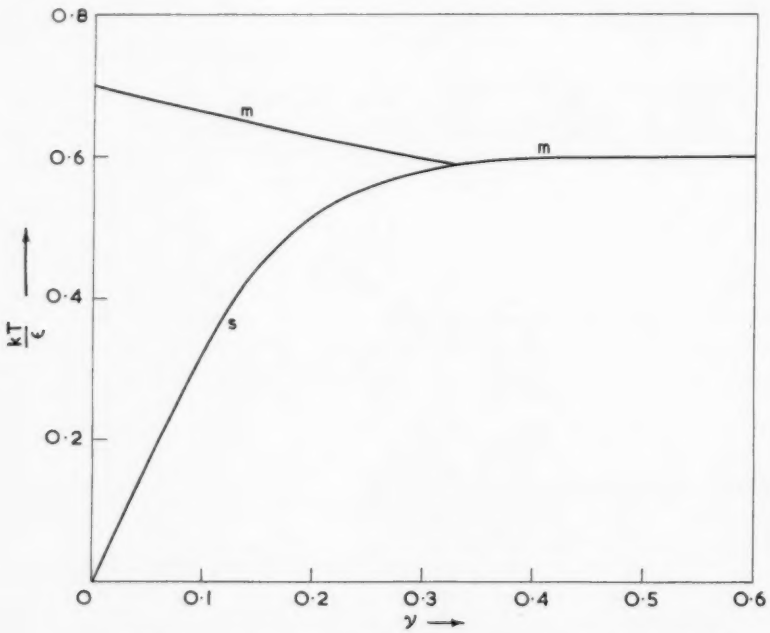

FIG. 2. Melting (m) and solid (s) transition temperatures as a function of ν.

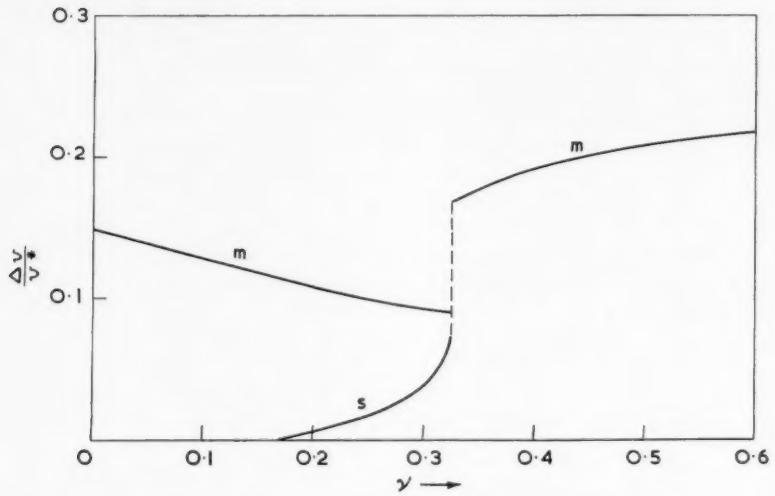

FIG. 3. Volume changes of melting (m) and solid (s) transitions as a function of ν.

Vol. 20
1961

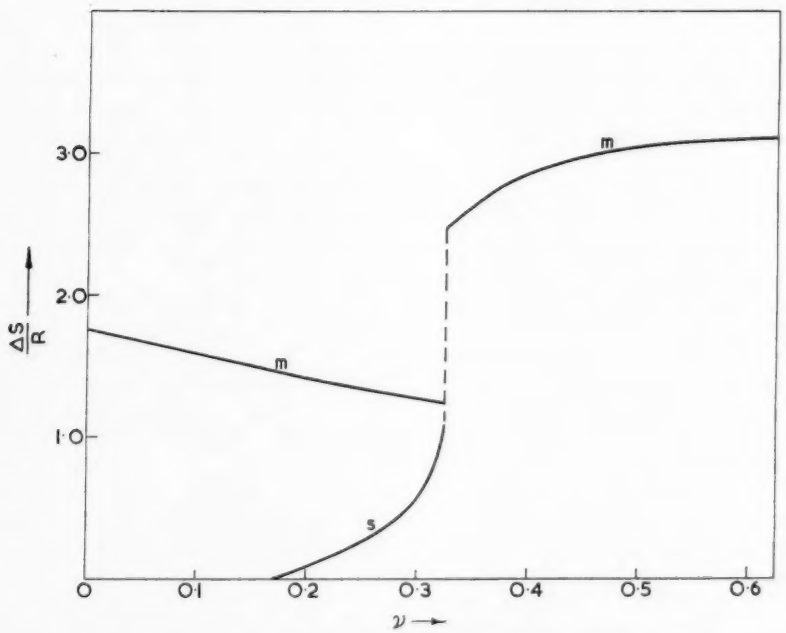

FIG. 4. Entropy changes of melting (m) and solid (s) transitions as a function of ν.

it corresponds to a solid with long-range disorder in orientations.

For smaller values of ν, the peak in the isotherm associated with the point S becomes less pronounced and for ν less than about 0·17, the transition temperature isotherm decreases steadily as the volume increases, with only a kink or discontinuity in slope to mark the loss of orientational order. Thermodynamically, this means that the transition changes from first to second order for these low values of ν. Fig. 1(b) shows a typical transition isotherm in this range.

By examining various isotherms in this way, we can obtain reduced transition temperatures kT_s/ϵ and kT_m/ϵ for each value of parameter ν. These are shown in Fig. 2. For $\nu > 0{\cdot}325$, the single curve gives the temperature for the combined transition.

Volume changes are also easily determined from the isotherms at transition temperatures, so we can plot $\Delta v/v^*$ against ν, where Δv is the increase in volume and v^* is the volume of the phase immediately below the transition. This is shown in Fig. 3. For $\nu < 0{\cdot}17$, the solid transition becomes second order and the volume change is then zero.

The change of entropy in the transition can be found in a similar manner and is shown in Fig. 4. Again there is no entropy change associated with the second-order transitions below $\nu = 0{\cdot}17$.

4. THEORETICAL PHASE DIAGRAMS

We now deal with our predicted phase diagrams, using reduced pressure and temperature coordinates, for various values of ν. These are constructed by drawing the summed $P'+P''$ isotherms for given ν and for a range of temperatures, and applying the "equal area principle" to the sigmoid portions to find the equilibrium pressures for the solid–solid and melting transitions. Figs. 5(a)–(e) illustrate typical behaviour.

In Fig. 5(a) ($\nu = 0$) the solid–solid transition cannot, of course, be seen, and we obtain a single solid–fluid phase boundary. For $\nu > 0$, but small, an orientational transition appears and we find, for example at $\nu = 0{\cdot}2$, a phase diagram such as is shown in Fig. 5(b). This predicts two solid phases in equilibrium at a reduced temperature kT_s/ϵ where T_s is finite for all finite pressures. Phase diagrams of this type cannot indicate the order of a transition and it has already been noted that at zero pressure the solid–solid transition changes from first to second order below $\nu = 0{\cdot}17$. We find that the orientational transition as predicted by the model exhibited this change of order for all ν between 0·17 and 0·325, but at correspondingly higher pressures. In addition the melting transition also changes to second-order at a pressure which depends on ν. This predicted change in the character of the melting transition was noted in the monatomic theory by LENNARD-JONES and DEVONSHIRE[3] and discussed further by DE BOER[5]. We shall discuss these predicted changes and associated volume changes in more detail when comparing the theory with experimental data in Section 6.

Figure 5(c) shows the phase diagram for $\nu = 0{\cdot}325$, the critical value where the two transitions merge at zero pressure. It can be seen that for all $P > 0$ the transitions have separated and we obtain a phase diagram that is essentially similar to that shown in Fig. 5(b) for $\nu = 0{\cdot}2$. For $\nu > 0{\cdot}325$ the transitions are merged at zero pressure as we have seen in Paper I, but it is interesting to find that at higher pressures the solid–solid transition is again separated, as can be seen in Fig. 5(d) for $\nu = 0{\cdot}4$. In this case, the melting curve should have a kink at the triple point. Finally, Fig. 5(e) shows the behaviour for $\nu = \frac{2}{3}$. This is a special case in our theory, where the two discontinuities in the isotherms coincide and we predict just one combined transition for all pressures. Above $\nu = \frac{2}{3}$, as was seen in Part I, the melting and orientational transitions remain merged (at zero pressure) up to the second critical value of $\nu = 1{\cdot}925$. Above this value something like liquid crystal behaviour is predicted, with the melting point preceding the orientational transition. However, our model becomes less realistic when applied to highly unsymmetrical molecules or molecules with strong associating forces as is implied by a high value of ν, and we do not consider this region further.

We note, incidentally, that our theory does not predict a genuine solid–fluid critical point for any value of ν, in the sense that there is no temperature above which the transitions disappear. This was noted by DE BOER for the monatomic theory.[5]

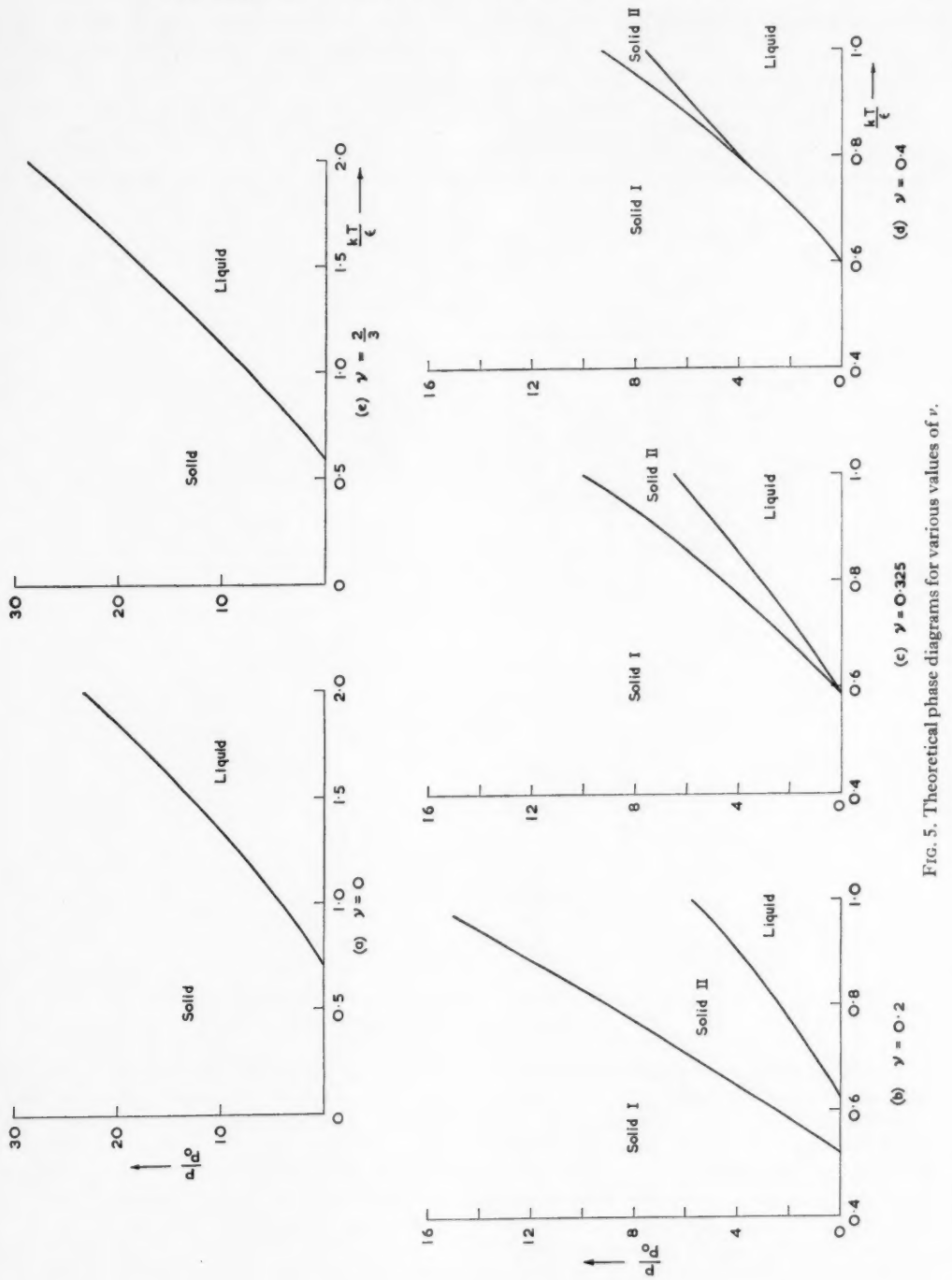

FIG. 5. Theoretical phase diagrams for various values of ν.

5. COMPARISON WITH EXPERIMENTAL PHASE DIAGRAMS

We now compare our predicted phase diagrams with such experimental data as are available. This involves an explicit assignation of the parameter ν for each substance compared, an interpolation from the phase diagrams described in the previous paragraph to construct the phase diagram for this value of ν, and the usual conversion of the experimental data to reduced temperature, kT/ϵ, and pressure, $Pv_0/N\epsilon$, units. The LENNARD-JONES and DEVONSHIRE interaction parameters ϵ and r_0 ($v_0 = Nr_0^3$) were, unless otherwise stated, obtained from HIRSCHFELDER *et al.*[6] Of the various ways in which ν might be assigned we choose the method in which the experimental reduced solid–solid transition temperature kT_s/ϵ (at $P = 0$) is fitted using the appropriate portion of the curve in Fig. 2.

The melting curve for the unmodified LENNARD-JONES and DEVONSHIRE theory,[3] that is for $\nu = 0$, may be compared with the melting curve of the inert gases. Our comparison using the data of ROBINSON[7] for argon agrees with a previously published result of DE BOER[5] except for minor differences arising from our use of compressibility data calculated from the more exact triple-shell integrals of WENTORF *et al.*[4] The agreement of the theoretical and experimental curves is within about 10 per cent up to 80,000 atm.

Figure 6 shows the predicted and experimental orientational and melting transitions for nitrogen.

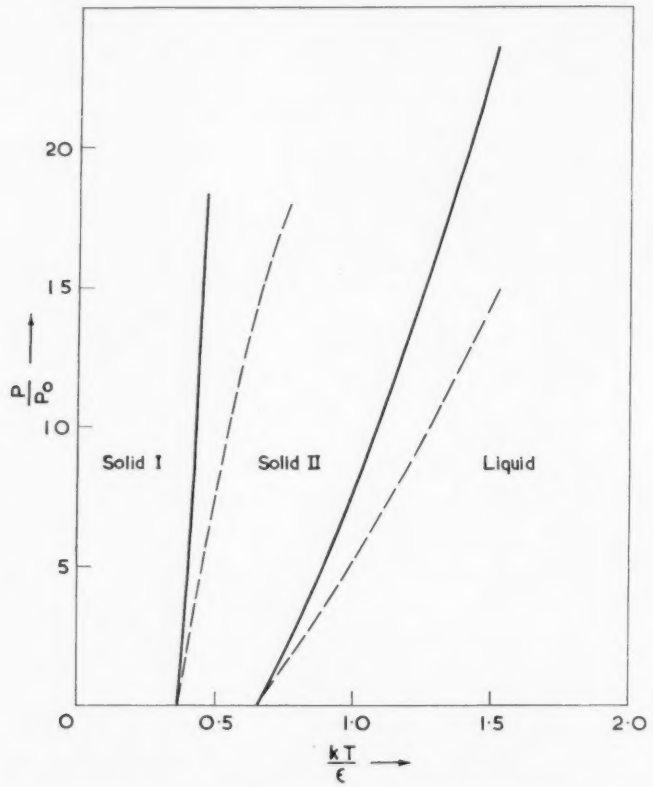

FIG. 6. Comparison of experimental (——) and theoretical (– – –) phase diagrams for nitrogen.

Vol. 20
1961

The data for the α–β-phase transition is from SWENSON[8], the melting point data from ROBINSON[7], and the value of ν calculated as described above, is 0·115. We have extended the comparison of theory and experimental results in the former up to 4650 atm. At this pressure a triple point was found and a further phase (the γ-phase) exists. Our model, of course, can only provide for two solid phases, and the comparison of STEWART[9], the melting data of CLUSIUS and WEIGAND[10] and an estimated ν of 0·04. Again agreement is reasonable, though the melting point data is insufficient for comparison of much more than the initial slopes, where however, agreement is perhaps fortuitously close. The low value of ν for methane is to be expected as its tetrahedral structure gives high symmetry and misorientation is relatively easy.

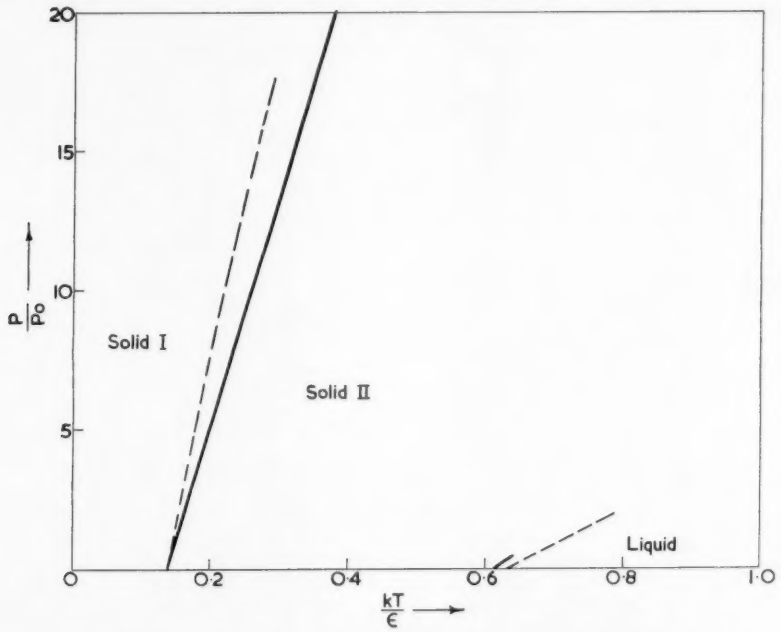

FIG. 7. Comparison of experimental (———) and theoretical (– – –) phase diagrams for methane.

becomes irrelevant. It will be seen that the predicted slopes for both transitions are too low. In the case of the orientational transition this may be due to an incorrect assignation of ν, for $d(kT_s/\epsilon)/d(Pv_0/N\epsilon)$ is a sensitive function of this parameter, but the melting curve cannot be fitted much better by any choice of ν. The lack of agreement is a manifestation of the too low melting entropy and/or too high relative volume change predicted by our model for nitrogen.

In Fig. 7, we show a similar comparison for methane, using the solid I–solid II transition data

In both Figs. 6 and 7 the scatter in the experimental points is much less than the deviation of our predicted curves from the experimental data.

There does not appear to be any other substance for which a full comparison with the experimental phase diagram is possible at present. There is some data on carbon tetrachloride,[11] but a theoretical difficulty arises because the 6–12 potential determined from virial coefficient data is known to give a poor description of other equilibrium properties and the transport coefficients. To apply the theory satisfactorily to this type of

molecule, it would be necessary to extend it to other basic intermolecular potentials.

There appears to be no example for which a phase diagram of the type shown in Fig. 5(d) is appropriate, but the total amount of available experimental data is very limited. The theory predicts that for substances for which the appropriate value of the parameter ν is just greater than the critical value (0·325), the two transitions merge at zero pressure, but would separate at higher pressures. Substances which may show the effect would be sufficiently asymmetric to prevent any solid disordering at zero pressure, but not so highly asymmetric that the effective ν value approaches 2/3, when the transitions would never be separated. Ethane is a possible example, since it shows no solid transition and is fairly symmetrical. If the appropriate ν value was 0·4, for example, the pressure for separation of the transitions is predicted to be about 1900 atm.

6. VOLUME CHANGES AND ORDER OF TRANSITIONS

As pointed out previously, the theory predicts that the melting transition should become second-order under sufficiently high pressures. Solid state transitions are predicted to be second-order for $\nu < 0{\cdot}17$ even at zero pressure and to become second-order under increased pressure for higher values of ν. Although neither transition has been proved to be second-order for any substance, some test of these predictions can be made by comparing trends of observed volume changes with experimental data when the transitions are definitely first-order.

In Fig. 8 we show predicted and experimental relative volume changes at the two transitions, as a function of pressure, for nitrogen (experimental melting curve data from GRILLY and MILLS[13]). Our model predicts a too rapid decrease in the relative volume change at the melting point, with pressure. This situation also occurs in the case of argon (not shown) which we have examined using BRIDGMAN's data.[12] This may well be due to numerical inadequacies in the free-volume theory, for at high reduced temperatures the relative volume change is very sensitive to small errors in the slope of the free-volume theory compressibility vs. reduced density isotherms, which make a large contribution to our calculated isotherms.

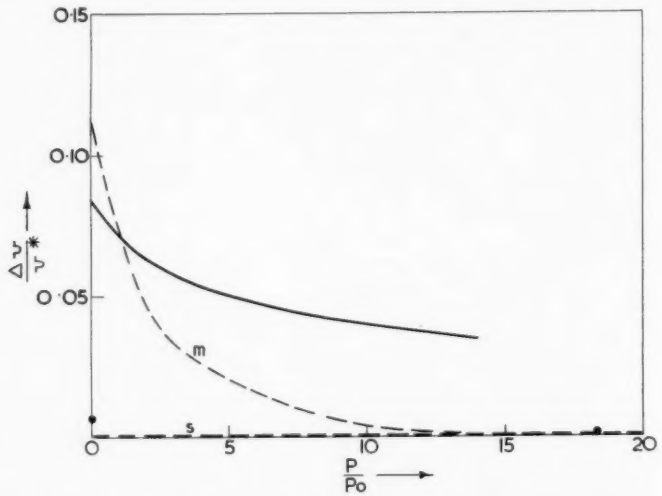

FIG. 8. Comparison of experimental (———) and theoretical (– – –) volume changes on melting and solid transitions for nitrogen. Points marked ● are experimental values for solid transition.

Clearly, if there is a pressure at which melting changes to a second-order transition, it is considerably underestimated by the present theory. Two experimental points for the relative volume change in the α–β solid transition of nitrogen, from SWENSON[8], are included in Fig. 8. Estimating ν by the transition temperature gives a value less than 0·17, so the transition is given as second-order by the theory. This is not found experimentally, although observed volume changes are small and do decrease with pressure.

Methane has a low value of ν (0·04) as measured by the solid transition temperature and is again predicted to be second-order at zero pressure. We have found no data on the corresponding volume change, although a finite entropy change is reported,[14] implying a first-order transition. However this change is smaller than for most other substances, so it seems possible that a change to second-order might be produced by moderate pressures.

7. COMPARISON OF THERMODYNAMIC PROPERTIES OF MELTING AND SOLID TRANSITIONS

A further test of our theory, in some ways more satisfactory in that it does not require the somewhat dubious assignation of ν, is to plot any two of the predicted parameters such as T_s, T_m, $\Delta v/v^*$, ΔS_s etc. against each other and to compare this with experimental data. Thus in Fig. 9 we have plotted

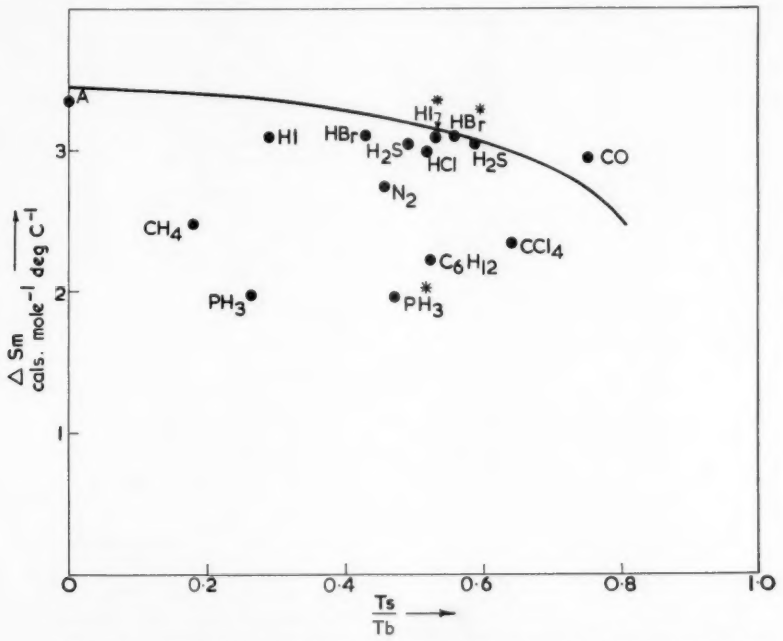

FIG. 9. Comparison of melting entropy ΔS_m with solid transition/boiling temperature ratio. Theoretical curve ————. For substances showing two solid transitions, a star denotes the upper transitions.

T_s/T_b vs. ΔS_m, the reduced entropy of melting, all quantities being evaluated at $P = 0$. The full line is the theoretical prediction for the range $\nu = 0$ to $\nu = 0{\cdot}325$, and we have assumed a constant relationship for the reduced boiling point, namely $kT_b/\epsilon = 0{\cdot}72$. The experimental data are from EUCKEN[14]. In a number of cases there are two solid transitions to consider and both are shown.

Figure 10 shows a similar plot of ΔS_m against ΔS_s. The agreement between theory and experiment is in general less satisfactory in these two

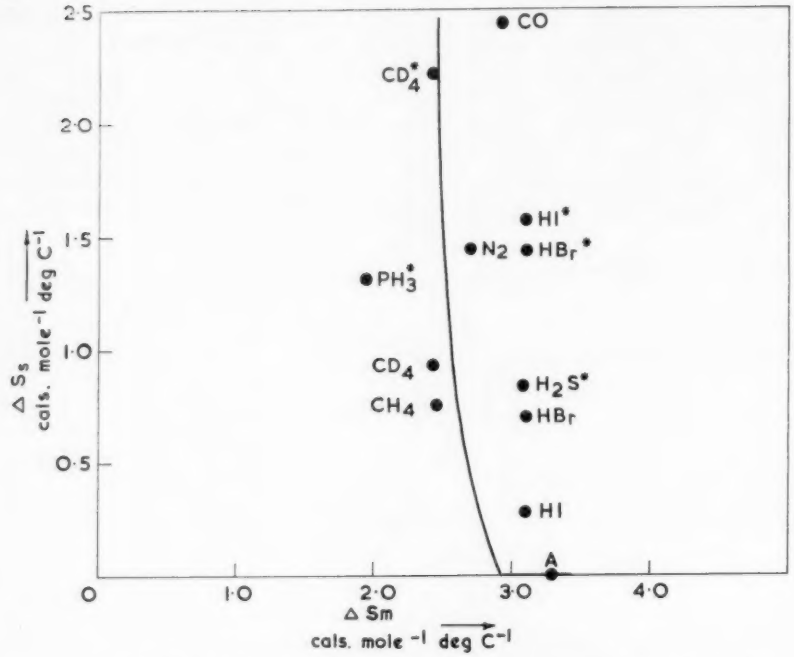

FIG. 10. Comparison of melting entropy ΔS_m with solid transition entropy ΔS_s. Theoretical curve ———. For substances showing two solid transitions, a star denotes the upper transition.

plots than it is in the analogous type of plot in Part I. We may again attribute this to our more formalized, less physically realistic, concept of the solid–solid transition compared with our concept of the melting transition. Nevertheless there undoubtedly is a correlation between the parameters as shown which is reproduced by our model.

Acknowledgements—We wish to acknowledge the help of Miss P. M. NOYES in the computational and graphical work associated with this research.

This work described in the paper is part of the research programme of the National Physical Laboratory and is published by permission of the Director.

REFERENCES

1. POPLE J. A. and KARASZ F. E. (Part I) *J. Phys. Chem. Solids* **18,** 28 (1961).
2. FOWLER R. H., *Proc. Roy. Soc.* A**149,** 1 (1935).
3. LENNARD-JONES J. E. and DEVONSHIRE A. F., *Proc. Roy. Soc.* A**170,** 464 (1939).
4. WENTORF R. H., BUEHLER R. J., HIRSCHFELDER J. O. and CURTISS C. F., *J. Chem. Phys.* **18,** 1484 (1950).
5. DE BOER J., *Proc. Roy. Soc.* A**215,** 4 (1952).
6. HIRSCHFELDER J. O., CURTISS C. F. and BIRD R. B., *Molecular Theory of Gases and Liquids,* John Wiley, New York (1954).
7. ROBINSON D. W., *Proc. Roy. Soc.* A**225,** 393 (1954).
8. SWENSON C. A., *J. Chem. Phys.* **23,** 1963 (1955).
9. STEWART J. W., *J. Phys. Chem. Solids* **12,** 122 (1959).
10. CLUSIUS K. and WEIGAND K., *Z. Phys. Chem.* B**46,** 1 (1940).
11. BRIDGMAN P. W., *Phys. Rev.* **3,** 153 (1914).
12. BRIDGMAN P. W., *Proc. Amer. Acad. Arts. Sci.* **70,** 1 (1934).
13. GRILLY E. R. and MILLS R. L., *Phys. Rev.* **105,** 1140 (1957).
14. EUCKEN A., *Z. Angew. Chem.* **55,** 163 (1942).

APPENDIX

Q and S as a function of κ for some values of ν

(a) $\nu = 0$

κ	Q
4·0 (c_Q)*	0·500
4·1	0·367
4·2	0·314
4·4	0·248
4·6	0·204
4·8	0·171
5·0	0·144
5·2	0·124
5·6	0·093
6·0	0·071
7·0	0·037
8·0	0·021
9·0	$0·012_5$
10·0	$0·007_2$
11·0	$0·004_3$
12·0	$0·002_6$

(b) $\nu = 0·2$

κ	Q	S
4·44 (c_Q)	0·500	
4·5	0·408	
4·6	0·341	
4·7	0·302	
4·8	0·267	
5·0	0·224	
5·5	0·157	
6·0	0·107	
7·0	0·058	
8·0	0·032	
9·0	0·020	
10·0	0·015	
10·22 (c_S)	0·014	0·500
10·3	0·010	0·414
10·4	0·009	0·370
10·5	$0·008_5$	0·345
10·8	$0·007_5$	0·290
11·0	0·007	0·264
12·0	$0·003_5$	0·176
14·0	0·001	0·090
16·0	$0·000_4$	0·054
18·0	$0·000_1$	0·032

(c) $\nu = 0·3$

κ	Q	S
4·71 (c_Q)	0·500	
4·8	0·380	
4·9	0·330	
5·0	0·294	
5·5	0·192	
6·0	0·133	
6·5	0·097	
7·0	0·074	
7·46 (c_S)	0·057	0·500
7·6	0·047	0·344
7·7	0·042	0·305
7·8	0·039	0·275
7·9	0·037	0·250
8·0	$0·036_5$	0·229
8·5	0·024	0·162
9·0	0·017	0·121
9·5	0·012	0·094
10·0	0·008	0·075
11·0	0·005	0·050
12·0	0·003	0·035
15·0	$0·000_6$	0·013

(d) $\nu = 0·4$

κ	Q	S
5·00 (c_Q)	0·500	
5·1	0·380	
5·2	0·332	
5·3	0·300	
5·4	0·276	
5·5	0·254	
5·7	0·216	
5·9	0·185	
6·1	0·160	
6·3	0·139	
6·44 (c_S)	0·128	0·500
6·5	0·110	0·311
6·6	0·095	0·252
6·8	0·073	0·190
7·0	0·058	0·151
7·5	0·032	0·089
8·0	0·018	0·055
8·5	0·013	0·040
9·0	0·010	0·037
10·0	$0·007_5$	0·025
12·0	$0·002_7$	0·009
14·0	$0·000_9$	0·004

* See note on p. 306.

Vol. 20
1961

(e) $\nu = 0{\cdot}667$

κ	Q	S
$5{\cdot}64(c_Q,c_S)$	0·500	0·500
	0·138	0·083
5·7	0·125	0·071
5·8	0·111	0·060
5·9	0·099	0·052
6·0	0·091	0·045
6·2	0·075	0·034
6·4	0·063	0·027
6·6	0·054	0·022
6·8	0·047	0·019
7·0	0·041	0·016
7·5	0·032	0·012
8·0	0·025	0·008
8·5	0·018	0·005
9·0	0·013	0·003
10·0	0·007	$0{\cdot}001_4$
12·0	$0{\cdot}002_5$	$0{\cdot}000_4$

c_Q and c_S indicate the critical values of κ ($\kappa \propto 1/T$) below which the positional and orientational order parameters Q and S, respectively, are at their maximum value of 0·5, corresponding to complete disorder.

Vol. 2
196

J. Phys. Chem. Solids Pergamon Press 1961. Vol. 20, Nos. 3/4, pp. 307–314. Printed in Great Britain.

RADIATION INDUCED CHEMISORPTION OF OXYGEN ON CHROMIA

M. NACHMAN, I. MAXIM and T. BRAUN

Institute of Atomic Physics, Bucharest, Rumania

(*Received* 7 *September* 1960; *revised* 19 *January* 1961)

Abstract—The effect of nuclear radiation on the chemisorption of oxygen on Cr_2O_3, Cr_2O_3–Al_2O_3 and Cr_2O_3–SnO_2 catalysts has been studied. An iodometric method was used to measure the amount of chemisorbed oxygen; simultaneously the increase in the catalytic activity of the catalyst in the decomposition of H_2O_2 was determined. It was found that the radiation present within a nuclear reactor promotes the chemisorption of oxygen on chromia (either pure or supported on Al_2O_3 or SnO_2) at temperatures at which such a chemisorption does not normally occur. The radiochemisorption of oxygen on chromia increases with the degree of dispersion of chromia on Al_2O_3 or SnO_2 and is accompanied by an increased catalytic activity of this catalyst in the decomposition reaction of H_2O_2. It seems that the radiochemisorption is largely due to the action of γ-rays and fast neutrons on the gas.

1. INTRODUCTION

It is known that the intense radiation present within a nuclear reactor promotes chemical reactions in solid–gas systems at temperatures at which these do not normally occur. Such reactions have been investigated especially in connection with their importance for reactor technology.[1] Very little attention was paid to semiconductor–oxygen systems although they are interesting both from theoretical and practical points of view, especially in connection with the studies made in the last few years on the influence of nuclear radiations on semiconductor catalysts' properties.[2]

It is the object of this work to report the results of our investigations about the effect of pile radiation on the chemisorption of oxygen on pure chromia, Cr_2O_3–Al_2O_3 and Cr_2O_3–SnO_2 catalysts.

2. EXPERIMENTAL

(a) *Preparation of samples and irradiation*

Powder catalysts were used in this work. The samples were prepared from Cr_2O_3 A.R. grade (Chinoin) and SnO_2 A.R. grade (Merck). The Cr_2O_3–Al_2O_3 and Cr_2O_3–SnO_2 mixtures were obtained through mechanical mixing of the components thus avoiding the reduction in hydrogen atmosphere and, therefore, the possibility that some hydrogen would remain chemisorbed on the sample surface.

For an exposure, 0·5–2 g of the catalyst were inserted in a 40 cm³ quartz ampoule. The ampoules (*d*) were connected to a vacuum system, containing a flask (*a*) with $KMnO_4$ for the preparation of oxygen, two traps (*b*, *c*) cooled with liquid nitrogen,

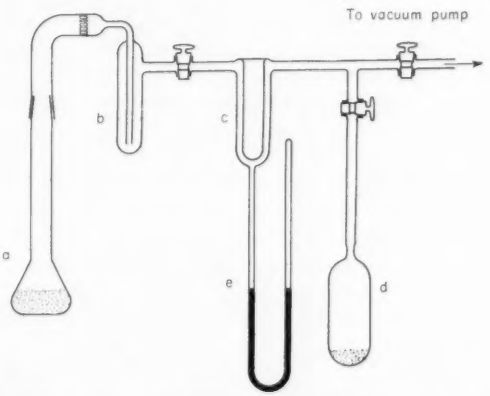

FIG. 1. Apparatus for filling the ampoules with oxygen: *a*, flask with $KMnO_4$; *b* and *c* traps cooled with liquid nitrogen; *d* quartz ampoule with sample; *e* mercury manometer.

and a mercury manometer (*e*) (Fig. 1). After evacuating the system to 10^{-2} mm Hg residual pressure, the flask was heated and the resulting oxygen was swept through the system. The whole vacuum system, including the ampoule, was flushed many times with oxygen. The stopcock to the vacuum pump was then closed, the pressure of oxygen in the system was allowed to rise to one atmosphere and the ampoule was sealed off from the system.

During these operations the catalyst was kept at room temperature. The aim of this initial treatment was to eliminate residual gases from the ampoule containing the sample. Otherwise such gases might remain as impurities in the oxygen.

The degree of oxidation of the samples after flushing with oxygen at room temperature is very small.[8] This initial surface state of the chromia samples was considered to be the reference state in this investigation.

The samples were irradiated in one of the experimental holes of the water-cooled and water-moderated 2 MW enriched uranium reactor of the Institute of Atomic Physics, Bucharest.

The thermal neutron fluxes and cadmium ratios in the irradiation holes were measured by activation of gold foils. The gamma dose rates were determined by chemical dosimetry. The results obtained in this manner are accurate within ± 15 per cent. The integrated thermal and fast neutron fluxes and the γ-ray dosage were calculated from the exposure time.

In order to avoid the effect of thermal neutrons, some irradiations were performed with the ampoules in 1 mm thick cadmium sheets.

Simultaneously with the samples for irradiation, blanks were also prepared.

(b) *Temperature of the sample during irradiation*

Because there also exists a thermal chemisorption of oxygen on chromia,[3,4] it was necessary to control the temperature during in-pile exposure, in order to separate the radiochemisorption from the thermal one. Therefore the temperatures in several points of the sample were measured during irradiation. We used Ni–CrNi thermocouples which seem to be unaffected by irradiation.[7] The temperature of the samples during exposure was never greater than 90°C, except for the samples irradiated in cadmium sheets, when the temperature rose to 250°C. By cooling the cadmium-wrapped ampoules with an air jet it was possible to maintain the temperature below 120°C.

(c) *Measurement of the amount of chemisorbed oxygen*

The quantity of oxygen chemisorbed by the catalyst was determined by an iodometric method.[3] An increased sensitivity and reproducibility was obtained by using the dead-stop end-point method. Analyses were performed as follows: 0·5 g KI, 20 ml HCl and 100 ml H_2O were added

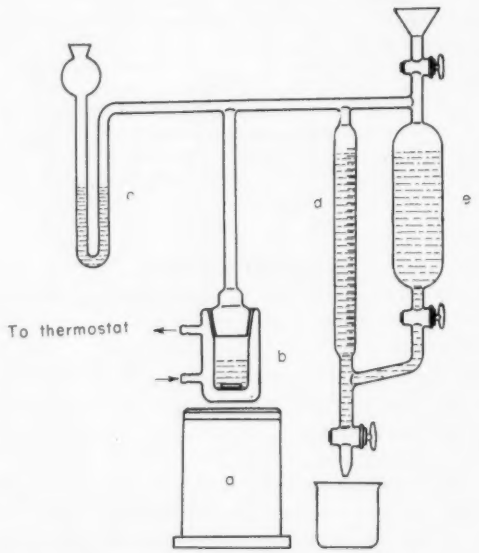

FIG. 2. Apparatus for studying the catalytic decomposition of H_2O_2; *a* magnetic stirrer; *b* reaction vessel; *c* manometer; *d* burette; *e* water reservoir.

to 0·5 g catalyst, the mixture was allowed to stand for 15 min in darkness and then titrated with a N/100 $Na_2S_2O_3$ solution.

(d) *Catalytic activity determination in the* H_2O_2 *decomposition*

VOLTZ and WELLER[5] and MATSUNAGA[6] have shown that the extent of surface oxidation of chromia and chromia–alumina is related to the activity for the catalytic decomposition of aqueous hydrogen peroxide. Therefore, simultaneously with the determination of the chemisorbed oxygen,

Vol. 2
196

the catalytic activity of catalyst samples was measured.

The measurements were made with the apparatus shown in Fig. 2. With this apparatus the amount of oxygen liberated during the decomposition of H_2O_2 is measured always at the same pressure. The reaction vessel (*b*) was maintained at 42°C with a Wobser ultrathermostat. The H_2O_2–catalyst suspension was stirred with a magnetic stirrer (*a*). As a result of the decomposition of H_2O_2, oxygen was liberated and the increase of the pressure in the reaction vessel was indicated by a manometer (*c*). A quantity of water was drained from the burette (*d*) until the pressure in the vessel has reached its initial value. From the volume of the drained water the amount of oxygen liberated could be determined.

The amount of oxygen liberated by the decomposition of 5 ml of a 30 per cent solution of H_2O_2 (at 42°C) was followed as a function of time. Catalyst sample weight was always 0·2 g.

3. RESULTS AND DISCUSSION

(a) *Thermal chemisorption of oxygen on chromia–alumina catalyst*

Owing to the existence of thermal chemisorption, as mentioned above, it was necessary to measure the amount of chemisorbed oxygen on unirradiated catalyst, heated at different temperatures during a time interval equal to the in-pile exposure time.

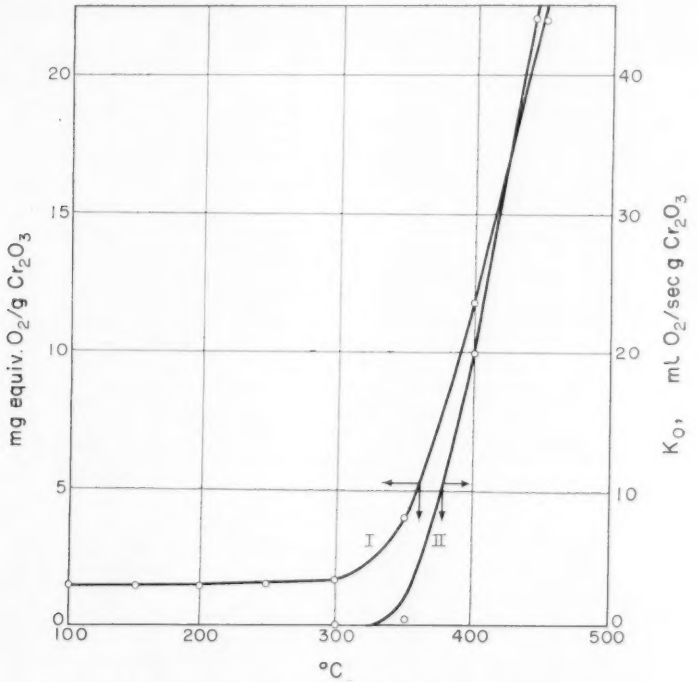

FIG. 3. Reaction rate, (K_0), of H_2O_2 decomposition (curve II) and amount of chemisorbed oxygen (curve I) vs. oxidation temperature of 2·5 per cent Cr_2O_3–Al_2O_3 catalyst.

In Fig. 3 are plotted the amounts of oxygen thermally chemisorbed (in mg equiv. O_2/gCr_2O_3) by unirradiated catalysts previously heated for 10 hr, against the heating temperature of the catalyst–oxygen system (curve I). On the same figure is also plotted the reaction rate constant K_0 (in ml O_2/sec g Cr_2O_3) of the decomposition of aqueous hydrogen peroxide (at 42°C) in the presence

of the catalyst (curve II). In these experiments a chromia–alumina mixture containing 2·5 per cent chromia was used.

It appears from the figure that up to a temperature of 300°C practically no chemisorption occurs. It may be concluded that thermal chemisorption does not occur during in-pile exposure because the temperature of the samples was always kept below 120°C.

amount of chemisorbed oxygen were then measured. Fig. 4 shows the results obtained for the catalytic activity of the unirradiated chromia samples (curve III), and for the chromia samples irradiated in oxygen (curve IV) and in vacuum (curve V).

On the same figure the amount of oxygen liberated as a result of thermal decomposition of H_2O_2 at 42°C in the absence of the catalyst (curve

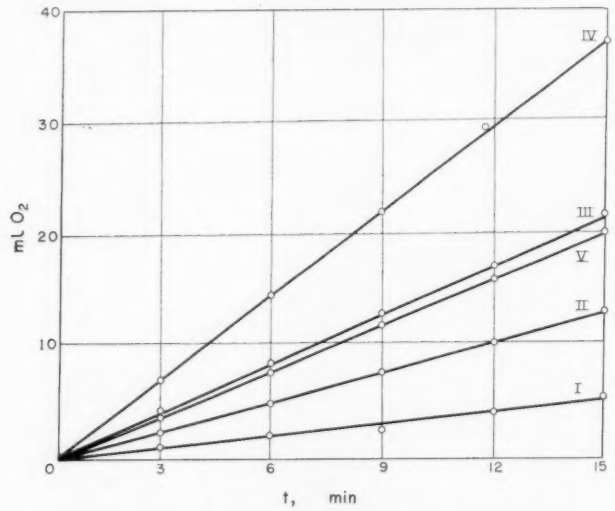

FIG. 4. Amount of oxygen liberated vs. time in H_2O_2 decomposition. I. Thermal decomposition; II, homogenous decomposition; III, decomposition by 2·5 per cent Cr_2O_3–Al_2O_3 catalyst, unirradiated; IV, decomposition by 2·5 per cent Cr_2O_3–Al_2O_3 catalyst, irradiated in oxygen; V, decomposition by 2·5 per cent Cr_2O_3–Al_2O_3 catalyst, irradiated in vacuum.

(b) *Radiochemisorption of oxygen on pure chromia*

Samples of pure chromia were subjected to reactor irradiation:

(i) in ampoules filled with oxygen at atmospheric pressure;

(ii) in vacuum (at a pressure of 10^{-2} mm Hg).

After exposure to an integrated neutron flux of $\sim 6 \times 10^{17}$ neutrons/cm^2 and a γ-ray dose of $\sim 10^9$ r, the samples were allowed to undergo radioactive decay for 60 hr. The catalytic activity (at 42°C) of the irradiated samples as well as the

I) is also given. Curve II represents homogenous catalytic decomposition of the H_2O_2 caused by the chromium ions in the solution due to the slight solubility of chromia in H_2O_2.[9] It can be seen from the figure that the catalytic activity of the samples irradiated in oxygen is much higher than that of the unirradiated or that of those irradiated in vacuum. The quantity of chemisorbed oxygen is 160 μg equiv./g Cr_2O_3. For the samples irradiated in vacuum, the catalytic tests show that some desorption of oxygen occurs. Because the temperature of the samples during irradiation was

Vol. 2
1961

always less than 120°C it may be concluded that thermal chemisorption during irradiation is negligible and, therefore, a radio-induced chemisorption occurs.

(c) *Radiochemisorption of oxygen on chromia supported on alumina*

Both WELLER and VOLTZ[4] and MATSUNAGA[6] have shown that thermo-activated chemisorption of oxygen on chromia takes place to a great extent when the latter is supported on γ-alumina. In order to check whether this fact remains also valid for radiochemisorption, some experiments with chromia mixed in different proportions with alumina were performed.

Experiments with pure alumina samples have shown that radiochemisorption of oxygen does not occur on these samples. The chromia–alumina mixtures were exposed in an oxygen atmosphere to an integrated neutron flux of $\sim 1{\cdot}5 \times 10^{17}$ neutrons/cm^2 and to a γ-ray dosage of $\sim 2{\cdot}5 \times 10^8$ r.

At the same time, test samples of the same composition were irradiated in vacuum. The reaction rates of the catalytic decomposition of H_2O_2 (expressed in ml O_2/sec g Cr_2O_3) and the amount of radiochemisorbed oxygen were determined and plotted vs. the chromia content in the mixture. For the samples irradiated in vacuum no increase of the catalytic activity after reactor exposure was observed. The results for the catalyst samples irradiated in oxygen are given in Fig. 5, where the reaction rate of the catalytic reaction is plotted vs. the chromia content of the mixtures, before (curve I) and after (curve II) irradiation. In Fig. 6, the difference (in ml O_2/sec g Cr_2O_3) between the reaction rates of the catalysed reaction with an irradiated and an unirradiated sample is represented vs. the chromia content of the mixture (curve I). Simultaneously, the quantity of chemisorbed oxygen is given as a function of the same parameter (curve II).

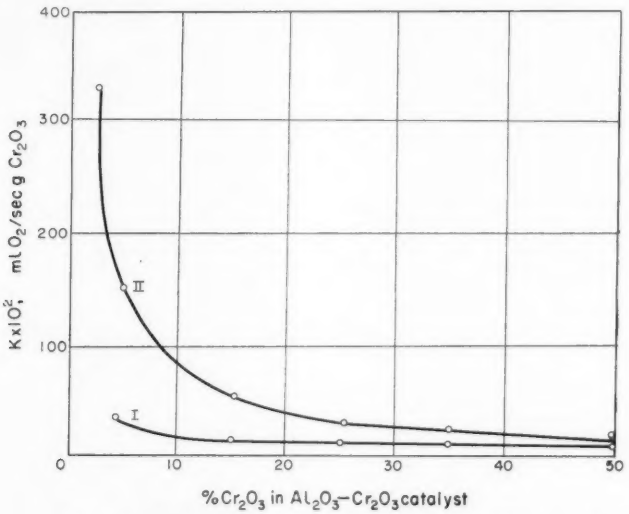

FIG. 5. Reaction rate, K, of H_2O_2 decomposition vs. the chromia content of unirradiated (curve I) and irradiated in oxygen (curve II) Cr_2O_3–Al_2O_3 catalyst.

From these figures, it is clear that an increase in chemisorption and, at the same time, an increase of the catalytic activity of chromia with the dispersion degree on alumina occurs under irradiation. The results are similar to those obtained by VOLTZ and WELLER[4] and by MATSUNAGA[6] for thermo-activated chemisorption on chromia–alumina catalysts.

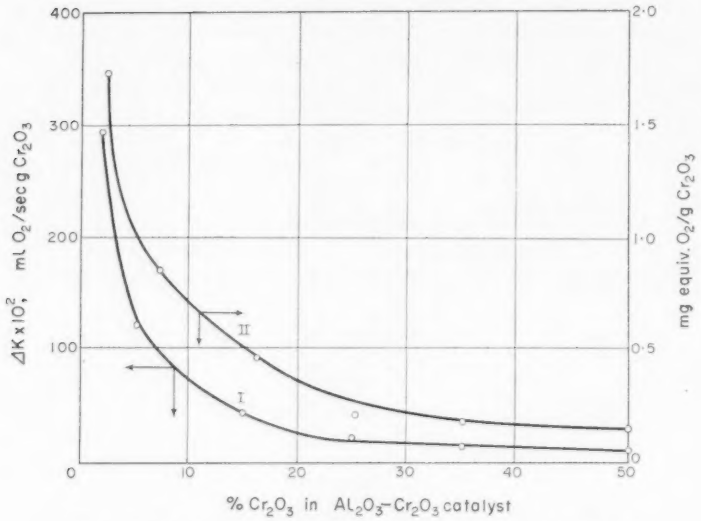

FIG. 6. Radiation induced increases in reaction rate of H_2O_2 decomposition, ΔK (curve I), and amount of chemisorbed oxygen during irradiation (curve II), vs. chromia content of the Cr_2O_3–Al_2O_3 catalyst.

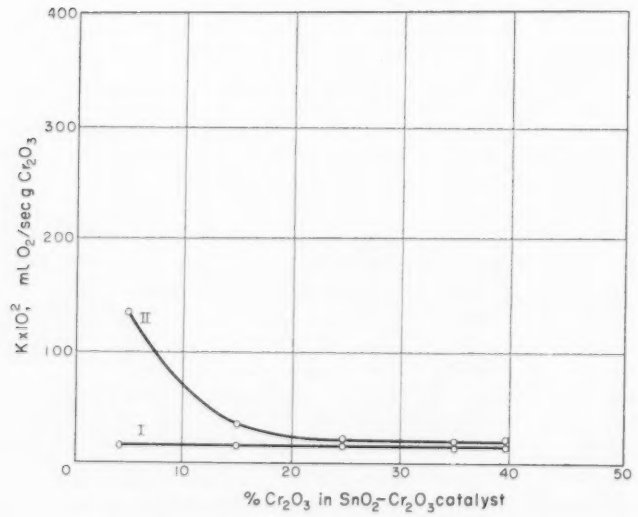

FIG. 7. Reaction rate, K, of H_2O_2 decomposition vs. chromia content of the unirradiated (curve I) and irradiated in oxygen (curve II) Cr_2O_3–SnO_2 catalyst.

(d) *Radiochemisorption of oxygen on chromia supported on* SnO_2

Results similar to those described above for chromia–alumina mixtures were obtained also for Cr_2O_3–SnO_2 mixtures.

Figure 7 shows that also for these catalysts (Cr_2O_3–SnO_2) the catalytic activity is higher for samples irradiated in oxygen (curve II) than for the unirradiated ones (curve I) and that this activity increases with the dispersion degree of chromia.

(e) *Irradiation time dependence of oxygen radiochemisorption on 2·5 per cent chromia–alumina catalyst*

In order to study the irradiation time dependence of the oxygen radiochemisorption on chromia–alumina catalysts, samples, with a content of 2·5 per cent chromia, were exposed in the reactor to different integrated neutron fluxes. As far as possible we tried to perform these irradiations under the same conditions, particularly at the same neutron flux and γ-ray dose rate, by varying only the time of exposure.

The irradiation was performed in a neutron flux of $\sim 2 \times 10^{13}$ neutrons/sec cm^2, and a γ-ray dose rate of $\sim 10^8$ r/hr.

The results are given in Fig. 8 where the difference (in arbitrary units) in the rate constants of the irradiated and unirradiated samples is plotted vs. the integrated neutron fluxes, expressed in neutrons/cm^2, which is proportional to γ-ray dose and also to exposure time. Although the experimental values diverge to a great extent, they seem to imply the existence of a plateau beginning with integrated neutron fluxes of 10^{18} neutrons/cm^2 (or a γ-ray dose of $\sim 10^9$ r), in spite of the fact that the amount of chemisorbed oxygen represents only one per cent of the oxygen present in the ampoule.

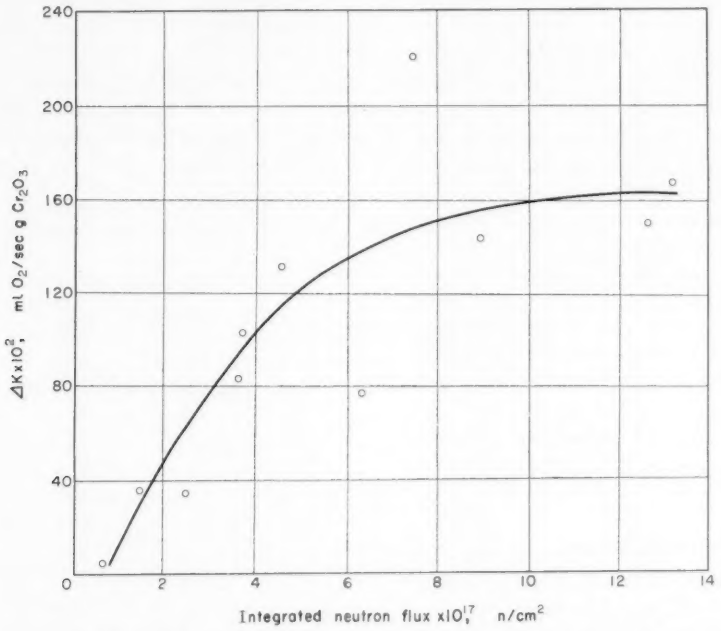

FIG. 8. Radiation induced increases in catalytic activity, ΔK, as a function of the integrated neutron flux.

(f) *Influence of the nature of radiation on the radiochemisorption*

In order to estimate the contribution of thermal

neutrons to the oxygen radiochemisorption on chromia and chromia–alumina, some of the samples were irradiated in cadmium covered ampoules.

No significant difference in the radiochemisorption between in-cadmium and without-cadmium irradiated samples was observed. One may conclude that the radiochemisorption is mainly due to the action of γ-rays and fast neutrons on the system.

(g) *Thermo-activated chemisorption of oxygen on samples irradiated in vacuum*

In order to see to what extent the lattice defects produced by fast neutrons in chromia samples affect the oxygen chemisorption process, the chemisorption at different temperatures was measured on samples irradiated previously in vacuum.

The samples were exposed to an integrated neutron flux of $\sim 10^{17}$ neutrons/cm^2. No difference was observed between thermo-activated chemisorption on irradiated and unirradiated samples. This lends support to the assumption that, up to an integrated neutron flux of about 10^{17} neutrons/cm^2, radiochemisorption is due rather to the effects produced by γ-rays and fast neutrons in the gas phase than to the radiation damage in the solid. It is however possible that, to some extent, the chemisorption is due also to defects in the solid.

4. CONCLUSIONS

From the experimental results presented above the following conclusions may be drawn.

(a) The radiation present within a nuclear reactor promotes the chemisorption of oxygen on chromia (either pure or supported on alumina or SnO_2) at temperatures at which such a chemisorption does not normally occur.

(b) The radiochemisorption of oxygen on chromia increases with the degree of dispersion of chromia on alumina or on SnO_2.

(c) The radiochemisorption of oxygen on chromia is accompanied by an increased catalytic activity of this catalyst in the decomposition reaction of hydrogen peroxide.

(d) Catalytic activity measurements seem to indicate that for a given neutron flux and γ-ray dose rate the amount of chemisorbed oxygen tends toward a constant value.

(e) The irradiation of the samples in evacuated ampoules does not increase the thermal chemisorption of oxygen on these samples. Thus one may conclude that, at least up to integrated neutron fluxes of, 10^{17} neutrons/cm^2 and γ-ray doses of $\sim 10^9$ r, the radiochemisorption is due rather to the action of γ-rays and fast neutrons on the oxygen than on the solid. It is however possible that to some extent, defects in the solid may also contribute to the oxygen chemisorption.

Acknowledgement—The authors are indebted to Miss E. TĂNASE for her technical assistance in this work.

REFERENCES

1. HURST R. and WRIGHT Y., *Proceedings of the International Conference on the Péaceful Uses of Atomic Energy, Geneva*, Paper No. 90, (1955); KOSIBA W. L. and DIENES G. J., *Advanc. Catalys.* **9,** 398 (1957); WOODLEY R. E., Report HW 40142 (1955); YOUNG F. W., Report ORNL 55–3–70 (1955).
2. TAYLOR E. H., *J. Chem. Educ.* **36,** 396 (1959); TAYLOR E. H., KOHN H. W. and MOORE G. F., *International Atomic Energy Agency Conference, Warsaw (Poland)*, (1959).
3. WELLER S. W. and VOLTZ S. E., *J. Amer. Chem. Soc.* **76,** 4695 (1954).
4. VOLTZ S. E. and WELLER S. W., *J. Amer. Chem. Soc.* **76,** 4703 (1954); MATSUNAGA Y., *Bull. Chem. Soc. Japan* **30,** 868 (1957).
5. VOLTZ S. E. and WELLER S. W., *J. Amer. Chem. Soc.* **76,** 1586 (1954).
6. MATSUNAGA Y., *Bull. Chem. Soc. Japan* **30,** 984 (1957).
7. BURAS B., RZEWUSKI H., BARTENBACH M. and TOMCZAK Z., Polish Academy of Sciences, Institute of Nuclear Research, Report No. 101/I–B (1959).
8. MATSUNAGA Y., *Bull. Chem. Soc. Japan* **31,** 58 (1958).
9. ROGINSKI S. Z. and ZHABROVA G. M., *Zh. Obschei Khim.* **27,** 10 (1954).

LETTERS TO THE EDITOR

Concerning the theory of anisotropic magnetization

(*Received* 13 *February* 1961)

WE WISH to point out a limitation in a recent calculation by CALLEN and CALLEN[1] of the anisotropic part of the spontaneous magnetization. Their procedure apparently regards as fundamental the expression of the temperature dependences of the magnetocrystalline anisotropy constants as powers of the magnetization. This leads them directly to an approximate expression [equation (7) of Ref. (1)] for the free energy density which is essentially of the form

$$F(T, H, \omega) \cong F_0(T, H, \omega)+f(\omega)m(T, H), \quad (1)$$

where $F_0(T, H, \omega)$ is the free energy which would be obtained in the case of temperature independent anisotropy (i.e. only the ground state anisotropy is contained in F_0) and the temperature dependence of the anisotropy is approximated by the last term. Here $f(\omega)$, which has the dimensions of a magnetic field, is a function of the magnetization direction, ω, in the crystal which includes all anisotropy terms, H is the component of the applied field along the magnetization direction and $m(T, H)$ is the deviation, at temperature T and in the field H, of the saturation magnetization, $M(T, H)$, from its zero temperature value, $M(0)$, evaluated in the absence of anisotropy.

The magnetization in any direction is given by the derivative of $-F(T, H, \omega)$ with respect to the applied field component in that direction. Applying this prescription to equation (1) and assuming the anisotropy to be field-independent[2] CALLEN and CALLEN find a contribution to the spontaneous magnetization, $M(T, 0)$, proportional to $f(\omega)$ which they identify as its anisotropic component, and which contribution is proportional to the isotropic susceptibility, $\chi(T, H)$, evaluated at $H = 0$. We are prompted to question the validity of this procedure when we notice that the susceptibility of a large sample, on the spin wave model,[3] obeys

$$\chi(T, H) \sim TH^{-1/2} \quad (2)$$

which tends to infinity as $H \to 0$. On the same model CALLEN and CALLEN claimed, without giving a detailed calculation, a different susceptibility which apparently remains finite in this limit.

The spin wave picture provides us with a model on which the power laws and equation (1) may be derived[4] and on which this difficulty in the magnetization calculation may be understood. On this model $f(\omega)$ represents a shift in the spin wave spectrum or dispersion law similar to the effect of an applied magnetic field. The anisotropy increases the size of the energy gap in the spin wave spectrum if the magnetization is in an easy direction and reduces it if the magnetization is held in a hard direction by an applied field. If $f(\omega) \ll k_BT$, where k_B is Boltzmann's constant, the free energy may be expanded in powers of $f(\omega)$ and is well approximated by equation (1). The procedure of CALLEN and CALLEN requires that a similar expansion of the magnetization be possible. If, however, the exact free energy (exact to the extent that the spin waves are a good approximation to use) is used to calculate the magnetization, the result is

$$M(T, H, \omega) = M(0)-\mu\eta(H+f(\omega), T) \quad (3)$$

where μ is the reduction in magnetization per spin wave excited and η is the total number of spin waves which is a function of T and of the gap $\mu[H+f(\omega)]$. When the gap is less than k_BT, the leading term in equation (3) involving the gap is proportional to[5] $[H+f(\omega)]^{1/2}$ and an expansion of the magnetization in powers of $f(\omega)$ is possible only if $|f(\omega)/H| < 1$. The calculation of the magnetization from equation (1) is apparently equivalent, on the spin wave model, to this expansion and the failure of the method for the low temperature spontaneous magnetization, as indicated by equation (2), is understood in this way. At the same time it is clear that the procedure of CALLEN and CALLEN is valid in the case of large applied fields. It may also be valid in the high temperature case, which they treated within the framework of the internal field model.

Acknowledgements—This work has benefitted from

discussions with Dr. J. C. SLONCZEWSKI and Dr. M. J. FREISER.

I.B.M. Research Center S. H. CHARAP
Yorktown Heights
New York

References

1. CALLEN E. R. and CALLEN H. B., *J. Phys. Chem. Solids* **16,** 310 (1960).
2. In case of a field-dependent anisotropy another anisotropic magnetization term appears which does not vanish at $T = 0$. See CHARAP S. H., *Phys. Rev.* **119,** 1538 (1960).
3. HOLSTEIN T. and PRIMAKOFF H., *Phys. Rev.* **58,** 1098 (1940). This result is obtained by letting $4\pi M_0 \to 0$ in equation (27), thereby removing the long-range dipolar interaction.
4. CHARAP S. H. and WEISS P. R., *Phys. Rev.* **116,** 1372 (1959).
5. See equation (18) of Ref. (2).

Evidence for canted magnetic moments in manganous stannate (Mn_2SnO_4)

(*Received* 25 *January* 1961)

MANGANOUS stannate, Mn_2SnO_4, crystallizes with the inverse spinel structure[1] which can be symbolized as $Mn^{2+}[Mn^{2+}Sn^{4+}]O_4$, where the brackets enclose octahedrally coordinated ions. There are, ideally, one tetrahedrally coordinated (A) and one octahedrally coordinated (B) $Mn^{2+}(3d^5)$ ion per molecule. It was predicted that pure, stoichiometric Mn_2SnO_4 would be antiferromagnetic with A- and B-site moments exactly compensating each other, each with the spin-only value of 5 Bohr magnetons (μ_B). However, GILLEO and MITCHELL[1] found an appreciable magnetization (n_B) in manganous stannate at low temperatures. They explained this net moment by assuming that partial oxidation of the material during its preparation produced a spinel composition containing Mn^{3+}, with a corresponding amount of SnO_2. The spinel phase could then be formulated as

$$Mn^{2+}[Mn^{2+}_{(1-b/2)}\, Mn^{3+}_{b}\, Sn_{(1-b/2)}]O_4.$$

Determining b from the average oxidation state of the manganese ions, it was then possible to account for the measured magnetization values on the basis of an antiparallel arrangement of spin-only moments (e.g. $b = 0{\cdot}255$ and $n_B = 0{\cdot}37\ \mu_B$/molecule). Similar considerations were consistent with the behavior of several compositions in which other cations were substituted for Mn^{2+} and Sn^{4+} ions. However, we have prepared manganous stannate and several compositions in the system Mn_2SnO_4–Mg_2SnO_4 which contain only a small amount of Mn^{3+}, and find that the magnetization values of these materials cannot be accounted for by the presence of Mn^{3+}. It follows that manganous stannate is intrinsically a ferrimagnetic compound.

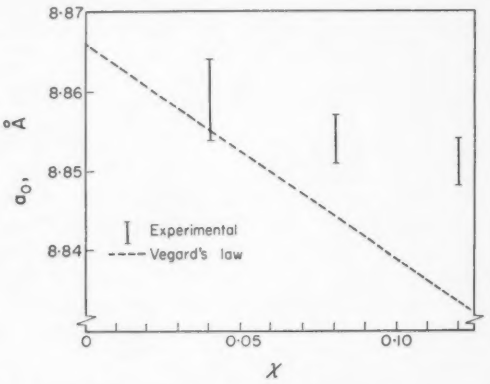

FIG. 1. Lattice constant, a_0, at 25°C, for the system $Mn_{2-2x}Mg_{2x}SnO_4$.

Pure Mn_2O_3 was prepared by heating manganous oxalate slowly up to 800°C in the presence of air. The finely divided product was reduced to MnO by heating it under a stream of hydrogen at 800°C. This treatment was repeated until no Mn^{3+} was chemically detectable. Appropriate quantities of MnO, pure MgO, and SnO_2 were ground together, reacted at 1000°C under a slow stream of pure nitrogen, re-ground, and similarly heated again. The addition to the reaction mixture of 5 wt. per cent NaF, which served as a flux, caused complete reaction to take place within a reasonable period of time (8–16 hr). The NaF was finally washed away with water. The resulting compositions were checked by chemical analysis. The oxidation parameters b were determined by reacting the solid samples with standard solutions of suitable reducing agents.[2] For our sample of

manganous stannate, b was equal to 0·038; for the sample studied by GILLEO and MITCHELL[1], b was equal to 0·255. The corresponding percentages of total manganese oxidized are 1·9 per cent and 12 per cent, respectively.

X-ray analysis failed to detect the presence of a second phase in any of the above preparations, although small quantities could be present and escape detection. Furthermore, the lattice constants of the system Mn_2SnO_4–Mg_2SnO_4 were determined and are shown in Fig. 1 (a = 8·60 Å for Mg_2SnO_4).[3] The dashed line in Fig. 1 represents the values of the lattice constant as calculated from Vegard's law, and the positive deviation

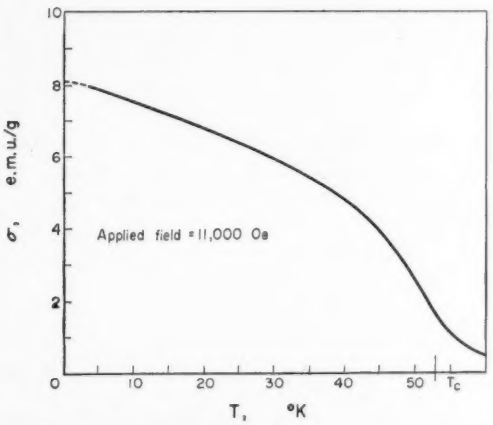

FIG. 2. Magnetization (σ) vs. temperature for manganous stannate with b = 0·038.

of the actual values from this prediction indicates that the Mg^{+2} ions preferentially occupy the octahedral sites, as expected.[1]

Magnetic properties were measured with the vibrating-coil magnetometer.[4] The variation of magnetic moment with temperature for Mn_2SnO_4 is shown in Fig. 2 for an applied field of 11,000 Oe. The behavior is clearly ferrimagnetic, the saturation magnetization corresponding to 0·41 μ_B per molecule. The saturation magnetizations of the other members of the system, plotted in Fig. 3, are seen to increase linearly with increasing Mg content. The corresponding values of the oxidation parameter b are also indicated in Fig. 3. It is interesting to note that the solid line in Fig. 3 extrapolates to 0·81 μ_B/molecule at x = 0·25, in agreement with previous findings[1] despite the large difference in b.

The dashed line in Fig. 3 indicates values of n_B computed for antiparallel moments on A and B sublattices on the basis of the formula

$$Mn^{2+}[Mn^{2+}_{(1-x-b/2)}Mn^{3+}_{b}Mg_xSn^{4+}_{(1-b/2)}]O_4.$$

The large discrepancy between this curve and the measured values precludes such a simple explanation of the ferrimagnetic properties of the system. Alternatively, a net moment for pure Mn_2SnO_4

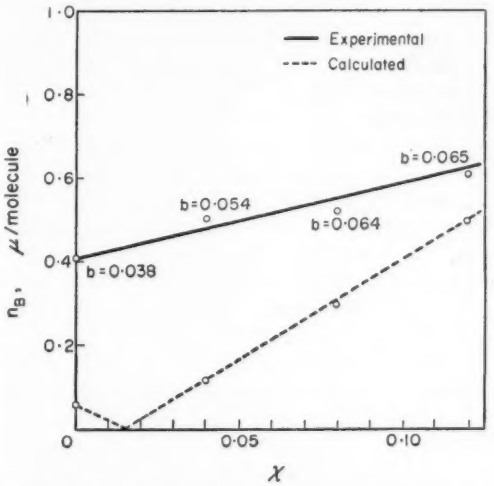

FIG. 3. Magnetization (n_B) vs. magnesium content for the system

$$Mn^{2+}[Mn^{2+}_{(1-x-b/2)}Mn^{3+}_{b}Mg^{2+}_{x}Sn^{4+}_{(1-b/2)}]O_4.$$

would be possible if an A-site Mn^{2+} ion contributed less than the spin-only value of 5·0 μ_B, such moments having been measured in several spinels by neutron diffraction.[5, 6] Also, a net moment could appear if the Mn^{2+} were not equally distributed between the two kinds of sites. However, in either of these two situations, the substitution of small amounts of Mg^{2+} for Mn^{2+} on B-sites would decrease the total B-site moment and, therefore, the net moment. Our experimental results contradict both of these hypotheses, since the moment increases with increasing Mg^{2+} content.

From this experimental result, it is apparent

that the A-site moment dominates the B-site moment, which in turn implies a canted-spin arrangement for the Mn^{2+} ions on the B-sites. Such a canted-spin configuration can occur only if the B-site ions are subject to competing exchange interactions.[7] The low T_c (53 ± 3°K from Fig. 1) for Mn_2SnO_4 ($b = 0{\cdot}038$) indicates a weak Mn(A)–O–Mn(B) interaction, and a comparable antiferromagnetic, direct Mn(B)–Mn(B) interaction is not unreasonable. KANAMORI[8] has suggested the possibility of direct interactions in MnO (rock-salt structure) in order to explain the unusually high value for θ/T_N. COLES and HORTON[9] have shown that the direct interactions between pairs of Mn^{2+} ions occupying neighboring Mg^{2+} sites in MgO (rock-salt structure) are as strong as indirect Mn–O–Mn interactions. These results are pertinent because a Mn^{2+} ion in the rock-salt structure and a B-site Mn^{2+} ion in the spinel structure have similar environments, i.e. both have some neighboring Mn^{2+} ions whose octahedra share a common edge. For this case, GOODENOUGH[10] has estimated the direct cation–cation interaction to be strongly antiferromagnetic whenever both cations have no more than five 3*d* electrons.

From a qualitative consideration of the orbital overlaps, it follows that the direct Mn–Mn interaction should be more sensitive to interaction distance than indirect Mn–O–Mn interactions. If the unit cell of a canted-spin material could be reduced, this differential sensitivity should lead to an increase in the net amount. In order to investigate this effect, a sample of the analogous compound Mn_2TiO_4 was prepared. The value of b was found to be 0·061, which corresponds to 3 per cent of the manganese oxidized. X-ray analysis showed this to be a cubic spinel with $a_0 = 8{\cdot}67$ Å, i.e. with a smaller unit cell than the stannate. The Curie temperature was found to be 81°K, showing an increase in the indirect A–B interaction due to the reduction in the unit cell. However, the saturation magnetization also showed an increase, the measured value being $n_B = 0{\cdot}45\,\mu_B$/molecule. This result further supports the hypothesis that the ferrimagnetism of manganous stannate and titanate arises from a canting of the B-site moments due to a competition between a direct B–B interaction and the indirect A–B interaction.

Finally, it should be noted that, with a canted-spin model, the net moment might be quite insensitive to the oxidation parameter. In particular, the increase in the B-site moment due to Mn^{3+} could easily be offset by an increased canting (as might be expected since the loss of an e_g electron should weaken the A–B interaction without affecting the direct B–B interaction). Thus the agreement between our findings and the results obtained by GILLEO and MITCHELL[1], despite the large difference in oxidation parameters, is consistent with a canted-spin model for the ferrimagnetism of the Mn_2SnO_4–Mg_2SnO_4 system.

Acknowledgements—We are indebted to R. J. ARNOTT for making the lattice constant measurements and to E. R. WHIPPLE, who performed the chemical analyses.

Lincoln Laboratory†
Massachusetts Institute of Technology
Lexington 73
Massachusetts, U.S.A.

D. G. WICKHAM*
N. MENYUK
K. DWIGHT

References

1. GILLEO M. A. and MITCHELL D. W., *J. Phys. Chem. Solids* **10,** 182 (1960).
2. WICKHAM D. G., M.I.T. Lincoln Lab. Tech. Rep. No. 164, August, 1957.
3. NOTTA G. and PASSERINI L., *R.C. Acad. Lincei* **9,** 557 (1929).
4. DWIGHT K., MENYUK N. and SMITH D. O., *J. Appl. Phys.* **29,** 491 (1958).
5. HASTINGS J. M. and CORLISS L. M., *Phys. Rev.* **104,** 328 (1956).
6. PICKART S. J. and NATHANS R., *Phys. Rev.* **116,** 317 (1959).
7. KAPLAN T. A., *Phys. Rev.* **119,** 1460 (1960); KAPLAN T. A., DWIGHT K., LYONS D. and MENYUK N., *J. Appl. Phys.* **32** (Suppl.), 13 (1961).
8. KANAMORI J., *J. Phys. Chem. Solids* **10,** 98 (1960).
9. COLES B. A. and HORTON J. W., *Phys. Rev. Letters* **4,** 116 (1960).
10. GOODENOUGH J. B., *Phys. Rev.* **117,** 1442 (1960) (See Table I).

---

* Present address—Ampex Computer Products Co., Culver City, California.

† Operated with support from the U.S. Army, Navy and Air Force.

Stress-induced alignment of anisotropic defects in crystals

(*Received* 20 *March* 1961)

MANY point defects in solids are anisotropic in their microscopic configuration. However, in the case of cubic crystals, an equal number of these anisotropic defects populating the various equivalent orientations available in the lattice results in most of the macroscopic properties of the solid which are associated with the defects being isotropic. Recently several techniques have been developed which can reveal this "hidden" anisotropy, under specialized conditions. These include the study of polarized luminescence[1] from the defect centers, photo-chemical conversion (bleaching) of the centers under the action of polarized light,[2] the study of the ZEEMAN splittings of the spectra of centers,[3] and the study of the splitting induced in sharp optical lines by applying a stress to the sample.[4] The purpose of this letter is to point out another method for revealing this "hidden" anisotropy and for studying the properties of these defects. The technique involves aligning the defects by applying a uniaxial stress to the crystal. In the distorted crystal the various orientations available to the defects are no longer equivalent, and, provided the defect can reorient, a preferential alignment of the defects in the crystal will occur. The degree of alignment will reflect the BOLTZMANN factor associated with the stress-induced energy differences between the various orientations. The technique is useful with any measurement that is sensitive to the alignment. (This technique, as well as the others,[1–4] is, of course, also applicable to non-cubic systems, if normally equivalent orientations are available to the defects.)

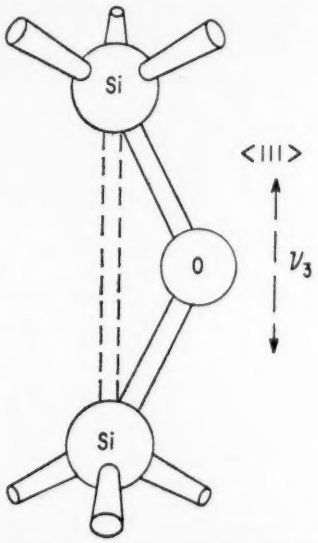

FIG. 1. Model for the oxygen configuration in silicon. The dashed lines indicate the normal Si–Si bond which is interrupted by the oxygen in forming the Si–O–Si "molecule". The ⟨111⟩ direction of the ν_3 vibration which is attributed to the 9μ band is shown.

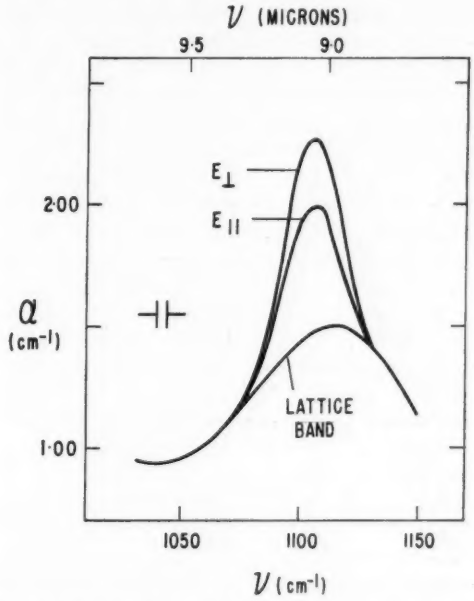

FIG. 2. The 9μ absorption band at room temperature after the ⟨111⟩ stress described in the text. The absorption is viewed along a ⟨110⟩ axis. $E_\perp$ and $E_\parallel$ indicate the E-vector of the polarizer perpendicular and parallel to the ⟨111⟩ stress axis, respectively. The spectral slit width is shown.

As an example of the technique, consider the 9μ infrared absorption band associated with the vibration of impurity oxygen in the silicon lattice. A model which has been proposed for the oxygen configuration[5] is shown in Fig. 1. In this model a normal Si–Si bond is disrupted and an oxygen

atom has bonded between them, forming a slightly bent Si–O–Si "molecule." The 9μ band has been assigned to the ν_3 vibration of this molecule,[6] whose dipole moment is along this ⟨111⟩ axis. As a test of this model, we have performed the following experiment: A crystal was cooled from 400°C with a compressional stress of 2700 kg/cm^2 applied along a ⟨111⟩ direction and then studied at room temperature with the stress removed. The results are shown in Fig. 2. The dichroic ratio for the absorption of polarized light reveals that a substantial preferred alignment has been frozen in. A similar experiment with the stress along a ⟨100⟩ direction gives no measurable alignment. These simple observations serve to confirm two important features of the model: (i) the lack of alignment under a ⟨100⟩ stress confirms the ⟨111⟩ axis for the defect; (ii) the sense of the alignment ($E_\perp > E_\parallel$) under ⟨111⟩ stress confirms the "interstitial" character of the oxygen in that the already compressed Si–O–Si bonds avoid the compressed direction in the lattice. In addition to these qualitative observations, a quantitative study of the energetics and kinetics of the alignment has been made,[7] and can be compared to internal friction[8] and diffusion measurements[9] previously assumed to be associated with this reorientation process.

Stress alignment can be a useful adjunct to microscopic tools as well. Electron paramagnetic resonance for instance, is already sensitive to the anisotropy of a defect in an unstressed cubic crystal, usually with resolved multiplets for each of the differently oriented defects. In this case stress-induced alignment is observed as a change in the relative amplitudes of the multiplets.* By monitoring these amplitudes under stress, the response of each defect orientation can be separated unambiguously, reflecting highly detailed information about the structure of the defect. In addition, monitoring the kinetics and energetics of the alignment as observed by more than one technique (electron paramagnetic resonance and optical absorption, for instance) is a means of correlating and identifying various properties of a defect.[10]

* First observed by G. W. Ludwig and H. H. Woodbury (unpublished) for the distorted Ni^- ion in germanium. It was their observation which stimulated our interest in stress as a tool for this type for study.

In summary, the technique described in this letter is quite versatile. The 9μ band is a convenient example in this regard. In the first place, it demonstrates an application to a vibrational absorption band that does not luminesce, bleach or split, and is therefore unavailable to the other techniques. Secondly, it demonstrates that significant alignment can be achieved even for relatively immobile defects requiring elevated temperatures ($\sim$400°C) to reorient. Thirdly, the applied strain ($\sim 10^{-3}$) is not excessive. Using care, elastic strains as high as $\sim 10^{-2}$ have been achieved in silicon.[11] Even in soft crystals such as the alkali halides along the hard slip ⟨111⟩ directions, elastic strains of $\lesssim 10^{-3}$ are possible.[12] This approach was used to observe[13] partial alignment of the O_2 centers in KCl as monitored in the O_2 electron paramagnetic resonance spectrum.[14] We thus conclude that this technique should be applicable to a wide class of systems.

General Electric Research Laboratory
Schenectady
New York

J. W. Corbett
G. D. Watkins

References

1. Feofilov P. P., *Dokl. Akad. Nauk. SSSR*, **92,** 545, 743 (1953).
2. Ueta M., *J. Phys. Soc. Japan*, **7,** 107 (1952).
3. Arkangel'skaya V. A. and Feofilov P. P., *Opt. i Spektrosk.* **4,** 602 (1958).
4. Kaplyanskii A. A., *Opt. i Spektrosk.* **7,** 406, 409 (1959).
5. Kaiser W., *Phys. Rev.* **105,** 1751 (1957); Hrostowski H. J. and Kaiser R. H., *Phys. Rev.* **107,** 966 (1957); *J. Phys. Chem. Solids*, **9,** 214 (1959); Hrostowski H. J. and Alder B. J., *J. Chem. Phys.* **33,** 980 (1960).
6. Herzberg G., *Infrared and Raman Spectra*, p.168 ff. Van Nostrand, New York (1945).
7. Corbett J. W. and Watkins G. D., to be published.
8. Southgate P. D., *Proc. Phys. Soc. Lond.* **36,** 385, 398 (1960).
9. Logan R. A. and Peters A. J., *J. Appl. Phys.* **30,** 1630 (1959).
10. See for example, Watkins G. D. and Corbett J. W., *Phys. Rev.* **121,** 1001 (1961); Corbett J. W., Watkins G. D., Chrenko R. M. and McDonald R. S., *ibid.*, **121,** 1015 (1961).
11. Dash W. C., private communication.
12. Johnston W. G., private communication.
13. Känzig W. and Watkins G. D., unpublished work.
14. Känzig W. and Cohen M. H., *Phys. Rev. Letters* **3,** 509 (1959).

BOOK REVIEWS

H. C. GATOS (with J. W. FAUST, Jr. and W. J. LAFLEUR): **The Surface Chemistry of Metals and Semiconductors.** John Wiley, New York, 1960. 526 pp., $12.50.

THE YEAR 1959 was notable for the extraordinary number of conferences devoted to the discussion of surface properties. This book is a summary of the proceedings of one of these meetings—a symposium, sponsored by the ONR and the Electrochemical Society in October of that year, which was intended "as a medium for an effective exchange of theory and technology between the fields of metal surfaces and semiconductor surfaces".

The proceedings consist of twenty-two summary papers, of approximately equal length, subdivided into five problem areas:

I. Chemistry and Physics of Surfaces
II. Imperfections and Surface Behavior
III. Electrode Behavior of Metals and Semiconductors
IV. Surface Reactions in Liquid Media
V. Surface Reactions in Gaseous Media

Each of the papers is followed by transcripts of the discussion. These greatly enhance the interest of the presentation and the value of the book. For the reader who is not an expert in the subject matter, the discussions clarify the material, put it into somewhat better perspective, or at the least suggest the interest of that report to the meeting audience.

The best that a symposium of this type can do is to present a faithful picture of the state of the science at the moment. This might be accomplished by comprehensive review articles or else by a collection of shorter accounts of the best current work. The latter course was followed in this symposium. As must be expected for a meeting covering so vast a field the emphasis placed on various topics, and to a lesser extent the quality of the papers themselves, are quite uneven. The areas that have traditionally been of interest to the Electrochemical Society are not only favored in the number of papers but also in the excellence of the presentation.

Of the twenty-two articles in the book, twelve deal with the behavior of the solid–liquid interface, compared with six on reactions in gaseous media, of which two cover oxidation. In the sections devoted to the electrode behavior of solids and to the contribution of defects to surface properties, the organizers do seem to have succeeded in selecting a fair sample of the more interesting current work. Even here such an important subject as hydrogen evolution, to which much recent work has been directed, is not even mentioned. By contrast, despite the considerable interest of some of the individual contributions concerned with the gas–solid interface, it is quite impossible to obtain a proper appreciation for this area of investigation from the papers in the present volume. The similarities and contrasts between semiconductors and metals do not emerge too clearly even in the former section. This might perhaps have been achieved by enlarging the introductory papers for each of the five sections, in which the material could be reviewed and connected on a larger scale than possible in the individual contributions. It must be added that even within their present scope, the introductions to parts I, IV, and V are not well conceived, and compare unfavorably with the excellent presentations of CABRERA and GERISCHER in parts II and III.

Despite these limitations, this book does contain a number of extremely valuable papers. The article by GWATHMEY and LAWLESS, for example, on the influence of orientation on oxidation, gives an excellent factual review of a field which is still very poorly understood, and for which an emphasis on the structural contributions is long overdue. LACOMBE and TURNER, respectively, present very good summaries of electrolytic etching of metals and semiconductors. The more detailed atomistic concepts involved in the etching process are outlined by CABRERA and GILMAN. The phenomenological discussions of surface damage in metals and nonmetals, by SAMUELS and BUCK, provide an up-to-date account of a classical field of inquiry. The papers by FARNSWORTH, DEWALD and EISCHENS give a good appreciation of the difficulties and potentialities of specialized experimental techniques applied to surface problems. Of particular interest is JURETSCHKE's article summarizing theoretical work on metal surfaces. This is a very easy, qualitative presentation of the problems

ol. 20
1961

of surface energetics and the exact estimation of surface potentials, which should bring these topics to the widest audience. More than that, JURETSCHKE also points up the almost complete absence of original work in this area during the last five years, a lack which should definitely be remedied.

This volume may not have achieved the desired synthesis of knowledge on metals and semiconductors, but it can be hoped that the meeting itself may stimulate this in the future. In any event, for the physicist or chemist interested in an introduction to current research on the solid–liquid interface, the papers in this symposium will be welcome.

GERT. EHRLICH

J. R. O'CONNOR and J. SMILTENS (Editors): **Silicon Carbide—A High Temperature Semiconductor.** Pergamon Press, New York, 1960. xix + 521 pp., $12.50.

SILICON carbide is a IV–IV compound having many characteristics similar to the elemental semiconductors of this column, and more specifically roughly midway between silicon and carbon. Unlike the silicon–germanium binary alloys, silicon carbide occurs only at, or very close to, 50–50 per cent composition, in a number of lattices ranging from a cubic type to hexagonal and rhombohedral forms having unit cells encompassing scores of atomic distances in one direction. These variations are known as *polytypes*.

Much interest in silicon carbide derives from its wide band gap and its chemically inert, relatively refractory nature. Military and other users require material for stable, high temperature devices, but silicon is not useful much above 200°C and diamond is too esoteric to be practical. Unfortunately, as the papers of this conference show, silicon carbide has proved to be a refractory subject of growth and investigation, and stands at present where germanium stood in 1946, in the words of one of the speakers at the conference. The main problem is that relatively perfect large single crystals of high purity material are desperately needed for experimentation. As a semiconductor, lifetime is of the order of 10^{-8} sec, mobility approximates 100 cm^2/volt sec, and typical charge carrier concentration is 10^{18} or 10^{19} cm^{-3}; impurities, traps, and stoichiometry all need further work.

This book records the proceedings of a conference sponsored under United States Air Force auspices held at Boston, Massachusetts in April 1959. The book perpetuates the unfortunate tradition of leisurely reproduction of timely conferences in hard-bound form. The alert signal for many librarians to a new book is the listing of its title in *Publishers' Weekly*, an indication that a given book is no longer a promise of advertising fancy but can actually be secured. This book was not so listed until November 14, 1960, a full nineteen months after the conference ended. It is to the credit of the previously mentioned refractory nature of silicon carbide that this delay plus this reviewer's procrastination and the subsequent delay in publication of these comments probably will not seriously detract from the pertinence of the volume to work going on at the moment the reader sees these words.

The book is well organized, being divided into five parts treating the silicon carbide binary system, single crystal growth, properties of the solid, semiconducting properties, and material and device processing. Each section starts with an introduction by a worker in the field and ends with a summary by one or more reviewers. The publication delay could not have been caused by over-scrupulous proof-reading of the galleys because there are many mis-spellings and typographical errors scattered throughout the volume. Placement of references in a list at the end of each contribution causes the reader to do much page-thumbing.

The contributions supply a great deal of information about silicon carbide and highlight our deficiencies of knowledge of the material.

SCACE and SLACK measured a decomposition temperature of 3100 ± 40°K, compatible with a heat of formation $H = -18 \pm 4$ kcal/mole calculated by DROWART and DE MARIA using mass spectrometric methods to determine the species existent in the vapor. SCACE and SLACK also measured the solubility of carbon in silicon and obtain an enthalpy of solution of 59 kcal/mole. They discuss a tentative phase diagram of germanium–carbon and report finding no evidence of compound formation. WRIGHT and BARTELS treat the carbon–silicon–germanium system. Some

discussion of the thermodynamic papers centered on whether cubic silicon carbide can transform directly to a hexagonal form at about 2000°C, or whether the transformation obtains only through the vapor phase.

At least three ways of growing single crystals are known, but none is really satisfactory. Wide flat crystals of hexagonal silicon carbide can be grown easily and are available commercially, but the largest cubic crystals are $1 \times 1 \times 8$ mm at the very best. Epitaxial growth is also possible; this is being investigated for its device possibilities. As mentioned earlier, the problems of stoichiometry, impurity control, growth size and habit are far from being solved.

Treating silicon carbide as a solid immediately brings up the problem of whether polytype formation occurs because of a peculiar growth mechanism or whether long-range ordering interactions could really occur. AMELINCKX and STRUMANE present many excellent pictures of interacting growth spirals and discuss Frank's theory that the polytypes arise from growth at an imperfect dislocation. In this case the repeat distance of the polytype should equal the step-height of the spiral, and this has been observed. On the other hand, types such as 6H and 4H, which have a small repeat distance, are better explained thermodynamically. KEYES discusses identification of polytypes by goniometric methods as contrasted to X-ray methods and presents evidence for the existence of partially ionic binding.

Other papers deal with determining the impurities present by neutron activation and spectrographic analysis, and the kinetics of surface oxidation. Radiation effects and device techniques are reported in yet other sections.

BIRMAN applies band theory to silicon carbide, while KEYES makes a more pragmatic comparison of silicon carbide to germanium and silicon. As in these latter materials, the valence band maximum is expected to be at the center of the Brillouin Zone, but the conduction band minima should be off-axis. By way of verification, PHILIPP and TAFT observed indirect transitions in the intrinsic absorption edges of both cubic and hexagonal material. They obtain 2·2 and 2·86 eV for the gap in each of these materials respectively. The hexagonal gap seems to be well defined, but there is still disagreement in various determinations of the cubic gap.

PATRICK and CHOYKE investigated the electroluminescence in junctions and found that independent hole and electron lifetimes, and the formation of impurity bands which provided a vehicle for injection, complicated the interpretation of the spectra observed. They also report the presence of indirect transitions in their intrinsic absorption measurements on hexagonal material. As almost a lone contribution in the direction of simplicity SPITZER, KLEIMAN, FROSCH and WALSH report that the reststrahlen bands can be analyzed classically with a single resonance frequency and show that the cubic dispersion parameters are essentially the same as those for the ordinary ray of one of the hexagonal polytypes.

D. M. WARSCHAUER

Vol. 20
1961

ERRATA

L. GILDART, J. M. KLINE and D. M. MATTOX, Some semiconducting properties of bismuth trisulphide, *J. Phys. Chem. Solids* **18,** 286 (1961).

All measured values of the Seebeck coefficients for bismuth trisulphide are negative, so that published values of 550 μV/°C and 700–850 μV/°C should read:

$$-550\ \mu\text{V/°C and } -700 \text{ to } -850\ \mu\text{V/°C}.$$

E. DANIEL, Sur le résistivité et le déplacement de Knight d'alliages liquides de sodium, *J. Phys. Chem. Solids* **13,** 353 (1960).

La formule donnant $\Delta\rho$ faut lire:

$$\Delta\rho = \frac{4\pi c}{kp} \sum_l l \sin^2 (\eta_{l-1} - \eta_l).$$

Pour l'alliage Na–Li, $\Delta\rho_{\text{calc}} = 0{,}74$ au lieu de 0,43 dans le Tableau 1 et $1/C \cdot \Delta K/K = -0{,}57$ faut lire: $-0{,}03$ dans le Tableau 2.

L'auteur tient à remercier le Dr. B. A. Green de lui avoir signalé cette erreur numérique.

ol. 20
1961